Application of cold plasma in oncology, multidisciplinary experiments, physical, chemical and biological modeling

Bruno Honnorat

Sorbonne Université

Ecole doctorale 564 : Physique en île-de-France

Laboratoire de Physique des Plasmas, UMR7648. Ecole Polytechnique, route de Saclay, Palaiseau

Université Pierre et Marie Curie, B.C. 90, 4 place Jussieu, Paris

Equipe plasmas froids

Application of cold plasma in oncology, multidisciplinary experiments, physical, chemical and biological modeling

Applications des plasmas froids à l'oncologie, approche expérimentale multidisciplinaire, modèles et modélisations physiques, chimiques et biologiques

Par Bruno Honnorat

Thèse de doctorat de Physique

Dirigée par Antoine Rousseau

Thèse soutenue le 8 Février 2018 à Paris

Devant un jury composé de :

Dr. Chantal Stehle	DR CNRS	Présidente
Dr. Jean-michel Pouvesle	DR CNRS	Rapporteur
Dr. Lluis Mir	DR CNRS	Rapporteur
Pr. Annemie Boggaerts	Prof University Antwerpen	Examinateur
Dr. Georg Daeschlein	Privatdozent Dr. med, Universitätsmedizin Greifswald	Examinateur
Dr. Antoine Rousseau	DR CNRS	Directeur de thèse
Dr. Géraldine Lescaille	PU-PH Université Paris VI	Invité
Dr. Lori Bridal	DR CNRS	Invité

Acknowledgments

Tout d'abord je tiens à remercier mon directeur de thèse, Antoine Rousseau de m'avoir permis d'effectuer cette thèse en disposant d'une grande liberté quant aux choix des objectifs scientifiques à poursuivre et des moyens pour y parvenir. C'est une chance rare, même dans le monde de la recherche, et j'espère l'avoir utilisée à bon escient.

Mes remerciements s'adressent aussi au Labex Plas@PAR qui a financé cette thèse ; ainsi qu'à l'Ecole Polytechnique et à l'UPMC pour le soutient qu'elles apportent aux projets « plasma-médecine ». Je remercie l'encadrement des parcours PACES et de Licence de l'UPMC de m'avoir donné l'occasion de réaliser des heures de TD et de TP aux niveaux L1, L2 ainsi qu'en première année de médecine.

Je remercie l'ensemble des personnels du LPP et son directeur Pascal Chabert.

Je remercie particulièrement les nouveaux thésards du LPP : Constance Duchesne et Bo Liu d'avoir réalisé les expériences systématiques de dosages des nitrates et des nitrites avec moi. Nous n'étions pas trop de trois pour réaliser ces 15h d'expériences non-stop.

Je remercie également les laboratoires du LIB et du CIMI ainsi que équipes de ces laboratoires : celle de François Lemoine au CIMI et celle de Lori Bridal au LIB qui nous ont reçus et ont consacrés des moyens et du temps à nos projet.

Du LIB, je remercie :

Lori Bridal pour nous avoir donné accès aux appareils de mesures du LIB, pour avoir consacré du temps au projet et à ses aspects administratifs les moins réjouissants et pour son esprit positif face aux difficultés expérimentales rencontrées.

Delphine Le Guillou pour s'être occupé de la préparation des cellules et des tumeurs CT26.

Alexandre Dizeux pour avoir réalisé la toute première série d'expérience in-vivo au LIB avec moi, pour sa dextérité à réaliser les injections d'agent de contrastes. Une campagne expérimentale assez dure, qui a demandé une résistance physique assez exceptionnelle étant donné les horaires exotiques auxquelles nous avons pu finir.

Je remercie Jérôme Griffon pour avoir réalisé l'imagerie ultrasonore associée à la deuxième campagne expérimentale. Encore une fois, il s'agissait d'un marathon expérimental particulièrement complexe qui a pu être réalisé avec succès malgré des instruments de mesures capricieux.

Concernant le CIMI, Je remercie,

Maude Delost pour son sens de l'organisation, sa rigueur scientifique et pour avoir effectué l'essentiel des comptages cellulaires et donc m'avoir enjoint à réduire le nombre de conditions expérimentales testées à quelque chose d'humainement raisonnable. J'ai beaucoup appris de ses méthodes de travail.

Géraldine Lescaille pour avoir repris la collaboration côté CIMI après le départ de Maude, pour avoir su organiser les conditions matérielles nécessaire à la réalisation des expériences au CIMI avec efficacité, pour sa esprit critique vis-à-vis des publications.

Je remercie Aurélien Gaubert, Aline Le-Moignic et Réda Bouras pour m'avoir aidé à réaliser les expériences *in-vivo* et *in-vitro* au CIMI et accompagné pendant ces longues

heures de traitement. Particulièrement Aline qui a su trouver du temps à un moment particulièrement délicat de sa thèse.

Je remercie aussi François Lemoine de nous avoir accueili dans son équipe,

Je remercie les zootechniciens des deux animaleries qui ont pris soin des souris.

Finalement je remercie ma famille et mes amis qui ont su me soutenir.

Abstracts

English

Plasma-medicine is the field of research describing the medical applications of plasmas, mainly at atmospheric pressure. Cold plasmas are a state of matter characterized by the presence of free electrons with a kinetic energy of several electron volts even though the ions and neutrals may be at room temperature. This transient state, apart from thermal equilibrium, produces highly reactive chemical species.

The objective of this multidisciplinary work was to evaluate the anti-tumor potential of cold plasmas. Two types of devices have been designed and manufactured by 3D-printing: Dielectric Barrier Discharge and plasma-jets. *In-vitro* and *in-vivo* studies were conducted with TC1 and CT26 cell lines. The production of reactive species produced in a liquid exposed to plasma has been studied in order to understand the *in-vitro* results and to compare the plasma devices with those of other teams. Various plasma devices have been made to study the effect of the energy deposited during the *in-vivo* treatment of skin and subcutaneous tumors. A device cooled with liquid nitrogen has been developed to limit skin damage induced by heating.

Finally, a numerical simulation modeling the heat transfers of tumors and tissues under plasmas exposure enables to quantify the hyperthermia and the associated lesions by validating the model on experimental results. A critical review of *in-vivo* plasma-medicine studies published in the literature is proposed to evaluate the role of hyperthermia in the therapeutic effects reported.

Français

« La médecine- plasma» est le domaine de recherche décrivant les applications médicales des plasmas, principalement à pression atmosphérique. Les plasmas froids sont un état de la matière caractérisé par la présence d'électrons libres ayant une énergie cinétique de plusieurs eV alors même que les ions et les neutres peuvent être à température ambiante. Cet état transitoire, hors équilibre thermique, produit des espèces chimiques très réactives.

L'objectif de ce travail multidisciplinaire a été d'évaluer le potentiel anti-tumoral des plasmas-froids. Deux types de dispositifs ont été conçus et fabriqués par impression 3D: des Décharges à Barrière Diélectrique et des jets plasmas. Des études *in-vitro* et *in-vivo* ont été menées avec les lignées cellulaires TC1 et CT26. La production d'espèces réactives produites dans un liquide exposé à un plasma a été étudiée afin de comprendre les résultats *in-vitro* et de comparer les dispositifs plasma entre eux. Différents dispositifs à plasmas ont été réalisés afin d'étudier *in-vivo*, l'effet de l'énergie déposée lors du traitement sur la peau et les tumeurs. Afin de limiter l'échauffement cutané et les lésions induites un dispositif refroidi à l'azote liquide a été développé.

Enfin, une simulation numérique modélisant les transferts thermiques des tumeurs et tissus sous exposition plasmas a permis de quantifier l'hyperthermie et les lésions associées en validant le modèle sur des résulats expérimentaux. Une revue critique d'études *in-vivo* de « médecine plasma » publiées dans la littérature est proposée afin d'évaluer le rôle de l'hyperthermie dans les effets thérapeutiques observés.

Introduction

Scientific context

Plasma-medicine is the field of research, which describes applications of plasma to medicine. Cold plasmas at atmospheric pressure are a transient state of matter characterized by the presence of free electrons with a kinetic energy of several electron volts, whereas ions and neutrals can be near ambient temperature. The idea of applying plasmas to the treatment of living targets started from the observation that cold plasmas can sterilize a certain number of surfaces. The use of cold plasmas is considered as a means of decontamination and even sterilization, of medical equipment sensitive to heat (like plastic materials). The sterilization of endoscopes seems to be an important outlet. Several startups already offer cold plasma sterilization capabilities, and the study of the sterilizing properties of plasmas is one of the most active research fields in plasma medicine.

The sterilization of temperature-sensitive object requires to pay close attention to the heating up produced. Finally, the treatment of living organisms has the same kind of constraint, since the biological target should stay below 42 °C, the temperature beyond which cell damage becomes irreversible. Moreover, since many wounds are difficult to treat because of local infections, the used of cold plasmas to promote wound healing has emerged as a natural outlet. This field of research quickly attracted the attention of biologists and dermatologists. Therapeutic effects were observed in animals and humans on a wide variety of wounds. One of the major issues of medicine for which plasmas could bring benefits is the treatment of diabetic wounds.

The application of cold plasmas to cancer treatments is not an obvious idea in itself. It was justified by the fact that anti-tumor effects were rapidly observed *in-vitro*, on several cell lines. In addition, it is known that plasmas produce reactive species from oxygen and nitrogen (RONS) involved in the mechanisms of cell signaling. The radical species produced by plasma also have an analogy with those produced in radiotherapy (on the other hand with radiotherapy, the radical species are also produced directly within the cell nucleus and cause direct damage to DNA).

Plasma-based cancer treatments have led to numerous *in-vitro* studies. Unfortunately, *in-vivo* studies are much rarer. The mode of action of cold plasmas is not known with certainty. The primary working hypothesis gives a leading role to the chemical species produced by plasma-treatment. The direct action of these radicals and reactive species, or, at least, the cascades of biological reactions induced by these species, would have an anti-tumor effect. It is also very often considered that the electric field can play a role via the electroporation of a part of the tumor. Depending upon the plasma device, a significant electric field (few tens of kiloVolts per centimeter) may be generated in the upper layers of the tissues.

The study of the chemistry of plasma-treated liquid is useful since the reactive species are supposed to play a key role in the therapeutic effects. At least, it enables to understand *in-vitro* results and perform a comparison with other groups. The study of the production of Reactive oxygen and nitrogen Species (RONS) is a problem in its own right. However, it appears that the reliability of measurement methods presented in many biochemistry papers is controversial according to the critical review of Wardman et al. [1] and Tarpey et Fridovich [2]. The biases are due to imperfect knowledge of the underlying chemistry. It is therefore advisable to be particularly careful using any chemical diagnostic. Especially since the chemical environment of plasma-treated liquids is often very different from that for which the chemical diagnostic was designed. We will show for example that in this context, the results of Griess'reagents can be completely biased. To

find the reason amongst the numerous published papers, it is advisable to focus on the papers made by chemists studying the diagnostic itself, to read the evidence and mechanisms, to track the biases listed by critical reviews and above all, beware of over-interpreting. Fortunately, the results obtained in other fields are of great help: radiochemistry, sonochemistry, radical chemistry, photochemistry can help to build a critical point of view.

I wish to point out the limited scope of *in-vitro* studies in predicting the *in-vivo* potential of such treatments. The fact that plasmas produce all the complex stimuli listed below at the same time is a major source of complexity.

- **Reactive oxygen and nitrogen species, radical species**
- **High voltage short Pulse**
- **UV and visible emission**
- **Heat**
- **mechanical vibrations**

I*n-vitro* experiments, although very useful to understand mechanisms, are obviously not sufficient to develop new therapeutics. *In-vivo* studies are necessary to obtain a higher degree of evidence. The observation of apoptosis *in-vitro* triggered by precise pathways does not guarantee that the same phenomenon takes place *in-vivo* with the same pathways and because of the same part of the stimuli.

Finally, all that is written below tends toward a single objective: conducting *in-vivo* experiments able to evaluate the anti-tumor efficiency of cold plasma treatments. Only this type of experiment can increase the level of evidence of plasma-cancer therapy towards human's applications.

Structure of the thesis

In the first chapter, a brief state of the art is presented. Particular attention is given to the devices that have been used in vivo for dermatological or antitumor purposes. The devices that have been the subject of the characterization of the chemistry they induce in the liquid phase are listed.

The second chapter describes the materials and methods commonly used in the three following chapters. For the sake of clarity, the protocols specific to each experiment are described in the experimental chapters. This chapter includes a description of the fabrication and geometric characteristics of the different plasma device used: "single-channel jet," "multi-channel jet" and "multi-channel jet". Dielectric Barrier Discharges and plasma-jets were designed and manufactured by 3D printing. This chapter also contains a discussion of power measurement problems: in the measurement method using Lissajous curves, the capacitance placed in series with the plasma-device cannot be chosen arbitrarily. It was necessary to develop electrical diagnostics to measure the power in real time above the biological targets (in-vitro and in-vivo). Finally, this chapter discusses the interference and bias related to chemical diagnostic. Particular attention is paid to the use of Griess reagent for the determination of nitrite, and the amplex red method for the quantification of H_2O_2. Calibration curves and methods are also described. Regarding the quantification of hydroxyl radical, this chapter explains why it is not possible to calibrate this method with Fenton reactions. Further discussion of the measurement method is presented in the chapter dedicated to the experimental results of liquid-phase chemical diagnostics.

The third chapter describes the chemical characterization of the liquid phase treated by plasma. The production of chemical species is systematically characterized for the single-channel jet. The production of H_2O_2, nitrites, and nitrates in the liquid phase is

measured when the experimental parameters are modified. The use of terephthalic acid (TPA) as a means of quantifying the hydroxyl radical is the subject of a discussion. This chapter also contains a discussion of the consumption of H_2O_2 by cells and tissues. How deep can H_2O_2 diffuse if the existence of cutaneous anti-oxidant defenses is taken into account?

The fourth chapter describes the *in-vitro* experiments performed during the thesis. *In-vitro* studies were performed with two different devices (single-jet and DBD) on two cell lines: TC1 and NRS1. The experiments were performed with several incubation times after treatment. The effect of chemical reagents at concentrations similar to those produced by plasma has been studied separately.

The fifth chapter is devoted to *in-vivo* experiments. The results and treatment conditions of the five experimental campaigns are exposed. The treated groups included a group treated with single jet, DBD and injections of plasma-treated medium. During the third experiment, the frequency of the power supply and the plasma jet nozzle were changed. The electrical power consumed by the device was significantly higher than that of the two previous experiments. The skin reached a temperature ~45 ° C, and skin damage was observed with processing times of a few minutes. This damage was attributed to the hyperthermia experienced by the tissues. During the last two experiments, the plasma device was cooled with liquid nitrogen before treatment. This pre-cooling of the device enables to treat the skin with the same power consumption (~ 4 W) without hyperthermia. This has been proven by surface temperature measurements made with an infrared camera. Others groups were also exposed to an inhibitor of the catalase (3-amino-1, 2, 4-triazole) just before being treated with plasmas, in the hope that the anti-tumor action would be increased.

The sixth chapter is dedicated to hyperthermia. The first aim is to understand the result of the experimental campaign that caused damage to the skin. A numerical simulation of the propagation of heat and the occurrence of damage has been made. The code for one of the simulated situations is available in Appendix I. Key findings from the literature related to hyperthermia and hyperthermia related to cancer treatment are discussed. The precise meaning of "the biological effect of hyperthermia" is specified. It turns out that significant biological effects occur below 42 ° C. The means to quantify the damage induced by hyperthermia are explained. Curiously, it turns out that the signaling pathways of mild-hyperthermia are very close to those seen in plasma medicine *in-vivo* experiments. Some published experiments show substantial heating of the skin and tumors. The Numerical simulations of the skin and subcutaneous tumors enable to quantify the damage of hyperthermia, to select thermometric methods that can detect it, and predict in what extent plasma-induced hyperthermia may be involved in anti-tumor effects.

Summary of the scientific issues addressed

The formulation of a scientific problem and its resolution requires an in-depth contextualization to detail the meaning of each term of the scientific question. Nevertheless, for an introduction, it is interesting to propose a list of the questions addressed. The content of the whole document is the context and the discussion of these questions.

Chapter	Questions addressed
2	What is the electrical power of the plasma device? How to measure it?
2	What is the limit of chemical diagnostics in the context of plasma-liquid interaction? How to calibrate?
3 chemistry	What is the production of reactive species of plasma devices?

3 chemistry	How the parameters of the experiments (peak to peak Voltage, flow, distance …) modify the production of species? Is there a link with the electrical power consumed by the devices?
3 chemistry	Is it possible to quantify the production of the hydroxyl radical with the diagnostic based on terephthalic acid?
3 chemistry	how fast H2O2 crosses cell membranes?
3 chemistry	What do we know about the diffusion of H_2O_2 through the skin? What models can be proposed for the transport and consumption of H_2O_2 through living tissue?
4 *in-vitro*	What treatment time affects cell viability? After how much incubation time does this difference in viability manifest itself?
4 *in-vitro*	Does the chemical species alone have an equivalent effect to that of the liquid treated by plasma?
4 *in-vitro*	Do two lines react in the same way?
5 *in-vivo*	Which plasmas-devices do elicit an anti-tumor response?
5 *in-vivo*	What is the temperature on the surface of the tumor? What treatment time causes damage?
5 *in-vivo*	What happens when the effect of hyperthermia is totally excluded by a cooling of the plasma source?
6 *hyperthermia*	What is hyperthermia? What are the thresholds of hyperthermia?
6 *hyperthermia*	How to simulate the propagation of heat and model biological tissues.
6 *hyperthermia*	How to measure tissue temperature in the context of plasma medicine? Which biases lead to underestimating the temperature?
6 *hyperthermia*	Do the published in-vivo studies exclude the possibility that tissues have been subjected to hyperthermia depending on the measurement method used? In the event of an adverse answer. In what extent the results could be attributed to hyperthermia?

About interdisciplinarity

This study was made possible by the collaboration of teams from two others laboratories. The team of Lori Bridal (LIB) and the team of François Lemoine and Geraldine Lescaille (CIMI) were involved. The *in-vivo* studies on CT26 and TC1 lines were performed in the animal-house associated with each laboratory.

It was not only a matter of accessing experimental equipment and installations or the solving of prosaic logistics problems. Above all, it was the building of a critical view on the scientific problems and experimental choices to answer them. Such topics force to decompartmentalize scientific disciplines. Even the basic and practical problem are at the crossroads of disciplines like:

- create a tolerable plasma source for the mouse
- To characterize the production of chemical species, it is necessary not only to measure the electric power consumed by the plasma but also to develop a method for determining the chemical species. Generally, it is hazardous to use a commercially available diagnostic kit without conducting a thorough reflection on the chemical reactions involved in the operation of the diagnostic. Biases can be surprisingly numerous and subtle, as in the case of amplex-red reagent.

- It is necessary to design a transportable device to reduce at best all the sources of uncertainties related to the plasma while respecting the constraints of sterility during *in-vitro* experiments.
- To model the thermal effect of plasma on mouse skin, it is necessary to know the equations of heat propagation but also the vascular structure of the skin.

An interdisciplinary research topic is not inherently difficult. It is merely a matter of applying the scientific method with the same rigor on other scientific objects. It is evident that this rigor can only be built by the time, a lot of discussions and criticism (received and formulated).

Chapter I State of the art

This chapter is divided into six parts.

First, the general context is described. This is followed by a brief presentation of the type of plasma sources used. Then, the literature regarding the chemistry elicited in the liquid phase by the interaction plasma-liquid is presented. The biological effects of so-called reactive oxygen and nitrogen species (RONS) are discussed after that.

Some remarkable results obtained in recent years with in-vitro studies are presented in I.5 and finally the studies showing evidence of an *in-vivo* plasma anti-tumor effect.

Other parts of this document contain bibliographic studies, and it seemed more appropriate to place them directly in the relevant chapters.

- Chapter III contains a description of the antioxidant defenses of the skin (section III.6.1, page 93, “Anti-oxidant defense of the skin, relevant orders of magnitude”).
- The biological effects of hyperthermia are described in Chapter VI (section VI.1, page 172, “What is hyperthermia? How to model and simulate it?”).

Several sections are dedicated to critical approaches of the literature:

- Regarding the transport of reactive species through living tissues (section III.6.4, page 101)
- Regarding the role of hyperthermia in plasma-medicine and how tissue temperature was measured (section VI.3, page 253)

I.1 General context

The use of cold plasmas produced by electric discharges for biomedical applications (Plasma-medicine) has considerably evolved over with major advances in the field of plasma-assisted haemostasis [3], biomaterials, dental surgery [4], sterilization, wound and ulcers healing [5], tumor treatment [6], skin treatment and dermatology [7]. Plasma-Medicine is an interdisciplinary field, which grows fast and brings together plasma physicists and chemists with medical doctors and biologists working on clinical aspects and fundamental biological issues.

Plasma usage in dermatology covers areas such as sterilization of tissues, treatment of skin diseases, cosmetic applications, blood coagulation and wound healing. It has been known for a long time that plasma has biocide effects; however, the exact mechanism of plasma disinfection is not yet fully understood. Plasma factors that believed to be relevant for sterilization are charged particles (electrons and ions), UV (A,B and C) radiation, strong electric fields and the reactive species of oxygen and nitrogen (O,N, O_2^-, O_3, OH°, H_2O_2, NO, OH etc.) and excited states of molecules and atoms ($O_2(a^1\Delta_g)$, $N_2(A^3\Sigma_u)$). The synergy between several plasma parameters could be responsible for the disinfecting effect of plasma [8]. Thus, UV radiation and electric field can directly damage cellular macromolecules and affect membrane, while DNA proteins and lipids are irreparably harmed by oxidative stress. Successful plasma treatment of chronic skin diseases like dermatitis [9], Hailey–Hailey disease [10] and eczema [5] shows that plasma efficiently eliminates bacterial colonization, e.g., Staphylococcus aureus, by inducing reactive oxygen and nitrogen species on the treatment surface (O_3, NO, etc.).

Cold atmospheric plasmas (CAP) for cancer treatment

If numerous studies use cold plasma to treat tumor cells [11], the nature of the interaction between CAP and cancer tissue remains poorly understood. In nude mice bearing subcutaneous bladder cancer tumors, regression was observed for tumors treated with CAP whereas the untreated neighboring tumors were unaffected [12]. Several genes associated with apoptotic and oxidative stresses were observed to be deregulated. Vandamme et al. evaluated the effect of CAP on tumor volume in glioma-bearing mice with bioluminescence imaging (BLI) and cellular biomarkers [6]. Compared to untreated mice, the CAP treatment induced a ~40% inhibition of tumor growth by the end of the study. It has been suggested that DNA damage and reactive species generated by the plasma may be the main cause of tumor cell apoptosis [13], [14]. ROS generated by CAP can, under certain conditions, modify endothelial cell proliferation [15];or lead to apoptosis [13]-[16]–[20]. This is consistent with the mechanisms used by radiotherapy to induce lethal DNA damage based on the formation of ROS in targeted cells that include superoxide, hydrogen peroxide and free hydroxyl. It should be noted, however, that radiotherapy produces the reactive species directly within the cell.

Such tumors have been treated with direct treatment. As an alternative, an indirect contact approach has been recently developed. It consists of plasma-activating a liquid medium (PAM), hereafter put in contact with the tumor [21].The utilization of PAM is relevant for the treatment of subcutaneous or barely accessible tumors to prevent any surgical operation before treatment. The value of PAMs has been demonstrated through antitumor effects on Glioblastoma, ovarian cancers and gastric cancers [21], [22]. However, it must be ensured that PAM injection is consistent with a therapeutic approach. For example, injecting PAM only 24h after the injection of tumor cells does not constitute a good biological model of the therapeutic effect that plasma would elicit. Treatment should be done when the tumor has already reached several mm in diameter. A majority of these studies have been performed in-vitro with murine cancer cell lines (lung, melanoma, head and neck, brain and bladder).

Oral squamous cell carcinomas (OSCCs)

Head and neck squamous cell carcinomas (HNSCC), including cancers from oral (pharynx, larynx, paranasal sinuses) and nasal cavities, are the sixth most common malignancy worldwide [23].They represent a major public health problem since, despite conventional treatment (i.e., surgery, with or without radiotherapy and chemotherapy), the prognosis remains very low with 35-55% relapse within two years and less than 20% overall survival at ten years [24]. Furthermore, due to their localization, these cancers affect some of the most vital functions of the body leading to a very poor quality of life. Long considered as a uniform group, HNSCCs are actually heterogeneous, depending first on their anatomic site and association with known risk factors (i.e., alcohol and tobacco, papillomavirus infection, HPV). Among HNSCCs, oral cancers (OSCCs) represent the ones located in the oral cavity and the oropharynx. Whereas oropharyngeal cancers (tonsils and base of the tongue) are known to be mostly associated with HPV infection, oral cavity squamous cell carcinomas (buccal mucosa, gums, front two-thirds of the tongue, the floor of the mouth below the tongue, hard palate) are mostly not [25], [26].Second, there is marked heterogeneity in therapeutic responses to one or more of the conventional treatments. Currently, despite this known heterogeneity, patients are treated with a similar global strategy. Standard treatment strategies for HNSCCs include surgery, radiation $^{and}/_{or}$ chemotherapy, mainly platinum-based drugs (Cisplatin) and 5-Fluorouracil (5-FU). The choice of these treatments and their combinations is based on site of disease and degree of invasion and metastases. However, approximately 60% of HNSCCs patients have locally advanced disease at presentation, and about 15 to 20% of them are not eligible for surgery because of tumor size $^{and}/_{or}$ poor general state of health. Different innovative therapies have been developed $^{and}/_{or}$ are currently under evaluation in HNSSCs. Those include the use of

monoclonal antibodies such as anti-VEGF, anti-EGFR, checkpoint inhibitors, therapeutic vaccines, or targeted therapies [27]. Because most of them appear not efficient enough or are under further studies, there is an urgent need to develop innovative strategies such as CAP. Thanks to their localization, OSCCs are accessible to CAP exposure [28]. Furthermore, these cancers relapse in a locoregional manner with little or no metastasis.

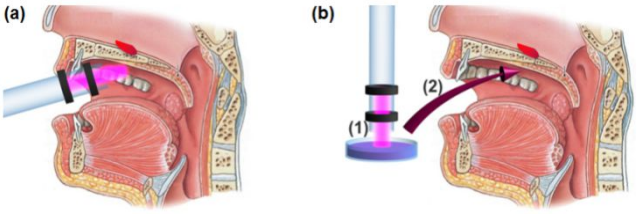

Fig 1 (a) Direct contact approach. The plasma is applied directly on the carcinoma located in the oral cavity (b) Indirect contact approach. A physiological medium is first plasma-activated (PAM) and then injected on the carcinoma located in the oropharynx.

I.2 Plasma sources for bio-medicine

Plasma sources generated at atmospheric pressure in air or air containing mixture produce ROS, RNS, UV, ions, electric field. The chemical composition of plasma sources in air containing mixture has been extensively studied experimentally [29] and numerically [30]. Numerical modeling predicts down-regulation of NO, O and O_2^- when switching from dry air to the air with 30 % humidity while concentrations N_2O, NO_3, N_2O_5, and O_3 would increase and new species like OH^-, HO_2, H_2O_2 and HNO_3 would be formed. The electric field seen by the treated object will be the sum of the applied electric field and strong local electric field which results from with the streamer propagation.

Following the commonly used terminology [31] currently available atmospheric plasma sources for biomedical applications can be divided into two groups [18], [32] depending on how plasma is delivered to the object to be treated.

Dielectric Barrier Discharges (DBD) are filamentary at atmospheric conditions with rather uniform plasma filament distribution over treated surface due to the surface charging and electrical repulsion of the filaments. UV emission of such plasmas is associated with excitation state of molecular nitrogen and OH° radical in the range of 300-400 nm and NOγ emission between 200 and 300 nm [33]–[35].

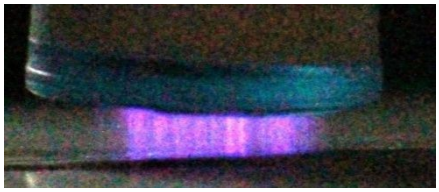

Fig 2 DBD treatment

Plasma Jets: in Plasma-Jet configuration, the plasma is confined in dielectric tube or capillary. Depending on excitation source electrode configuration may be DBD-like for pulsed and low-frequency jets [36] and corona-like for devices which operate at radio frequency [37]. Plasma jets are operated in noble gas flow (Helium, Argon, Neon, etc.) or in a mixture of noble gas with air or oxygen admixture. The ability to modify gas mixture is an advantage of plasma jets since it enables the tailoring of ROS and RNS produced in plasma zone or in the plume due to mixing with ambient air [38].

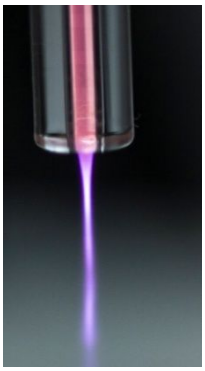

Fig 3 plasma-jet

I.3 Chemistry of plasma-liquid interaction

Why is it interesting to study the plasma-liquid interaction and in particular the chemical composition of the liquid phase? First, such measurement could give clues on the intake of a chemical species at the boundary of the treated tissue. However, It appears that the conductivity of the target modifies the chemistry of the gas phase [39]. Consequently, it is likely that the intake above the biological tissue is different from that above liquid.

So, it is important to avoid to overextend the scope of the results obtained with liquids to in-vivo experiments. On the other hand, it is fully relevant to use the results of plasma-liquid experiments for the interpretation of *in-vitro*[1] experiments or PAM treatments. The chemistry of the interaction plasma-liquid has others applications than plasm-medicine: water-decontamination [40], sterilization and decontamination of medical devices [41], plasma-chemicals process, plasma-agriculture [42]. The chemical mechanisms of the plasma-liquid interaction at the origin of these species are not necessarily all known and remain an open question despite the progress of the last ten years [43].

It is relevant to make a distinction between short-lived species and long-lived species (more than a few minutes). The long-lived species can be measured several hours after treatment. Hydrogen peroxide (H_2O_2), nitrites (NO_2^-) and nitrates (NO_3^-) are part of the long-lived species. Among short-lived species, there are singlet oxygen, peroxynitrites (HOONO), ozone (O_3), hypochlorite anion (ClO^-) and radicals such as superoxide anion O_2^-, NO° and hydroxyl radicals HO° [43]. When experiments of the therapeutic and biological effects of PAM are carried out, the short-lived species generated by the plasma which no longer exists, cannot be at the origin of the biological effects. Moreover, Adachi et al. [44] and Judée et al. [45] shows that PAM retains a therapeutic effect for several days. In addition, the long-lived species contained in the PAM produce short-lived species. H_2O_2 can react with nitrites and give peroxynitrites: half-life of peroxynitrite is few tens of ms in biologic conditions [46], [47]. Then, among other reactions, peroxynitrite give HO° radical and nitrate [48]. The lifetime of this radical is of the order of ns in biological media [49]. Another example: when H_2O_2 solution is exposed to UV rays, it decomposes by photolysis and gives HO°. Otherwise, the therapeutic effects of PAMs are also due to the short-lived species produced by PAM species that react together or with biological molecules. So, if the distinction between short and long live species is not relevant regarding therapeutics effects, it is relevant for an experimental point of view: the probes of short-lived species need to be in the treated liquid during the treatment, and this fact could be another source of bias and complexity

The roadmap of Adamovitch et al. summarizes the physics and the chemistry of plasma-liquid interaction [50]. It provides precious information on how to model the liquid plasma interaction. Adamovitch et al. and Bruggeman et al. propose an overview of the chemistry that takes place in the gas phase, at the interface, and in the liquid phase (see Fig 4) [50] [51].

[1] In this case, the liquid is the culture medium in which the cells are immersed. Caution should be exercised with regard to the reactions that occur with the culture medium.

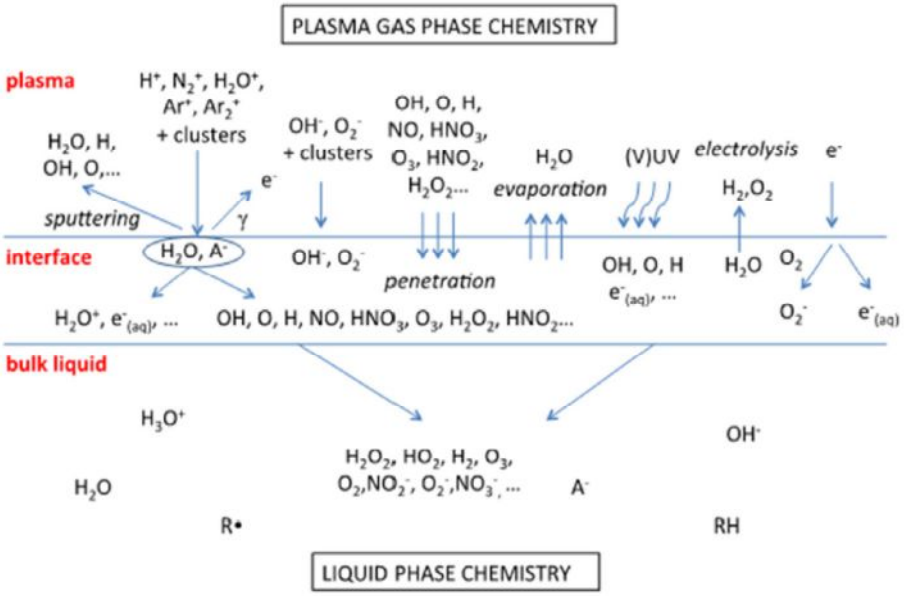

Fig 4 Overview of plasma-liquid chemistry, from [50], [52]. © IOP Publishing Ltd

I.4 Biological effect of reactive oxygen and nitrogen species (RONS) alone

Regarding, the field of sterilization and decontamination, the problem is rather straightforward. Hydrogen peroxide and other reactive nitrogen and oxygen species have an anti-microbial effect known from tenth. The open questions, in this case, are to know, if other properties of plasma could play a significant role or not. For instance, is the effect of electroporation negligible or not? What is the precise contribution of UV radiation to the decontamination of the surface? There is a lot of work to do regarding the precise understanding and optimisation of plasma treatment applied to decontamination and sterilization. When a sufficient amount of this reactive species is produced, the cells die because of the toxicity of this species. The question is to know what the cellular mechanisms are implied in the dead of this cells

Regarding, “plasma-cancer,” the question is more complex. Studies who show an anti-tumor effect propose an explanation based on a RONS-mediated anti-tumor effect, which means that the input of chemical species could induce a biological response leading to cell death via necrosis or complex response like apoptosis [53]–[55].

Toxicity of H_2O_2

Hydrogen peroxide is not classified as a mutagen or carcinogen according to the European Union Risk Assessment report [56]. According to the report of INRS [57, p. 123], There are no signs of reproductive toxicity, carcinogenicity or mutagenicity. INRS (“Institut national de recherche et de sécurité”) is the French research and Safety Institute for the prevention of accidents at work and occupational diseases which edit material safety data sheet.

It appears that genotoxicity is widely observed in-vitro [56], [57]. Watt et al. explain that three mechanisms are involved in the toxicity of hydrogen peroxide: lipid peroxidation, corrosive damage, and oxygen gas formation [58]. In the event of accidental injection or ingestion, significant neurological damages may occur. Dermal exposition causes skin damage, inflammation and blistering among which erythema, focal epidermal necrosis,

purpura (red spots due to bleeding under the skin) and subcutaneous emphysema, a condition in which gas is present under the skin.

Hydrogen peroxide is not only a poison, but this also a major intracellular messenger involved in several signaling pathways [59]. Stones et Yang indicate extracellular and intracellular concentration ranges that may cause cell proliferation or morbidity (see Fig 5, [60].

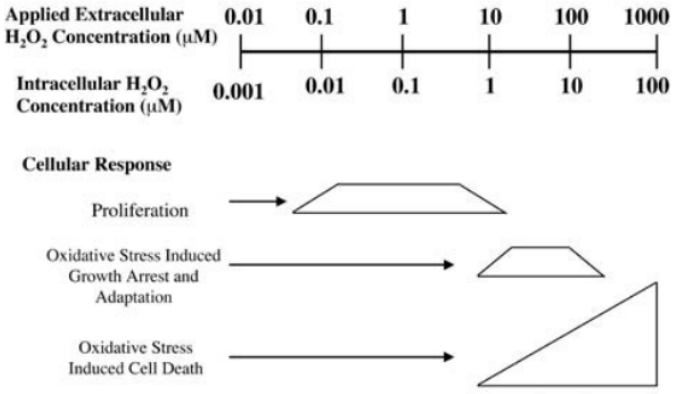

Fig 5 Legend and figure from the paper of Yang et al. Vertebral response to H_2O_2 [60] © Mary Ann Liebert, Inc.

Hydrogen peroxide is sometimes considered as means to deliver oxygen to skin. For instance to assist in the treatment of ulcers [61].

Toxicity of nitrate and nitrites

The toxicity of nitrates is well documented. Standards have been established to limit human and animal exposure. Deleterious effects are mainly due to the transformation of nitrate into nitrite [62]. According to [63], nitrite is ten times more toxic than nitrate. The lethal oral doses for human beings are established in 80–800 mg nitrate/kg body weight and 33–250 mg nitrite/kg body weight.

I.5 *In-vitro* evidence of cytotoxic responses

In-vitro experiments are used as a model for the disease and the treatment. An *in-vitro* experiment provides a lower level of evidence than in-vivo experiments in the development of therapies. On the other hand, the degree of control of these experiments is higher. Consequently, it is easier to understand the mechanisms which explain how a therapy works with *in-vitro* model. Currently, most of the work done in plasma-medicine is *in-vitro* experiments [64]. We will focus on the work related to oral cavity cancer.

Selectivity against cancerous cells

The most exciting results are that CAP can have selective effects against cancer cells. This means that in an in-vitro experiment, there are treatment times for which it is possible to kill cancer cells without killing healthy cells. However, the result depends also on what is chosen as “normal cell”. In a recent review, Yan et al. counted the number of papers showing evidence of selectivity of plasma treatments against cancer cells [65]. It appears that a very high selectivity has been observed for 25 different lines. In contrast, an absence of selectivity has been reported in only two lines. However, it is likely that negative results on the selectivity of plasma treatments have not been published.

The selectivity of plasma treatment is generally attributed to the idea that cancer cells could have weakened anti-oxidant defenses; the RONS provided by plasma treatment would then overcome their defense and induce an apoptotic response. Normal cells would have their anti-oxidant defense intact, which would protect them in higher concentrations than cancer cells can withstand. However, this concept of "redox equilibrium" is very controversial for the biologists; it is likely that this concept poorly represents the behavior of the cell in all its complexity. The complexity of the biological response to CAP was clearly shown by Keidar et al. since dozens of genes are modified toward an over-or-under expression after plasma treatment [12].

Regarding anti-cancer selectivity and head and neck cancer lines; Guerrero-Preston et al. have shown that cold plasma selectively decreased the viability of SCC25 and JHU-028 cancerous cells [66]. The viability was measured by MTT assay seven days after plasma-treatment. The normal cells, OKF6 and NOKsi, were poorly affected by 30 and 45 s treatments, whereas the cancerous lines O22 and O28 were dead after a 10s-treatment. It may be noted, however, that normal and cancerous cells have not been cultured precisely in the same medium. It would be interesting to verify that the anti-oxidant capacity of the culture medium is the same in both cases.

Plasma treatment elicit DNA damages

Han et al. observed that plasma treatment promote DNA double-strand breaks [67]. The treatment of SCC-25 oral cancer was performed with a plasma jet of N_2 powered at a frequency of 28 kHz, and peak to peak Voltage ~ 22.4 kV, $\Phi(N_2) = 1500\ sscm$. DNA damages were observed in the nuclei just after plasma treatment. 30 s of plasma treatment cause damage in 60% of the cells exposed to plasma.

Chang et al. performed experiments on four cell carcinoma lines (MSK QLL1, SCC1483, SCC15, and SCC25) [20]. All of these cell lines are models of oral cancer of human origin. The wells were treated with an (He+O_2) plasma jet powered at 2 or 4 kV. The precise frequency is not specified (in the range 20-30 kHz). Neither gas composition nor gas flow is specified (even in the paper done by physicist [68]). The treatment time is 1 s. The authors show the production of DNA damage Double-strand breaks and especially that the p53 signaling channel is activated.

Role of reactive oxygen species

Girard et al. exposed several lines (MRC5Vi, HCT116) to cold plasma-jet [69]. The DBD-plasma-jet was powered by high voltage pulse generator (amplitude 8 kV, rise time 280 ns, full with at half maximum of 540 ns). They found a dose-dependent increase in cell mortality. Chemistry experiments were performed to measure the amount of H_2O_2 and nitrites present in culture wells. For one minute of treatment, the concentrations of H_2O_2, NO_2^- and NO_3^- reached are respectively ~400 µM, ~400 µM and, ~100 µM. Subsequently, in a very clever way, they performed a comparison between the effects of chemical mixture which have the same composition than plasma-activated medium. They observed that NO_2^- and H_2O_2 act synergistically to induce cell death, and conclude that these two species alone are sufficient to explain plasma-induced cell death.

Bekeschus et al. have compared the treatment done with a Dielectric Barrier Discharge, and kINPen11 [70] on CT26 cell line. They show that H_2O_2 play a dominant role in the decrease of viability observed after 21 h of incubation. Comparisons were made with bolus addition of H_2O_2. The effect of kINPen is well explained by the amount of H_2O_2produced by the device. In contrast, DBD produced an unknown species that increases the toxicity of the treatment compared to the bolus addition of H_2O_2.

I.6 Cold Plasma and oncology

Clinical case

Metelmann et al. report the follow-up of 12 patients afflicted with advanced squamous cell carcinoma of the head and neck [28]. This protocol has been authorized to decontaminate infected cancerous ulceration. This study was not designed to study the anti-cancer potentialities of cold plasma but improve the understanding of how such treatment could take place. The patients were treated with kINPen MED powered at 1 MHz with a sinusoid waveform (2->3 kV peak) modulated with 2.5 kHz at 8 mm of the tissue and flow between 3 and 6 slm of Argon.

Cold plasma treatments were delivered in 3 single treatments within 1 week, followed by an intermittence of 1 week without CAP exposure. Note that plasma exposure conditions have been maximized: every square centimeter of the ulceration was exposed for 1 min. In some patients, the exposure time has exceeded 30 minutes

Metelmann et al. have shown that plasma treatment brings benefits related to i) the reduction of pain ii) reduction of fetid odor which reflects the fact that the antibacterial action of kINPen has been effective iii) gain of weight and reduction of medications.

It also appears that the effect of cold plasma was not immediately observable. Visible change appears after two weeks of treatments (i.e., 3 weeks after the first exposure). The totality of the treated area did not respond uniformly. Some patients presented areas of partial remission. These results are quite encouraging. Note also that plasma is used in pulsed mode which totally excludes the occurrence of hyperthermia but also decreases the production rate of chemical species. Perhaps it would be possible to increase the chemical action of such devices by making them operate at higher power in continuous mode while reducing the temperature of the carrier gas upstream of the plasma source (in order to avoid hyperthermia[2]).

Regarding this clinical assay, Schuster et al.[71] also report that the number of apoptotic cells was higher in the group treated by plasma.

Which mechanisms?

The crucial role played by the development or reactivation of an antitumor immune response in the eradication of the tumor and in the therapeutic clinical response is now well established. If both innate and adaptative immunity is essential for eradication of tumor cells, the latter is, however, crucial in order to favor a better protection against relapses, that are frequent in HNSCCs, as well as to envision combination with chemotherapy for patients non-eligible to surgery. T cells as effectors (cytotoxic CD8), helpers (T_h) or regulators (T_{REG}), may play diverse roles in the evolution of the tumor, being pro-tumor or the opposite. Intensive studies over the past years of tumor-infiltrating lymphocytes (T_{IL}) highlight the clinical relevance for the infiltration of high numbers of T cells at the tumor site in many solid cancers, CD8 memory T cells being a key denominator for overall survival whereas T_{REG} infiltration being associated with a poor clinical outcome [72].

Several studies have been focused on the key processes which could elicit efficient immune responses against tumor cells. First, there are growing evidence that some

[2] what we tried to achieve in the section V.3, page 147. See also the discussion concerning hyperthermia in Chapter VI.

chemotherapeutic and radiotherapeutic regimens trigger cancer cell death while stimulating an active immune response against the tumor [73], [74]. As shown in Fig 6.

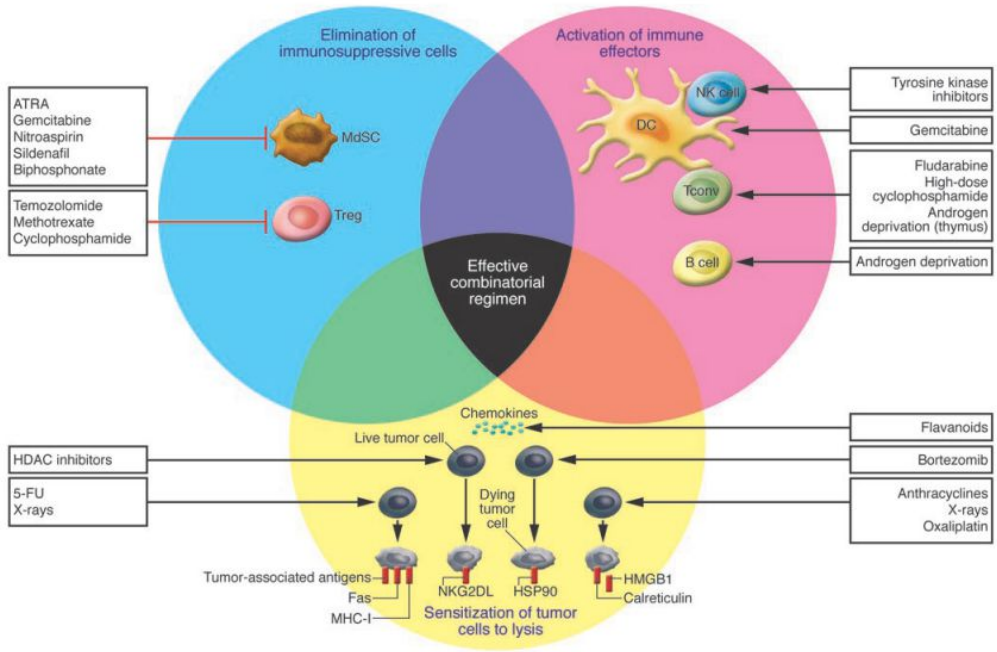

Fig 6 Adapted from Zitvogel et al. [74]. Mechanisms of the impact of conventional anticancer therapies on immune responses. Anticancer therapeutics can inhibit suppressive mechanisms of tumor-induced immune tolerance (blue circle), boost T and/or B cell responses (pink circle), or stress tumor cells in such a way that tumor cells become immunogenic and sensitive to lysis (yellow circle). The main drugs driving these effects are also shown.

The immunogenic cell death relies on the emission of signals from dying cancer cells and their perception by the host immune system in a first step. Secondly, an appropriate localization and migration of immune cells is required. In particular, T-cells is a prerequisite for antitumor immunity. However, immune cells accumulate more efficiently in the surrounding stroma than in the tumor islets and can be influenced by modulation in vascularization. So, the structure of the tumor stroma-vascular filling and network distribution, local microstructure, cellularity, as well as fibrosis and necrotic core - play key roles in the positioning and migration of immune cells [75].

Pre-clinical model: B16-F10 melanoma C57/BL6 line

First of all, it should be noted that among plasma-treated tumors experiments, one has been repeated by several independent groups with different plasma sources. This line, the melanoma B16-F10 was treated by Keidar et al. [12], Daeschlein et al. [76], Chernets at al. and Mashayekh et al. [77]. The four groups reported a positive effect of plasma treatment which induces a slowdown in the rate of tumor growth. In contrast, the magnitude of the slowdown is different depending on the device used.

Keidar et al. treated B16-F10 melanoma and SCaBER tumor model [12].

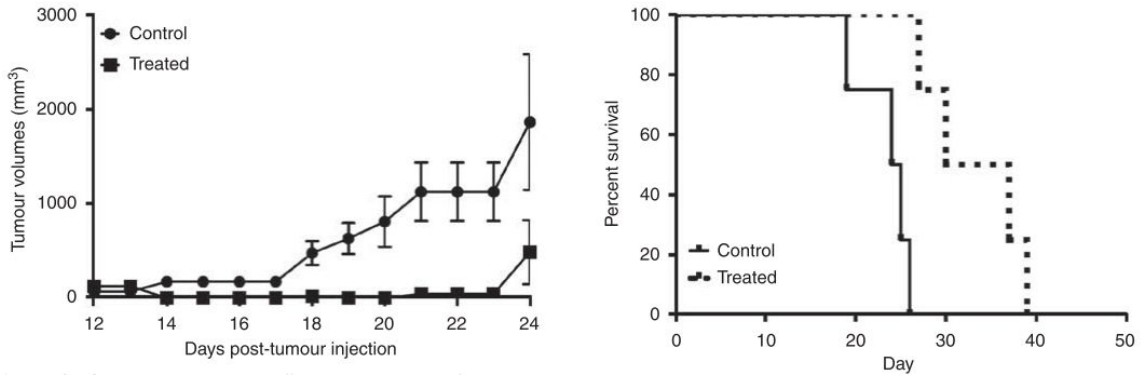

Fig 7 Adapted from Keidar et al. [12]. © 2011 Cancer Research UK

However one can note the presence of damages on the skin right after the end of the plasma treatment (Fig 8). This type of observation has been correlated with treatment inducing hyperthermia by Dobrynin et al. [78]

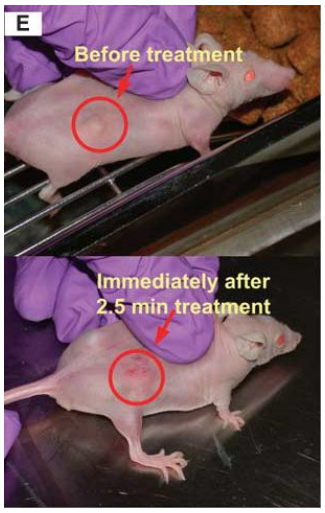

Fig 8 Adapted from Keidar et al. [12]. This picture shows the damage on mice bearing SCaBER tumor. © 2011 Cancer Research UK

Daeschlein et al. compared the antitumor effect of two plasma sources against B16-melanoma [76]. DBD and Kinpen09 were used alone or in combination with other therapies. The anticancer effect of plasma treatment alone is smaller than observed in the work of Keidar et al. [12]. Indeed, regarding the survival, the groups treated with DBD or plasma-jet shownd no significant improvement of their survival rate. Regarding, the kinetics of tumor growth, Daeschlein et al. shownd that the tumor growth acceleration[3] (TGA) is significantly smaller in DBD (D) and plasma-jets (J) groups than control (K) (see Fig 9). Besides the paper signals that the plasma does not elicit skin injury[4].

[3] TGA is the coefficient a_2, in the fitting of tumor volume by a second-degree polynome in time $V(day) = a_0 + a_1 \times day + a_2 \times day^2$.

[4] private communication of Dr Daeschlein: we measured maximal around 40°C during and directly after Jet therapy and never > 35°C after DBD using a laser equipped tool

Table 2. Tumor growth kinetics in the different treatment groups and controls showing tumor growth acceleration (TGA) and daily volume progression (DVP) (mean ± SD) in comparison with controls

Mouse group	TGA (mean b_2 and SD)	DVP (mm^3 mean and SD)	Survival days after treatment (Median)	Netto survival day difference to controls (after treatment) (mean)
K	0.0327 ± 0.0310	375.2 ± 188.9	28.5 no treatment	–
E	0.0220 ± 0.0085	345.5 ± 132.1	16.0	No
C	0.0089 ± 0.0051†	254.6 ± 183.6	15.0	No
ECJ	0.0082 ± 0.0039*	133.5 ± 62.9*	41.0*	19.0*
D	0.0155 ± 0.0127†	343.1 ± 158.1	19.0	No
J	0.0125 ± 0.0056*	317.2 ± 85.7	26.0	3.6
ECD	0.0133 ± 0.0124†	218.3 ± 177.9	35.0	7.6
ECJ	0.0081 ± 0.0051*	135.2 ± 138.3*	46.0*	24*
EJ	0.0105 ± 0.0047†	442.7 ± 517	28.0	No
ED	0.0161 ± 0.0075	514 ± 662	15.0	No
CD	0.0134 ± 0.0098†	436 ± 695	22.0	No
CJ	0.0151 ± 0.0107	281 ± 428	17.0	No

Survival days after treatment were shown in comparison with untreated controls (*t*-test, significance shown for α = 5%* and 10%†).

Fig 9 Adapted from [76]. K is the control group. D the group treated by DBD and J the group treated by kINPen09.

Chernets at al. got a stronger effect than observed by Daeschlein et al. on the same line of melanoma [79]. Indeed, in addition to tumor slowing, an increase in survival rate was observed (Fig 10).

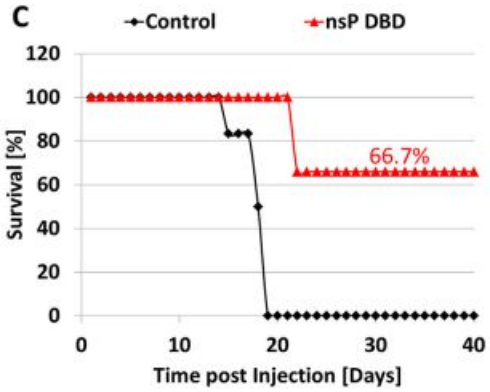

Fig 10 Adapted from Chernets et al. [79]

However, measurements show that the temperature at the center of the tumor is 27 ° C higher than average tissues temperature. It turns out also that damage is visible just after treatment (Fig 11).

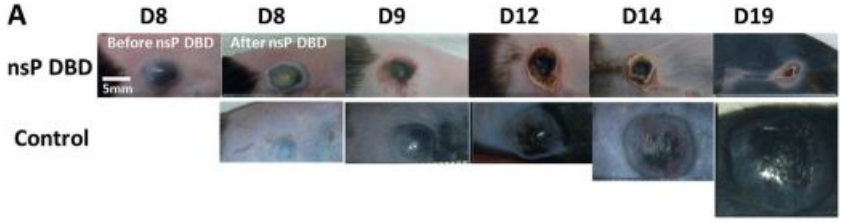

Fig 11 Adapted from Chernets et al. [79]

Mashayekh et al. show that the therapeutic effect of plasma is equivalent to that of chemotherapy (Fig 12) [77]. Mashayekh also indicates that the mice were treated conscious and that the skin showed no sign of damage after treatment (private communication of Mashayekh).

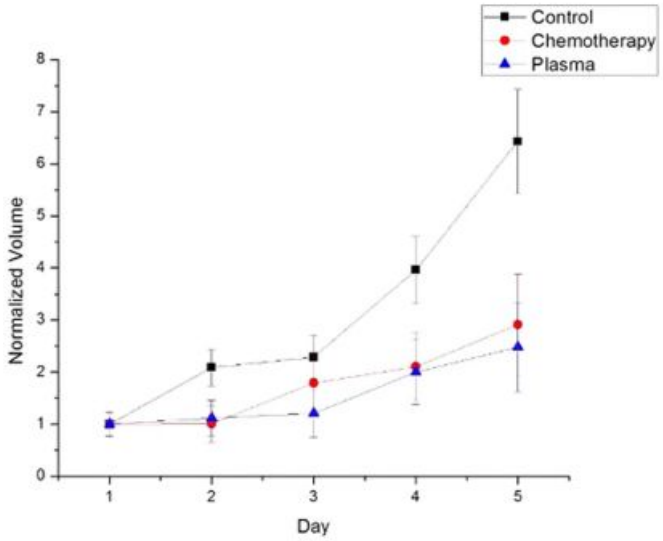

Fig 12 Adapted from Mashayekh et al. [77]

Slowdown in tumor growth and increase in lifespan were also observed in the works of Partecke et al. [80], tumour-chorio-allantoic model of tumor, Walk et al. [81] regarding treatment of the neuroblastoma line neuro2a, Mirpour et al. [82] regarding 4T1 breast tumor model, Kang et al, [83] regarding FaDu line, Vandamme et al. [84] [85], 2010, regarding the human glioblastome U87 implanted in nude mice, Robert et al. [86] regarding the treatment of MIA Paca2-luc and HCT116-Luc endoscopic system, Brullé et al. 2012, [87] regarding MIA PaCa-2.

The injection of plasma-treated medium in the vicinity of the tumors is another modality of therapy envisaged. Utsumi et al. bring evidence of the benefits of such approach with a model of ovarian cancer [21].

Consequently,

- We began by designing and electrically characterizing our plasma sources (Chapter II)
- Then we wanted to characterize the chemistry they induced in a liquid phase and/or living cells
- Then we conducted in-vitro experiments to observe the anti-tumor effect of the treatment
- Finally, in-vivo experiments led us to discuss the role of temperature and to simulate it

The bibliography of specific topic is treated in

- Chapter III contains a description of the antioxidant defenses of the skin (section III.6.1, page 93, “Anti-oxidant defense of the skin, relevant orders of magnitude”).
- The biological effects of hyperthermia are described in Chapter VI (section VI.1, page 172, “What is hyperthermia? How to model and simulate it?”).

Chapter II Materials and methods

This chapter briefly presents the manufactured plasma devices, the method of measurement of the electric power consumed, the methods of chemical assays and the biological material.

Few points deserve particular attention:

- The manufacturing process of the plasma-device takes an original form.
- A discussion of chemical biases regarding the exploration of the chemistry of the liquid exposed to plasma. The chemical diagnostics should not be used as black boxes: this chapter illustrates the severity of some biases in the context of plasma-liquid experiment. The bias related to Griess reagent is particularly emphasized.
- Similarly, in the section dealing with electronics, it will be explain that the choice of components necessary to achieve a correct power measurement is not as obvious as it looks at first glance. The effect of the measuring system: oscilloscope and measuring probe is modeled and plays a major role.
- The complex chemistry of the reaction of terephthalic acid with the hydroxyl radical begins to be addressed in this chapter. We specify important notions about the Fenton reaction.

II.1 Engineering of plasma sources

II.1.1 Fast prototyping with 3D-printing in the laboratory

At the beginning of this work, the plasma-devices available in the laboratory were not suitable for medical applications. Regarding plasma-jet, the capillaries were too thin, and easily broken and not suited for reliable and routine use. Glass-DBDs consisting of a tungsten tip coated in glass were tested. The result was rather disappointing. Two of these electrodes were broken during *in-vivo* experiments after few hours of use. Moreover, it was not really possible to choose precisely the thickness of glass surrounding the tungsten tip (~1.5-2 mm).

The need of a versatile, high speed and economical manufacturing process led to choose 3D-printing. In the case of plasma jets, 3D-printing enables fast modifications of the geometry of the nozzle in a trial-error process. It was possible to create more complex nozzle geometries than those commonly used. Ultimately, it would be possible to optimize the production rate of one class of chemical species (e.g., nitrogen species) compare to another to improve the therapeutic efficacy in a rational way.

Advantages

- On average, there were less than four days between the design of the part and the functional plasma source. This speed enables to use trial and error approach.
- 3D-printing enables to manufacture a large number of parts and obtain a better reproducibility. One of the sources was manufactured in 6 copies. Each experimenter could reproduce the experiments and the plasma-device which is used. The 3D design of one of the devices is given in Appendix M. This code is open with OpenSCAD, free open-source software.
- The spatial resolution of the part reaches 50 µm along Z axis and 70 µm along XY axis.

Drawbacks

- Plastics are generally good insulators. But the way the plastic is printed can degrade the quality of the electrical insulation. Some precautions should be taken during printing: a reduced z-layer thickness, a high printing temperature and a relatively slow printing speed are required to ensure adhesion of the new layers and the partial melting of the underlying layer. Gas sealing is another reason to choose this kind of printing parameter.
- Constraints on the geometry of the object that can be printed.

II.1.2 Settings of 3D-printer

3D-printing is part of additive manufacturing techniques. The material is added layer by layer from bottom to top. Each part was printed with a Creatr-HS purchased from Leapfrog3D (Fig 13, left). The printing technique belongs to the family of Fused Deposition Modelling (FDM) technology. A plastic filament contained in a coil is fed into an extrusion nozzle head by motors. The extruder is heated to a temperature appropriate to the material (about 220 °C for PLA or PETG). The printing speed, the temperature of the extruders, the size of the plastic layers (see Fig 13, right), and the kinetics of cooling are the main parameters.

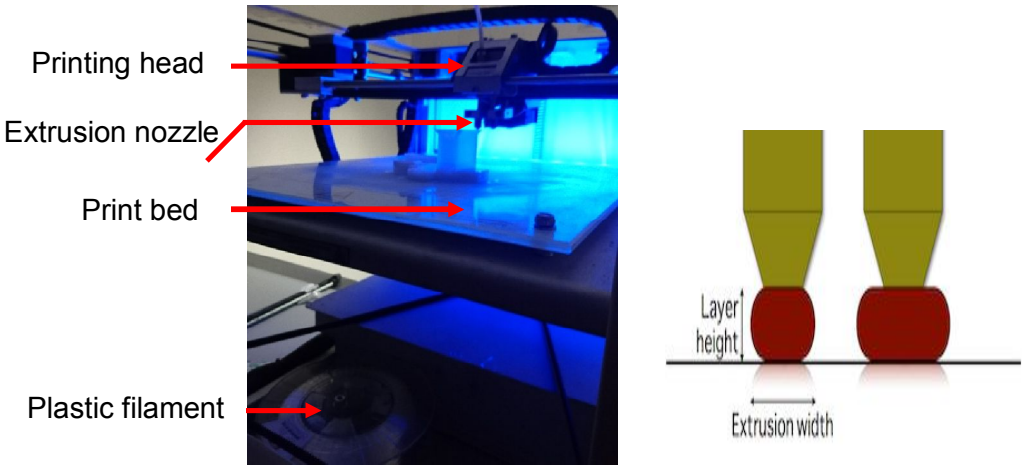

Fig 13 Left: 3D-printer in operation. Right: size of extruded filament. Layer height and extrusion width are directly related to the spatial resolution of 3D-printing.

The distance between the print head and the print surface is critical for printing quality (Fig 14). This distance depends on the height of the layers and is usually around 100 µm. Plasma source printing requires different settings from those used to print a decorative object. For example, the walls of the objects must be thick enough to ensure sealing and electrical insulation.

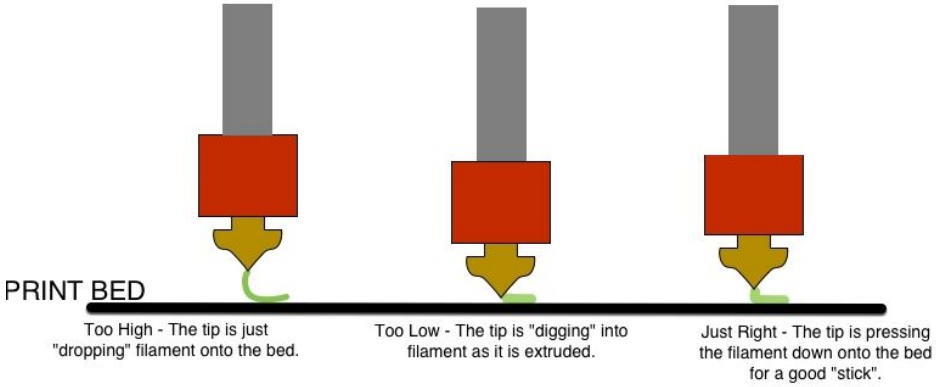

Fig 14 Adjusting head distance is critical for printing quality. Too high: the print does not stick well to the surface and can detach at any time. Too low: the pressure on the filament may cause it to twist and jam in the print head. Moreover, if the plastic remains in the nozzle for too long, the extruder may clog.

II.1.3 Manufacturing of Dielectric Barrier Discharge (DBD)

A DBD device is made of one or more layers of dielectrics placed between the high voltage electrode and the ground. This layer limits the current flow and enables the re-starting of the discharge from one-half period to another. Epoxy resin was used to constitute the dielectric layer. Epoxy resin was purchased from DIL France (Resolcoat 1060ES7, Résoltech). This resin has high mechanical and chemical resistance. Dielectric strength and dielectric constant at 100 Hz are respectively 25.5 kV/mm and 4.8. The polymerization takes place in about one day when the constituents are mixed. Immediately after mixing, the viscous liquid is centrifuged (around 3000 rpm) to prevent bubbles[5] from being trapped in the dielectric layer. A copper rivet was used as the conductive part. The outside of the part is printed in Polylactic Acid (PLA) or Polyethylene terephthalate glycol-modified (PETG). The model of this part is in the left part of Fig 15. The dimensions are shown on the right of the figure.

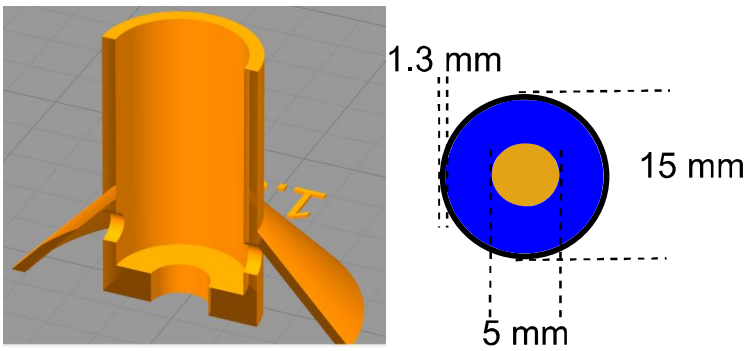

Fig 15 Left: a sectional view along the X axis of the plastic part of DBD: the two channels that make possible to insert the resin and to evacuate the air bubbles during the polymerization are visible. Right: a sectional view of the DBD along the Z-axis. In orange: copper rivet, d= 5 mm, in blue: epoxy resin. In black: PETG, thickness of 1.3 mm.

Once the plastic part is printed, the copper rivet is placed inside (Fig 16). The plastic part is designed in such a way that the end of the rivet extends to a lower depth than the plastic part. The distance **e** represents the thickness of dielectric; it is in the set {1.3, 1.4, 1.5 mm}. These values prevent dielectric breakage up to 30 kV peak to peak. A margin

[5] This would significantly reduce the quality of the electrical insulation.

of safety is taken since the device is used above living organisms (mice). The bottom of the part is closed by duct tape during the polymerization. The DBD is connected to HV power supply by a shielded HV Cable (reference 2124 from hivolt.de).

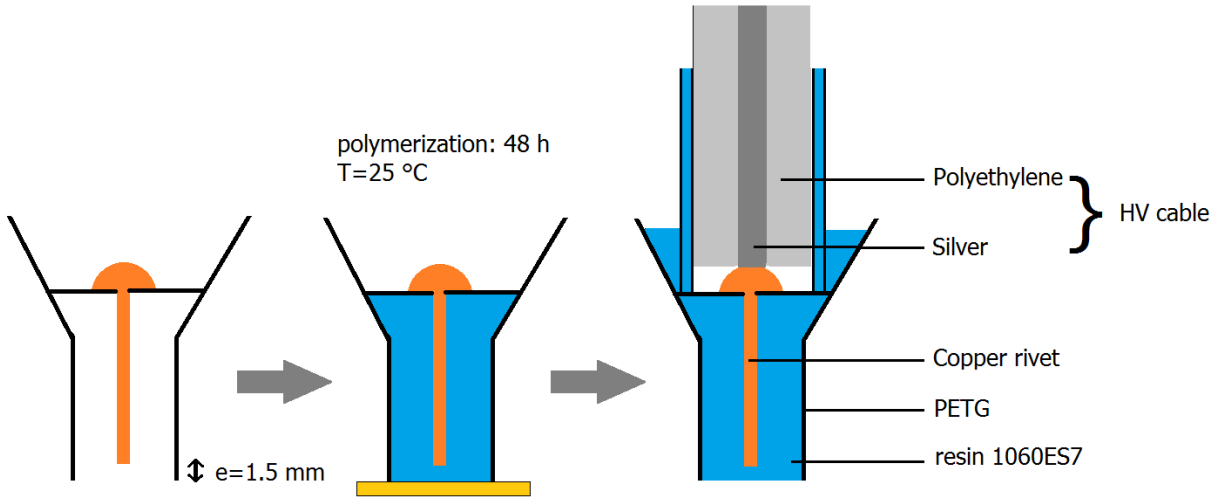

Fig 16 Sketch describing the manufacture of DBDs. Printing time of PETG part is about three h. The polymerization time is approximately two days. e is the thickness of dielectric layer.

II.1.4 Manufacturing of single-channel-jet

The simplest DBD-plasma-jet is a gas tube surrounded by an electrode powered by AC-voltage. A rare[6] gas flows into the tube. When the difference in electric potential between the high voltage electrode and the biological target is high enough, the discharge is ignited. 3D-printing enables to produce such device called “single-channel jet” or “single-jet” in the dissertation. The electrode was printed in a conductive plastic. Plastics are excellent insulators which become conductive when they contain graphite or graphene fibbers. Two conductive plastics were used: PLA-Graphite (resistivity $\rho = 44\ m\Omega.m$ from Proto-Pasta) and PLA-Graphene ($\rho = 6\ m\Omega.m$, BLACKMAGIC3D). The electrical resistance of the part printed with PLA-Graphene is of the order of a few ohms from one side to another. A polymer of Poly-Lactic Acid (PLA-white, Esun) was used to make the insulating part (Fig 17). Note that the insulating ring between the high voltage electrode and the gas tube is made of PLA.

[6] generally argon, helium or neon.

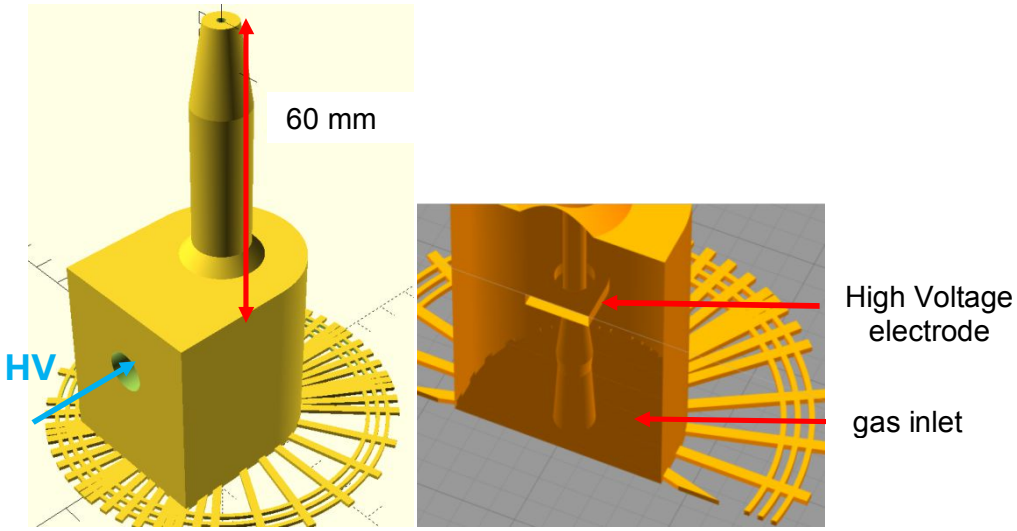

Fig 17 **Left**: view of the single jet. Blue arrow: connection to the high voltage electrode. The gas outlet towards biological targets is at the top of the figure. The distance between High Voltage electrode and gas outlet is 60 mm. The gas intake is below (not visible). At the bottom of the figure, the structure made of several circles and radius ensures that the print remains attached to the printing bed. **Right**: sectional view of the single jet. In this representation, the structure of the gas tube is visible by transparency. The gas inlet (below) has a conical shape which enables to fix the arrival of rare gas. The position of the high voltage electrode is visible. The conductive part is separated from the gas by a thickness **e** (PLA). Printing time: 12 h.

The conductive part is separated from the gas tube of diameter **d** by a thickness **e** of PLA (Fig 18). All around the PLA-graphene electrode, 15 mm of PLA ensure the electrical insulation. The distance between high voltage electrode and gas outlet is 60 mm. 8 plasma jets with six couples of parameters (**d**, **e**) were manufactured. **d** is in the set {2, 3 , 4 mm}; **e** in {1, 1.5 mm}.

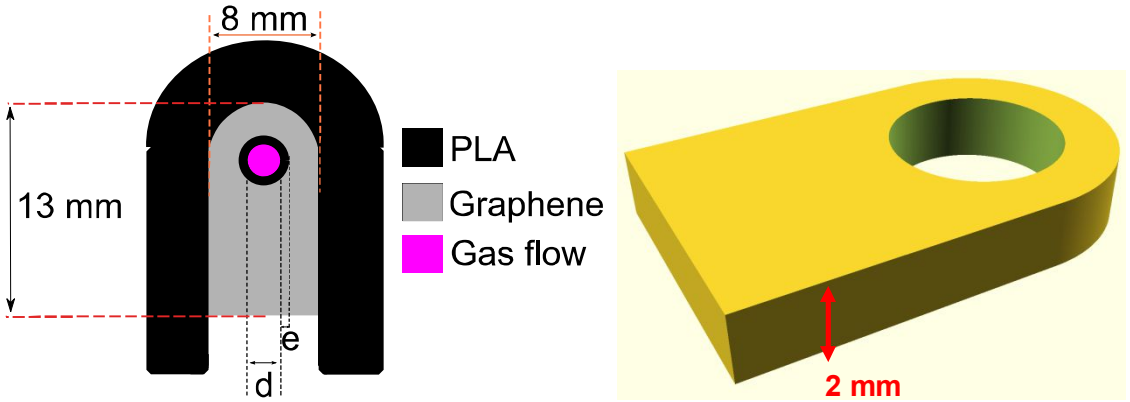

Fig 18 **Left**, sectional view of the single-jet along z-axis at the position of the conductive part. Internal diameter of gas tube: **d.** Thickness of the PLA dielectric wall **e**. **Right**: view of the conductive part in PLA-Graphene, height = 2 mm.

II.1.5 Manufacturing of multi-channel plasma-jet

The single-channel plasma-jet has one disadvantage. Like the other plasma-jet, the area of plasma-skin interaction is very small (~1 mm). It is necessary to move the plasma-device above the animal to treat the tumor or the wound. This can be an issue in terms

of homogeneity and reliability if the movement[7] of the device is not automated. A large nozzle with several channels was printed to address this problem. It was possible to treat large tumors (~ 8mm) without moving the mouse or the nozzle. The body of the plasma-device was printed in PETG (Fig 19). Dielectric layer is made of blue resin 1060ES7 (thickness = 1.4 mm). High voltage electrode is embedded in the resin.

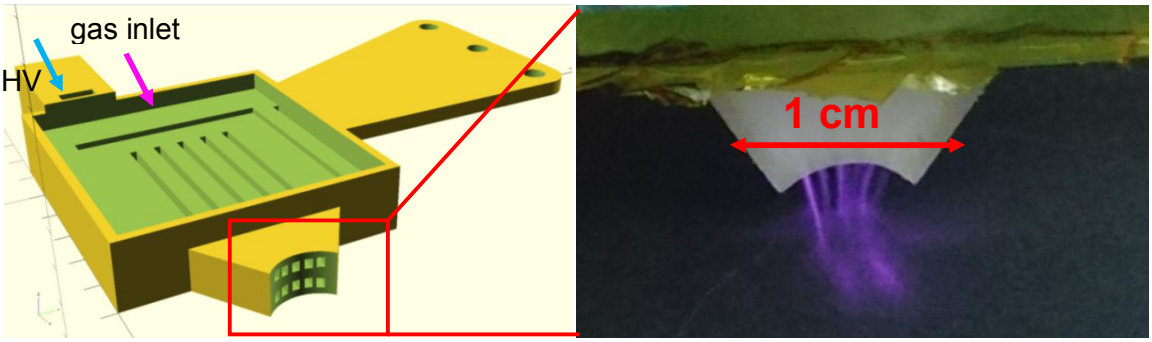

Fig 19 **Left**, view of a multi-channel plasma jet. The gas circulates in five rectangular channels ($1.5 \times 3\ mm$). The high voltage electrode is placed 1.4 mm above these channels. The polymerized resin 1060ES7 made the dielectric layer and gas sealing. At the position of the nozzle each, channel is divided in two. The ten channels are distributed over a length of about 1 cm. **Right**, view of the nozzle facing a black paper stuck on the electrical ground.

II.1.6 Manufacturing of refrigerated multi-channel plasma jet

Excessive heating of the skin was observed in some *in-vivo* experiments. Several solutions can be envisaged[8]. It was chosen to refrigerate the whole device with liquid nitrogen whose boiling point is at $-196\ °C$ at atmospheric pressure. A nitrogen tank was added to the printed part and filled with liquid nitrogen for about 10 min (Fig 20). Just before treatment, the liquid nitrogen was removed. Since the heat exchanges between plastic and helium is very efficient, the plasma jet was considerably cooled. Chapter V shows that the amount of thermal damage was considerably reduced with this device. At the bottom of the tank, heat exchange surface is a rectangular area $16\ mm \times 44\ mm$. The entire device is cooled during 10 min. Fig 20 shows that the tank has already warmed up after 1 min of treatment.

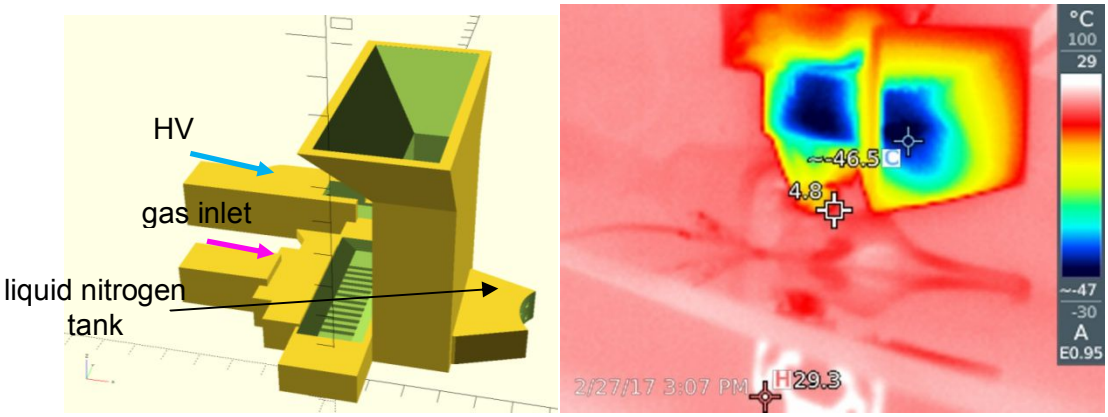

Fig 20 **Left**, view of the refrigerated multi-channel plasma jet. **Right**, infrared image of refrigerated multi-channel plasma jet after 1 min. The plastic in contact with the gas has a temperature slightly below 0 ° C (yellow color).

[7] It would be interesting to keep the plasma device at a constant distance from the skin. Since the tumors are curved, it would be interesting to tilt the plasma device.
[8] move the plasma source fast enough. Perform short and repeated treatments.

The contact of liquid nitrogen with the solid material at room temperature cause mechanical stress. However, the thickness of tanks walls (~3 mm) is sufficient to prevent them from breaking. The multi-channel plasma jet supports repeated cooling-heating cycles without damages, gas leaks or loss of electrical insulation. Frost is formed on the outside (Fig 21). This could be an issue[9]. It is even possible to follow how the multi-channel jet warms up during the treatment.

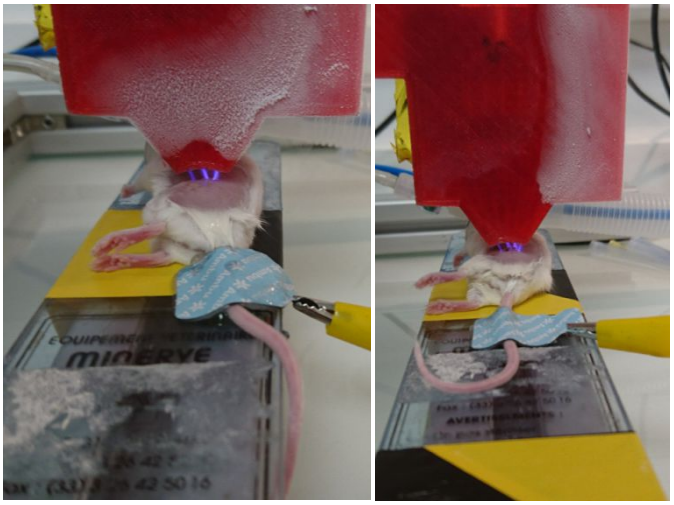

Fig 21 Left: multi-channel plasma jet after 1min. Right after 6 min, the warming of the device is clearly visible since the frost disapear in the heated area.

The manufacturing process consists of four steps.

- Printing of PETG parts (around 20 h)
- One layer of Mylar (~ 50 µm) is taped to the surface to prevent the resin from blocking the channels.
- A plastic bar with appropriate dimensions is covered with aluminium and fix 1.4 mm above the Mylar layer (Fig 22).
- The resin is added to constitute the insulator. After one day of polymerization, the device can be used. The thickness of the dielectric layer is equal to 1.4 mm.

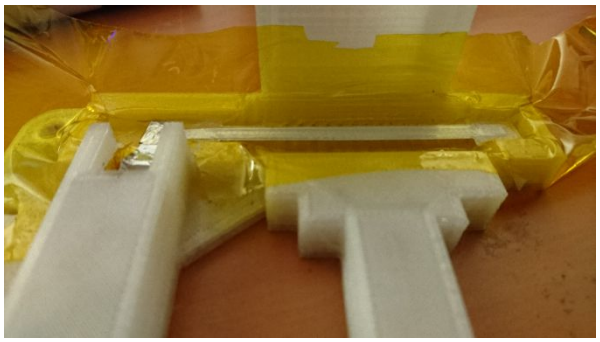

Fig 22 Refrigerated multijet, just before the addition of blue resin 1060ES7. Mylar is the yellow sheet. The rectangular bar which is covered with aluminium tape can be seen in the center. The space between the bottom of the bar covered by aluminium and the top of the channels covered by Mylar sheet is 1.4 mm.

[9] The buildup of melting ice near parts at high voltage can be dangerous. It is necessary to dry the device regularly. If water enters in gas channel, the discharge may not be able to ignite.

II.1.7 Mechanical supports

In addition to plasma-device, many parts have been designed and manufactured. Fig 23 shows five printed parts which have mechanical functions. They enable to choose the vertical and horizontal position of the plasma-jet relatively to the well. This is particularly important for the reproducibility, and the reliability of the experiments since the chemistry of plasma-liquid interaction strongly depends on the position (see Chapter III). I have tried to take into account the constraints[10] imposed by the work in the sterile environment. For example, DBD supports do not block the flow of laminar hoods.

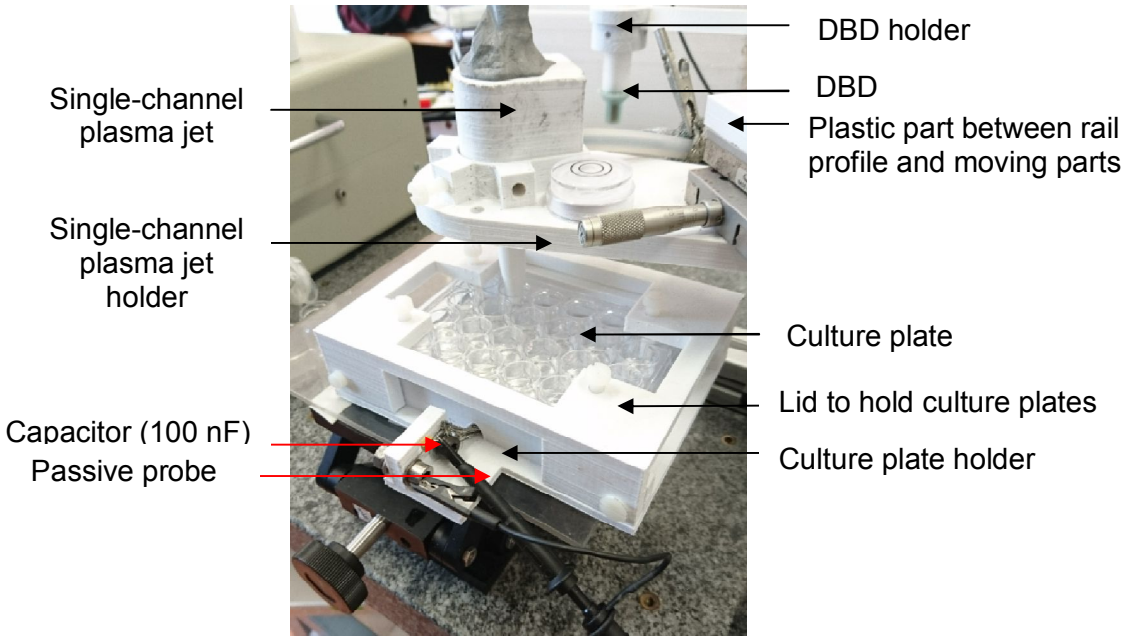

Fig 23 In addition to the single jet visible in the foreground and the DBD visible in the background, many supporting parts (five in this picture!) were drawn and printed.

II.2 Electrical characterization

Voltage measurement was acquired with an Oscilloscope (WaveRunner 6 Zi, band-pass =2.5 GHz, Lecroy). Passive probes PP08 and PPE20kV provide respectively a /10 and /1000 attenuation.

II.2.1 Power supply

Three homemade generators were used for this work. They were made by Sebastien Thomassier during his internship in electronics engineering. The generator with a sinusoidal waveform is composed of three stages. The signal of a function generator is amplified by an audio amplifier which gives low voltage and high current signal. The output of the amplifier is connected to a transformer to obtain a high voltage and low current signal.

- Sinusoidale generator, f = 500 Hz, maximum peak to peak voltage = 30 kV.

[10] in addition to the constraints of safety and ergonomics

- Sinusoidal generator, f = 10 kHz, maximum peak to peak voltage = 14 kV in continuous operation. The voltage can be increased to 18 kV for a few minutes. Excessive heating triggers the shutdown of the components.
- A 500 Hz power supply whose voltage waveform is a kind of square with resonance peak (Fig 24). Maximum peak to peak voltage is 30 kV. Beyond, the electrical insulation of the transformer is insufficient.

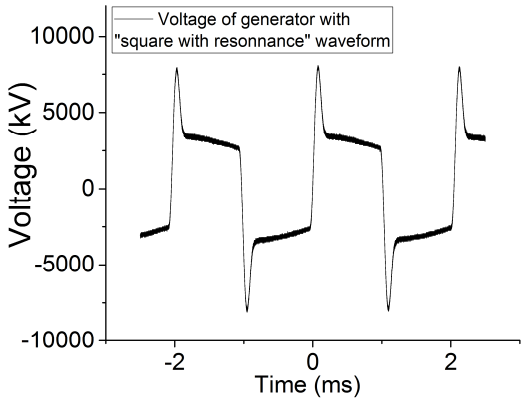

Fig 24 Waveform of the 500 Hz power supply.

II.2.2 Power measurement

A capacitor **Cm** is connected in series with the target of the DBD or plasma jet. The quantity of stored charges is known by measuring the Voltage **Um** at the terminals of this capacitor, with the relation $Q = Cm \times Um$. The current flowing through the measuring capacitor is known according to the expression $I = Cm\frac{dUm}{dt}$.

DBD and DBD-plasma-jet can be modeled by a dipole **D** whose characteristics change over time depending on whether the plasma is on or off. The amount of energy **E** consumed from time $t = 0$ to $t = \tau$ is defined by $\int_0^\tau (Valim - Um)Idt$.

The amount of charges Idt flowing during dt starts at the potential $Valim$ (with a potential energy $ValimIdt$). Theses charges cross the dipole **D** and reach electrical potentiel U_m. At this point, potential energy is $UmIdt$. The difference is the energy that the charges lose by crossing **D** (Fig 25).

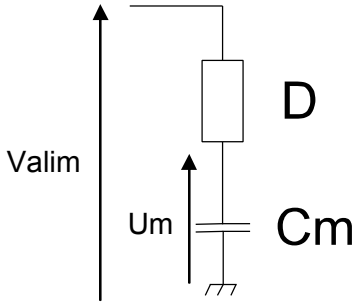

Fig 25 The capacitor Cm with a known capacitance is placed in series between plasma source and ground. It enables the measurement of the mean power consumption.

Cm can be chosen so that Um is negligible with respect to Valim. In that purpose, the impedance of Cm must be negligible with respect to those of **D**. Regarding DBD; we can estimate an upper bound of **D**-capacitance. **D** is modeled by a capacitor representing the capacitance of the dielectric layer in series with the capacitance of the gas layer between the surface of the DBD and the counter electrode.

By neglecting edge effect[11], the capacitance of the dielectric layer is:

$$Cdie = \frac{\varepsilon_0 \varepsilon_r S}{e}$$

Where e is the thickness of the dielectric layer; S the area of conductive plate and $\varepsilon_0 \varepsilon_r$ the absolute permittivity of the dielectric material.

Numerical application in the case of a cylinder of radius 2.5 mm, thickness 1.4 mm made of resin 1060ES7:

$$Cdie = \frac{8.85\ 10^{-12} \times 4.8 \times \pi (2.5\ 10^{-3})^2}{1.410^{-3}} = 0.60\ pF,$$

With the same approximation: an air slab defined as a cylinder of a radius 2.5 mm and thickness 1.5 mm has a capacitance of 0.17 pF. Since the capacitances are combined in series, the equivalent capacitance is of few pF.

Lissajous curves enable to measure these values experimentally. The presence of plasma decreases the capacity of air slab. The measurements obtain from Lissajous curves, and the RLC-meter confirms this ordering.

To conclude, this order of magnitude (few pF) is an upper bound of the equivalent capacitance **D** whatever the state of the discharge and the plasma-devices, since the geometrical parameters of the dielectrics are substantially the same.

Since the impedance of a capacitor is $Z = \frac{1}{jC\omega}$,

The approximation $Um \ll Valim$ is valid[12] if $Cm \gg Cd$. A measuring capacitor of a few nF should be suitable for carrying out the measurement. This value correspond to those presented in the reference[13] [89] which is a review of methodologies regarding DBD power measurement.

With the approximation $Um \ll Valim$, The amount of energy **E** consumed from 0 to τ is

$$E = \int_0^\tau Valim\ I\ dt = \int_0^\tau Valim\ Cm\ \frac{dUm}{dt}\ dt,$$

which gives for a period τ of electrical signal:

$$E = \int_0^\tau Valim\ dQ(t) = \int_{Qmin}^{Qmax} Valim\ dQ.$$

thus, when Lissajous curve is plotted, i.e., the curve with following parametric equation,

$$(t \to (x = Um(t), y = Valim(t)),$$

E is also the internal area delimited by the parametric curve multiplied by Cm.

---

[11] Of course, in this case (e = 1.5 mm, for a disk of 2.5 mm radius), it is not correct to neglect the edge effects. It slightly increases the capacitance since the lines of fields are curved at the edges of the disk, polarizing a greater volume of dielectric. The reference [88] enables to take the edges effects into account. In previous configuration edge effects add a capacitance of 0.48 pF to Cdie.

[12] With the assumption that the impedance of the resistive part of D is negligible with respect to the capacitive part. This is confirmed by the fact that the transient electrical resistance attributed to plasma is ~1-1000 kΩ

[13] *"Since the capacitance of typical actuators used in published studies is very low (5 pF to 200 pF), typical monitor capacitors are selected with a value between 10 nF and 330 nF. The capacitance is usually selected to provide a voltage that is adequately low for measurement by instruments."* [89]

II.2.3 Equivalent circuit of measurement system

It will appear that the disturbances induced by the measuring system impose a more restrictive condition on Cm than $\mathrm{Cm} \gg \mathrm{Cd}$. Before the discussion of this point; it is necessary to model the measurement system. The voltage Um is measured with a passive probe connected to the oscilloscope (PP08, /10 attenuations). The probe enables to obtain an attenuation of the voltage in such a way that it becomes measurable by the oscilloscope. The electrical circuit modeling the measuring system is described in Fig 26.

At low frequency, the circuit {probe + cable + oscilloscope} is equivalent to two resistors connected in series. Since input resistance is 1 MΩ, Rprobe should be 9MΩ to obtain a /10 attenuation.

At high frequency, the characteristic time τ of the two circuits {probe} and {oscilloscope + cable} must be equal in such a way that the signal is not deformed.

$$\tau = \mathrm{R_{probe}C_{probe}} = \mathrm{R_{osc}C_{osc}}$$

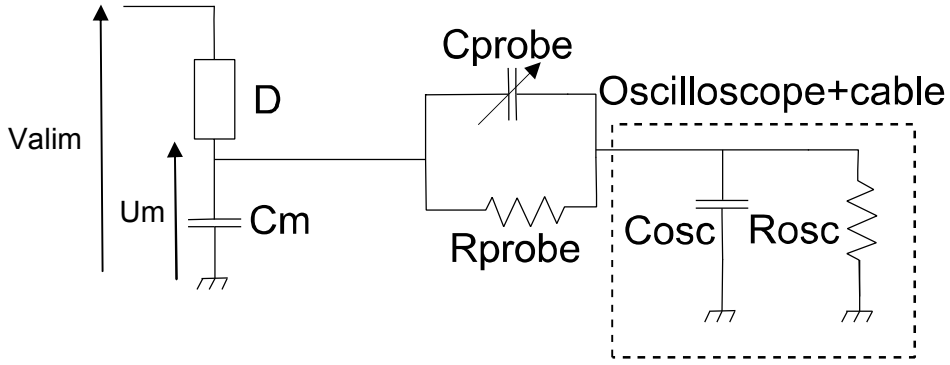

Fig 26 Modeling of the measuring system consisting of the probe and the oscilloscope. Cosc= 115 pF. Capacitance of the cable = 100pF, input capacitance of oscilloscope = 15 pF . Rosc= 1 MΩ. Rprobe = 9 MΩ. The adjustable capacitor Cprobe enables to obtain a reliable attenuation at high frequencies. The capacity can be adjusted with a screw.

Since $Cosc = 115\,pF$, this relation imposes $Cprobe = 12.8\,pF$ for a well-adjusted probe. The influence of the probe and the oscilloscope can be modeled as a capacitance Ceq and a resistance Req connected in parallel with Cm. An elementary calculation give Req=10 MΩ and Ceq= 11.5 pF (Fig 27).

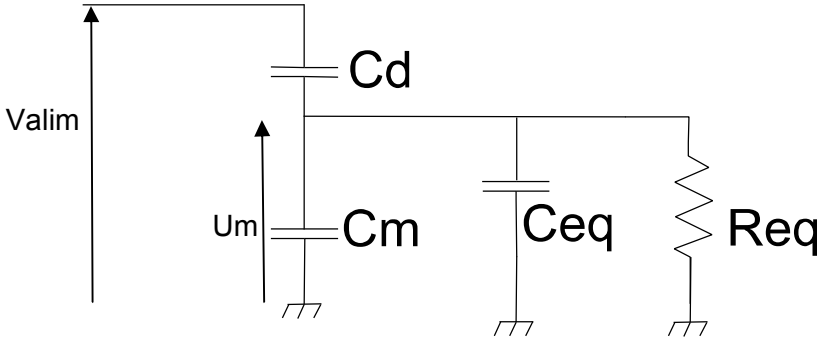

Fig 27 Equivalent circuit of the measuring system and Dielectric Barrier Discharge.

II.2.4 How to choose the capacity?

Let us consider what happens if **D** is a pure capacitor $Cd = 1\,pF$. **D** contains no dissipative elements; the energy consumption is strictly zero over one period.

The Current flowing through **D** is

$$id = (Cm + Ceq)\frac{dUm}{dt} + \frac{Um}{Req}$$

thus during one period, E is the sum of four integrals:

$$E = \int_0^\tau (Valim - Um) id\, dt$$
$$= \int_0^\tau Valim\,(Cm + Ceq)\frac{dUm}{dt}dt + \int_0^\tau Valim\frac{Um}{Req}dt - \int_0^\tau (Cm + Ceq)Um\frac{dUm}{dt}dt$$
$$- \int_0^\tau \frac{Um^2}{Req}dt$$

The third integral is zero over one period.

Consider that Valim is a sinusoidal signal of amplitude 15 kV at 500 Hz. In a first step, it is assumed that $Cm = 1\,nF$. Note that Cm respects the condition $\mathrm{Cm} \gg \mathrm{Cd}$. The error which is made by neglecting the effect of the measuring circuit is calculated with an electrical simulation (Ltspice software).

Order of magnitude:

The absolute value of impedance is:

$$Zm = \left|\frac{1}{jC\omega}\right| = \frac{1}{2\pi\times500\times10^{-9}} = 3.2\times10^5\,\Omega, \quad Z_d = \left|\frac{1}{jC\omega}\right| = \frac{1}{2\pi\times500\times10^{-12}} = 3.2\times10^8\,\Omega$$

$$Z(Ceq) = \left|\frac{1}{jCeq\omega}\right| = \frac{1}{2\pi\times500\times11.5\times10^{-12}} = 2.8\times10^7\,\Omega,\ Z(Req) = Req = 10^7\Omega,$$

Neglecting the effect of the measuring system is equivalent to take $Req = \infty, and\ Ceq = 0$. Consequently, at the first order of approximation $Um = Valim\frac{Zm}{Zm+Zd} \cong \frac{Valim}{1000}$

$$E = Valim^2\,[\int_0^\tau (Cm + Ceq)\frac{d\left(\frac{Um}{Valim}\right)}{dt}dt + \int_0^\tau \frac{Um}{Req\,Valim}dt - 0 - \int_0^\tau \frac{Um^2}{Valim^2 Req}dt\,]$$

The second and fourth integrals are negligible compared to the first. Moreover, the fourth integral is of order 2 in Um/V_{alim}, thus negligible with respect to the second integral.

Consequently, an error of the order of $\int_0^\tau Valim\frac{Um}{Req}dt$ is commited by neglegtinc the effect of probe and oscilloscope.

$$Error \cong \int_0^\tau Valim\frac{Um}{Req}dt = \frac{15\,000^2}{2}\frac{1}{1000}\frac{1}{10^7}\times\tau = 22.5\ \mu J \ \text{ with } \tau = 2\ ms$$

The measured power is less than the actual power from $22.5\times10^{-6}\times500 = 11.3\,mW$. This error is far from negligible compared to the consumption of DBDs which is of the order of 100 mW with the same power supply.

Simulation of electrical circuit:

The software (LTspice® IV) is used to simulate the electrical circuit (Fig 28). D, Cm and Ceq are pure capacitance of 1 pF, 1nF and 11.5 pF respectively. The codes on the left are used to define the measurements made on the simulation.

"real energy" is the integral of the power received by the dipole **D** during one period of power supply (between 8 and 10 ms). The simulation gives "real energy"= -2.5 10^{-13} J, this is the order of magnitude of the numerical error committed during the simulation.

“measured energy” is the value of the energy consumed by the dipole **D**, that would be measured if the effect of the measuring system was not taken into account. The simulation gives “measured energy”= - 21.9 µJ. This value is greater than the numerical error and conforms to the order of magnitude obtained in the previous paragraph. When the power consumed by the DBD is of the order of 100 mW and elicit an underestimation of the power by approximately 10%.

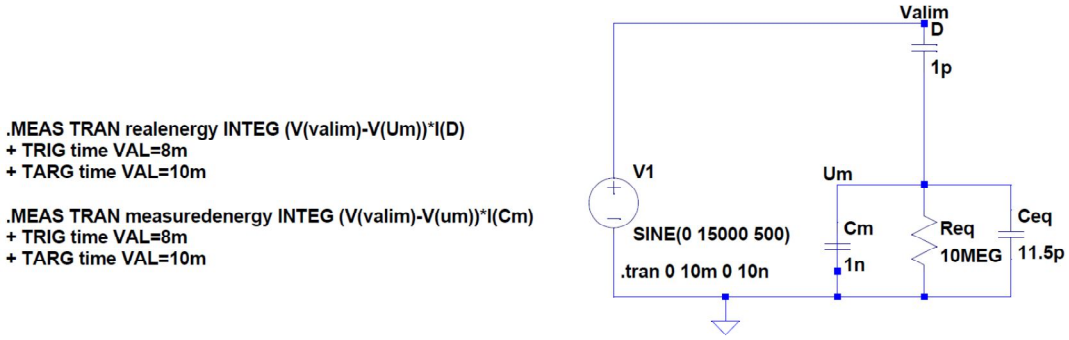

Fig 28 Left: line which enables to calculate power consumption if the effect of the probing system is taken into account or not. Right: simulated electrical circuit.

This error can be corrected with a modification of the calculations. Another solution is to increase the value of the measuring capacitor. For example, with $Cm = 100\ nF$, the **“measured energy”** is equal to -0.22 µJ which gives an error of -0.11 mW (which is $\ll 100\ mW$).

Finally, the choice of capacitance **Cm** is a compromise between the error due to probing system and the need to have a signal of sufficient amplitude for the oscilloscope. 100 nF is a good compromise because the amplitude at the terminal of **Cm** is 150 mV in the absence of plasma**.**

Among the components available in the laboratory, some capacitor previously used show a strong sensitivity to thermal variation (1 nF for few °C). Subsequently, less temperature-sensitive capacities were selected (0.1 nF for 10 K over 100 nF). The capacitance was measured with a capacitance meter (accuracy of 0.1 nF); the value was used to perform power calculations.

Power consumption is calculated in real time. The oscilloscopes used the software option “Xdev” which enables to perform the calculations. The code is written in Appendix K. After each acquisition; this code plots the integral function of instantaneous power. A temporal gate located at the end of acquisition window enables to record the energy consumption during one acquisition. The signal is acquired during the entire plasma treatment. The result is given as a mean value ±uncertainty.

The acquisition time is 2ms (= one period of the 500 Hz generator). The acquisition rate is 25 MS/s. The voltage is represented with 8 bits of memory (i.e., 256 levels of voltage, since the signal is numeric). The size of the signal should cover the entire display to obtain the best accuracy.

II.3 Chemical diagnostics

II.3.1 Fluorometry

A fluorometer is an instrument for exciting the molecules contained in a liquid at a given wavelength and to measure the fluorescence spectrum. The light source is a xenon

lamp. A monochromator enables to select the excitation wavelength λex. The bandwidth Δλex can be chosen by changing the opening of the input and output slits of the monochromator (Fig 29, left). Fluoromax-4 a fluorimeter from Horiba is used to carry out all the experiments. The excitation beam passes through a 4 ml cuvet in PMMA (Optical path of 1 cm with four optical faces). The emitted light is observed at right angle. Another monochromator enables to filter the emission spectrum. Emission wavelength and bandwidth are chosen: λem, Δλem. The light from the monochromator strikes a photomultiplier (Fig 29, right).

The photons extract electrons from a thin metallic plate called photocathode, and then these electrons are accelerated by a potential difference. These electrons gain energy. One electron extracts secondary-electrons by striking successive dynodes. The optical signal has therefore been converted into an electrical signal and amplified. The relation between optical intensity and the electrical signal delivered by the photomultiplier is nonlinear when it exceeds 10 million counts per second (CPS). A photodiode captures a portion of the light exiting the excitation monochromator. The signal of this photodiode (a current in µA) is proportional to the luminous intensity. The signal of the photodiode thus makes it possible to compensate the evolution of the intensity of the xenon lamp (and its spectrum also) over time (heating, aging of the lamp). A signal is detectable when it exceeds the average noise level by 3 times the standard deviation of the noise around its mean value.

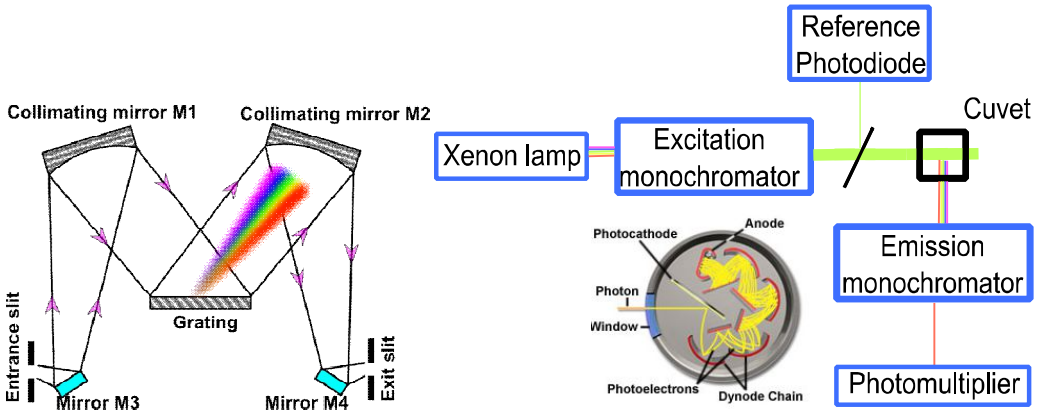

Fig 29 Left: diagram of a monochromator, the wavelength to be observed is selected by rotating the diffraction grating (1200 line / mm). The bandwidth Δλ can be chosen by changing the opening of the input and output slits of the monochromator. Right: diagram of fluorimeter and photomultiplier.

II.3.2 Quantification of Hydrogen peroxide produced by plasma

The production of H_2O_2 was measured with two independent methods. The first use the conversion of titanium(IV) oxysulfate ($TiOSO_4$) to a compound having a very high absorbance. The range of measurement is [25 µM; 5000 µM]. In the second, the production is quantified using Amplex red reagent. Amplex red react with H_2O_2 and an enzyme called horseradish peroxidase (HRP) to form the resorufin, a fluorescent compound.

II.3.2.1 Titanium(IV) oxysulfate method

Reagent. Titanium (IV) oxysulfate, $TiOSO_4$ is an intermediate product in the synthesis of the titanium dioxide TiO2, a widespread industrial product. For example, TiO2 is used as

a pigment, a food additive (sometimes in nanometric form!), a catalyst for photolysis reaction. Titanium (IV) oxysulfate ($TiOSO_4$) solution was obtained from Sigma-Aldrich (ref: 34244). In commercial solution, the concentration of TiOSO4 is close to 2 w% which corresponds to [$TiOSO_4$] ~0.13 M. The reagent is stored in an acid medium. The manual indicates that the concentration[14] of sulfuric acid is between 5 and 10 w%. $TiOSO_4$ solution is also called titanyl sulfate because Ti=02+, the titanyl ion, should exist in this solution. However, his existence was unproven in 1999 and remain controversial in 2008 according to [90] and [91].

With this concentration of H_2SO_4, and according to the literature $Ti(OH)_3HSO_{4(aq)}$ is the main species in the commercial solution of $TiOSO_4$ [90]. As the kinetics of hydrolysis is very slow [90], these species remain after a dilution by ten[15]. Consequently, this is this chemical which is in the balance of the chemical equation (and not Ti^{4+}).

Reaction with H_2O_2. $TiOSO_4$ reacts stoichiometrically with H_2O_2 and give peroxo-titanium complex. The commercial solution is dilute by ten during the experiments; therefore the pH is close to 0.82 with the assumption that the strong acid is wholly dissociated. In these conditions, according to [92], peroxo-titanium complex is $Ti(O_2)OH^+$. So, the complex formed is not H_2TIO_4 which would be a yellow solid formed after several days of reaction [92]. Consequently, the balance equation is:

$$\mathrm{Ti(OH)_3HSO_{4(aq)} + H_2O_{2(aq)} = Ti(O_2)OH^+_{(aq)} + HSO_4^-{}_{(aq)} + 2H_2O_{(l)}.}$$

For a preliminary experiment, a solution of H_2O_2 at 1.5 mM was prepared by diluting 3% hydrogen peroxide solution (Sigma-Aldrich, ref 88597) in demineralized water. 900 µL of this solution was mixed with 100 µL of the commercial $TiOSO_4$ solution. The solution is yellow; its absorbance spectrum is plotted in Fig 30.

In the same way, the blank is obtained by mixing 900 µL of water and 100 µL of $TiOSO_4$ solution. The peroxo-titanium complex has a maximum absorbance at 408 nm; this is consistent with [92] and [93].

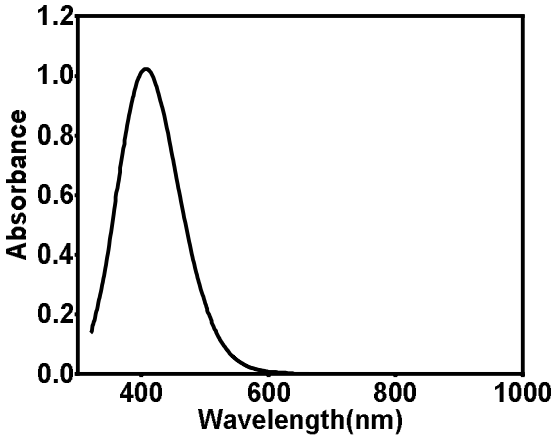

Fig 30 Absorbance curve after an addition of 100 µL of the commercial solution of $TiOSO_4$ to a solution of hydrogen peroxide in water (Volume of the sample: 900 µL, [H_2O_2] = 1.5 mM). The maximum of absorbance is obtained for $\lambda_{max} = 408\,nm$. Optical path = 1 cm.

[14] 7.5 %w corresponds to 0.76 M for sulfuric acid

[15] Several days would enable to add another OH group and form the thermodynamically stable product at this concentration of sulfuric acid

Protocol. For the quantification of H_2O_2, the protocol consists in mixing 900 µL of unknown sample (PAM), with 100 µL of the commercial solution of $TiOSO_4$. The absorbance is then measured at 408 nm using a UV-line-9100 spectrophotometer in PMMA cuvet with 1 cm of optical path. The reaction is instantaneous. If dilutions are required to fall within the operating range, they are made in water.

The buffered solutions used by biologists such as PBS (from Thermo Fisher-14200067) and RPMI (Thermo Fischer-31870017) cannot be used with this diagnostic. In this case, a precipitate is formed which give a turbid solution and disturb the measurements of absorbance (Fig 31). The precipitate is likely made of the salt NaCl and KCl. In [69] a different PBS containing 0.9 mM CaCl 2 and 0.49 mM MgCl 2 was used and no precipitation was observed.

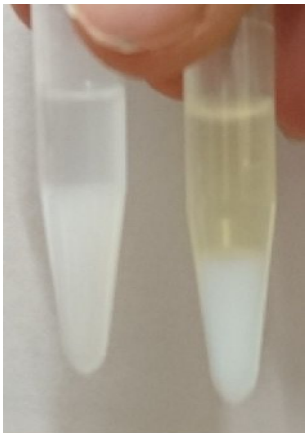

Fig 31 Left vial: 900 µL of PBS1X+100 µL of $TiOSO_4$ (2 w%) solution. Right: same solution after addition of 1µL H_2O_2 3 w%. The white precipitate distorts the absorbance measurements. Attempts to eliminate by centrifugation and filtration have failed.

Calibration curve. Hydrogen peroxide solutions were prepared by diluting 3 w% commercial solution in water. The concentration is in the range [100 µM ; 10 mM]. The previous protocol was used, solutions were made in duplicate. Above 5 mM, the absorbance is higher than 3 and spectrophotometer measurement does not work anymore (not enough intensity). Absorbance was plotted as a function of H_2O_2 concentration in the sample (Fig 32). In the range [100 µM; 5 mM], the absorbance is proportionally linked to $[H_2O_2]$. The slope is $6.79e^{-4}$ μM^{-1} and R^2= 0.99885.

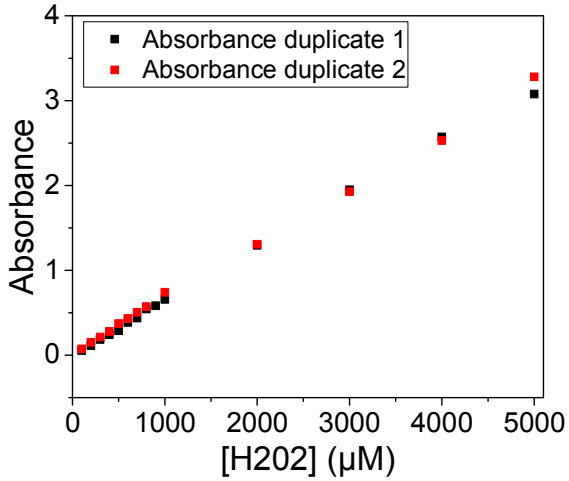

Fig 32 Calibration curve of $TiOSO_4$ diagnostic. Absorbance at λ= 408 nm as a function of $[H_2O_2]$ in the 900 µL sample. Cuvets contain 900 µL of the sample and 100 µL of the $TiOSO_4$ commercial solution.

Interferences and stability. An interference with formaldehyde CH_2O was reported in [94]. No interferences were reported for seven other species including acetone and methanol. Nitrites and nitrates interferences were tested. No significant interferences of nitrite and nitrate at 2 mM were found. This is due to the very high rate of reaction which forms a peroxo-titanium complex. The reaction between nitrite and H_2O_2, which occurs in acidic medium (like here), is rather slow [43]. That's why there is no interference when nitrite is added. Peroxo-titanium complex is also stable for several hours according to our own experiments.

II.3.2.2 Amplex red method for H_2O_2 quantification

Reagent. Amplex red (10-Acetyl-3,7-dihydroxyphenoxazine, Fig 33) was purchased from Sigma-Aldrich (92001 Ampliflu ™ Red kit). There is 1 mg of reagent in each of the 10 vials. A stock solution of Amplex red is prepared, by adding 388.7 µL of DMSO in a vial, leading to a 10 mM Amplex red solution. Stock solutions are protected from light and stored at 2-8 °C during one month. Amplex red may be used for in-vitro experiments.

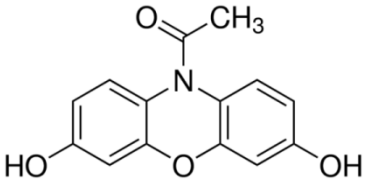

Fig 33 Structure of 10-Acetyl-3,7-dihydroxyphenoxazine (Amplex-red)

Horseradish peroxidase (HRP) is isolated from horseradish roots (*Amoracia rusticana*). HRP is a single chain polypeptide containing four disulfide bridges. At least seven isozymes of HRP exist. HRP Type VI-A was from Sigma-Aldrich (6782-10MG), this is a lyophilized powder.The amount of enzyme is close to 300 units/mg solid. One unit forms 1.0 mg purpurogallin from pyrogallol in 20 sec at pH 6.0 at 20 °C. 1 mg of HRP is diluted in 2 ml of deionized water. This solution was diluted by 10 in water. Twenty solutions of 1 mL were prepared and stored in the fridge at - 20°C. Each aliquot contains 15 unit of HRP.

Sodium azide (NaN3), cyanide, L-cystine, dichromate, ethylene thiourea, hydroxylamine, sulfide, vanadate, p-aminobenzoic acid, as well as Cd^{2+}, Co^{2+}, Cu^{2+}, Fe^{3+}, Mn^{2+}, Ni^{2+}, and Pb^{2+} ions are found to inhibit the enzyme activity. So, Azide, which is often used to scavenge nitrite, cannot be used with this diagnostic.

II.3.2.2.1 Reaction with H_2O_2. Interferences and stability

HRP form a complex with H_2O_2. This molecule, HRP-H_2O_2, reacts stoichiometrically with Amplex Red and release resorufin, a fluorescent compound (Fig 34). This method has a higher sensitivity to H_2O_2 than the diagnostic which uses $TiOSO_4$. Indeed, the range of detection of $TiOSO_4$ is [100 µM; 5mM] whereas the following protocol gives [5 µM, 80 µM].

Amplex red can be used in PBS whereas $TiOSO_4$ causes precipitation. However, the selectivity of Amplex red is lower than those of $TiOSO_4$. For instance, the five following dietary antioxidants induce an artifactual[16] increase of fluorescence: Gallic acid, Ascorbic acid, (-)-Epicatechin, Quercetin and Vanillic acid [95].

[16] The interaction between HRP and antioxidants could explain some paradoxical observation: in some case adding an antioxidant increase the oxidation of AR to resorufin [95]. We have the impression to detect more oxidants by adding antioxidants...

Oxidation of Amplex red can be induced by exposure to light [96]**.** Ambient light or light use for measurement can induce this photooxidation. The residual resorufin in Amplex-red stock solution is excited by the light and react with Amplex red which gives a new molecule of resorufin. Both NADH (b-nicotinamide adenine dinucleotide) and reduced glutathione (GSH) react with HRP to generate H_2O_2 that can subsequently oxidize Amplex-red [97]. This diagnostic must, therefore, be used with caution to quantify the production of H_2O_2 during *in-vitro* experiments [1].

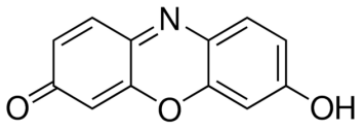

Fig 34 Structure of resorufin. Excitation wavelength: maximum at 571 nm. Emission wavelength: maximum at 585 nm.

II.3.2.2.2 Protocol and calibration curve

Before the experiment, 1 ml solution of HRP 15 U/ml is diluted by ten in water or PBS leading to 10 ml at 1.5 U/ml (solution HRP-A). 50 µl of the 10 mM stock solution of Amplex red is diluted in 10 mL of water or PBS, leading to 10 mL at 50 µM (solution AR-A).

The following reagents are introduced in a fluorimetric cuvet with this order: 50 µl of HRP-A, 3 ml of water or PBS, 100 µL of AR-A, 50 µL of a sample containing H_2O_2 in the range [5 µM, 80 µM] and 1 ml of water or PBS (for homogenization). After 20 of min incubation in the dark: the fluorescence signal is detected with excitation wavelengths at 571 nm and emission wavelength 585 nm. The final solution is characterized by the following concentrations: $[Amplex\ red] = 1.25\ \mu M$ and $[HRP] = 6.2 \times 10^{-2}\ U/ml$.

The solvent is the same to prepare the dilutions of the reagents and PAM samples. Fig 35 shows the fluorescence signal in Count Per Second (CPS) as a function of [H_2O_2] in the sample. The fluorescence is acquired with the following set of parameters: excitation wavelength λex = 571 (bandpass Δλex= 1 nm) and an emission wavelength λem = 585 (bandpass Δλem= 1 nm). The saturation of the signal is simply due to an excess of H_2O_2, and not to the saturation of the photomultiplier.

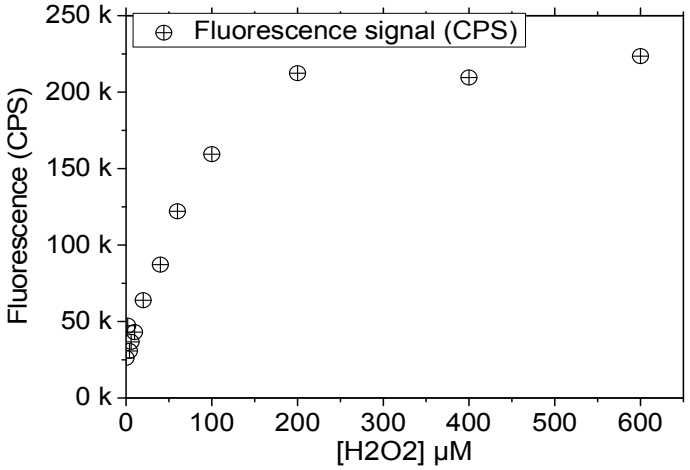

Fig 35 Fluorescence signal in CPS of Amplex-red reagent after reaction with HRP-H_2O_2 complex. λex = 571, Δλ= 1 nm, λem = 585, Δλ= 1 nm. Time of acquisition: 3s (integration time = 0.1 s per measure).

Fig 36 shows the fluorescence signal in the range of concentration [5 µM; 200 µM]. Beyond 100 µM, the fluorescence no longer depends linearly on the amount of H_2O_2 added. The fluorescence is acquired with the set of parameter (λex = 571, Δλex= 1 nm, λem = 585, Δλem= 2 nm).

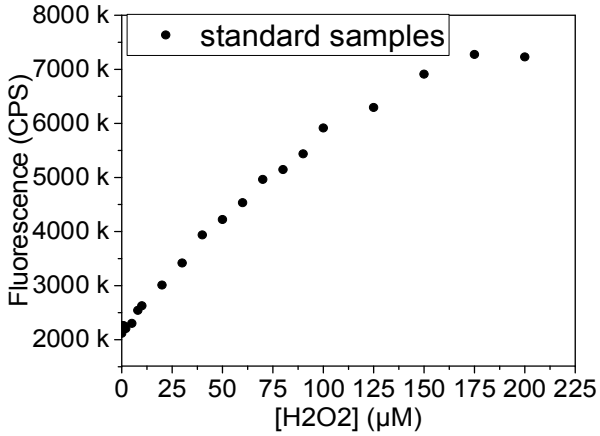

Fig 36 Fluorescence signal in CPS of Amplex-red reagent after reaction with HRP-H_2O_2 complex. λex = 571, Δλ= 1 nm, λem = 585, Δλ= 2 nm. Time of acquisition: 3s (integration time = 0.1 s per measure), 10 accumulations.

In the last version of the protocol, the excitation and emission slits have respectively 1 nm and 5 nm bandpass. The concentrations and the volumes used to prepare the dilutions are the same than those of the previous paragraph. Each acquisition lasts six[17] seconds. Care must be taken to avoid the saturation[18] of the photomultiplier. On Fig 37, a calibration curve is acquired in triplicate. Error bar represents the standard deviation. The error bar is smaller than the size of the dots for six points. The signal represented (S1/R1) is the ratio of the signal of the photomultiplier in CPS by the signal of the reference photodiode in µA. The calibration curve must be done for each experiment at the same time as the samples.

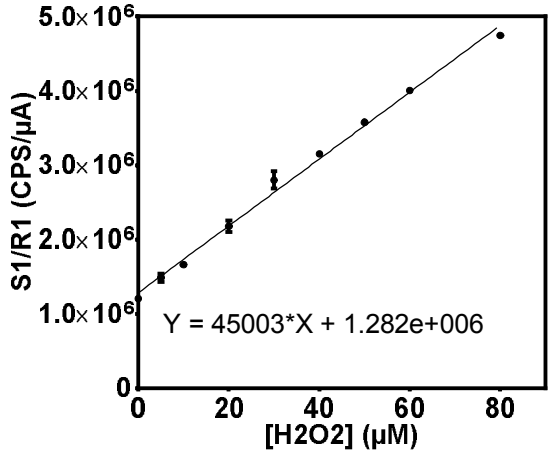

Fig 37 Example of calibration curve obtained with standard solutions of H_2O_2, S1/R1 in CPS/µA as a function of [H_2O_2]. According to the standard protocol: λex = 571/1 nm, λem = 585/5 nm, acquisition time = 6 s (60 points, integration time of 0.1 s per point). The calibration protocol was repeated for each experiment (same incubation time, similar handling conditions and light exposure...).

[17] The 60 measurement points are acquired in 6 s, integration time of 0.1 s for each point.
[18] which occurs when the signal is greater than 10^7 CPS

II.3.3 Measure nitrite and nitrate concentrations

There are several commercial kits for measuring the concentration of nitrite in a liquid, in an extracellular sample or intracellularly. Most kits producing a fluorescent compound are based on the transformation of 2,3-diaminonaphthalene (DAN) in 2,3-naphthotriazole (NAT), a highly fluorescent product in acidic condition. The kits based on an absorbance usually use Griess reagent or one of its variants. In all cases, the reaction has a step in acidic medium. Griess reagent is a blend of sulfanilic acid and 2-Naphthylamine. At low pH, nitrous acid HNO_2 reacts with sulfanilic acid to form a diazonium (Fig 38). 2-Naphthylamine reacts with this diazonium (diazo-coupling) to form a compound absorbing in the visible.

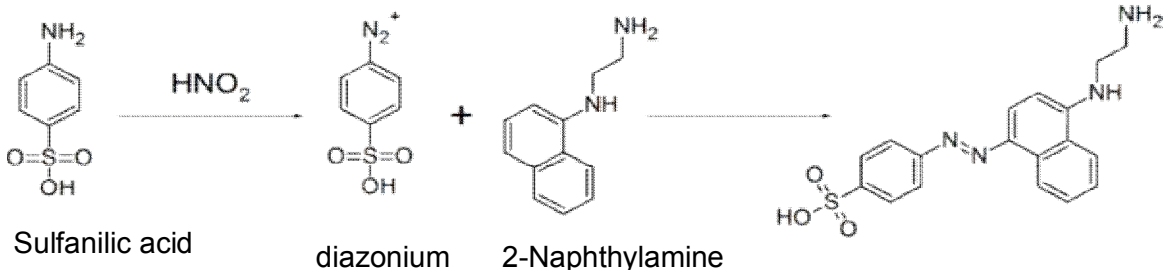

Fig 38 Chemical reactions of Griess assay. The sulfanilic acid reacts with nitrite in acidic conditions.

Scavenger

Two scavengers are usually used against nitrite: sulfamic acid and Sodium Azide. It is better to avoid putting these species in solution when the plasma is on because they can interfere with short-lived RONS. For example, according to [98], the reaction between Azide[19] and ozone can be used to synthesize peroxynitrite.

II.3.3.1 Dealing with Griess Reagents interference

The reagent used is a blend of Griess reagent and concentrated acetic acid (Sigma-Aldrich, 03553-100mL). A nitrite solution at 10 µM was prepared by diluting the commercial solution at 0.1 M in demineralized water. The absorbance spectrum of the compound is measured by UVLINE 9100 spectrophotometer (Cloup®, Fig 39). The sample was made by mixing 975 µl of 10 µM nitrite with 25 µl of the Griess reagent commercial solution. The blank is obtained by mixing 975 µl of water with 25 µl of Griess reagent. The absorbance peak is at 522 nm.

[19] This product is particularly dangerous because of its high toxicity, and its ability to generate explosive compounds.

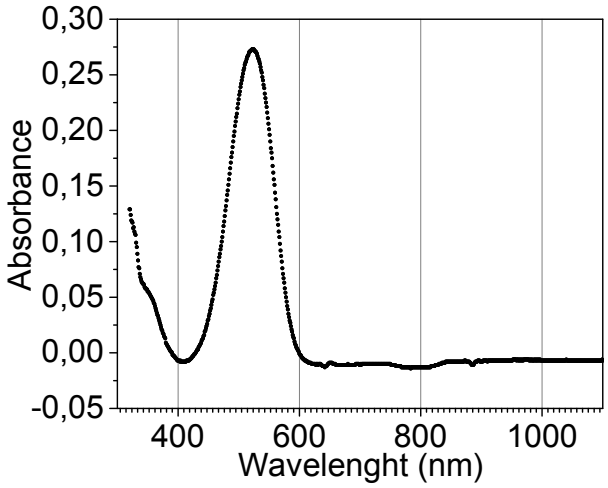

Fig 39 absorbance spectrum of a nitrite solution (10 µM).

The reaction kinetics was studied to develop the diagnostic. Standard solutions of nitrites were prepared. 975 µl of these solutions were mixed with 25 µl of Griess reagent. The absorbance was measured 10 min or 30 min after the mixing at a wavelength of 522 nm. Blank solution was prepared by mixing 975 µl of water and 25 µl of Griess reagent. Each sample is measured twice in 4 mL cuvet with four optical faces. Each cuvet is rotated by 90° between the two measurements denoted “A” and “B” in Fig 40.

It appears that the solution did not reach a steady state after 10 min of incubation since the absorbance at 30 min is significantly higher than those at 10 min.

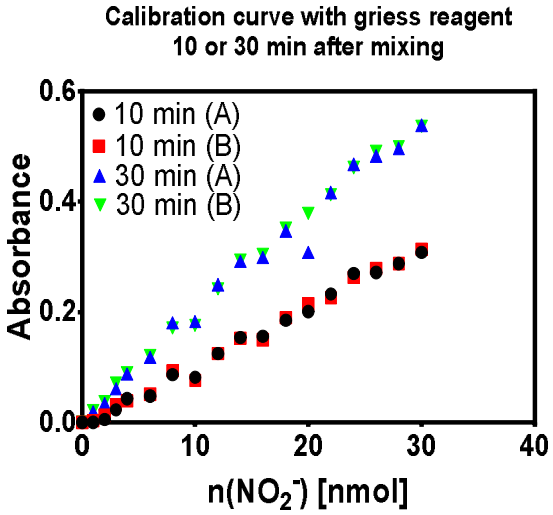

Fig 40 Absorbance at 522 nm measured 10 or 30 min after mixing as a function of the amount of nitrite in the cuvet. 25 µL of Griess reagent + 975 µL of nitrite solutions.

Moreover, it appears that the difference of the absorbance measured at two different times (10 and 30 min) and in the same cuvet is proportional to the concentration of nitrite. Indeed $\Delta abs = Abs(30\,min) - Abs(10\,min)$ plotted in Fig 41 is a line, the kinetics of the reaction should be of order 1 relatively to nitrite concentration.

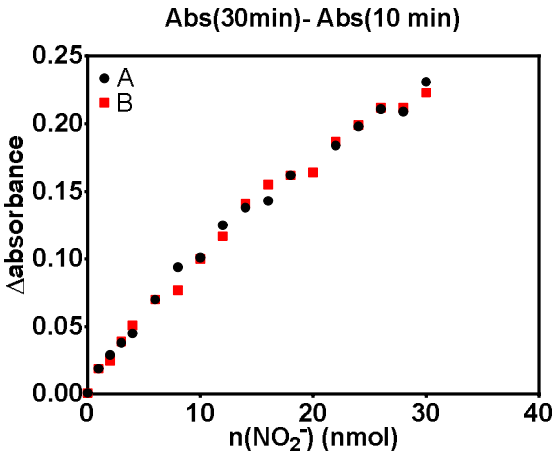

Fig 41 $\Delta abs = Abs(30\,min) - Abs(10\,\mathrm{min})$ as a function of nitrite concentration. The line mean that the kinetics is of order 1 with respect to [NO_2].

The absorbance of the cuvet containing 30 nmol of nitrites was followed over time (Fig 42). It is clear that the steady state is not reached, even after 80 min of reaction. Consequently, the protocol must be modified since it is easier to obtain a reliable and sensitive measurement when the stationary state of the dosing reaction is reached.

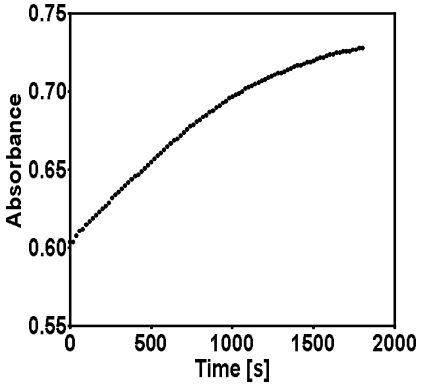

Fig 42 Kinetics of Griess reaction 50 to 80 min after the mixing. Absorbance at 522 nm as a function of time. The cuvet contains 30 nmol of nitrite. Total volume = 1 mL, volume of Griess reagent = 25 µL.

A slow reaction is not an issue when the probed product is stable. In the context of plasma-liquid interaction, the nitrites react with H_2O_2 in acidic medium to form peroxynitrite that quickly gives nitrate and hydroxyl radicals. Consequently, it is preferable to have a faster reaction to minimize this bias. The speed of reaction is increased by multiplying the amount of Griess reagent by four so that the reaction reaches the steady state after only 15 min (Fig 43).

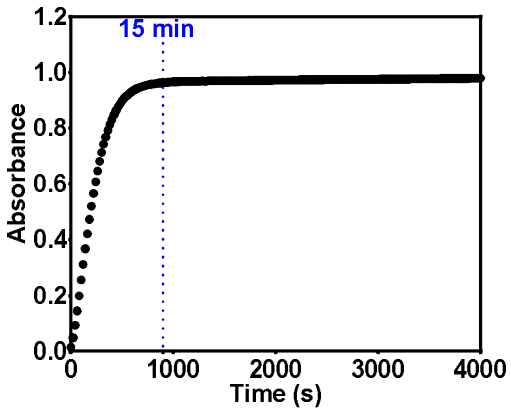

Fig 43 Absorbance at 522 nm as a function of time. 30 nmol of nitrite in the cuvet, total volume = 1 mL, volume of Griess reagent = 100 µL. The concentration of Griess reagent is greater than in the previous experiment consequently the reaction reaches a steady state in less than 15 minutes.

The operating range of the diagnostic was determined: 100 µL of Griess reagent was mixed with 900 µl of standards samples. The absorbance was measured at 522 nm after 20 min of incubation (Fig 44). It appears that the range of nitrite concentration which gives a linear response is between 0 and 60 µM (red dots). An uncertainty[20] of 0.010 can be attributed to each measure. Since the sample of concentration $[NO_2^-] = 1\,\mu M$ has an absorbance of 0.035 which represents three times the level of uncertainties, we can define the operating range of the diagnostic with the interval [1; 60 µM].

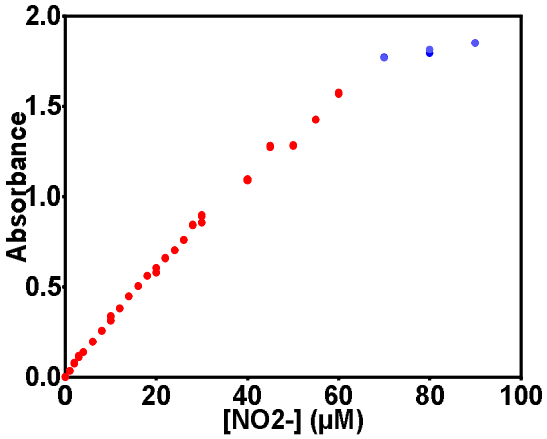

Fig 44 Absorbance after reaction with nitrite in deionized water. Absorbance of nitrites samples (522 nm) as a function of the nitrite concentration contained in the 900 µL sample. 100 µL of Griess reagent was added 20 min before absorbance measurement. The red dots are in the range of linearity of the diagnostics, not the blue ones.

PAM contains H_2O_2. The addition of 100 µL of Griess reagent containing concentrated acetic acid decreases the pH (pH~2). At low pH, the peroxynitrite formation reaction is significantly accelerated[21] [99]. Consequently, it is necessary to study if the presence of H_2O_2 interferes with the diagnostic or not. Solutions containing nitrites and hydrogen peroxide were prepared. The concentration of H_2O_2 is 2 mM. This is ten times the typical concentration obtains after treatment of 4 min (Chapter III). Nitrite concentration is

[20] this value is obtained by repeating the measurement in several cuvets containing the same solution. The standard deviation of the distribution was ~10^{-2}.
[21] since the speed of the reaction which form peroxinitrite is proportional to [H+].

chosen in the interval [1 µm; 80 µM]. The previous protocol of measurement was used. Three groups were prepared and measured (Fig 45).

The red dots correspond to pure nitrite samples. **The black dots** correspond to the samples which contain H_2O_2 and nitrite. The protocol of measurement started just after the mixing of the two species: Griess reagent was added at the same time than H_2O_2. **The blue dots** correspond to the samples which contain H_2O_2 and nitrite. In this case, the protocol was started[22] 60 minutes after the mixing.

Since **the blue dots** are below **black** and **red** dots, it appears that the presence of H_2O_2 disturbs the protocol. This supports the assumption that H_2O_2 destroyed nitrite to produce peroxynitrite before the production of the diazonium. The fact that the blue dots are slightly below[23] the black ones show that nitrites are destroyed, even at higher[24] pH.

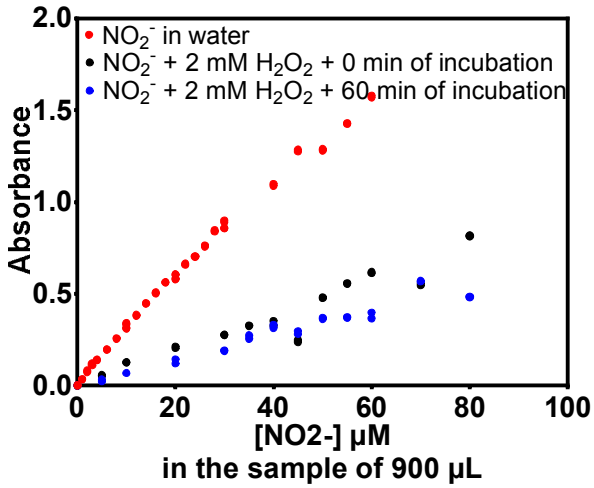

Fig 45 Absorbance of the samples at 522 nm as a function of nitrite concentration. Red : nitrite without H_2O_2, Black : [H_2O_2]= 2 mM, Blue : [H_2O_2]= 2 mM + 60 min of incubation before the addition of Griess reagent.

The interference with H_2O_2 is avoided by adding Catalase enzyme in the liquid before the addition of Griess reagent (10 µl of a solution prepared by the dissolution of 10 mg in 1 mL). Another solution is to use diluted solutions of nitrites in buffer (PBS 1X or 10X) that will prevent the pH from falling too much.

Fig 46 **the red dots** represent the absorbance of the pure nitrite solutions in PBS. **The blue dots** correspond to the solutions containing nitrites and H_2O_2 (2 mM). The protocol was initiated after 60 min incubation of the mixing of H_2O_2 with NO_2^-.

The fact that the two sets of points are on the same line show that the interference due to the presence of H_2O_2 has been avoided. PBS enables to obtain a pH~4 (rather than 1-2) after the addition of Griess reagent. The pH is low enough to produce the diazonium at a significant rate in such a way that the production of peroxynitrite is negligible compared to diazonium production. The slope of the calibration curve enables to know the concentration of nitrite. It was also checked that nitrates do not form a colored compound with Griess reagent. Finally, this protocol is specific for NO_2^- with respect to NO_3^- and H_2O_2 in the range [1, 60 µM]. Similarly, it has been shown that the addition of

[22] which means that 100µL of Griess reagent are added to 900 µL of sample.
[23] except two points attributable to an experimental error
[24] but at a much lower rate of what is observed in acidic conditions

Catalase mentioned above does not disturb[25] the measurement. The protocol obtained is specific for nitrites.

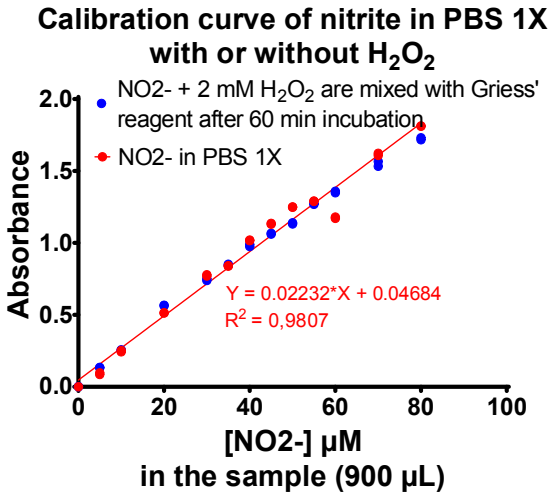

Fig 46 Absorbance at 522 nm as a function of nitrite concentration. Red dots: solutions of nitrite in PBS 1X. Blue dots: [H_2O_2]= 2 mM + 60 min of incubation. Since the pH does not decrease too much, the reaction producing the peroxynitrites (and destroying the nitrites) is kinetically disadvantageous compared to the reaction which forms the diazonium.

II.3.3.2 Quantification of nitrate

In the previous section, we explained how and especially why it was necessary to adapt the nitrite measurement protocols. The problem arises in the same form regarding the determination of nitrates, since the majority of the kits transform the nitrates into nitrites before dosing them.

Standard solutions are prepared from sodium nitrate powder (Sigma-Aldrich, ref S5506-250G-D). The solubility is about 1kg/l in water. Culture media such RPMI-1640 contains nitrates. Consequently, the quantification of the production due to plasma-liquid interaction may be inaccurate in such media.

Nitrate reductase method (kit Sigma-Aldrich)

Material. Nitrite/Nitrate Assay kit was obtained from Sigma-Aldrich (23479). This kit was used in accordance with manual instructions with the exception of two points. First, catalase (C1345, Sigma-Aldrich) was added to the sample to destroy H_2O_2 and avoid the formation of peroxynitrite from H_2O_2 and nitrite. Second, 300 µL of PBS 1X were added just before the measurement of absorbance to obtain a sufficient volume to fill the cuvets of the spectrophotometer (UV-line 9100, Cloup®).

Protocol. First PAMs are prepared for several sets of parameters (time, height above the liquid, voltage, He flow). Then, 10 µL of a solution of bovine liver catalase (10 mg/ml) is added to destroy H_2O_2. Quantification of nitrites is done independently using the protocol described in the previous section using the Griess reagents for microscopy. 80 µL of PAM diluted in the buffer for reaching the range of measurement are mixed with Nitrate Reductase and co-factor. In the process, NO_3^- is converted to NO_2^- by the enzyme Nitrate Reductase. After 2h of incubation at ambient temperature Griess

[25] Unless the concentration of Catalase is too high, but the value mentioned in the text enables to destroy the H_2O_2 produced by the plasma in a few minutes without disturbing the absorbance measurement. The calibration curves were redone.

reagents are added. The absorbance at 540 nm is given by the UV-line9100 spectrophotometer. The result is the sum of nitrite and nitrate concentration. The calibration solutions are included in the kit.

Electrochemistry

pH measurements were made with a glass electrode (Consort, ref: SP10B). Some concentration of nitrate was measured with an ion selective electrode (CONSORT, ref: ISE31B). The range of measurement is [6 µM; 1M]. Following species cause interferences: I^-, ClO_4^-, CN^-, BF, NO_2^-. This electrode has a polymer membrane, which consists of ion-exchange materials in an inert matrix: PVC or polythene. The potential at the membrane surface is related to [NO_3^-]. We noticed that the interference of nitrite could be corrected if [NO_2-] is known. The major drawback is that the time required to measure one point is particularly long (several minutes + time of cleaning of the probe between each point). This diagnostic confirmed the measurements obtained with the kit of Sigma-Aldrich.

II.3.4 Quantification of hydroxyl radical produced by plasma

II.3.4.1 Terephthalic acid (TPA) method

Terephthalic acid (TPA) (ref 185361) and 2-hydroxyterephtalic acid (ref 752525) were purchased from Sigma-Aldrich. A fluorometer (fluoromax-4 from Horiba) was used for fluorescence measurement. Fig 47 shows the balance of the reactions which occurs between terephthalic acid, a non-fluorescent compound, and hydroxyl radical. The main product is 2-hydroxyterephtalic acid (TPA-OH) which is a fluorescent compound with an excitation wavelength of 317 nm and an emission wavelength at 433 nm.

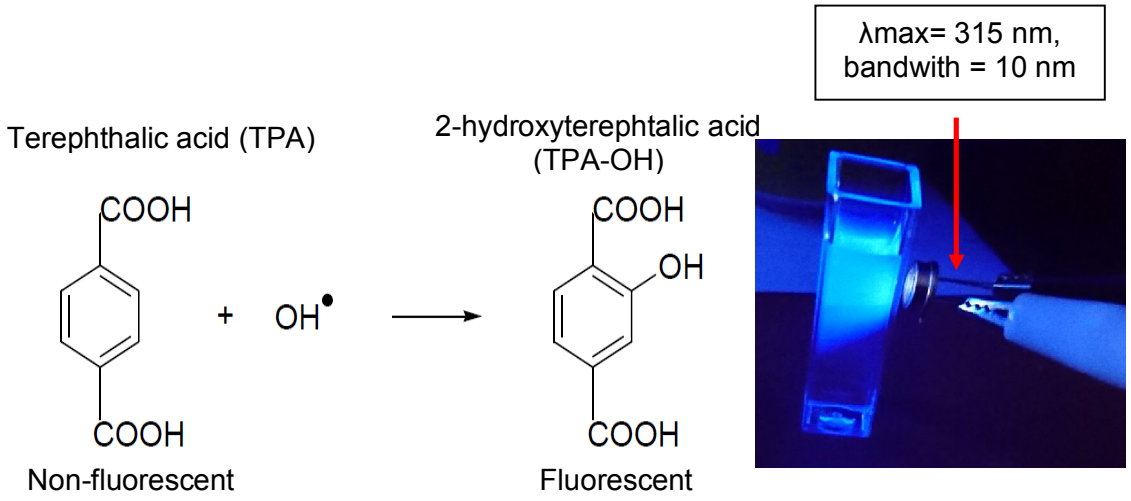

Fig 47 Left: balance equation of the hydroxylation of terephthalic acid (TPA) to 2-hydroxyterephtalic acid (TPA-OH). Right: cuvet filled with a solution of TPA in KOH treated by plasma. [OH-]=20 mM and [TPA] =4.1 mM. LED emits at 315 nm with a bandpass of 10 nm. Before plasma treatment, no fluorescence is visible. After treatment, the fluorescence is clearly visible. The measurements are made in PMMA cuvets

Standard solutions are prepared with 2-hydroxyterephtalic acid (TPA-OH). KOH solutions are added to the samples so that the pH is the same in samples and standard solutions. Excitation and emission spectra were acquired to optimize the sensitivity by selecting the excitation and emission wavelengths. Excitation spectrum is plotted in Fig 48. The central wavelength of excitation is changed while emission wavelength is fixed at

434 nm. This curve answer to the question: **what wavelength is the most effective to excite the targeted molecule?**

Since the spectrum of the xenon lamp exciting the medium is not flat, the fluorescence signal (in CPS) at one wavelength is divided by the reference signal (in µA). The reference signal is acquired with a photodiode measuring a fraction of the light at the output of the excitation monochromator. For small wavelengths (λ<240 nm) the intensity emitted by the xenon lamp is so small that the signal reaches the level of the noise. This can explain why the fluorescence signal (in CPS/ µA) is noisy at low wavelength (Fig 48).

The mean value of the signal is high at small wavelength. This is probably explained by the fact that the electrical delivered by the photomultiplier has a small offset (due to dark current). Consequently, the signal at small wavelength comes from the noise and has no chemical sense. It also appears that the most efficient wavelength for exciting TPA-OH is 318 nm.

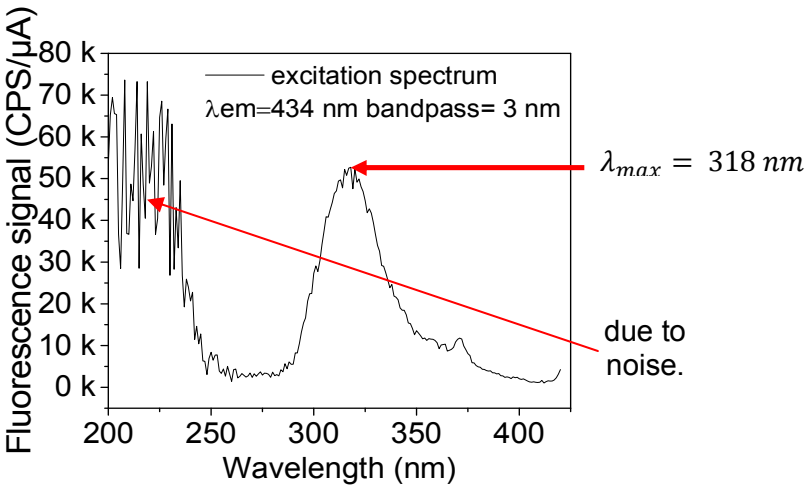

Fig 48 Excitation spectrum of TPA-OH. The central wavelength of excitation is changed while emission wavelength is fixed at 434 nm. The signal at small wavelength is probably due to noise and has no sense. For wavelength higher than 250 nm, the signal is significant. Thus, the most efficient wavelength for exciting TPA-OH is 318 nm.

The emission spectrum is plotted in Fig 49. The central wavelength of emission is changed while excitation wavelength is fixed at 310 nm. This curve is an answer to the question: **what wavelength is the most effective to obtain the best sensitivity and selectivity of the fluorescent molecule?**

Since a fixed wavelength is used, it is possible to represent only the response of photomultiplier as a function of excitation wavelength, without dividing it by reference signal. Moreover, it appears that the signal delivered above 10 million CPS is no longer linear. So, it is careful to plot some values in CPS to avoid the saturation. The maximum emission is found at 435 nm; this is consistent with reported value. The excitation/emission couple chosen is therefore 317/435 nm with bandpass Δλ= 5 nm for excitation and emission. Up to one day, the fluorescence of the solutions did not evolve significantly when the solutions are stored at 4 °C in the dark.

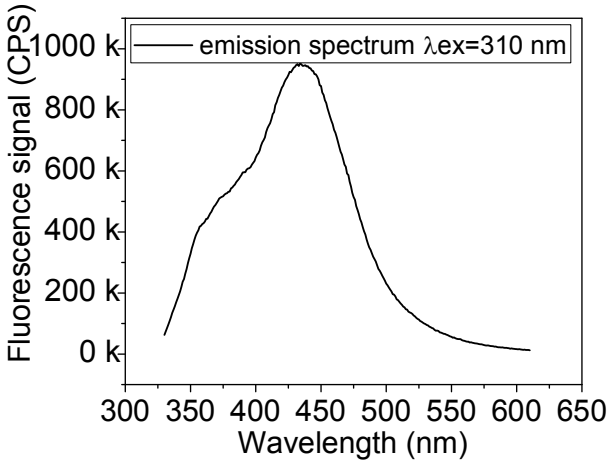

Fig 49 Emission spectrum of TPA-OH. The maximum emission wavelength 435 nm.

II.3.4.2 Which calibration?

The Fenton reaction is the reaction that occurs between Fe^{2+} and hydrogen peroxide and releases hydroxyl radicals HO° (Fig 50). This reaction[26] is often used to explain why some RONS, which are not very reactive (like H_2O_2) can induce severe damage to living organisms. In fact, the situation is not so simple since the metal atoms at the origin of the homolytic rupture of the O-O bonds in H_2O_2 are often linked or even chelated by many biological molecules. It turns out that it is not obvious to guess if these interactions speed up or slow down the Fenton reactions [100]. Here, the question is to known if it is relevant to use this reaction in calibration purpose[27].

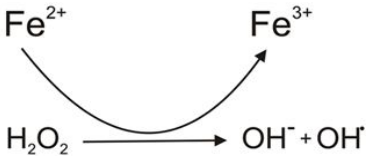

Fig 50 The Fenton reaction. The oxidation of Fe^{2+} in Fe^{3+} enables fast production of HO° from H_2O_2.

At first sight, this reaction to look like a very convenient method and some experiments were done to test this idea. The solutions whose compositions are indicated below have been prepared in spectroscopic cuvets:

- 500 µL of TPA solution at a concentration of 4.1 mM,
- a volume **V** of Fe^{2+} solution diluted in demineralized water with [Fe^{2+}] = 200 µM and V in the range [5; 500 µL].
- The same volume **V** of a hydrogen peroxide solution diluted in demineralized water with [H_2O_2]= 200 µM.
- $1500 - 2V$ μL of demineralized, so that the final volume is 2 mL.

[26] and the Fenton-like reactions which take place with another metal atom, for example Cu.
[27] The question arises from a discussion with one of our Japanese colleagues who claims that his measurement was “obviously” valid since the Fenton reaction was used to calibrate the diagnostic.

The experiments were done in triplicate. Fluorescence measurements were made after 10 min of incubation. Fluorometer parameters are λex=317 nm, λem=435 nm, Δλ= 5 nm for excitation, emission and bandpass. Fig 51 shows the fluorescence signal as a function of the amount of H_2O_2 introduced.

It appears that the reproducibility of the triplicate is excellent. The value of the fluorescence is in the range of linearity of the photomultiplier with the exception of the last point[28]. The six other points are in the range of linearity. The slope is **30 kCPS/µA per nmol** of H_2O_2 introduced in 2000 µL which represents a slope of **60 kCPS/µA/µM** in terms of concentration. With such characteristic (linearity, sensitivity), Fenton's reaction seems very attractive and therefore some group use Fenton reaction for calibrations purpose. However...

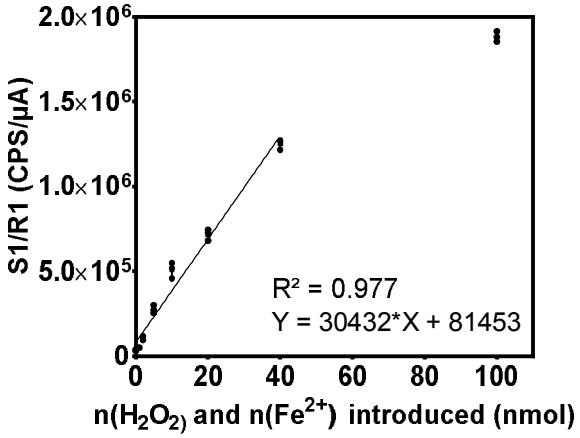

Fig 51 fluorescence signal in CPS/µA as a function of the amount of H_2O_2 or Fe^{2+} introduced in solution. The slope of the linear fit is 30432 CPS/µA/nmol. In order to compare this value with the other calibration method, it is interesting to have the slope as a function of the concentration of H_2O_2 introduced in 2 mL. it would be [TPA-OH] if all the reactions (Fenton and hydroxylation) had a yield of 100%. Slope is: 60864 CPS/µA/µM

However, this approach failed because Fenton reaction does not produce only free HO° radical [101], [102]. HO° stay in the vicinity of Fe ions. The relevant reagent is a complex of Fe whose one of the water molecule is replaced by HO°. These complexes also have strong oxidizing properties, but, unfortunately, their reactivity is quite different from those of free HO° and explained the rate of Fenton reaction [103].

Saran et al. show that these complex considerably changes[29] the reactivity during the hydroxylation of terephthalic acid [102]. It appears that the reaction which produces TPA-OH from TPA is a multi-step reaction. One of these steps implies the oxidation of the aromatic ring by dissolved oxygen. The yield of formation of TPA-OH change when oxygen is replaced by one of these complexes. Moreover, the rate of reaction becomes sensitive to pH (Fig 52), and manual mixing of the component can induce concentrations inhomogeneity which modify the yield [104].

Consequently, even if the yield[30] of the reaction "TPA + free radical HO°" is known; since radiolysis experiments produced free HO° like the plasma-liquid interaction. The calibration with Fenton reaction is false because they are unable to reproduce the yield of reaction between TPA with free HO°.

---

[28] signal of photomultiplier is close to 12 millions of CPS, that give 1.8 million (CPS/µA)
[29] Compare to the reactivity observed with the free HO° produced by $\gamma - radiolysis$
[30] 35% in the presence of oxygen according to radiolysis experiments [105]

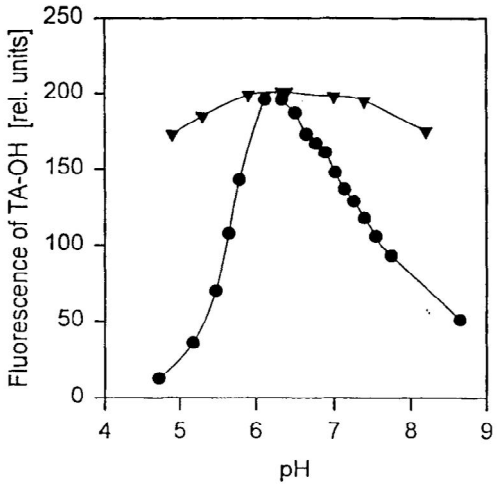

Fig 52 Figure and legend adapted from the work of Saran et al. [102]. It appears that the hydroxylation of terephthalic acid by crypto-OH° (e.g., the radical constituted by the bonding of OH° to the metal atom having catalyzed the breaking of the O-O bond) strongly depends on pH whereas hydroxylation by free OH° is almost independent of pH. The curve for free OH° (triangles) was obtained by gamma-irradiation of TPA-containing 50mM phosphate buffer; that for crypto-OH° (circles) by injecting boli of 8 µM FeSO4 into phosphate buffer containing 460 µM TPA; pH was adjusted by mixing Na2HPO4 and NaH2PO4.

The solution is to calibrate the fluorescence measurements with TPA-OH solutions. By doing this, the fluorescence signal obtained can be associated with the amount of TPA-OH present in solution.

Standards samples were prepared from TPA-OH (ref 752525), a yellow solid.

19.6 mg of TPA-OH (182.13 g/mol) was dissolved in 250 mL of deionized water. We obtain a 0.43 mM solution. Standard solutions were prepared by dilution of this solution in a KOH solution (20 mM) in water. Fluorometer parameter are λex=317nm, λem=435nm, with Δλ= 5 nm for excitation and emission. S1/R1 signal of standard samples (i.e., the ratio of photomultiplier signal and reference photodiode signal, section II.3.1) is plotted on Fig 53. There is a linear relationship between the concentration of TPA-OH and fluorescence up to 3 µM. The slope[31] is **601 000 CPS/µA/µM**. At higher concentration than 3 µM, the fluorescence increases nonlinearly and then decreases[32]. It is found that the slope of this curve is ten times the slope of the curve obtained with the Fenton reaction, which means that the succession of Fenton and hydroxylation reactions has a yield of the order of 10%.

This is the experimental confirmation that the use of the Fenton reaction should be avoided for calibration purpose. At this point, the reader should notice that we do not have a calibrated diagnostic of the hydroxyl radical. The yield of the reaction which produces TPA-OH from TPA and HO° is still to be discussed. At first glance, the solution seems simple too: the efficiency of the reaction was measured during the radiolysis experiment, and for our working conditions (saturated solution in air) the yields should be around 35% [106].

However, it turns out that the question of the yield is more complex than expected. We will see that plasma-liquid interaction experiments do not produce HO° in the same

[31] the experiments presented in section III.5.3 are made with another brand of optical cuvet, in this case: the slope of the calibration curve is: 426885 ± 7522 CPS/µA /µM of TPA-OH

[32] This decrease is probably due to self-absorption: the wavelength of emission of TPA-OH molecule is immediately reabsorbed by the fluorophore itself.

range of concentrations than water radiolysis. Since the rate of recombination of HO° depends greatly on this concentration, we will see that a sufficient concentration in TPA should be chosen to avoid that the reaction producing TPA-OH loses the competition against the recombination reaction of two hydroxyl radicals. We will see that what appeared at the beginning as an additional complexity, enables obtain information on the liquid phase over the lifetime of HO° (few ns). This discussion is exposed in section III.5 (page 82).

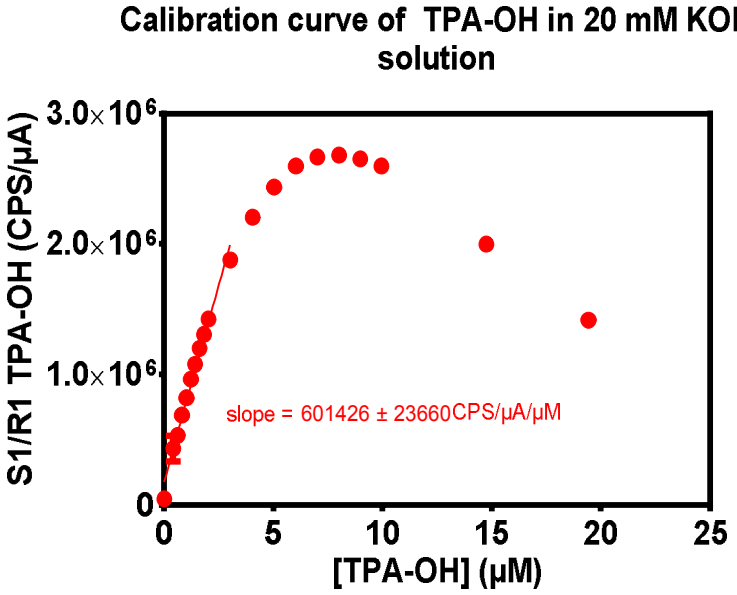

Fig 53 fluorescence signal S1/R1 of standard samples as a function of [TPA-OH]. There is a linear relationship between TPA-OH concentration and fluorescence signal up to 3 µM. For higher concentration fluorescence increases nonlinearly and then decreases. This decrease is probably due to the self-absorption of TPA-OH molecule.

II.4 In vitro experiments

These experiments took place at hospital Pitié-Salpêtrière in the team of François Lemoine from CIMI laboratory (CIMI-Paris - UPMC UMRS CR7, INSERM U1135, CNRS ERL 8255).

II.4.1 Cell Number

In vitro experiments were performed with two cell lines: TC1 and NR-S1. TC-1 cell line (CRL-2785; American Type Culture Collection [ATCC]) is an immortalized, C57Bl/6-derived, mouse epithelial cell line that expresses HPV-oncoproteins E6 and E7. NR-S1 cells were derived from a spontaneous oral carcinoma in C3H mice. These cells do not express HPV-16 oncoproteins [107]. More information can be found about the lines in the references [108]–[110].

The cells were plated in 12 or 24 wells plastic plates (Costar®) at a density of 30 000 cells/well (24-well plates) and 60 000 cells/well (12-wells plate). Cells were grown for 24 hours at 37°C, 5% CO_2. Cultures were performed in complete culture medium that corresponds to Roswell Park Memorial Institute RPMI-1640 medium containing 10% Fetal Bovine Serum (FBS) and supplemented with 100 U/ml penicillin, and 100 µg/ml streptomycin (Invitrogen). Before treatment, the cells received fresh medium.

The “direct” treatment consists of exposing the well containing the cells to the plasma-jet or the DBD. The “indirect” or “PAM” treatment consists of replacing the culture medium by a medium previously treated by plasma. The “chemical treatment” designate the fact to expose the cells to combinations of nitrites and hydrogen peroxide prepared from standard solution.

After treatment, cells were grown for 24, 48 or 72h at 37°C, 5% CO_2 and 95% O_2. After this incubation, the medium was removed, and the cells were treated with trypsin at 37°C. Trypsin action was stopped by adding FBS before the samples were centrifuged, washed and counted. The trypan blue exclusion technique was carried out (10% trypan blue). The numbers of stained and unstained cells were counted by using Malassez cell. Dead cells take up the stain, whereas living cells do not.

II.4.2 Plasma-jet, DBD or chemicals treatment

Plasma-jet

The plasma-jet device used for all the *in-vitro* experiments is the single-channel jet described in Chapter II.1.4 (see Fig 17 and Fig 18). We use the square power supply at 500 Hz AC. Peak to peak Voltage is 19.5 kV or 30 kV. Height above the liquid is 1.7 or 9.7 mm (linear translation stage at ± 10 µm). He flow rate is 200 or 400 sscm. The chemical yield H_2O_2 is around 2 nmol/J. Power consumption was measured in real time, which enables to obtain precisely the targeted energy (and so H_2O_2 concentration, see Chapter III, section H_2O_2). Treatment times between 30 and 300 s are chosen to reach the targeted energy with an uncertainty of the order of 2 J.

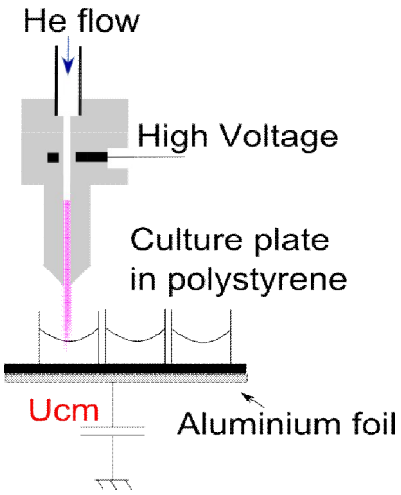

Fig 54 experimental setup for *in-vitro* and chemistry experiments

Experiments with the DBD

The Dielectric Barrier Discharge (DBD) used in the *in-vitro* experiments is described in section II.1.3. Few modifications are made to the experimental set-up. Due to the size[33] of the DBD, it is necessary to work with 12-wells plates (instead of 24). Consequently,

[33] In fact the plasma source is compatible with the wells of 24-well plates. However, in these conditions a part of the discharges occur between the edge of the DBD and the plastic walls of the well. Since not all discharges reach the surface of the liquid, it is likely that the concentration of chemical species produced in the liquid phase would have been very different for the same power consumed. In addition, this situation poses problems of experimental reproducibility. Hence the choice of larger wells.

the number of cells per well has been doubled (60 000 cells 1 days before treatment). The volume of medium is also doubled in such a way that the cells have the same amount of nutrients as the cells located in the 24-well plates.

Additions of chemicals

The chemicals were prepared from the commercial solution of nitrite at 0.1 M (Sigma Aldrich, ref 72586) and 3w% h hydrogen peroxide solution (Sigma Aldrich, ref 88597).

II.5 In vivo experiments

II.5.1 Collaboration with CIMI laboratory

These experiments were done at hospital Pitié-Salpêtrière in the team of F Lemoine from CIMI laboratory (Sorbonne Universités, UPMC/Paris 06, UMR-S INSERM U1135, CNRS ERL 8255, Center d'Immunologie et Maladies Infectieuses (CIMI-Paris), Paris, France).

Mice

Seven- to 8-week-old female C57BL/6 mice were purchased from Janvier (Le Genest Saint Isle, France) and kept under specific pathogen-free conditions at the UMS28 animal facility (UFR 969, Pitié-Salpêtrière). Experiments were performed according to the European Economic Community guidelines and approved by the local ethics committee. Mice were anesthetized with 2 % (v/v) isoflurane in medical air at 1 l/min.

Tumor model

C57BL/6 mice were injected with 5.10^4 TC-1 cells. Cells were subcutaneously (SC) implanted into the flank of animals or in the cheek of the animal. Mice were monitored every two days for tumor progression and individual weight. Tumor growth was determined using a caliper and according to the formula: $\frac{(length \times width^2)}{2}$, which is an approximation of the volume of an ellipsoide. Mice were sacrificed when tumors reached volumes of 2000 mm^3 (respectively 800 mm^3 if the tumor is in the cheek) or when body weight loss is more than 10%

For the sake of simplicity, the precise protocol of each experiment is described in Chapter V before the exposure of results. Some experiments were done with an inhibitor of catalase. Catalase is a very efficient enzyme whose function is to remove H_2O_2. Since one of the key species which could be implied in the therapeutic effects of plasma is H_2O_2. It was expected that an addition of a biocompatible inhibitor of catalase could drastically enhance the effect of plasma. The inhibitor chosen was 3-amino-1, 2, 4-triazole (Sigma Aldrich, ref A8056, Fig 55) [111]. A lipid-rich cream (Dexeril®), was used to enhance the penetration of the chemical. The solid was dissolved in water and mixed with the Dexeril® before application to the skin of the mice.

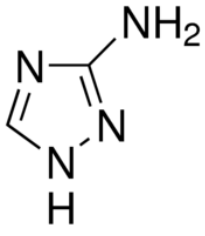

Fig 55 inhibitor of catalase: 3-amino-1, 2, 4-triazole (Sigma Aldrich, ref A8056)

II.5.2 Collaboration with LIB laboratory

These experiments were made the CEF (Centre d'Explorations Fonctionnelles, Cordeliers' Research Center, facility agreement no. A75-06-12) in the team of Lori Bridal from LIB laboratory (the Laboratoire d'Imagerie Biomedicale, CNRS, IN- SERM, UPMC Univ Paris 06, Sorbonne Universités, Paris F-75006, France). The mice were housed at the CEF. All experiments were conducted in accordance with the institutional guidelines and the recommendations for the care and use of laboratory animals established by the French Ministry of Agriculture. Mice were anesthetized with 2 % (v/v) isoflurane in the medical air at 1 l/min. The temperature of the animal was maintained at 37 °C. Mice were sacrificed when tumors reached volumes of 2000 mm 3, or when body weight loss was more than 10%.

Ultrasound diagnostic.

The system of imagery is described in the thesis of Alexandre Dizeux ([112]) from the team of Lori Bridal at LIB. Stiffness and mode-B and quantitative ultrasound measurements were carried out with a clinical ultrasound System (Aixplorer, SuperSonic Imagine). Contrast imaging was performed with A Sequoia 512 clinical ultrasound system (AcusonSiemens Healthcare, MoutainView, CA, USA).

B-mode Imaging

Transducers made of piezo-electrical material have the ability to modify their volume when an electric field is applied. Respectively, in response to mechanical stress, piezoelectric components produce a difference of potential. These transducers are used to produce ultrasound in biological tissue and measured the backscattered signals. The backscattered signals are produced when the wave reaches a structure which has a different impedance (mechanical impedance). The frequency is of the order of few MHz. The choice of one frequency is a compromise between the resolution (better at high frequency) and the attenuation of the signal (higher at high frequency).

Shear Wave elastography

This kind of elastography enables to obtain a map of the young Modulus **M** in the vicinity of the tumor. The ultrasound transducer focalizes the wave at one point; a shear wave propagates from the focal point with a speed which depends on the **M.** These shear waves propagate in the plane normal to the direction defined by TF the segment between the transducer and the focal point. The observation of the propagation of this shear-wave (by the backscattered signal to the transducer) provides a horizontal section of the young Modulus in the vicinity of the tumor.

Quantitative ultrasound

Quantitative ultrasound uses the frequency-dependent information contained in the backscattered signals. They provide information about tissue microstructure at smaller spatial scales than B-mode imaging ([112]).

Contrast-enhanced ultrasound (CEUS)

In this kind of experiments, a contrast agent, made of microbubbles containing SF6 gas (Sonovue®), is injected in the tail vein of the mouse. The transducer produces ultrasound with an intensity which enables to elicit a non-linear response of the bubbles. The bubbles are excited at the frequency f and vibrate at the frequency 2f. The response is observed at the frequency 2f. Similarly to mode-B the time between the emission at frequency f and the reception of the signal at frequency 2f enables to find the position of the micro-bubbles. Since micro-bubbles circulate in the blood, the signal will give

information about the vascularization of the tumor. The protocol consists of defining a region of interest covering the tumor (red zone surrounded in Fig 56). Then the intensity of the signal reflected by this area is plotted as a function of time (right part of Fig 56). This curve enables to obtain functional parameters which characterize the vascularization of the tumor. The definition of this six parameters is explained in the legend of Fig 56 from the thesis of Alexandre Dizeux [112].

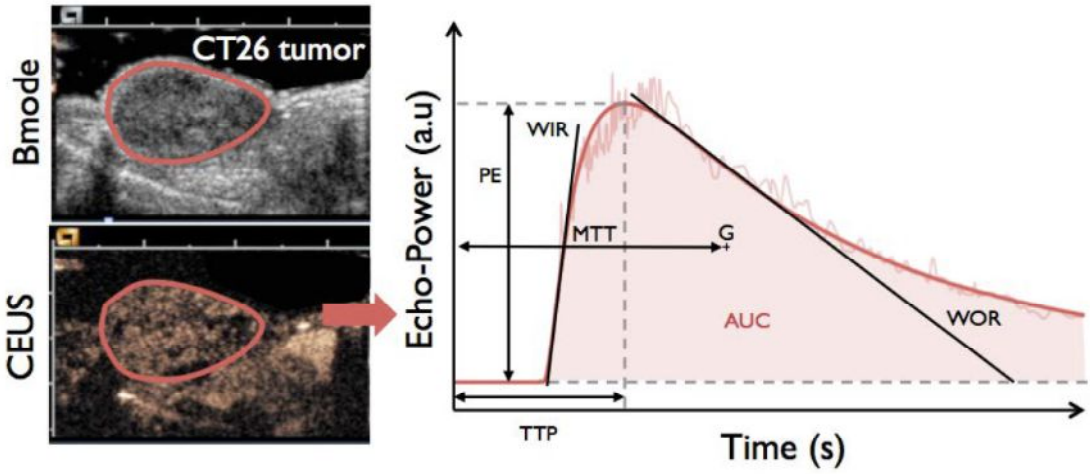

Fig 56 Legend and figure from the thesis of Alexandre Dizeux [112]. The contrast passage is quantified in a range of interest by fitting echo-power data to a lognormal model. Functional parameters are extracted from the fit curve. Peak-enhancement (PE) corresponds to the maximum echo-power value of the curve; time to peak (TTP) is the time to reach PE; wash-in and washout rate (WIR and WOR) are related to the maximum slope at the initial and late phase of contrast uptake, respectively. The mean transit time (MTT) is the mean value of the lognormal distribution of transit times in the imaging plane, and the (AUC) parameter is the area under the curve.

Chapter III Liquid phase chemistry after and during plasma-liquid interaction

In the field of "plasma-medicine", one of the central assumptions is that the reactive species produced by the plasma contributes significantly or even predominantly to the therapeutic effects. For example, it is generally accepted that the oxidative chemical species produced by the plasma can trigger inter and intracellular signals leading to cell death or activation of the immune system against cancer [64]. Unfortunately, the vast majority of the arguments supporting this hypothesis are related to *in-vitro* experiments.

This hypothesis is often questioned. Unfortunately, it is often a question of wondering which of the chemical species produced by the plasma could contribute to the biological responses. The question of the "chemical dose", the quantification of the chemical effect is rarely tackled frontally. This precise question is the subject of few *in-vitro* studies; some results are presented in Chapter IV Regarding the action of hydrogen peroxide and nitrites on TC1 line.

The question: how to measure the chemistry of life *in-vivo* still remains a major scientific issue of the biology. The question of the "chemical dose" can be reformulated in a less ambitious form:

Even with imperfect knowledge of the reactive species created by the plasma, is it credible that the reactive species produced by the plasma have a biological effect, *in-vivo*? Alternatively, is the amount so small, so quickly destroyed by the anti-oxidant network that they have no chance to produce any effect?

In this Chapter, we will focus on measurements of H_2O_2, NO_2^-, NO_3^- and HO° in liquid using different plasma jets described in the previous chapter. We will discuss the relevance of the molecular probes diagnostics (following Chapter II), and put forward a tentative discussion about the diffusion of such RONS in living tissues.

This chapter proposes some paths of reflection. First, we need to know the chemistry produced by our plasma sources and if possible the link between the power consumption of the device and the production of chemical species in liquid phase. Consequently, we represent the chemistry induced in the liquid phase by two quantities:

- **The production rate in pmol/s**. This is the amount of chemical species (in nmol) produced per second of operation of the plasma device.
- **The Yield in nmol/J**. This is the amount of chemical species (in nmol) produced by the number of joules that we measure consumed by the plasma. Other fields like sonochemistry and radiolysis used such notion.

This presupposes that we have characterized our chemical diagnostic (specificity, yield, kinetics...). This question is far from being obvious, even for the most straightforward diagnostic. The correct use of Amplex-red and Griess reagents[34] is explained in Chapter II.

The first four paragraphs contain the results of parametric study implying the quantification of H_2O_2, NO_2^- and NO_3^-. Two single-jet and the multi-channel jet. In each

[34] It is recalled that Amplex-red is very sensitive to light, exposure to ambient light and even more so to that produced by the plasma can completely distort the diagnostic. The fact that the nitrite detection test operates in an acidic medium can lead to a significant underestimation of the nitrites since if H_2O_2 react with nitrite to form peroxinitrite.

experiment one of the parameter change, all other being constant (Table 1 and Fig 57). The results are exposed in terms of production rate and yield respectively in pmol/s and nmol/J. The results are not immediately interpreted and discussed.

Table 1 List of the parameter modified during parametric studies

Plasma-jet (single or multi-channel)	DBD
peak to peak voltage	peak to peak voltage
the distance between the output of the nozzle and the surface of the liquid ↕	the distance between the surface of the liquid and the surface of the dielectric
time of treatment	time of treatment
gas flow, controlled by a mass-flow controller (Brooks®)	-
radial position: relatively to the center of the well ↔	-

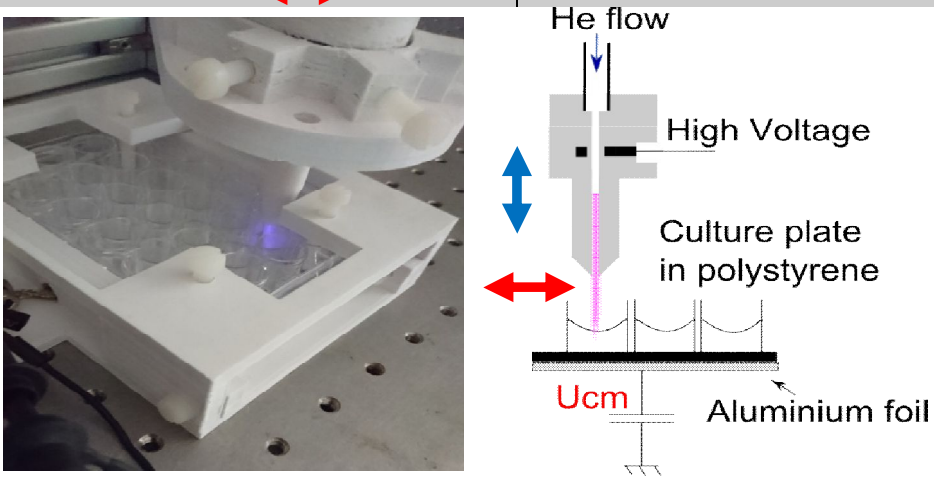

Fig 57 Picture and schema of the single jet operating above a 24-well culture dish.

The fifth section describes experiments related to the quantification of hydroxyl radical, principally with the use of terephthalic acid (TPA). A significant part of the discussion is devoted to the setting up and validation of the diagnostic. The choice of an appropriate concentration of TPA depends on the rate of production of OH° radical. The results and the interpretations of experiments using the scavengers of hydroxyl radical like methanol are also presented and discussed in Appendix B.

The sixth section is a discussion of the results of parametric studies, in the light of published literature.

The seventh section contains a discussion of the interaction of H_2O_2 with cells, its diffusion and its destruction by the anti-oxidant defenses of the skin.

The use of the fluorescent probe (NBD-Cl) has been studied and is presented in Appendix L. According to the literature, this probe enables the quantification of superoxide radical O_2^- without interference of H_2O_2. However, it seems there is an interference with H_2O_2, in the context of plasma-medicine ([H_2O_2] ~ 1 mM).

III.1 Single-channel jet, H_2O_2 production

This section[35] regards the H_2O_2 chemistry of the single-channel in the liquid phase. The device is defined by the following dimensions:

di = 3 mm, **e** = 1.5 mm, **H** = 60 mm (see Chapter II)

Where **di** is the inner diameter of the tube; **e** is dielectric thickness; **H** is the distance between the High-voltage-electrode and nozzle output. The voltage waveform "500 Hz generator n°3" is described in Chapter II (II.2.1, Power supply).

The production of H_2O_2 is studied in 24-well-plates (Costar flat-bottomed). The nozzle has been positioned in the center of the well. The dosing protocol[36] is described in Chapter II, section II.3.2.2. This protocol is based on Amplex-red method. All the measurements presented here were acquired at the same time than those of calibration curve (same incubation time, similar handling conditions and light exposure...). The calibration curve has been acquired in triplicate. Dilutions have been made to reach the range of detection.

III.1.1 Adjustable parameter: treatment time

The treatment time varies in the range: 1-6 min. The set of constant parameters is (voltage = 29.2 kV, $\Phi_{He} = 500\ sscm$, height = 5 mm). The amount of H_2O_2 increases quite linearly as function of time (Fig 58). The slope of the line defines the rate of production of H_2O_2: ~1.2 nmol/s with this set of parameters. Even while trying to fix the other parameters, we find that the electrical power consumed is not constant above each well. This lack of stability is probably due to the sensitivity of the electrical power with respect to the others parameters.

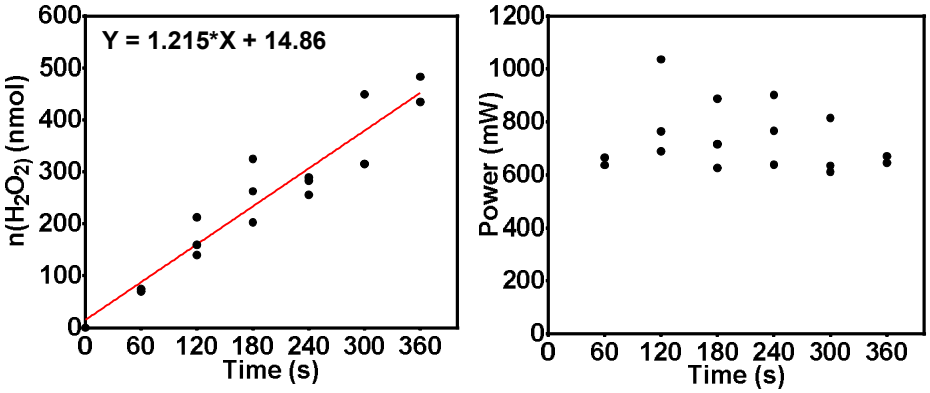

Fig 58 **Left:** amount of H_2O_2 (nmol) as a function of time. **Right**: power consumption. Treatment time = 1-6 min, frequency of power supply = 500 Hz, peak to peak voltage = 29.2 kV, $\Phi_{He} = 500\ sscm$, height = 5 mm, power supply = "500 Hz generator n°3" (II.2.1, Power supply). Error bars represent the standard error of the mean. Each well of the 24-well plate (flat bottom) contains 500 µL of PBS 10X.

The amount of H_2O_2 is plotted as a function of the energy in Fig 59. It appears that with this choice of abscissa, the linear fit is better. This shows the interest of using and

[35] and in the sections III.2, III.4 and III.5 for the nitrite, nitrate and hydroxyle radical respectively.
[36] The acquisition parameters are as described in the "last version" of the protocol described in Chapter II (i.e. λex = 571/1 nm, λem = 585/5 nm, acquisition time = 6 s (60 points, integration time of 0.1 s per point.)

measuring power during each experiment. Even if the power varies for some reason, the link between power consumption and chemical production remains strong. The slope of the line defines the yield (~1.9 nmol/J with this set of parameters).

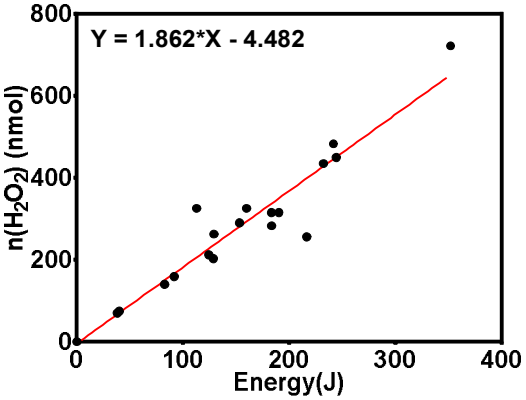

Fig 59 Amount of H_2O_2 as a function of energy consumption. Treatment time = 1-6 min, frequency of power supply = 500 Hz, peak to peak voltage = 29 kV, $\Phi_{He} = 500\ sscm$, height = 5 mm, power supply = "500 Hz generator n°3" (II.2.1, Power supply). Each well of the 24-well plate (flat bottom) contains 500 µL of PBS 10X.

III.1.2 Adjustable parameter: helium flow rate

Similarly, experiments are carried out with variable helium flow $\Phi_{He} = 200 - 800\ sscm$ (Fig 60). The set of constant parameters is (voltage = 29 kV, height = 5 mm, treatment time = 2 min). In the chosen range of flow, the power consumed is constant (with respect to the uncertainty of repeated experiments...). However, we note that the rate of production and the yield decrease when the flow increases. The yields obtained are between 1 and 3 nmol / J. Production rates between 900 and 1500 pmol/s.

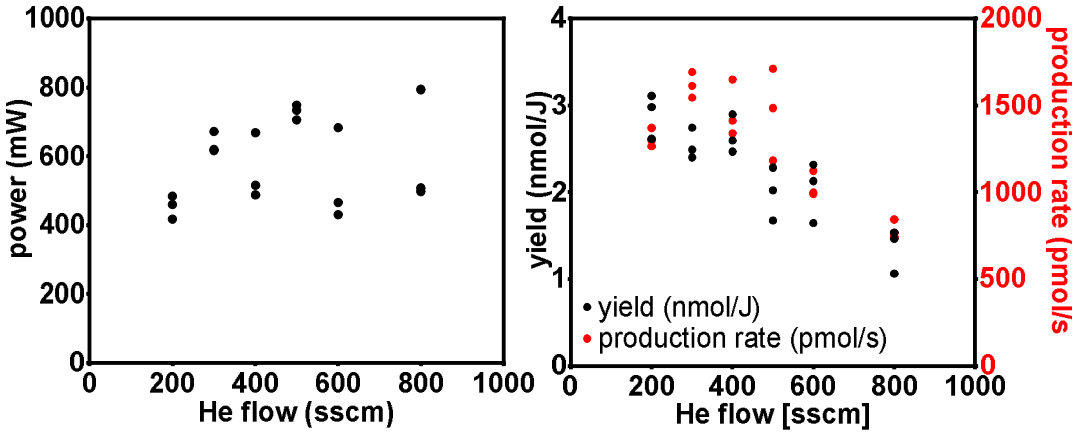

Fig 60 Left: power as a function of helium flow. Right: Yield (nmol/J) and rate of production of H_2O_2 (pmol/s). Treatment time = 2 min, frequency of power supply = 500 Hz, peak to peak voltage = 29 kV, $\Phi_{He} = 200 - 800\ sscm$, height = 5 mm, power supply = "500 Hz generator n°3" (II.2.1, Power supply). Each well of the 24-well plate (flat bottom) contains 500 µL of PBS 10X.

III.1.3 Adjustable parameter: height above liquid

The variable parameter is the height which is the distance between the nozzle and the surface of the liquid (Fig 61). The set of constant parameters is (voltage = 29 kV, $\Phi_{He} = 500\ sscm$, treatment time = 2 min). The power decreases substantially above 8 mm. With regard to the yield and the rate of production they continually increase up to 8 mm. The yield is between 0.7 and 4 nmol/J.

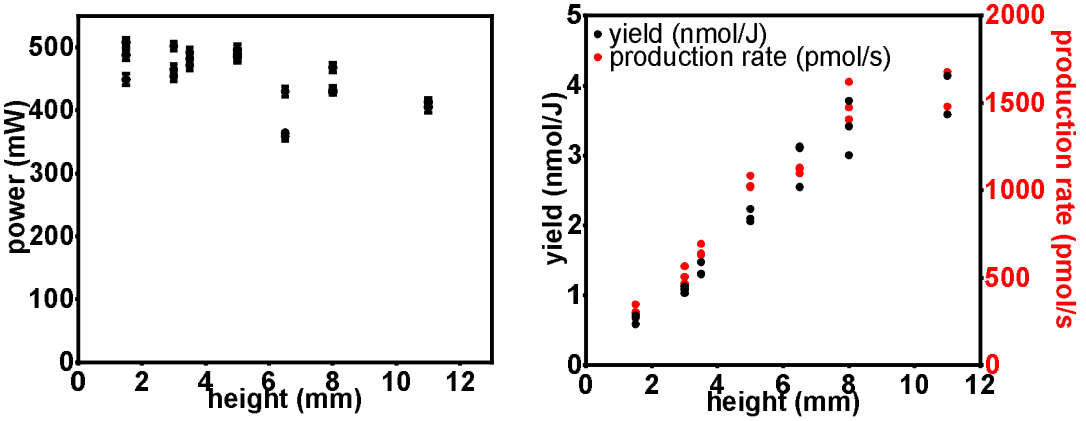

Fig 61 Left: power as a function of height. Right: Yield (nmol/J) and rate of production of H2O2 (pmol/s). Treatment time = 2 min, frequency of power supply = 500 Hz, peak to peak voltage = 29 kV, $\Phi He = 500\ sscm$, height = 1.5-11 mm, power supply = "500 Hz generator n°3" (II.2.1, Power supply). Each well of the 24-well plate (flat bottom) contains 500 µL of PBS 10X.

III.1.4 Adjustable parameter: peak to peak voltage

In this experiment, the voltage of the power supply is in the range 17.5-29.5 kV. The set of constant parameters is (height=5.7 mm, $\Phi_{He} = 500\ sscm$, treatment time = 2 min). Unlike the previous cases, the power consumed changes considerably (between ~150 mW and 1 W). The rate of production increases with power and voltage, while the yield tends to decrease. The yield and the rate evolve in the range 1.3-2.6 nmol/J and 300-1300 pmol/s respectively.

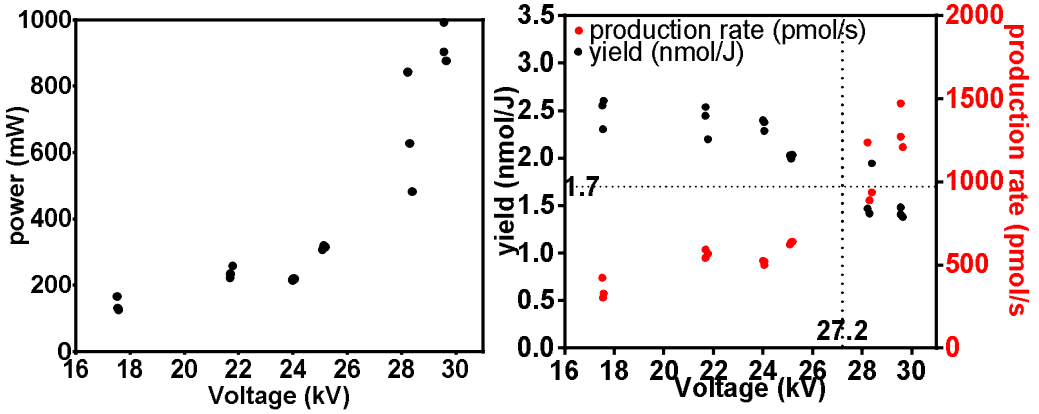

Fig 62 **Left**: power as a function of voltage. **Right:** Yield (nmol/J) and rate of production of H2O2 (pmol/s). Treatment time = 2 min, frequency of power supply = 500 Hz, peak to peak voltage = 17.5-29 kV, $\Phi He = 500\ sscm$, height = 5.7 mm, power supply = "500 Hz generator n°3" (II.2.1, Power supply). Each well of the 24-well plate (flat bottom) contains 500 µL of PBS 10X.

III.2 Single-channel jet, NO_2^- production

This section regards the nitrite chemistry of the single-channel jet. The experimental setup is the same in the previous section. The nozzle has been positioned in the center of the well (except in section III.2.4).The dosing protocol[37] is based on Griess reagent method (described in Chapter II, section II.3.3). Dilutions have been made to reach the range of detection. Initially, the wells contain 1400 µl of PBS 10X. The average volume is 1200 ± 100 µL after treatment.

III.2.1 Adjustable parameter: treatment time

The treatment time varies in the range: 1-10 min. The set of constant parameters is (voltage = 27.6 kV, $\Phi_{He} = 500\ sscm$, height = 5.7 mm). The amount of nitrite as a function of time is shown in Fig 63. These treatments were repeated in triplicate (except t= 10 min, duplicate). Nitrite production increases over time, which is consistent. However, the data points are far from being on a line.

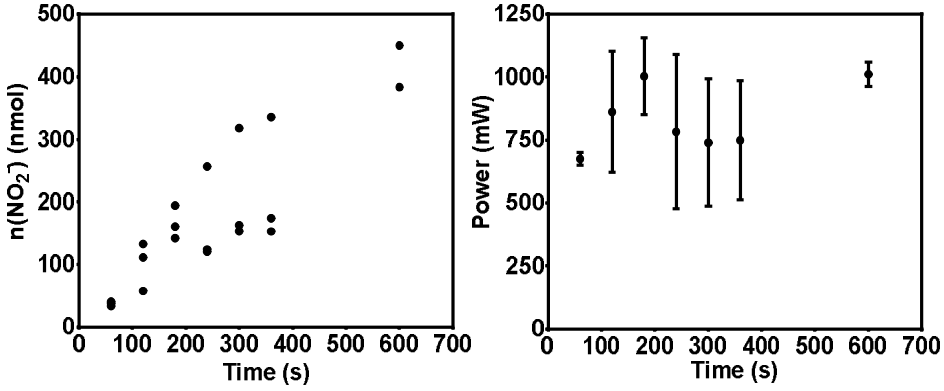

Fig 63 Left: the amount of nitrite (nmol) as a function of time. Right: power consumption. Except for the last point (duplicate), all measurements are triplicated. Treatment time = 1-10 min, frequency of power supply = 500 Hz, peak to peak voltage = 27.6 kV, $\Phi He = 500\ sscm$, height = 5.7 mm. Error bars = standard deviation of the mean.

As the amount of H_2O_2, the amount of nitrite depends linearly on the energy (Fig 64). The energy is a better parameter of control than the time of exposure, for this plasma device powered at 500 Hz.

[37] In brief, the absorbance of a 1 mL solution containing 100 µL of Griess reagent (Sigma-Aldrich, 03553-100mL) and 900 µL of sample is measured at a 522 nm after 20 min of incubation.

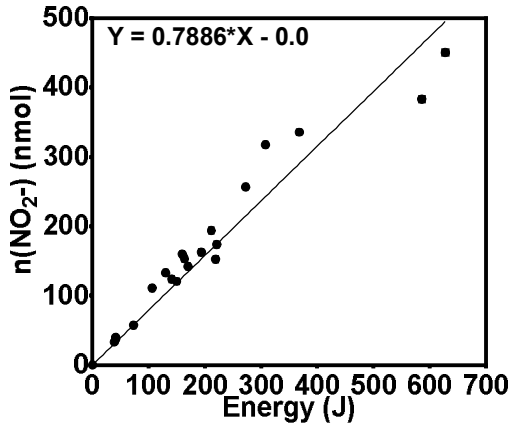

Fig 64 Amount of nitrite in nmol as a function of energy consumption. All other things being equal, the treatment time is at the origin of the changes in the value of energy. Treatment time = 1-10 min, frequency of power supply = 500 Hz, peak to peak voltage = 27.6 kV, $\Phi He = 500\ sscm$, height = 5.7 mm.

The yield and the production rate are plotted in Fig 65. The production rate is ~800 pmol/s, the yield ~0.9 nmol/J for $t \leq 6\ min$. Curiously, the yield decrease: 0.7 nmol/J at 10 min. This point cannot be explained by the fact that the voltage decreases[38] during this time since a decreasing voltage increase the yield (see Fig 69). For the same reason, the fact that there is more evaporation in 10 min than in 6 min (thus an increasing height) does not explain that point (Fig 67). The reaction between NO and H_2O_2 could explain this observation.

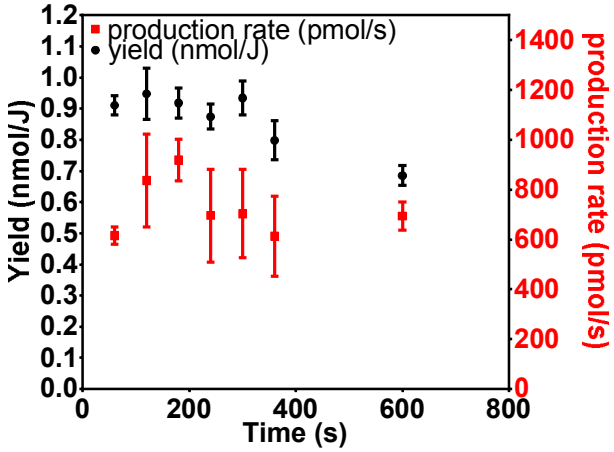

Fig 65 Yield (nmol/J) and production rate (pmol/s) of nitrite as a function of treatment time. Treatment time = 1-10 min, frequency of power supply = 500 Hz, peak to peak voltage = 27.6 kV, $\Phi He = 500\ sscm$, height = 5.7 mm. triplicate, except last point duplicate. Error bars represent the standard error of the mean.

III.2.2 Adjustable parameter: helium flow rate

The variable parameter is the flow ($\Phi_{He} = 100 - 1000\ sscm$). The set of constant parameters is (voltage = 27.4 kV, height = 5.5 mm, treatment time = 3 min). The power

[38] During 10 min the average value of the applied voltage is 27kV. During the first six minutes ~27.6 kV. This is due to the heating of the components (especially the resistors) of this homemade generator.

increase with the flow and reaches a plateau for $\Phi_{He} \geq 400\ sscm$ (Fig 66). This behavior is different from that observed during the determination of H_2O_2. This is probably due to the fact that the voltage is higher (29 kV) in previous experiment. The height was also slightly lower (5 mm).

Yield and production rate increase and reach a maximum at 300 sscm, then decrease at higher flow rates. The yield and the rate of production are in the range 0.07-1.2 nmol/J, 50-810 pmol/s. Note that the range of relative variation of the production rate is greater for the nitrite than for H_2O_2. A flow rate of 300 sccm optimizes the production since the yield, and the rate are equal to 1.2 nmol/J and 810 pmol/s.

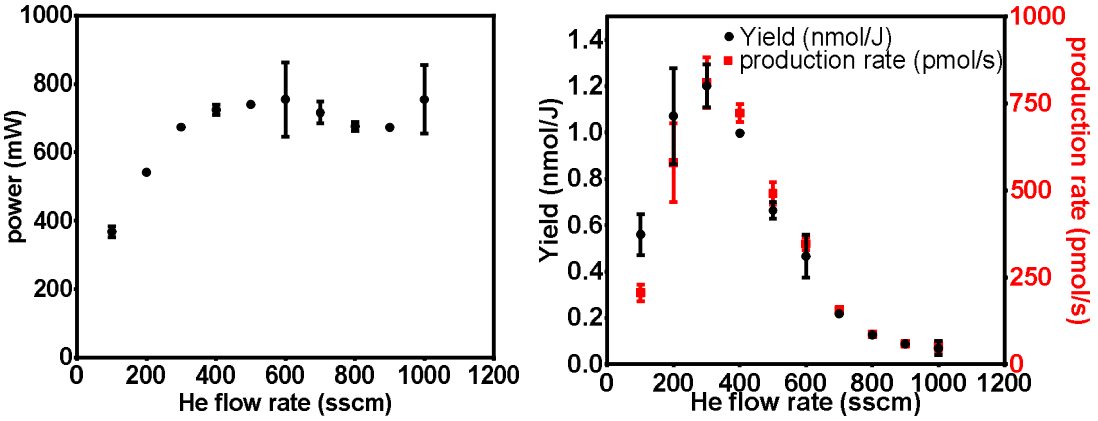

Fig 66 Left: power consumption (mW) as a function of helium flow rate (sscm). **Right**: yield (nmol/J) and production rate (pmol/s) as a function of helium flow rate (sscm). Treatment time = 3 min, height =5.5 mm, voltage = 27.4 kV, power supply = "500 Hz generator n°3" (II.2.1, Power supply). Each well of the 24-well plate (flat bottom) contains 1.4 ml of PBS 10X. Duplicate experiment.

III.2.3 Adjustable parameter: height above liquid

The variable parameter is the height (height = 1.5-12.5 mm). The set of constant parameters is (voltage = 27.4 kV, $\Phi_{He} = 500\ sscm$, treatment time = 3 min, except height = 1.5 or 2.5 mm where treatment time = 5 min). The evolution of the power is similar to those of the previous experiment as a function oh height (constant before 11 mm, decay beyond, Fig 67). Similarly, the yield and the rate of production are similar[39].

[39] except that the decrease in production rate is not observed in the H_2O_2 experiment probably since height $\leq 12\ mm$.

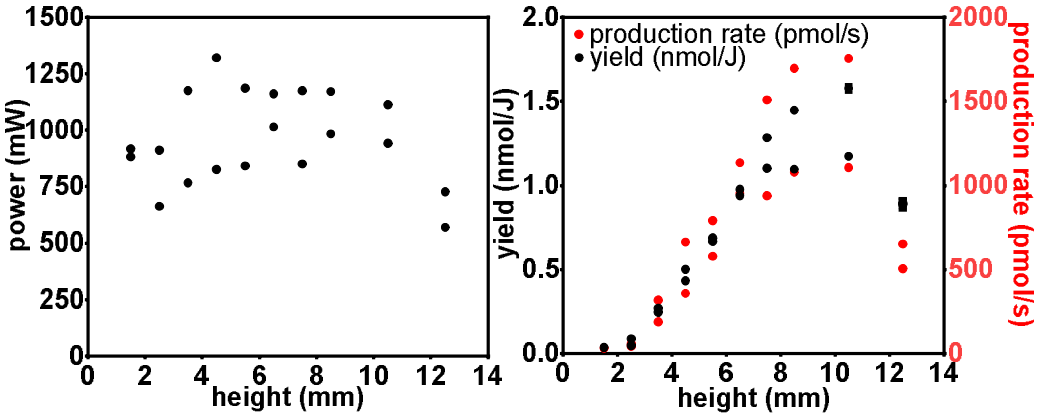

Fig 67 **Left:** power consumption (mW) as a function of height above the liquid. **Right:** yield (nmol/J) and production rate of nitrite (pmol/s) as a function of height. Treatment time = 3 min except for the height = 1.5 or 2. 5 mm where treatment time is 5 min to obtain a measurable concentration, $\Phi_{He} = 500\ sscm$, height =1.5-12.5 mm, voltage = 27.3 kV, power supply = "500 Hz generator n°3" (II.2.1, Power supply). Each well of the 24-well plate (flat bottom) contains 1.4 ml of PBS 10X. Duplicate experiment.

III.2.4 Adjustable parameter: radial position

In this section, the variable parameter is the radial position of the nozzle. Since the outer radius of the single-jet[40] is 4 mm and since the wells have a diameter of 16 mm; the position of the center of the nozzle can vary from the position 4 mm to the position 12 mm. The set of constant parameters is (voltage = 27.4 kV, $\Phi_{He} = 500\ sscm$, height = 8.7 mm, treatment time = 3 min).

At this height and when the nozzle is close to the edge, a fraction of the discharges touches the edge of the well and not the surface of the liquid. The power is constant (Fig 68), whereas the yield and the production rate decreases close to the wall. Subsequently, it is necessary to center the plasma source to achieve reliable experiment. Nevertheless, there is a tolerance of ~±2 mm regarding the radial position. In addition, this effect decreases with decreasing height (not shown here).

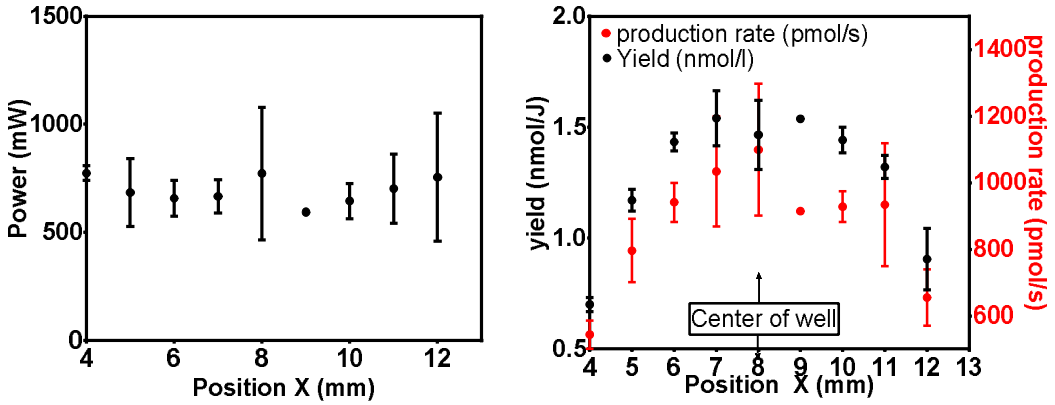

Fig 68 **Left**: power in mW as a function of radial position. **Right**: yield (nmol/J) and production rate (nmol/s) as a function of radial position in mm. Treatment time = 3 min, $\Phi_{He} = 500\ sscm$, height = 8.7

[40] outer radius = 4 mm, inner radius of gas tube = 1.5 mm.

mm, voltage = 27.3 kV, power supply = "500 Hz generator n°3" (II.2.1, Power supply). Each well of the 24-well plate (flat bottom) contains 1.4 ml of PBS 10X. Duplicate experiment.

III.2.5 Adjustable parameter: peak to peak voltage

In this experiment, the voltage of the power supply is in the range 19-29.5 kV. The set of constant parameters is (height=5.7 mm, $\Phi_{He} = 500\ sscm$, treatment time = 3 min). The power changes considerably (between 200 mW and 750 mW). The rate of production increases with voltage, while the yield tends to decrease (Fig 69). The yield and the rate evolve in the range 0.6-1 nmol/J and 200-400 pmol/s respectively.

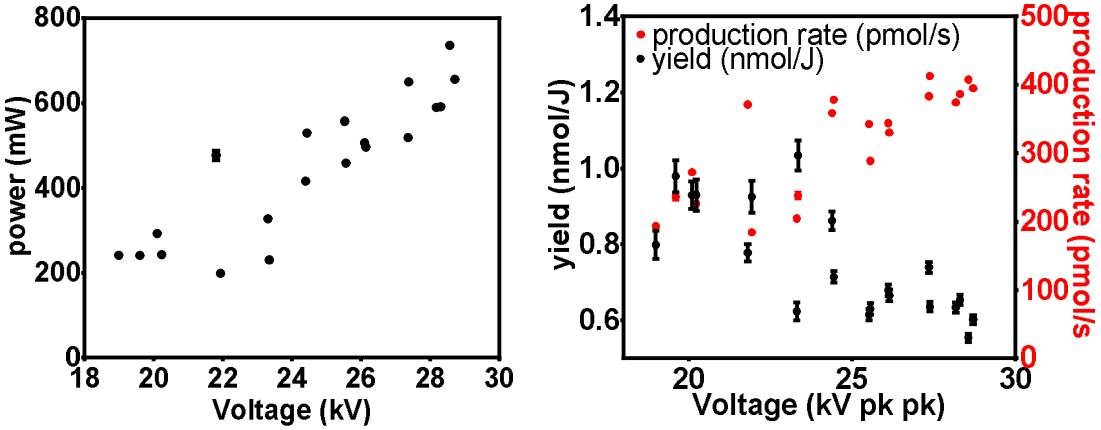

Fig 69 **Left**: power consumption as a function of voltage. **Right**: yield (nmol/J) and production rate (nmol/s) as a function of voltage. Treatment time = 3 min, $\Phi_{He} = 500\ sscm$, height = 5.7 mm, voltage = 19-29.5 kV, power supply = "500 Hz generator n°3" (II.2.1, Power supply). Each well of the 24-well plate (flat bottom) contains 1.4 ml of PBS 10X.

III.3 Multi-channel jet: H_2O_2 and NO_2^-

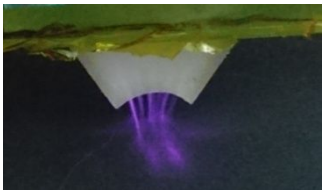

In this experiment, the amount of NO_2^- and H_2O_2 have been measured in each well treated by the multi-channel jet. As the nozzle is larger, it is necessary to use culture plates with larger wells (6-well plate, Costar®, flat-bottom). This nozzle requires[41] higher gas flow rates (~1000-2800 sscm) than that used for the single-channel jet (~100-1000 sscm). The measurement of H_2O_2 is based on Amplex-red diagnostic, that of nitrites on Griess reagent method (the two methods were used in the two previous sections and are described in Chapter II). Dilutions have been made to reach the range of detection. Initially, the wells contains 5000 µl of PBS 1X.

[41] below, the discharge becomes particularly unstable, which considerably increases the dispersion.

III.3.1 Adjustable parameter: treatment time

The time varies in the range: 1-6 min. The set of constant parameters is (voltage = 23 kV, $\Phi_{He} = 2600\ sscm$, height[42] = 5.5 mm). The power is constant over time (~1500 mW); moreover with the chosen parameters the dispersion of the measurements is quite low (Fig 70). It is also found, similarly to the single-channel jet that the amount of nitrite and H_2O_2 increases linearly as a function of the treatment time. We can observe that the amount of H_2O_2 is greater than the amount of nitrite.

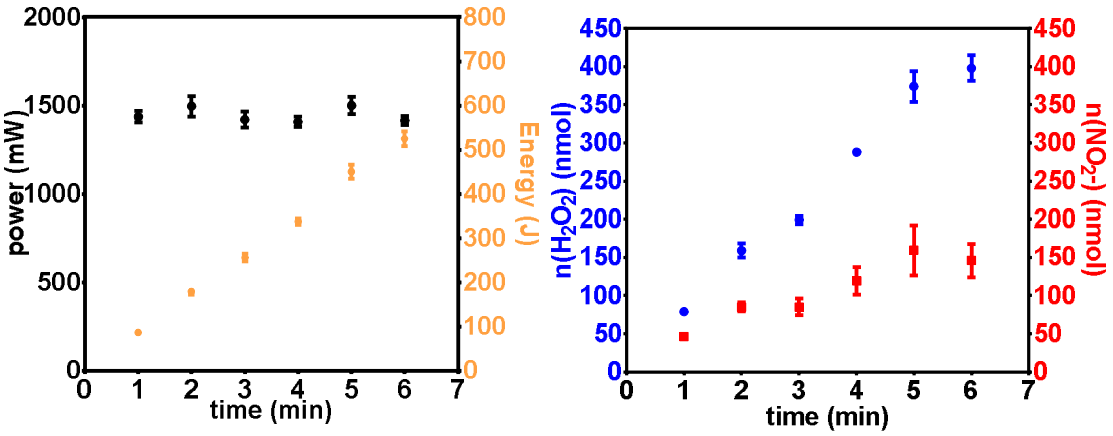

Fig 70 **Left**: power as a function of treatment time (black dots), energy consumed during the treatment of each well (yellow). **Right**: amount of H_2O_2 and nitrite produced in each well. Treatment time = 1-6 min, $\Phi_{He} = 2600\ sscm$, height = 5 mm, voltage = 23 kV, power supply = "500 Hz generator n°3" (II.2.1, Power supply). Each well of the 6-well plate (flat bottom) contains 5 ml of PBS 1X. Triplicate experiment, error bar = standard deviation of the mean.

The yields and the production rate are described in Fig 71. They belong to the same range than the single-channel jet.

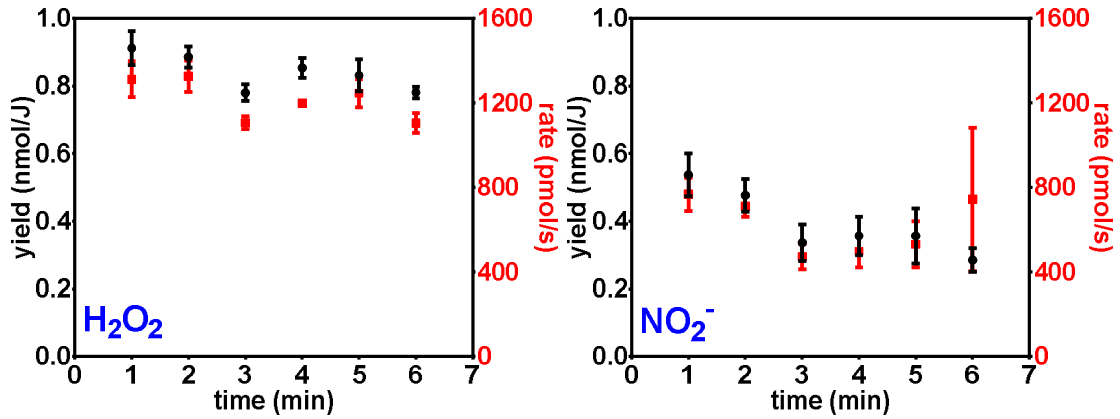

Fig 71 Yield (nmol/J) and production rate (pmol/s) as a function of treatment time. **Left**: H_2O_2, **Right:** nitrite. Treatment time = 1-6 min, $\Phi_{He} = 2600\ sscm$, height = 5 mm, voltage = 23 kV, power supply =

[42] Due to the curve of the nozzle the height is defined as the distance between the lowest point of the nozzle and the surface of the liquid. As with the single-jet, this position is identified by lowering the nozzle until it touches the surface of the liquid (the measurement is repeated and the flow of gas is cut to make the height calibration).

"500 Hz generator n°3" (II.2.1, Power supply). Each well of the 6-well plate (flat bottom) contains 5 ml of PBS 1X. Triplicate experiment, error bar = standard deviation of the mean.

III.3.2 Adjustable parameter: helium flow rate

The variable parameter is the flow ($\Phi_{He} = 1200 - 2800\ sscm$). The set of constant parameters is: (voltage = 23 kV, height = 5 mm, treatment time = 3 min). The power is fairly constant = 1270 ± 15 mW (SEM), (Fig 72). In contrast, the amount of NO_2^- and H_2O_2 evolve in opposite directions for $\Phi_{\mathrm{He}} \leq 2000\ \mathrm{sscm}$. With this device, the production of H_2O_2 evolves in the opposite direction of that observed with the single-channel jet. Moreover, even if the nitrite evolves in the same direction than the single-channel plasma jet, the decrease does not reach the magnitude[43] observed with the single-channel jet (in 24-well plates).

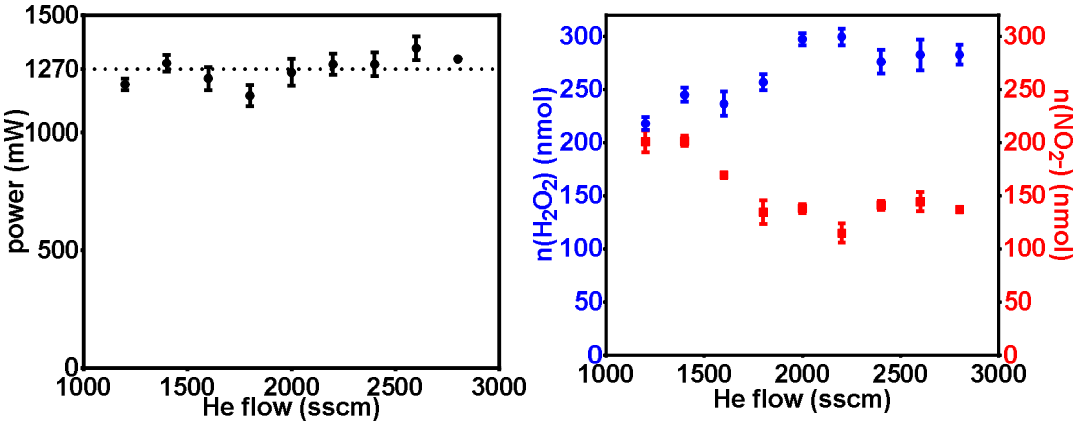

Fig 72 **Left**: power as a function of helium flow. **Right**: amount of H_2O_2 and nitrite (nmol) produced in each well. Treatment time = 3 min, $\Phi He = 1200 - 2800\ sscm$, height = 5 mm, voltage = 23 kV, power supply = "500 Hz generator n°3" (II.2.1, Power supply). Each well of the 6-well plate (flat bottom) contains 5 ml of PBS 1X. Triplicate experiment, error bar = standard deviation of the mean.

The yields and the production rate are described in Fig 73. They belong to the same range than those observed during single-channel experiments.

[43] There is probably much air in the vicinity of the plasma produced by the multi-channel jet in large wells than in the poorly-ventilated well treated with the single jet.

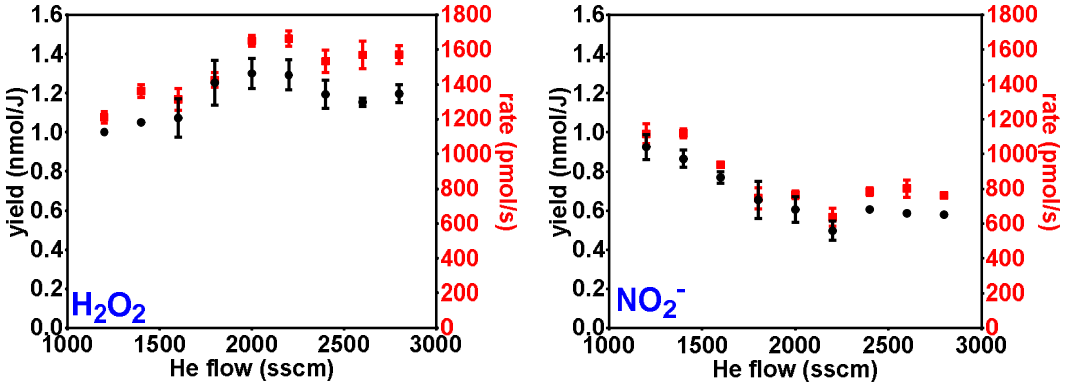

Fig 73 Yield nmol/J) and production rate (pmol/s) as a function of He flow. **Left**: H_2O_2, **Right:** nitrite. Treatment time = 3 min, $\Phi He = 1200 - 2800\ sscm$, height = 5mm, voltage = 23 kV, power supply = "500 Hz generator n°3" (II.2.1, Power supply). Each well of the 6-well plate (flat bottom) contains 5 ml of PBS 1X. Triplicate experiment, error bar = standard deviation of the mean.

III.3.3 Adjustable parameter: height above liquid

The variable parameter is the height = 2-12 mm (Fig 74). The set of constant parameters is (voltage = 23 kV, $\Phi_{He} = 2600\ sscm$, treatment time = 3 min). The power decreases continuously above 4 mm. The yield and the rate of production of H_2O_2 increase and reach a plateau above 4 mm. Yield and production rate of nitrite increase continuously for increasing height (Fig 75). This is similar to the beginning of the curve observed with the single-channel plasma jet.

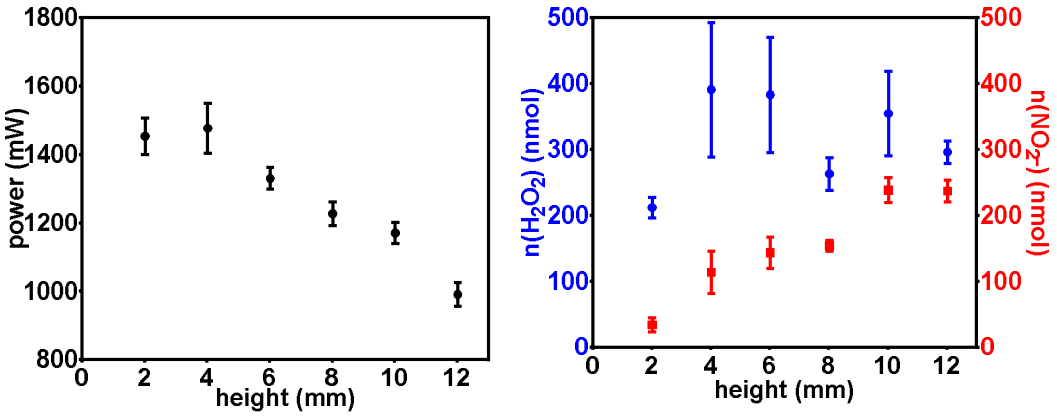

Fig 74 **Left**: power as a function of height. **Right**: amount of H_2O_2 and nitrite produced in each well. Treatment time = 3 min, $\Phi He = 2600\ sscm$, height = 2-12 mm, voltage = 23 kV, power supply = "500 Hz generator n°3" (II.2.1, Power supply). Each well of the 6-well plate (flat bottom) contains 5 ml of PBS 1X. Triplicate experiment, error bar = standard deviation of the mean.

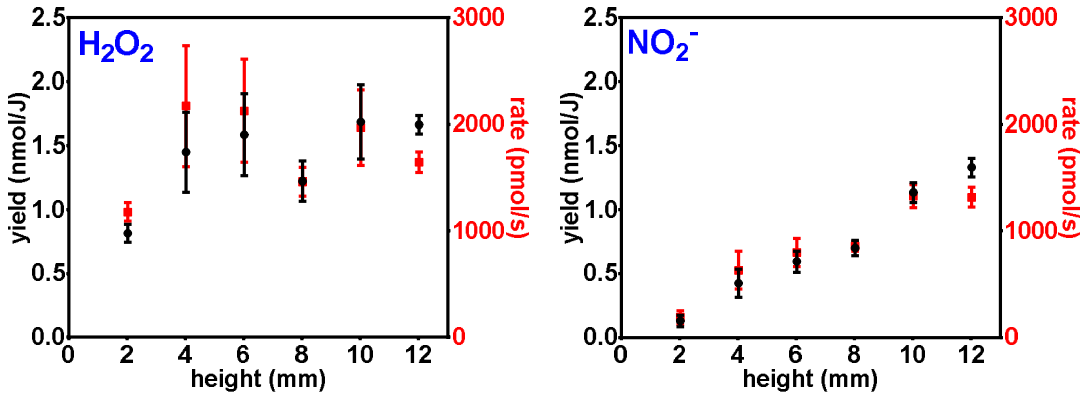

Fig 75 Yield (nmol/J) and production rate (pmol/s) as a function of height. **Left**: H_2O_2, **Right:** nitrite. Treatment time = 3 min, $\Phi He = 2600\ sscm$, height = 2-12 mm, voltage = 23 kV, power supply = "500 Hz generator n°3" (II.2.1, Power supply). Each well of the 6-well plate (flat bottom) contains 5 ml of PBS 1X. Triplicate experiment, error bar = standard deviation of the mean.

III.3.4 Adjustable parameter: peak to peak voltage

In this experiment, the voltage of the power supply is in the range 14-28.2 kV. The set of constant parameters is (height=5 mm, $\Phi_{He} = 2600\ sscm$, treatment time = 3 min). The power is between 98 mW and 3770 mW and the amount of H_2O_2 and nitrites increases with the voltage (Fig 76).

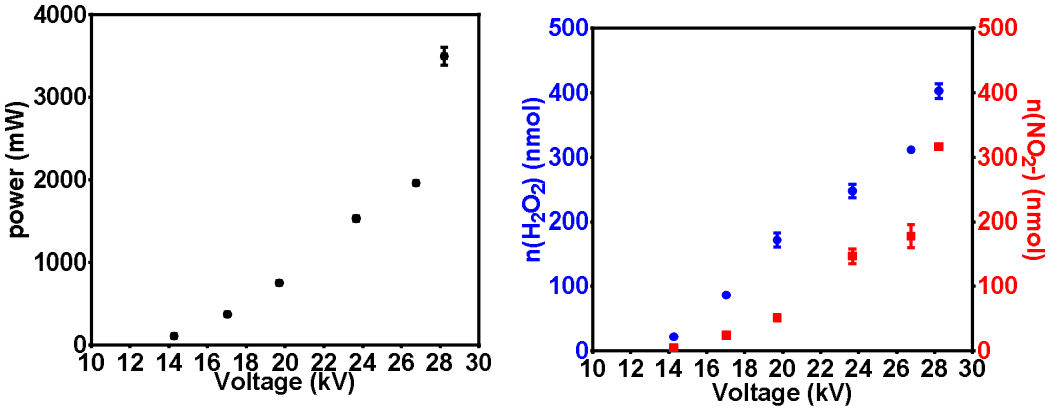

Fig 76 **Left**: power as a function of voltage**. Right**: amount of H_2O_2 and nitrite produced in each well. Treatment time = 3 min, $\Phi_{He} = 2600\ sscm$, height = 5 mm, voltage = 14-28.2 kV, power supply = "500 Hz generator n°3" (II.2.1, Power supply). Each well of the 6-well plate (flat bottom) contains 5 ml of PBS 1X. Triplicate experiment, error bar = standard deviation of the mean.

Regarding H_2O_2, the rate of production increases continuously, whereas the yield reaches a maximum around 16 kV and then decrease (Fig 77). This is consistent with the observations made with the single-channel plasma jet.

Regarding NO_2^-, the rate of production increases continuously whereas the yield increase and reach a plateau above 24 kV. This behavior is different from those of the single-channel jet whose yield decrease continuously.

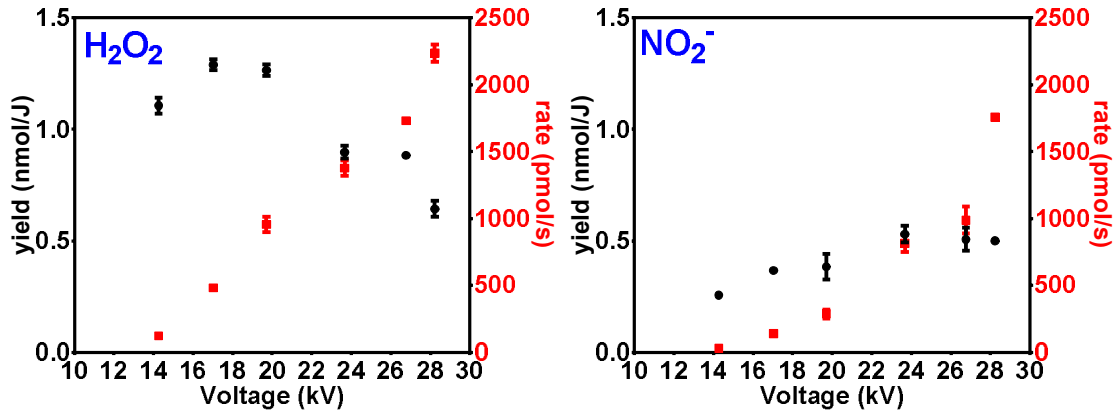

Fig 77 Yield (nmol/J) and production rate (pmol/s) as a function of peak to peak voltage. Left: H_2O_2, **Right:** nitrite. Treatment time = 3 min, $\Phi_{He} = 2600\ sccm$, height = 5 mm, voltage = 14-28.2 kV, power supply = "500 Hz generator n°3" (II.2.1, Power supply). Each well of the 6-well plate (flat bottom) contains 5 ml of PBS 1X. Triplicate experiment, error bar = standard deviation of the mean.

III.4 Single-channel jet: NO_2^- and NO_3^-

In this experiment, the amount of nitrite and nitrate has been measured in each well treated with the single-channel jet. This experiment implies to do two measurements for each sample: the first measurement gives the concentration of nitrite; the second gives the sum of nitrite and nitrate concentration. The experimental setup is described in the sections III.1 and III.2. The nozzle is positioned in the center of the well. It appears that the evolutions of nitrite and nitrates productions are relatively similar and that nitrate is produced in larger quantities than nitrite (~three times). Note that in some cases, both species have been represented with different scales so that the nitrite variation is visible.

The measurement method is based on the modified nitrate reductase method (kit Sigma-Aldrich). The protocol[44] is described in Chapter II. Dilutions have been made to reach the range of detection. Initially, the wells contain 1250 µl of deionized water. I warmly thank Constance Duchesne and Bo Liu for helping at the beginning of their thesis. Alone, it would not have been possible to make as many measurements while performing the series of dilution, calculations, and mixture required by nitrate determination.

III.4.1 Adjustable parameter: treatment time

The time varies in the range: 1-6 min. The set of constant parameters is (voltage = 28.5 kV, $\Phi_{He} = 500\ sccm$, height = 5.5 mm). The power is constant (~620 mW), Fig 78.

The amount of nitrite and nitrate increases linearly as a function of the treatment time. The slopes are ~810 pmol/s and 230 pmol/s respectively for nitrate and nitrite. Note that the amount of nitrate is approximately 3.6 times greater than the amount of nitrite. The graph which represents the yield and the production rates confirm these results (Fig 79)

[44] Compared to the supplier's instructions, the main change is to add catalase before nitrite and nitrate determination. The catalase is added just after the plasma treatment to minimize the reaction with H_2O_2 at neutral pH.

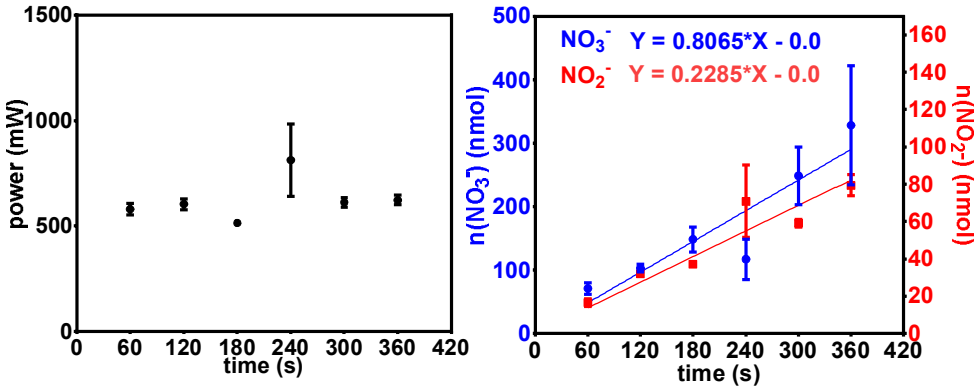

Fig 78 **Left**: power as a function of He flow. **Right**: amount of nitrite and nitrate produced in each well. Treatment time = 1-6 min, $\Phi He = 500\ sscm$, height = 5.5 mm, voltage = 28.5 kV, power supply = "500 Hz generator n°3" (II.2.1, Power supply). Each well of the 24-well plate (flat bottom) contains 1.25 ml of deionised water. The addition of Catalase takes place just after the plasma treatment. Triplicate experiment, error bar = standard deviation of the mean

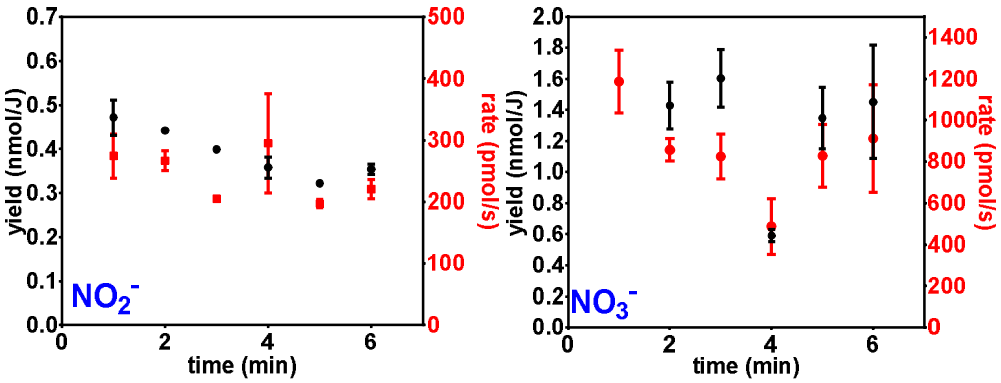

Fig 79 Yield (nmol/J) and production rate (pmol/s) as a function of treatment time. **Left**: nitrite, **Right:** nitrate. Treatment time = 1-6 min, $\Phi He = 500\ sscm$, height = 5.5 mm, voltage = 28.5 kV, power supply = "500 Hz generator n°3" (II.2.1, Power supply). Each well of the 24-well plate (flat bottom) contains 1.25 ml of deionised water. The addition of Catalase takes place just after the plasma treatment. Triplicate experiment, error bar = standard deviation of the mean.

III.4.2 Adjustable parameter: helium flow rate

The variable parameter is the flow ($\Phi_{He} = 100 - 800\ sscm$). The set of constant parameters is: (voltage = 28.5 kV, height = 5.5 mm, treatment time = 3 min). The power is fairly constant = 485 ± 48 mW (SEM), (Fig 80). The evolution of yield and rate of production are similar for nitrites, nitrates and similar to previous measurements (Fig 81).

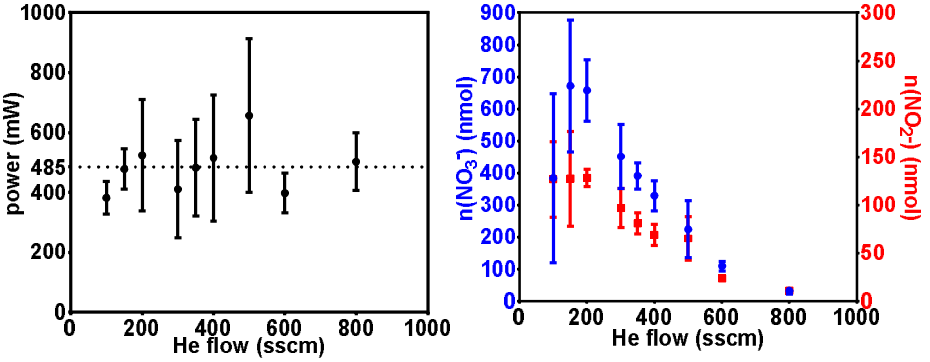

Fig 80 **Left**: power as a function of He flow**. Right**: amount of nitrite and nitrate produced in each well. Treatment time = 3 min, $\Phi He = 100 - 800\ sscm$, height = 5.5 mm, voltage = 28.5 kV, power supply = "500 Hz generator n°3" (II.2.1, Power supply). Each well of the 24-well plate (flat bottom) contains 1.25 ml of deionised water. The addition of Catalase takes place just after the plasma treatment. Triplicate experiment, error bar = standard deviation of the mean

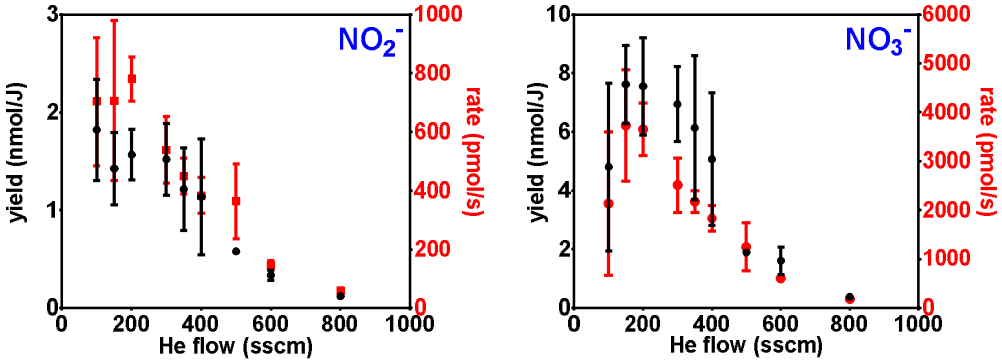

Fig 81 Yield (nmol/J) and production rate (pmol/s) as a function of He flow**. Left**: nitrite, **Right:** nitrate. Treatment time = 3 min, $\Phi He = 100 - 800\ sscm$, height = 5.5 mm, voltage = 28.5 kV, power supply = "500 Hz generator n°3" (II.2.1, Power supply). Each well of the 24-well plate (flat bottom) contains 1.25 ml of deionised water. The addition of Catalase takes place just after the plasma treatment. Triplicate experiment, error bar = standard deviation of the mean.

III.4.3 Adjustable parameter: height above liquid

The variable parameter is the height = 3-13 mm (Fig 82). The set of constant parameters is (voltage = 28.5 kV, $\Phi_{He} = 500\ sscm$, treatment time = 3 min). The power is constant until 11 mm and decreases above. The power, the yield and the rate of production evolve similarly to the previous experiment involving the single-channel plasma jet (Fig 83). For example, the production rate reaches its maximum at the same height ~11 mm.

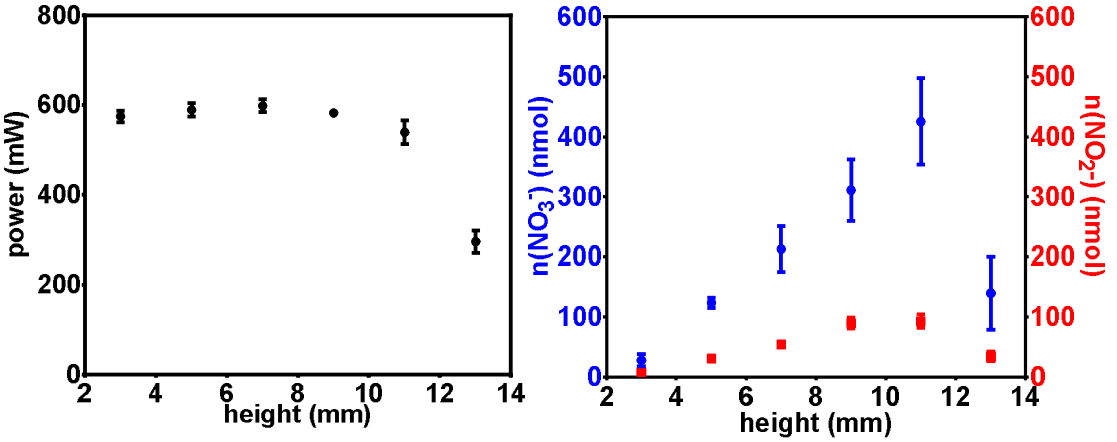

Fig 82 **Left**: power as a function of height. **Right**: amount of nitrite and nitrate produced in each well. Treatment time = 3 min, $\Phi He = 500\ sscm$, height = 3-13 mm, voltage = 28.5 kV, power supply = "500 Hz generator n°3" (II.2.1, Power supply). Each well of the 24-well plate (flat bottom) contains 1.25 ml of deionised water. The addition of Catalase takes place just after the plasma treatment. Triplicate experiment, error bar = standard deviation of the mean.

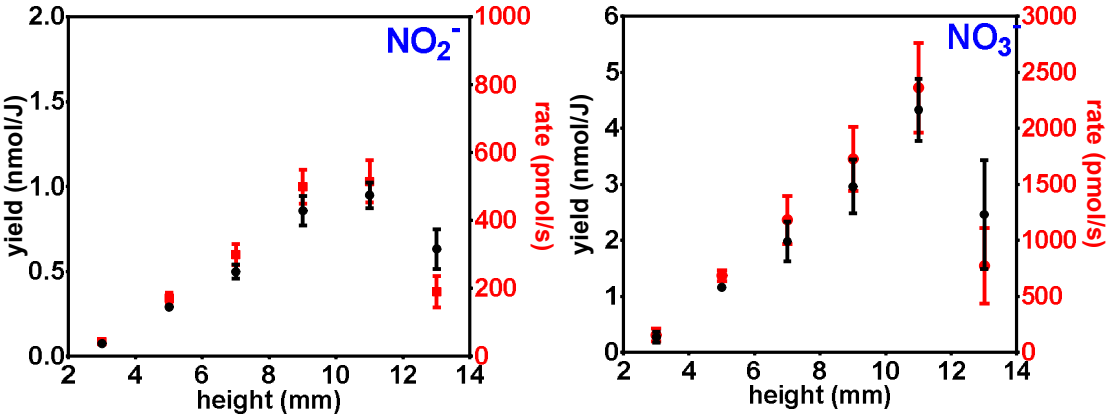

Fig 83 Yield (nmol/J) and production rate (pmol/s) as a function of height. **Left**: nitrite, **Right:** nitrate. Treatment time = 3 min, $\Phi He = 500\ sscm$, height = 3-13 mm, voltage = 28.5 kV, power supply = "500 Hz generator n°3" (II.2.1, Power supply). Each well of the 24-well plate (flat bottom) contains 1.25 ml of deionised water. The addition of Catalase takes place just after the plasma treatment. Triplicate experiment, error bar = standard deviation of the mean.

III.4.4 Adjustable parameter: peak to peak voltage

In this experiment, the voltage of the power supply is in the range 19-28.5 kV. The set of constant parameters is (height=5.5 mm, $\Phi_{He} = 500\ sscm$, treatment time = 3 min). The power is between 200 mW and 600 mW. The amount of nitrates and nitrites increases with the voltage (Fig 84 and Fig 85). Once again the evolution of nitrates and nitrites depends on the voltage in a similar way. The results obtained with the nitrites confirm those obtained during the previous experiment (section III.2).

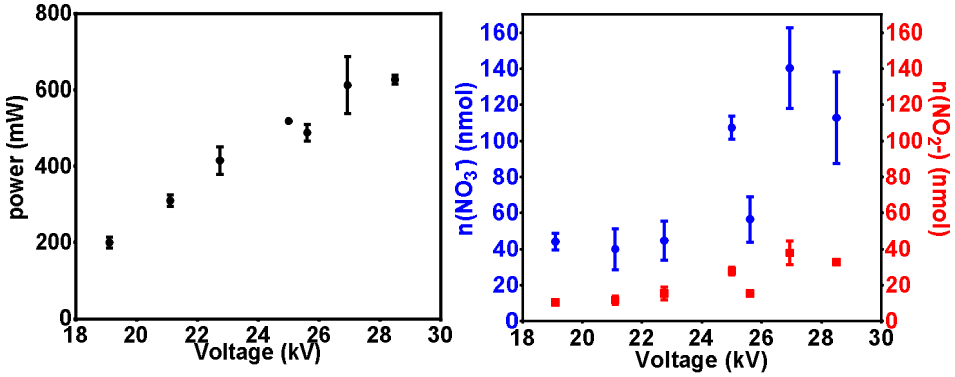

Fig 84 **Left**: power as a function of voltage. **Right**: amount of nitrite and nitrate produced in each well. Treatment time = 3 min, $\Phi He = 500\ sscm$, height = 5.5 mm, voltage = 19-28.5 kV, power supply = "500 Hz generator n°3" (II.2.1, Power supply). Each well of the 24-well plate (flat bottom) contains 1.25 ml of deionised water. The addition of catalase takes place just after the plasma treatment. Triplicate experiment, error bar = standard deviation of the mean.

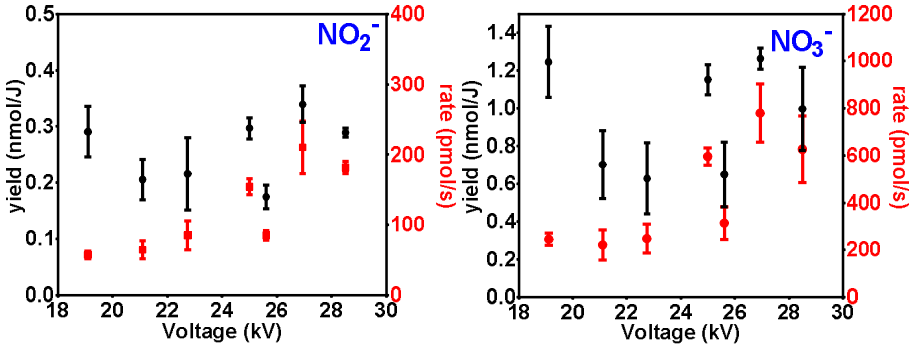

Fig 85 Yield (nmol/J) and production rate (pmol/s) as a function of peak to peak voltage. **Left**: nitrite, **Right:** nitrate. Treatment time = 3 min, $\Phi He = 500\ sscm$, height = 5.5 mm, voltage = 19-28.5 kV, power supply = "500 Hz generator n°3" (II.2.1, Power supply). Each well of the 24-well plate (flat bottom) contains 1.25 ml of deionised water. The addition of Catalase takes place just after the plasma treatment. Triplicate experiment, error bar = standard deviation of the mean.

III.4.5 Ratio nitrate/nitrite

To confirm the link between nitrate and nitrite production, the ration of nitrate/nitrite was computed for the four previous experiments (Fig 86). The ratio is equal to 3.9±1. This means that on average 3.9 molecules of nitrates are produced for one nitrite molecule. It would be interesting to discuss about the mechanism that could provide such ratio.

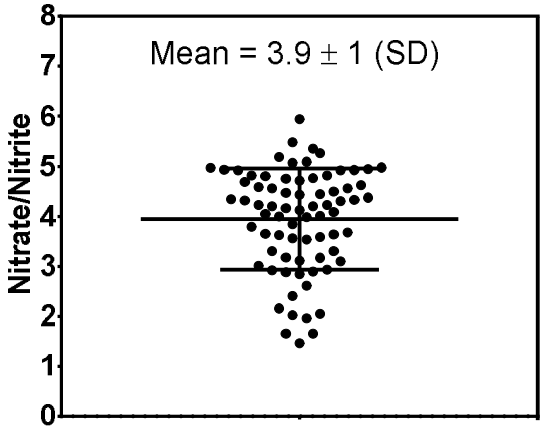

Fig 86 Ratio of the amount of nitrate over nitrite. Concatenation of the four previous experiments.

III.5 Quantification of hydroxyl radical

Before parametric experiments, we need to discuss how works the chemical diagnostic. The whole beginning of this discussion was done in Chapter II (section II.3.4, page 52). The use of terephthalic acid (TPA) as a scavenger of HO ° is not evident because its yield is not 1, and this is not a one-step reaction.

III.5.1 Yield of terephthalate as a dosimeter

Let's start with an experimental result. We perform the same plasma treatment with several concentrations of TPA. After correction with the signal of white samples, and use of TPA-OH calibration-curves (see Chapter II). The following concentrations of TPA-OH were obtained (Fig 87). It turns out that power was approximately the same for each well. There is an increase in the formation of TPA-OH which is necessarily linked to a chemical process, not to a modification of the discharge above the well. The concentration reaches a kind of plateau for TPA~20-30 mM. How to interpret this?

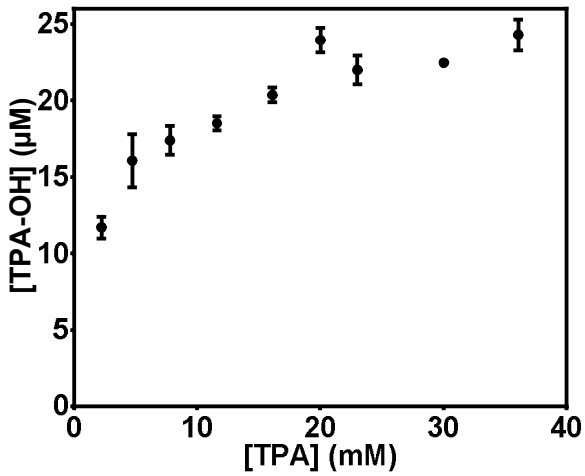

Fig 87 TPA-OH concentration obtained as a function of TPA concentration for the set of parameters: single jet, 2 min, height = 5 mm, Vpp=27.7 kV, He flow = 500 sscm. (V=500 µL). Power ~500 mW. Power supply n°3.

First, radiolysis or sonochemistry studies have shown that the yield of the reaction

$$TPA + OH -> TPA - OH \text{ (which is the sum of several step)}$$

is limited. In an aerated solution (air saturated), it appears that the yield is 35% ([105], [106], [113]–[115])

I will not detail the chemical mechanisms involved, but this 35% yield is (mainly) not due to the first step of the reaction (position of the hydroxylation). It is unlikely that the yield of the others steps changes with increasing TPA concentration. Therefore it will always be necessary to take it into account. Here we observe a change in yield that depends on the concentration of TPA. It means that there is a competition for the scavenging of HO° during the first step of TPA+HO° reaction.

It will, therefore, be necessary to take into account the fact that in the plasma experiments the yield could be limited by the competition during the first reaction stage, but also the yield of 35% above. Since they have not the same origin, more information is available about this topic in the references ([105], [114], [116]–[120]).

Lifetime and length of diffusion of HO° in pure water

In this paragraph, the lifetime of a homogeneous solution of HO° in pure water is calculated. It is also assumed that only HO° recombination plays. Data on reaction kinetics were obtained from the paper of Buxton et al. [121]. The recombination reaction is:

$$HO° + HO° \rightarrow H_2O_2 \quad \mathrm{k_2} = 5.5 \times 10^9\ \mathrm{L.s^{-1}.mol^{-1}} \quad \text{in pure water [121]}$$

Consequently, HO° disappears according to:

$$\frac{d[HO°]}{dt} = -2 \times k_2[HO°]^2$$

So, with n_0 the inital concentration in HO° and $n(t)$ the concentration in HO°:

$$\int_{\mathbf{n_0}}^{\mathbf{n}} \frac{\mathbf{d[HO°]}}{\mathbf{[HO°]^2}} = \int_{\mathbf{0}}^{\mathbf{t}} \mathbf{-2 \times k_2 \times dt}$$

Consequently,

$$\boldsymbol{\frac{1}{n_0} - \frac{1}{n(t)} = -2k_2t}$$

Thus,

$$\boldsymbol{n(t) = \frac{n_0}{1 + 2k_2n_0t}}$$

This equation enables to obtain a time which characterizes the lifetime of HO°: this is merely the expression:

$$\boldsymbol{\tau = \frac{1}{2k_2n_0}}$$

Note that $\boldsymbol{\tau}$ depends on the initial concentration. if $\boldsymbol{n_0 = 10^{-4}M}$, then $\boldsymbol{\tau = 0.9\ \mu s}$. The recombination of HO ° was represented as a function of time in Fig 88 during 15 µs.

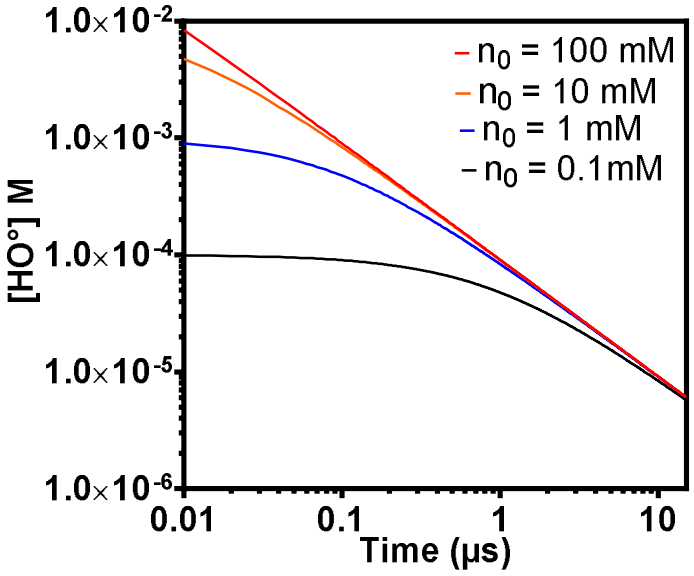

Fig 88 [HO°] as a function of time in a homogeneous solution of water for several n_0

It can be seen that at each initial concentration corresponds a characteristic time needed to observe a significant decrease. It is also interesting to have an idea of how deep H0°can spread during such time. The paper of Buxton et al. provides the diffusion coefficient of HO° in pure water:

$$D(OH°) = 2.3 \times 10^{-9} m^2.s^{-1} \qquad [121]$$

According to this value, the characteristic length of diffusion is: $L(\tau) = \sqrt{D\tau}$

τ	Characteristic length of diffusion during τ
100 ns **~lifetime of plasma above water**	$L(\tau = 100\ ns) = \sqrt{D\tau} \cong 15\ nm$
10 µs	$L(\tau = 10\ \mu s) = \sqrt{D\tau} \cong 150\ nm$
100 µs	$L(\tau = 100\ \mu s) = \sqrt{D\tau} \cong 480\ nm$
2 ms **= One period of the power supply.**	$L(\tau = 2\ ms) = \sqrt{D\tau} \cong 2.1\ \mu m$

It is therefore quite certain that HO ° will not be able to diffuse more than a few tens of nm from the air-liquid interface. But what happens when TPA is added to the solution?

Does the TPA have the same concentration at the interface gas-liquid?

Xiao et al. describe the scavenging of HO° by three organic compounds: terephthalic acid (TPA), ibuprofen and ciprofloxacin [117]. The aim of these experiments is to find if TPA scavenges HO° in bulk solution or HO° at the gas-liquid interface. The sonolysis of the solution (at 20 or 620 kHz) is at the origin of HO° in bulk solution or at the bubble-water interface. It turns out that Ciprofloxacin and ibuprofen are respectively hydrophilic and hydrophobic. It is the hydrophobic or hydrophilic nature of a compound that will determine whether it accumulates on the surface or not. This character can be quantified by the octanol-water partition coefficient (**Kow**), i.e. the ratio of the concentrations the compound in octanol over the concentration in water. A low Kow number (less than 10) corresponds to a hydrophilic compound and high Kow (more than 10^4) to a hydrophobic compound.

According to the paper of Xiao et al, Log(Kow(TPA)) is -1.52 when pH=8.5 and according to PubChem database, Log(K_{ow}(TPA))=2 [122]. As the TPA solutions were prepared with KOH at 20 mM so $pH{\sim}12$. Under these conditions TPA is rather hydrophilic and therefore will not tend to concentrate at the air-liquid interface. It would be interesting to use the same approach than Tauber et al. which estimate the interfacial concentration from gas-fugacity [123], [124]. In the following, we consider that the interfacial and bulk concentrations are the same.

Lifetime and length of diffusion of HO° in TPA

According to the paper of Mark et al., the first step of the reaction leading to TPA (with a yield < 1) is the hydroxylation of TPA by HO° [115]

$$TPA + HO° \rightarrow "Intermediate\ product" \qquad \text{(R1)} \qquad \mathrm{k_1} = 3.3 \times 10^9\ \mathrm{L.s^{-1}.mol^{-1}}$$

If it is assumed that TPA is in large excess compared to HO° and that the others reactions are negligible, the decay of OH° due to TPA is:

$$\frac{d[HO°]}{dt} = -k_1[TPA][HO°]$$

Thus, HO ° decreases exponentially with a characteristic time $\tau = \frac{1}{k_1[TPA]}$,

$$n(t) = n_0 \exp\left({}^{-t}/_{\tau}\right)$$

Generally, the experiments were done with $[TPA] = 4.11\ mM$. Consequently $\tau \cong 74\ ns$.

At first glance, the dosing reaction is much more effective to scavenge HO°. Generally such [TPA] is sufficient to dominate the recombination reaction completely. But if it's true why the production of TPA-OH does depends on [TPA]?

III.5.2 Competition between HO° recombination and the hydroxylation of TPA

Actually, the situif it is assumedation is more complex because HO° is produced in a very short time and at high concentration. It is therefore necessary to study the competition of the two reactions and see if this can explain the fact that the concentration of TPA has an influence on the quantity of TPA-OH produced.

$$TPA + HO° \rightarrow "Intermediate\ product" \qquad \text{(R1)} \qquad \mathrm{k_1} = 3.3 \times 10^9\ \mathrm{L.s^{-1}.mol^{-1}}$$

$$HO° + HO° \rightarrow H_2O_2 \qquad \text{(R2)} \qquad \mathrm{k_2} = 5.5 \times 10^9\ \mathrm{L.s^{-1}.mol^{-1}}$$

$$\frac{d["Intermediate\ product"]}{dt} = k_1[TPA][HO°]$$

$$\frac{d[H_2O_2]}{dt} = k_2[HO°]^2$$

The effect of plasma-liquid interaction is model by a source term S, such as

$$\frac{d[HO°]}{dt} = S$$

We will study the situation in the steady state

$$\frac{d[HO°]}{dt} \cong 0$$

Thus

$$\frac{d[HO°]}{dt} = 0 = S - k_1[TPA][HO°] - 2k_2[HO°]^2,$$

We obtain a polynomial of the second degree in [HO°]:

$$[HO°]^2 + \frac{k_1[TPA]}{2k_2}[HO°] - \frac{S}{2k_2} = 0$$

The discriminant is:

$$\Delta = \left(\frac{k_1[TPA]}{2k_2}\right)^2 - 4 \times \left(-\frac{S}{2k_2}\right) = \left(\frac{k_1[TPA]}{2k_2}\right)^2 + \frac{2S}{k_2}$$

Consequently, $[HO°] = \frac{1}{2}[\left(-\frac{k_1[TPA]}{2k_2}\right) + \sqrt{\Delta}]$, thus

$$\frac{d[Intermediate\ product]}{dt} = k_1[TPA]\frac{1}{2}[\left(-\frac{k_1[TPA]}{2k_2}\right) + \sqrt{\Delta}]$$

The concentration of TPA-OH, obtained after a time t is given by the integration of this equation. However, it is necessary, to take into account the fact that the yield is of the order of 35% (oxygenated solution). Moreover, we can assume that the volume where HO° exists is not the total volume of the solution (~500 µL). We defined an effective volume V_{eff}, this is the volume of solution accessible by HO° during the discharge.

Consequently, we need to define an effective time of reaction, which is different from the treatment time (2 min in this case). Because we need to assume that [HO°] is established only during plasma-surface-interaction (and plasma has a short lifetime ~200 ns at the surface of the liquid). In this condition [TPA-OH] is:

$$[TPA - OH] = YT_{eff}\frac{V_0}{V_{eff}}\frac{{k_1}^2[TPA]^2}{4k_2}(\sqrt{1 + C_2[TPA]^{-2}} - 1)$$

Where, $C_2 = \frac{8Sk_2}{k_1^2}$ and Y=35% is the yield of formation of TPA-OH from "Intermediate product", and $\frac{k_1^2}{4k_2} = 4.95 \times 10^8\ L.s^{-1}.mol^{-1}$.

This equation enables to fit of our experimental results (Fig 89). The result is quite satisfactory and gives a value to S.

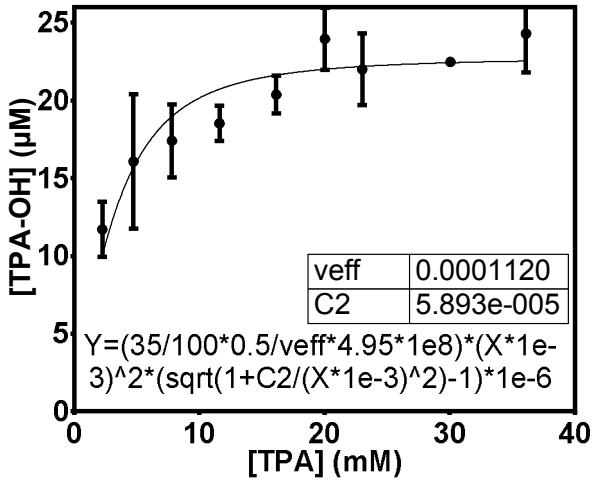

Fig 89 TPA-OH concentration obtained as a function of TPA concentration for the same parameters of treatments: single jet, 2 min, height = 5 mm, Vpp=27.7 kV, He flow = 500 sscm.

$$S = \frac{1}{2} C_2 \frac{k_1^2}{4k_2} = \frac{4.95 \times 10^8}{2} 5.893 \times 10^{-5} = 1.5 \times 10^4 \, mol.L^{-1}.s^{-1}$$

Thus, the "steady" concentration of HO° can be evaluated with

$$[HO°] = \frac{1}{2}\left[\left(-\frac{k_1[TPA]}{2k_2}\right) + \sqrt{\left(\frac{k_1[TPA]}{2k_2}\right)^2 + \frac{2S}{k_2}}\right] = \frac{k_1[TPA]}{4k_2}\left[\sqrt{1 + C_2[TPA]^{-2}} - 1\right]$$
$$= 6.9 \times 10^{-4} \, M$$

Is it coherent?

The fitted value ($Veff_{FIT} = 1.12 \times 10^{-4} \, mL$) represents the effecive volume of reaction divided by Teff the proportion of time where plasma is "on" compared to total time. It is also assumed that the production time of HO° is 100 ns (of the order of magnitude of the life of the ionized column). We assume that our generator has a frequency of 500 Hz and that there is 1 discharge per half-period. Thus,

$$Teff = 2 \times 500 \times 10^{-7} = 10^{-4}$$

In these conditions, the "true" volume is

$$Veff = Veff_{FIT} \times Teff = 1.12 \times 10^{-8} \, mL$$

As we know the diffusion thickness of HO ° during the treatment time: let us try to find the associated surface, which should correspond more or less to the surface of the liquid in contact with the plasma.

$$L(\tau = 100 \, ns) = \sqrt{D\tau} \cong 15 \, nm$$

$$Area = \frac{1.12 \times 10^{-8} \times 10^{-6}}{15 \times 10^{-9}} \cong 7.5 \times 10^{-7} m^2 = 0.75 \, mm^2$$

This is consistent with what we can see in the photos. The average production rate predicted by the fitting is:

$$production \, rate = S \times Veff \times Teff = 16 \, pmol.s^{-1}$$

This is (about one) order of magnitude below the values that we will obtain in the experiments (see next sections). So there is a problem. The chemical reactions do not stop the production of TPA-OH instantaneously after the end of the discharge. The concentration of OH° will decay because of the reaction with TPA at the "long" times, i.e., several $\tau = 74\,ns$. Perhaps it is necessary to consider an “effective time of reaction” longer than100 ns per discharge. For example, doubling this time in our model, will cause a doubling of the production rate.

Finally, it is certain that at this frequency, with this generator, there are several discharges per half-period (and rather less than 10 than hundreds, see Appendix A). This would lead us to predict a production rate consistent with the experimental results. Of course, the whole of the preceding approach is questionable on several points, and a numerical simulation could be of great help.

How does HO° react in this range of concentration?

Now, it is assumed that $[HO°] = 6.9 \times 10^{-4}\ M$ and the reaction rates of HO ° with several chemical is obtained:

1-Recombination reaction:

$$\frac{d[HO°]}{dt} = -2k_2[HO°]^2 = -5240\ mol.L^{-1}.s^{-1}$$

2- Scavenging reaction (with [TPA]=4.11 mM)

$$\frac{d[HO°]}{dt} = -k_1[TPA][HO°] = -9360\ mol.L^{-1}.s^{-1}$$

3-$HO° + H_2O_2 \rightarrow HO_2° + H_2O$ with $k_3 = 2.7 \times 10^7$, [121] and $[H_2O_2] \cong 1\ mM$

$$\frac{d[HO°]}{dt} = -k_3[HO°][H_2O_2] \cong -18.6\ mol.L^{-1}.s^{-1}$$

Consequently, this reaction is likely negligible, whatever [H_2O_2]

4- $HO° + NO_2^- \rightarrow NO_2° + OH^-$ with $k_4 = 9.1 \times 10^9$ [43, p. 252] and $[NO_2^-] \cong 1\ mM$

$$\frac{d[HO°]}{dt} = -k_4[NO_2^-][HO°] \cong -6300\ mol.L^{-1}.s^{-1}$$

Consequently, if $NO_2^- = 1\ mM$, this reaction is not negligible compared to the reaction between TPA and HO°. In this case, the concentration of TPA should be increased to effectively scavenge HO°.

However, in most of the experimental cases encountered so far, the concentration of nitrites remained ~ 100 µM, and so this reaction was negligible.

To conclude, measurements of relative yield as a function of TPA concentration enables to propose an order of magnitude of the mean concentration of hydroxyl radical in the effective volume where TPA and Hydroxyl radicals react. The orders of quantities proposed are consistent. It appears that the quantity of TPA-OH produced when TPA = 4.11 mM (concentration used in the following sections) represents only 65% of the maximum that could be obtained by increasing [TPA]. This value was obtained with the fit seen in Fig 89.

III.5.3 Single-channel jet, Hydroxyl radical HO°

The following four sections contain the results of a parametric study performed on the single-channel jet. The experimental setup is exactly the same in the three previous experiments characterizing the production of nitrite, nitrate, and H_2O_2. The fluorescence of the sample was measured[45] as described in Chapter II (section II.3.4.2). The calibration curve enables to determine the concentration of TPA-OH present after plasma treatment.

Each well of the 24-well plate (flat bottom) contains 1400 µL of a solution with the following composition[46]:

[TPA] = 4.11 mM + [KOH]= 20 mM + deionised water,

After treatment, the final volume was around 1200 µL. The amount of hydroxyl radical is obtained from the amount of TPA-OH by making two assumptions regarding the yield of the reaction producing TPA-OH:

i) Since $[TPA] = 4.11\ mM$, it is assumed that the first step of the hydroxylation of TPA by HO° reaches only 65% of its maximum value because of the competition with the recombination reaction ($HO° + HO° \rightarrow H_2O_2$).

ii) Since the liquid phase is initially saturated with air, and assuming that the amount of dissolved oxygen does not decrease significantly[47] in only 3 minutes, it can be considered that the mechanisms which produce TPA-OH, after the first step of reaction (i.e., the addition of HO°) have a yield of 35% [105], [115].

It is therefore considered that only $65\% \times 35\% \sim 22.8\%$ of the molecules of HO° produces one molecule of TPA-OH. This correction has been applied to the results of the four following sections.

III.5.3.1 Adjustable parameter: treatment time

The treatment time varies in the range: 1-6 min. The set of constant parameters is voltage = 27.5 kV, $\Phi_{He} = 500\ sccm$, height = 5.6 mm. The amount of HO° detected increases linearly as a function of the treatment time (Fig 90). The slope represents a production rate ~240 pmol/s. The power is $580 \pm 70\ (SD)\ mW$.

[45] λex=317nm, λem=435nm, with bandpass Δλ= 5 nm for excitation and emission.

[46] The choice [KOH]=20 mM, is necessary for the solubilization of terephthalic acid. The use of di-sodium terephtalate which is easier to solubilize enables to do experiments at neutral pH. Preliminary experiments show that the results are identical at neutral pH.

[47] This hypothesis is debatable, but let us remembers that the volume is around 1200 µL. and that the helium flux is moderate and does not bubble in the liquid, which limits gas exchange. Moreover, according to [105], *"the terephthalate system does not show a significant O2 dependence of the hydroxylation reaction. Thus, even as the oxygen content of the water drops during sonication, the amount of OH radical production can still be measured with confidence."*

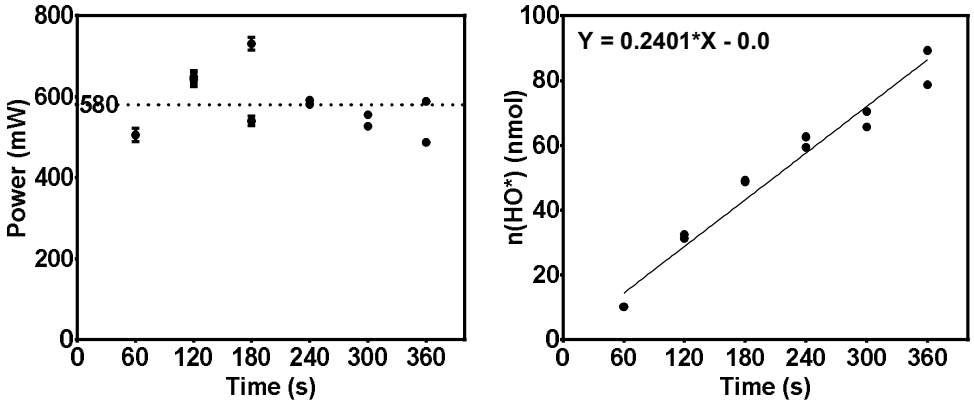

Fig 90 **Left** power consumption (mW) as a function of time. **Right** amount of HO° (nmol) measured as a function of time. Treatment time = 1-6 min, frequency of power supply = 500 Hz, peak to peak voltage = 27.5 kV, $\Phi_{He} = 500\ sscm$, height = 5.6 mm, power supply = "500 Hz generator n°3" (II.2.1, Power supply). Each well of the 24-well plate (flat bottom) contains 1400 µL of the TPA +KOH solution. Duplicate.

On average, the yield is ~0.4 nmol/J (Fig 91). Note that the amount of H_2O_2 that would be produced by the recombination of all HO° in pure water is much lower than the amount of H_2O_2 observed. Indeed, HO° would produce only[48] ~0.2 nmol/J, whereas the yield of H_2O_2 is ~ 1.7 nmol/J with the same parameters (see Fig 62, p 68). Consequently, HO° is probably not the only species which contributes to the production of H_2O_2 in liquid phase. We can imagine that H_2O_2 is formed in gas phase, or from the superoxide radical in liquid phase in these precise experimental conditions.

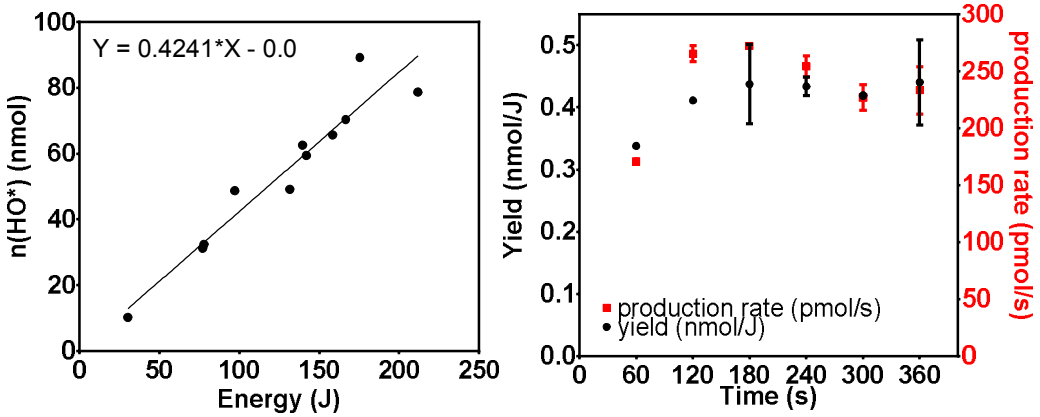

Fig 91 **Left**: amount of HO° radical as a function of energy consumption. Treatment time is between 1 and 6 min. **Right: Yield** and production rate of HO° as a function of time. Treatment time = 1-6 min, frequency of power supply = 500 Hz, peak to peak voltage = 27.5 kV, $\Phi_{He} = 500\ sscm$, height = 5.6 mm, power supply = "500 Hz generator n°3" (II.2.1, Power supply). Each well of the 24-well plate (flat bottom) contains 1400 µL of the TPA +KOH solution. Duplicate.

III.5.3.2 Adjustable parameter: helium flow rate

The variable parameter is the flow ($\Phi_{He} = 100 - 700\ sscm$). The set of constant parameters is: (voltage = 25.6 kV, height = 5.7 mm, treatment time = 3 min). Power

[48] It takes two HO ° to make one H_2O_2

consumption is quite constant $P = 400 \pm 50\, mW\ (SD)$ (Fig 92). The yield is in the range 0.3-0.6 nmol/J and increase with helium flow rate $\Phi_{He} \leq 500\ sccm$. The production rate is between 100 and 250 pmol/s and increase. The trends are opposite to that of H_2O_2 (decrease of yield and production rate, see Fig 60, page 66). This is another argument against the statement: "HO ° in the liquid phase is the main species at the origin of H_2O_2".

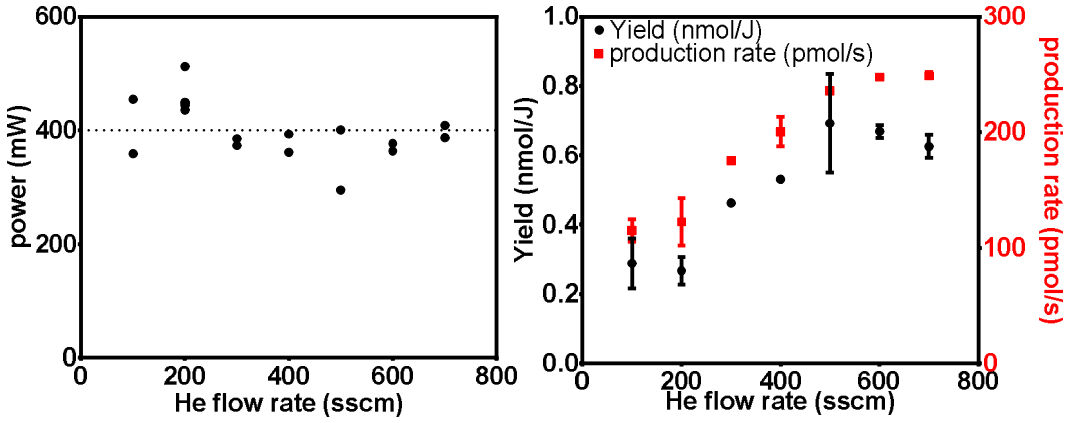

Fig 92 **Left:** power (mW) as a function of Helium flow rate. **Right:** yield (nmol/J)and production rate (pmol/s) of HO° as a function of flow rate. Treatment time = 3 min, frequency of power supply = 500 Hz, peak to peak voltage = 25.6 kV, $\Phi_{He} = 100 - 700\ sccm$, height = 5.7 mm, power supply = "500 Hz generator n°3" (II.2.1, Power supply). Each well of the 24-well plate (flat bottom) contains 1400 µL of the TPA +KOH solution. Duplicate.

III.5.3.3 Adjustable Parameter: height above liquid

The variable parameter is the height = 1.5-10.5 mm (Fig 93). The set of constant parameters is: (voltage = 28.1 kV, $\Phi_{He} = 500\ sccm$, treatment time = 3 min). The power is constant ~575 ± 60 mW. Beyond 6 mm in height, the yield and production rate were halved compared to the value they have below 3 mm. Once again, the trend is the opposite of that found for H_2O_2 production (see Fig 61, page 67).

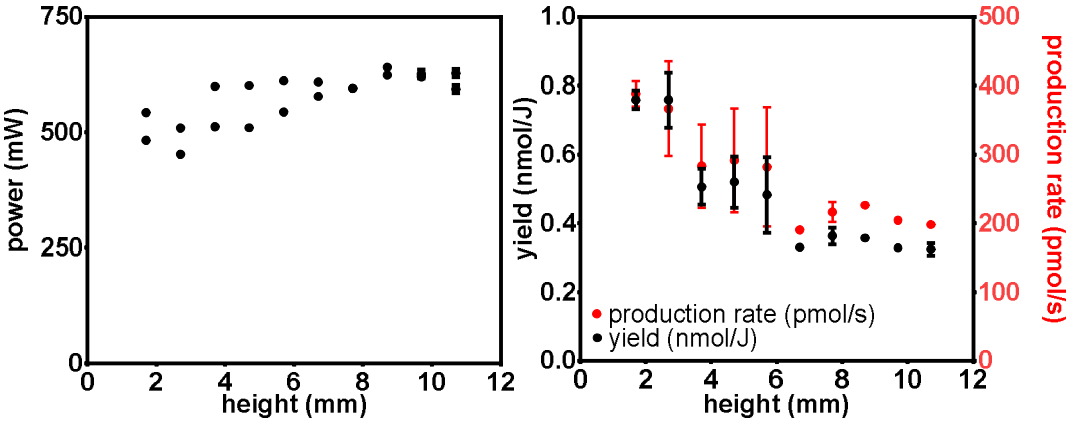

Fig 93 **Left:** power (mW) as a function of height. **Right:** yield (nmol/J) and production rate (pmol/s) of HO° as a function of height. Treatment time = 3 min, frequency of power supply = 500 Hz, peak to peak voltage = 28.1 kV, $\Phi_{He} = 500\ sccm$, height = 1.5-10.5 mm, power supply = "500 Hz generator n°3" (II.2.1, Power supply). Each well of the 24-well plate (flat bottom) contains 1400 µL of the TPA +KOH solution. Duplicate.

III.5.3.4 Adjustable parameter: peak to peak voltage

In this experiment, the voltage of the power supply is in the range 16.5-29 kV. The set of constant parameters is (height=5.7 mm, $\Phi_{He} = 500\ sscm$, treatment time = 3 min). The power changes considerably (between 200 mW and 750 mW). The rate of production increases with voltage, while the yield tends to decrease (Fig 69). The yield and the rate evolve in the range 0.2-1.1 nmol/J and 150-250 pmol/s respectively.

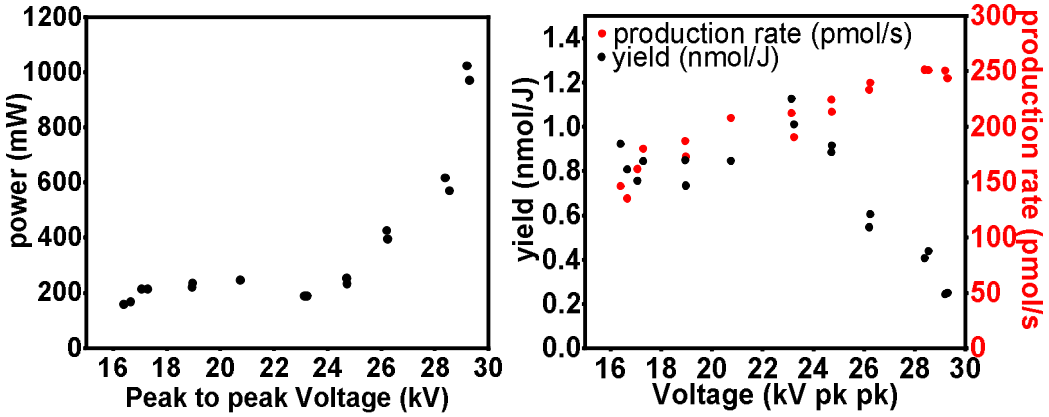

Fig 94 **Left:** power as a function of voltage. **Right:** yield (nmol/J) and rate of production of HO° (pmol/s). Treatment time = 3 min, frequency of power supply = 500 Hz, peak to peak voltage = 16.5-29 kV, $\Phi He = 500\ sscm$, height = 5.7 mm, power supply = "500 Hz generator n°3" (II.2.1, Power supply). Each well of the 24-well plate (flat bottom) contains 1400 µL of the TPA +KOH solution. Duplicate.

III.6 In a living organism, what is the depth of penetration of H_2O_2?

In the field of plasma-medicine, it is widely accepted that RONS and particularly H_2O_2 can probably diffuse through living tissue over several mm [64]. H_2O_2 is described as a relatively stable species, especially compared to the hydroxyl radical [100]. According to this assumption, it is logical to assume that this species could be at the origin of anti-tumor effects. Indeed, *in-vitro* studies prove that H_2O_2 can induce cell death per necrosis or apoptosis beyond a concentration of a few hundred µM. At higher concentration, >~10%, H_2O_2 is even considered as a corrosive product [56].

Unfortunately, a crucial point is often neglected: the anti-oxidant defenses. Cells have the ability to remove ROS very efficiently. In particular, the skin and its outermost layer provided several mechanisms to deal with oxidizing aggressions. This set of molecules, enzymes, and metabolic pathways is called the antioxidant network.

We begin with a brief description of the antioxidant defenses of the skin. Emphasis is placed on quantitative data, such the amount of catalase or other anti-oxidant systems present in the different layers of the skin.

Then, the notion of cell membrane permeability (H_2O_2) is described. This value enables to determinate the flux of H_2O_2 crossing the plasma membrane as a function of the extracellular concentration in H_2O_2. This model enables to find the lifetime of H_2O_2 in the

presence of cells[49]. The result is consistent with the results our team (C. Duchesne) and with the literature.

An *in-vivo* diffusion model which integrates the effect of the anti-oxidant is then described. The simulations by finite element method could extend the results of this section.

Finally, a critical approach of the papers which address this question is proposed. The use of gelatine layer as a "good" tissue-model to understand RONS is disputed.

III.6.1 Anti-oxidant defense of the skin, relevant orders of magnitude

How H2O2 enters into the cells?

The transportation of H_2O_2, from the extracellular medium to the intracellular medium is an area of active research. It appears that the natural diffusivity across the phospholipid membrane cannot explain the intake of H_2O_2 which is greater than expected [125]. The cells can exchange molecules with the extracellular environment by means of various channels, i.e., complex assemblies of proteins crossing the membrane and whose activation depends on internal or external cellular signals. The aquaporins are part of the channels responsible for exchanging water[50] between the external and internal environment. Because the molecular structure of water and H_2O_2 are relatively close [127]; H_2O_2 cross the membrane preferentially through aquaporins.

Even if the underlying phenomenon is complex[51], the transport of H_2O_2 is described by a quantity called permeability that represents the ability of H_2O_2 to pass through a membrane:

The permeability P_{H2O2} is the ratio of the incoming flow (in $mol.m^{-2}.s^{-1}$) by the extracellular concentration of H_2O_2 (in $mol.m^{-3}$).

$$\mathrm{P} = \frac{\Phi}{[\mathrm{H_2O_2}]}\ \mathrm{m.s^{-1}}.$$

Permeability: orders of magnitude

Henzler et al. report that the H_2O_2-permeability of the cells of the plant *Chara Corallina* is ~$3.6 \times 10^{-6}\ m.s^{-1}$ [127]. For this plant, the main barrier of water and/or H_2O_2 transport is mainly due to the plasma membrane.

Antunes et al. depict the kinetics of H_2O_2 consumption by the Catalase and Glutathione peroxidase (GPX) enzyme [128]. They expose Jurkat T-cells to an external source of H_2O_2. The permeability of these cells is $2 \times 10^{-6}\ m.s^{-1}$. This paper also indicates that the permeability of the human erythrocytes is tree-fold greater: $\sim 6 \times 10^{-6}\ m.s^{-1}$. Most mammalian cells have permeability of the order of $\sim 10^{-6}\ m.s^{-1}$. Erythrocytes are part of the higher value in terms of permeability.

---

[49] it has been checked that the culture medium itself does not destroy H_2O_2. Beware of media containing sodium pyruvate which is a scavenger of H_2O_2.

[50] and others non-charged charged and partially polar molecules [125], [126]

[51] the active pumping of molecules controlled by a cell responding to the modifications of its environment!

Antunes et al. also indicate that approximately 1 s is needed to build the gradient of [H_2O_2] at the plasma membrane. Since the cells contain organelles which are separately enclosed, there is also H_2O_2 transport across these membranes. In particular, the peroxisomes contain catalase which is enclosed in this specific part of the cell. The Glutathione peroxidase (GPX) enzyme is present in the entire cytosol. On the other hand, they have lower activity than catalase and contribute mainly to the destruction of H_2O_2 at low concentration. In the approximation of low concentrations, Antunes et al. show that GPX contributes for 90% to the destruction of H_2O_2. The 10% remaining are due to the activity of catalase (less accessible because of his location in peroxisomes). In these conditions, Fig 95 shows the concentration of H_2O_2 expected in the cytosol and peroxisomes.

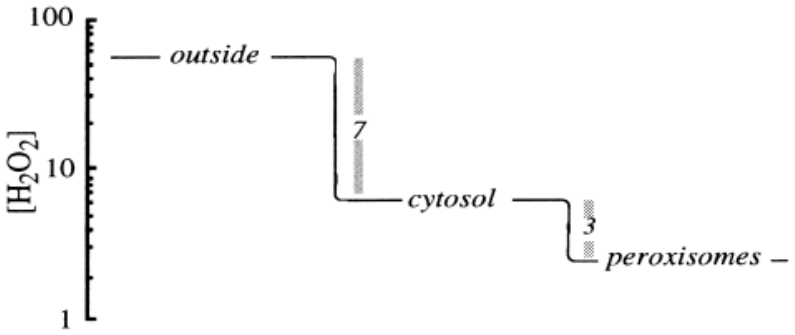

Fig 95 Figure and legend adapted from the paper of Antunes et al. [128].Profile of H_2O_2 concentration in Jurkat T-cells upon incubation with an external source of H_2O_2. [H_2O_2] log scale axis has arbitrary units.

Too high, the concentration of H_2O_2 can inhibit the GPX [129]. It is likely that the inactivation of the GPX occurs in a few minutes, if [H_2O_2] is ~100 mM, which means that the extracellular concentration should be ~700 mM according to Fig 95. Such concentration may be accessible for the higher layers of the skin exposed to plasma.

Regarding the kinetics, the reaction rate of the Michaelis-Menten constant (Km) of catalase[52] is higher than the Km of GPX [130]. Consequently, at high concentration ($\sim 10\ mM$) of H_2O_2, the activity of catalase continue to increase while that of GPX no.

The situation is different for erythrocytes since catalase is present in the cytosol. They contain higher level of catalase than the others cells according to Agar et al. [131]. In these cells the catalase predominantly contributes to the elimination of H_2O_2 [132]; among the others anti-oxidant defenses [133]. So, since the H_2O_2-permeability is approximately three times higher in erythrocyte than in other cells, the blood is extremely efficient for destroying H_2O_2. Therefore it is very unlikely that H_2O_2 can spread without being destroyed over a substantial distance in the blood[53] or in irrigated tissues such as the dermis or tumor.

The permeability of yeasts to H_2O_2 is modified according to whether they are in exponential division phases, or whether they maintain a stable population. In the case of exponential growth, the membrane is 5 times less permeable. Sousa-Lopes et al. point out that this remarkable behavior allows these yeasts to protect themselves from oxidative stress when they are the most vulnerable [134]. Finally, the reader can consult the excellent review of Bienert et al. to get more information about H_2O_2 transport [125].

---

[52] Km is the concentration of substrate (H_2O_2)at which the reaction rate is at half-maximum

[53] The surgeons are very well aware of the danger of treating a bloody wound with too much oxygenated water: gaseous embolisms or emphysema caused by an oxygen concentration so excessive that it is no longer soluble in tissues can be deadly.

Anti-oxidants defense of the skin

The skin is frequently and directly exposed to prooxidative environment including UV radiation, air pollutants, and drugs. Skin contains antioxidants systems which counteract the harmful effects of ROS. Thiele et al. detail the prevalence of each anti-oxidants present in the skin and how they act [135]. The following species play a significant role in the defense of the skin: vitamin C, Glutathione GSH[54], Urate[55], Vitamine E[56], the couple Ubiquinols/Ubiquinones, Carotenoids and Vitamin A, The enzymatic Glutathione system[57], superoxide dismutase and catalase. Further discussions outside of the scope of this thesis can be found in [100], [111], [136]–[144]

Some factors may contribute to the destruction of the antioxidant defenses of the skin. Valacchi et al. show that UV, cigarette smoke, and ozone can potentiate their effects and lead to a depletion in Vitamine-E, α-tocopherol [145]–[147].

Sometimes it is interesting that chemical species cross the skin. A drug must cross the epidermis before reaching the dermis and blood circulation. The hydrophilic or hydrophobic character of the applied molecule, the presence of emollient, and the thickness of the stratum corneum are key factors in the penetration of organic compound [148]–[153].

Orders of magnitude related to the prevalence of catalase

The concentration of catalase is generally represented in terms of unit of enzymatic activity. One unit of catalase is the quantity of catalase that will decompose 1.0 µmole of H_2O_2 per minute at pH 7.0 at 25 °C, while the H_2O_2 concentration falls from 10.3 mM to 9.2 mM.

Shindo et al. measured that the catalase activity is: 30.4 ± 4.3 U/mg protein in murine epidermis and 33.3 U/mg protein in murine dermis [140]. According to [135] and [140], the catalase activities is higher in human epidermis (62 ± 6 U/mg protein), but lower in the dermis (14.5 ± 2.9 U/mg protein) compared to the mouse. This is potentially an issue for the translation[58] of an effective murine treatment to humans treatments.

In-vivo and ex-vivo experiments, origin of the skin whitening exposed to H_2O_2

It is well known[59] that the application of H_2O_2 on the surface of the skin causes a whitening phenomenon. Zonios et al. explain that this transient phenomenon is attributed to vasoconstriction [154]. Zonios et al. have applied different concentrations of H_2O_2 (0.5 -6 %w, i.e., ~ 1.6 M) at the top of the skin and measured the reflectance of the skin. This method enables to detect an oxidized form of hemoglobin or melanin. They emit serious doubt about the fact that H_2O_2 can spread to the dermis without being totally destroyed by the anti-oxidant defenses of the skin. The results they obtain can be explained by the release of O_2 resulting from the reaction between H_2O_2 and catalase. They explain that

[54] An essential cofactor of GPX enzyme
[55] deprotaned form of uric acid
[56] "The major antioxidant role of vitamin E is generally considered to be the arrest of chain propagation by scavenging lipid peroxyl radicals" [135]
[57] This system reduces H_2O_2 and lipid hydroperoxides at the expense of two molecules of GSH,
[58] If anti-tumor effect are maily caused by prooxidative action of plasma-treatment.
[59] a commercial solution at 3% enables to observe this effect when we keep a few droplets in the palm of the hand for a few minutes.

O_2 alone may cause vasoconstriction[60]. Zonios et al., also suggest that contact of H_2O_2 with blood[61] will result in accelerated scavenging of H_2O_2.

Nocchi et al. studied the ability of catalase contained in the stratum corneum to destroy H_2O_2 [157]. For this, 500 µm of human skin[62] was brought into contact with a solution of H_2O_2 (0.5 or 1 mM in PBS) on its outer face; and a Clark type electrode measuring the oxygen on its inner face (see Fig 96). They also mention that acidic pH ($pH \leq 2$) probably decrease catalase efficency *in-vivo.* They removed the stratum corneum layer by layer by tap-stripping and observed the signal of Clark electrode (proportional to [O_2]). This experiment confirms the strong activity of catalase in the epidermis, but does not enables to conclude with regard to the diffusion of H_2O_2 itself and its total destruction or not by epidermis and dermis.

Fig 96 Legend and figure from the paper of Nocchi et al. [157]. Photo of oxygen electrode covered with skin membrane.

III.6.2 Modeling of an *in-vitro experiment*

In order to quantify the contribution of H_2O_2 to the whound healing induced by cold-plasma treatment, our colleague C.Duchesne exposed humans fibroblastes and keratynocytes to H_2O_2. [H_2O_2] was measured over time. Each wells contained, $N = 200\,000$ cells in 2 mL. It appears that the time to decrease the concentration of extracellular H_2O_2 from 100% to 37% is **~2 h**.

The purpose of this section is to model the removing of H_2O_2 due to cell permeability and compare the results with those of the in-*vitro* experiments. First, it is assumed that all the molecules of H_2O_2 crossing the membrane are destroyed. We consider that membrane

---

[60] In contrast the role of H2O2 alone is less clear, since H_2O_2 alone can be both vasoconstrictor and vasodilator [155]

[61] Zonios et al. [154] *"However, we have seen no evidence of their production here, which means that either H_2O_2 decomposed before it was given the chance to react with haemoglobin or that the produced oxidized haemoglobin forms were quickly reduced owing to the action of reducing agents available in vivo such as ascorbate. In general, skin appears to have a very strong antioxidant capacity and H_2O_2 may be decomposed following numerous other pathways besides the straightforward one that involves its reaction with catalase. Some evidence supporting this argument is offered by oxygen bubbles observed histologically in the skin after reaction with the 35% solution of H_2O_2 (*[156]*)."*

[62] this thickness includes the epidermis and part of the dermis

permeability works as described above. The differential equation which predicts the temporal evolution of H_2O_2 takes the form:

$$\frac{\delta n}{\delta t} = -n \times P_S \times A_{tot} \times \frac{1}{V}$$

Where n is H_2O_2 concentration ($mol.m^{-3}$), P_S is the permeability ($m.s^{-1}$), A_{tot} is the total area of all the cells and V is the volume of the well in which the experiment takes place. The solution of this equation is:

$$n = n_0 \exp\left(-{}^{t}/_{\tau}\right)$$

where n_0 is the initial concentration and

$$\tau = \frac{V}{P_S \times A_{tot}}$$

is the time which characterizes the decay of H_2O_2.

For the calculation, we assume that $P_S = 2 \times 10^{-6}\ m.s^{-1}$. This is the H_2O_2-permeability of the mammalian cells according to Antunes et al. [128]. In the first approach, we assumed that the cells are spherical with radius $r = 10\ \mu m$. Thus, the total area is $A_{tot} = N \times 4\pi r^2$, where N is the number of cells in the well. Since N = 200 000,

$$A_{tot} = 200\,000 \times 4\pi(10^{-5})^2 = 2.51 \times 10^{-4}\ m^2$$

and then

$$\tau = \frac{2 \times 10^{-6}}{2 \times 10^{-6} \times 2.51 \times 10^{-4}} \cong 4000\ s = 1h + 6\ min$$

This time is consistent with the experiments (**~ 2h**). This order of magnitude is also consistent with the experimental results obtained by others groups ([125], [127], [128], [134]), especially regarding the fibroblast [158]. Similarly, these teams propose the same kind of interpretation, based on permeability calculations.

In this model, we have considered perfectly spherical cells whose entire surface is freely accessible. In fact, the free area of the cells is probably smaller than modeled since the cells adhere at the bottom of the well. Moreover, the cells are almost confluent. This decrease of the free surface could explain why the model predicts a faster decay than observed. Wagner et al. show experimental results that are consistent with this hypothesis [159]. Indeed, they observed that detached cells destroy H_2O_2 faster than attached ones.

III.6.3 In vivo: diffusion model

The purpose of this section is to question the hypothesis "H_2O_2 can spread over several mm in living tissue". Is this realistic? Or not?

Similarly, it is assumed that the totality of H_2O_2 entering the cells is suppressed by the intra-cellular anti-oxidant[63]. For the sake of simplicity, it is also assumed that there are no anti-oxidants in the extracellular environment and that the cells occupy all space. It described an epithelium-like structure.

[63] whatever the antioxidant mechanism at work (GSH or catalase, non-enzymatic system...)

Let's start with an orders-of-magnitude calculation.

First, we must find the number of cells present in the skin per unit volume. If it is assumed that the cells are spherical with a radius $r = 10\ \mu m$. The number of cells per unit volume is:

$$n_c = \frac{1}{\frac{4}{3}\pi r^3} = 2.39 \times 10^{14}\ m^{-3}$$

This order of magnitude is quite good since the density of fibroblasts in the human dermis is 3×10^{12} and $10^{14}\ m^{-3}$, respectively for reticular and papillary dermis according to [160].

For the calculation, we choose the value: $n_c = 10^{13}\ m^{-3}$, with this assumption the volume of one cell is $10^{-13}\ m^3$. The surface of this single cell[64] is ~$10^{-8}\ m^2$. Consequently, the total area of the cells per unit of volume is:

$$S_C = n_C \times 10^{-8} = 10^5\ m^2/m^3$$

As seen in the *in-vitro* model, it is assumed that the permeability is $\mathrm{P_S} = 2 \times 10^{-6}\ \mathrm{m.s^{-1}}$ [128]. The volumic consumption of H_2O_2 takes the form:

$$-S_C P_S n$$

The equation representing the diffusion of H_2O_2 is:

$$\frac{\partial \mathrm{n}}{\partial \mathrm{t}} = \mathrm{D}\Delta \mathrm{n} - \mathrm{S_C P_S n}$$

where D is the diffusion coefficient. For this order-of-magnitude calculation, it is assumed that the material is homogeneous and isotropic[65]. As in the work of Marquez-Lago et al. who simulate the skin with a mortar-diffusion model[66], we assume[67] that $D = 10^{-7}\ cm^2.s^{-1} = 10^{-11}\ m^2.s^{-1}$ [161].

With this model, the ROS introduced at the top of the skin are carried by passive diffusion and consumed by the anti-oxidant defenses when they cross the membrane of a cell. The RONS produced by the cold plasma is modeled with a constant surfacic term: $\Phi = CST\ mol.s^{-1}.m^{-2}$. For this order-of-magnitude calculation, we consider the 1-dimensional problem. In this framework, the problem is summarized by:

$$\begin{cases} \dfrac{\partial \mathrm{n}}{\partial \mathrm{t}} = \mathrm{D}\dfrac{\mathrm{d}^2\mathrm{n}}{\mathrm{dx}^2} - \mathrm{S_C P_S n} \\ + \text{boundary condition:} \quad -D\dfrac{dn}{dx}(x=0, t \geq 0) = \Phi \\ + \text{ initial condition:} \quad \mathrm{n} = 0 \end{cases}$$

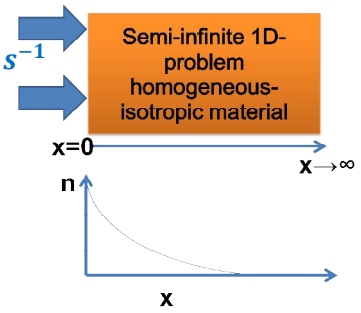

[64] spherical cells approximation
[65] Strictly speaking, this is false for the skin.
[66] It would be possible to develop one simulation based on the work of Marquez-Lago et al. [161].
[67] we suppose that the diffusion coefficient is the same for water and H_2O_2, which is likely true in terms of order of magnitude.

We want to know the characteristic time and length of attenuation lengths of time. After the transient regime we have:

$$0 = \mathrm{D}\frac{\mathrm{d}^2\mathrm{n}}{\mathrm{dx}^2} - \mathrm{S_C P_S n}$$

Consequently, the characteristic length is L_{CAR} such that:

$$\frac{\mathrm{D}}{\mathrm{L_{CAR}^2}} = \mathrm{S_C P_S}$$

thus, $$\mathrm{L_{CAR}} = \sqrt{\frac{\mathrm{D}}{\mathrm{S_C P_S}}} = \sqrt{\frac{10^{-11}}{10^5 \times 2 \times 10^{-6}}} \cong 7\ \mu m$$

and the concentration take the form: $n(x) = \frac{\Phi L_{CAR}}{D} \exp\left(-\frac{x}{L_{CAR}}\right)$.

In this model, the surface concentration is directly related to the incident flux. This incident flow can be evaluated with our chemistry experiments. It can be considered that the single-channel plasma jet produces approximately 1 nmol of H_2O_2 per second over an area of 1 mm ². Thus $\Phi = 10^{-3}\ \mathrm{mol.m^{-2}.s^{-1}}$ and

$$\mathrm{n(x=0)} \cong 700\ \mathrm{mol.m^{-3}} = 0.7\ \mathrm{mol.L^{-1}}$$

This order of magnitude is not absurd, besides the commercial H_2O_2 solutions are concentrated at $3\%\ \mathrm{w} \cong 0.9\ \mathrm{mol.L^{-1}}$.

According to this model, on what depth H_2O_2 will damage the cells?

According to Stone and Yang (see [60] and our own in-vitro experiments, see Chapter IV), it is unlikely that an extracellular concentration of H_2O_2 below 10 µM cause cell death, or slow cell growth. This concentration is reached for $\mathrm{x = L_{DEATH}}$ such that:

$$\mathrm{n(x = L_{DEATH})} = 10\ \mu\mathrm{M} = 10^{-8}\ \mathrm{mol.m^{-3}}$$

thus,

$$n(x = L_{DEATH}) = n(x=0) exp\left(-\frac{L_{DEATH}}{L_{CAR}}\right) \text{ and } \frac{L_{DEATH}}{L_{CAR}} = -Ln\left(\frac{n(x=L_{DEATH})}{n(x=0)}\right) \cong 25$$

Consequently, $L_{DEATH} \cong 25\ L_{car} \cong 175\ \mu m$,

According to this model, it is therefore unlikely that the damage caused by H_2O_2 could damage the skin to a depth of more than 175 µm. This depth[68] is in the human dermis and exceeds the depth of the mouse dermis by a few tens of µm.

Now, I am going to criticize this model, some aspects of this model lead to an underestimation of the depth of penetration, while others lead to an overestimation:

This model could <u>under</u>estimate the depth of penetration because:

i) It is assumed that H_2O_2 is removed as soon as the molecules have crossed the membrane for any external concentration of H_2O_2. This is obviously false.

[68] [162] see Chapter VI, section VI.1.1 for the comparison of human and mouse skin.

For the upper layer of cells, the antioxidant defenses of the cell are overloaded by the molar concentration of H_2O_2. It is likely that the intracellular concentration is high. This causes DNA damage and kills the cell. The amount of H_2O_2 that these cells will take to the external environment will be lower than modeled. However, the catalase works well even at high concentration of H_2O_2 (several mol.L^{-1}, [163], [164]). In case of destruction of the cell membrane, it is not easy to guess whether catalase, released from the cell, will see its anti-oxidant activity increased or not ...

ii) H_2O_2 transport is modeled as a purely diffusive phenomenon. According to this model, $L(\tau = 10\ \mathrm{min}) = \sqrt{D \times \tau} = 77\ \mu m$. A weak but continuous electric field, due to the establishment of a constant potential difference on the surface of the skin, could contribute to an accelerated migration of chemical species. In the same way, could the mechanical vibrations caused by the treatment modify the transport of the chemicals?

iii) The reaction of cells to such oxidative stress is not really predictable. New metabolic pathways can be triggered by this stress. In some cases, the cells develop a tolerance to oxidative stress [165], [166]. However, the open questions regard the time scale of these phenomena. Are they relevant compare to the time scale of plasma treatment?

iv) It is false to model the material as homogeneous at the scale of the cell. Since the value L_{car} has a size similar to those of a cell, its validity may be debatable. However, having a such value of L_{CAR} is not shocking by itself, since it is considered that the H_2O_2 consumption results from an averaging of the amount of H_2O_2 absorbed by the surfaces of several cells. L_{car} has a statistical meaning. Finally, while it is certain that **n(x)** is wrong at cell scale, it does not mean that the description is incorrect for the sizes representing thicknesses of several cells.

This model could overestimate the depth of penetration because:

i) This is a 1D model. Since, the diffusion can occur in all directions, [H_2O_2] decreases faster as a function of depth than in this model.

ii) The dermis is a very well irrigated tissue. Blood flow could help eliminate H_2O_2 in a much more effective way. Indeed, the erythrocytes are the most common blood cell. The H_2O_2-permeability is higher[69] in erythrocyte than in other cells [128]. They contain higher level of catalase than the others cells according to Agar et al. [131]. In these cells the catalase predominantly contributes to the elimination of H_2O_2 [132]; among the others anti-oxidant defenses [133]. Wagner et al. specify the numerical values for the human erythrocyte [159].

iii) If electroporation takes places, it could enhance the H_2O_2-intake of the cells located in the upper layer of the skin and the molecules consumed by these cells could not diffuse below.

iv) The model does not take into account the effect of other anti-oxidant systems present in the extracellular matrix [138]–[140].

To go further, it is necessary to use the numerical simulations. It would be interesting to address the question of the geometry of the diffusion and to take into account the kinetics of enzymatic reactions. The inhomogeneous nature of the skin could be addressed by a mortar-diffusion model.

[69] approximatively three times higher than the main mammalian cells, $P_{S_{blood}} = 6 \times 10^{-6} m.s^{-1}$ [128]

III.6.4 Critical approach

As said in the introduction, it seems widely accepted by the community that the RONS produced by the plasma can diffuse freely over distances of several mm [64]. However, this belief is based on a very limited number of experimental works. The numerical simulations of plasma-antitumor effect are still an embryonic topic [167]. The work of Murphy et al. does not even consider the presence of anti-oxidant defenses [168].

The main criticisms addressed relate to three crucial points.

1) The diffusion of **all** chemical species must be considered. The chemical probes used can diffuse into the skin/gel ... but also the colored or fluorescent product formed during the reaction of the probe with the RONS. Since the diffusivity of colored products and RONS have the same order of magnitude, it is not possible to neglect the diffusion of one species compared to the other.
2) In some case, the chemical diagnostic may have been biased because its use as an *in-vivo* or *ex-vivo* probe is inappropriate. Moreover, it appears that the kinetics of the chemical reaction used to detect the RONS is slow. For example, H_2O_2 does not react instantly with the Amplex Red reagent[70] or Griess Reagent. The chemical problem posed by these manipulations is more complex than assumed. In fact, the detection reaction takes place in a system that reacts and diffuses at the same time... For example, if someone increases the concentration of the probe, a smaller diffusion length could be observed since the RONS would have been consumed at higher speed in the upper layer of the skin/gel.
3) The use of gelatine layer is very questionable. These models totally neglect the existence of the antioxidant defenses of the skin. Moreover, the main result of the experiments involving the gels implies that the diffusion of the RONS is accelerated by plasma treatment compared to the case where a droplet of the RONS to be detected is placed at the surface of the gel. However, if the concentration in the droplet does not represent the concentrations elicited by plasma treatment, the non-detection of RONS crossing the membrane does not prove that the plasma has accelerated the diffusion. Both experiences are only incomparable.

Let's start with the work of by Dobrynin et al. [169].

Dobrynin et al. have injected 200 µl under the skin of the sacrificed rat, performed a plasma treatment and then cut the piece of skin and observed the position of the colored reagent[71]. The result is visible in Fig 97.

[70] in manual instructions, and according to our own protocol, the incubation time is ~15-20 min for diagnostics under normal conditions of use

[71] *[169]* "To measure the H_2O_2 in and the pH of tissue, the dyes were injected using a syringe into a 1-cm-thick 4×4-cm sample of skinless chicken breast tissue at various points to the depth of up to 1 cm. Ex vivo measurements were done in a rat tissue: a hairless Sprague-Dawley male rat was killed right before the procedure; 200 µL of dye solution (Amplex UltraRed) was injected subcutaneously using a sterile syringe, and the animal's skin was treated with floating electrode DBD plasma at various time points after a 5-minute incubation period (Fig 97). Right after the treatment, samples of skin tissue were extracted and analyzed as follows. Treated samples were cut in a vertical direction into slices with a thickness of 1 mm; fluo-rescence was measured"

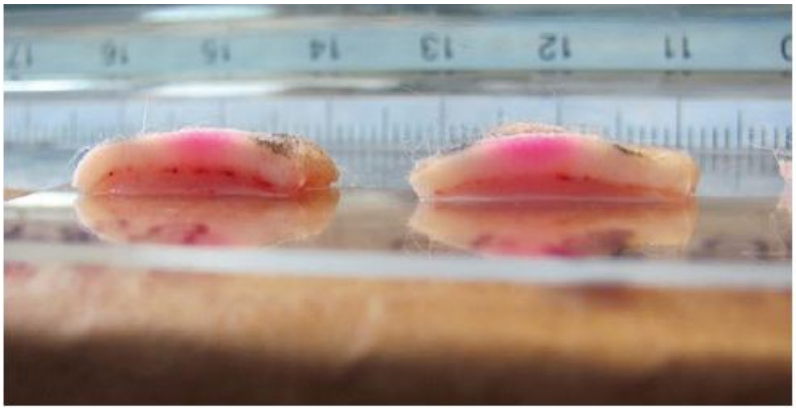

Fig 97 Adapted from the paper of Dobrynin et al. [169]. Cross-section of the skin sample just before measurement.

They concluded[72] that H_2O_2 can diffuse over several mm. This conclusion is highly questionable because of the previous argument (n°1 and 2). The diffusion coefficients of amplex-Ultrared and his fluorescent product are not known because the structure of the molecule has not been provided by the manufacturer. We can, however, suppose that the value close to that of Amplex-red and resorufin, since Amplex-Ultrared is a derivative of the Amplex-red with a slightly higher molar mass.

Regarding the diffusivity of the two species:

- the diffusion coefficient of resorufin in water is $D_{res} = 4 \times 10^{-10}\ m^2.s^{-1}$ [170].
- the diffusion coefficient of H_2O_2 in a phosphate buffer at 25 °C is $\sim 14 \times 10^{-10}\ m^2.s^{-1}$ [171]

Since the characteristic length of diffusion is $\propto \sqrt{D}$, H_2O_2 will spread over a distance 1.8 times greater than that of the resorufin. Consequently, it is not possible to neglect the diffusion of the resorufin througth gel/skin. It is therefore possible that the resorufin is formed only in the upper layers of the skin. In fact the Amplex-Ultrared (like Amplex-red) is not transformed into its product with a chemical reaction in a single step. The reaction starts with a reaction between the enzyme HRP and H_2O_2. Therefore, the diffusion of HRP-H2O2 should also be considered

Secondly, this probe is not suitable for *in-vivo* or *ex-vivo* measurements. Its use for measuring H_2O_2 in extracellular fluids is even explicitly discouraged by Tarpey et al. [172]. Moreover, an experiment of Snyrychová et al. on leaves show that Amplex-Ultrared is more sensitive to photooxidation[73] than Amplex-red[74] [173].

Finally, all the sources of bias already mentioned in chapter two, enjoin to avoid this kind of reagent for tissues, and for direct exposure measurement ([96], [97], [174], [175]).

---

[72] [169] "In summary, we show that plasma effects may be transferred several millimeters deep inside a tissue, as measured in ex vivo chicken tissue and rat skin models. We detected penetration behavior of 2 simple active components, namely H_2O_2 and pH, but other species may be detected and measured using other fluorescent dyes or techniques. In addition, we have shown that a simple agar gel model may express physicochemical properties similar to those of real tissue, resulting in comparable penetration effects of active species."

[73] an order of magnitude calculation (not reproduced here) shows that the amount of UV emitted by the plasma could be sufficient to cause the color change in the absence of H2O2.

[74] Which is rather sensitive. I observe personally that the results are totally biased by ambient light.

layer of gel, a good tissue-model?

Gaur et al. propose to use gelatine layer as a skin model [176]. A layer of gelatine or PVA is placed above the liquid. The authors detect RONS in liquid phase and claims, insofar, that this system mimics the chemical transports induced by plasma through the skin. The scheme of the experiment used is visible below. First of all, it is necessary to point out that just mimicking the elasticity of the skin does not allow to obtain a "good" model of the skin, in any way. With this gelatine model, the effect of the antioxidant defenses of the skin is totally neglected[75]. The skin contains a complex system of enzyme and small molecules located in the vicinity or at the surface of the cells (whose most famous representatives are vitamins and catalase). It is precisely this chemistry that makes skin an anti-oxidant barrier.

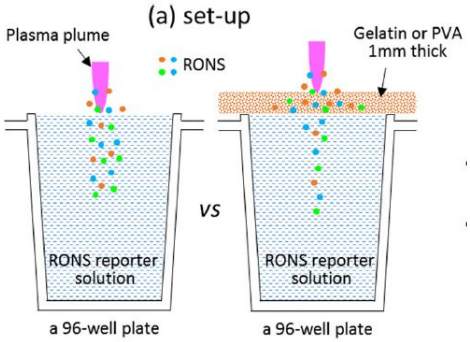

Fig 98 Figure adapted from Gaur et al. [176]

Moreover, the supplementary data[76] of this paper are very clear; the chemical probe was in contact with gelatine during the entire experiment. In that situation, it is obvious that “RONS reporters” diffuse and is present at the top of the gelatine when treatment begins. Consequently, these reporters are able to react. The product formed, diffuse quite freely in gelatin too[77] and can go into the bulk solution. This point of chemistry was not considered by the authors. Yet, it changes considerably the interpretation of the experiment. For instance, no need to evocate the photolysis to understand why HO° is detected below this layer of gelatine... These biases also concern the work of Szili et al. [177] and [178].

The results of this kind of experiment should be interpreted by considering the diffusion of the ROS, the chemical probe, and the fluorescent product. It is also necessary to the study at which point the gelatine promote the diffusion of one chemical species compare to another. It is an interesting physicochemical problem but very far from biological reality. It doesn’t prove that the RONS produced in the plasma can diffuse through the skin across several mm.

In the paper [177] of the same team, Szili et al. claim the two following things:

Statement 1 *[177] “Gelatin was chosen because it consists of collagen, which is a major protein in skin, bone, and connective tissue [179]; gelatin also provides a barrier to H_2O_2 (when spotted as solution on top of the gelatin surface) and potentially to other RONS.”*

[75] Gelatin will react with the most reactive species like HO °, but probably not with H_2O_2

[76] *“The RONS reporters were used at a volume of 400 µl per well of a 96-well plate. This volume ensured the solution always remained in contact with the gelatin or PVA targets that were placed over the wells.”*

[77] since rons repporters are « small molecules » i.e not proteines.

Statement 2*[177] "Experiments with the tissue models have revealed the key RONS delivered into tissue (speciation) and likely relative (but not absolute) concentrations (doses) and depths of delivery. From these findings it is clear that plasma treatment can induce physical and chemical modifications deep within tissue to millimeter depths. Since our earlier studies, other groups have started utilizing gelatin and agarose tissue models with different plasma sources and also observed relatively deep penetration of RONS to millimeter depths [180], [181]"*

The statement 1 is debatable since the concentration of H_2O_2 spotted at the surface of the gelatine is smaller than that expected during a plasma treatment (1 mM vs 1 M) [178].

The statement 2 is debatable since the existence of anti-oxidants is forgotten. Is it reasonable to say that such experiments are models of what is happening in the skin, whereas the main phenomenon (the scavenging of ROS by anti-oxidant defenses) is neglected?

In a recent experiment, the same team reproduces the "droplet experiment" with pig skin [182] (see Fig 99). Once again, there is bias since H_2O_2 concentration does not necessarily represents surface concentration under plasma-treatment (1 mM, against 1 M according to our calculations). Moreover, this sample of skin is another source of bias since: *"obtained as a waste product from a pig that was sacrificed for food"* [182].

Indeed, for food preparation, pigs skin undergo a significant heat treatment (~ 60 ° C) to facilitate the separation[78] of the skin from the rest of the body [183]. This heat treatment is able to denature the enzymes and the structure of the skin; such sample is a bad model of living skin.

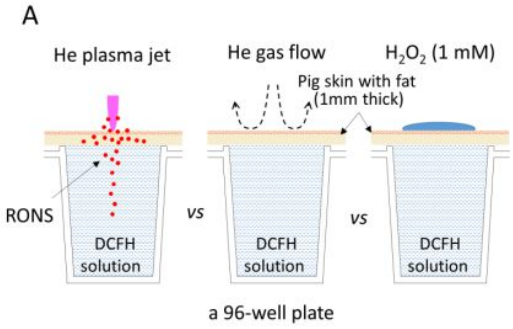

Fig 99 from the accepted manuscript [182]

Similarly, the conclusions of Duan et al. [184]:

[184] -"Besides, it is exciting to found that the RONS produced by the plasma can penetrate through up to 1.25mm thick of the biological tissue."

are false according to the argument n°1 (i.e., all chemical species diffuses through the skin not only the RONS…) [184]. Note also that the use of TPA is particularly biased in this study, since the TPA is used at low concentration (~200 µM) and that absolutely no observation is made regarding the yield of the reaction TPA + OH, whose yield is assumed to be 1 ... which is far from being true ...

[78] The plant specifications for the scalding operation are that the carcasses are immersed for 6.5 min in water maintained at 60°C, which contains a commercial scalding tank additive that both acts as a wetting agent and raises the water pH to 12

Regarding the chemistry of the probe used in the paper of Szili et al. (2018) [182]. It appears that RONS activity was observed with Luminol:

[182]-" ROS react with Luminol to form a luminescent product underneath the skin. The Luminol-ROS reaction product lifetime is approximately 30 seconds. No luminescence was detected in the control group of rodents with the tumours treated with the control He gas flow (figures 3A and C). This result indicates that the He gas flow on its own does not deliver ROS into the tumours. After He plasma jet treatment, a strong luminescent signal was detected (figures 3B and C). This signal was statistically higher compared to the He gas flow control (n = 5, p <0.05), indicating that ROS were evidently delivered through the tumours by the He plasma jet. "

Now let's see what says, those who have a critical eye on the use of such a chemical probe (i.e., Wardmann [1]):

Luminol and related probes

The chemistry of this probe has been studied rather extensively [211,212]. A paper commencing with the sentence "Luminol is known to elicit chemiluminescence under almost an unlimited variety of conditions" [213] should alert us to approach its use in biology with caution. Indeed, an earlier review [214] concluded that "luminol-dependent chemiluminescence gives at present very little ability to discriminate between individual oxygen or radical species. Furthermore, luminol-dependent chemiluminescence used in biological systems is extremely prone to many interferences, which are very difficult to control." Other authors concluded that "luminol ... can neither serve to study the formation kinetics nor be used as a valid continuous assay of ROS ... generated by stimulated neutrophils ... luminol speciously report on H_2O_2 or $O_2^{\bullet -}$ production even in a cell-free system" [215], and "Luminol is not well suited for the detection of $O_2^{\bullet -}$ within living cells " [185].

Despite these cautions, the probe remains in widespread use. It is therefore important to outline the basis for its limitations.

Fig 100 From Wardman [1].

Now back to the paper by Szili et al.:

[182]-*"This result was relatively surprising because it shows the He plasma jet delivered ROS across an intact epidermal layer that normally provides an effective barrier to, for example, harmful agents and moisture ingress."*

Knowing the huge interference associated with the use of Luminol, it seems difficult to draw strong conclusions from the experiment of Szili et al. For example if the plasma causes an increase in tissue oxygenation (due to hyperthermia or a breakdown of H_2O_2 by the catalase contained in the skin), this could also contribute to the increase of the fluorescence signal observed in the entire body. Moreover, there is no evidence that hyperthermia didn't play (see Chapter VI)

III.6.5 Perspectives about the measurement of H_2O_2 measurement?

Van de Bittner et al. have developed a new family of *in-vivo* probes called Peroxy Caged Luciferin-1 [185]. This bioluminescent probe appears to be chemoselective and enables the quantification of H_2O_2 in real time and in the whole mouse. As pointed out, the development of new H_2O_2-*in-vivo* diagnostics is a very active field of research [186], [187]. Indeed, the probes like Amplex-red or Amplex-Ultrared present serious limitation which considerably limits the possibility of obtaining credible results in-vivo. The probe of Van de Bittner et al. is better in terms of chemical selectivity. On the other hand, it requires the use of genetically modified mice to express the precursor of the fluorescent product [188]. A probe based on a similar principle has been developed by Wu et al. [189].

Another class of molecules, the hydrocyanine, enables the *in-vivo* detection of H_2O_2. The probe is converted by H_2O_2 into a detectable fluorescent molecule [190], [191]. There are also electrochemical probes for H_2O_2, and NO that can be used *in-vivo*, some are already commercialized [192]. It would be interesting if one of these "new generation" probes could be used with plasma treatments.

III.7 Conclusion

This chapter was dedicated to the chemistry of plasma-liquid interaction. Long-lived species, i.e., H_2O_2, NO_2^-, NO_3^-, were measured with minor modifications of the protocols (see Chapter II section II.3, page 39).The production of HO° was measured through the production of the fluorescent specieTPA-OH. The diagnostic used during the systematic experiment presented in this chapter are summarized in Table 2.

Table 2 Summary of the diagnostic used during systematic experiments

Section/device	Diagnostics	Variable
III.1/single channel jet	Amplex-red/H_2O_2	Time/height/gas flow/Voltage
III.2/single channel jet	Griess/NO_2-	-
III.3/multi-channel jet	Amplex red + Griess	-
III.4/single-channel jet	Griess + modified Nitrate-kit	-
III.5/single-channel jet	TPA	-

It was found that the yield of the reaction between terephthalic acid (TPA) and hydroxyl radical depends on TPA concentration. In fact, the reaction producing the fluorescent compound is likely in competition with the recombination reaction of the radicals HO°. This is due to the high concentration of HO° in the first nm below the air-liquid interface. This model enables to estimate HO° concentrations during the plasma discharge: $[HO°] \cong 6.9 \times 10^{-4} M$. It provides also the production rate of HO° by volume that the plasma-liquid interaction should bring to maintain this concentration of HO°: $S = 1.5 \times 10^4\ mol.L^{-1}.s^{-1}$. This simple model explain why the concentration of TPA-OH obtained, depends on [TPA] for the same plasma treatment. The orders of magnitude regarding the “effective Volume Veff” (i.e. the volume of liquid under the plasma where OH° exists at high concentration) seems consistent.

The plasma-devices have been characterized in terms of production rate in pmol/s and yield in nmol/J (Table 3).

Table 3 Range of chemical yield (nmol/J) and production rate (pmol/s) measured during systematic experiments. "0" means that the concentration was below the range of detection of the diagnostic. The power supply has a frequency of 500 Hz for the totality of systematic experiments.

Section/device	Species	Range of chemical yield (nmol/J)	Range of production rate (pmol/s)
III.1/single channel jet	H_2O_2	0.7-4	300-1500
III.2/single channel jet	NO_2^-	0.03-1.5	50-1500
III.3/multi-channel jet	H_2O_2/ NO_2^-	0.5-1.9 /0.2-1.3	0-2500 /0-2000
III.4/single-channel jet	NO_3^-	, 0.2-9	20-4000
III.5/single-channel jet	HO°	0.2-1.1	100-400

These experiments show also that it is possible to optimize the amount of nitrite and nitrate produced in liquid phase by the single-channel jet by choosing $\Phi(He) = 300\ sscm$, when peak to peak voltage is 27.4 kV and height is 5.5 mm. In such condition, the production rate of nitrite is $\sim 750\ pmol.s^{-1}$ and the yield is $\sim 1.2\ nmol.J^{-1}$. By comparing the production rate of nitrites and nitrates for all the devices, it appears that the ratio of the two seems relatively constant: about 4 molecules of nitrate are measured for one molecule of nitrite.

Regarding the single-channel plasma jet powered with 500 Hz power supply, the production rate of H_2O_2, NO_2^-, NO_3^- and HO° were measured in the range: 300-1500, 50-1500, 20-4000 and 100-400 pmol.s^{-1} respectively; the yields were in the range 0.7-4, 0.03-1.5, 0.2-9, 0.2-1.1 nmol.J^{-1} respectively. The multichannel-plasma jet is more powerful up to 3500 mW (vs. 800 mW for single-channel jet), which contributes to the increase in production rates. On the other hand, the yield is very similar to that of single-jet.

The aim of the parametric studies was not only to understand the plasma-liquid interactions but also to choose the set of parameters which optimize the production of chemical species (assuming that the production follow the same law above a living tissu, which is probably false). The underlying idea was to maximize the biological effect by increasing the amount of species produced.

A critical reading of the experiments studying the diffusion of chemical species in gels or mouse skin was proposed. The hypothesis that the oxidizing species produced by the plasma diffuse deeply (beyond the dermis) was also questioned. The results suggest that the antioxidant defenses of the skin can considerably limit the ability of H_2O_2 to diffuse deeply into the living tissues ($175\ \mu m <$). Incidentally, it was explained how the studies [176] and [169] that defend the opposite hypothesis could have been biased. Further studies should be carried out on the subject, especially regarding the other RONS.

Perspective

The comparison between experiments and simulations/model is absolutely fundamental. It can only be improved by choosing experimental setup in close collaboration with the team interested in the simulation of plasma-liquid interaction. The chemistry of the first nanometers below the interface liquid-gas is crucial. The presence of an interface considerably complicates the chemical and physical aspects. However, sonochemistry faces the same challenges: a mixture of UV-absorption, radical chemistry, in the vicinity of the air-liquid interface.

To complicate things, we face an epistemological problem: as mentioned previously, the scientific literature related to the RONS may contain biased work due to the misuse of chemical probes. The authors of the critical reviews (Wardman et al. [1] and Tarpey et Fridovich [2]) sadly describe this situation as **"the triumph of hope over reality"**. According to these authors, several thousand of papers are involved. We can only wish that plasma-medicine literature evolves in a healthier direction than that related to RONS.

It would be interesting to collaborate with the researchers of the emerging field called "Quantitative Redox Biology" [159], [193]. The ambition of this field is to "gain the next level of understanding of redox processes" by developing mathematical models.

Chapter IV Results of *in-vitro* experiments

This chapter describes the results of *in-vitro* experiments carried out on two cell lines. In the first place, the purpose of these experiments was to assay the cytotoxicity of plasma treatments on cancer lines before the *in-vivo* studies. The aim was to show that plasma treatment could have an anti-tumor effect. Indeed, it is unlikely that a significant effect occurs *in-vivo* without a cytotoxic response *in-vitro*. Two cancerous lines were used: TC1 and NRS1.

The two plasma sources and the two cell lines (TC1 and NRS1) are described in Chapter II. The left panel of Fig 101 presents a photo and a schematic diagram of the single-channel plasma-jet. The right panel of the figure shows the Dielectric Barrier Discharge (DBD) facing a conductive surface connected to the ground. These two devices have been fed by the power supply n°3 described in Chapter II (section II.2.1). The waveform of voltage was a square waveform summed with a resonance peak at the time of switching. The power supply has a frequency of 500 Hz. The method for measuring power was described in Chapter II.

These two sources were also used during some of the *in-vivo* experiments presented in the next chapter. Some features of the experiments are described in Chapter II. These experiments were carried out in the team of François Lemoine at CIMI laboratory (Pitié-salpêtrière hospital). It has been checked that plasma treatments (DBD or single-channel plasma jet) do not cause any heating of the liquid. For this purpose, a thermocouple was immersed in the liquid during the treatment. DBD treatment does not cause any measurable increase in temperature; the plasma-jet decreases the temperature of the liquid (up to 17-18 °C). The biological diagnostics of the samples consist of trypan blue cell counts.

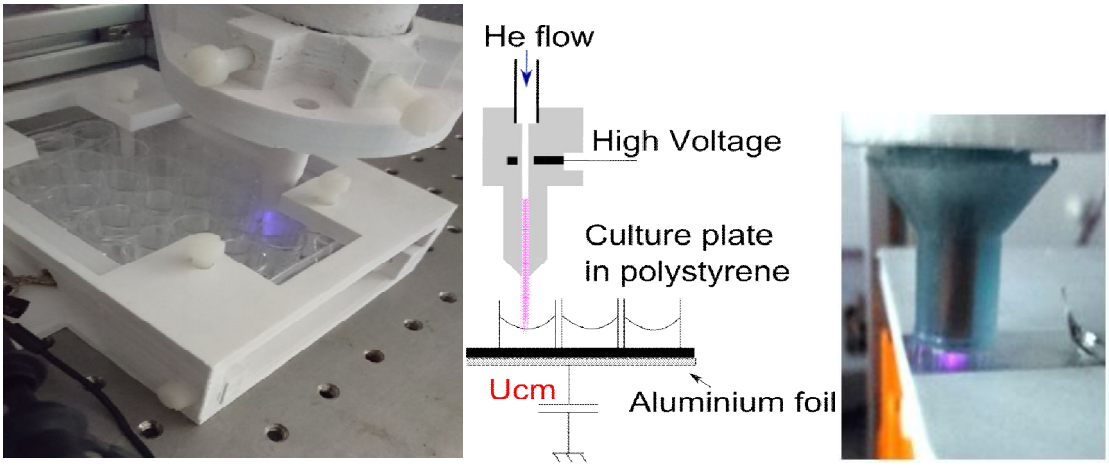

Fig 101 Left, photo of treatment made with the single-channel plasma-jet above a 24-wells plate. Center, a diagram of the single-channel-jet, electrical circuit, that was used for power measurements. Right: photo of the dielectric barrier discharge facing a conductive surface connected to the ground. Diameter of blue resin = 15 mm. Diameter of copper cylinder = 5 mm embedded in the resin.

IV.1 Viability of TC-1 cells after 24, 48 or 72H of incubation

This experiment shows a comparison of the viability of cells treated by plasma-jet (single-channel), PAM or H_2O_2 treatment. The cells were counted with the Trypan blue method described in Chapter II. The number of cells in each well and the schedule of this experiment are shown in Fig 102. Each well contained 500 µL of liquid. The medium is composed of RPMI-1640 supplemented with L-glutamine (0.3 g/L), fetal calf serum (1 %) (SVF). In this experiment, the medium does not contain antibiotics.

Regarding the exposure to plasma, the energy consumption was measured between 0.1 and 200 J. Chemistry experiments have shown that this exposes the cells to H_2O_2 concentrations between 0.4 and 800 µM. The Plasma activated Medium (PAM) was prepared by treating 500 µL of medium with the plasma jet. The effect of PAM on cells viability was compared with direct treatment after 24 h and 48 h incubation, but no significant difference appeared[79].

The effect of the direct treatment was compared with those of H_2O_2 after 72 h of incubation. During these experiments, the power of the source is measured in real time, and the duration of exposure is increased to reach the target value of energy. We work with constant applied energy (and not constant treatment time). This choice is justified by the fact that in this experimental situation, energy is a parameter directly proportional to the quantity of H_2O_2 produced, even if the power of the source varies slightly from one treatment to another.

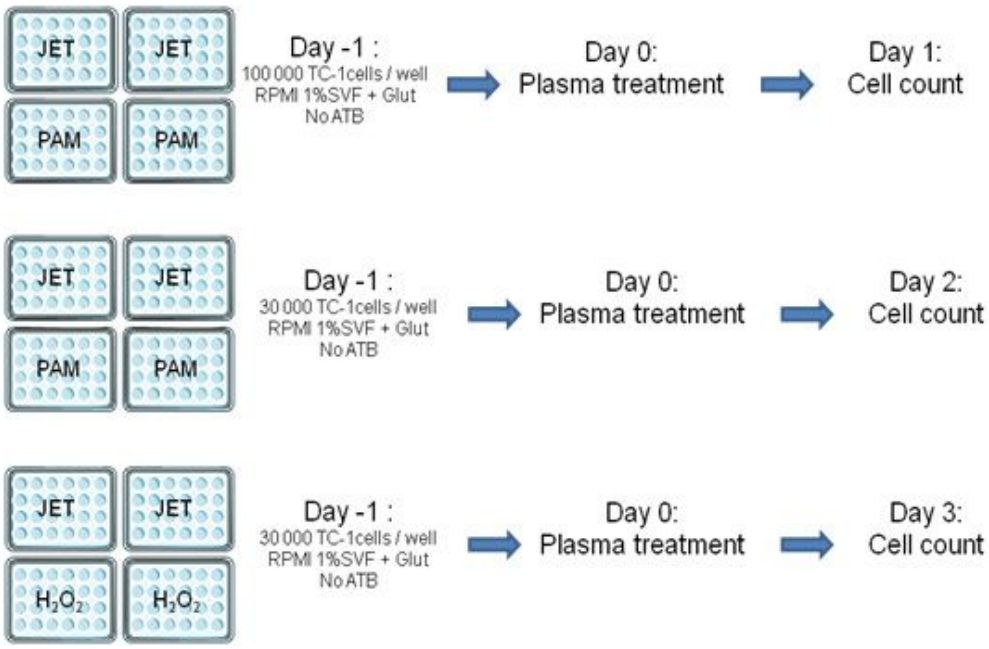

Fig 102 Diagram and schedule of the dose-response experiment to the single jet, PAM and addition of H_2O_2. The majority of treatments are made in duplicates. Each plate contains 24 wells with a diameter of 15.6 mm. There was 500 µL of liquid in each well.

For the experiments which involve an incubation time of 24 and 48 hours, the flow of helium is 400 sscm, the distance between the nozzle and the surface of the liquid is about 3 mm. Peak to peak voltage is around 18.5 kV for the following energies: {2.5, 5, 10, 15, 20, 25, 30, 40, 50 J}. It takes about 5 min to reach the energy of 50 J. For higher

[79] Not shown in this manuscript

target energies, the peak-to-peak voltage is increased to decrease the total treatment time. The following targets of energy {50, 70, 80,100, 200 J}, are reached with a peak-to-peak voltage of 30 kV. It takes about 5 min to obtain 200 J. Most treatments are done in duplicate.

Fig 103 shows the cell count obtained after 24h, 48 and 72 h of incubation (trypan blue diagnostic). This is a comparison between the effect of direct treatments (plasma-jet, red dots) and PAM treatments (orange dots).

During direct treatments, the wells containing the cells and the medium are treated with the single-channel plasma jet. The plasma plume touches the surface of the liquid. PAMs are prepared from the complete medium (without cells). Just after the preparation of PAM, the medium in which the cells are immersed is replaced by the PAM (less than 1 min after its preparation). Since the treatments exhibit significant variability, it would be necessary to use more replicates. The results were grouped by the range of energy. No significant differences appear between treated and untreated wells since the error bars of the treatments done at the energy $E = 200\,J$ are just below those of the untreated group. Moreover, there is no significant difference between direct and indirect treatments.

Therefore, it can be concluded that no deleterious effect on viability occurs after 24 or 48 hours of incubation in this range of energy.

Regarding the experiment done with 72h of incubation. The treatment conditions were slightly modified. Half of the plates were treated with a flow rate of 400 sscm, with a height of 9.7 mm between the surface of the liquid and the nozzle. The other plates were treated at 200 sscm and a height of 1.7 mm. Similarly, the targeted energies (100 and 200 J) were carried out with a peak-to-peak voltage of 30 kV while the other energies (2, 4, 5, 6, 8, 10, 20, 50 J) were reached with a peak-to-peak voltage of 19-20 kV. At 30 kV, 200 J corresponds to a 4 min treatment at 30 kV whereas 6 min of treatment is needed to obtain 50 J at 19-20 kV.

No significant difference appears[80] in terms of cell viability between the wells treated with the parameters (height = 9.7 mm, $\Phi = 400\ sscm$) or the parameters (height = 1.7 mm, $\Phi = 200\ sscm$).

The cell division rate is unusually high as evidenced by the control group (over 2 million cells). The results of the untreated group are dispersed. However, the effect on cell viability is significant after 72h of incubation. The error bars represent the standard deviation of the data. Since the analysis of the results did not show any significant differences for the same energy in the two conditions of treatments (200 sscm/1.7 mm vs. 400 sscm/9.7 mm), the results of the two plates have been pooled.

[80] this result is not shown here for the sake of brievety

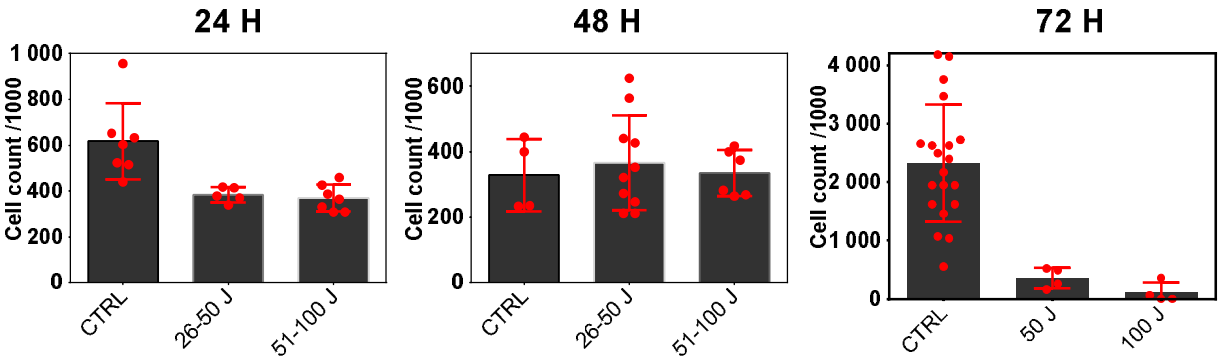

Fig 103 Cell count of living cell after 24 h, 48h and 72 H of incubation. The error bars represent the standard deviation of the data. The red dots represent the results of direct plasma treatments. The number in brackets refers to the range of energy pooled in the bar. For example, "Jet (26-50)" means that the cell counts of treatments with energy between 26 and 50 J are pooled.

The results are summarised in the following statements:

- The effect on viability is significant after 72h of incubation. The difference between treated and untreated wells is not significant at 24 or 48h, in the range of energy 0 -> 200 J.
- Direct and indirect treatments (PAM) are not significantly different regarding cell viability after 24H or 48H of incubation (not shown)

IV.2 Comparison between plasma-jet, DBD treatments and artificial PAM treatments

By "artificial PAM", I mean a mixture of H_2O_2 and NO_2^- prepared from pure species (not prepared by plasma).

IV.2.1 Plasma jet versus H_2O_2

Fig 104 shows the results of trypan blue diagnostic after 72h of incubation. The blue dots (black bars) represent the results of plasma jet treatments. The green dots represent the cell counts after exposure to H_2O_2 diluted in the medium.

The treatment at $E = 10\ J$ is placed under the same brakets since the wells are exposed to a concentration of 40 µM of H_2O_2, which corresponds to the concentration of H_2O_2 produced by the plasma for this energy. The second brace corresponds to 50 J/200 µM.

To conclude, after 72h of incubation, H_2O_2 added from the bottle has a similar effect than those of direct treatments. For the same energy, viability is the same for this two conditions of treatment (height=1.7 mm, flux = 200 sscm) and (height = 9.7 mm, flux = 400 sscm) (not shown)

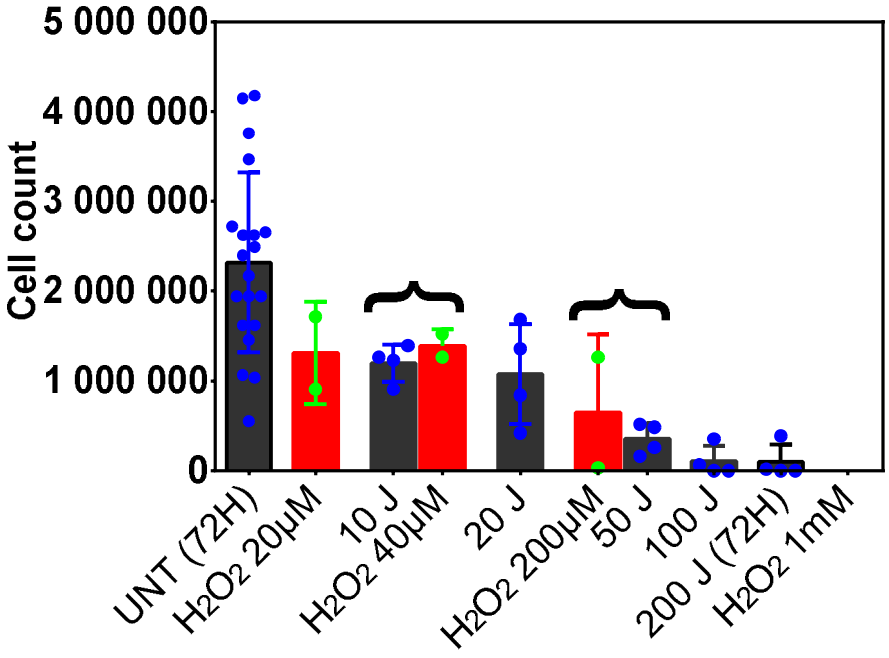

Fig 104 Cell count of living cell after 72 h of incubation. The numbers in the brackets describe the range of energy consumption measured during the experiment.

IV.2.2 Role of NO_2^-

In the previous section, we have found that the mortality is observable after 72 hours of incubation (in this range of energy/concentration). Consequently, in the present section, all cell counts are carried out after 72 h of incubation. It was found that exposure to direct or indirect treatment has a similar effect on the viability. Lastly, the viability of cells exposed to an artificial PAM composed of hydrogen peroxide diluted in the culture medium is very similar to that of cells exposed to direct treatments.

The experiment depicted in this section is a comparison between the mortality induced by direct treatment with i) the DBD ii) the single-jet and iii) artificial PAM. A quick overview of the experiment is given in Table 4. Stepping back, this kind of experiments address the fundamental question: which chemical species (or combination of chemical species) produced by the plasma could explain the mortality of the cells?

Plasma-liquids interactions produce essentially three long-lifetimes species: H_2O_2, nitrites, and nitrates. Among these species, H_2O_2 and nitrites have the highest toxicity[81]. Consequently, in the following experiment, TC-1 cells have been exposed to increasing concentrations of H_2O_2, nitrites, and combinations of these two. It is a matter of understanding whether the addition of nitrites, increases the toxicity already induced by H_2O_2. The concentration ranges chosen correspond to those measured in Chapter III. The case of $[NO_2^-]$ =1 mM higher than that obtained with plasma treatments, is also examined.

In this experiment (plate 1, 2 and 3 in Table 4) the concentrations of hydrogen peroxide and nitrites take the following concentrations:

[81] nitrates are less toxic, see Chapter I.

- $[H_2O_2] \in \{0, 100, 200\ \mu M\}$
- $[NO_2^-] \in \{0, 10, 50, 100, 150, 200, 600, 1000\ \mu M\}$

Table 4 Content of each plate used for the comparison of plasma-jet, DBD, and treatments with artificial PAMs

ID of culture plate/ Number of wells per plate	Description
Plate 1, 24 wells	$[H_2O_2] = 0\ \mu M$, [NO_2-] is in the range [0, 1000 µM]
Plate 2, 24 wells	$[H_2O_2] = 100\ \mu M$ [NO_2-] is in the range [0, 1000 µM]
Plate 3, 24 wells	[H_2O_2]= 200 µM [NO_2-] is in the range [50, 150 µM]
Plate 4 and 5, 24 wells	Dose-response experiment. **Plasma jet**. The duration of exposure was increased to reach the target value of energy consumption.
Plate 6, 7, 8, 12 wells	Dose-response experiment. **DBD** The duration of exposure was increased to reach the target value of energy consumption.
Plate 9 = 24 wells plate **Plate 10 = 12 wells plate**	Untreated

The experiments are carried out in 24-well culture plates. Each well contains 500 µL of the medium (RMPI+ 10% FCS + L-Glutamine + antibiotics). A diagram of the experiment is shown in Fig 105. 24 h after the seeding of the wells with 30 000 TC-1; H_2O_2 and nitrites are added to the wells (at constant volume). The viability is measured 72 hours after the addition. At this time, the cells in control wells are not confluent. Otherwise, the results could be biased. Three wells are used for each combination of concentrations (triplicate experiments).

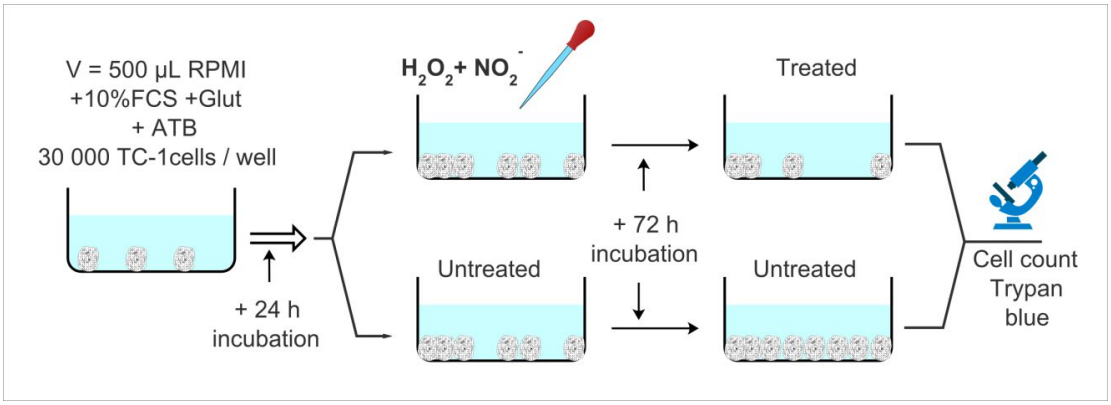

Fig 105 Diagram and schedule of the dose-response experiment to artificial PAM. Three wells are used for each concentration (triplicate experiments). Each plate contains 24 wells with a diameter of 15.6 mm

The results of cell counts are shown in shows a greater number of dead cells for the higher concentrations of H_2O_2. Note that the cells counted are those that are colored by

trypan blue, dead cells whose cytoplasm has mixed with the extracellular medium are not counted. It also appears that the concentration of nitrite has no influences on cell viability, even in combination with H_2O_2.

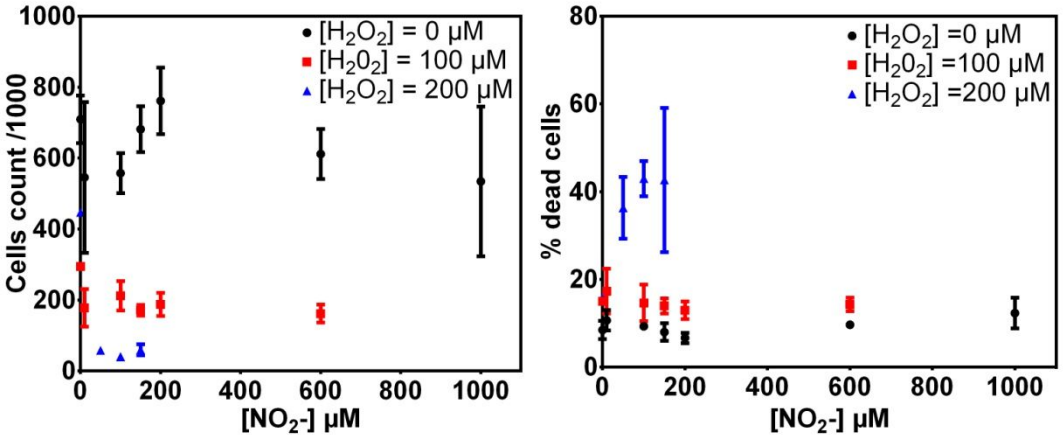

Fig 106 Left, cell count as a function of [NO_2-] after 72 H of incubation. Right: percentage of dead cells. Trypan blue diagnostic.

Bear in mind that the scope of such a statement is limited, the previous study regards

- One line (TC-1). Other cells, more resistant to oxidative stress probably behave differently.
- In the range of concentration $[NO_2^-] < 1\ mM$, $[\mathrm{H_2O_2}] \in \{0, 100, 200\ \mu\mathrm{M}\}$
- In the framework of *in-vitro* experiments. Nothing proves that the *in-vivo* behavior is the same.

Let us now examine the results of single-jet treatments (schematic in Fig 107). The culture conditions are the same. The experiments are carried out in 24-well culture plates. Each well contains 500 µL of the medium (RMPI-1640+ 10% FCS + L-Glutamine + antibiotics). The treatment takes place 24 h after the seeding of the wells with 30 000 TC-1. The duration of exposure is increased to reach one value of energy. The experiment is repeated for each value of the energy at least in three different wells (triplicate).

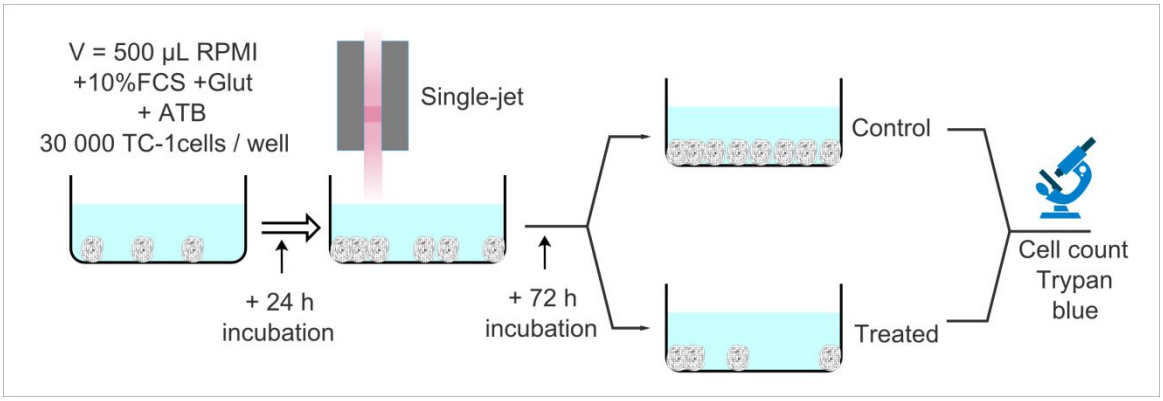

Fig 107 Diagram and schedule of plasma jet experiment. Three wells are used for each value of energy. Each plate contains 24 wells with a diameter of 15.6 mm.

The red dots of Fig 108 represent a group of wells treated with the same parameters. Peak to peak voltage is 26 kV, the flow of helium is 640 sscm, and the distance between the nozzle of the jet and the surface of the liquid is equal to 1 cm. For these points, the

value of energy respects the setpoint at $\pm$ 1 J. All the points are triplicates, except $E = 50\,J$, which is a duplicate. This group of points is homogeneous in terms of processing conditions and compliance with the set value. The error bars represent the standard deviation of the data.

The black dots contains the previous data and the two points for which the energetic setpoint was missed[82] as well as the 8 points acquired with different parameters: $V_{pp} = 30\ kV$, $h = 12\ mm$, $\Phi = 640\ sccm$. The error bars represent the standard deviation of the data.

It seems that the small differences in the parameters do not fundamentally alter the trends observed with the red dots. This is consistent with the result of the previous experiment since the data are represented as a function of the energy and since Chapter III have shown that the yield of H_2O_2 (in nmol/J) vary little in this range of parameters. The viability of the cells decreases rapidly as a function of the energy applied, in accordance with the experiments of the previous section. There is about one-fifth of the cells in wells treated with 20 J compared to untreated.

Note that there is only a slight increase in the percentage of dead cells among the cells counted. This can be explained by the fact that the diagnostic does not count the cells that are dead and whose cytoplasm has mixed with the extracellular environment. Moreover, with this experiment, it is not possible to know whether plasma killed cells, or slowed their growth.

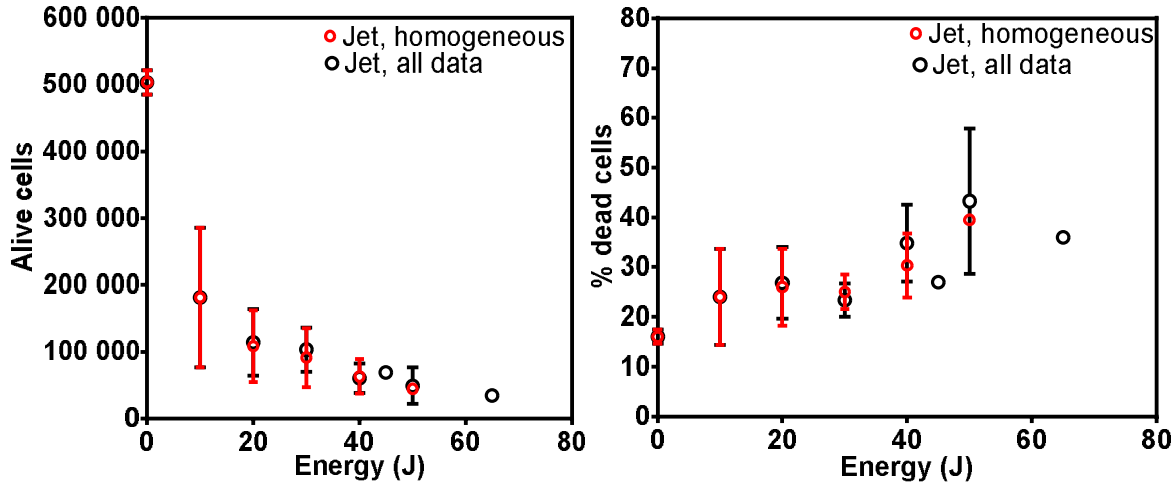

Fig 108 Results of trypan blue diagnostic. Left: number of living cells after 72 H of incubation. Right: percentage of dead cells. Red: Vpp = 26 kV, Φ = 640 sscm, height = 1 cm. Errors bars = standard deviations. Triplicate experiments except for one duplicate for E=50 J. Black: Red dots + data acquired with the parameters Vpp = 30 kV, Φ = 640 sscm, height = 1.2 cm + data acquired with the set of parameter red and for which the energy does not respect the setpoint.

Let us now discuss the results of DBD experiments (Fig 109). The culture conditions are different because the size of the DBD is close to the diameter of the wells of the 24-

[82] In practice, some treatments were missed. In this case, the experiment was repeated in another well. For example, when the energy consumed over a single well was 45 J whereas the setpoint was 40 J.

wells-plates. Larger culture wells should be chosen to avoid the discharges between the edge of the DBD and the wall of the wells. These discharges could bias the link between power measurements and the production of chemicals. The wells of the 12-wells-plates have an area twice as large. Thus, the number of cells per well must be the twice as big so that the cells grow under similar conditions. It is also necessary to double the volume of liquid so that the cells have the same amount of nutrient. Moreover, by doubling the volume of liquid, the same distance is maintained between the surface of the liquid and the bottom of the well. The cells are at the same distance from the plasma-liquid interface as in the case of the 24-well plates.

The experiments are carried out in 12-well culture plates. Each well contains 1 000 µL of the medium (RMPI-1640+ 10% SVF + L-Glutamine + antibiotics). The treatment takes place 24 h after the seeding of the wells with 60 000 TC-1 cells. The duration of exposure is increased to reach the value of energy in the set {10, 20, 30, 40, 50, 60}. The experiment is repeated in 3 different wells (triplicate) for each energy.

.

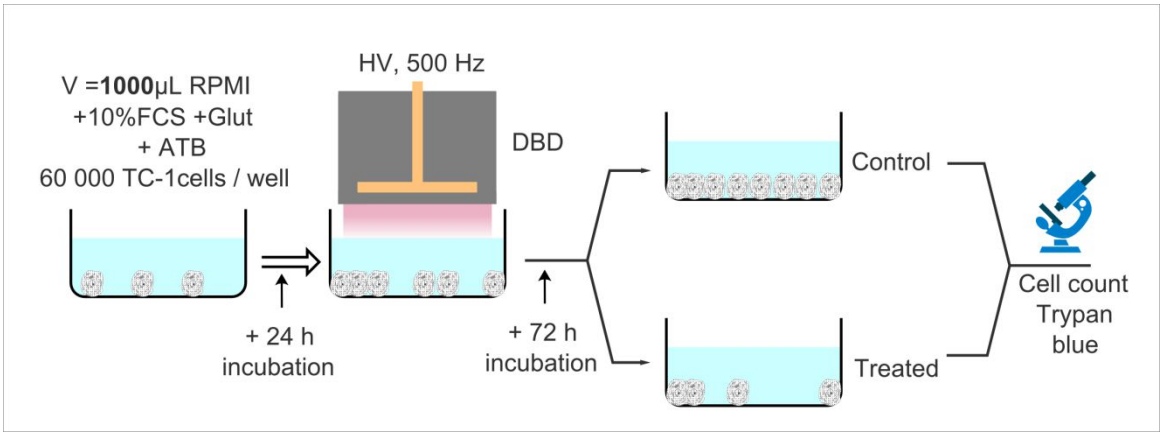

Fig 109 Diagram and schedule of DBD-dose-response experiment. Three wells are used for each concentration (triplicate experiments). Each plate contains 12 wells with a diameter of 22.1 mm. Each plate contains 24 wells with a diameter of 15.6 mm

The results of trypan blue diagnostic are shown in Fig 110. Again, the number of cells decreases with higher energy. The dispersion is quite large, unlike the wells treated by the plasma jet.

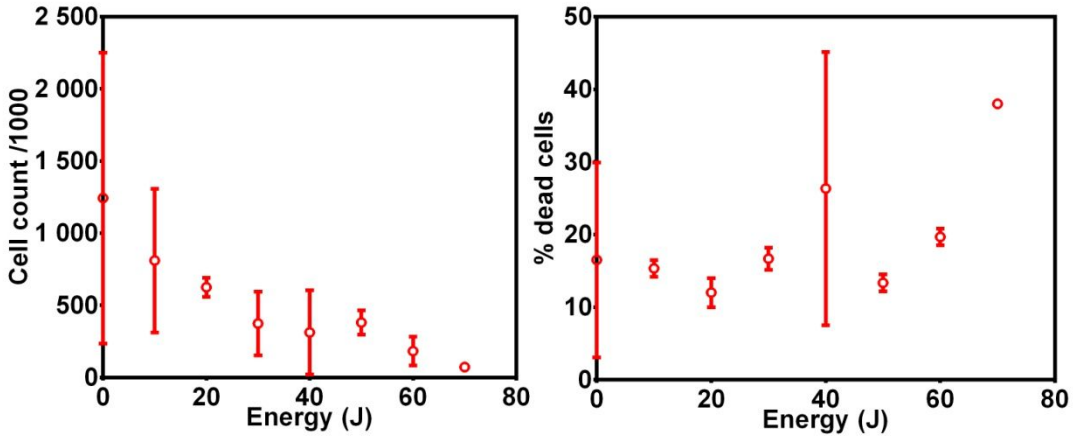

Fig 110 Results of trypan blue diagnostic. Left: number of living cells after 72 H of incubation. Right: percentage of dead cells. The cells counted are those whose membrane is still intact. Errors bars = standard deviation. Triplicate experiments except for the measurement at E=70 J. Parameters Vpp = 30 kV, height ~1 mm.

IV.2.3 DBD vs. Plasma-jet

The comparison between the results of plasma-jet, DBD and the treatments with the artificial PAM is shown in Fig 111. The **black** dots represent the treatments made with the plasma-jet. Regarding the DBD, since the initial number of cells is double, it is necessary to divide the number of cells by two to obtain a valid comparison. So, the ordinate corresponds to the number of living cells in 500 µL of medium (**red dots**). It can be seen that the **red dots** are above the **black** ones for the same energy. This can be easily understood: since the volume of liquid is double, the concentration of ROS is twice smaller. In order to obtain a more relevant comparison, it is interesting to divide the energy of the treatments by two (**green dots**). The abscissa of **green** dots represents the amount of energy consumed by the DBD for 500 µL of liquid. With this correction, the points associated with the jet and the DBD have a similar effect on viability (comparison of **black** and **green** dots).

The **blue dots** represent the result obtained with the artificial PAM. The points associated with several nitrite concentrations were pooled since there is no significant effect of nitrites. The three points (Untreated, $[H_2O_2]$=100 µM, $[H_2O_2]$=200 µM) are plotted as a function of the H_2O_2 concentration (**blue and upper abscissa**).

The experiments of Chapter III show that the yield of H_2O_2 is close to 2 nmol / J for the DBD and the plasma-jet. This gives 4 µM / J regarding concentration in 500 µL of liquid. This information enables to match the two abscissas (energy and $[H_2O_2]$). The position of **blue dots** is consistent, again with the hypothesis that $[H_2O_2]$ alone could explain the decreasing viability of the cells.

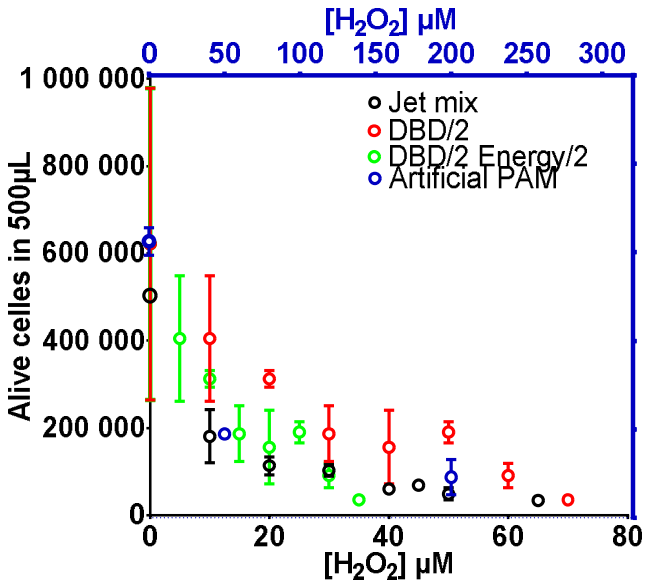

Fig 111 Results of trypan blue diagnostic. Comparison of the number of living cells after a treatment made with the jet (black), the DBD (red and green) or and artificial PAM (blue) as a function of energy and the equivalent amount of H_2O_2. Error bars are the standard deviation of measurement.

The conclusions of this experiment are summarised here. They are valid in the studied ranges with experimental uncertainties.

- $[NO_2^-]$ have no significant effect on the viability of the cells.
- The concentration of H_2O_2 could explain all observations on cell viability, irrespective of the source of H_2O_2: DBD, plasma-jet, artificial PAM.
- The representation of cell viability as a function of energy makes sense since the experiments of Chapter III have shown that the yield of H_2O_2 is of the order of 2 nmol/J for the DBD and the single-channel jet (for this range of parameter). Since there are variations in the power of the sources (for this experiment: $Power(plasma-jet) = 419 \pm 100\,mW$, $Power(DBD) = 110 \pm 40\,mW$); this representation is preferable to a representation of the cell viability as a function of the treatment time.

IV.3 Comparison of the viability of two lines: NRS1 and TC-1

A group of experiments was carried out with another cell line: NRS-1. Since the rate of growth and the needs of this line are very close to those of TC-1, the number of cells and the conditions of incubation are the same for TC-1 and NRS-1 (schematic in Fig 112). The wells were treated with DBD and plasma jet. Wells containing TC1 were also treated, to compare the behavior of the two cell lines. The treatment takes place 24 h after the seeding of the wells. The duration of exposure is increased to reach one value of energy. The experiment is repeated in triplicate for each setpoint of energy.

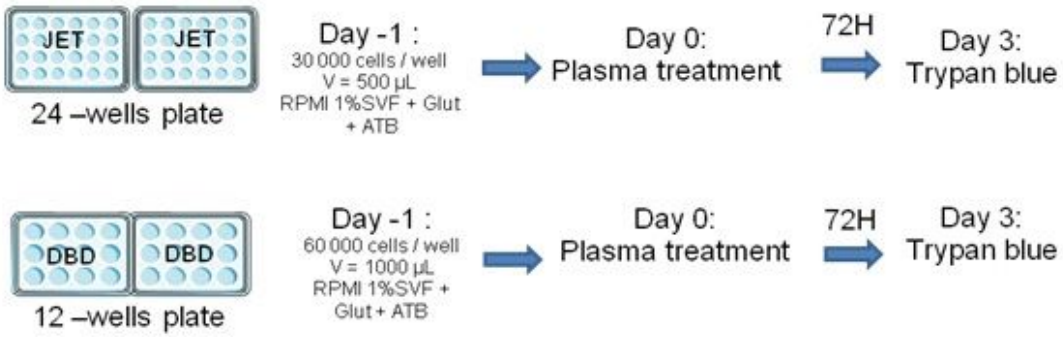

Fig 112 Diagram and schedule of DBD-dose-response experiment. Three wells are used for each concentration (triplicate experiments). 24-Wells plate: 30 000 cells/well in 500 µL of the medium. 12-Wells plate: 60 000 cells/well in 1000 µL.

The results of trypan blue diagnostic are shown in Fig 113. The trends are very similar for the two species since there is a significant reduction of the number of the cells when the energy reaches 10 J. There is a great similarity between the results obtain with the DBD and the plasma-jet regarding the viability of the NRS1. Once again, the number of cells represented was halved in the DBD-treated wells since the initial amount of cells is twice as big. The energy applied to the DBD-treated wells was halved because the volume of liquid is twice as large (RONS are diluted by two).

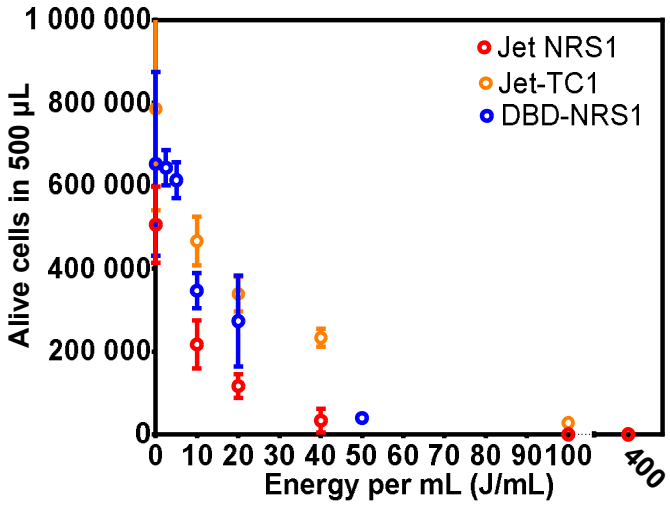

Fig 113 Results of trypan blue diagnostic. Number of living cells after 72 H of incubation. Errors bars = standard deviation. Triplicate experiments. Parameters of JET-NRS1: Vpp = 25.1 kV, height =5 mm, Helium=400 sscm, Power=352±51 mW. JET-TC1 Vpp = 24.9 kV, height = 5 mm, Helium=400 sscm, Power=495 ± 48 mW. DBD-NRS1: Vpp=29.3 kV, height~1-2 mm Power= 105±17 mW.

The curve showing the normalized results as a function of the initial number of cells for 500 µL is represented in Fig 114. The evolution of viability is very similar not only for the two devices but also for the two lines. For 20 J, however, we find that TC1s seem to be significantly less affected by plasma-jet than NRS1. This experiment should be repeated in this range of energy, to clarify this point.

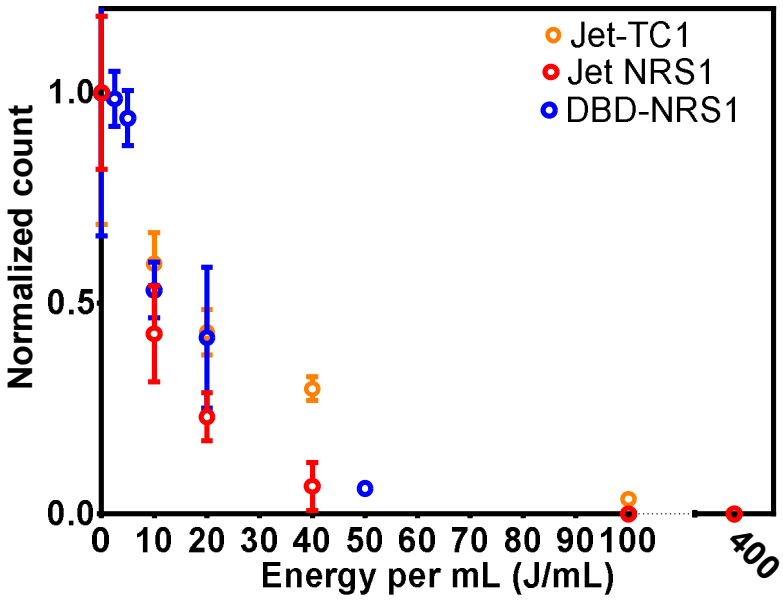

Fig 114 Results of trypan blue diagnostic. Left: number of living cells after 72 H of incubation. Errors bars = standard deviation. Triplicate experiments. Parameters of JET-NRS1: Vpp = 25.1 kV, height =5 mm, Helium=400 sscm, Power=352±51 mW. JET-TC1 Vpp = 24.9 kV, height = 5 mm, Helium=400 sscm, Power=495 ± 48 mW. DBD-NRS1: Vpp=29.3 kV, Power= 105±17 mW.

IV.4 Discussion

Our group is not the first to do experiments with this line (TC-1). Kim et al. have treated TC-1 cells with a micrometric sized plasma-jet [19]. Indeed, the hollow-core of an optical fibber was used as a gas pipe. The inners diameters of the fibbers were in the range 15 – 200 µm. The frequency of the power supply was ~$32\ kHz$. The power consumption was between 15 and 35 W. This is very different from our device. The single-channel plasma-jet has an inner diameter of 3 mm, is powered at 500 Hz, and consumes ~500 mW.

Moreover, the processing conditions are entirely different. Indeed, in the work of Kim et al. the medium overlying the cells was removed just before the treatment. In our experiment, the medium was not removed.

Kim et al. observed that the percentage of viable, necrotic, and apoptotic or dead cells with Annexin V-FTIC assay and TUNNEL assay. One treatment of $6 \times 10\ s$ (repeated in 6 spots) reduces the viable cells of ~ 75%[83] 24h after treatment.

It could be assumed that the oxidative stress is higher in the experiments of Kim et al. because they observed that the viability of the cells is below those of control group only after 24 hours of incubation (against 72 h for us). The smaller volume of the target and the greater power of the devices could explain this observation. However, in the absence of additional measures regarding the chemistry, it would be hazardous to do others comparisons.

Regarding the comparison of the efficiency of artificial PAM with plasma treatment. Girard et al. conducted a much more extensive study than ours on the line HCT116 and LU1205 [69]. Contrary to what we saw in the previous sections, they proved the existence of an anti-tumor synergy between H_2O_2 and NO_2^- in aqueous solution. In this respect, two important remarks must be made:

- the viability assay was performed after 24 h of incubation (in our case no visible effect before 72h of incubation)
- the concentration of H_2O_2 and NO_2^- is higher in the well treated by Girard et al. than in our experiments. For $\Phi(He) = 50\ sccm$, the device produce 400 µM of H_2O_2, 400 µM of NO_2^- and 100 µM of NO_3^- per minute. In our case, for the same volume, the single-channel plasma-jet produces 120 µM of H_2O_2 and 60 µM of nitrites and nitrates per minute. Only the wells treated with 200 J have a final concentration (~ 800 µM in 500 µL) which is comparable. The rate of production of nitrite and nitrate of our device is lower than those of Girard et al. Beyond the fact that the cell lines are different in the two studies, this could explain why we do not see a very significant effect of plasma treatment before 72h of incubation, contrary to Girard et al. [69].

To conclude, it is also necessary to be very careful with the experimental biases that culture medium could elicit. For instance, sodium Pyruvate is frequently used in cell culture medium and is known to be a scavenger of H_2O_2. Some formulations of Dulbecco's Modified Eagle Medium (DMEM) contain pyruvate [194]. Fetal Calf Serum (FCS) contains a complex mixture of proteins that can also scavenge radical species.

[83] this result is difficult to appreciate, since error bars and uncertainties are not available

The same caution must be applied regarding the commercially kits for ROS measurements. For example, in the work of Girard et al. the nitrate/nitrite assay kit of Cayman is used in accordance with the manufacturer's instructions [69]. According to Sun et al. [195] (and the manufacturer's instructions), the kit of Cayman is based on Griess Reaction. In these conditions, it has been shown that H_2O_2 can react very efficiently with nitrites which can lead to underestimating the production of nitrites (Chapter II, section II.3.3., page 46). It would be interesting to test the kit in the presence of H_2O_2. If a chemical interference is found; the addition of catalase should enable the destruction H_2O_2 and so, avoid the interference. Of course, it must be checked that catalase itself does not distort the diagnostic with appropriate controls.

According to [195] and [196], the protein content of the samples could also bias the measurements. However, preliminary experiments of C.Duchesne (private communication) show that FCS content of culture media does not bias Griess diagnostics. Since these kits have not been designed to give accurate results in the context of plasma medicine; it would be wise to control all the sources of bias for each kit.

Some attempts to couple plasma therapies with various therapies have been made *in-vitro*. For example, [197] describes the use of air plasma coupled with antibody conjugated nanoparticles. On the other hand, without in-vivo studies, the results of this kind of studies seems very disconnected from the therapeutic applications. Indeed, it seems very unlikely that a biological tissue protected by several anti-oxidant defenses behave similarly *in-vitro and in-vivo*.

IV.5 Conclusion

The aim was to show that plasma treatment could have an anti-tumor effect. Since it is unlikely that a significant effect occurs *in-vivo* without a cytotoxic response *in-vitro*. Two cancerous lines were used; TC1, and NRS1 and deleterious effects have been shown in vitro.

The conclusions of this chapter are summarised in the following points:

- Plasma treatments performed with DBD and the single-channel plasma jet decrease the viability of the cells. The effect on viability is significant after 72h of incubation. The difference between treated and untreated wells is not significant after 24 or 48h, in the range of energy 0 -> 200 J.
- Direct and indirect treatments (PAM) are not significantly different regarding cell viability after 24H or 48H of incubation.
- After 72h of incubation, H_2O_2 added from the bottle has a similar effect than those of direct treatments. For one same energy, the viability is the same for these two conditions of treatments: (height=1.7 mm, flux = 200 sscm) and (height = 9.7 mm, flux = 400 sscm)
- TC-1 cells have been exposed to increasing concentrations of H_2O_2 and nitrites, as well as combinations of both chemicals. The concentrations take the following concentrations:
    - $[H_2O_2] \in \{0, 100, 200\ \mu M\}$
    - $[NO_2^-] \in \{0, 10, 50, 100, 150, 200, 600, 1000\ \mu M\}$

  It appears that nitrites play no role in the toxicity of chemical mixtures. H_2O_2 alone explains the toxicity of the mixture. Moreover, with the experimental uncertainties, the production of H_2O_2 generated by the plasma explains the toxicity of the plasma treatments (DBD and plasma-jet).
- There are slight differences between the mortality of NRS1 and TC1 lines.

- [NO_2^-] have no significant effect on the viability of TC-1 after 72h of incubation.
- [H_2O_2] alone explain the decrease in viability whatever the source of H_2O_2: DBD, plasma-jet and artificial PAM.

After such experiments, it appears logical to proceed to *in-vivo* studies.

Chapter V In-vivo experiments

Five experimental campaigns have been carried out during the last three years. For the sake of clarity, the protocols and the specificity of each experiment are described before the presentation of the results. These campaigns involve treatments of two lines: TC-1 implanted in the cheek or the flank of C57BL/6 mice and CT26 tumor implanted in the flank of BALB/C mice.

The approach was to increase the power of the source to obtain an anti-tumor effect. This led us to observe the appearance of cutaneous lesions due to hyperthermia. It was therefore necessary to develop temperature monitoring. Finally, a refrigerated source was then used. A thorough discussion based on the literature takes place in Chapter VI.

It is recalled that TC-1 cell line (CRL-2785; American Type Culture Collection [ATCC]) is an immortalized epithelial cell line of C57BL/6 mice that expresses HPV-oncoproteins E6 and E7 [107]. If the tumor is located in the place of origin of the cells of the tumor line, the tumor model is orthotopic; otherwise, this model is called ectopic. TC-1 in the cheek is an orthotopic model of HPV cancers. CT26 tumors are subcutaneously implanted in the flank of the mouse; this is an ectopic murine colorectal carcinoma.

In-vivo and *in-vitro* experiments are two classes of models. In other words simplifications of the disease occurring in humans and the biological responses accompanying the treatment. *In-vivo* models are better models than *in-vitro* models because the tissue and the whole organism are taken into account. Growing complexity is encountered when the experiments are done at the level of the cell, the tissue; the whole organism or the level of an organism disturbed by the disease.

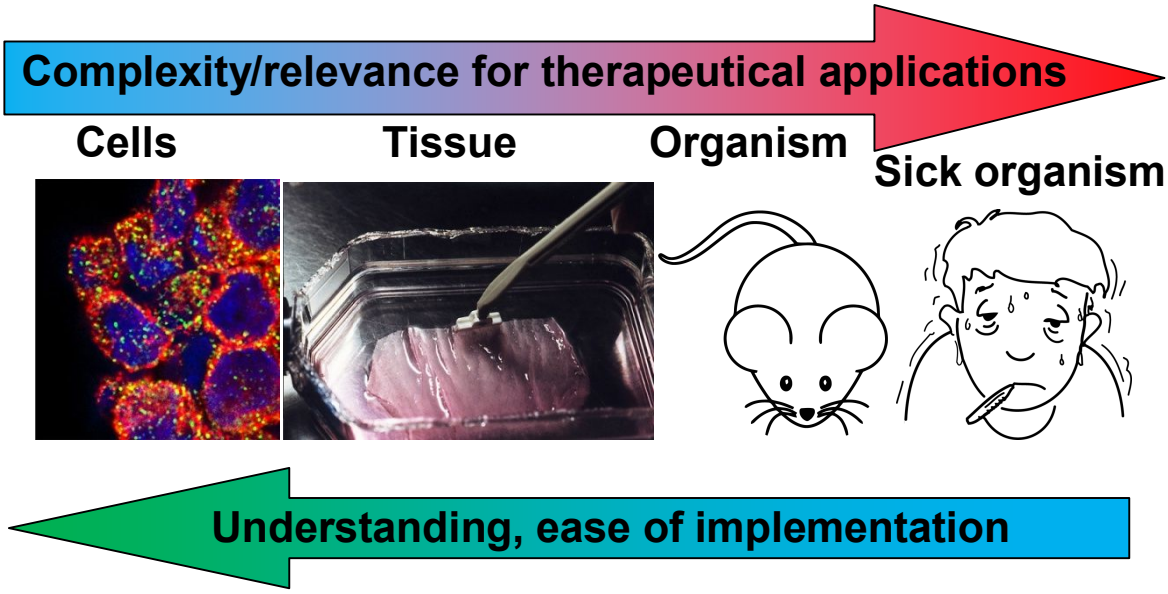

Since, the complexity increases, it is much harder to understand biological responses. On the other hand, the relevance of the treatment is more precisely questioned during an *in-vivo* than *in-vitro* experiments. For instance, the microenvironment of the tumor and the immune response are key parameters that cannot be taken into account with *in-vitro* experiments.

Numerous *in-vitro* experiments describe cellular mechanisms that can lead to cell death by necrosis or apoptosis. However, if it is not possible to prove the existence of *any in-*

vivo effect, these experiments are rather useless for therapeutic applications. In-vitro experiments aim to obtain more precise knowledge of cellular mechanisms and clues regarding what might happen *in-vivo*. However, it must be proved secondly, that these precise mechanisms intervene and play a key role at the scale of the organism by dedicated *in-vivo* experiments.

Ultimately, this is the relevance and the strength of the *in-vivo* experiments which will give the extension of the medical applications of plasmas. The question is whether the benefit-risk ratio of this type of treatment will convince physicians to assign a function to plasma-medicine therapies (PAM and direct treatment) in the framework of modern oncology.

V.1 Preliminary experiment: CT26-tumor of Balb/C mice treated with a DBD at low power

This experiment took place between November and December 2014. This work was done in collaboration with Alexandre Dizeux, Ph.D. student in the team of Lori Bridal at the Laboratoire d'imagerie Biomédicale (LIB) in Cordeliers' Research Center.

V.1.1 Power supply and plasma source

The AC-power supply has a frequency 610 Hz. The waveform is non-sinusoidal, and peak-to-peak voltage is 30 kV (Fig 115, right). It was the first version of the home-made power supply: voltage and frequency cannot be set precisely. The plasma source is a dielectric barrier discharge between the skin and the surface of the glass rod, in which a tungsten tip is embedded. Glass thickness is around 1.5 mm (± 0.2 mm). Several glass tips broke over the mice. The lack of flexibility of the power-supply and the lack of reliability of glass-tips have resulted in the evolution of the devices for subsequent experiments.

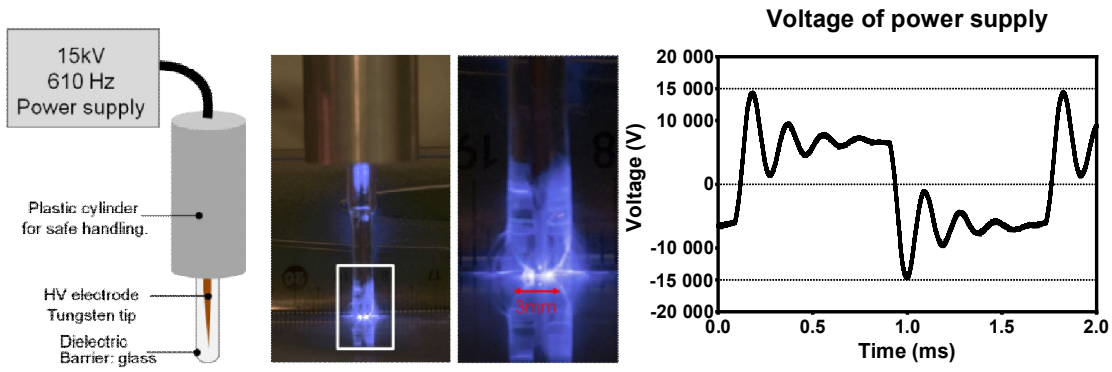

Fig 115 Left: Schematic diagram of glass-DBD and photography of the discharge above a metallic plate. Right: waveform of the voltage provided by the power supply.

V.1.2 Treatment schedule

Seven- to 8-week-old female mice from the Balb/C line were purchased from Janvier (Le Genest-Saint-Isle, France). The animals were housed at the CEF (Centre d'Explorations Fonctionnelles, Cordeliers' Research Center). All experiments were conducted in laboratory animal house in accordance with the institutional guidelines and the

recommendations for the care and use of laboratory animals established by the French Ministry of Agriculture.

A group of 35 mice with subcutaneous CT26 colorectal tumor on the flank was divided into three homogeneous groups in terms of tumor size: a placebo group ($N = 11$) and two groups that received, respectively, CAP exposure at 100 J/cm² ($N = 12$) and 300 J/cm² (N = 12) per day of therapy. Ultrasound diagnostic is time consuming (around 30 min per mouse). Therefore, the number of mice that can be treated and observed per day is limited. That's why 35 mice are divided in two groups of 17 (**Gr1**) and 18 mice (**Gr2**). Tumor implantation is made at two consecutive days for these two groups. Therapy was applied for 5 consecutive days, twelve days (Fig 116) after tumor implantation.

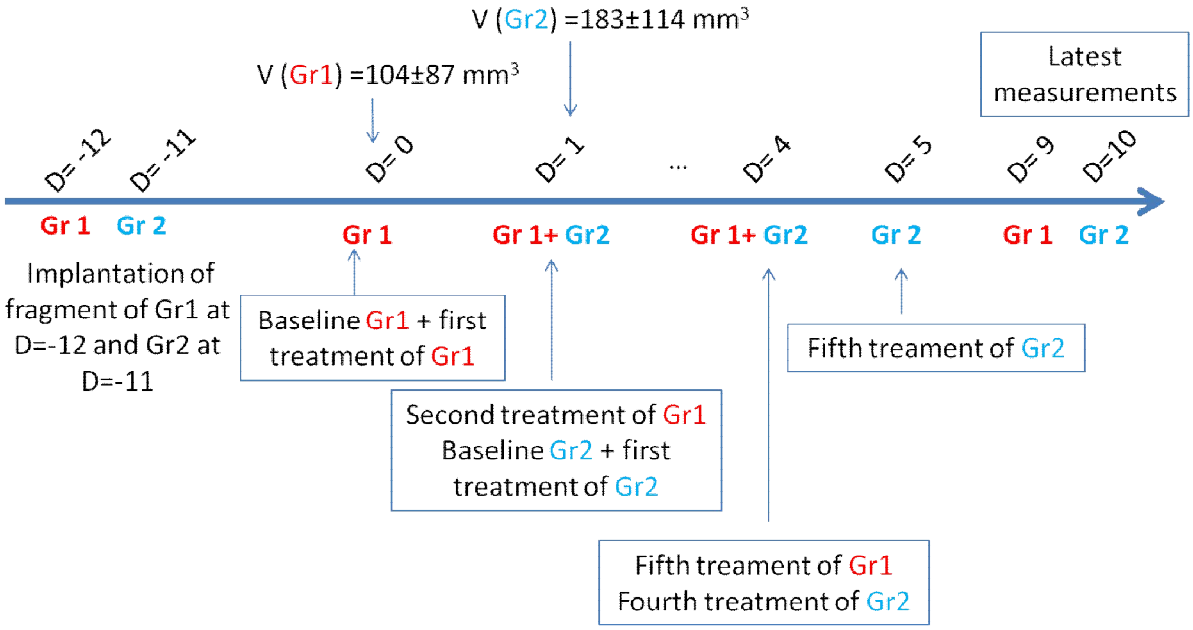

Fig 116 Treatment schedule of the experiment. 35 mice are divided into two groups. CT-26 tumors are implanted at time D=-12 and D-11 for groups one and two respectively.

V.1.3 Monitoring of tumor, ultrasonic diagnostics

Baselines measurements were made at day 0 for **Gr1** and day 1 for **Gr2** with the three different imaging: B-mode, shear wave elastography (SWE), and Contrast-enhanced ultrasound (CEUS).

Ultrasound imaging with B-mode was used for the calculation of volume. Tumor dimensions were assessed with two B-mode images. The first gave length and thickness. The second gave width and thickness (again). Tumor volume was approximated using the ellipsoid formula $V = \frac{\pi}{6}abc$ where a is the length, b is the width and c is the thickness. Surface of the ellipsoide that must be treated was calculated according to Knud-Thomsen formula:

$$S = \pi \left(\frac{a^p b^p + b^p c^p + c^p a^p}{3} \right)^{1/p}$$

where $p \approx 1.6075$ yields a relative error of at most 1 %.

We consider that the surface exposed to plasma is constant and equal to 9 mm² (It is based on photographs of the electric discharge). We also make the assumption that the half of the surface of ellipsoid can be exposed to plasma, the rest being inside. The number N_t of treatment points of each tumor is obtained by dividing S/2 by 9 mm²:

$$N_t = \frac{S(mm^2)}{2 \times 9}.$$

Then, shear-wave elastography measurements give the mean stiffness of this region of interest. After injection of contrast agent, **CEUS** enables to obtain the six functional parameters of tumor vascularization. Chapter II.5 summarises the definition of these parameters.

V.1.4 Protocol applied to each mouse

In the beginning, the general state of each mouse was checked. Particular attention was paid to the research of specific signs of pain and distress. The mouse was then anesthetized with 2 % (v/v) isoflurane in the medical air at 1 l/min. The temperature of the animal was maintained at 37 °C during anesthesia using heated support (Minerve, Esternay, France). The hair of the mouse was shaved around the tumor or the position of ECG electrode. The ECG electrode (whitesensor, distrimed) was then fixed on the flank; a small amount of the conductive gel (uni'gel, distrimed) was put between the skin and the electrode to improve electrical contact. At the beginning of treatment, the mouse was moved to an anesthetic device. This device was in plastic material to isolate the animal from the earth. The ECG electrode was then connected to the measuring capacitor Cm. The equivalent electrical circuit as described in Chapter II.

The surface of the tumor was divided into several zones according to the number of treatments points **N_t** defined in previous section (Fig 117, left). The generator was switched on, and the power consumption was measured in real time by the oscilloscope. The processing time was changed to obtain the wanted energy per unit area. There were slight changes in the power consumption as a function of the position of the treated point. The glass tip was held securely attached about 1.5 mm from the skin. Once the point was processed, the generator was cut off, and the tip was moved to the next point. The measurements of the oscilloscope were reset between each point.

Tumors are divided into several areas of approximately 9 mm ²

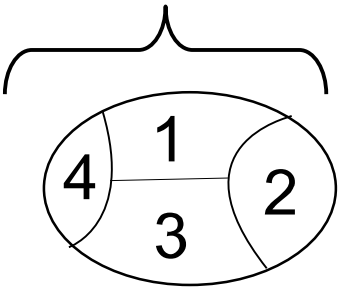

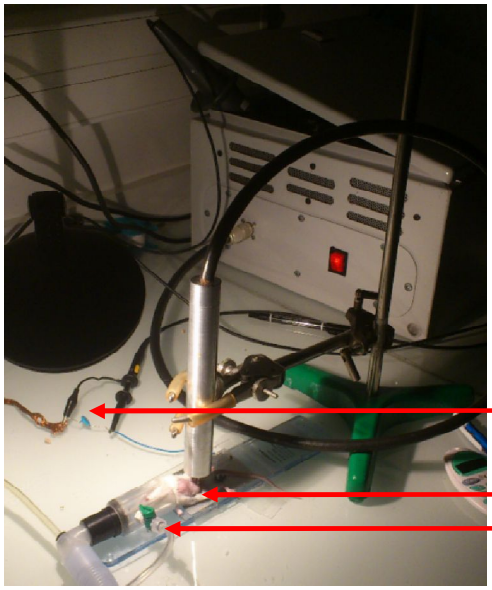

Fig 117 Left: diagram of one tumor, the order of the treatments is indicated. Right: photography of experimental setup.

At the end of the treatment, the mouse was moved to the heating plate. Its front and rear legs, and its tail are firmly taped to the surface of the thermostat plate. B-mode imaging is used to measure the transverse dimensions of the tumor (width and depth). If the tumor is large enough, three measurements of elasticity (using SWE) are made according to three transverse sections of the tumor. The same protocol was repeated along the longitudinal axis (1 image in B mode giving length and depth + 3 elasticity measurements).

Then, another ultrasound transductor delivering greater power is fixed above the mouse, after the choice of a region of interest, which contains the tumor; the contrast agent is injected into the caudal vein of the mouse. The ultrasound power reflected by the bubbles is measured for a few minutes (CEUS diagnostic describe in Chapter II).The set of ultrasonic measurements take about 30 min for each mouse. The mouse was left to wake up on the hot plate; the state of health was checked after his awakening.

V.1.5 Power measurements

The section below describes the results of the electrical measurements carried out on the mice. As outlined in Chapter II, the measurement of two voltages enables the calculation of power consumption. The voltage provided by the generator (black curve) and the voltage at the terminal of the measuring capacitor (9.6 nF), which was connected in series to the mouse (red curve), are plotted in Fig 118. These voltages are called respectively "**High Voltage"** and "**Ucm**".

Peak to Peak Voltage of "**High Voltage**" signal was only 28 kV whereas it was 30 kV at the beginning. This drop in voltage is a consequence of the heating which occurs in the primary circuit of the transformer. After several tens of minutes, the increasing temperature of coil leads to increase the resistance of the primary circuit which elicits a decrease of the current flowing through the transformer. Since the output voltage is directly proportional to this current, the output voltage decreases to the observed value. This is one of the problems raised by this homemade generator.

The waveform of **"Ucm"** is very similar to "**High Voltage**" signal. This is a consequence of capacitive currents. As explained in Appendix A, the circuit "**mouse + capacitor+Cm**" may be modeled as pure capacitance with a good approximation. Without plasma, the layer of air between glass rod and the skin is also a pure capacitance. Therefore, this circuit is a Voltage divider referenced to ground. Capacitive currents caused by the vicinity of high voltages are at the origin of a signal proportional to "High Voltage."

The changes of Ucm, however, are not only due to capacitive current but also to discharges currents. Discharges currents cause steps in the voltage across the capacitor. This is a result of an exchange of charges between the surface of the dielectric and the skin. This exchange is partly due to the charges transported in the head of streamers in the form of an ionization wave. Another part of discharge current occurs after the establishment of the ionized between the two surfaces. Steps in "Ucm" are shown in the right part of Fig 118, which is a zoom of signals plotted on the left between 2.6 and 2.9 ms.

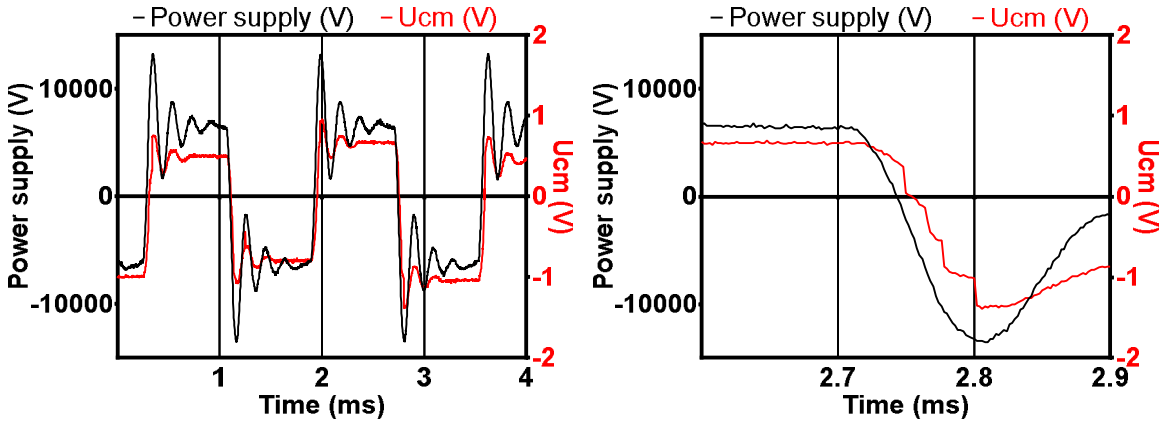

Fig 118 Voltage of power supply (in black) and the voltage at the terminal of measuring capacitor (in red) as a function of time. Right: zoom of the waveform between 2.6 and 2.9 ms. The step of voltage observed on measuring capacitor corresponding to successive discharges are clearly visible.

As explained in Appendix A, the capacitive currents do not contribute to the power balance, on average. On the other hand, the capacitive currents have a significant effect on the instantaneous power. The numerical calculation of the integral of power consumption is set out in Fig 119. The Visual Basic script, which enables the integration of power, use trapezoidal rule. This script was implemented in the oscilloscope. The energy consumed during the acquisition can be read directly into the interface. The benefit of this approach is that we know power consumption in real time. The black curve is the value of consumed energy between time t=0 and time in the range [2.6 ms ; 4.4 ms]. The decrease in the energy consumed just after 2.7 ms, as well as the overshoot between 2.8 and 2.9 ms, is due to the transient capacitive currents. When the black curves decrease, it means that energy is released from the capacitor. The dipole equivalent to the circuit "DBD + system of measurement" acts as a generator for a short time. By contrast, when energy consumption of the circuit "DBD+ measuring system" is higher than the damping values (dashed line, Fig 119 left), it means that energy is stored in a capacitive form.

The instantaneous power gives no information regarding each discharge because of the response time of the system. This is shown very clearly by comparing the left and right parts of Fig 119. The four individual discharges cannot be distinguished on the left of, in contrast to the right. Instantaneous power, with this measurement method, is meaningless regarding physics of the discharge. Only the damped value of the energy gives physical information.

The difference of the energy before and after discharge current, when the transient capacitive currents have been damped, represents the energy consumption due to the formation and maintenance of the plasma (as well as energy consumption due to the dielectric losses, see Appendix A). The red arrow represents this quantity in (Fig 119, left). We obtain that 98 µJ were consumed during these discharges.

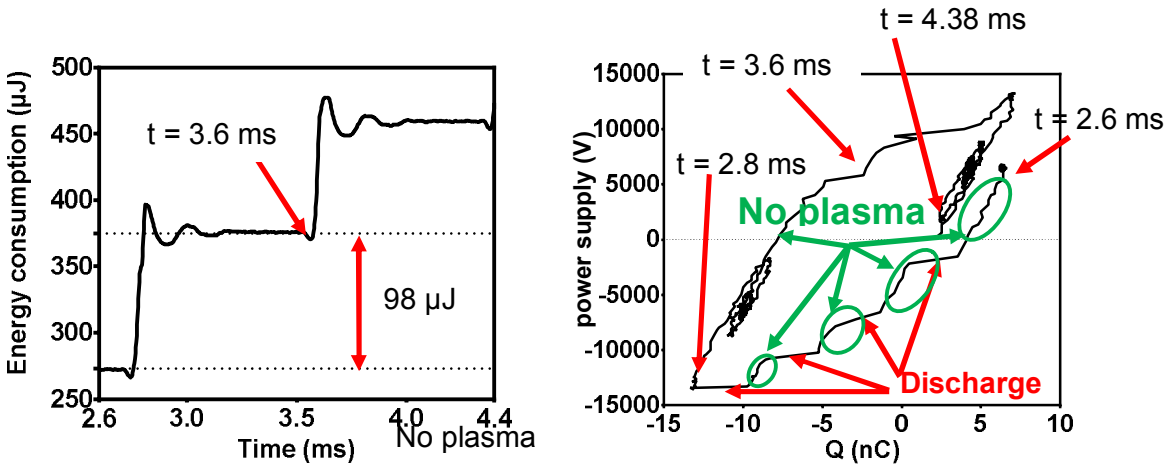

Fig 119 Left: Detail of the integral of the power as a function of time. The decrease in the energy consumed just after 2.7 ms, as well as the overshoot between 2.8 and 2.9 ms is due to the transient capacitive currents (this is energy stored in capacitive form and then released). Right: XY representations of signals between t=2.6 ms and t=4.38 ms.

Several periods of "High Voltage" signal are recorded during each acquisition. The purpose was to increase the precision of measurements of mean value. The using of long acquisition time is not the best choice. Appendix A shows that a wiser choice is to acquire only one period. This increases the speed of calculation of one acquisition and enables to acquire more samples. Moreover, uncertainties due to numerical integration decrease.

The integral of power given by the oscilloscope is plotted in the left panel of Fig 120. Acquisition time is 20 ms, 2060 µJ is consumed. Each step corresponds to a half period of the power supply. The frequency of power supply is 610 Hz. For one treated point, a given position above the tumor, hundreds of acquisitions are made. Each dot in black plotted on the right of Fig 120 is the energy consumed during one acquisition. The dispersion is partly due to the respiration of the mouse or change in the distance between glass rod stems from respiration and movement of the mouse under anesthesia. The mean value of the 420 measurements (1555 µJ), is plotted in red and blue. Red error bar is the standard deviation of the set of measurements (167 µJ). In blue, error bar is the standard error of the mean equals to 8 µJ. The mean value of power is known much more precisely because more than 400 measurements are available. Since 1555 µJ are consumed in 20 ms, power is equal to 77.8 ± 0.5 mW.

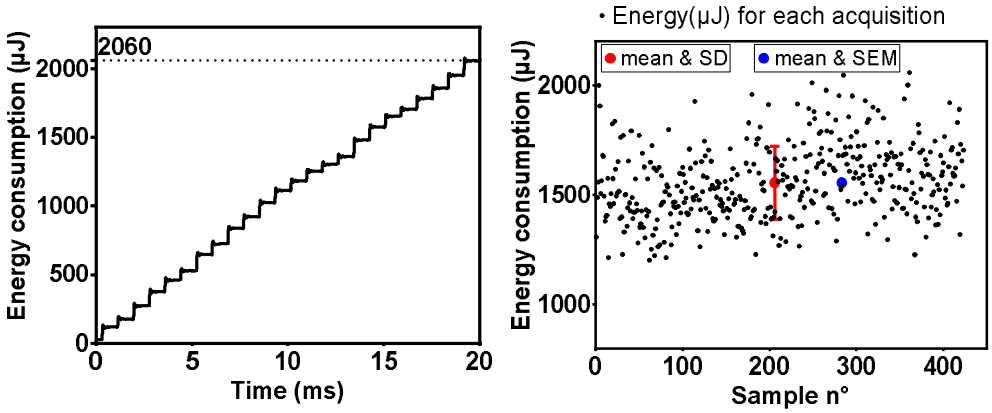

Fig 120 Left: Result of the calculation of the energy consumed during 20 ms. The black curve is the integral of the power consumption calculated by the oscilloscope. At each change of sign of the voltage, discharges leave glass-electrode. Right: each black dot is one measure of energy during one acquisition. Error bar in red is the standard deviation of the set of measurements (167 µJ). In

blue, error bar is the standard error of the mean: 8 µJ. mean value of energy consumption is 1555 µJ for 20 ms. Therefore power is 77.8 ± 0.5 mW.

The measurement method described in the previous paragraph was used on each mouse and for each position of glass rod above the tumor. Following this treatment, energy was summed for all points of one tumor. This energy is divided by the S/2; this is half of the surface of the ellipsoid describing a tumor. The result, energy per unit area, is set out in Fig 121 as a function of time express in terms of the number of treatments undergone by one mouse. The black dots represent mice in 300J/cm² group. The blues dots correspond to 100 J/cm². Error bars are the standard deviation of the sets.

Regarding 300 J/cm² group, energy per area is very close to the setpoint for the first three days of treatment. The energy applied to the mice was not precisely at the level of the setpoint because it was necessary to leave time for ultrasound diagnostics. The area of the tumor was estimated from caliper measurements. The last two treatments are far from the setpoint. The surface of the tumor became so large that it was impossible to treat the tumor in less than an hour, which is dangerous for animals.

Regarding 100 J/cm² group, the first three treatments respect the setpoint. It was not possible to treat all mice in this group in the last two days due to the long handling times.

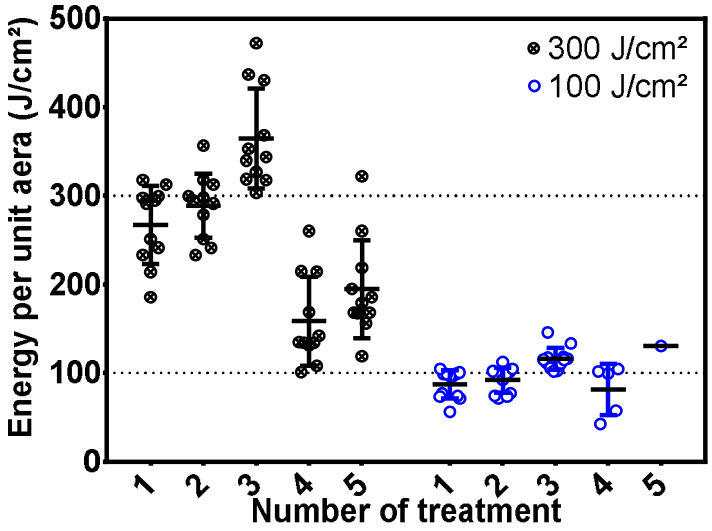

Fig 121 Treatments (in J per cm²) effectively applied to the mice of different groups (black 300 J/cm², blue 100 J/cm²). After day 4 the surface was so high that it was not possible to treat mice in less than 45 min. 45 min was the upper bound of treatment time. The time of anesthesia undergone by the mouse (1h15) is dangerous beyond that.

Energy consumed by the DBD above each mouse is set out in Fig 122. The graph reveals that there has been a gradual increase in the consumption. It is merely due to the growth of the volume of the tumors which required longer treatment to comply with the setpoint values. The mean energy is between 170 J and 270 J for 300 J/cm² group.

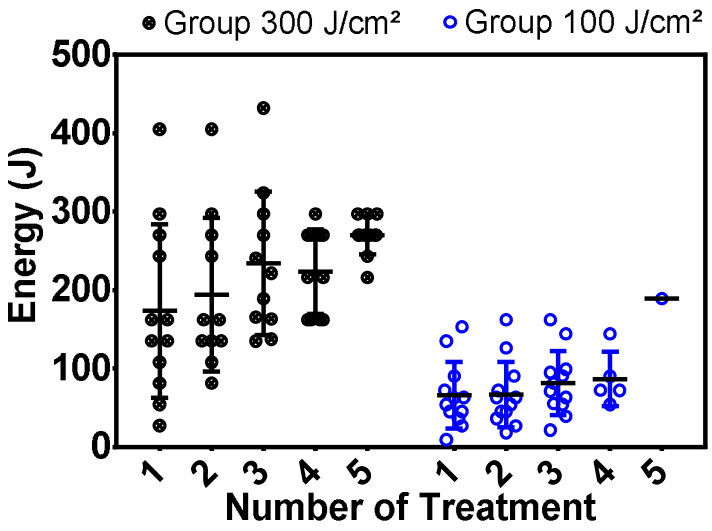

Fig 122 Treatments (in J) effectively applied to the mice of different groups (black = 300 J/cm² group, blue = 100 J/cm² group).

The energy consumed was summed for each mouse and all treatments. Fig 123 provides the results for each group. On average, mice in 300 J/cm² group received 1020 J, during five successive days. One mouse died during the first treatment. No other mice died or were sacrificed before the end of the therapy.

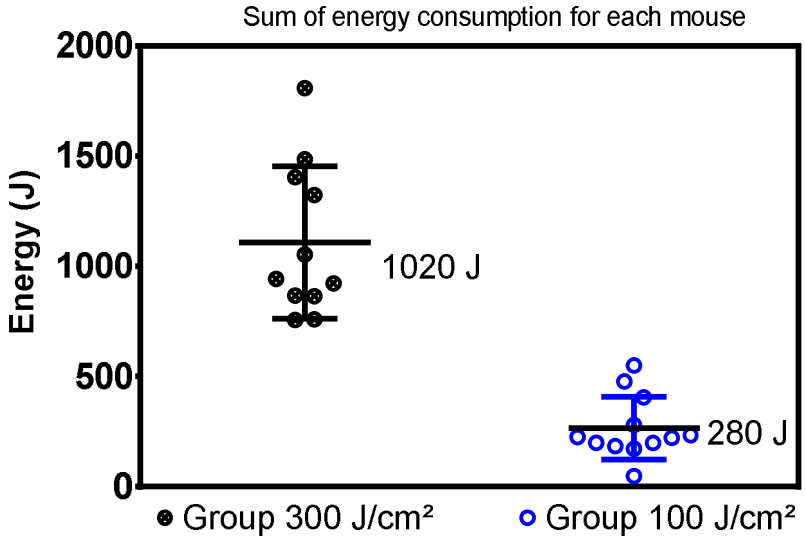

Fig 123 Sum of energy consumed for all treatments. Each point is a mouse. On average, mice in 300 J/cm² group received 1020 J. Error bars represent the standard deviation.

V.1.6 Treatment of CT-26Tumor: a negative result

The following section is a brief description of results given by ultrasound diagnostics.

No difference was visible between the skin of treated and placebo group. No mark, no sign of damage, no inflammation or crust was visible just after one or five treatments.

The tumor volume (B--mode), tumor stiffness (SWE) and tumor vascularization (with CEUS) were measured at baseline and the end of the experiment (D=9). As presented in, the results did not reveal significant differences between size, stiffness or functional

parameters of the tumors Fig 124. Only results related to the placebo group and the 300 J/cm² group are presented here (results of 100 J/cm² group are similar). This is clearly a negative result.

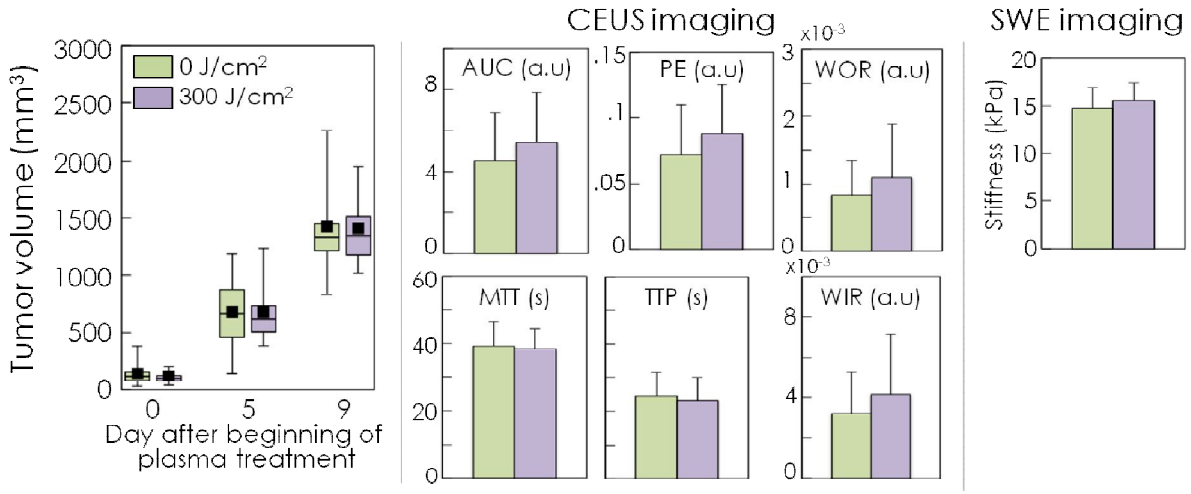

Fig 124 Left: tumor volume as a function of time for placebo and 300J/cm² group. Center: comparison of 6 parameters describing vascularisation for placebo and 300 J/cm² group at day nine given by Contrast Enhanced Ultrasound imaging. Right: comparison of stiffness for placebo and 300 J/cm² group at day 9. Ultrasound diagnostics show no differences between placebo and treated groups.

V.1.7 Conclusion

The results of this preliminary study are negative: no antitumor effect or changes in vascularisation was observed. This study, however, was rich in lessons regarding the limitation of the experimental setup. Furthermore, it enabled to refine the questions relating to the measurement of power consumed by the plasma above the mouse.

After this first experiment, several changes appeared to be priorities:

- Improve the power supply to obtain a generator whose peak to peak voltage and frequency can be set up.
- Replace glass DBD by something more reliable and reproducible. The assemblage (glass rod fused around tungsten tip) broke several times above the animal (risk of electrocution)
- Increase the area of the treated surface (9 mm² for glass-DBD) to shorten treatment time.
- Increase the power consumption of the device. Indeed, the mean power of this device was around 100 mW. This is an order of magnitude smaller than the devices of others groups. It was assumed that this could explain the failure of treatment despite long treatment times.
- Develop a transportable plasma-jet source, which could be installed and provide a comparison with DBD experiments.

V.2 Experiments with a Cheek-TC1 model of oral squamous cell carcinoma: toward more power

This section describes experiments with a different tumor model than that used in the previous section. TC-1 cancer cells were injected in the cheek of mouse and formed a solid tumor, causing inflammations similar to those observed in humans [107], [108]. This is an orthotopic model of C57BL/6 mice. These experiments took place at the animal house of Pitié-Salpêtrière hospital between May and August 2016. The maximum volume before euthanasia[84] is 800 mm^3. This value is justified by the fact that growing at this location causes significant eating disorders and quickly reaches the eye.

First, the results of four modalities of treatments are described; (i) treatment during 30 min with a DBD shown in section II.1.3; (ii) treatment time of 15 min or 30 min with the single-channel plasma jet described in II.1.4; (iii) injection of plasma-activated RPMI in the vicinity of the tumor. All plasma sources are powered by the high voltage power supply n°3 operating at 500 HZ described in II.2.1.

The second subsection describes experiments with the multijet (described in Chapter II.1.5) made with the 10 kHz sinusoidal power supply. The power consumption is larger than those of the preceding experiments of one order of magnitude. Unlike previous experiments, the skin cannot sustain the treatment without damage beyond a given time of exposure.

V.2.1 Single-jet and DBD experiments with 500 Hz power supply generator

V.2.1.1 Treatment schedule

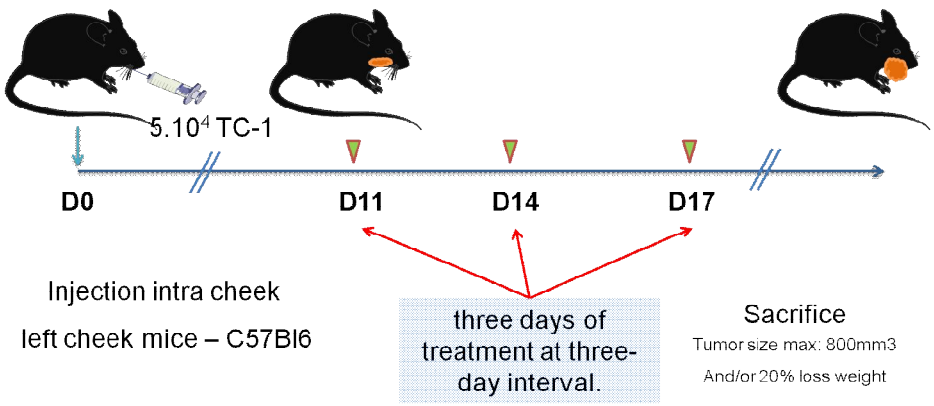

Fig 125 Treatment schedule of the experiment. The injections took place at time D=0. There were three days of treatment at three-day interval after D11.

For this experiment, the power supply n°3 described in II.2.1 was used. The waveform is non-sinusoidal, and peak-to-peak voltage can be set to 30 kV maximum.

Regarding the experiment using DBD, peak to peak voltage was adjusted to 30 kV. The currents do not cause muscle contraction. By contrast, peak to peak voltage was limited

[84] according to the protocol accepted by ethics committee

to 22-23 kV with the single-channel plasma jet. A Higher voltage caused muscles contractions. The flow rate of helium was set at 400 sscm.

Plasma activated medium was prepared by exposing one mL of RPMI-1640 to the plasma-jet during 1h15 or 1h 20 min. As evaporation occurs at a significant level, more than half of the fluid evaporates during treatment. The remaining volume is measured with the 1000 µL pipette.

A group of 40 Seven- to 8-week-old female C57BL/6 mice were purchased from Janvier (Le Genest Saint Isle,France) and kept under specific pathogen-free conditions at the UMS28 animal facility (UFR 969, Pitié-Salpêtrière). 50, 000 TC1 cells were injected into the cheek of each of the 40 mice. After twelve days of growth, treatments begin. The group of 40 mice was divided into six homogeneous groups in terms of tumor size (Table 5). For an exploratory study of several experimental conditions, it is necessary to reduce the size of the groups to the minimum to reduce the number of animals implies in the study. Consequently, the minimum group size was fixed at six. Mice were sacrificed if tumor volume was higher than 800 mm^3.

Table 5 Size of the groups.

Group		Number of mice
Direct treatments	Untreated	8
	DBD 30 min	6
	Single-channel jet 15 min	6
	Single-channel jet 30 min	6
Indirect treatments injection of 40 µL	Control group, injection of RPMI	6
	RPMI treated by the single-channel jet (PAM)	7

The distance between the surface of the DBD and the skin ranged from 2 to 4 mm. This distance was not precisely fixed because the animal moved and breathed during anesthesia, Furthermore, the DBD was moved during processing so that the plasma touched the entire surface and the tumor. The same range of distance was used for the plasma-jet Two photography are shown on the top of Fig 126. At the right, we can see the ECG electrode, which is connected mouse torso to the measuring capacitance.

Photos of Fig 126 illustrate another practical problem. In the presence of hair, the plasma discharges tend to strike the top of the hair rather than the surface of the skin. This could reduce the effectiveness of the therapy. It is, therefore, necessary to shave the surface of the skin at the level of the tumor. The two photos below represent a mouse before shaving treated with the single-channel plasma jet. This mouse was used for preliminary experiments.

A conductive gel was applied on mouse skin to prevent the current from flowing through the internal organs. A conductive path was established from the ECG electrode to the surface of the tumor with this gel. The surface of the tumor was also covered by this hydrogel. The gel is removed from the tumor just before treatment, so the plasma was applied to a slightly moist skin (except for the first treatment of 30 min-plasma-jet group, Fig 128).

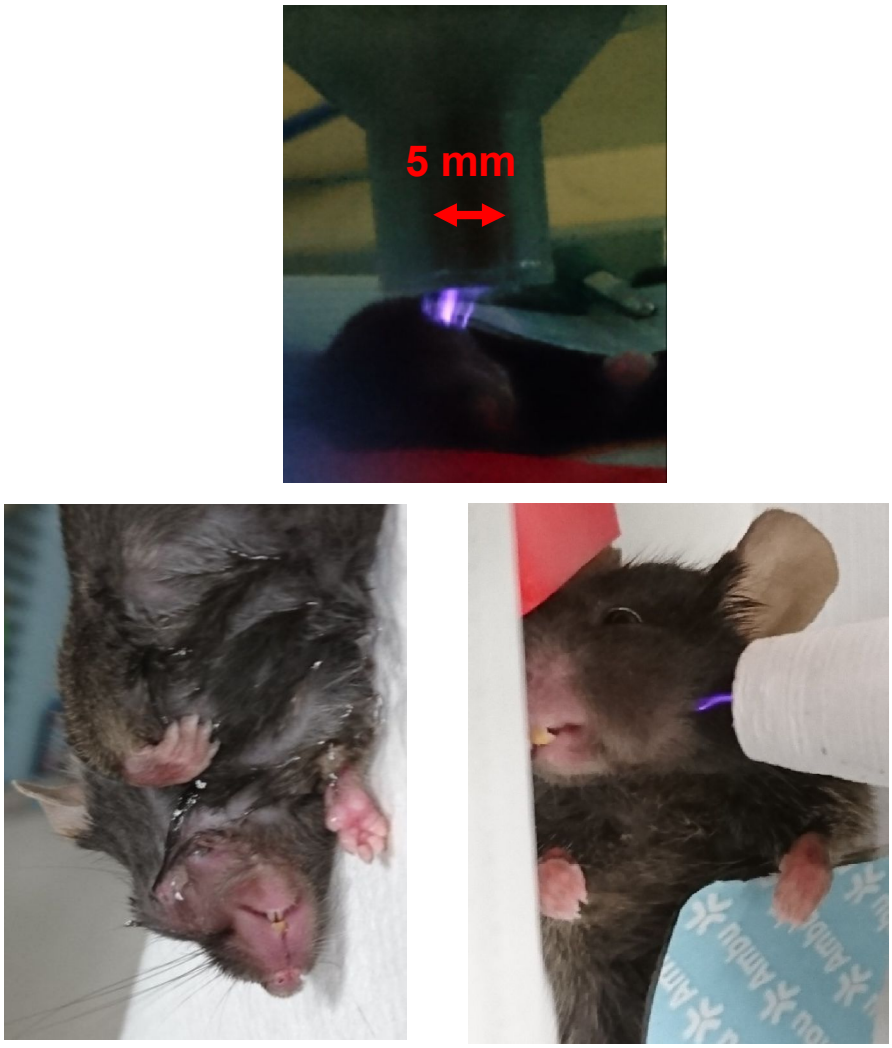

Fig 126 Top: treatment with the DBD. Bottom: right and left, hair and vibrissae are an issue when it is desired to direct the plasma discharge onto the skin. This figure enables to understand the problem caused by the presence of hair during plasma-treatment.

V.2.1.2 Results of the electrical diagnostics

The section below describes the results of the electrical measurements carried out on the mice. As outlined in 0, the measurement of two voltages enabled the calculation of power consumption. A capacitor of 100 nF was connected in series to the mouse (Fig 127).

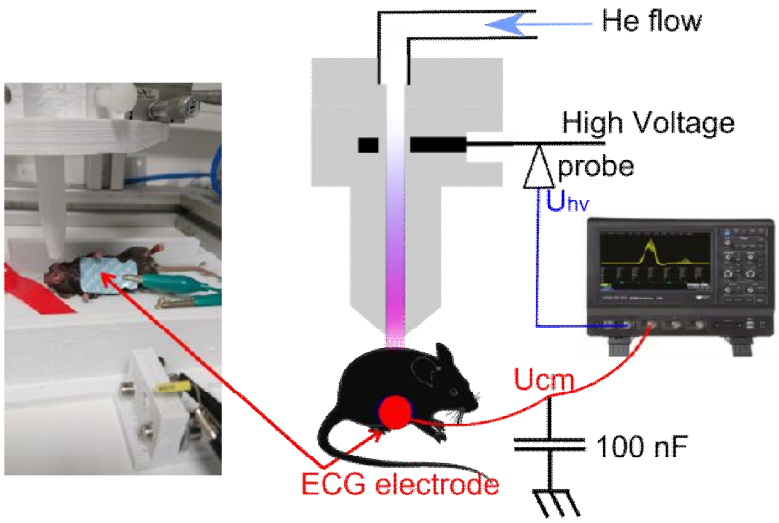

Fig 127 Left, photography of experimental setup, the tumor is implanted in the cheek of the mouse. Right, a schematic diagram of the single jet and electrical circuit devoted to power measurement.

Power measurements regarding treatments with the single-channel plasma jet were summarised in Fig 128 (blue). The power is of the order of 400 mW. The first day of treatment of the group “jet 30 min” is different from those of group “jet 15 min”: the skin of the mice was dry. In this case, the power was significantly lower for this group at day 1. The average of the energy for the two groups is plotted in red and green.

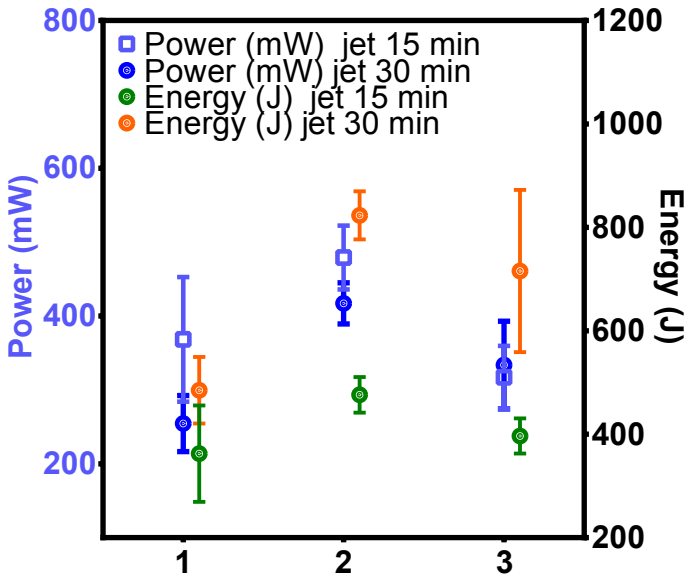

Fig 128 Blue: power consumption of single-channel plasma-jet. Orange and green: energy consumption in J. The first treatment took place at day 11; the three treatments are at three-day interval. The first day of treatment of group « jet 30 min » is different: the skin was dry for all the mice. Consequently, the power was significantly lower for this group at day one.

Power measurements regarding treatments with the DBD were summarized in Fig 129 (blue). The power consumed, 150 mW, is considerably lower than that of the plasma-jet. It is also found that the reproducibility of one treatment to the other is ensured. The mean energy was 320 J for each treatment.

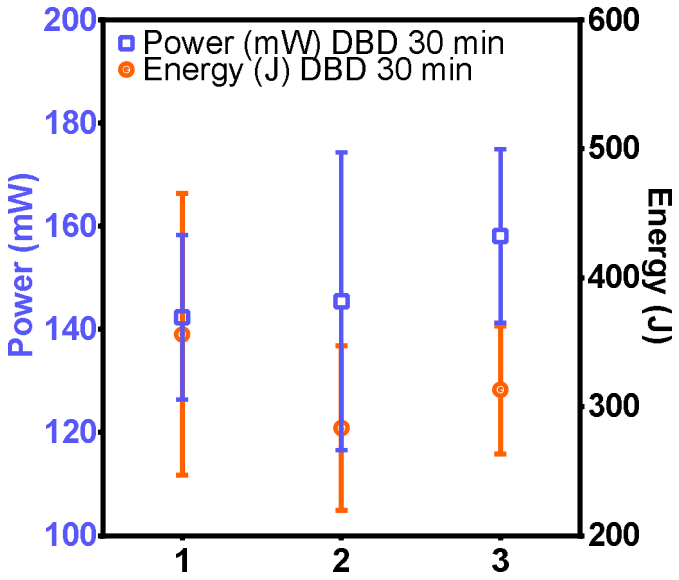

Fig 129 blue: power consumption of DBD during treatment. Orange: Energy consumption in J. The first treatment took place at day 11; the three treatments are at three-day interval. The reproducibility of power consumption and energy reached seems better than those of single-channel plasma-jet.

Plasma activated medium (PAM) was prepared with the set of parameters specified in. The final volume was measured with 1000 µL pipette. The amount of H_2O_2 in the well was deduced from the measurement of energy and the fact that the yield was close to 2 nmol/J for this parameter (Chapter III).

Table 6 Plasma activated medium was prepared from RPMI-1640. One mL of liquid in 24 wells plate was exposed to the single channel plasma-jet for a time specified in the second column. He flow was 400 sscm. Height above liquid was 2 mm. A significant part of the liquid was evaporated during plasma exposure. Consequently, height above the liquid is between 2 mm and 4.5 mm.

Day of PAM injection	Time of treatment (s)	Final Volume µL ±10 µL	Energy (J) ± 15 J	Amount of H_2O_2 (µmol)	Amount of H_2O_2 injected in each mouse (µmol)
D1	4830	565	3030	6	0.4
D2	4805	440	4075	8	0.6
D3	4521	440	4130	8	0.6

V.2.1.3 The growth of TC1-tumor in the untreated group

The size of the tumor was measured with a caliper (Fig 130). Tumor volume was approximated using the formula $V = \frac{1}{2} L \times W \times \min(L, W)$ where L was the length and W the width. It is an approximation of the volume of an ellipsoid, considering that the thickness of the tumor is of the order of magnitude of the width. Mean value and errors bars are plotted until the day of the first sacrificed mouse. The volume of tumors grows exponentially.

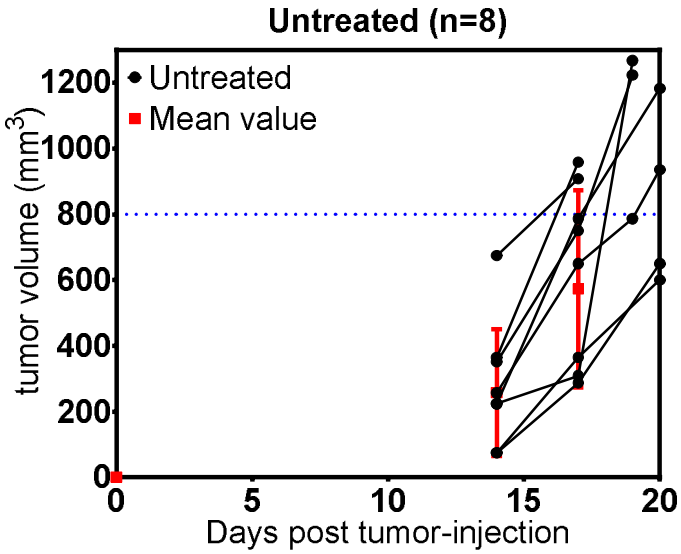

Fig 130 Tumor volume as a function of time for the untreated group. Black dots represent individual values. Red dot and errors bars are the mean value and the standard deviation of this group. The mean values and error bar no longer make sense when a mouse in this group had to be sacrificed.

V.2.1.4 Tumor volume of DBD group

Tumor volume of the group treated with the DBD was plotted on Fig 131 for each replicate. There is no significant difference in the size of untreated and DBD group. In these conditions, the plasma treatment does not affect tumor growth.

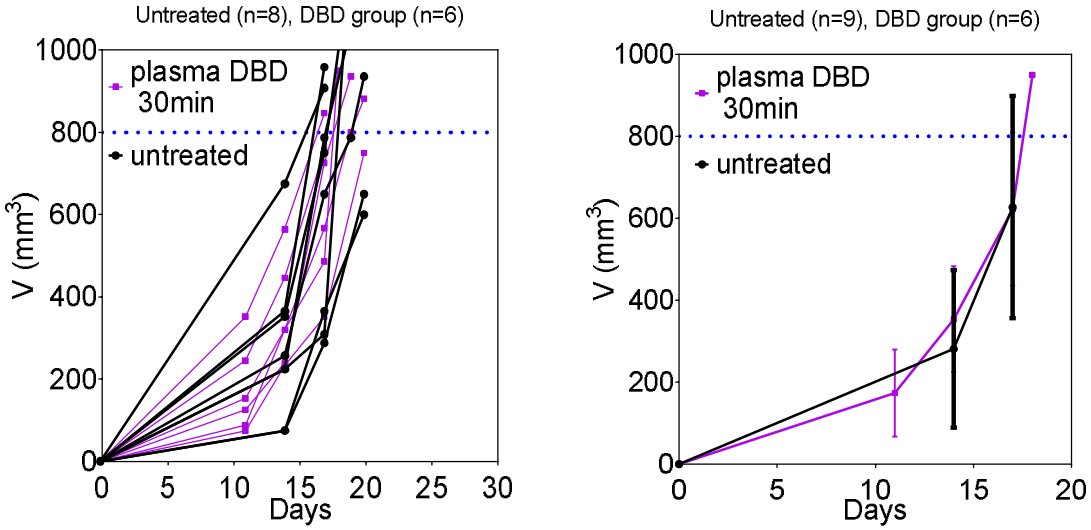

Fig 131 Tumor volume as a function of time. Comparison between untreated and plasma DBD group for each mouse (left). Comparison between the mean value of each group: error bar represents the standard deviation of the groups.

V.2.1.5 Effect of plasma jets treatments on tumor growth

Tumor volume of the two groups treated with plasma-jet is plotted in Fig 132 for each replicate. There was no significant difference in the size of untreated and plasma jet groups.

.

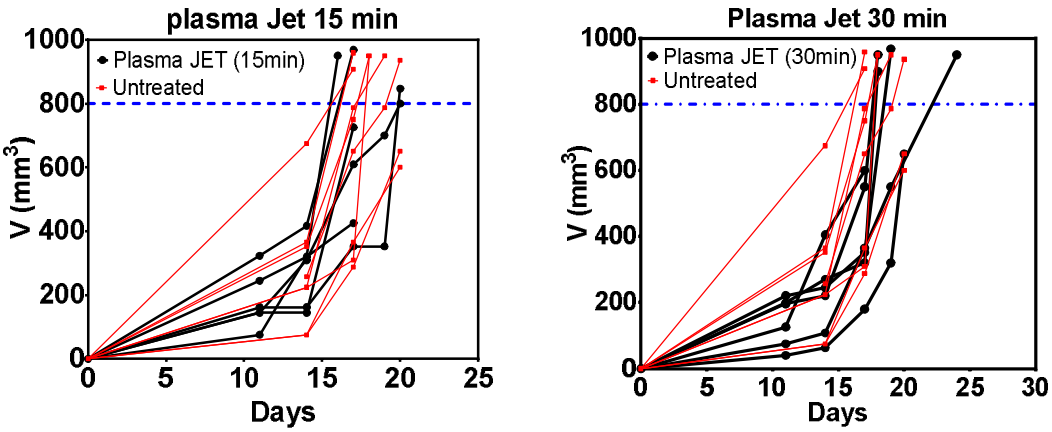

Fig 132 Comparison of tumor volume of group "plasma jet 15 min" and "plasma jet 30 min" with the untreated group. There is no significant difference between the treated and untreated groups.

The survival curve, however, shows a little effect for the group "plasma jet 30 min". Such increase survival is not significant since there is only 6 mices in each group.

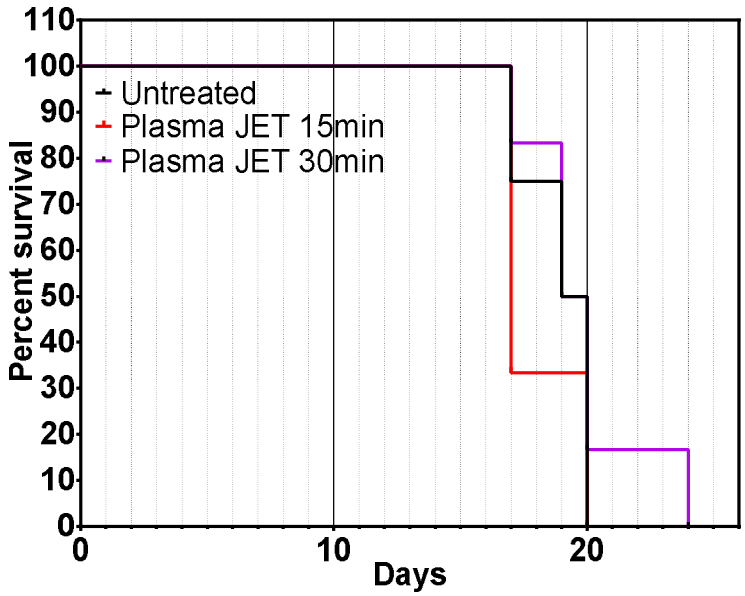

Fig 133 Survival curve as a function of time for untreated(Black), single-channel plasma jet for 15 min (red), 30 min (purple).

V.2.1.6 Effect of PAM injection on tumor growth

Tumor volume of the group treated with the injections of PAM was plotted on Fig 134 for each replicate. There is no significant difference in the size of untreated and PAM group. The amount of H_2O_2 in each injection was 0.4 µmol for the first treatment and 0.6 µmol for the two others. These values are based on the assumption that the yield of H_2O_2 production is of the order of 2 nmol / J.

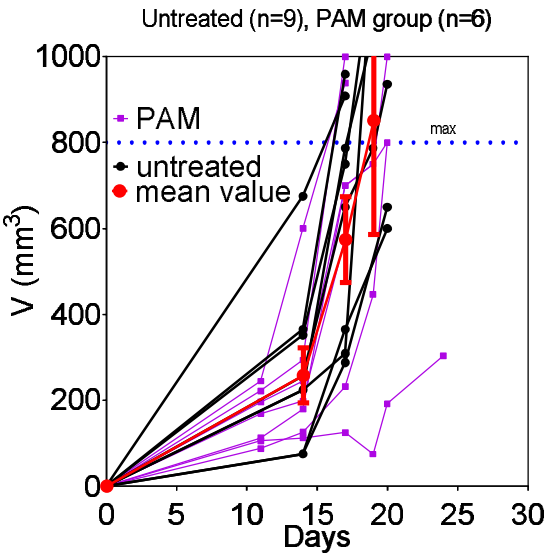

Fig 134 Tumor volume as a function of time. Comparison of PAM (pink) and untreated group (red and black)

V.2.1.7 Conclusion

The main results are summarised in the following points:

- No visible effects on mouse skin, no signs of damages.
- Indirect treatment with PAM injection had no measurable effect.
- Regarding tumor size, direct treatment with the DBD during 30 min and the single-channel plasma jet for 15 min had no measurable effect.
- Perhaps a little effect regarding the survival of plasma jet groups

V.2.2 Multichannel plasma jet experiments 10 kHz experiments

These experiments took place at the animal house of Pitié-Salpêtriere hospital between August and October 2016. These experiments were done in collaboration with the team of François Lemoine from the Centre d'Immunologie et des Maladies Infectieuses (CIMI) in Paris.

V.2.2.1 Protocol and electrical diagnostic

The experiment is composed of two groups of six eight-weeks-old female C57BL/6. The orthotopic tumors were prepared as in the previous section. However, treatment began seven days after the injections (instead of eleven days). The 12 mice are divided into two homogeneous groups. The conditions of sacrifice are the same than in the previous experiment in term of tumor size ($V_{MAX} = 800\ mm^3$).

The plasma source and the generator have been changed compared to the previous experiment. For this experiment, the power supply n°2 is used (described in II.2.1). The waveform is sinusoidal, and the peak-to-peak voltage was adjusted to 13 ± 0.3 kV. Higher voltages cause muscles contractions. The flow rate was set at $\Phi(He) = 2250\ sscm,$ the minimum value, which provides a stable discharge.

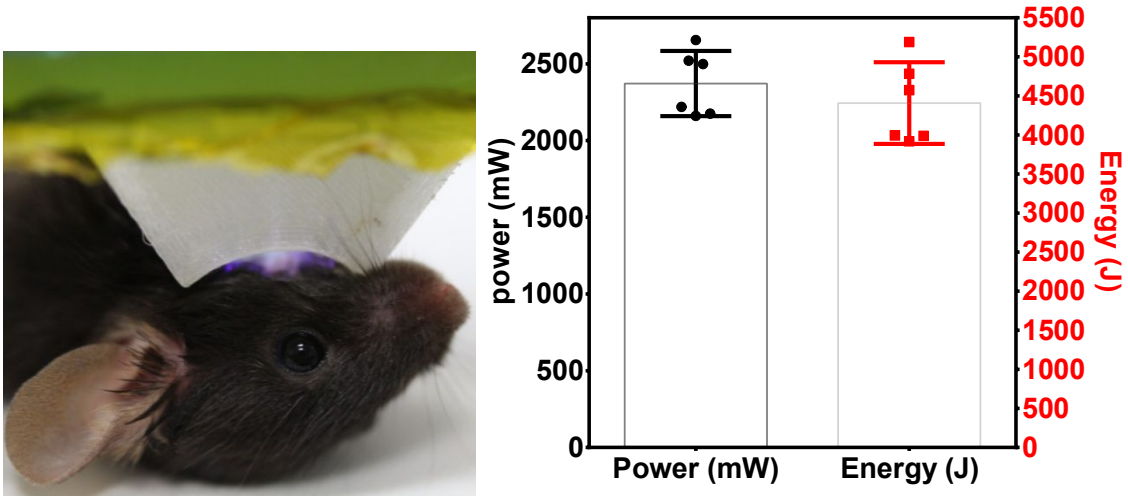

Fig 135 The power consumption is plotted in black. Energy consumption is plotted in red. The treatment has a duration of 30 min. Mean power = 2371 mW, Mean energy = 4408 J. Error bars corresponds to the standard deviation of the treatments applied to the six mice.

V.2.2.2 Results of the 30-min-treatment

Just after the treatments of 30 min, no differences were visible between the skin of treated group and placebo group. No mark, no sign of damage, no inflammation or crust was visible right after the treatment (Fig 136, left).

The state of skin was very different two days later. The skin of the treated area was destroyed. The damage is similar to that of a severe third-degree burn. Subcutaneous tissue was severely damaged, in some cases, muscle tissue is apparent. Ischemia accompanies the loss of substance. A significant loss of weight of the order of ~ 1.5 g is also observed, probably due to the difficulties that the mouse has to feed. Owing to the size of the damage, three mice were immediately sacrificed.

The size of the damaged area spread until the third day. Wound healing occurred, and the mice started to gain weight again. The treatment was not repeated. After the cicatrization, two of the three mice developed the tumor at the same location. The tumor of the mouse shown in Fig 136, was removed entirely. This mouse was still alive 60 days after plasma-exposure.

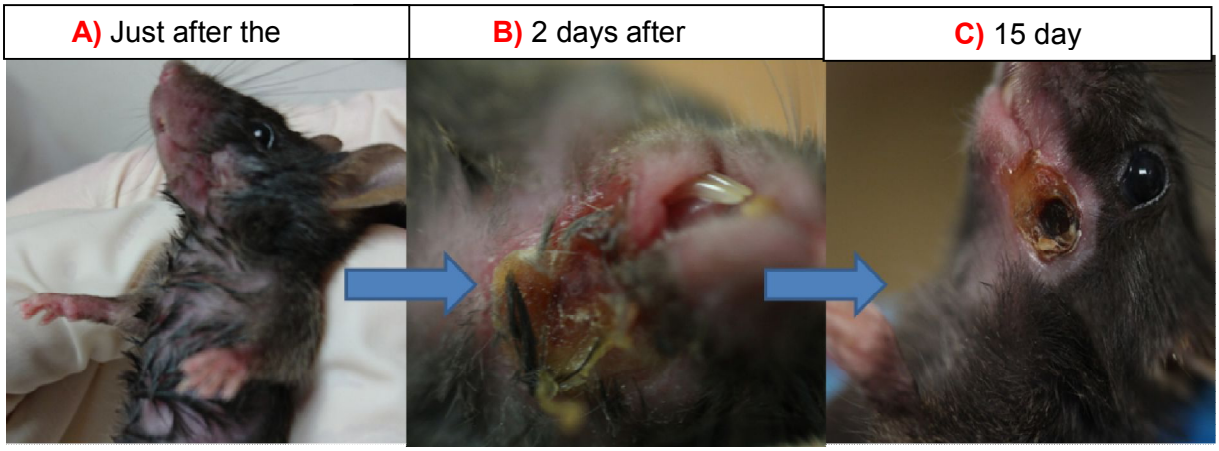

Fig 136 Picture of the cheek of the mouse n°A0. Picture A: just after the treatment. Picture B: 2 days after. Picture C: 15 days after. These massive damages entirely obliterated the tumor which did not re-growth.

V.2.2.3 Discussion

A) First, in-vitro experiments had shown that there was no heating of the liquid exposed to the multichannel jet (even for higher power consumption). The cooling of the liquid was observed and attributed to the evaporation of the liquid. The rate of evaporation is increased by the flow of dry helium.

B) Moreover, the paper [80] (Kin-Pen experiments) use the same kind of assumption. The authors of this paper use the temperature obtained at the surface of their petri dish to assume that the maximum temperature reached by the tissues do not exceed 41 ° C. They assume an initial temperature of 37 °C for biological tissue. Then, they use their temperature measurements in 12-wells dishes (temperature rise of + 2.93 ° C + -0.40 ° C) to justify the fact that the temperature of the biological tissue does not exceed 41 ° C.

C) Unfortunately, the infrared camera was not available. Consequently, the temperature was measured with a thermocouple applied at the surface of the skin few seconds after the end of the treatment. However, the time required by the moving of the mouse and the outcoming the thermal equilibrium with the skin (15-20 s) is sufficient to ensure that the temperature measured by the thermometer reaches a temperature range which seems tolerable (40 ± 1 °C). However, next experiments and simulations show that this temperature did not represent the temperature of the skin during treatment.

Indeed in the framework of plasma-medicine the symptoms encountered could have three origins: an electrical burn, a thermal burn or a chemical burn.

Electrical burns involve the destruction of tissues by Joule effect and dielectric rupture. They are fairly well characterized in the literature, especially to prove the existence of cases of torture by electricity [198]. In our case, this source of damage can be excluded, the value of the current involved exclude the possibility of damages produced by joules effects inside the body. In addition, precautions are taken (addition of conductive gel) to minimize the size of the tissues through which the current flows.

The literature shows that the corrosive action of H_2O_2 (see toxicology section II.3.2) could be a source of damages. Regarding our case, it will appear that the damage is probably from thermal origin. At this point of the discussion, without the measurements given by the thermal camera, it is not possible to exclude that chemical effects play a role.

Three needs emerge:

1. Reliable data regarding the temperature of the treated surface. The link between these temperature measurements and the damage observed must be studied.
2. The modeling and the simulation of the thermal behavior of the tumor exposed to plasma should bring precious information.
3. experimental device that excludes the possibility that hyperthermia plays.

V.2.3 Damage to the skin

This discussion is devoted to the damage following the treatments of 1, 2 or 5 min. These experiments aimed to determine the maximum duration of treatment, which

enables the repetition of treatment every two days. The multijet powered by a sinusoidal source at a frequency of 10 kHz was used

V.2.3.1 Orthotopic model

Fig 137 shows the treatment of an orthotopic TC-1-model (tumor in the cheek) by the multi-channel jet. The distance between the center of the nozzle and the skin is of the order of 4-6 mm. The gas flow and the voltage are the same as in the previous experiment. In all cases, no mark is visible on the skin just after the treatment. In this context, the repetition of treatment which seems to induce a second- or third-degree burn is not acceptable.

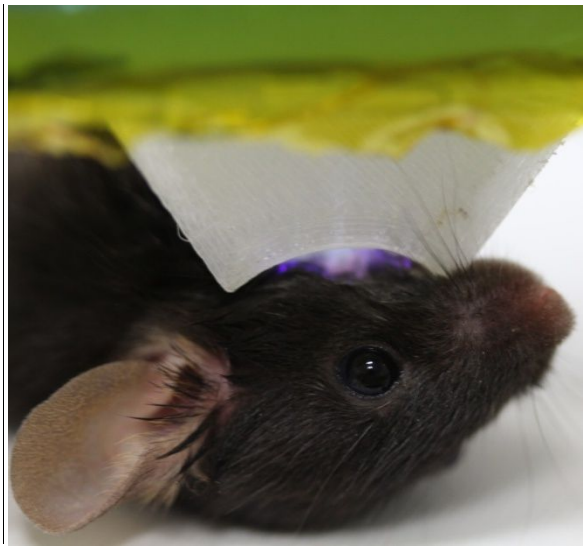

Fig 137 Picture of the mouse during the treatment of the orthotopic model.

Fig 138 shows that one-minute treatments do not cause significant damage. Both photos are taken two days after the last mentioned treatment. The two photos were taken with the same mouse. After one treatment of one minute, no difference can be observed between the untreated skin and treated area. After three treatments, the skin seems to have peeled (on a very small area). It is not even possible to describe this as a burn of the first degree: the treated zone has the same color than the untreated area.

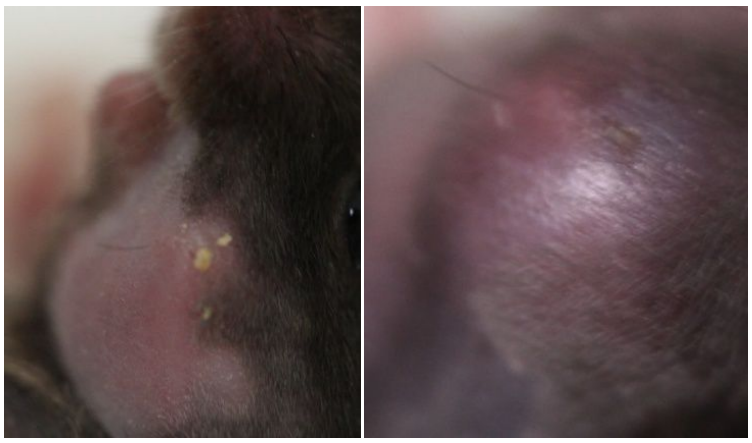

Fig 138 Left: two days after the first treatment. the four yellow objects are gravel, which has stuck to the skin. Right: two days after three treatments of 1 min

Fig 139 shows the skin of the mouse two days after one treatment of 5 min (Left), and two days after one treatment of three minutes (Right). It appears that the five min treatment induces a rather severe burn, relatively thick (second or third degree) and relatively extensive. From an ethical point of view, it would not be acceptable to treat this mouse again. Three-minute treatments induce visible but limited damage (slight irritation). It seems ethically acceptable to repeat these treatments.

Fig 139 Left: two days after one treatment of five min. The scar and the depth of the damage are like a second or third-degree burn. Damage is limited. However, from an ethical point of view, it would not be acceptable to treat this mouse again. Right: 3 min of treatment is a good compromise between toxicity and treatment time.

The proximity of the eye is a difficulty for this type of model. It is ethically unacceptable that a mouse loses an eye during treatment. It is also necessary to protect the eye of the mouse from the flow of Helium which could cause its drying.

The ectopic tumor models developing in the flank enables to reduce the number of experimental precautions to be taken and enables to monitor tumors growth over a longer time since the mice must be sacrificed when the volume reaches 2000 mm^3 (800 mm^3 for the orthotopic model).

V.2.3.2 Ectopic model: damages and surface temperature after one or several treatments

Fig 140 shows two mice bearing an ectopic model of cancer (TC1-tumor in the flank). It can be seen that the multijet achieves its objective: the possibility of treating a large area without moving the mouse. The discharge takes the form of several filaments starting from each of the channels and sweeping the surface over time. If the nozzle is too far from the surface, the filaments become a single, more intense filament, which may cause burns.

The treatment conditions were slightly optimized compared to the previous case. The flow of Helium has been increased up to 2600 sscm to decrease the voltage of ignition. This enables to be away from the tension causing muscular reactions.

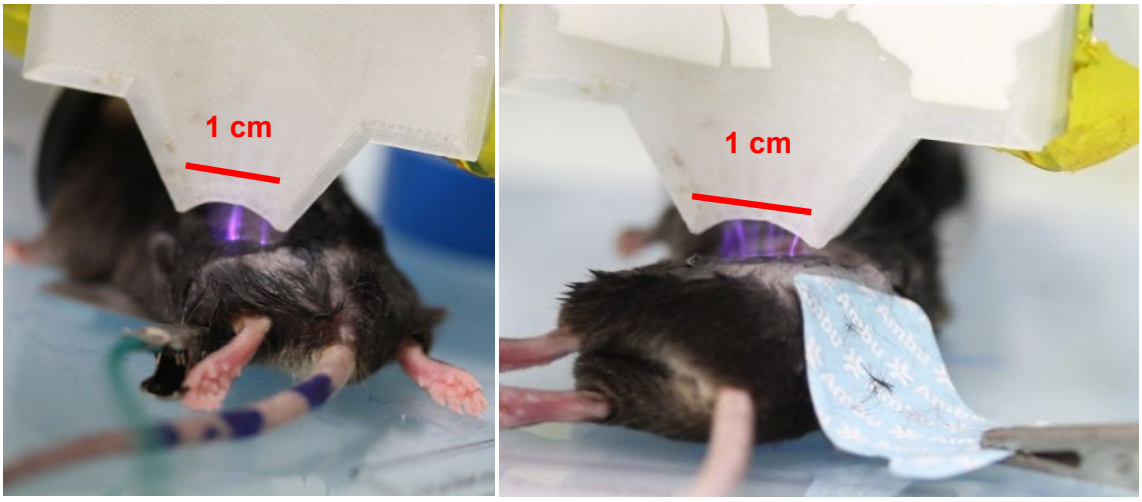

Fig 140 Photo of a C57BL/6 mouse bearing an ectopic TC1 tumor. During this treatment, the power consumption is around 2 W. The generator has a frequency of 10 KHz. Sinusoidal voltage, peak to peak voltage is 13 kV peak to peak.

Fig 141 shows three infrared images of a tumor. They were taken at the end of the treatment. The first picture, on the left, was taken around 5 s after the end. The two others are taken respectively 33 s and 57 s after the first picture. The rate of thermalization of the surface can be observed. The generalization of this kind of measurements is presented in section V.3.2.5; they are interpreted by a model described in Chapter VI. In this precise measurement, the surface of the skin reaches a maximum temperature of 45 ° C after 3 min. The temperature after 5 min of treatment is not so different. To summarize, the surface temperature is systematically measured between 45 and 48 ° C at the end of a treatment of 3 or 5 min. Exposure of the cells to a temperature above 42 ° C induces irreversible damage to the cells. The damage increases exponentially with temperature. The modeling of damage is described in Chapter VI.

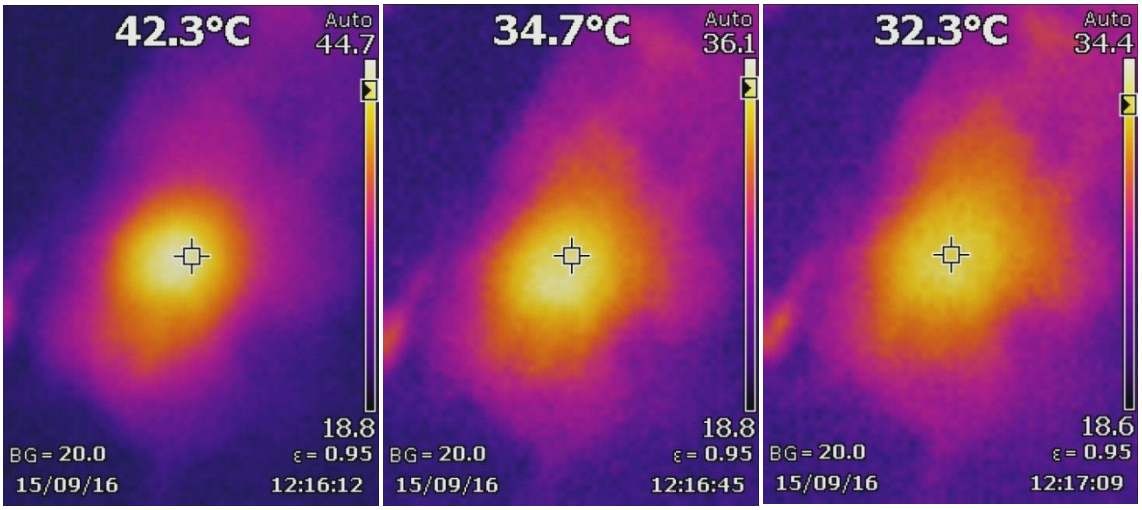

Fig 141 Temperature of the treated area acquired with the infrared camera. From left to right: the maximum temperature is 44.7, 36.1 and 34.4 ± 0.1 °C. The picture in the center is taken 33 s after the left one, the picture on the right, 57 s after the left one. The left image was acquired about 5 seconds after the end of treatment. This kind of measurement was repeated during the experiment described in section 0. The results of measurements are compiled in section V.3.2.5 and interpreted in Chapter VI.

As previously, damage caused by treatments lasting 3 min were evaluated. The following tables show the damage to the skin of two mice. The damages shown are representative of those of a group of 12 mice, which has undergone a similar treatment. The pictures

were taken two days after each treatment. Significant damages always appear after two or three treatments.

Table 7 Damages two days after repeated treatment of 3 min. Peak to peak voltage and power which was measured two days before the picture was taken are written below the picture. Orange column = the two pictures are taken two days after the first treatment of 3 min. Green column = the pictures are taken two days after the second treatment. The damages after one treatment are relatively small. The black area is parts of the skin with different coloration: this is not a carbonized area. For the mouse n°374 (First line), significant damages appear after only two treatment (probably a second-degree burn). Whereas the extension of damage is more limited for mouse n°362 (probably a first degree-burn). The blue arrow is the spatial scale of the wound.

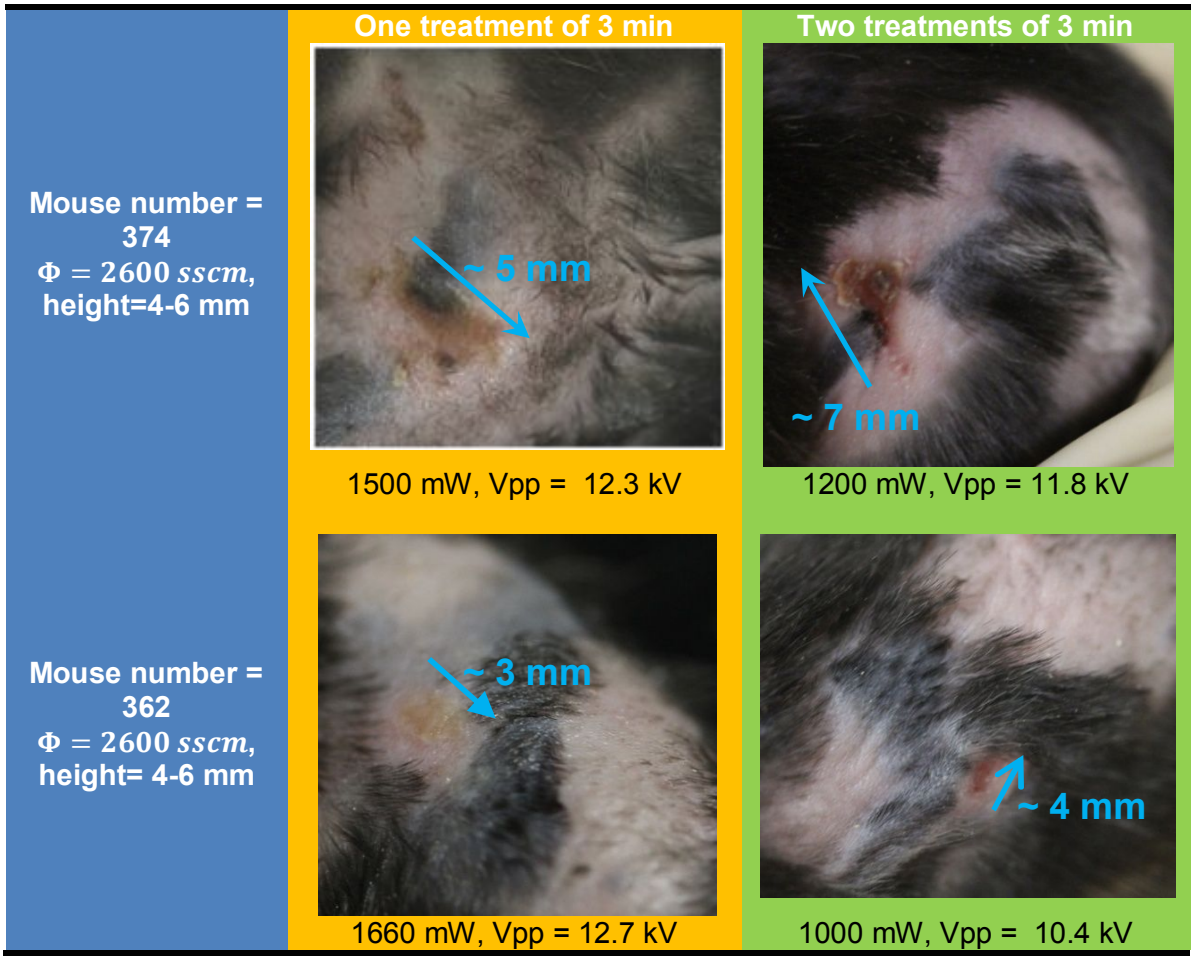

All the experimental observations of damage and temperature measurements are summarized in the four following points.

- Skin temperature after one treatment of 3 min or 5 min was around 45-48 °C.
- Treatment of one min gave no damages. Repetition of 1-min therapy does not produce damage.
- One treatment of three min gave no damages, but the repetition of this treatment at two days intervals gave damages after two or three treatments.
- Treatment of 5 min systematically causes damages. The damage probably corresponds to a second or third-degree burn.

These observations are the set of facts that the simulations of Chapter VI must reproduce, it enables to constrain the model and the simulations.

V.3 Systematic experiments with refrigerated plasma-jet: treatment of CT-26 and TC-1 tumors line

The discussions of the previous section and the results of the experiments provided treatment conditions that minimized damage to the skin. The addition of a cooling system reduced the damages considerably. A preliminary experiment missed due to a failure of the control group, suggested that a decrease in the size of TC-1 tumors could be observed with non-refrigerated plasma-jet. In this experiment, however, the temperature of the skin was between 45 and 48 ° C after plasma treatment. Consequently, It is not excluded that hyperthermia plays a role.

The purpose of the experiments described in following sections is to cancel this bias by cooling the skin. The refrigerated plasma-jet is a 3D-printed plasma source described in section II.1.6, which includes a tank for containing liquid nitrogen. The boiling point of liquid nitrogen is $-195.8\,°C$ at atmospheric pressure. This very low temperature could lead to mechanical stress and breakdown of plastic material. The design[85] of the source guarantees the good mechanical strength of the device and solves this issue. Since liquid nitrogen was removed from the device before treatment, the cooling was not excessive or able to cause frostbite. Infrared images show that the skin temperature is around 10 ° C when the treatment begins.

This solution was chosen due to his practical interest[86]. Unfortunately, the chemistry of this source is less well characterized, but preliminary measurements suggest that yield of nitrites and H_2O_2 (in nmol per J) has the same order of magnitude than the single-channel jet.

It would have been possible to choose another technological solution. For instance, in dermatology, micro-droplets of a cryogenic fluid are projected on the skin [199]. Their evaporation elicits a cooling of the upper layer of the skin and enables to use dermatological treatments based on the heating of the tissues while preserving the upper layers of the skin. It is also possible to use the Joule-Thomson expansion of argon gas at high pressure to obtain a fast cooling of biological tissue for the treatment of prostate cancer by cryotherapy [200].

Let's go back to our device.

Since the device cool the skin, are we creating a new bias?

The review [201] describes the effect of cold on several tissues. The rate of refrigeration and warming seems to play a key role. Necrosis occurs when ice is formed within the cells. The paper [202] explains how to quantify the damage caused by the cold. The temperature has to be below 0°C to damage the tissue.

With our device, since the minimum temperature of the skin is between 7 and 9 °C[87], it can be considered that the device is safe regarding the low-temperature side. Moreover, cryotherapy required a temperature of - 40 °C to kill the cancers cells in one treatment [203] [204].

---

[85] i.e. the choice of plastic thickness ~several millimeter

[86] The device was designed, manufactured and tested in a single week thanks to 3D printing. Moreover, the use of liquid nitrogen is credible from a practical point of view. Indeed, all laboratories and hospitals have liquid nitrogen to store biological samples.

[87] see section V.3.2.5

The first experiment consisted of treating BALB/C mice with CT-26 tumors implanted in the flank. The second was to treat C57BL/6 developing TC-1 tumors in the flank.

V.3.1 CT26- treatment with refrigerated multi-channel jet

This experiment took place between November and December 2016. This work was done in collaboration with Jerôme Griffon, a Ph.D. student in the team of Lori Bridal at the Laboratoire d'imagerie Biomédicale (LIB) in Cordeliers' Research Center.

V.3.1.1 Power supply and plasma source

The power supply of this experiment produced a sinusoid waveform with a frequency of 10 kHz. Plasma source was the multichannel plasma jet described in section II.1.6. Mass flow controllers (Brook's instruments) provided a helium flow of 2600 sscm. This flow was the minimal value of flow that enables the ignition of plasma for a peak to peak voltage around 11 or 12 kV. For lower flow rates, the ignition occurs at higher voltage (16-17 kV). Moreover, the ignition occurs suddenly when the voltage of the generator is increased. The current flowing through the skin caused a rather violent muscular reaction.

To avoid a waste of gas, we do not choose a gas flow rate higher than this value. Second, we know from our chemicals experiments, that the yield of nitrite production decrease for increasing value of Helium flow. Consequently, the choice of helium flow is a compromise between mouse health and the production of reactive species from nitrogen. The best operating point of the device is achieved by a flow of 2600 sscm.

The choice of the distance between the output of the refrigerated plasma-jet and the skin is also the result of compromises. Too close, the output of plasma-jet which is at a temperature below -20 ° C may touch the skin, which, while freezing, may stick to the device and induce frostbite. Moreover, chemistry experiment from chapter IV, show that the yield of production of nitrogen species decrease when the distance decrease. This is probably due to a less efficient mixture of nitrogen from the ambient air with He flow leaving the plasma jet. Too far, the stability of ignition is not ensured. Second, the cooling of the skin due to cooled He is ineffective because He is less dense than air, the range of distance for cooling is limited by the characteristics of Helium flow at the output of the plasma-jet. Third, If we increase the distance too much the aspect of the discharge changes, instead of having about ten plasma filaments, striking the surface of the tumor in ten different points, we have a single discharge, Much brighter, probably warmer, since huge damages were instantaneous observed on the skin of mice (carbonization).

V.3.1.2 Treatment schedule

Seven- to 8-week-old female mice from the Balb/C line were purchased from Janvier (Le Genest-Saint-Isle, France). The animals were housed at the CEF (Centre d'Explorations Fonctionnelles, Cordeliers' Research Center). All experiments were conducted in an animal house in accordance with the institutional guidelines and the recommendations for the care and use of laboratory animals established by the French Ministry of Agriculture.

A group of 39 mice with subcutaneous CT26 colorectal tumor on the flank was divided into four homogeneous groups in terms of tumor size (a) untreated group (**N = 10**) (b) (**N = 10**) (c) (**N = 10**) per therapy (d). Ultrasound diagnostic requires much time (around 30 min per mouse). Therefore, the number of mice that can be

treated and observed per day is limited. That is why 39 mice are divided into two groups of 20 (**Gr1**) and 19 mice (**Gr2**). Tumor implantation was made at two consecutive days. Therapy was applied to each mouse for two weeks at two days interval, seven days after tumor implantation.

Table 8 Description of the four groups.

Group	Number of mice	Description
Untreated	10	Control group
PAM	10	Prepared from PBS1X, injection in 6 points
Plasma	10	Direct exposure of the tumor to the refrigerated multi-channel plasma-jet
Plasma-inhibitor	9	Tumor was exposed to a catalase inhibitor during 10 min before plasma treatment (Hydroxylamine NH_20H 10%w in DMSO)

V.3.1.3 Tumor monitoring

The set of diagnostics used for the monitoring of the tumor is the same than those of previous experiments done at LIB laboratory. The monitoring protocol was described in section V.1.3. The tumor size was measured with a caliper. Tumor volume was approximated using the approximation: $V = \frac{1}{2}abc$ where a is the length, b is the width and c the thickness.

V.3.1.4 Protocol applied to each group

Untreated group

The ten mice of this group undergo only the manipulations necessary for the acquisition of ultrasound measurements.

Direct-plasma group

First, the plasma source filled with liquid nitrogen. The cooling took about 10 min. Photos of the tumor were systematically taken before treatment. The size of the tumor was measured with a caliper. A small amount of gel was spread on the surface of the tumor. The gel was removed with paper towels before treatment. The purpose of this was to treat a slightly moist skin in the hope that this could promote the formation of ROS.

The mouse was moved to a plastic anesthetic device to isolate the animal electrically. The ECG electrode was then connected to the measuring capacitor Cm. Liquid nitrogen was removed from the plasma sources (otherwise the cooling is too strong)

The health of the mouse was checked a few minutes after his awakening. This group contained ten mice. Measurements made with the ultrasound diagnosis are performed for approximately 30 min.

Catalase-inhibitor group

The skin of mice was exposed to hydroxylamine (NH_2OH), a catalase inhibitor, for 10 min before plasma treatment. The 10% by weight solution of Hydroxylamine was prepared by dissolving the solid in DMSO. Since the DMSO has an excellent cutaneous absorption, the idea was to promote the passage of the product through the skin of the mouse. In the protocol, 40 µL of solutions are applied to the surface of the skin for 10 minutes. Then the skin is dried before being treated with plasma. This group contains ten mice.

PAM group

The conditions regarding the preparation of PAM are summarized in Table 9 and its legend. The PAM is prepared by exposing PBS1X to the plasma source for more than 30 min. 30 µL of liquid is injected into each mouse every two days. These injections take the form of 6 injections of 5 µL in the vicinity of the tumor (less than 1 mm outside the tumor). The injections are not done in the tumor itself to avoid the breaking of the outer layer of the tumor and the spread of metastasis.

Unfortunately, the chemistry generated by this plasma source has not been studied precisely, however measurements made with semi-quantitative diagnostics (Quantofix®, test strip for H_2O_2, nitrites, nitrates) show that the yield of chemical species (in nmol/J) is at least as high for this device than for the single-channel plasma jet. The yield could be even higher (up to an order of magnitude higher). It is certain that a rigorous chemical characterization work must be done with this plasma source. The estimation of the quantity of H_2O_2 contained in the 30 µL of injected liquids (last column of Table 9) is based on the low assumption that the yield is around 2 nmol / J. The amount of H_2O_2 injected has a significant variability. The sum of the total quantity of H_2O_2 injected is of the order of 7.2 or 7.9 µmol. This group contains nine mice.

Table 9 Plasma activated medium was prepared from PBS 1X. The liquid contained in 6 wells plate was exposed to the multichannel plasma jet for a time specified in the second column. He flow was 2600 sscm, mean value of peak to peak voltage was 12.7 kV. Height above liquid was 6 mm. A significant part of the liquid was evaporated during plasma exposure.

Day of PAM injection (after implantation)	Time of treatment (s)	Initial Volume (µL)	Final Volume µL ±20 µL	Energy (J) ± SD		Amount of H_2O_2 injected in each mouse (with the assumption of a yield equals to 2 nmol/J) (µmol)
7 Gr1	1860	1500	270	7988	15	1.8
7 Gr2	1824	1700	500	10086	25	1.2
9 Gr1	2551	2000	460	10255	16	1.3
9 Gr2	1937	1500	280	10314	22	2.2
11 Gr1	1833	1500	790	10704	9	0.8
11 Gr2	1882	2000	700	11047	16	0.9
14 Gr1	2220	2000	680	11510	70	1.0
14 Gr2	1869	2000	580	12335	15	1.3
16 Gr1	1800	2000	950	9549	14	0.6
16 Gr2	2100	2000	~ 550	13471	52	1.5

18 Gr1	2105	2000	520	14745	19	1.7
18 Gr2	1823	2000	890	11393	7	0.8

V.3.1.5 Results of electrical diagnostics

The section below describes the results of the electrical measurements[88]. The measuring capacitance had a value of 104 nF. Fig 142 shows the power of the plasma source during direct treatments. Compared to non-refrigerated devices, we found that the power of the devices is twice higher. This increase in power could be attributed to the fact that the refrigeration dries the gas. In non-refrigerated devices, it was likely that the desorbption of water adsorbed inside the gas tubes contributes to decrease the power of the device.

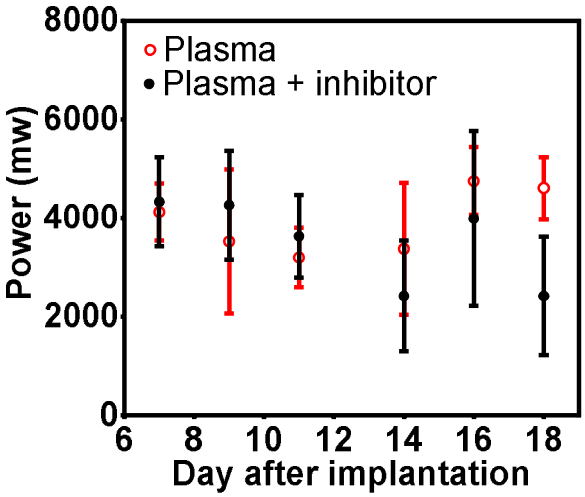

Fig 142 Power consumption of the multichannel plasma-jet. In red: power consumption of "plasma" group. In black: power for "plasma+inhibitor" group. Error bars represent standard deviation. The mean value for the merged group was close to 4 W.

Fig 143 shows the energy consumed during direct plasma treatments. It appears that the energy consumed by the plasma is constant from one day to another (average value of 785 J). The error bars show the dispersions of measurements. The primary sources of variability are the structure[89] of the flow in the vicinity of the surface of the tumor or the variability of the electrical properties of the skin.

[88] method is described in Chapter II
[89] laminar or turbulent

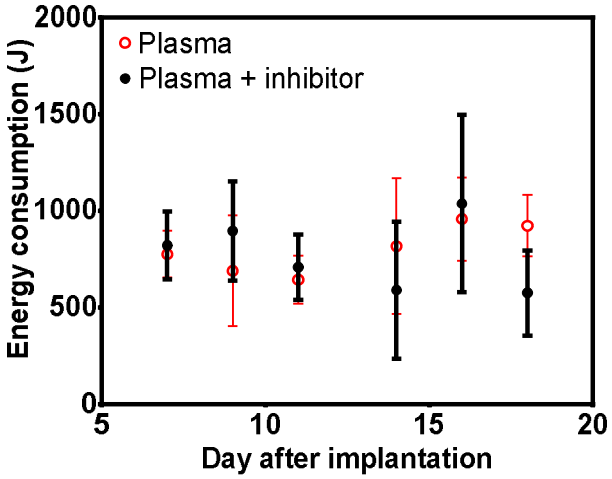

Fig 143 Energy consumption of the device during one treatment. In red: "plasma" group. In black: "plasma+inhibitor" group. Error bars represent standard deviation. The energy consumption is 785 J (average value of pooled groups)

Fig 144 shows the sum of energy and time over the six treatments of the experiment campaign. It appears that each mouse was treated during 1300 seconds (total energy consumption ~5400 J). There is considerable progress compared to the first experiments in terms of applied energy and therefore the quantity of chemical species produced in the skin.

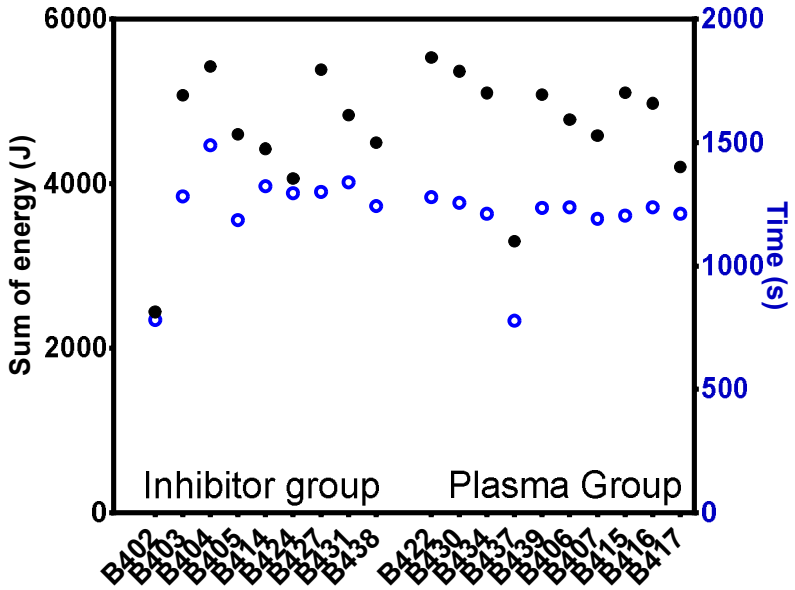

Fig 144 sum of energy (black dots) and treatment time (blue dots) during the six treatments of the experiment campaign. The nine mice of "plasma+inhibitor" are plotted in the left part of the graph. The ten mice are drawn in the right part.

V.3.1.6 Treatment of CT26-tumor

Tumor volume (calliper measurements) is plotted as a function of time in Fig 145 for each group. It appears there is no significant difference between treated and controls groups.

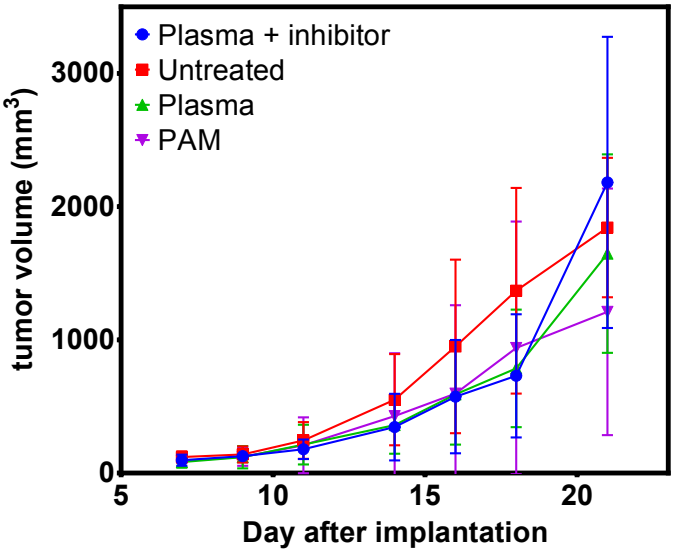

Fig 145 Tumor volume plotted as a function of time for the four different groups. Error bars represent the standard deviation of measurement. Each group contained ten mice.

Even ultrasound measurements show no effects. The results of the preliminary results of ultrasound measurements (mode B, CEUS, contrast-enhanced ultrasound) show similar results. The results of shear wave elastography are visible in Fig 146. There is no difference between treated and untreated groups.

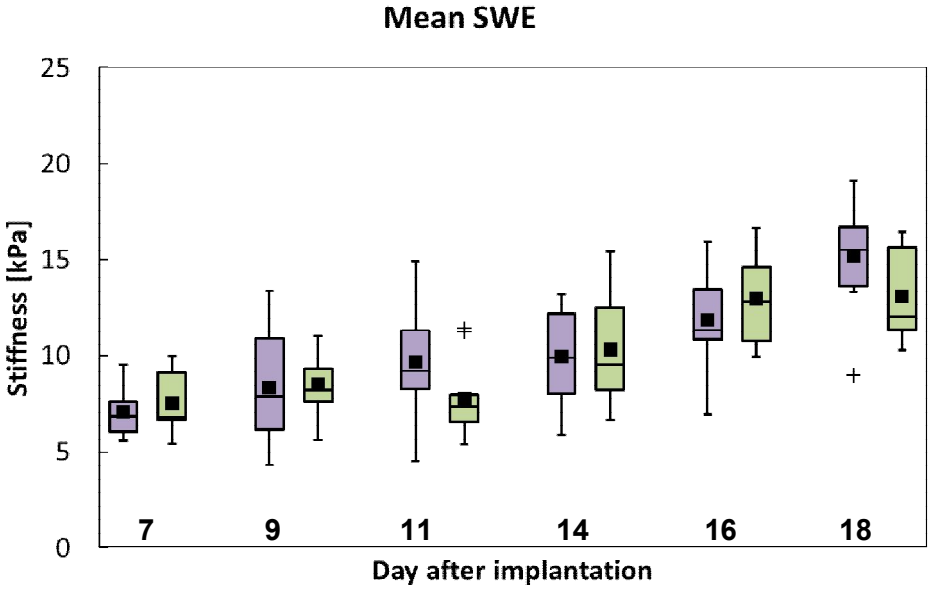

Fig 146 Stiffness of the tumor (in kPa) as a function of time. Pink = treated group. Green = Control group. Error bars = standard deviation of measurement. Each group contains ten mice.

V.3.1.7 Conclusion

This experimental campaign was the first to use a cooled plasma-jet device. The device was developed on isolated mouse during the previous experiment. It was found that the amount of damage to the skin decreased considerably. The following points emerge from this experiment

- The refrigeration system of the plasma sources is effective; there was less damage.
- The plasma treatments done with the refrigerated-multijet have strictly no observable effect on tumor growth. Even measurements taken with ultrasound showed no difference between the untreated group and the group exposed to the plasma.
- The addition of an inhibitor of catalase, the hydroxylamine dissolved in the DMSO (10 %w) does not enable to obtain a slowdown of tumor growth. The catalase inhibitor is applied to the skin overlying the tumor for ten minutes.
- PAM injections (6 injections of 5 µL around the tumor, every two days) have no significant effect compared with untreated group.

V.3.2 TC-1 Treatment with refrigerated multi-channel jet

This experiment took place between February and March 2017. This work was done in collaboration with the team of François Lemoine, in the Centre d'Immunologie et des Maladies Infectieuses (CIMI) at the hospital of Pitié-Salpêtrière.

V.3.2.1 Power supply and plasma source

The power supply is the same as in the previous study. Plasma source was the multichannel plasma jet described in section II.1.6. The choice of processing parameters (peak to peak Voltage, height above the skin, Helium flow) follow the constraints described in the previous section (section 0).

V.3.2.2 Treatment schedule

A group of 30 Seven- to 8-week-old female C57BL/6 mice were purchased from Janvier (Le Genest Saint Isle,France) and kept under specific pathogen-free conditions at the UMS28 animal facility (UFR 969, Pitié-Salpêtrière). 5×10^4 TC1 cells were injected into the flank of each of the 30 mice. After seven days of growth, treatments began.

After seven days, only 25 mice had palpable and measurable tumors. The 25 mice were divided into three homogeneous groups in terms of tumor size. There were ten mice in the untreated group. The ten mice of the group “plasma 3 min” were exposed during 3 min. The treatments take place during three weeks[90]. The majority of mice in this group had eight treatments. One of the mice had only six treatments. Indeed, for ethical reasons, the state of the skin was not considered favorable for repeated treatment. The total treatment times of each animal and power measurement are described in the next section.

In addition to these two groups, the group “plasma 6 min” with five mice had treatments of increasing duration: first of 5 min and then of 6 min. These treatments started slightly

[90] Monday, Wednesday and Friday of each week

later than those of the group “plasma 3 min”. Consequently, the majority of mice in this group had only six treatments.

A mouse is sacrificed if the volume of the tumor exceeds 2000 mm^3 or if signs of pain are observed. Fig 147 summarizes the experiment schedule.

Table 10 Number of mice for each group of this experiment.

Name of group	Size of group
Untreated	10
Plasma 3 min	10
Plasma 6 min	5

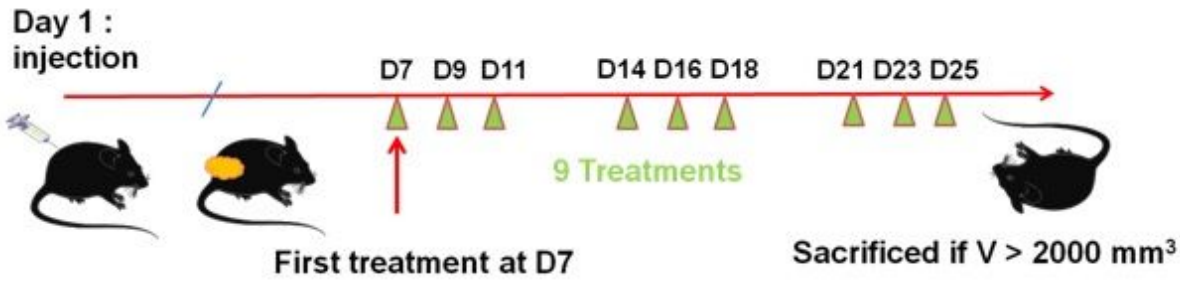

Fig 147 experimental Schedule. At day one, 50 000 cells had been injected into the flank of C57BL/6 mice. Tumors grew until day seven without treatment. At day seven, mice are divided into homogeneous groups in terms of tumor size. There were ten mice in the groups “plasma 3 min” and untreated. There were five mice in the group “plasma 6 min”. Treatments took place after day seven at two days intervals during three weeks. A mouse is sacrificed if the volume of the tumor exceeds 2000 mm^3.

V.3.2.3 Protocol applied to each mouse

First, the plasma source was cooled. The plastic tip shown in Chapter II was placed in a horizontal position and filled with liquid nitrogen. Due to evaporation, it was necessary to fill the tank with liquid nitrogen three times. It was refilled when there were less than 3 ml of liquid nitrogen. The cooling took about 10 min.

The general state of each mouse was checked. Particular attention was paid to the research of specific signs of pain and distress. The mouse was then anesthetized with 2 % (v/v) isoflurane in the medical air at 1 l/min. The temperature of the animal was maintained at 37 °C during anesthesia using a heated support (Minerve, Esternay, France). The hair of the mouse was shaved around the position of the tumor and those of ECG electrode. The ECG electrode (whitesensor, distrimed) was then fixed on the flank; a small amount of the conductive gel (uni’gel, distrimed) was put between the skin and the electrode to improve electrical contact.

Photos of the tumor were systematically taken before treatment. The size of the tumor was measured with a caliper. Tumor volume was approximated using the ellipsoid formula $V = \frac{\pi}{6} L \times W \times \min(L, W)$ where L was the length and W the width. It is an approximation of the volume of an ellipsoid, considering that the thickness of the tumor is of the order of magnitude of the width. A small amount of gel was spread on the surface of the tumor. The gel was removed with paper towels before treatment. The purpose was to treat a slightly moist skin in the hope that this could promote the formation of ROS.

The mouse was moved to a plastic anesthetic device to isolate the animal electrically. The ECG electrode was then connected to the measuring capacitor Cm. Liquid nitrogen was removed from the plasma sources and fixed in a vertical position. The generator was switched on, and the power consumption was measured in real time by the oscilloscope. The output of the jet was held about 3-4 mm from the skin. An infrared image of the skin was acquired (with camera testoo® 868, resolution of 0.1 °C) few seconds after the end of treatment.

The total anesthesia time was about 17 min for each mouse. This time is quite acceptable for their health, and no mice died because of anesthesia. The mouse was left to wake up on the hot plate. His state of health was checked a few minutes after his awakening.

The first treatments took place seven days after the injection of TC1. Mean value of tumor volume was around 14 mm^3 (Fig 148).

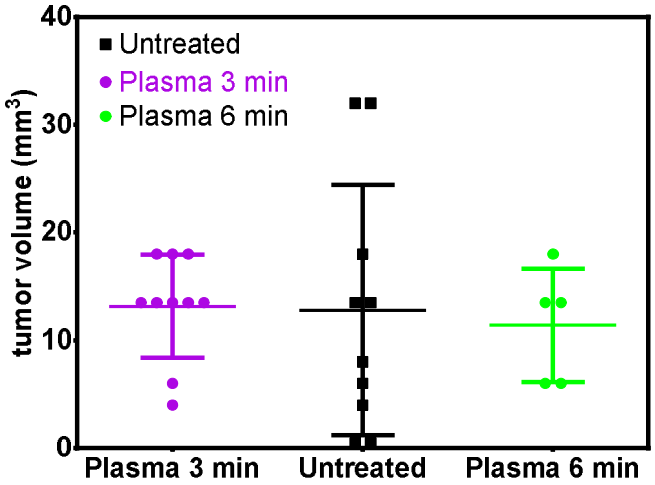

Fig 148 volume of the tumors in the three groups seven days after the injection of TC1. Mean volume is around 14 mm^3. Day seven is the first day of treatment. The groups are homogeneous.

V.3.2.4 Results of electrical diagnostics

The section below describes the results of the electrical measurements carried out on the mice. We use the same method in the previous section.

The power consumption is plotted in Fig 149. The left part of the graph shows that mean value of power is close to 4 W± 300 mW for each group. This uncertainty is much higher than the uncertainties which come from measurement method (under 40 mW). The dispersion comes purely from experimental conditions. The output of the jet is not exactly at the same distance from the skin from one treatment to another. Moreover, chemistry experiments from Chapter III show that distance is likely the main parameter that contributes to the dispersion of power. It can be seen that the power was very low during four treatments (below 2 W). This was due to the presence of moisture inside the plasma source[91]. When the plasma jet is cooled, water solidifies on its surface. After several thaws, water can contaminate the nozzle. A systematic drying of the nozzle was done after each treatment to prevent this problem.

[91] Our own experiments and the literature shown that water admixture reduces power.

The right part of the figure shows the mean value and standard deviation of power for each mouse during all the treatments. It is clear that there is no significant difference in power from one mouse to another. No mice were exposed to a discharge whose production required a very different power.

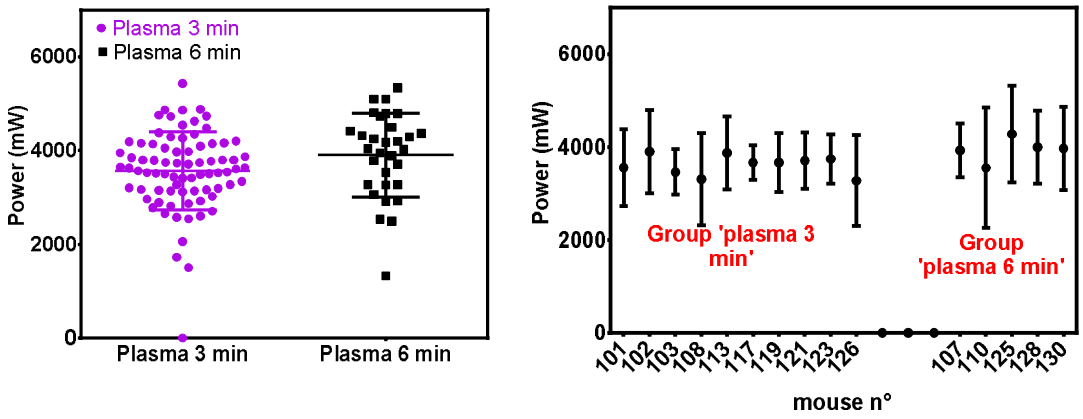

Fig 149 Left: power consumption of the device for each mouse and each treatment. Mean value of power is 3600mW in "plasma 3 min" group and 3900 mW "plasma 6 min" group. The power was very low during four treatments. This was due to the presence of moisture inside the plasma source. When the plasma jet is cooled, water solidifies on the surface. After several thaws, water can contaminate the nozzle. Precautions were taken subsequently to prevent this problem from recurring: systematic drying of the nozzle after treatment. Errors bars are the standard deviation of power. Right: power consumption for all treatments as a function of mouse ID. All treatments are equivalent in terms of power consumed; there is no major difference from one mouse to another despite the fact that the tumors have slightly different sizes and locations.

Treatment times are shown in the left of Fig 150. Mice from group "plasma 3 min" had only treatment of 3 min. In some cases, the discharge went off for a few seconds. In order to compensate, treatments were longer. That is why there is a small dispersion around 3 min. Fives mice of "plasma 6 min" had treatments of increasing duration: two treatments of five min and four of 6 min. At the right of this figure, energy consumption was plotted as a function of treatment time. As we have already noted, the energy consumed in 3 min is of the order of magnitude of the energy consumed by the single-channel jet in 30 min.

It is also observed that choosing fixed processing times is accompanied by a significant dispersion in the energy consumed. Chemistry experiments show that the energy consumed in plasma is a better parameter than time to account for the production of chemical species. Perhaps it would be appropriate to fix the energy consumed by each treatment, to increase the reproducibility of treatments? For that, it would, of course, be necessary that it is the chemistry produced by the plasma that is at the origin of anti-tumor effects.

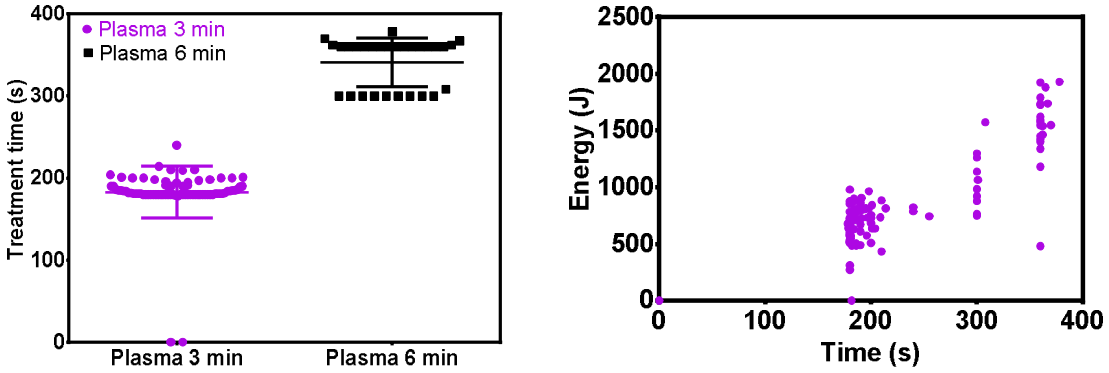

Fig 150 Left: treatment time for each mouse in the groups and for each treatment. In the group "plasma- 3 min, one mouse was not treated two times (pink dot at t= 0s). Mice of "plasma groups" were treated 5 min two times and then 6 min. Right: energy consumption of the multichannel plasma-jet for each treatment as a function of time.

The sum of the treatment times during the experimental campaign is plotted at the left of Fig 151. Each column is associated with one mouse. Mouse 117 had only six treatments of 3 min. The others had eight treatments of 3 min in the group "plasma 3 min". Mice 107 and 130 had one treatment more than the others. Mouse 130 survived a little longer; mouse 107 was treated two days before the others to check that the treatment was tolerable. The graph on the right represents the sum of energy consumption for all treatments. Mean value of total energy was 5500 J for "plasma 3 min group"and 8800 J for "plasma 6 min" group. These value should be compared with the order of magnitude, 2000 J, of energy consumption observed with the single-channel plasma jet when used for 30 min.

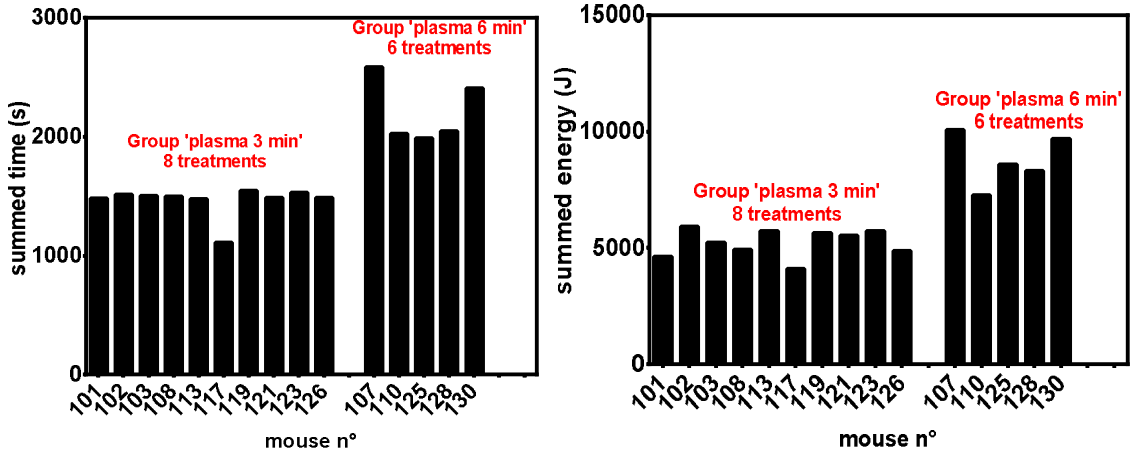

Fig 151 Left: the sum of the treatment time during the experimental campaign. Each column is associated with one mouse. Mouse 117 had only 6 treatments of 3 min. The others had 8 treatments of 3 min in the group "plasma 3 min". Mice 107 and 130 had one treatment more than the others. Mouse 130 survived a little longer; mouse 107 was treated two days before the others to check that the treatment was tolerable. Right: the sum of energy consumption of plasma source for all treatments. Mean value of total energy was 5500 J for "plasma 3 min group"and 8800 J for "plasma 6 min" group.

V.3.2.5 Skin temperature

During this experiment, the temperature of the skin was systematically measured few seconds (less than 5 s) after the end of treatment. At the end of the processing, the high-voltage generator was switched off, the mouse was quickly removed from the sources,

and an infrared image was taken. Infrared images were acquired with an infrared camera testoo® 868 (thermal resolution of 0.1 °C).

Some infrared images were taken from the mouse during treatment. These images, however, were taken at grazing incidence, and from far enough (due to high voltage). Consequently, it is conceivable that this could cause errors. Nevertheless, it was found that the temperature measured before the plasma generator was stopped and after the mouse had been removed (less than 5 s) were almost the same. It seems that the skin did not cool significantly in 5 s.

Fig 152 shows infrared images of mice under anesthesia or not. Under anesthesia, skin temperature decrease and reach a value of between 28 °C and 30 °C. This drop comes from the slowing of metabolism due to anesthesia.

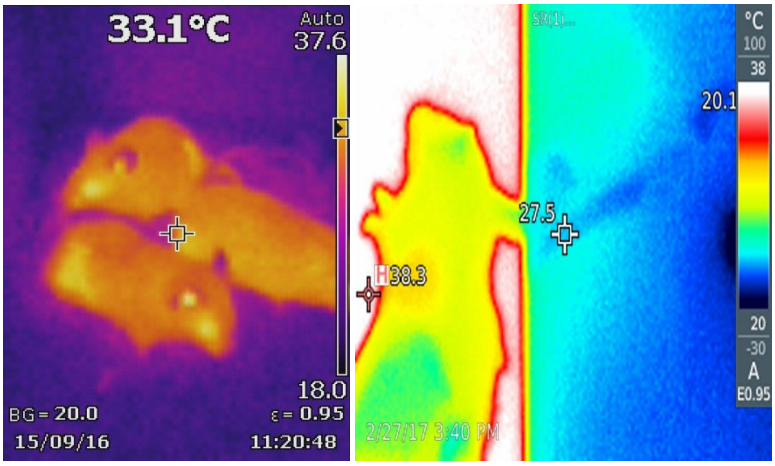

Fig 152 Left: the infrared image of mice. The temperature of the skin was just below 37 °C. Right: infrared picture of a mouse under anesthesia. The animal was placed on a heating plate. The mean temperature of the skin was around 25 °C. The metabolism of the mouse slows down during anesthesia and causes this drop.

The kind of images acquired with the infrared camera is shown in Fig 153. These pictures were taken only 5 seconds after the end of treatment. The images of the center (B and C) were taken after one treatment of 3 min. The blue zone, colder than the rest of the body, represents the upper part of the tumor exposed to the flows of cooled helium. Picture D was acquired after one treatment of 6 min. The tumor was slightly heated compared to the rest of the body. Tumor temperature is around 34 °C, thus below the threshold of thermal damage.

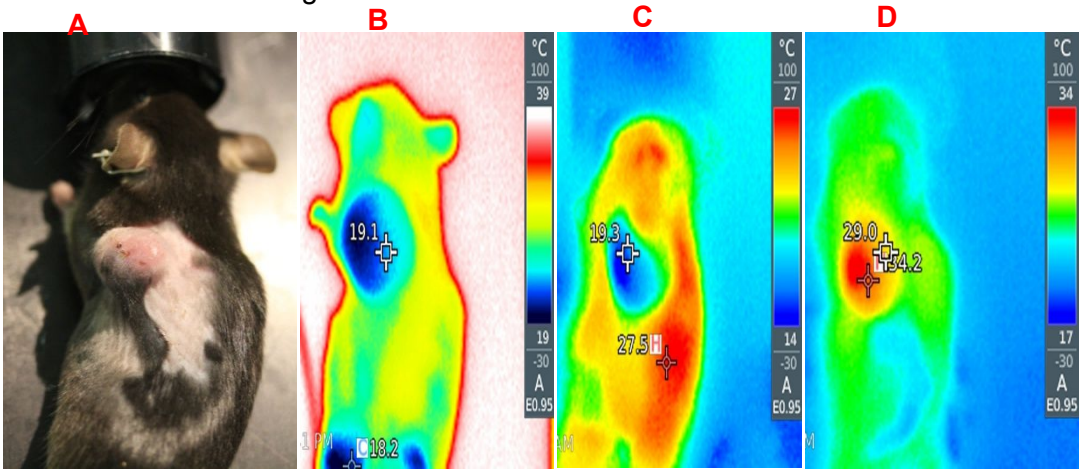

Fig 153 part A : picture of the mouse sleeping on the heating plate. part B: infrared picture of the mouse on the heating plate (at 39 °C) after a treatment of 3 min with the refrigerated plasma jet. The

area exposed to the device is colder than the rest of the body. The temperature on the top of the tumor is around 19 °C. Part C: another mouse exposed during three minutes. The photo was taken while the mouse was still on the plastic anesthesia device (non-heating). This explains why the background temperature is around 14 °C. For this mouse also the temperature of the treated zone is of the order of 19 ° C. Part D: This mouse was treated during six minutes. In this case, the temperature of the tumor is higher than the temperature of the body. The maximum temperature of the tumor is 34 ° C. This average temperature should exclude the onset of thermal damage.

The infrared camera enables to obtain the maximum temperature at the position of the tumor and at the end of treatment. This value is plotted as a function of groups and energy in Fig 154. It appears that mean temperature was respectively 17± 7 °C and 32 ± 6°C after 3 and 6 min of treatment. This proves that the cooling system is efficient, and has avoided the hyperthermia in the majority of cases. Only one treatment gave a final skin temperature of 43 °C. Only two treatments gave temperature between 39°C and 42°C (mild hyperthermia). It should also be noted that these temperatures were reached at the end of treatments, so the time spent above the limits was probably short. The pictures of the skin associated will be described just below.

The temperature is higher after 6 min because the device does not contain liquid nitrogen during processing (which could cause excessive cooling), so the plasma source heats up during processing. Consequently, helium coming out of the nozzle becomes less and less cold. In addition, infrared pictures show that the temperature of the heated area at the beginning of the treatment had a mean value of 10°C. This should avoid the overcome of frostbite.

The dispersion of the results on skin temperature could be explained by the fact that many factors play in the thermal transfer of helium and plasma to the surface of the skin. And that some of these parameters are difficult to control. Distance to the nozzle of the jet is probably a key parameter.

The shape of the tumor, which could modify the gas flows and thus the heat exchanges, has a significant effect. The nature of the gas flow: turbulent or not is probably very important.

The surface condition of the tumor should modify heat exchange coefficient and conduction of the heat (what if there is a crust or holes in the skin?). The blood perfusion[92] of the tumor itself should modify the ability of the tumor to exchange heat, and it could be different from one tumor to another.

Furthermore, heating depends on how the filamentary discharges spread over the surface. It should be mentioned that the mechanism at the origin of thermal transfer is not well known during the plasma-skin interaction.

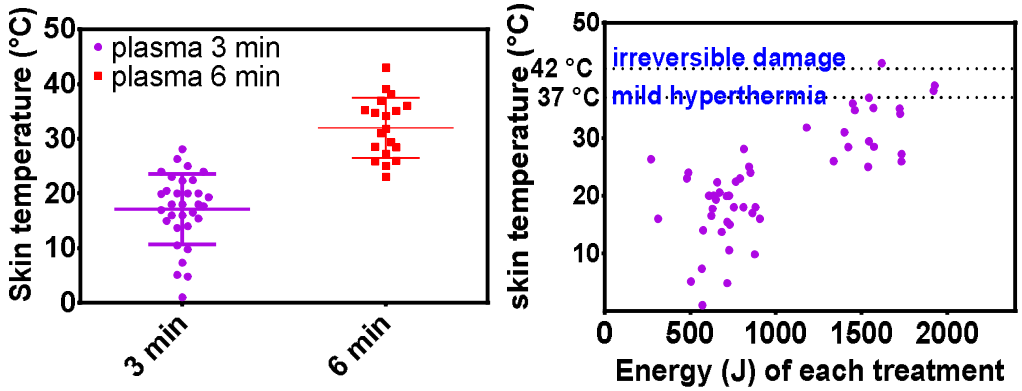

[92] About blood perfusion, see Chapter VI, section VI.1.5.3, page 189

Fig 154 Skin temperature was measured from the data acquired with an infrared camera (less than 5 s after treatment). The maximum temperature of the treated area was read on the acquired images. This value was plotted as a function of groups (Left) and energy consumption during the treatment (right). The dispersion of the results is quite important. This is due to the fact that the cooling undergone by the biological tissue depends on many parameters among which: distance to the nozzle of the jet, shape of the tumor (Is the tumor aerodynamic or not?), surface condition of the tumor (is there any crust?) and how the filamentary discharges spread over the surface during processing. The threshold of mild hyperthermia and irreversible damage are represented by dotted lines. All available data are represented on both graphs. Only one treatment gave a final skin temperature of 43 ° C. Only two treatments gave temperature between 39°C and 42 °C

The skin condition was monitored during the experiment. Each day of treatment, notes are taken on the condition of the skin: depth and condition of the lesions if any. A photo of the tumor was taken before each treatment.

Table 11 presents the skin of three mice at seven, nine and eleven days after injection. This corresponds to the first, second and third treatment of each mouse. These mice were representative of the whole "plasma-3 min" group.

As in the previous experiment[93] the damage are considerably limited compared to the treatments done without cooling. After three treatments of three minutes, most of the tumors presented a few crusts of very small sizes (~ 1-3 mm²) and of low thickness (estimated below 200 µm). This level of damage is acceptable from the ethical point of view and corresponds to the specifications that would be achieved by a treatment applied to humans. With these processing times, and for equivalent plasma powers, the level of damage appears to be less than that of the previous experiment: either because this mouse line is less sensitive or because the refrigeration procedure is better controlled.

Table 12 summarizes treatments conditions of these three mice. There is no obvious link between the occurrence of damage and the power applied or the energy consumed.

Table 11 Pictures of treated area as a function of time for 3 mice of "plasma 3 min" group. Pictures were taken before each treatment (blue marks allowed to target the tumor). No differences were visible between a picture taken before treatment and 1 hour after. Treatments begin at day 7. Since the effects of one treatment are not visible instantaneously (A) at day seven, the skin without treatment was observed, (B) at day 9, the effect of treatment of day seven can be seen. (C) At day eleven, the sum of the effect of day seven and nine was observed. These three mice were chosen because the condition of their skin is representative of that of the other seven mice of the group. Regarding mouse 123 at day seven, the short red line was probably a scratch or a bite of another mouse. At day 9 very small crusts (~ 1 mm²) were found in mice 123 and 121: brown and black areas at the top of the tumor. These areas are wider on the mouse n°108: length~2-3 mm width~1 mm. These small crusts had a very low thickness (<200 µm). At day 11, the appearance of the crusts had not changed fundamentally but had slightly expanded.

	Mouse n°123	Mouse n°121	Mouse n°108
Day 7	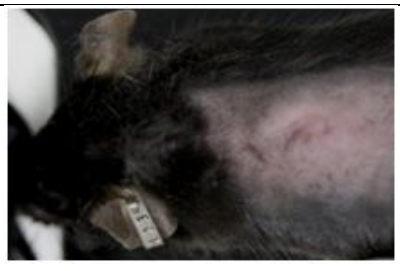		

[93] regarding the treatment of BALB/C mice bearing CT-26 tumor (sectionV.3.1 page 149)

Day 9			
Day 11			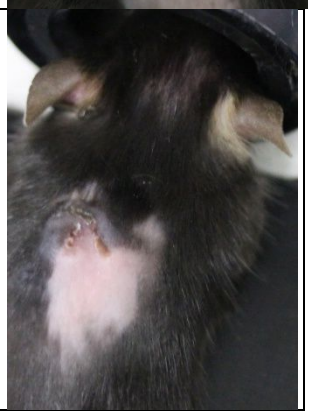

Table 12 Summary of processing conditions. Peak to peak voltage was not exactly the same from one treatment to another (max difference in the order of 1 kV). The voltage is difficult to reproduce from one treatment to the other because the primary winding heats up during the experiment, which tends to decrease the output voltage. No obvious link appears between deposited energy or power and extension of damage. Damage has a very limited extent quite similar in all mice in the group (at least for the first week of treatment).

He flow = 2600 sscm	Mouse n°123	Mouse n°121	Mouse n°108
Day 7	Vpp=13.7 kV Power=4.30 W Energy=790 J	Vpp=13.2 kV Power=3.3 W Energy=589 J	Vpp=14.4 kV Power=4.27 W Energy=777 J
Day 9	Vpp= 14.1 kV Power=3.5 W Energy= 734 J	Vpp=13.5 kV Power=2.7 W Energy=485 J	Vpp=13.3 kV Power=2.10 W Energy=432 J
Day 11	Vpp=13.2 kV Power=2.82 W Energy= 507 J	Vpp=13.8 kV Power=3.75 W Energy=675 J	Vpp=14.5 kV Power=3.80 W Energy=684 J

As reported in the previous paragraph: only three treatments gave temperature between 39°C and 43 °C. It is interesting to observe the skin condition of these mice before and after treatment. This is a way to assess the sensitivity of the skin to hyperthermia. Photos of tumors were grouped in Table 13. The mouse subjected to the highest hyperthermia (43 ° C, Mouse n°128) had a fairly extensive crust ($4\,mm \times 3\,mm$). For the other two mice, damages were distributed over a larger surface but are more superficial. Again, electrical diagnostic (power and energy) did not predict hyperthermia and the occurrence of damage. For example, the greater power used does not lead to greater temperature and damage. It appears that the damage observed on these skins after two days is more important than those of the other mice of the group.

To conclude, this refrigeration system seems efficient to avoid the damages. It would be useful to generalize this system to other plasmas sources to extend their conditions of use and optimize the production of chemicals species without thermal damages. The Table 14 recalled the damages obtain after 5 min of treatment without refrigeration.

Of course, the changes that these refrigeration systems induce on the chemical production of plasma should be studied. We know from semi-quantitative experiments that the production of hydrogen peroxide and nitrite had the same order of magnitude with or without refrigeration. In any case, the approach which consists in the separation of the thermal effects from the chemical effects seems useful for *in-vivo* experiments.

Table 13 The first column describes the parameter of the treatment leading to mild hyperthermia at the position of the tumor and after treatment of 6 min. The second column contains the infrared images that allowed to observe the hyperthermia. The third column contains the photos of the tumors taken the same day. The fourth column contains a photo of the tumor two days later. A clearly defined crust appears on the skin of the mouse subjected to the highest hyperthermia (43 ° C). For the other two mice, damages seem distributed over a larger surface but are more superficial

	Infrared image and this picture were taken the same day		two days after the previous column
Mouse n°128 at Day 18 Time = 6 min Vpp =14.5 kV Power= 4.5 W Energy = 1620 J Tmax= 43 °C	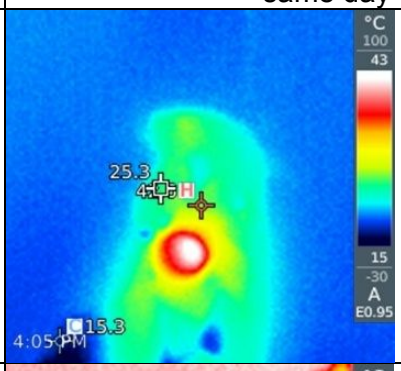		
Mouse n° 125 at day 16 Time= 6 min Vpp = 15.4 kV Power=5.34 W Energy=1922 J Tmax= 38.2 °C	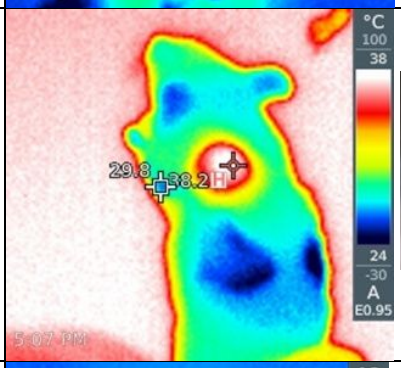		
Mouse n°110 At day 223 Time =6 min Vpp=15 kV Power= 5.1 W Energy=1930 J Tmax=39.1 °C	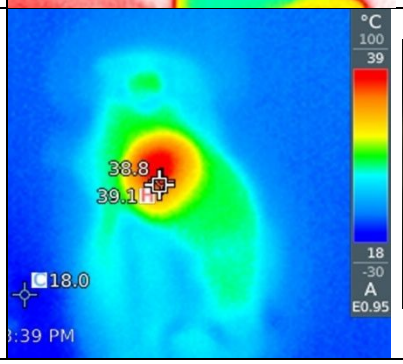		

Table 14 Very serious damage after one treatment of 5 min, without refrigeration. Right, the second or third-degree burn of 7 mm diameter observed two days after one treatment of five min.

5 min, Vpp = 14.5 kV Power = 2160 ± 10 mW E = 647 ±3 J	 **Just after treatment**	 **Two days after**

V.3.2.6 Effect of cooled multi-channel jet , tumor volume

This section describes the observations made on the tumors during the last two weeks of treatment. In some of the treated mice, large size holes occurred in the tumors. These holes have developed from what appears to be surface necrosis. This kind of necrosis occurs naturally for this type of tumor as shown in Fig 155, left (this mouse was in the untreated group). Conversely, some of the mice of the treated groups have the skin of the tumor relatively intact with very few lesions at the end of the protocol (Fig 155, right).

Fig 155 Left: mouse from the untreated group which develops a bleeding open wound 18 days after the injection of TC1 cells. Surface necrosis occurs naturally with this tumor model. It was necessary to kill this mouse (Mouse n°127). Right: tumor of one of the mouse n°113 of "plasma 3 min group" at day 25, last day of treatment.

It appears, however, that treatment of three or six min causes the formation of hollows much deeper and wider, than those observed in the untreated group. Table 15 merge photos of the skin of the tumor taken each day of treatment during the last two weeks of treatment (between day 14 and day 25). At days 14 16 and 18, there was probably the growth of a necrotic and weakened area below the crust. From day 25, the hollow itself was appearing. The following days, the hollow continues to spread, but the tumor growths rapidly and tends to bend the cavity.

Table 15 Monitoring of the formation of holes in the mouse tumor 130 ("plasma 6 min" group)

20/02- Day 14	22/02-Day 16
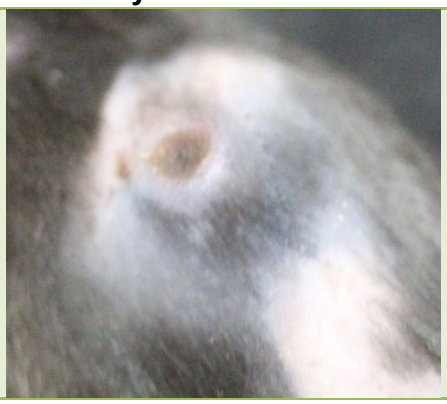	
24/02- Day 18	**27//02 Day 21**
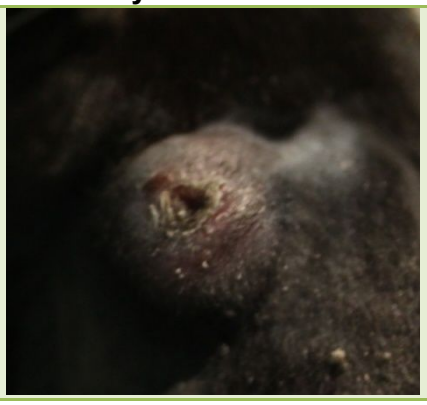	
01/03-Day 23	**03/03 – Day 25**
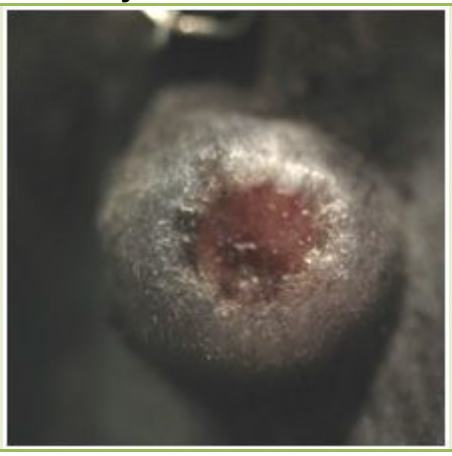	

The size of the tumor was measured with a caliper. Tumor volume was approximated using the formula $V = \frac{\pi}{6} L \times W \times \min(L, W)$ where L was the length and W the width. It is an approximation of the volume of an ellipsoid, considering that the thickness of the tumor is of the order of magnitude of the width. These measurements, however, do not take into account the formation of hollows in the tumor, since the hypothesis is that the tumor is an ellipsoid. According to this formula, tumor volume was plotted as a function of time on Fig 156 for each group. Error bars were the standard deviation of the set. Once again, the results of the groups show no statistically significant differences between them.

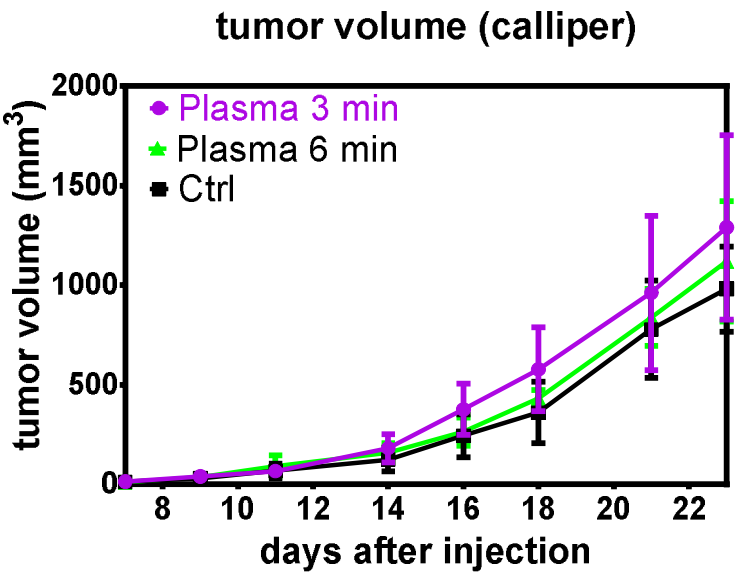

Fig 156 Volume of TC1 tumor as a function of time. There was no significant difference between the different experimental groups. Methods of measurement, however, did not take into account the holes created in some tumor.

What if the volume of hollow was taken into account?

The size of the hollow was likely between 6 and 8 mm of diameter, with the assumption of spherical holes, the volume of these was between 110 and 190 mm^3. Even in this case, error bars are large enough to exclude the eventuality of an anti-tumoral effect. Table 16 summarizes the results for each mouse at day 22.

Table 16 Summary of the state of the tumor TC1 and the skin located above at day 22. The first 10 mice are in the group "plasma 3 min". The last five are in the group "plasma-6 min". Only two mice of the untreated group develop surface necrosis: one was sacrificed. Regarding the second, the hole induce was small (around 4 mm in diameter). "NO" means, there were no holes in the tumor. "N0 + no damage" means that there were no holes and no (or very small) scar and crust. "YES" means that there was a big hollow that cannot be explained by the usable surface necrosis.

"plasma 3 min"	**Mouse n° 119**	**117**	**121**	**123**	**103**
	NO	YES	YES + crust	YES	YES (small)
	Mouse n° 101	113	126	102	108
	NO	NO + no damage	NO + no damage	YES	NO +No damages
"Plasma 6 min"	Tox n°107	Tox 128	Tox 110	Tox 125	Tox 130
	NO + no damages	YES (small)	NO	YES (small)	YES

V.4 Conclusion

The objective of this chapter was to develop protocol of plasma treatment. We have evaluated:

i. The anti-tumor effects
ii. Skin damages

During the five experimental campaigns, the device and the protocol have evolved towards powerful device. The experiments were performed on two types of tumors that have never been treated with plasma: TC-1 and CT-26 tumors. The experiments were carried out with two DBD devices, the single-channel plasma jet and multi-channel jet devices (refrigerated or not). The efficacy of PAM has also been tested *in-vivo.* It has also been attempted to expose the skin to catalase inhibitor, to see if it is possible, thereby increasing the efficiency of plasma treatments. The processing conditions (power, source type, the probable concentration of PAMs, range of energy) are summarized in the table below.

Device/protocol	*In-vivo* target	Power	Range of energy/ H_2O_2
Glass DBD/500 Hz	CT-26, flank	~75-100 mW	100 & 300 J/cm²
DBD/500 Hz	TC-1, cheek	~ 140 mW	400 J
Single-channel jet/500 Hz	TC-1, cheek	~ 400 mW	500-800 J
PAM injection	TC-1, cheek		$0.6\ \mu mol$
Multichannel plasma jet/ 10 kHz	TC-1, cheek & flank	1000-1500 mW	180-3000 J
Refrigerated multichannel plasma jet/ 10 kHz	CT-26 flank	~ 4000 mW	~800 J
Refrigerated multichannel plasma jet/ 10 kHz + an inhibitor of catalase (hydroxylamine in DMSO)	CT-26 flank	~ 4000 mW	~800 J
PAM injection	CT-26 flank		~1-2 µmol
Refrigerated multichannel plasma jet/ 10 kHz	TC-1, flank	~ 4000 mW	800-1600 J

These experiments highlight negative results of our tissue-tolerable plasmas sources. These results, although negative, are useful. For example, it is reasonable to think that an experimenter wishing to treat these tumors should use a source producing different chemistry from those produced by our device. For this reason, the results presented in Chapter IV could guide his choice. It could also be tempted to remove the skin before the treatment of a subcutaneous tumor (for example, with a micro-punch. Since the skin is an anti-oxidant barrier, we can hope for better results. Although showing no anti-tumor effect, the last experiment with the refrigerated multijet showed that the plasma treatment promotes the extension of pre-existing surface necrosis.

The only positive results (up to tumoral ablation) were obtained with sources causing a heating of the skin (final temperature between 45 and 48 °C). This tumor ablation result most probably from thermal burn: since the refrigerated devices produce less damages and are close in terms of chemical production. It turns out also that the measure of the temperature of biological tissue is not necessarily something obvious. In particular, the question of the spatial resolution of the diagnostic is a crucial point which can lead to biases.

The experimental observations related to the link between heating due to plasma-treatment and damages are summarized by the following points:

- Skin temperature after treatment of 3 or 5 min was around 45-48 °C.
- Treatment of one min gave no damages.

- One treatment of three min gave no damages, but the repetition of this treatment at two days intervals gave damages after two or three treatments.

Treatment of 5 min systematically gave damages.

The following chapter is dedicated to these methodological questions. It addresses the issues related to hyperthermia and it's biological effects, the simulation of heat-propagation through tissue.

Chapter VI Modelling and simulation of the thermal aspects of plasma-tissue interaction

The primary objectives of this chapter are

- The development of a model of the thermal properties of mouse skin and tumors. The model should describe (a) the propagation of heat by conduction (b) heat exchange by convection and radiation with the external environment (c) heat exchange with the blood flow. Finally, the model should provide a quantitative approach of the thermal damages affecting the tissues and blood vessels.
- The implementation of this model in a simulation using the finite element method. The results given by the simulation should be consistent with all the experimental observations. This includes temperature measurements on the surface of the tumor and all qualitative observations regarding the state of the skin after one or several treatments. For example, the simulation should reproduce the kinetics of heating and cooling of the tumor.
- There is no guarantee that each mouse has exactly the same thermal properties or even that they are precisely known during the experiment. It is necessary to know in what extent the simulated damage (represented by the field $\boldsymbol{\Omega}(\vec{\boldsymbol{r}})$) evolve when the treatment or the thermal properties of the biological tissue are changed. For example, what happens if the rate of blood perfusion of the tumor, the thermal conductivity, the parameters which defined $\boldsymbol{\Omega}$ or the area of plasma-skin interface are changed? The scientific literature indicates in which intervals these parameters vary. Fortunately, this problem is constrained by temperature measurements. The precise question is “In what extent are the damage different? **knowing that** this simulation correctly predicts the temperature field.
- The simulations should cover a wide range of cases of practical interest:
    - Non-refrigerated multijet, refrigerated multijet, single-jet (our own devices).
    - What information can be obtained from simulations on the accuracy of measurement methods? What is the required spatial resolution of measurement methods?
    - What happens if the skin is covered with a gel or is slightly moist? How to model the mass transfer of water?
    - What happens when a short treatment (~few s) that induces heating of the tissue is repeated?
- Propose a critical approach of the scientific literature regarding *in-vivo* plasma-cancer studies.

VI.1 describes the different biological effects of hyperthermia and the content of the model. Finally, its numerical implementation is described. There is particular emphasis on the biological effects that can be induced by moderate hyperthermia (T ~ 39-44 ° C). The effects of hyperthermia are not purely local. The following table summarizes what moderate hyperthermia can induce at the level of an organism or tissue.

VI.2 gives the results of the simulations obtained in various experimental configurations (not only our experiments but also those of T. Freeman's group). The measurement methods and the pitfalls that can lead to underestimation of temperature are presented in VI.2.6. The accuracy that can be expected from measurements made with thermometer-gun, infrared cameras, and invasive devices are modeled and discussed in the context of plasma medicine.

The section VI.3 is a critical approach of *in-vivo* plasma-medicine experiments. We proceed to a new reading of the published *in-vivo* experiments which regards the treatment of B16 melanoma. For each paper, there are two simple questions:

- Does the published information really exclude the possibility that tissues have been subjected to hyperthermia, depending on the measurement method used?
- In what extent the results obtained could be attributed to hyperthermia?

The question of the reliability of measurement methods used in the papers is addressed by the section VI.2.6. The principles that guided the construction of this critical approach are listed below:

The calculations were done with Freefem++, a software developed by Frederic Hecht and his team at UPMC [205]. Visualization is done with Matlab®. The code that represents the physical content of the simulation in Freefem++ is in Appendix I. The code of visualization is in Appendix J.

VI.1 What is hyperthermia? How to model and simulate it?

Several groups produced works related to the quantification of thermal damage since the end of the forties [206]. The objective of these studies was to predict the lesions that appear on the skin depending on the temperature exposure. Quantifying the biological effects of heat is also essential for treatments that explicitly involve hyperthermia. In oncology, heat can be used to destroy tumors. This heat can be produced by focusing microwaves, ultrasound or laser. In some cases, the heat applied is so intense that it makes it possible to carry out the instantaneous ablation of the treated zone. For most treatments, the heat produced induces tissue necrosis and not their vaporization. This necrosis occurs several hours after treatment. Cells may die directly from heat because excessive temperature causes the denaturation of vital proteins. They can also die because they are in a hypoxic environment. Indeed, blood vessels are very sensitive to the damages induced by heat. For example, coagulation occurs at 60°C, and small capillaries are sensitive to lower temperature. The destruction of blood network bringing oxygen and nutrients to the cells induce ischemia and lead to strong hypoxia. It must be noticed that hypoxic environment is not systematically associated with anti-tumor effect. Hypoxic environment can leads to the selection of the more aggressive cells clones among the different population of cells in competition.

Heat exposure has less destructive applications in the field of dermatology: laser-heating can be used for the remodeling of tissue [207]. Fortunately, the literature concerning the simulation of thermal damage is rather extensive, since reliable models were needed to optimize the applications in the field of health.

Most papers modeling thermal damage consider human skin. It appears that human skin and mouse skin are significantly different. Since mouse skin is thinner, it is easier to elicit hyperthermia and second-or third-degree burns in mice than in humans. The first section of this chapter is a comparison of the structure of human and mouse skin.The second enables to precise the ideas regarding thermal diffusion, the threshold of hyperthermia. The discussion is conducted with calculations of orders of magnitude. The third describes how to quantify and predict thermal damage. The fourth paragraph describes the physical content of the simulation: what are the physical phenomena to be taken into account and how to model them. The fifth section gives the numerical values which

define the model used in most of the simulations. The sixth briefly describes the implementation of the finite element method. How to choose spatial and temporal resolution, what are the boundary conditions?

VI.1.1 Human and mouse skin structure

This section is a quick overview of the structure of the skin. For the sake of brevity, the main components are only mentioned. This discussion does not address the biological properties and functions of the skin and how these could be affected by plasma. The antioxidant functions of the skin in humans and mice were quickly discussed at the end of Chapter III. This point indeed requires further discussion. It would be interesting that a biologist leads this kind of discussion. Since the composition of the skin, for example, the kind of immune cell and so the type of immune response triggered, should be very different in mice and humans [208]. Similarly, the mechanisms of wound healing are considerably different for mice and humans [209].

The structure of skin consists of three main layers: epidermis, dermis, and subcutaneous tissue (Fig 157). The thickness of layers depends on the localization of the skin on the body [210]. For instance, the skin of the foot is thicker.

The stratum corneum (20 µm- 40 µm of thickness) is the most out layer of the epidermis (75 µm- 150 µm of thickness). Stratum corneum is made of dead cells, which is an impermeable barrier between environment and organism. The epidermis is nonvascularized and stratified. The most frequent cells are keratinocytes. In the epidermis, the non-keratinocytes cells that can be found are melanocytes (pigment forming), Langerhans cells (immunological functions) and Merkel cells, which are involved in the immune response.

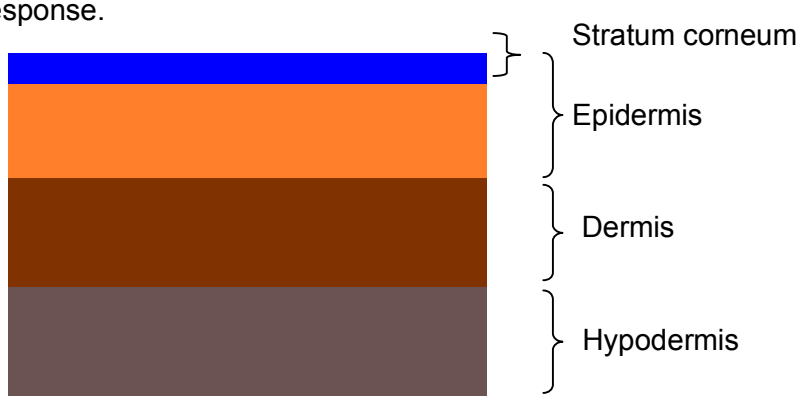

Fig 157 simplified structure of human skin. The thickness of different layers: Stratum corneum (from 10 µm to 40 µm), epidermis (from 75 µm to 150 µm), dermis (from 1 mm to 4 mm), hypodermis.

The dermis is much thicker (1~4 mm for humans) than the epidermis and is mainly composed of two fibrin proteins: collagen and elastin. Blood vessels, nerves, and lymph vessels are included in the dermis. Hair follicles, sebaceous and sweat glands are held together by collagen.

Collagen is a rather stiff and hard protein which is a major constituent of the extracellular matrix of connective tissue and provides structural strength in soft tissues. In the dermis, collagen is the major constituent and accounts for approximately 60%~80% of dry weight of fat-free skin and 18%~30% of the volume of the dermis [210]. This molecule also serves to quantify the thermal damage (see section VI.1.4).

The ground substance contributes to 20% of the dry weight of skin and to 70%~90% of the skin's volume. This is a gel-like substance, which contains proteins like

glycoproteins, proteoglycans and glycosaminoglycans and hyaluronic acid [210]. The hyaluronic acid chain has proteoglycans side-chain, which are cross-linked by glycoproteins to others structures such as collagen or elastin fibrils.

The third layer is the hypodermis is mainly composed of fat. This layer is made of fatty connective tissue and has thermal insulation functions. The fatty tissues have a lower thermal conductivity than the rest of the tissues. This layer carries major blood vessels (and nerves) to the overlying skin.

The thickness of mouse skin is described in [162]. Fig 158 compares the thickness of the four layers separated by strains and gender. This study aimed to prove that gender of mice is a major factor for biophotonics experiments. The value of the left column ('gray') is particularly useful because this species (C57BL/6 - female) was used for each experiment involving TC1-cancer cells. It appears that the thickness of stratum corneum is close to 20 µm. The dermis is thinner (180 µm) in mice than in humans. Therefore, thermal damage reaches the deeper layers of the skin faster in the mice than in humans. Moreover, the spread of chemical species produced by plasma at the surface through the skin could be less effective in humans than in mice.

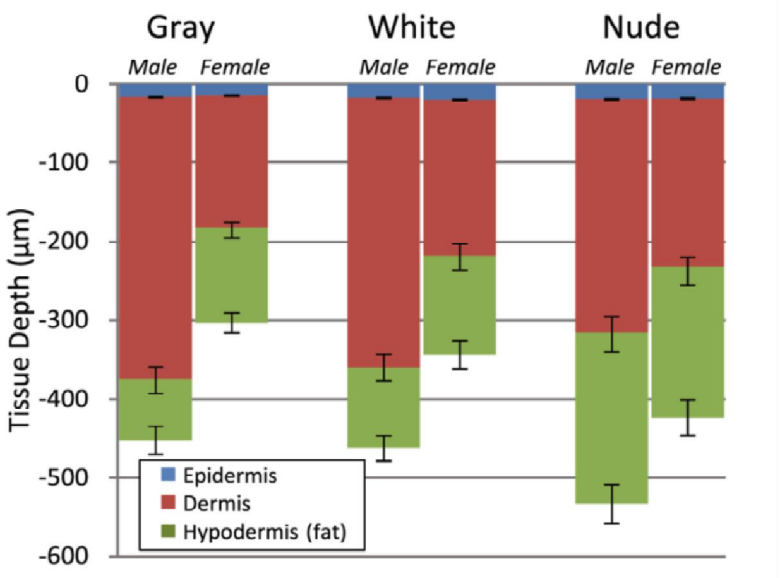

Fig 158 Averaged values of the epidermis, dermis, and hypodermis thicknesses as measured by histology, separated by strain and gender. Gray refers to C57Bl/6 mice, and White refers to CD-1 mice. Variation in the thickness of the dermis is the most significant difference between genders. Error bars correspond to the standard error of the mean. Figure and legend are from [162]

Table 17 Mean and SEM values of the thickness of epidermis, dermis, adipose tissue and muscle layer quantified by histology in [211]

	BALB/c		C57BL/6	
	Female	Male	Female	Male
Epidermis	12.08 ± 3.14	10.19 ± 3.29	13.08 ± 3.50	12.53 ± 3.97
Dermis	156.65 ± 55.23	343.44 ± 100.09	162.02 ± 15.12	226.33 ± 36.86
Adipose tissue	168.01 ± 52.31	40.17 ± 9.65	189.37 ± 64.14	103.05 ± 61.24
Muscle	91.68 ± 21.95	90.47 ± 51.96	83.34 ± 27.14	90.53 ± 18.23

The difference in thickness and in the nature of the biological response (e.g., wound healing or immune response) should be an issue. For example, the cicatrization of

mouse skin does not take place exactly in the same way in mice as in humans or pigs [209].

The layers of the skin are used to assess the severity of damage to the skin. Burns are classified as first, second, third degree based on the extent of damage to the different layers of skin. The degrees of skin burns are described by Parsons [212], as shown in Table 18.

Table 18 Classification of burns according to [212]

Burn degree		Description
First degree	Partial thickness skin destruction	Characterized by redness in the burned region. Discomfort is temporary, and healing is rather quick, with no permanent damage.
Second degree		Also referred to as partial thickness burns. The epidermal layer is damaged, and injury extends into the dermal layer as well. There is damage to sweat glands and hair follicles. Blisters, severe pain, reddening, and swelling characterize these burns.
Third degree	Whole thickness skin destruction	Burns destroy all the epidermal and dermal layers. There is tissue damage below the hair follicles and sweat glands into the subcutaneous tissue. The burned area will appear charred or dry, white color. There is no possibility for spontaneous healing, so skin grafting is required.

VI.1.2 Orders of magnitude related to hyperthermia

This section aims to present the framework of the simulations using the orders of magnitude.

VI.1.2.1 Space and time scales of thermal diffusion

First, the numerical values of the characteristic times of thermal diffusion τ_D are calculated.

Thermal properties of the skin for human, pig, and rabbits are described in [213]. The specific heat is very close for all of these species. It is assumed, for this calculation, that the tissue has a specific heat $C_p = 3600\, J.kg^{-1}.K^{-1})$. The thermal conductivity is $\lambda = 0.235\ \mathrm{W.m^{-1}.K^{-1}}$ which corresponds to the conductivity of the epidermis. The density is assumed to be $\rho = 1500\, kg.m^{-3}$.

The thermal diffusivity is then

$$\alpha = \frac{\lambda}{\rho C_p} = \frac{0.235}{1500 * 3600} \cong 4.4 \times 10^{-8} m^2.s^{-1}$$

The characteristic time of diffusion τ_D on the scale L_D is $\tau_D(L_D) = L_D^2/\alpha$

Consequently, the time of diffusion through a thickness of the order of magnitude of the size of a cell is:

$$\tau_D(L_D = 20\ \mu m) \cong 9.1\ ms$$

Regarding the time of diffusion through a layer with a characteristic size of the order of skin thickness~ $300\ \mu m\ (mouse)$:

$$\tau_D(L_D = 300\ \mu m) \cong 2.1\ s$$

It is recalled that the power supplies have a frequency of 500 Hz and 10 KHz. So, with the assumption of one discharge per half-period, we obtain the characteristic times of $\tau_{rep}(500\ Hz) = 1\ ms$ and $\tau_{rep}(10kHz) = 0.05\ ms$.

This means that thermal diffusion is a slow phenomenon, compared to the characteristic time scale of discharges frequency. Consequently, 9 and 182 discharges had time to occur, before the heat had the time to diffuse of the thickness of a single cell. Thus, in the simulation, the heat transfer due to the plasma-skin interaction of many filaments striking the skin is correctly modeled by a continuous function of time and space.

It is now assumed that the discharges are evenly distributed over a surface S depending on the distance output-skin. Closes to the surface, the discharges spread over $S_1 = 1\ cm^2$. Far from the surface, the discharges form a single filament strinking an area $S_2 = 10^{-2}\ cm^2$. It is assumed that $100\ \mu m \times 100\ \mu m$ is the order of magnitude of the plasma-skin interfaciale area for a single filament. In fact, this area is likely larger, and it seems obvious that filaments are not distributed evenly. The number of electrical discharges striking the same spot during the characteristic times of diffusion is summarized in Table 19. This enables to understand that the most dangerous is obtain with the power supply at 10 kHz and $S_2 = 10^{-2}\ cm^2$. A quasi-instantaneous carbonization of the skin was observed on very small spots (even when the source was refrigerated). The input of thermal energy is so high that the thermal diffusion does not have the time to act effectively before the damage occurs. In all other experimental situations, no damage was observed, instantaneously after treatment. On the contrary, thermal diffusion has had time to play its role; the damaged zones extend beyond the zones immediately affected by the plasma.

Table 19 Orders of magnitude of the number of discharges striking one spot of area $100\ \mu m \times 100\ \mu m$ over a total area S_1 or S_2 during $\tau_D(20\ \mu m)$ and $\tau_D(300\ \mu m)$.

Frequency of the power supply	area	Number of discharges striking the same spot of area $100\ \mu m \times 100\ \mu m$ during the time $t = \tau_D = 9.1\ ms$	Number of discharges striking the same spot of area $100\ \mu m \times 100\ \mu m$ during: time $t = \tau_D(L_D = 300\ \mu m) \cong 2.1\ s$
10 kHz	$S_1 = 1\ cm^2$	0.018<1	4.2
	$S_2 = 10^{-2}\ cm^2$.	1.8	420
500 Hz	$S_1 = 1\ cm^2$	9×10^{-4}<1	0.2
	$S_2 = 10^{-2}\ cm^2$.	0.09<1	20

VI.1.2.2 Order of magnitude of surface heat flux

In the first place, it is interesting to have an order of magnitude of the value of the maximum heat transfer due to plasma-skin interaction. The purpose is to compare the thermal flux obtained to those which are known causes of thermal damage. It is recalled that the mean power consumption of the plasma-source (see 0) is described by

- $\boldsymbol{400\ mW}$ for the single channel jet + 500 Hz power supply
- 2-4 W for the multichannel jet + 10 kHz power supply.

So for this calculation, it is assumed that $\boldsymbol{1\ W}$ is the order of magnitude of the total thermal power crossing the interface skin-plasma of area S. Two cases are studied:

- $\boldsymbol{S_1 = 1\ cm^2}$, the order of magnitude of the area covered by plasma when the skin is treated with the multi-channel jet, and when there are several filaments striking the surface in a random way.
- $\boldsymbol{S_2 = 10^{-2}\ cm^2}$, when all the filaments are grouped into a single stronger filament striking the surface of the skin (this discharge regime is obtained by slightly removing the plasma source from the surface of the skin).

Consequently, the power per unit of surface is

$$\boldsymbol{\Phi_1 = 10^4\ W.m^{-2}} \quad \text{and} \quad \boldsymbol{\Phi_2 = 10^6\ W.m^{-2}}$$

Let us now compare these orders of magnitude with known thermal fluxes.

- The solar radiation received by the earth is equal to $340\ W.m^{-2}$ on average [214].
- Flashfires result from the inflammation of combustible gas. The radiative heat flux of these fireballs causes burns, sometimes several km. These fires involve heat fluxes of the order of several $kW.m^{-2}$ for less than 5 s. The modelling of these fires is particularly important for the design of protective clothing for firefighters. For instance, [215] describes a finite element model of skin subjected to flashfire. [215] and [216] show that an incident flux of $4.18\ kW.m^{-2}$ for 34 s is high enough to induce blistering or second degree burn. The time to obtain a second degree burn is only 2.78 s when the incident flux is $24\ kW.m^{-2}$ ([215]). According to [217], theses fireballs causes second and third degree burn when the absorbed heat is approximatively equal to $23\ kJ/m^2$ and $113\ kJ/m^2$ respectively.
- An example of a clinically used photothermal treatment is described in ([210], p240).The laser-skin interaction is divided into three categories depending on the temperature of the tissue and the duration of heating i) the mild hyperthermia is due to a slight increase in temperature in the range 41-44 °C for some tens of minutes. In this case, cell death is induced by changes in enzymatic pathway ii) strong hyperthermia occurs when the temperature is in the range 50-100°C for few seconds. The death of tissue stems from extensive necrosis caused by the coagulation. Indeed, the destruction of the blood vessels deprives the cells of their intake of oxygen and nutrients. iii) The photoablation of tissue occurs when the tissue is heated above 100°C. The tissues are vaporized. For the most powerful pulses (laser fs, mJ to cite a personally tested example), the upper part of the skin forms a plasma plume. The skin bursts, shock waves are emitted. In addition to these three categories, non-thermal effects were observed, due to photochemical reactions. According to ([210], p240), a pulse at $1064\ nm$, whith an intensity of $150\ W.cm^{-2} = 1.5\ MW.m^{-2}$ during 0.1 s induce a temperature of $90\ °C$ in the upper part of the dermis. At the wavelength $532\ nm$, the same intensity causes the photo-ablation.

Finally, the orders of magnitude of thermal fluxes and duration of heating described in the previous paragraph induce damages or at least biological responses associated with mild-hyperthermia. These values are similar to those that can be imagined for plasma treatments. In this context, it is pertinent to ask whether plasma treatments can inflict thermal damage or not. The way in which the damages are quantified is specified in the next section.

VI.1.2.3 What are the thresholds of hyperthermia?

The term “mild-hyperthermia” regards tissue exposed to a temperature between 39 and 42 °C. The mild-hyperthermia has biological effects which regard, for instance, the chemical reactivity of intracellular ROS and the heat shock protein HSP70. This point will be discussed at the end of this chapter.

Hyperthermia, in the strict sense, occurs when it is possible to observe deleterious effects (cells necrosis or apoptosis) that are the consequence of an exposure to the temperature **Th** during a reasonable time t (up to several hours, not days). The most frequently reported value in the literature is 43 °C.

For example, [218] describes the clinical use of thermal dosimetry. It is a matter of predicting the way in which energy is deposited (by microwave treatments) to ensure that the tumor is in a state of hyperthermia. The target temperature of the tumor is between 42 or 43 ° C (p125, p146, p161). However, at 43 °C, the time to obtain complete necrosis could be quite long (several hours). However, the time required decrease with increasing temperature. The paper [219], which describes bio-heat transfer which occurs during laser exposure, argue that an exposure of 56 ° C for 1 s is enough to kill cancer cells.

Moreover, the three following papers, [220] [221] [222], respectively from 2015, 2014 and 2011 discuss the concept of thermal dose called “Cumulative Equivalent Minutes at 43 °C (CEM_{43})”. The damages are represented by the time needed to obtain the same damage at $\mathrm{T} = 43\,^{\circ}\mathrm{C}$. It is then possible to know the time t required to elicit the same amount of damages at another temperature T.

$$\mathrm{CEM}_{43} = \mathrm{t} \times \mathrm{R}^{43-\mathrm{T}} \text{ where R is a constant for T>43°C}$$

The paper [221], [222] contains discussions of the relationship between CEM_{43} and the quantification of damages by a first order Arrhenius law (explain in next section). The damage can be modeled by a chemical reaction of the first order; [222] has collected the values of the kinetic coefficients for some tissue/cells. [221] and [223] also give an order of magnitude of the depth of damage as a function of the surface temperature:

$$Burn\ depth\ (in\ mm, T\ in\ ^{\circ}C, t\ in\ s) = -2.9302 + 0.0473T - 0.0317t + 0.000913Tt$$

The results given by this expression are poorly consistent with the results obtain with the non-refrigerated multichannel jet after the treatments of 3, 5 and 30 min. It is recalled that the final surface temperature was observed between 45 and 48 ° C. For the calculation, 46 ° C is chosen.

$$\text{Burn depth } (\mathrm{T} = 46°\mathrm{C}, \mathrm{t} = 3 \text{ min}) = 1.1 \text{ mm}$$

$$\text{Burn depth } (\mathrm{T}=46°\mathrm{C}, \mathrm{t}=5 \text{ min}) = 2.4 \text{ mm}$$

$$\text{Burn depth } (\mathrm{T} = 46°\mathrm{C}, \mathrm{t} = 30 \text{ min}) = 18 \text{ mm}$$

This expression tends to overestimate the depth of the damage inflicted. This failure was predictable; since this expression is fitted to the human skin, heated by hot water in the

range 60-90 °C. The laws apply only to restricted temperature ranges. This is one of the pitfalls of the quantification of thermal damage; others are described after.

Caveat 1 Steepness of the dose effect,

In fact, the relationship between damages and time and the temperature is really steep. The paper [224] give an example. At 43.5 °C, the fraction of mice developing necrosis of the ear is 0% after 40 min and 100% at 60 min. Experiments can quickly lead to widely dispersed results. The paper [225] also affirm that the cytotoxicity increased rapidly as temperatures were increased from 42°C to 45°C. This review also affirms that cancer cells are more sensitive to moderate increases in temperature (42-45°C) than normal cells. This paper also discusses the correlation between immunotherapy and thermotherapy.

Caveat 2 Mouse skin vs. human skin

The review [224], show that the sensitivity to thermal damages depends on the species (see Fig 159). It appears that the mouse is more sensitive than humans (several °C). It is potentially a huge bias for plasma-medicine. Treatments that induce an anti-tumor effect via a hyperthermia-type response at 45 °C in the mouse may be ineffective for humans. Moreover, the results presented in this figure Fig 159 is consistent with the fact that the skin of the mouse was completely destroyed after a treatment of 30 min with the non-refrigerated multichannel-jet (final temperature between 45 and 48 °C). Indeed, this curve gives a time of the order of ~15 min for mouse skin necrosis.

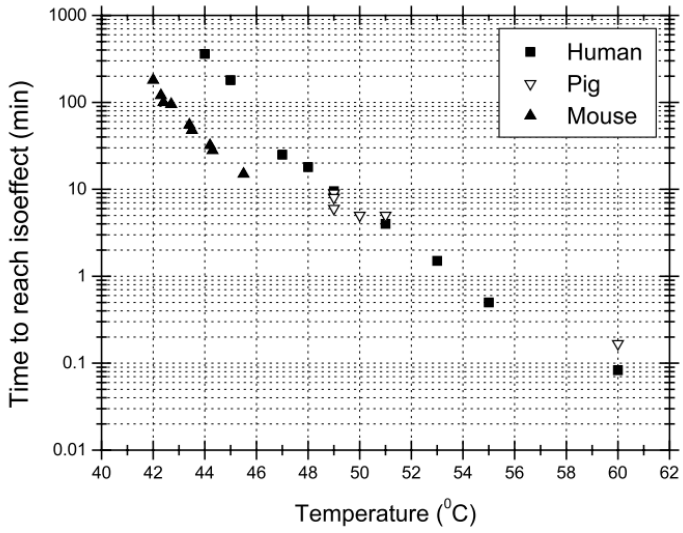

Fig 159 the points represent the time to obtain epidermal necrosis as a function of temperature for human, pig and mouse skin. The figure is from the review [224]. The data itself were derived from papers [226] and [227]

An additional difficulty, the damage also depends on the type of biological tissue. The differences between tissues are considerable, several °C (see Fig 160)

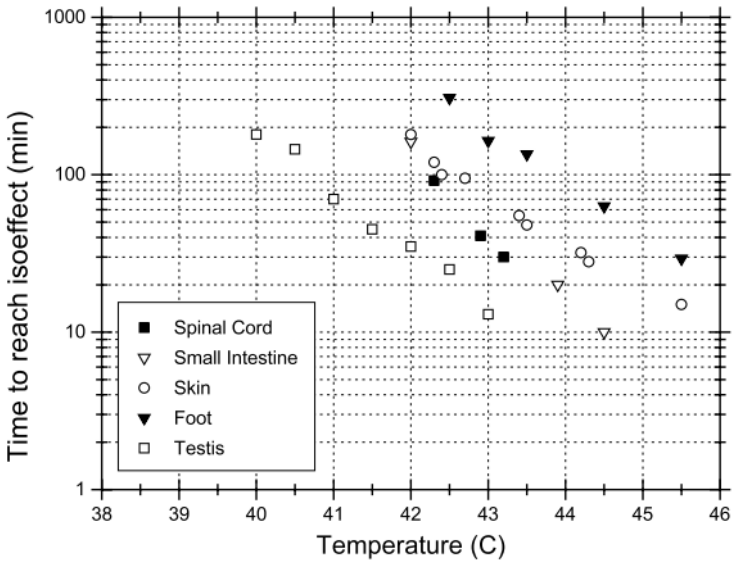

Fig 160 The figure is from the review [224]. Time-temperature relationships to achieve isoeffective damage in several mouse tissues.

Moreover, there is no obvious ranking by type of tissue. Regarding the nervous system, for instance, peripheral nerves appear heat resistant, whereas the brain is very sensitive [224].

Caveat 3 the heating rate

Under the effect of a moderate increase in temperature (mild-hyperthermia 39-42 °C), the cells develop temperature tolerance mechanisms (involving, among others, the heat shock proteins HSP70). HSP proteins play the role of chaperones, helping the folding of the proteins emerging from the ribosomes, enabling to avoid the defect of folding and denaturation that could result from the mild-hyperthermia. The review [224] assume that the heating rate is a significant factor because the thermotolerance develops to a greater degree during slow versus fast heating rates. The example discussed in [224] regards damage to vascular systems. These damages play a key role in the tumoricidal effects. It appears that the threshold for arteriolar stasis (respectively venular stasis) that was between 45-46°C (respectively 43.4 °C) for heating rates in the range 0.1-0.7 °C/min dropped to 42°C (respectively 42.1 °C) at a heating rate of 1 °C/min. Since the heating rates due to plasma treatment are still higher than 1 °C/min, the damage should be greater than what the simulations might suggest.

Not to leave with a pessimistic impression. Quantification of thermal damage, although problematic, is an area of active research, promising results of phase III clinical trials are presented in the paper [220] from 2015.

VI.1.2.4 Can the plasma-skin interaction produce damage at short time scales?

“short timescale” mean the time scale of the interaction of a single discharge with the skin. it has been found, by acquiring images with the ICCD camera and a plasma-jet, that the plasma has a lifetime of the order of 200 ns above a glass surface. We will take this value as the time scale. In 200 ns, the thermal diffusion takes place over a very short distance:

$$L_D = \sqrt{\alpha \times 200\ ns} = \sqrt{4.4 \times 10^{-8} \times 200 \times 10^{-9}} = 94\ nm$$

The only thing that could happen is possibly an ablation of the first cells of the stratum corneum. Two kinds of experiments are known to produce this type of effects to the skin.

First, the paper [228] describes the ablation of the skin at a microsecond timescale. The device produces hot steam jets that interact with the skin during approximatively $10\ \mu s$. The purpose of these devices is to pierce the corneum stratum to facilitate transdermal passage of drugs. The external parts of the skin are heated to a temperature of the order of several hundred °C. According to the authors, the thermal effects (not the mechanical effets due to the impact of the jet) are the cause of tissue ablation. Unfortunately, we do not have sufficient time-resolved skin temperature measurements to know if the plasma treatments are approaching this case or not. The temperature measurements were acquired with the thermal camera which has a limited temporal resolution of ~100 ms. On the other hand, the amount of energy consumed during each discharge is known. At maximum, each microdischarges represents energy of the order of 100 µJ. This gives an upper limit to the thermal transfer due to plasma-skin interaction.

It is assumed that the area of interaction of a single filament is:

$$\mathrm{S}= \mathbf{100}\ \mu\boldsymbol{m} \times \mathbf{100}\ \mu\boldsymbol{m} = \boldsymbol{10^{-8}\ m^2},$$

100 µJ in 200 ns, this is a flux $\Phi = \frac{100\times10^{-6}}{200\times10^{-9}}\frac{1}{10^{-8}} = 5 \times 10^{10}\ W.m^{-2}$

Then, we consider, the volume of epidermis define by the thickness of epidermis (e~15 µm), multiplied by a square of area S. This volume has the volumic specific heat:

$$C = \rho C_p Se = 1500 * 3600 * 10^{-8} * 15 * 10^{-6} = 8.1 \times 10^{-7} J.K^{-1}$$

Consequently, the addition of 100 µJ of thermal energy should increase the temperature of this volume by:

$$\Delta T = \frac{100 \times 10^{-6}}{8.1\ \times 10^{-7}} = 123\ K$$

It seems unlikely that a substantial part of the skin can be ablated with the heating caused by a single discharge. Firstly, because it is below the temperatures described in the paper [228], secondly, we are assuming that all the energy is transferred the skin and in the thermal form which is probably false. However, the heating caused by a single discharge should be detectable by a triggered infrared camera with a temporal resolution lower than the ms. It would be an interesting to do the experiment with a thin film (50 µm) of material which could mimic the skin. Measuring the temperature of the two sides of the film could provide valuable information on the kinetics of the thermal energy deposit, and indirectly on the plasma surface interaction.

The other type of experiments known to ablate the upper part of the skin involves laser pulses. Very short pulses (ns-fs) can cause damage by dielectric breakdown of materials (especially optical glasses). However, thermal damage is the main risk for pulses longer than 1 µs. There are medical treatments for the skin using the thermal energy released by the absorption of lasers. The process is called photo-thermolysis. One of the goals of this treatment may be the removal of skin defects or its rejuvenation. The paper [207] describes the treatment of the skin which consists in the thermolysis of zones of micrometric sizes. The treated volume is a cylinder of diameter 100 µm and depth 300 µm. The depth is limited by the phenomena of absorption and diffusion. The infrared pulse has a duration in the range 1.5-5 ms and energy in the range 6-12 mJ.

Thus, the optical intensity is in the range, 0.15-1 $GW.m^{-2}$

The temperature increase would be ΔT, in the cylindric volume of the skin:

$$\Delta T = \frac{6 \times 10^{-3}}{\rho C_p Se} = \frac{6 \times 10^{-3}}{1500 * 3600 * \pi \times (50 \times 10^{-6})^2 * 300 * 10^{-6}} = 470\ K$$

This order of magnitude is consistent with the value evoked in the paper [228], which describes the thermo-ablation by hot steam at a timescale of 10-100 µs. The conclusion is the same with respect to the comparison with the energy deposited by a single plasma filament. It is likely that a single discharge **does not** cause ablation.

In the following, the damages occurring at longer time scales (seconds) is studied. At this scale, the thermal diffusion is a key factor.

VI.1.3 Biological effects of hyperthermia

Long-term cellular changes

Lepock et al. reviewed the molecular and cellular changes related to hyperthermia [229]. Higher temperature increases the metabolism [94]and elicits transitions[95] in cellular structures, particularly membrane and macromolecules. The orders of magnitude of time/temperature mentioned in section VI.1.2.3 are confirmed. The protein denaturation[96] occurs at a temperature as low as 40-45°C (mammalian cells) [229]. However, the temperature of denaturation is only ~40°C in rodent cells and 41-42°C for human cells [229]. This could be an issue since most *in-vivo* plasma-medicine experiments are done with mouse models.

Hyperthermia also alters the fluidity of the membrane[97] and increases cell permeabilization [229]. De Andrade Mello et al. exposes the link between changes in the fluidity of the membrane due to hyperthermia and the promotion of tumor death [230]. Leyko et Bartoz. compare the effects of ionizing radiation and hyperthermia on the membranes [231].

The existence of thermotolerance shows that the metabolic path is modified in a fairly durable way (at least several days) by moderate hyperthermia and that mild-hyperthermia (e.g., temperature in the range 39-42 °C) change the behavior of the cells. Lepock et al. describe the mechanism of thermotolerance [229]. It has been shown that relatively short exposure to 40-41°C can inhibit growth and changes the activity of cellular pathways.

---

[94] in particular, the reaction rate of enzyme involved in cellular life

[95] The changes in molecular structures, for example, unfolding of the proteins (also called protein denaturation) are characterized by high activation energy ("100–200 kcal/mole"), which reflects the strong temperature dependence of this kind of process. Metabolism reactions have activation energies of one order of magnitude lower. Since thermal damages are characterized by higher activation energy, it is the reactions of structural transitions, and not the accelerated reactions of the metabolisms which explain the kinetics of thermal damage.

[96] Lepock et al. distinguish two effects of protein denaturation at the origin of cells killing [229] . First direct loss of essential functions of the metabolism ("Inactivation *of enzyme activity,membrane receptors, and ion transporters*"). Second, the structural damages to the membrane, the cytoskeleton, the nuclear matrix.

[97] directly due to the denaturation of the structural protein of the membrane

It should be noted that there are sensitizing chemical substances (methanol, ethanol, propanol, butanol) or protective substances (glycerol) with regard to the denaturation of cellular proteins [229].

Hyperthermia and thermal ablation ($T \geq 42°C$)

Borasi et al. study the coupling of strong hyperthermia induced by focalized ultrasound with radiotherapy [232]. The tissues reach a maximum temperature of 58 °C. They also found activation of the immune system due to hyperthermia. Several models of glioma[98] were treated.

Ahmed et al. and Appelbaum et al. describe tumor ablation at high temperature (T>50°C), with radiofrequency heating in combination with doxorubicin chemotherapy ([233] [234]). They prove that the combined effect of treatments is much better than treatments alone. Hyperthermia enables to improve drug delivery.

Rossman et al. review the effects of hyperthermia on the tissues properties [235]. Regarding the electrical properties, the conductivity increase with tissue temperature. whereas the permittivity is rather constant. Regarding thermal properties, thermal conductivity and specific heat increase with the temperature for $T \leq 80\ °C$. Regarding the blood perfusion it appears that generally[99] mild-hyperthermia increase blood flow whereas excessive heating elicit vascular stasis. This paper raises also an important issue: hyperthermia would be less effective on large animals (humans) than smalls (mice).

Sun et al. have shown that a treatment which consists in an alternation of heating (~60 °C) and cooling (with liquid nitrogen) is efficient against tumor [236]. It appears that damaged was increased when the cooling precedes heating.

The damage elicited by hypothermia is beyond the scope of this section. However, information can be found in the papers [237]–[240].

Mild hyperthermia and tumor

Stewart et al. show that mild hyperthermia (42.5 °C/30 min) have long-term effects on tumor blood perfusion [241]. One day after treatment, the blood perfusion decreases considerably. Contrary to what is observed in normal skin. Reduced blood flow and hypoxia leads to tumor starvation and decrease the pH of the tissue. The combination of radiotherapy and chemotherapy should be avoided at this time. On the other hand, the drugs will be diffused less effectively within the tumor, on the other hand, because the low oxygenation increases the radioresistance of the cells. It is, therefore, better to apply chemotherapy and radiotherapy before hyperthermia.

Grile et al. show that hyperthermia (44 °C from 30 to 40 min) and radiation have synergistic effects on tumor [242]. It appears that big tumors are more sensitive to heat than the small ones, while the smaller ones are more sensitive to radiotherapy. It's consistent with the results presented in the paper [241] since the small tumor benefit from good oxygenation, while large, less oxygenated will be more radioresistant and more sensitive to additional hypoxia. This paper also shows that serotonin injections increase the sensitivity to heat.

[98] including U-87 which was also treated by Vandamme et al. [84]

[99] there are exceptions… It happens that blood perfusion decrease at the begining of hyperthermia.

Sun et al. show that one-third of the lethal dose of heat induces thermoresistance. It appears that the tissues are not damaged by a dose that should destroy them [241].

Song et al. have studied the modifications of blood flow induced by mild-hyperthermia. It turns out that the effect is complex, in some cases, blood flow increase, in another case it decreases [243]. Song et al. also observe a decrease in tissue pH (by 0.2 unit of pH) in addition to an increase in tissue oxygenation due to mild hyperthermia [244].

Vujasckovic et al. observe the oxygenation and pH of the in-vivo canine tumor [245]. The tumor oxygenation (pO2) and blood perfusion are described after hyperthermia (24 h). Oxygenation increases when the temperature is lower than 44 ° C, on the contrary, it decreases when the temperature is above 44 ° C. Regarding blood perfusion, mild hyperthermia significantly increase blood perfusion. On the contrary, there is no change in perfusion when $T \geq 44\ °C$. On average, the pH decrease of 0.1 after hyperthermia.

Song et al. also observe an increase in oxygenation of tumors due to hyperthermia. The combined use of hyperthermia and nicotinamide increases radiosensitivity of the skin and tumor [246].

Mild hyperthermia and immune response

Tempel et al. describe how the immune system is activated by mild-hyperthermia [247]. The heat shock proteins in particular HSP70 is crucial. Heating cells to 41.5 °C also increased the phosphorylation of histone H2AX. And it turns out that γH2AX is considered as a marker of DNA breaks (double strand breaks) which also triggers immune responses

The first effect of hyperthermia on immunity is localized to the heated tumor, but, secondly, local hyperthermia can also stimulate a systemic antitumor reaction that can strike tumor cells that are distant from the heated tumor. Indeed:

[247]. "At 39°C, heat increases the MHC class I polypeptide-related sequence A (MICA), a molecule which increases cell sensitivity to natural killer cells. At a temperature of 43 °C, heat will increase the level of MHC class I molecules, which attract cytotoxic T-cells."

[247]. "Moreover,Hsp70s can stimulate the adaptive immune system by transferring chaperoned tumor proteins to antigen-presenting cells, which evokes a tumor-specific T-cell response [69,85–87]. This T-cell response presumably has the ability to target all tumor cells, including metastases."

Regarding this topic, the following references contain more information about this topic. [248]–[251] and [252].

Mild hyperthermia and oxidative stress

Lord-Fontaine et al. show that hypothermia increases the toxicity of ROS, especially H_2O_2 [253] and proves that protection systems against ROS can be deactivated by hyperthermia [254]. The review of Bettaieb et al. summarize the link between hyperthermia and oxidative stress [255] with the following statement:

- Elevated temperatures can increase the rates of biochemical reactions, this would increase cell metabolism and increased oxidative stress
- This increase is seen below (at 40°C) and above 42 °C.
- This stress is likely due to a dysfunction of the mitochondrial respiratory chain
- Hyperthermia could increase the reactivity of reactive oxygen species. For example, the toxicity of H_2O_2 is higher at 41-43°C compared to the physiological temperature.
- Hyperthermia inactivated cellular antioxidant defenses

The thermosensitivity depends on species and organ

Some tissues and organs are more sensitive to hyperthermia than others: this question was illustrated by the comparison of human and mouse skin and mouses organs (see section VI.1.2.3). According to [255], the nervous and gastrointestinal tissues are most sensitive[100] to hyperthermia.

Hyperthermia and wound healing

It turns out that mild-hyperthermia can promote wound-healing [257]. It may be interesting to take this into account for dermatological applications of plasmas [258].

Mild hyperthermia and photodynamic therapy

This difficulty in separating the effects of hyperthermia has arisen in other domains, for example, that of photodynamic[101] therapy. As this is beyond the scope of this study, the relevant papers will be quoted without further comment: [259]–[262].

***in-vivo* experiments have shown that mild hyperthermia causes:**
Long-term cellular changes: thermotolerances, expression of several heat shock protein, HSP70
oxidative stress
pH decrease
pO_2 increase (vasodilatation)
membrane permeabilization
Radio and chemosensitization of chemoresistant lines
Innate and adaptive immune responses • **MHC class I↗ = attract cytotoxic T-cells** • **Hsp70s stimulate the adaptive immune system** • **abscopal effect/systemic response**

VI.1.4 Quantification of thermal damage

Collagen is the major component of skin [210]. Consequently, the state of collagen can be used as a marker of thermal damage. Moritz & Henriques ([206], [263])described a way to quantify thermal damage, which is widely accepted and used by communities interested in the quantification of thermal damages. The purpose is to link the degree of burns with temperature history of the skin.

---

[100] see also Yarmolenko et al. discusses the susceptibility to hyperthermia of several organs and tissues [256]

[101] *According to [259] "Photodynamic therapy (PDT) have been shown to be synergistic with sub-lethal hyperthermia. The greatest effect in vivo is when hyperthermia is applied immediately prior to light irradiation. In many of the earlier clinical studies of PDT, it was not realised that, at high enough incident light power, the absorption of light by the target tissue could itself produce significant temperature rise, even to the extent of causing coagulation or charring. … Conversely, hyperthermia could be applied deliberatelywith PDT,either using the light itself or by independent RF, microwave or ultrasonic irradiation, to enhance the tumoricidal effects of PDT"*

Skin damage can be modeled as a chemical reaction of collagen. This reaction, called denaturation, is the transition of collagen structure from triple helix configuration to a randomly coiled conformation. The reaction rate $k(T)$ depends on the temperature.

The temperature of thermal denaturation strongly depends on (a) the water content in collagen (b) the degree of cross-linking between the molecules [264]. In fact, the denaturation of collagenous tissue is even more complex and depends not only on the temperature history but also on mechanical loading during heating, pH variations and preheating.

This modeling assumes that the denaturation is of order one and follows the law of Arrhenius. The damage function, Ω, is dimensionless and defined by:

$$\mathrm{k(T)} = \frac{\mathrm{d\Omega}}{\mathrm{dt}} = \mathrm{Aexp}\left(-\frac{\mathrm{Ea}}{\mathrm{k_B T}}\right)$$

Where A and Ea are constants; A has the dimension of a frequency, interpreted as a parameter related to the frequency of molecular collision. Ea is the activation energy of the reaction (J). When the thermal energy exceeds this energy, the reaction occurs at a significant rate. The damage function Ω is also expressed in an integrated form for each time and each position:

$$\Omega(\mathrm{x,y,z,t}) = \int_0^{\mathrm{t}} \mathrm{A} \times \exp\left(-\frac{\mathrm{Ea}}{\mathrm{k_B T(x,y,z,\tau)}}\right) \mathrm{d\tau}$$

The reaction is faster with larger values of T for the same Ea. The two constants A and Ea were obtained experimentally. The meaning of Ω is explained in [265]. This number is the logarithm of the relative concentration of undenatured collagen.

$$\Omega(t) = \ln\left(\frac{\mathrm{C(0)}}{\mathrm{C(t)}}\right).$$

Where C(t) is the concentration of undenatured collagen at time t. The percentage of denatured collagen is:

$$\%col(t) = \frac{C(0) - C(t)}{C(0)} = 1 - \exp\left(-\Omega(t)\right)$$

Thus, $\Omega = 1$ corresponds to the transformation of 63.2% of collagen into damaged collagen. Damage function can be calculated in each position: $\Omega(\mathrm{x,y,z,t})$. Three thresholds of damages, which corresponds to the three degrees of the burn are generally used (Table 20, according to [266] and [210]) . Ω is calculated at the position of the basal layer of the epidermis (the living cells at the boundary of dermis and epidermis). The value $\Omega = 10^4$ at the same location represents a third-degree burn (for human), which mean that the damages reach subcutaneous tissues.

Table 20 Link between the degree of burn and the value of the damage function.

Degree	Description	Quantification
1	Transepidermal damage	Ω = 0.53 at the basal layer of epidermis
2	transepidermal necrosis	Ω = 1 at the basal layer of epidermis
3	Third-degree burn	Ω = 10^4 at the basal layer of epidermis

Ea and A are obtained for several species and location of the skin on the body. The value Ω = 1 corresponds to the same amount of damage for all species and kind of skin because Ea and A are chosen for this purpose.

The damage function Ω is an integral over time. The consequences of single hyperthermia are well known. The effects of repeated hyperthermia with an interval of several days have been less studied. It is likely that the damage does not have time to be fully repaired in two days when the tissue is significantly damaged.

VI.1.5 Physical content of the simulation

In this section, the physical significance of the parameters used to model the thermal behavior of the tumor is explained. The numerical values of these parameters are given in next section (VI.1.6). The parameters related to the plasma source are given in the sections devoted the results.

VI.1.5.1 Conduction through living tissue

The heat transfer by conduction takes place as soon as there is a temperature gradient. It represents the global effect of the transport of energy by the elementary carriers: molecules, phonons, electrons. The conductive surface flux **jc** is proportional to the local temperature gradient $\boldsymbol{\nabla} T$, according to the Fourier law in the case of a homogeneous and isotropic medium.

$$\boldsymbol{jc} = -\lambda(T)\boldsymbol{\nabla} T$$

$\lambda(T)$ depends on temperature, but is considered to be constant in the temperature range that is concerned. The different layers of the skin will be considered as homogeneous and isotropic media (Otherwise it would be possible to consider conductivity as a tensor). The minus sign comes from the second principle of thermodynamics. The Fourier law is the approximation of the response to a disturbance at first order. This is a linear response, only the first derivative of the temperature appears in this equation. This law postulates an instantaneous response to a thermal disturbance. This means that the heat flux occurs instantaneously in response to a temperature gradient, at a given point. This hypothesis holds true as long as the time scales are large compared with the timescale of collisions $\boldsymbol{\tau col}$ between the elementary carriers. The Fourier law ceases to be valid for the modelling of thermal transfer due to the interaction of a short laser pulse (scale of the ps or below) with a solid medium.

Some authors (see reference book [210]) propose non-Fourier simulations of thermal transfer through the skin using expressions like $\boldsymbol{jc}(t+\tau_q) = -\lambda(T)\boldsymbol{\nabla} T(t+\tau_T)$. The argument for these approaches is that the non-homogeneous of the skin, the presence of sub-structure (cells, blood vessels…) could give relaxation times between 0.1 s and

100 s (instead of 10^{-11} s for crystal lattice). This relaxation time that characterizes exchange between each sub-structure would be an equivalent of the time of collisions between energy carriers in crystal. This description is strongly controversial. The observation of thermal waves has not been clearly proved for biological tissues. Moreover, these generalizations of the Fourier law pose fundamental problems for non-equilibrium thermodynamics and could lead to strange physical behaviours like negative thermal-temperature [267]. Furthermore there is few data on the values of coefficients τ_g and τ_T regarding the skin. That's why it was decided to describe conduction only on the basis of Fourier propagation equation.

Some authors also use the notion of "effective thermal conductivity" ([268], [269], [270]). In fact, the tissue studied is often irrigated by multiple blood vessels. The displacement of the blood is accompanied by a convective transfer of heat. Consequently, a description which assumes that the transfer of heat is of pure conductive form is necessarily incomplete. Effective conductivity is a mean to deal with the convective transport of heat by assuming that the tissue has a thermal conductivity (λ_{eff}), several times higher than the real conductivity of the tissue. In what extend this approah can correctly mimic the thermal behavior of the tissue is still an open question. There is much less information available on the values of thermal conductivities that could be attributed to tissues. The Appendix F gives the results of simulations based on the theory of effective thermal conductivity.

VI.1.5.2 Metabolic heat generation

The activity of the cells generates heat. This can be modeled by a constant volumic-source in the equation of heat propagation. Heat generation, however, depends on several parameters: ambient temperature, physical activity of the mouse. Thermoregulation can be maintained at ambient temperature in the range -5°C, 30°C [271]. Rodents cannot sweat; they adjust their temperature by changing their metabolism and behavior. Metabolic activity of awake mouse was measured at 30 kJ/day (for a body weight of 30g). With the assumption of a density of 1 for the whole mouse, this gives 7700 W/m^3. Deng et Liu [272] choose the value of 4200 W/m^3 for normal human tissue and 42 000 W/m^3 in the tumors. Consequently, the metabolic heats of humans and mice have the same order of magnitude.

However, the following paragraph will show that the heating due to metabolic heat is not preponderant compared to the effect of blood perfusion. The effect of metabolic heat is relevant at the scale of the whole organism, not as the scale of a centimetric tumor. This statement is true for small animals but not necessarily in humans.

VI.1.5.3 Heat exchange with blood

Blood flow coming from the artery acts as a damping system for temperature variations. In most models, the blood enters the tissue at the arterial temperature which matches the internal temperature of the mouse. The blood exits at the tissue temperature. It is assumed that blood transfers its thermal energy to the tissue. Dermis and tumor tissue are highly vascularised. The fat layer is poorly vascularized. The epidermis is not vascularized. Arterial blood temperature is 37 °C when the mouse is conscious. During anesthesia (with isofluorane) and for this strain, the internal temperature is 35 °C [273]. Internal temperature strongly depends on the number of heartbeats per minute, the duration of the anesthesia and the concentration of anesthetic gas. We assume that this temperature is the same for C57BL/6 and BALB/C strain. Volumic source term of heat has the following expression:

$$q_{perf} = \omega \rho_{blood} C_{blood} (Ta - T)$$

Where Ta is the arterial temperature; T the temperature of the tissu; $\rho_{blood} C_{blood}$ the volumetric specific heat of blood; ω the perfusion rate. Perfusion rate is often express with unit ml/s/ml, which expresses the number of ml of blood flowing per s per ml of perfused organ. Blood perfusion has a magnitude of 0.001 ml/s/ml for the dermis and this kind of tumor.

Numerical example:

With $\boldsymbol{\omega = 0.001}$ ml/s/ml, $\rho_{blood} = 1060$ kg/m^3, $C_{blood} = 3770$ J/kg/K and Ta-T=5 K (for example if the tissue has a temperature$T = 40\,°C$). Consequently, $q_{perf} = 20\,000$ W/m^3. That's why metabolic heat, whose mean value is around 7000 W/m^3 does not have a preponderant effect.

VI.1.5.4 Effect of temperature and damage on blood perfusion

The organism reacts to temperature variation. In particular, blood perfusion is temperature and damage-dependent. When the temperature increases blood flow begins to increase until reaching a maximum. The blood flow then decreases with increasing damage and vanishes entirely above 60 ° C due to blood coagulation [210]. This effect was modeled by Schutt and Haemmerich [274] by using the "degree of stasis function."

The degree of stasis is defined with:

$$DS = 1 - \exp\left(-\Omega_{\text{perf}}\right)$$

Where Ω_{perf} is a damage function defined by coefficient A = 1.98 10^{106} s^{-1}, ΔE = 6.67 10^5 J/mol.

$$\Omega_{\text{perf}} = \int_0^t A e^{-\Delta E/(RT)} dt$$

Perfusion rate is linked to the degree of stasis with four linear approximations:

$$\omega = \omega_0(1 + 30\ DS) \quad for\ DS\ \epsilon\ [0{,}0.02]$$
$$\omega = \omega_0(1.86 - 13\ DS) \quad for\ DS\ \epsilon\ [0.02{,}0.08]$$
$$\omega = \omega_0(0.884 - 0.79\ DS) \quad for\ DS\ \epsilon\ [0.08{,}0.97]$$
$$\omega = \omega_0(3.87 - 3.87\ DS) \quad for\ DS\ \epsilon\ [0.97{,}1]$$
$$\omega = 0 \quad for\ DS \geq 1$$

Where $\omega_0$is the blood perfusion of the undamaged skin. The same model of damage is used in our model. Since the volumes destroyed are generally small, this effect does not play a key role.

VI.1.5.5 Radiation

The physics of heat exchange at the skin interface is described in the four following sections. Exchange of heat by radiation takes the form:

$q_{rad} = \sigma(Ts^4 - Text^4)$ (with the assumption of emissivity = 1= black body, in reality the emissivity of the skin is around 0.95)

With Ts the skin temperature, Text The temperature of the surface which emits the radiation seen by the surface of the tumor, $\sigma = 5.67 \times 10^{-8}\ W.m^{-2}.K^{-4}$ the constant of

Stefan-Boltzmann and q_{rad} the value of the power which leaves the body per surface unit (W.m^{-2}).

Numerical example:

With Ts = 33 °C and Text = 20 °C, heat flow is $q_{rad} \sim 78\ W.m^{-2}$.

In the condition of natural convection (see next section), heat exchange for the same difference of temperature is $q_{conv} \sim 91\ W.m^{-2}$. Radiative exchanges are a significative part of heat exchange. It is necessary to take them into account. In the simulation, the part of the tumor which is not exposed to plasma is exposed to $Text = Tamb = 20\ °C$. The part of the tumor exposed to plasma jet, is exposed to Text = Temperature of Helium gas = Temperature of the plasma source. The tumor is in the nearby of plasma-source, and we assume that the plasma source (at least his head) is in thermal equilibrium with gas. This point is particularly crucial in the case of treatment with refrigerated multijet since the initial temperature of the device is below -30 ° C and represents a significant part of the visible surface from the treated zone.

VI.1.5.6 Convection

The convection is modeled by a heat exchange coefficient h.

$$q_{conv} = h(Ts - Tgas)$$

Where Ts is the temperature of the surface of the skin; Tgas is the temperature of the fluid; h is the heat transfer coefficient (W/m²/K); q_{conv} is the amount of heat transferred per unit area. The coefficient h depends strongly on the nature of the flow, which is conditioned by the value of the dimensionless numbers of the fluid mechanics. Three cases are studied: (a) the case of a skin exposed to air at room temperature (natural convection) (b) the skin under the helium jet orthogonal (c) case of an argon jet. Plasma-specific effects are not taken into account. Plasma can act on the turbulence of the overall flow. The thermal conductivity λ of the plasma is quite high; thus, the effusivity of the plasma $\sqrt{\lambda \rho c_p}$ can be expected to be much higher than that of the air.

Thermal effusivity $\mathbf{E} = \sqrt{\boldsymbol{\lambda \rho c_p}}$ is the parameter which fixes the surface temperature when two semi-infinite bodies **1** and **2**, initially at temperatures $\mathbf{T_1}$ and $\mathbf{T_2}$ are brought in perfect conductive thermal contact. This value is only true for short duration, those for which the approximation of semi-infinite media is valid. In this case surface temperature is:

$$Ts = \frac{T_1 E_1 + T_2 E_2}{E_1 + E_2}$$

It is, therefore, possible to assume that the presence of plasma could increase the value of the heat transfers.

It would be interesting to have an idea of thermal conductivity of this cold plasma at atmospheric pressure, in the conditions of plasma-medicine experiments. The lifetime of these plasmas on the surface of the solid and the unsteadiness of their thermal properties at short time scales requires the use of simulations. The following three sections describe heat exchanges by assuming that heat exchanges are made with hot (or cold) helium if the device is refrigerated.

VI.1.5.6.1 Natural convection

Natural convection of the skin (i.e., without imposing a flow of fluid) is modeled in the works [210], [275], by that of an isothermal cylinder of diameter D=10 cm. It seems relevant since these works seek to model the skin at human scale. In this framework

$$q_{conv} = 2.44\ (Ts - Tair)^{1.25}\ W.m^{-2} \quad (\boldsymbol{Eq\ 1})$$

In our situation, the relevant dimension is rather D = 1 cm (~ size of the tumor). It is therefore necessary to recalculate an expression of the heat transfer coefficient elicited by natural convection with this hypothesis. Insofar, we use a tabulated expression linking some of the adimensioned numbers which characterized the problem. Let's start by calculating these numbers

The heat transfer coefficient h is related to the number of Nusselt with

$$\mathrm{Nu} = \frac{\mathrm{h\ D}}{\lambda_{\mathrm{air}}},$$

where D is the diameter of the cylinder; and λ_{air} the thermal conductivity of air. Morgan [276] shows that Nusselt number is a function of Rayleigh number Ra. This number characterises the relative importance of heat transfer by conduction or convection. If the Rayleigh number is below a critical value, heat transfer is in the form of conduction. This number is the product of Grashof number and Prandtl number $\mathrm{Ra} = \mathrm{Pr\,Gr}$.

Prandtl number is defined by $\mathrm{Pr} = \frac{\nu}{\alpha} = \frac{\text{momentum diffusivity}}{\text{thermal diffusivity}}$, this number depends only on the fluid characteristic. For small Pr, the heat diffuses quickly compared to diffusion of momentum.

Grashof number is defined by $Gr = \frac{g\,\beta(Ts-Tair)D^3}{\nu^2}$, where g is acceleration due to earth's gravity; β is the coefficient of thermal expansion (1/T for ideal gases); ν is the momentum diffusivity (i.e the kinematic viscosity). The Grashof number compares the value of viscous force and buoyant force which is a consequence of the difference of density due to gas heating. Gas parameter are given in [277] (French edition).

$$\nu_{\mathrm{air}} = 1.589 \times 10^{-5}\ \mathrm{m^2/s} \text{ at } 300\ \mathrm{K}$$
$$\alpha_{\mathrm{air}} = 2.25 \times 10^{-5}\ \mathrm{m^2/s} \text{ at } 300\ \mathrm{K}$$
$$\mathrm{Pr} = 0.707 \text{ at } 300\ \mathrm{K}$$

diameter D=1 cm, Ts=33°C ,Tair =20 °C and $\beta = \frac{1}{T} = 1/(273.15 + 33)$ give

$$\mathrm{Gr(D = 1cm)} = \frac{\mathrm{g\,\beta(Ts - Tair)D^3}}{\nu^2} = \frac{9.81 \times 1/306.15 \times 13}{(1.589 \times 10^{-5})^2}\mathrm{D^3} = 1649 \times 10^6 \times \mathrm{D^3}$$

Thus, $Gr(D = 1cm) = 1649$ and $Ra = PrGr = 0.707 * 1649$ =1166

According to [276] and [277], $Nu = ARa^n$ with A=0.850 and n=0.188, for Ra in the interval [10^2, 10^4].

Thus, $\mathrm{h} = \frac{\lambda_{\mathrm{air}}\mathrm{Nu}}{\mathrm{D}} = \frac{2.63\times10^{-2}\times\mathrm{ARa}^{0.188}}{0.01} = 5.21 \times (\mathrm{Ts - Tair})^{0.188}\ \mathrm{W/m^2/K}$

For example, with Ts=33 °C and Tair= 20 °C, $h = 8.4\ \mathrm{W/m^2/K}$. This is relevant for natural convection according to [277].

Furthermore, thermal transfer leaving the surface takes the form:

$$\mathrm{q_{conv}} = \mathrm{h(Ts - Tair)} = 5.21 \times (\mathrm{Ts - Tair})^{1.188}\ W.m^{-2}$$

At this point, we have found the expression which provides the value of power loss per unit of surface relevant with the size and curvature of mouse tissue. The following note explains how to obtain **Eq1** with our own calculations.

Additional note:

Briefly, for D = 10 cm, $Gr(D = 10\ cm) = 1.649 \times 10^6$, thus $Ra = 1166 \times 10^3$ which is in the interval [10^4, 10^7]. Consequently, $Nu = ARa^n$ with A=0.480 and n=0.250. Thus,

$$\mathrm{q_{conv}} = \frac{2.63 \times 10^{-2} \times 0.480 \times \left(0.707 \times 9.81 \times \frac{\frac{1}{300}}{(1.589 \times 10^{-5})^2} 10^{-3} \right)^{0.250}}{0.1} (\mathrm{Ts - Tair})^{1.25}$$

$$\mathrm{q_{conv}} = \mathrm{h(Ts - Tair)} = 2.20 \times (\mathrm{Ts - Tair})^{1.250}\ \mathrm{W.m^{-2}}$$

The heat flux is a polynomial function of (Ts-Tair), with the same power than the expression given in [210], [275] ($q_{conv} = 2.44\ (Ts - Tair)^{1.25}\ W.m^{-2}$). The proportionality factor differs from 8%. Unfortunately, I was unable to access the references used in [210], [275] to investigate this small difference.

VI.1.5.6.2 Helium jet

The study of the thermal transfer of a jet of gas to the surface of a solid is a problem of applied physics that is studied since the mid-fifties. Many industrial applications involve gas jets for (a) drying surfaces (b) cooling hot surfaces in particular during welding (c) heating parts or furnaces with the flames of a burner in the most efficient way possible [278]–[289].

Most applications, however, involve relatively high Reynolds number (above 10,000) whereas the number characterizing the gas flow is relatively small (around 100). Fortunately, some studies contain results for small Reynolds number. The influence of the turbulence and the shape of the treated substrate were explored experimentally and numerically. In particular, following configurations were studied: (a) plate (b) concave or convex surface (c) multi-jet configuration.

On the other hand, no paper describing the thermal exchanges of a gas stream lighter than air was found in this experimental configuration. It seems reasonable to think that this configuration should probably increase the level of turbulence of the flow, even at low Reynolds number. The formation of the boundary which contains helium and air possessing different hydrodynamic and thermal properties could be a source of instability. Especially since the thermal and physical properties of the air-He mixture are more complex than an elementary weighting related to the partial pressure of the gases [290].

The heat transfer coefficient is evaluated from the information found in the literature. Before this, the flow was characterized by the values of dimensionless numbers. The geometry of the tip is visible in Fig 161. The total flow rate is 2600 sscm. Each of the ten channels has a size of $1.5\ \mathrm{mm} \times 1.5\ \mathrm{mm}$.

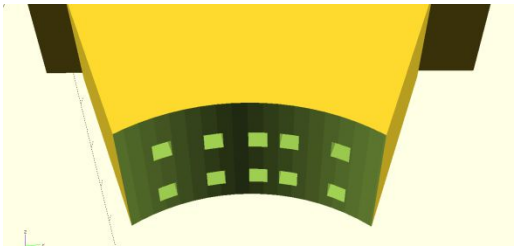

Fig 161 Nozzle of the multi-channel jet is made of ten channels with sizes of 1.5 mm X 1.5 mm. Helium flow was around 2600 sscm during experiments.

Consequently, gas velocity is:

$$\mathrm{U_{He}} = \frac{2600}{10}\frac{10^{-6}}{60}\frac{1}{(1.50\ \times 1.50 \times 10^{-6})} = 1.93\ \mathrm{m/s}$$

Thus, Reynolds number is $\mathrm{Re} = \frac{\mathrm{U_{He}L}}{\nu_{\mathrm{He}}} = \frac{1.93 \times 1.5 \times 10^{-3}}{12.2 \times 10^{-5}} = 15.8$

Where $\mathrm{U_{He}}$, the flow velocity is defined at the exit of the nozzle; L is the characteristic size of flow at the exit; ν_{He} the kinematic viscosity. Numerical values of gas properties were found in [277] .

$\nu_{\mathrm{He}} = 12.2 \times 10^{-5}\ \mathrm{m^2/s}$ at 300 K
$\alpha_{\mathrm{He}} = 18 \times 10^{-5}\ \mathrm{m^2/s}$ at 300 K
$\lambda_{He} = 12.2 \times 10^{-2}\ W/(m.K)$ at 300 K
$\mathrm{Pr} = 0.680$ at 300 K

The calculation of Rayleigh and Richardson number give a better view of the flow.

$Ra = \frac{g\,\beta(Ts-The)L^3}{\nu\alpha} \sim 0.24$, where Ts-The = 50 K and $\beta = \frac{1}{T}$ is taken at 40 °C.

Richardson number, Ri is defined by $Ri = \frac{Gr}{Re^2} = \frac{Ra}{\mathrm{Pr}\,Re^2} = \frac{0.24}{0.680 \times 15.8^2} = 1.4 \times 10^{-3} \ll 1$. Since Ri characterize the importance of natural convection compared to the forced convection, it appears that natural convection is negligible.

Fig 162 shows the structure of a jet impinging a free surface. The literature describes the evolution of Nusselt number (and therefore h; thermal transfer coefficient) along the plate as a function of the distance from the point of impact. The results giving the Nusselt number are taken only in the stagnation region. This region is located at the point of jet impact; its size is related to the size of the flow exiting from the nozzle. In this region, the heat transfer coefficient takes its greatest value. Moreover, the farther, the less the model will be valid, due to the rise of the helium and the curvature of tumor surface.

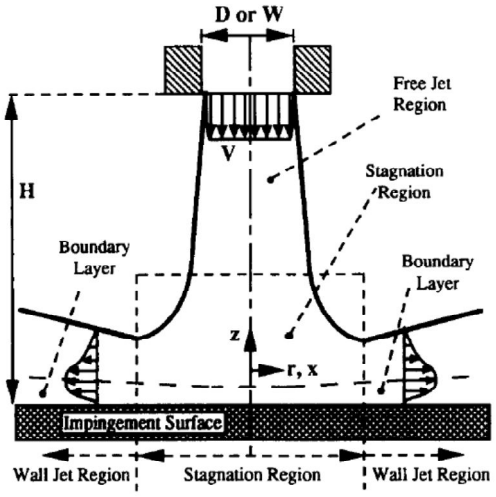

Fig 162 Structure of the flow of an impinging jet given by Viskanta et al. [282].

[283] gave an expression of the Nusselt number at the stagnation point by using the results obtained in the paper of Brdlik et Savin [286].

$$Nu = Re^{\frac{1}{2}} Pr^{\frac{1}{3}} a_1 \left(\frac{z}{d}\right)^{-0.11} \left(1 - \frac{\left(\frac{r}{d}\right)^2 \left(\frac{z}{d}\right)^{-0.2}}{b1}\right)^{1.2}$$

Where, d is a characteristic size of the flow (1.5 mm); z is the distance between nozzle and surface; r is the distance between the center of impact region and the point where the local Nusselt number is calculated; coefficients a1 and b1 depends on z/d. This expression applies to stagnation region (r/d<1) and has been validated experimentally for Re ≥ 3800. This expression was obtained with the hypothesis of a laminar layer and should be valid at lower Reynolds number.

For z/d=4, close to our own experimental situation $a1 = 1.42$ and $b1 = 3.2$

And Nusselt number at stagnation point is

$$Nu(r = 0) = Re^{\frac{1}{2}} Pr^{\frac{1}{3}} a_1 \left(\frac{z}{d}\right)^{-0.11} = 15.8^{\frac{1}{2}} 0.680^{\frac{1}{3}} \times 1.42 \times (4)^{-0.11} = 4.26$$

Sahoo et al. [285], described slot-jet at $\mathrm{Re} = 100$. This paper describes the behavior of the gas leaving a long slot (compared to its width). In the impingement region, depending on the aspect ratio and the geometry chosen, the number of Nusselt is between 4.5 and 6. The two orders of magnitude are consistent.

The Nusselt number describing the thermal transfer of a sphere in a forced heat convection flow is known for a larger range of Re. According to [277], for 1<Re<25,

$$\mathrm{Nu} = (2.2 + 0.48 \times \mathrm{Re}^{0.5})\mathrm{Pr} = 2.8 \quad \text{with } \mathrm{Re} = 15.8$$

Line of flow around sphere

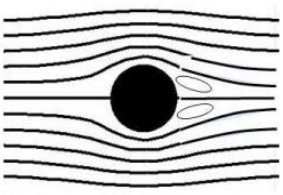

This number is a global Nusselt number; it describes the thermal transfer over the entire surface of the sphere. This is a mean value taking into account the lower heat transfer occurring in the downstream of the flow, that's why this Nusselt number has a smaller value than in the previous configuration.

According to these three experimental configurations, the Nusselt number has likely magnitude of few units.

Finally, in simulations involving the convection of helium, the value $Nu = 5$ was chosen.

Thus, the value of heat transfer coefficient is given by:

$$h_{conv} = \frac{\lambda_{He} Nu}{L} = \frac{15.2 \times 10^{-2} \times Nu}{1.5 \times 10^{-3}} = 101.3 \times Nu$$

But this heat coefficient is relevant only for the region of stagnation (i.e., an area of ~ $1.5 \times 1.5 = 2.25\ \mathrm{mm}^2$). Since there are ten channels, the total area for which this heat transfer coefficient occurs is 22.5 mm².

In the simulation, however, the treated area represents the size of the treated area which is experimentally observed. This size is of the order of the size of the nozzle ~ 0.5-1 cm. More precisely, the treated area is the portion of a sphere of radius 5 mm defined by a half-angle at the top of 50 °. This area is $2\pi \times 5^2 \times (1 - \cos(50°)) = 56.11$ mm².

In the simulation, we consider that incident flux is uniform over the boundary. Consequently, an equivalent heat transfer coefficient is defined over the entire boundary with

$$h_{simu} = h_{conv} \times \frac{\text{"Sum of the area of stagnations regions"}}{\text{"boundary area"}} = h_{conv} \times \frac{22.5}{56.11} = 40.6 \times Nu$$

For example, with Nu = 5, $\mathrm{h_{simu}} = 203\ \mathrm{W.m^{-2}.K^{-1}}$.

The heat transfer coefficient is higher than those of natural convection; this is consistent.

VI.1.5.6.3 Argon jet

What happens with a different gas? This section contains the calculations for Argon by using the same approximations. The thermophysical properties of Argon were found in Handbook [291].

$$\mathrm{U_{Ar}} = \frac{2600}{10} \frac{10^{-6}}{60} \frac{1}{(1.50 \times 1.50 \times 10^{-6})} = 1.93\ \mathrm{m/s}$$

$$\mathrm{Re} = \frac{\mathrm{U_{Ar} L}}{\nu_{\mathrm{Ar}}} = \frac{1.93 \times 1.5 \times 10^{-3}}{1.418 \times 10^{-5}} = 204$$

$\nu_{\mathrm{Ar}} = 1.418 \times 10^{-5}\ \mathrm{m^2/s}$ at 300 K

$\lambda_{\mathrm{Ar}} = 17.84 \times 10^{-3}\ \mathrm{W/(m.K)}$ at 300 K

$\rho_{\mathrm{Ar}} = 1.603\ \mathrm{kg/m^3}$ at 300 K

$\mathrm{Cp_{Ar}} = 521.5\ \mathrm{J.kg^{-1}K^{-1}}$ at 300 K

Thus, $\alpha_{\mathrm{Ar}} = \frac{\lambda_{\mathrm{Ar}}}{\rho_{\mathrm{Ar}} C_{\mathrm{pAr}}} = 2.14 \times 10^{-5}\ \mathrm{m^2/s}$ at 300 K and $\mathrm{Pr} = \frac{\nu}{\alpha} = 0.66$ at 300 K

Regarding Rayleigh and Richardson number:

$Ra = \frac{g\,\beta(Ts-The)L^3}{\nu\alpha} \sim 17.4$, where Ts-The = 50 K and $\beta = \frac{1}{T}$ is taken at 40 °C.

$Ri = \frac{Gr}{Re^2} = \frac{Ra}{\Pr Re^2} = \frac{17.4}{066 \times 204^2} = 6.3 \times 10^{-4} \ll 1$ natural convection is negligible.

For z/d=4 and $\mathrm{a1} = 1.42$ and $\mathrm{b1} = 3.2$, the Nusselt number at stagnation point is:

$$Nu(r=0) = Re^{\frac{1}{2}} Pr^{\frac{1}{3}} a_1 \left(\frac{Z}{d}\right)^{-0.11} = 204^{\frac{1}{2}} 0.66^{\frac{1}{3}} \times 1.42 \times (4)^{-0.11} = 15.2$$

Then, $h_{conv} = \frac{\lambda_{He} Nu}{L} = \frac{17.84 \times 10^{-3} \times Nu}{1.5 \times 10^{-3}} = 11.9 \times Nu$ W.m^{-1}.K^{-1}

and $h_{simu} = h_{conv} \times \frac{\text{"Sum of the aera of stagnations regions"}}{\text{"boundary aera"}} = h_{conv} \times \frac{22.5}{56.11} = 4.77 \times Nu$

Thus, with the assumption Nu=15.2, $\mathrm{h_{simu}} = 72.4\ \mathrm{W.m^{-2}K^{-1}}$

Considering all other parameters constant elsewhere, heat transfer is 64% less efficient with argon than with helium. This is essentially due to the smaller thermal conductivity of argon. Obviously, beyond this consideration, the physics of argon plasmas and in particular the metastable-chemistry will be considerably different from those of Helium plasma. Regarding the comparison between Helium and argon plasma. It would be simplistic to say that argon plasma generates less or more heat transfer than He plasma.

VI.1.5.7 Evaporation

Evaporation takes place if the there is moisture at the surface of the skin. A quantity of thermal energy equivalent to the latent heat of evaporation multiplied by the quantity of evaporated water is removed from the surface of the skin. Sweating is a very efficient means for some animals (like humans) for evacuating the heat. However, it turns out that rodents do not sweat since rodents have not sweat gland [292]. The evaporation is not taken into account for most simulations.

An expression of the evacuated power per unit area is given in [293] and Wilson & Spence [275] for human skin

$$\mathrm{q_{ev}} = 9.66 \times 10^{-8}\ (\mathrm{Ts} - \mathrm{Text})^{0.25} \times (10^{0.0265\ \mathrm{Ts}} - \mathrm{RH} \times 10^{0.0265\ \mathrm{Text}})\ \mathrm{W.m^{-2}}$$

Where Ts is the temperature of the skin; Text is the temperature of the air in contact with the skin; RH is the relative humidity of the ambient air.

The following orders of magnitude help to understand the efficiency of the sweating in the cooling of the skin.

Numerical example:

With $\mathbf{Ts} = \mathbf{30}$ °C and Text = 20 °C, RH=0%, $q_{ev} \sim 19\ W.m^{-2}$

with $\mathbf{Ts} = \mathbf{45}$ °C and Text = 20 °C, RH=0%, $q_{ev} \sim 58\ W.m^{-2}$

with $\mathbf{Ts} = \mathbf{70}$ °C and Text = 20 °C, RH=0%, $q_{ev} \sim 318\ W.m^{-2}$ (order of magnitude of natural convection at this temperature ~ 324 W.m^{-2}. The losses by radiation, natural convection and evaporation are compared in Fig 163. In the case of human skin, and when the humidity is 50%, the radiation losses are predominant (red curve).

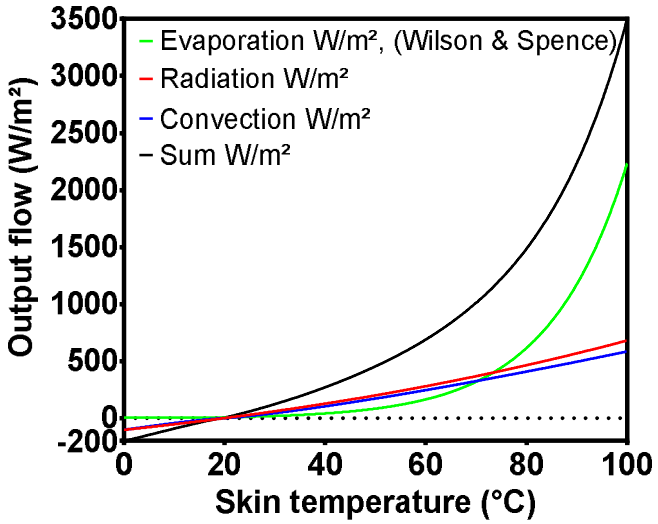

Fig 163 Thermal flux coming out of the skin (algebraic value) according to the temperature. Case of human skin, when RH=50%. $q_{conv} = 2.44\ (Ts - Tair)^{1.25}\ W.m^{-2}$. $q_{rad} = \sigma(Ts^4 - Text^4)W.m^{-2}$, $\mathrm{q_{ev}} = 9.66 \times 10^{-8}\ (\mathrm{Ts - Text})^{0.25} \times \left(10^{0.0265\ \mathrm{Ts}} - \mathrm{RH} \times 10^{0.0265\ \mathrm{Text}}\right)\mathrm{W.m^{-2}}$

Several expressions are given in the literature. Deng et al. [293] provide another expression of heat transfer by evaporation:

$$\mathrm{q_{ev}} = \mathrm{Qdif} + \mathrm{Qrsw}$$
$$\text{with} \quad \mathrm{Qdif} = 16.7\mathrm{hW_{rsw}}(0.256\mathrm{T_s} - 3.37 - \mathrm{P_a})\ \mathrm{W.m^{-2}}$$
$$\text{with} \quad \mathrm{Qrsw} = 0.354 * (0.256\mathrm{T_s} - 3.37 - \mathrm{P_a})\ \mathrm{W.m^{-2}}$$

Where W_{rsw} is the skin humidity (0 mean that the skin is dry, 1 mean that the skin is entirely wet); P_a is the vapor pressure (in kPa) of water in ambient air. T_s is skin temperature. h is the heat transfer coefficient (W/m²/K), as defined in previous section.

Q_{dif} represents the heat loss which already occurs (even if the skin is dry). Q_{rsw} represents the heat loss added when the skin is wet. Unfortunately, the review [210] does not provide information on the validity of either expression. Fig 164 shows that the two models predict very different values (even for several values of W_{rsw}). A more recent study [294] indicates a value of the order of $350\ W.m^{-2}$ (nude and wet human skin at 30 °C). Which could be compatible with the model of Deng et al. Regarding the evaporation of the gel located on the surface of mouse skin, it would be necessary to propose our own model since the geometry is slightly different.

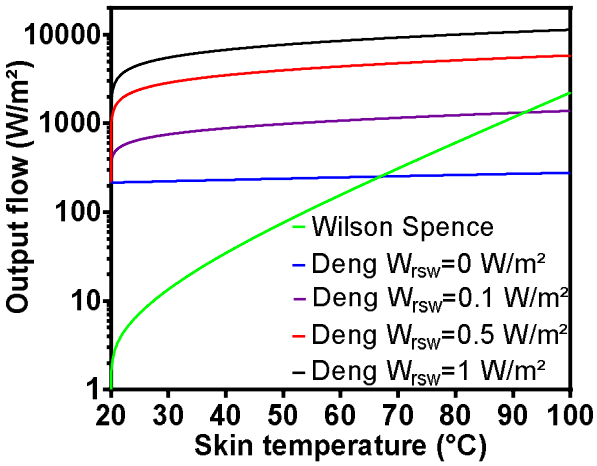

Fig 164 Comparison of heat loss by evaporation at the surface of human skin, according to the two model of evaporation.

VI.1.5.8 Plasma source

This section describes how thermal transfers caused by plasma treatment are taken into account in simulations. There are some studies which describe thermal energy balances during plasma-surface interactions ([295] and [296]). Unfortunately, it describes plasma at low pressure, and very little is known about thermal transfer for cold plasma at atmospheric pressure.

Consequently, the thermal transfer is modeled either by a constant surface term or by the convective transfer of heat described in the previous section. No experimental data on gas temperature were acquired during these experiments. We do not know what the origin of thermals transfers is. Are they due to the impacts of charged particles on the surface or to the convective heat transfer? It could be a mixture of the two terms. The available data do not enable to differentiate the two source terms.

One of the following two assumptions is made; in order to propose gas temperatures and heat flux which enable to reproduce surface temperature over time.

- Thermal transfer due to plasma is constant over time as long as the plasma is turned on. $q_{plasma} = \text{Constant}\ \text{W.m}^{-2}$ on skin boundary, if plasma is on, else $q_{plasma} = 0$. We assume that gas temperature (if study regards plasma jet) is ambient temperature. Thus, convection contributes to decrease the temperature of the skin.
- Thermal transfer is only caused by convection of hot gas. $q_{Conv} = h_{simu}(T_{gas} - T_{skin})\ \text{W.m}^{-2}$ at skin boundary when plasma is on. Gas temperature is constant.

With more information on the dynamics of heating, for example, more data on the evolution of surface temperature as a function of time, it would be possible to quantify the importance of the two terms (one will be constant over time, the other evolve with the surface temperature). With gas temperature measurements given by spatially resolved spectroscopic measurements, for example, it would be possible to refine convective transfer models. It would be possible to reproduce the evolution of surface temperature by simply projecting helium heated without plasma.

With a better experimental knowledge of convective transfers, it would be possible to identify the contributions specific to the plasma. This information on the origin of thermal transfers would make possible to control them better: one could choose to amplify or limit thermal transfers by playing on the nature of the flow (for example by introducing vorticity and playing with nozzle geometry and turbulence)

Regarding damages predictions, we have enough data to model and simulate the field of temperature and thus the field of damage.

The approach consists of reproducing the evolution of surface temperature either by choosing the value of q_{plasma} or by choosing the gas temperature. Since surface temperature is somewhat sensitive to these parameters, observations constrain the values of q_{plasma} or gas temperature in restricted ranges. Then, we observe if the thermal damage corresponds to the experimental observations.

The main source of uncertainty in this model is the value of h. However, this uncertainty will not affect the ability of the model to predict damage, since, for a given h, qplasma or gas temperature are constrained in such a way that experimental observations of surface temperature are respected. Tgas and qplasma are simulation products in this approach. q_{plasma} and h are also constrained by the measurements of power consumption.

VI.1.6 Physical properties of living tissues

This paragraph summarizes the numerical values used to model the tumor according to the physical model made in the previous section. Unless otherwise stated, the values below were used to perform the simulations. The exact properties of the tissues are not always known for the mouse. However, the range of values they can take is often very limited. Finally, the results section contains a paragraph dealing with the effects of changes in biological parameters. We show that these modifications have little effect on the prediction of the zones affected by the thermal damage.

Tumor and the skin above it are modeled as a sphere of radius 5 mm. This is an axisymmetrical 2D-Simulation. We defined four layers, which have constant thermal properties. Table 21 gives the value of parameters regarding conductive heat transfer. The last column contains references. When experimental values for mouse skin were not found, the value for human skin was used. Regarding the specific heat of the fat layer, instead of using the value of [210] (~2500 J.kg-1.K-1) which corresponds to human or obese C57BL/6 mouse (~40 g [297]), we use the value of specific heat for lean C57BL/6 mouse (20.79+ 3.58 g) found in [297]. Conductivity, specific heat, and volumetric density of the dermis and the tumor (and generally those of soft tissue) differ little from that of blood for the mammals. Thermal conductivity is in a range between 0.2 and $0.6\,W.m^{-1}.K^{-1}$. Thermal conductivity is below the thermal conductivity of water: $0.591\ \ W.m^{-1}.K^{-1}$ [298].

Table 21 Thermal properties and size of this four model describing C57BL/6 subcutaneous tumor.

Parameter unit	Layer	Value	Reference
Thickness µm	epidermis	13	[211] C57BL/6 female
	dermis	162	[211] C57BL/6 femal
	fat layer	189	[211] C57BL/6 female
	tumor	4636	Substraction
Volumetric mass density kg.m^{-3}	epidermis	1500	[210] [213]
	dermis	1116	[210] [213]
	fat layer	971	[210] [213]
	tumor	1050	Assumption =Blood density. Same assumption in [293]
Specific heat J.kg^{-1}.K^{-1}	epidermis	3600	[206][210]
	dermis	3300	[206][210]
	fat layer	3660	[297] (lean)
	tumor	3770	Assumption =Blood specific heat
Conductivity W.m^{-1}.K^{-1}	epidermis	0.235	[210]
	dermis	0.445	[210]
	fat layer	0.21	[299]
	tumor	0.561	[300]

Metabolic heat generation was described with the set of parameters given in Table 22. This term is negligible at this scale (small tumor of a small animal: a half-sphere with a diameter of 5 mm). Metabolic heat plays at the scale of the whole body (for the small animal).

Table 22 Parameters of metabolic heat generation.

Parameter	Layer	Value	Reference
Metabolic heat generation ($W.m^{-3}$)	epidermis	0	[275]
	dermis	200	[275]
	fat layer	5	[275]
	tumor	7700 (conscious)	[271]

The value of the perfusion rate is a critical parameter for evaluating the stationary and dynamic thermal response. With the conduction term, it is the term that leads to limiting thermal damage, by decreasing the temperature of the superheated tissues.

Blood perfusion in humans

Deng et al. study the possibility to detect tumor with thermal techniques [293]. In their simulation, they used a perfusion rate of $5 \times 10^{-4}\ ml/s/ml$ for normal tissue and $2 \times 10^{-3}\ ml/s/ml$ for human tumoral tissue. Holmes et al. provide the value $0.25\ ml/min/g$ (~ $4 \times 10^{-3}\ ml/s/ml$) for one human tumor [300]. This is consistent. Torvi et al. propose a model of human skin subjected to fire and use a perfusion rate of $1.25 \times 10^{-3}\ ml/s/ml$ in dermis and fat layer of human skin [215].

Blood perfusion and mice

Stott et al. describe the distribution of blood flow in each organ of the mouse [301]. Regarding skin, the paper show that perfusion rate is $0.07\ ml/min/g$ (i.e. $1.2 \times 10^{-3} ml/s/ml$). For comparison purposes, the heart, the best-irrigated organ has a perfusion rate of $3.6\ ml/min/g$ (i.e. 0.06 ml/s/ml).

The book of Orr et al. report the rate of perfusion for mouse skin and mouse tumors [302]. Perfusion rate of the skin and muscle are respectively around 0.08 ml/min/g and 0.11 ml/min/g. This is consistent with the paper cited above. Perfusion rate of the small tumor is between 0.03 and 0.22 ml/min/g. Small tumors have better blood irrigation. Big tumors have a perfusion rate in the range 0.01 and 0.08 ml/min/g. We choose the value 0.08 ml/min/g ~ 1.3×10^{-3} ml/s/ml for the simulation of dermis and tumor tissue[102].

Order of magnitude

The Mean Transit Times (MTT) of contrast agent was measured by CEUS (see Fig 124) during the experiments regarding the treatment of mice bearing CT-26 tumors. It turns out that the rate of perfusion can be obtained from this parameter if the volume of blood contained in the tumor is known. Montet et al. have determined the Vasculature Volume Fraction (VVF) of the CT-26 tumor, during experiments on angiogenesis [303]. The value of the VVF taken from this paper: VVF~ 3% means that only 3% of the tumor is made of blood vessels. Note however that this value may not correspond to that of our experiments since the experimental conditions are slightly different. In addition, because the fluorescence diagnostic has a depth of detection limited to few mm, this value represents the VVF only in the upper layer of the tumor.

Anyway, this value is used to obtain an order of magnitude and check if this value is consistent with the range $0.01 - 0.22\ \mathrm{ml.min^{-1}.g^{-1}}$, reported in the book [302]. According to the experimental results described in Fig 124: $\mathrm{MTT} \cong 40 \pm 10\ \mathrm{s}$ for CT-26 tumor. Consequently, if the tumor has a radius of 5 mm

[102] Except during reliability study where blood perfusion vary in the range $0.01 - 0.22\ \mathrm{ml.min^{-1}.g^{-1}}$ reported in the book [302].

$$V_{tumor} = \frac{4}{3}\pi r^3 = \frac{4}{3}\pi(5e-3)^3 = 0.52\ mL,$$

and blood volume is close to $V_{blood} = V_{tumor} \times VVF = 15.6\ \mu L.$

Thus, perfusion rate is obtained with

$$\omega_{CT26} = \frac{V_{blood}}{MTT \times V_{tumor}} = 7.5 \times 10^{-4}\ \text{ml.s}^{-1}.\text{ml}^{-1}$$

The experimental value is consistent with the values given in the bibliographic references (an order of magnitude $10^{-3}\ ml/s/ml$). We will consider that TC1 and CT26 tumors have the same perfusion rate and the same thermal properties.

Table 23 Properties for the computation of heat exchange due to blood perfusion, blood damages, and tissue damages.

Parameter	Layer	Value	Reference
Volumetric mass density of blood kg.m^{-3}		1050	[213] [210]
Specific heat of blood J.kg^{-1}.K^{-1}		3770	[210]
Blood perfusion ml/s/ml ω_0 (value before the effect of temperature add damages on blood vessels)	epidermis	0	[293]
	dermis	0.0013	[301] [302]
	fat layer	0.0005	[293]
	tumor	0.0013	[302]
Tblood (°C) mouse awake		37	[273]
Tblood (°C) under anesthesia		35	[273]
Damage function of blood vessel and degress of stasis (as described in VI.1.5.4)	A = 1.98 10^{106} s^{-1}, ΔE = 6.67 10^5 J/mol. $\Omega_{\text{perf}} = \int_0^t Ae^{-\Delta E/(RT)}dt$ $DS = 1 - \exp(-\Omega_{\text{perf}})$ $\omega = \omega_0(1 + 30\ DS)$ $for\ DS\ \epsilon\ [0,0.02]$ $\omega = \omega_0(1.86 - 13\ DS)$ $for\ DS\ \epsilon\ [0.02,0.08]$ $\omega = \omega_0(0.884 - 0.79\ DS)$ $for\ DS\ \epsilon\ [0.08,0.97]$ $\omega = \omega_0(3.87 - 3.87\ DS)$ $for\ DS\ \epsilon\ [0.97,1]$ $\omega = 0$ $for\ DS \geq 1$		[274]
Damage function of tissu	A = 2.984 10^{80} s^{-1}, ΔE = 5.064 10^5 J/mol. $\Omega = \int_0^t Ae^{-\Delta E/(RT)}dt$		[274]

VI.1.7 How to formulate and solve the partial differential equations of the model?

VI.1.7.1 Weak formulations of a problem defined by partial differential equation

The equation which defined heat transfer in living tissue is known as Pennes-Bioheat equation ([304]). This equation describes the thermal diffusion in the presence of blood perfusion.

$$\rho c \frac{\partial T}{\partial t} = div(\lambda \nabla T) + \omega \rho_{blood} c_{blood}(T_a - T) + q_{met}$$

Where ρ is the density; c the specific heat; λ the thermal conductivity; ω the perfusion rate; ρ_{blood} and c_{blood} are density and specific heat of blood at arterial temperature T_a; q_{met} is the metabolic heat generation in $W.m^{-3}$.

The software does not solve this equation directly. The software solves a variational formulation of this partial differential equation. For example, if we want to solve the problem of conductive heat transfer on the domain Ω with only one boundary called $\partial\Omega$ and a surface heat flux defined by $h(T - T_{air})$. Strong formulation of this problem mean that we want to find the field of temperature T defined on Ω such that

$$\begin{cases} \rho c \frac{\partial T}{\partial t} - \lambda \Delta T = 0 \ in \ \Omega \\ with \ T \ initially: \ T(x,y,z,0) = f(x,y,z) \\ \lambda \boldsymbol{\nabla T}.\boldsymbol{n} + h(T - T_{air}) = 0 \ \ on \ \ \partial\Omega \end{cases}$$

with $\boldsymbol{n}$ the unit vector normal to the surface and oriented towards the interior.

On the contrary, a weak formulation of this problem consists of finding the function T such that:

$$\forall\, g \ \in H^1(\Omega) \qquad \int_\Omega \rho c \frac{\partial T}{\partial t} g - \int_\Omega \lambda \Delta T g + \int_{\partial\Omega} \lambda \boldsymbol{\nabla T}.\boldsymbol{n}\, g + \int_{\partial\Omega} h(T - T_{air}) g = 0$$

Where $H^1(\Omega)$ is the Sobolev space of functions of $L^2(\Omega)$ whose first weak derivatives are also in $L^2(\Omega)$.

$$H^1(\Omega) = W^{1,2}(\Omega) = \{u \in L^2(\Omega) | \forall\, \alpha \ such \ that \ |\alpha| \leq 1, D^\alpha u \in L^2(\Omega)\}$$

But, by using Green's identity $\int_\Omega \Delta T g = \int_{\partial\Omega} \boldsymbol{\nabla T}.\boldsymbol{n}\, g - \int_\Omega \boldsymbol{\nabla T}.\boldsymbol{\nabla g}$

Thus, $\forall\, g \ \in H^1(\Omega) \qquad \int_\Omega \rho c \frac{\partial T}{\partial t} g + \int_\Omega \lambda \boldsymbol{\nabla T}.\boldsymbol{\nabla g} + \int_{\partial\Omega} h(T - T_{air}) g = 0$

Note that with this form, it is quite easy to add the boundary conditions which consist of known heat flux. Of course, this equation is discretized according to time. If dt is the time step; T^n the field of temperature at time t; T^{n+1} the temperature t+dt. The weak formulation becomes:

$$\forall\, g \ \in H^1(\Omega) \qquad \int_\Omega \rho c \frac{T^{n+1} - T^n}{dt} g + \int_\Omega \lambda \boldsymbol{\nabla T}.\boldsymbol{\nabla g} + \int_{\partial\Omega} h(T - T_{air}) g = 0$$

VI.1.7.2 Space and time resolution

Finite element methods solve the partial differential equation at discrete points. The choice of the mesh defining the size of the finite element is crucial for the accuracy of the results. The differential equations are solved for each vertex which defines a triangle and for the midpoints of each side of the triangle. The other points are interpolated with a quadratic polynomial function.

The Mesh is refined in the region of interest. This region contains mouse skin which has a total thickness of 364 µm. A thickness of 500 µm is added to the region of interest to correctly describe the propagation of heat and damage inside the tumor. The region of interest is clearly visible on Fig 165. Our main objective is to determine whether the thermal damage can reach the tumor or not. In that purpose, a spatial resolution of the order of 20 µm is required (small compared to the size of the layer of the skin). With the

mesh shown in Fig 165 and Fig 166, the spatial resolution is even better in the dermis and the epidermis to take into account the differences in thermal properties between the two layers. It would not make sense to increase the spatial resolution further since it would mean to calculate in an increasingly precise way an environment that is modeled as homogeneous and isotropic, whereas this is false at this scale (for example the size of a cell is around 10 µm). Temporal resolution is directly imposed by the desired spatial resolution. The characteristic length on which the heat diffuses must be of the same order of magnitude as the size of a finite element.

For example, in the dermis, thermal diffusivity is $\alpha_{dermis} = \frac{\lambda}{\rho C} = 1.2 \times 10^{-7}\ m^2.s^{-1}$.

Thus, diffusion time on a length L = 20 µm is $\tau = \frac{L^2}{\alpha} = 3\ ms$. On the other hand, it is quite expensive in terms of calculation time. We use time a step of 10 ms for most simulations which corresponds to a spatial resolution of 35 µm. A decrease of the resolution from this point does not alter the representation of the damaged areas.

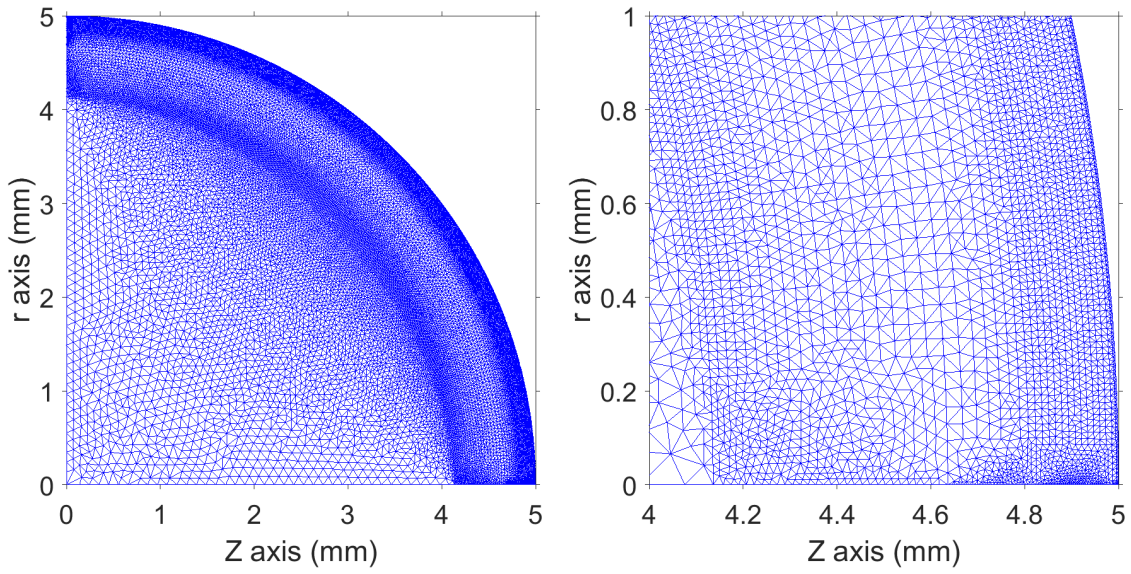

Fig 165 Triangulation of the region of interest modeling tumor and the different layers of the skin. The entire region of interest is visible on the left-hand side of the figure. Right zoom on an area of thickness 1 mm. The positions of the different layers are clearly visible because mesh resolution is increased at the level of the outermost layers to precisely describe the field of temperature. Size of epidermis, dermis, and fat layer are respectively, 13, 162, 189 µm.

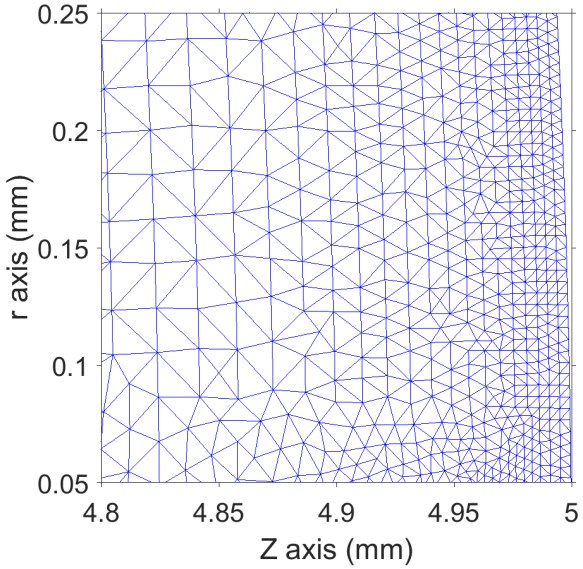

Fig 166 Triangulations applied to the outermost layers of mouse skin. For epidermis and dermis, the size of each triangle is below the size of the cell itself (order of magnitude d~10 µm). The mesh enables to describe temperature and damage field in a precise manner. At this spatial resolution, it is not the resolution of the simulation that is lacking, but the physical model which ceases to be valid. It doesn't make sense to perform calculations of the field of temperature at the subcellular or cellular scale because the medium is far from being isotropic and homogenous.

VI.1.7.3 Physical fields in finite elements method

Finite element method approximates all functions u as:

$$u(x,y) \cong \sum_{i=1}^{M} u_i \phi_i(x,y)$$

Where $\phi_i(x,y)$ are the basis functions of a space of polynomial functions which are defined on triangle describing the mesh. The basis functions of this space are continuous piecewise and quadratic functions of space coordinate. The support of each function ϕ_i is defined on triangle T_i and is zero on other triangle. Six coefficients define each function. The software does an exact resolution in the center of each side and at each vertex which define a triangle. These six values enable to find the six coefficient of the polynomial interpolator.

VI.1.7.4 An axisymmetric problem

Problem is axisymmetric with axis $r = 0$. This has consequence regarding the definition of boundary conditions and the equations. It is necessary to multiply all the function under the integral by $2\pi r$ to take the effect of axisymmetry into account.

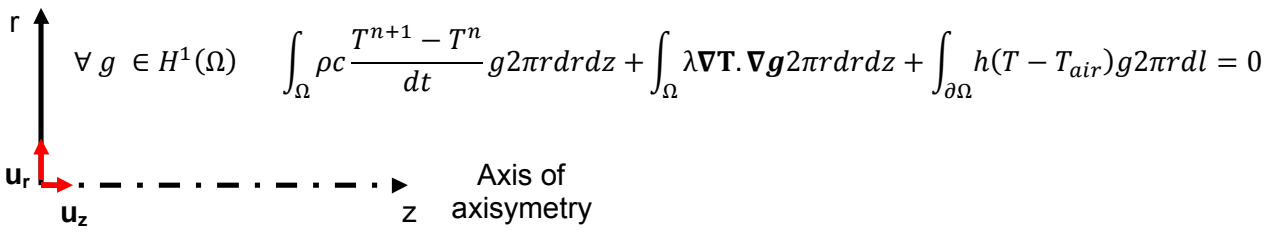

VI.1.7.5 Dealing with nonlinearity

We have seen that radiative exchanges are not negligible. Thermal transfer depends on temperature to the fourth power (σT^4). This nonlinear problem can be solved iteratively after a semi-linearization. Boundaries conditions take the form:

$$\lambda \boldsymbol{\nabla T}.\boldsymbol{n} + \sigma\left(T^4 - T_{air}^4\right) = 0 = \lambda \boldsymbol{\nabla T}.\boldsymbol{n} + \sigma(T - T_{air})(T + T_{air})(T^2 + T_{air}^2).$$

The problem is solved at iteration index m+1 (for a given time), by using surface temperature calculated at iteration m.

$$\lambda \boldsymbol{\nabla T^{m+1}}.\boldsymbol{n} + \sigma(T^{m+1} - T_{air})(T^m + T_{air})\left(T^{m2} + T_{air}^2\right) = 0$$

Convergence seems quite fast; we used only two iterations. No significant difference was found between a solution obtained with 2 or 3 iterations (the difference was only of the order of $10^{-4}\ K$). Heat exchanges due to evaporation are solved in the same way. The solver UMFPACK was used for the resolution.

VI.1.7.6 Initial conditions

For the simulation of a conscious mouse, the initial temperature is constant at 33°C. Regarding the mouse under anesthesia, final skin temperature was observed between 25°C and 30 °C. In the simulation, it is considered that the cooling of the mouse just begins. The initial temperature is chosen as a constant at 30°C.

VI.1.7.7 Boundary conditions

Fig 167 describes the position and kind of boundary conditions which was chosen to solve the problem. The region of interest is the area defined by the boundary red, green, yellow and orange n°2. No heat transfer occurs through Red boundary (perfect insulation). This mirror boundary represents the fact that axis r=0 is axisymmetrical.

The green boundary defined the surface of plasma-surface interaction. Half angle to the top, θ, defined a portion of sphere of area $\boldsymbol{2\pi r^2(1 - cos(\theta))}$. Heat transfer through green boundary occurs by radiation, convection, evaporation and plasma surface interaction.

On yellow boundary, heat transfer occurs by radiation and natural convection with ambient air at room temperature.

The function of the square delimited by orange line is to mimic an infinite medium on the boundary n°2 of the region of interest. This choice enables to obtain a realistic description of the temperature field located up to few mm below the green boundary. Boundary n°1, 4 and 3 are also mirror boundary, but they are too far to have any effect on the region of interest. The imposition of a Dirichlet condition at boundary n ° 2 leads to an unrealistic temperature distribution. The surface temperature is imposed by choice of the temperature at the border. This must be adjusted to match the surface temperature. While the surface temperature of the mouse without treatment reappears naturally in the simulation with a semi-infinite medium.

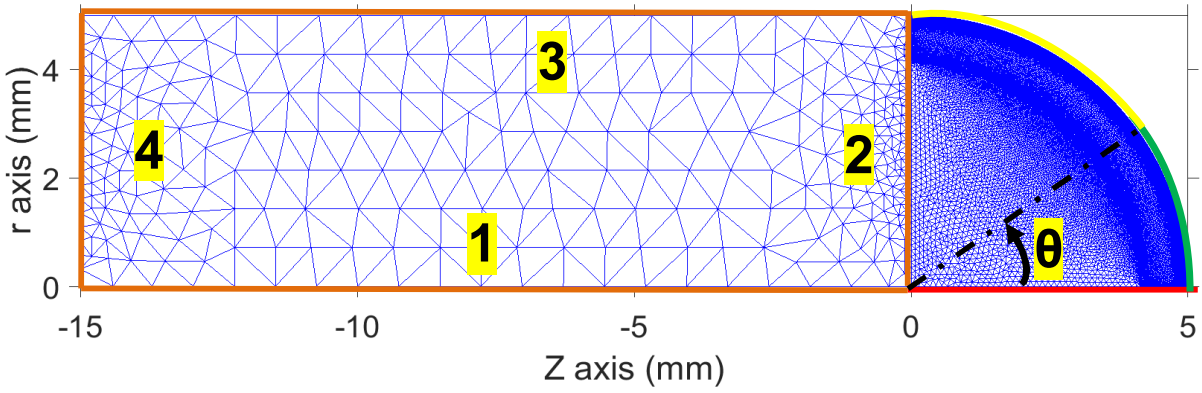

Fig 167 Description of boundary conditions. The region of interest is the area defined by boundary red, green, yellow and orange n°2. The red boundary is a mirror boundary; no heat transfer occurs through = isolative boundary. This enables to use the symmetry of the problem which is axisymmetric of axis r = 0. The green boundary defined the surface of plasma-surface interaction. Half angle to the top, θ, defined a portion of sphere of area $2\pi r^2(1-cos(\theta))$. Heat transfer through green boundary occurs by radiation, convection, evaporation and plasma surface interaction. At yellow boundary, heat transfer occurs by radiation and natural convection with ambient air at room temperature. The function of the area delimited by orange line is to mimic an infinite medium at the boundary n°2 of the region of interest. Boundary n°1, 4 and 3 are also mirror boundary. This choice enables to obtain a realistic description of the temperature field located up to few mm below the green boundary.

VI.2 Results of numerical simulations

The first objective of these simulations is to correctly predict the thermal damage induced in the skin and in the tumor. Unfortunately, the heat flux due to the plasma-skin interaction is not known. This is one of the unknowns of the model.

We know the temperature and its evolution over time. Our experiments provide the temperature on the surface of the skin. The experiments performed by the team of T. Freeman [79] provide measurements acquired inside the tissues. The modeling of heat propagation enables to find the temperature field inside the tumor and to know the severity of the damages.

As the thermal flux incident on the plasma-skin interaction surface is strongly related to the evolution of the temperature field, it is possible to find constraints on the value of the thermal flux. Simple models of the plasma-surface thermal interaction are proposed: we assume, for example, that the thermal flux is constant and uniform in the area affected by the plasma. This model has only two unknowns, the size of the plasma-surface interaction zone and the value of the incident thermal flux. For example, for a large area of plasma skin interaction, it is not always possible to determine an incident heat flux value respecting the heating kinetics.

As the model regards living tissue, we could fear that the results have a weak validity. For example, because of the biological variability of the thermal properties and the uncertainties regarding the blood perfusion of the tumor. Fortunately, this is not the case, the link between the damage and the temperature distribution is particularly robust (see Appendix E). We have varied the thermal properties of the tumor at the extremities of known ranges. For example, the conductivity of soft tissue cannot be anything; it is necessary between 0.1 and 0.7 W / m / K for the most insulating and most conductive.

The first thing to do is to simulate a situation for which there is an analytical solution. This enables to know the precision that can be expected from the numerical calculation

depending on the temporal and spatial resolutions chosen. This comparison is made in Appendix D for the sake of brevity.

The next simulation regards the behavior of the skin of a mouse under anesthesia without plasma-skin interaction. In this case, when a steady state is reached, the losses due to convection and radiation are compensated by heat exchanges with the arterial blood at 35 ° C. This enables to check that heat exchange due to the blood perfusion are realistic.

Then, the thermal behavior of the non-refrigerated multijet, the single jet, and the refrigerated multi-jet is simulated. A study is dedicated to the rate of cooling of the skin at the end of the treatment.

We then propose a discussion of methods of temperature measurements. Which ones are adapted, which ones should be avoided? The simulations illustrate how specific methods give biased results: especially those with insufficient spatial resolution.

We then propose a simulation of all the experiments described in Chernets et al. [79] and performed by the team of T.Freeman.

We are then interested in more open questions. To begin, we analyze the damage that can cause fractional treatments, e.g., repeated sequences of heating due to plasma and cooling in ambient air. Then we have found the maximum heat flux that can sustain the skin without damages.

Then a summary of the results developed in Appendix E is presented. Appendix E is a discussion of the reliability of the simulation when the thermal properties of the tumor are changed. It would be interesting to describe what happens when the skin is wet or covered with gel (comparison with the experiments of Chernets et al. [79]).

VI.2.1 Skin temperature under anesthesia

The first step is to simulate the skin of the mouse under anesthesia without treatment. Our experiments show that skin temperature is between 25°C and 30°C. Of course, the more the mouse waits under anesthesia, the more the skin cools down. The initial temperature of 33°C is selected for the entire simulation domain. The skin exchange heat by natural convection with air at ambient temperature $\mathrm{Tamb} = 20\ ^{\circ}\mathrm{C}$. When a steady state is reached, the losses due to convection and radiation are compensated by heat exchanges with arterial blood at 35 ° C. All the properties of the tumor and of the boundaries are as described in the sections VI.1.6 and VI.1.7. The simulation lasts 600 s. Fig 168 shows that temperature is not significantly different from the initial temperature below one cm depth. A surface temperature compatible with the experimental observations emerges naturally, without the need to impose an arbitrary Dirichlet condition at the boundaries defined by ($\mathrm{z} = -15\ \mathrm{mm}$).

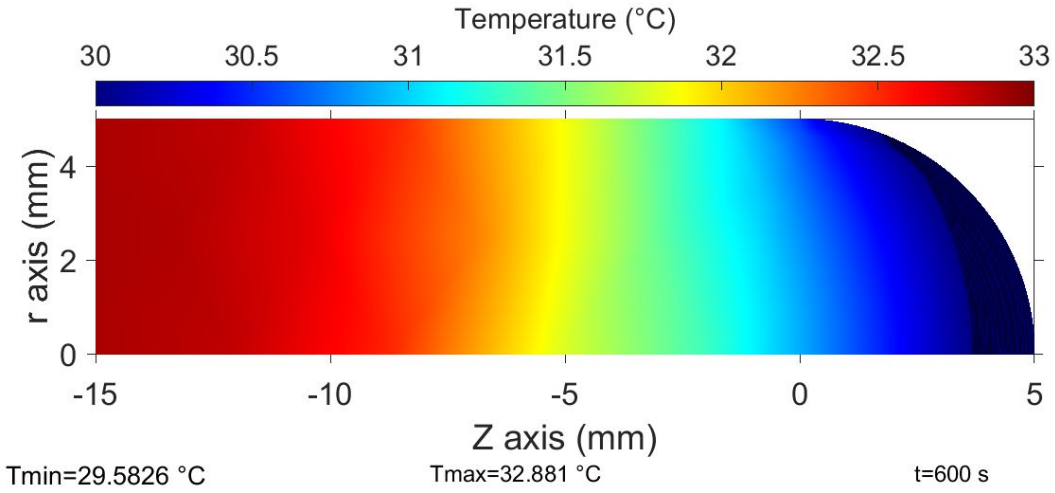

Fig 168 map of temperature on the whole area of simulation after t=600s. $T_{ini} = 30\ °C$, $\mathbf{Tamb} = 20\ °C$. No plasma.

The left Fig 169 shows the map of temperature at the same time. The temperature of the tumor is fairly uniform and of the order of 30 ± 0.5 °C. The right-hand side of this figure is a graph which represents the temperature as a function of time. Several points were chosen on axis r=0 with different depth. Of course, the deeper is the point, the higher is the temperature. Cooling kinetic seems realistic.

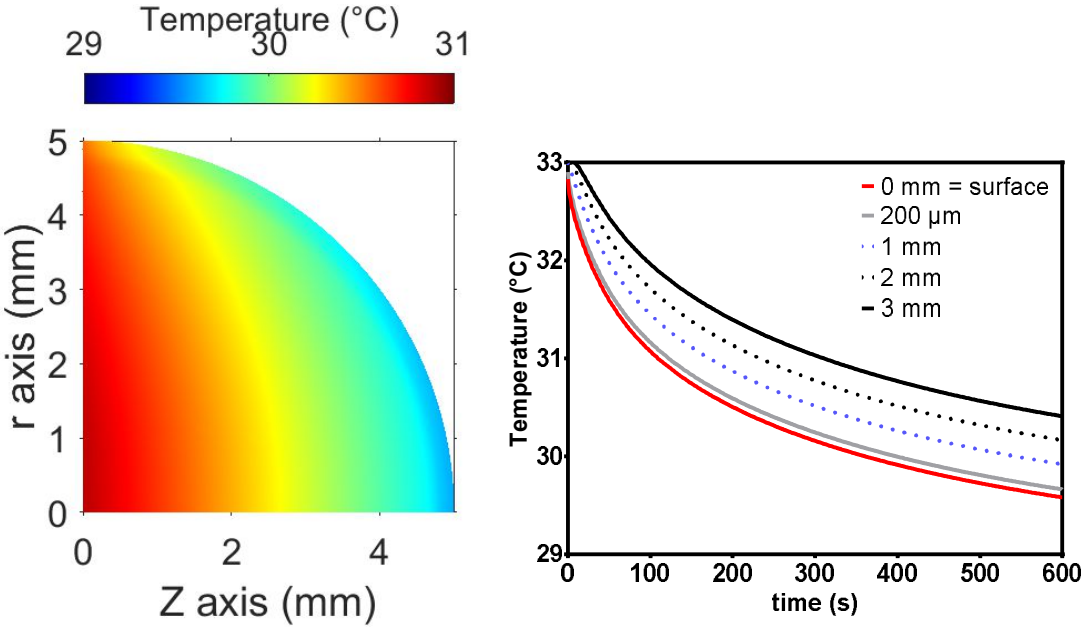

Fig 169 Left: map of temperature at time t=600 s for the region of interest which contains the tumor. Right: temperature as a function of time for points on axis r=0 and at different depth under the surface of the skin.

VI.2.2 Non-refrigerated multichannel jet

Now we will simulate the evolution of the temperature of the skin which undergoes the treatment of multi-channel plasma jet. What do we know from our experiments? What do thermal images show?

- Skin temperature after treatment of 3 or 5 min was around 45-48 °C.
- Treatment of one min gave no damages.

- One treatment of three min gave no damages, but the repetition of this treatment at two days intervals gave damages after two or three treatments.
- Treatment of 5 min systematically gave damages.

The tumor model is the same as in the previous paragraph. The initial temperature is set at 30 ° C. What are the unknown parameters?

- If the effect of plasma-surface interaction is modeled by a constant heat transfer $q_{plasma} = Cst\ W.m^{-2}$. The value of q_{plasma} must be set to respect what we know from the experiment. He temperature is set to ambient temperature = 20 °C. Convective transfer cools down the skin.
- If the effect of plasma-surface interaction is modeled by a convective heat transfer due to Helium at the temperature T_{He}. The value of T_{He} must be set to respect what we know from the experiment.

VI.2.2.1 Constant heat transfer, Helium temperature = Tamb

For q_{plasma} between 6750 W/m² and 7750 W/m², the value of surface temperature obtained after three and five min of treatment is consistent with the experimental observations. The prediction of damages enables to further refine. When $q_{plasma} = 7000\ W.m^{-2}$, the simulation does not predict sufficient damage (after 3 min of treatment Fig 170). Indeed, the maximum value of the predicted damage is $\Omega = 0.2$.

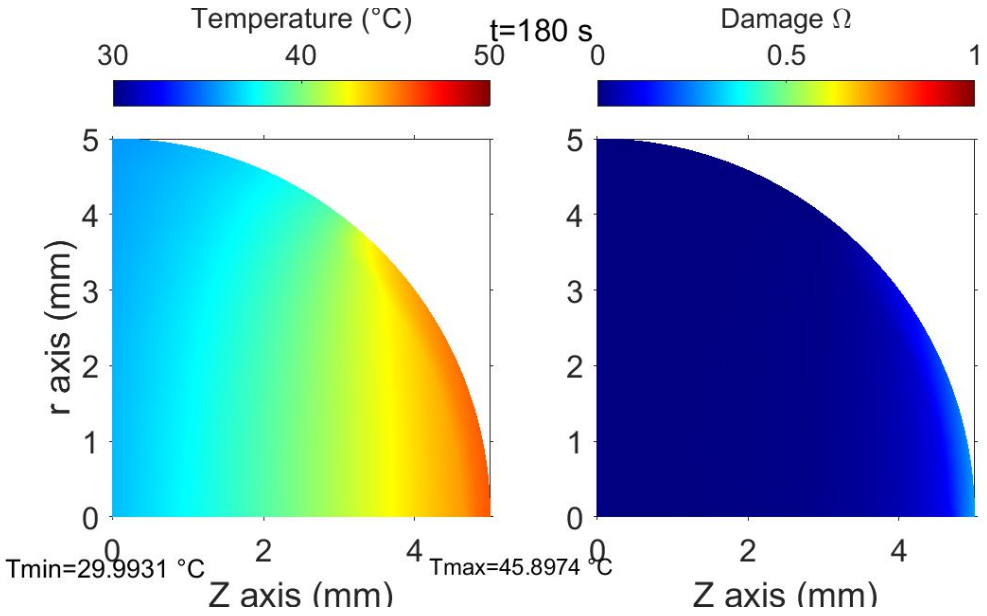

Fig 170 Field of temperature and damage after 3 min of treatment. $q_{plasma} = 7000\ W.m^{-2}$.

For $q_{plasma} = 7500$ W/m², the damages would be too severe (Fig 171). A significant part of the surface of the skin would be burned to the second degree, which does not correspond to the observations.

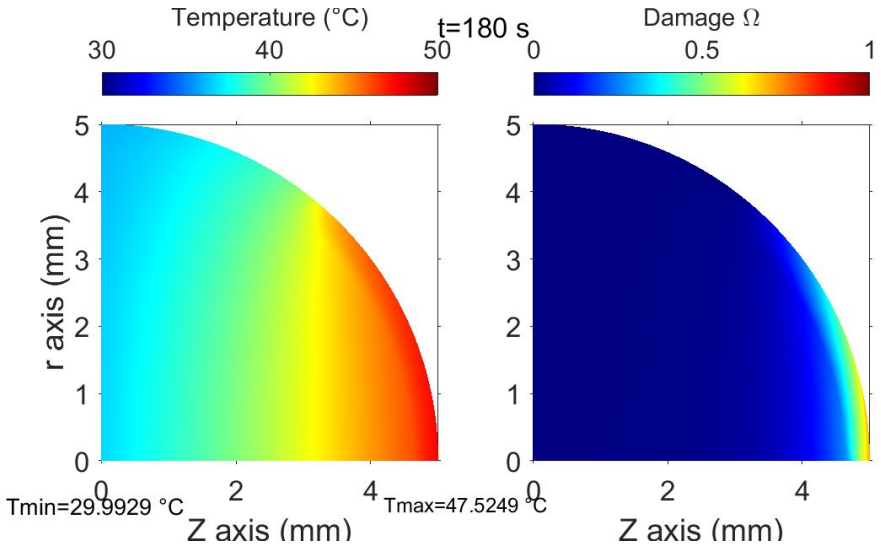

Fig 171 Field of temperature and damage after 3 min of treatment. $q_{plasma} = 7500\ W.m^{-2}$

q_{plasma}= 7250 W/m² is a good compromise. Fig 172 shows that there are no damages at t = 1 min, the damages and the temperature at 3 and 5 min are consistent with experimental results.

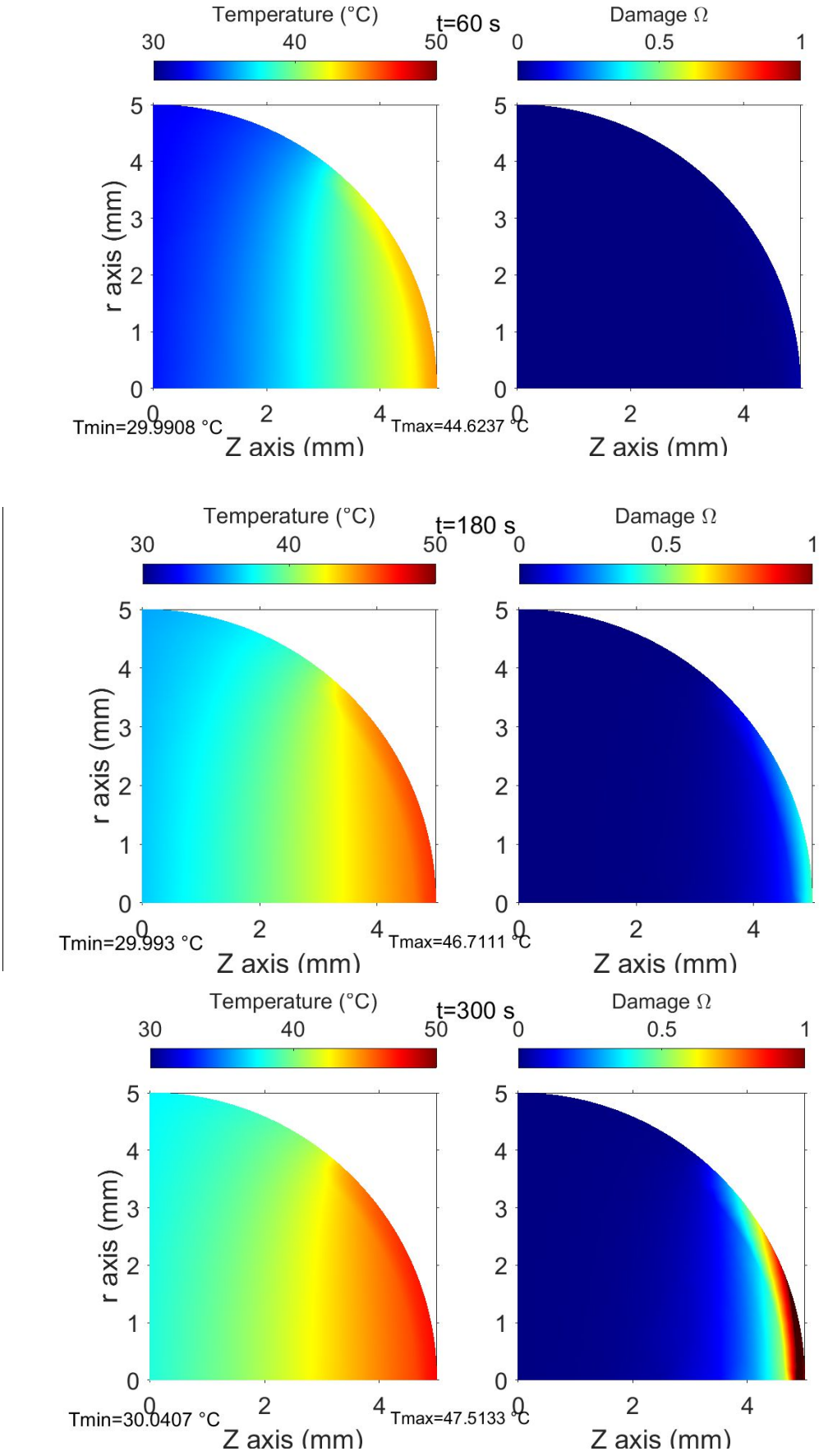

Fig 172 from top to bottom: field of temperature and damage after one three and five min of treatment with $q_{plasma} = 7250\, W.m^{-2}$.

Temperature and damages are plotted as a function of time on Fig 173 and Fig 174. Several points located on axis r=0 are chosen. The legends show the depth relative to the surface. The accumulation of damage ceases as soon as the plasma is stopped due to the rapid cooling of the surface. From 0 to 200 µm of depth, Ω is greater than 1. It means that the dermis is totally destroyed after 5 min (third-degree burn). Damage is more limited at 1 mm depth but would be problematic if the treatment was repeated.

Regarding treatments of three minutes, the damage is in the range from 0.35 to 0.58 for the outermost layers of the skin. The observation of damage after multiple plasma exposures could be explained by the progressive accumulation of damage that the mouse could not totally heal in two days.

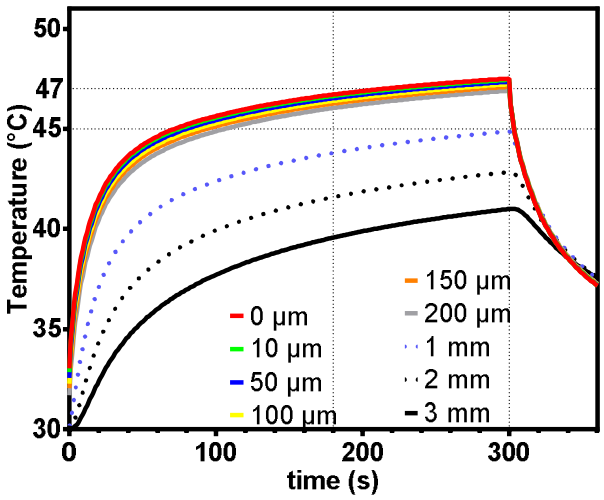

Fig 173 Temperature as a function of time for several points located on axis r=0. The legend designates the depth relative to the surface. The red curve is the surface temperature.

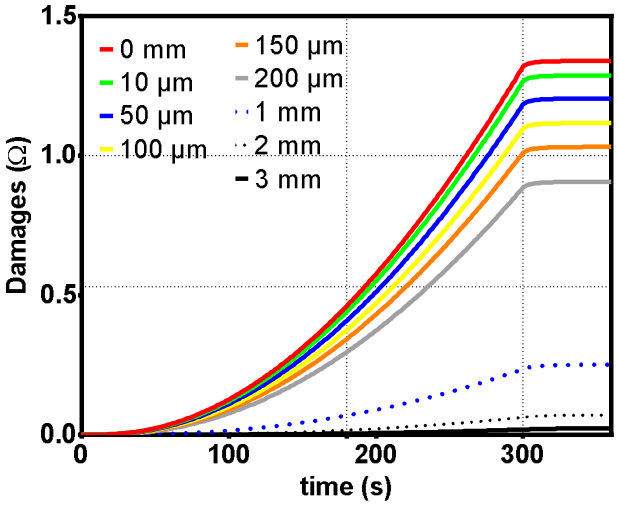

Fig 174 Damages as a function of time for several points located on axis r=0. The legend designates the depth relative to the surface. From 0 to 200 µm of depth Ω is greater than 1. It means that the dermis is totally destroyed (third-degree burn) after 5 min. For 3 minutes of treatments, the damage is between 0.35 and 0.58 for the outermost layers of the skin. Damage is limited at 1 mm of depth since $\Omega = 0.08$.

The treated surface has an area $S = \mathbf{2}\,\boldsymbol{\pi r^2}(\mathbf{1} - \boldsymbol{cos}(\boldsymbol{\theta}))$ with $\theta = 50\,°$ and $r = 5\,mm$.

Thus $S = 56.11\,mm^2$, and the total thermal power take the form:

$$P_{plasma} = q_{plasma} S = 7250 \times 56.11 \times 10^{-6} = 407\ mW$$

This is consistent with the fact that the total power of the device is of the order of 4W > 407 mW. Only 12% of total energy would take the form of thermal heating. Of course, with the assumption that the incident heat flux is constant: for example, this could be due to the impact of electrons and ions on the surface.

The consequences of a 30-minute treatment are also simulated (Fig 175). It is found that serious damage extends up to 4 mm deep. Since the tumor ablated by the plasma treatment had an initial diameter smaller than 4 mm (~ 1-2 mm at day seven), it is coherent that the plasma treatment of 30 min resulted in the total thermal ablation of some tumors (as seen in Fig 136, section VI.2.2.1).

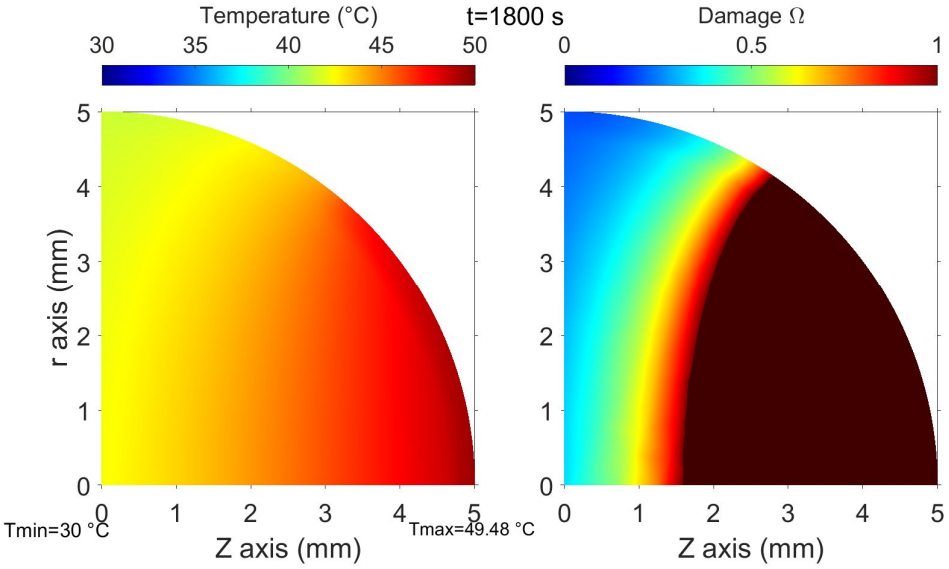

Fig 175 Field of temperature and damage after a treatment of 30 min, with $q_{plasma} = 7250\ W.m^{-2}$.

VI.2.2.2 Constant helium temperature

For T_{He} between 50 and 57 °C, the value of surface temperature obtained after three and five min of treatment is consistent with the experimental observations. The prediction of damages enables to further refine. The simulation does not predict sufficient damage after 3 min of treatment with $T_{He} = 54\ °C$ (Fig 176). Indeed, the maximum value of the predicted damage is around $\Omega = 0.3$.

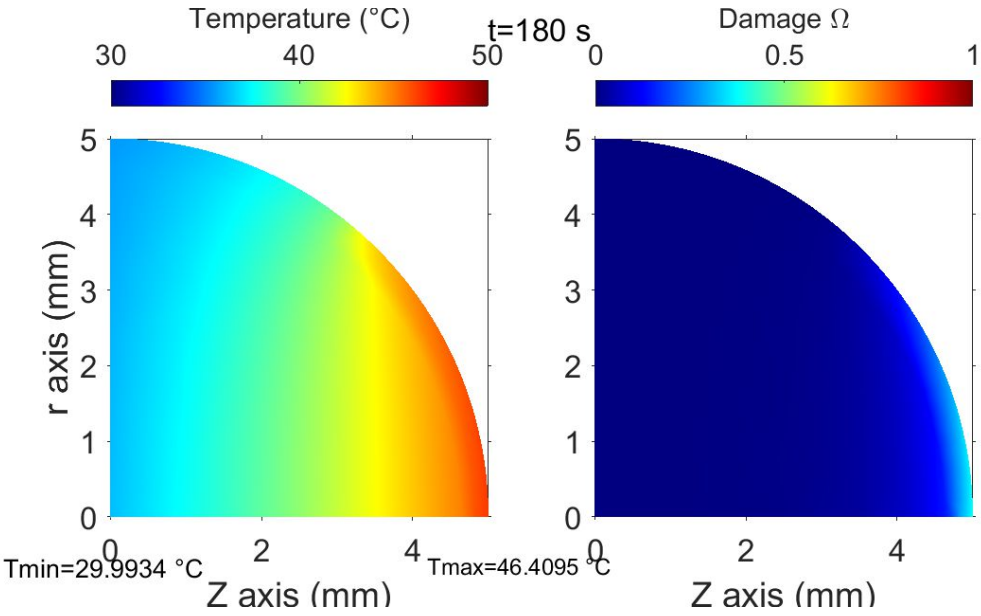

Fig 176 Field of temperature and damage after 3 min. $T_{He} = 54\,°C$.

On the contrary, with $T_{He} = 56\,°C$, the damages would be too severe (Fig 177). A significant part of the surface of the skin would be burned to the second degree, which does not correspond to the observations.

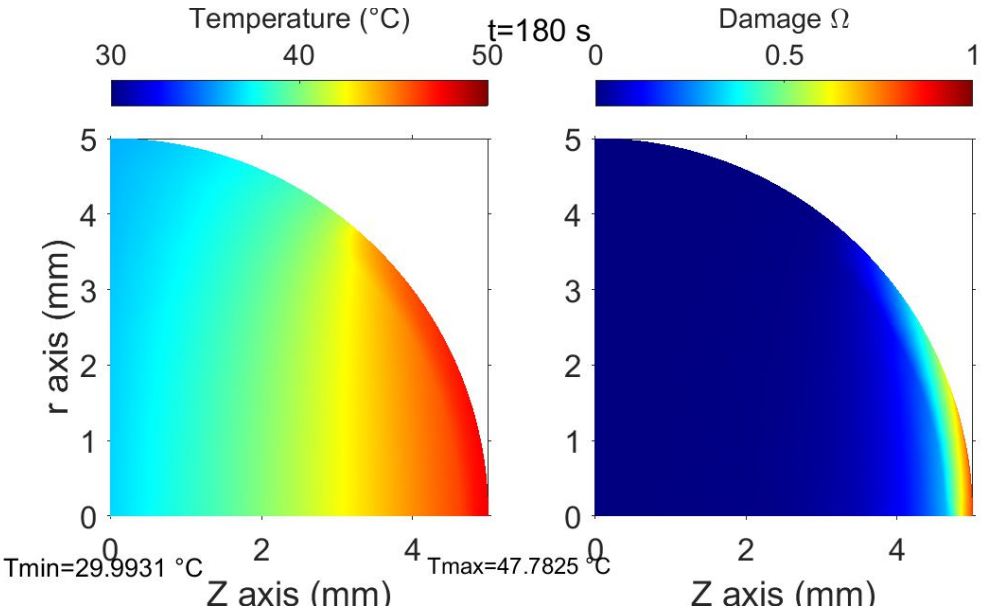

Fig 177 Field of temperature and damage after 3 min. $T_{He} = 56\,°C$.

$T_{He} = 55\,°C$ is a good compromise. Fig 178 shows that there are no damages at t = 1 min, the damages and the temperature at 3 and 5 min are consistent with the observations.

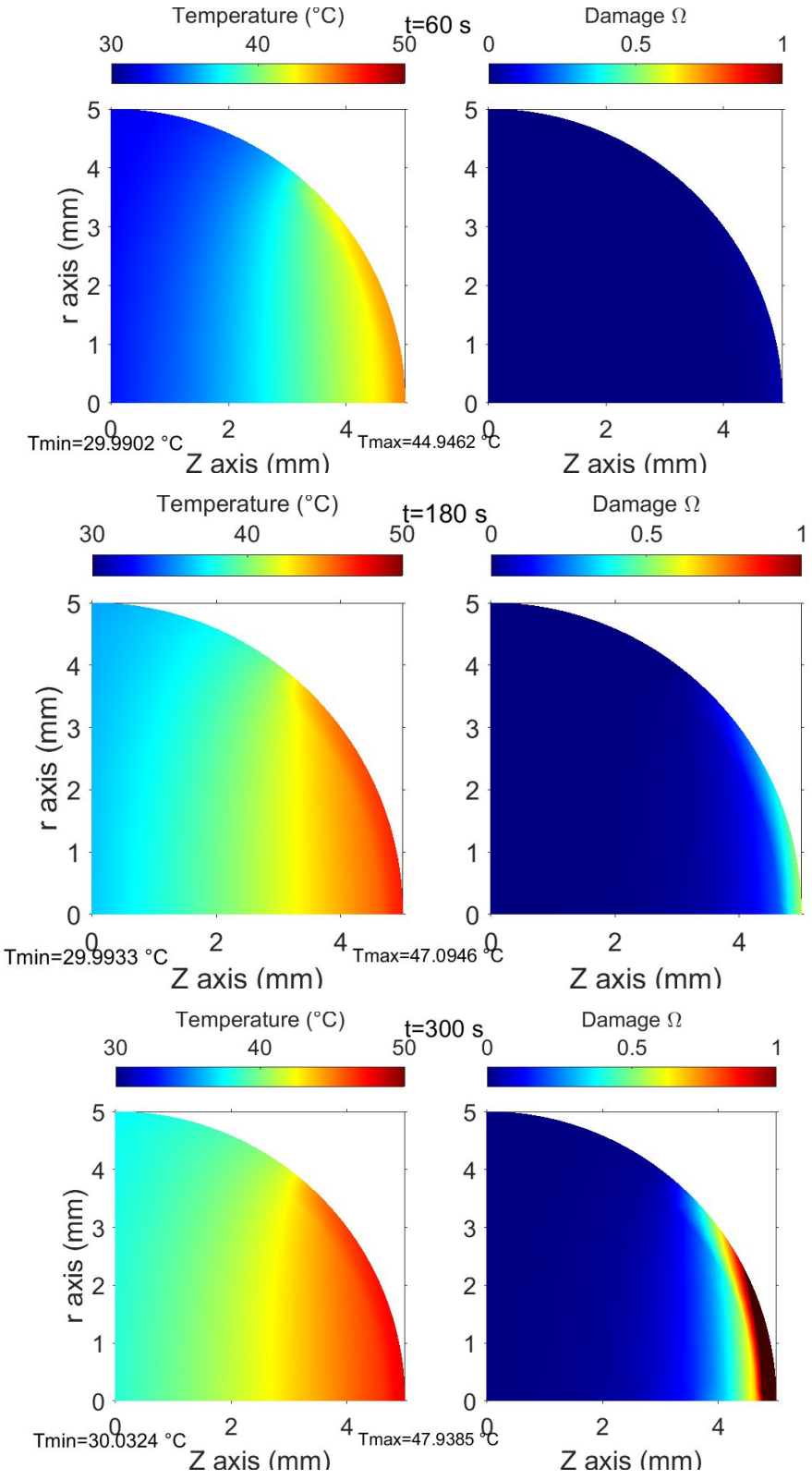

Fig 178 Field of temperature and damage after 1, 3 or 5 min. $T_{He} = 55\ °C$.

As explained in the previous section, the accumulation of damage ceases as soon as the plasma is stopped due to the rapid cooling of the surface (Fig 179). Regarding treatments of three minutes, the damage is in the range from 0.35 to 0.55 for the outermost layers of the skin (Fig 180). The observation of damage after multiple plasma

exposures could be explained by the progressive accumulation of damage that the mouse could not totally heal in two days.

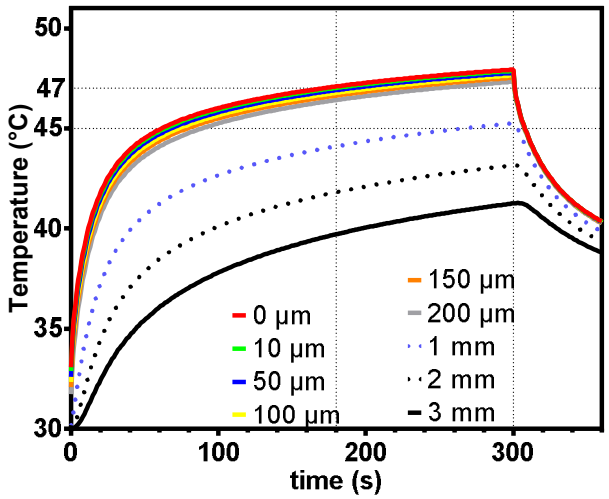

Fig 179 Temperature as a function of time for several points located on axis r=0. The legend designates the depth relative to the surface. The red curve is the surface temperature.

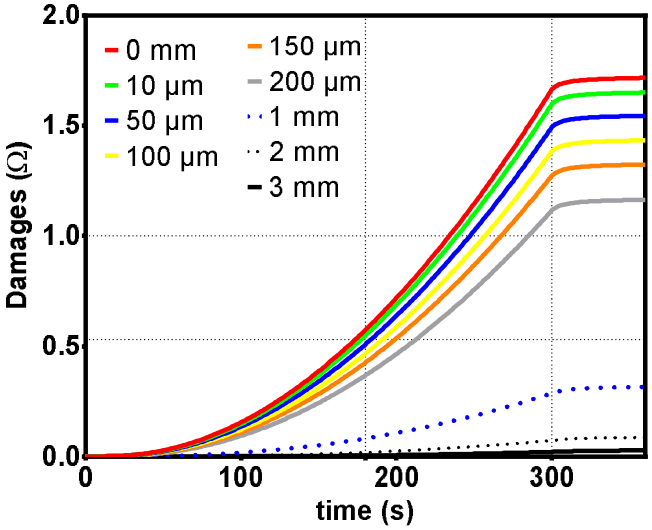

Fig 180 Damages as a function of time for several points located on axis r=0. The legend designates the depth relative to the surface. From 0 to 200 µm of depth Ω is greater than 1 after 5 min. It means that the dermis is totally destroyed (third-degree burn). Regarding 3 minutes of treatments, the damage is between 0.35 and 0.55 for the outermost layers of the skin. at 1 mm, the damage is limited since $\Omega = 0.08$.

The power required to heat the helium at 55 ° C flowing with a flow rate D of 2600 sscm is

$$P_{Heating} = D\rho_{He}C_{He}(T_{He} - T_{amb}) = \frac{2600 \times 10^{-6}}{60} \times 0.1625 \times 5193 \times (55 - 20) = 1.3\ W$$

Where $\rho_{He} = 0.1625\ kg.m^{-3}$ is the density of Helium at 300K [277]; $C_{He} = 5193\ J.kg^{-1}.K^{-1}$ is the specific heat of helium at 300K [277]. This is consistent with measurements of the total power consumption of the device, which is of the order of 4 W > 1.3 W. Only 32% of total energy would take the form of thermal heating according

to the assumption that heat mainly comes from convective transfer. The convective transfer model leads us to assume that helium has a temperature of 55 ± 1 °C.

It can also be noted that the cooling curves are different when heat transfer is due to plasma-surface interaction with $q_{plasma} = Cst$ or when it comes from convectives transfer. This is probably due to the fact that the temperature distribution inside the tumor is slightly higher in the second case than in the first.

VI.2.3 Refrigerated multi-channel jet

Now we will simulate the evolution of the temperature of the skin which undergoes the treatment of refrigerated plasma jet. Relevant experimental results are summarized

- At the beginning, the temperature of the skin is between 8 and 10 °C.
- The mean temperature is 17 °C after 3 min.
- The mean temperature is 31 °C after 6 min.

We assume that thermal transfers are essentially caused by convective transfers between the gas and the skin. The problem then is to model how the temperature of the gas evolves over time. First, it is necessary to know the characteristic length needed to reach thermal equilibrium between gas phase and the wall. We consider the forced convection in a square pipe with sides of length a = 1.5 mm (representing one of the channels of the multichannel jet). When the profile of the velocity inside the pipe is established, ([277], p376) gives the length to establish the thermal equilibrium. This is the length that the fluid must travel to lose the memory of its initial conditions. The temperature is imposed by the temperature of the wall (here a constant surface temperature).

$$L_{th} = 4.1 \times 10^{-2} \times a \times Re \times Pr$$

Using the same flow description as in VI.1.5.6.2, Re =15.8 and $Pr = 0.680$. Thus $L_{th} = 0.7\ mm$. The fluid reaches the temperature of the wall in a few mm. Heat transfer to the wall are very effective since the channels are small and the flow is relatively slow.

Now we will model the evolution of wall temperature by those of a semi-infinite medium subjected to a constant heat flux ϕ. According to ([277], p62), this approximation is true as long as: $t \ll \frac{L^2}{\alpha_{plastic}}$, where L is the characteristic size of the medium; $\alpha_{plastic}$ is the thermal diffusivity of the medium. Thermal diffusivity of PET is given in [305]: $\alpha_{plastic} = 0.16 \times 10^{-6}\ m^2.s^{-1}$ and $L = 1\ cm$. Consequently, $\frac{L^2}{\alpha_{plastic}} = 625\ s$. The approximation may be considered as true for the first few minute and false after. This is consistent with experiments; the thermal camera images show that the device warms up to 31 ° C in 6 min.

According to this model, surface temperature takes the form

$$T_s(t) = \frac{2\phi\sqrt{t}}{\sqrt{\lambda\rho C}} + T_0,$$

For PET, $\sqrt{\lambda\rho C} = 586$ (according to [305]). Now, if we assume that the thermal flux ϕ is of the same order as the thermal flux which would be at the origin of the heating of the skin (see previous experiment with non refrigerated multichannel jet). We should have: $\phi = 7250\ W.m^{-2}$. Surface (and Helium) temperature takes the form:

$$T_s(t) = 24.7\sqrt{t} + T_0 = T_{He},$$

With this assumption, however, the heating of gas and skin is too fast (even assuming the initial temperature is 196 ° C, Fig 181). The result is totally inconsistent with experimental results. The predicted temperature is too low at the start and too high at 360 s.

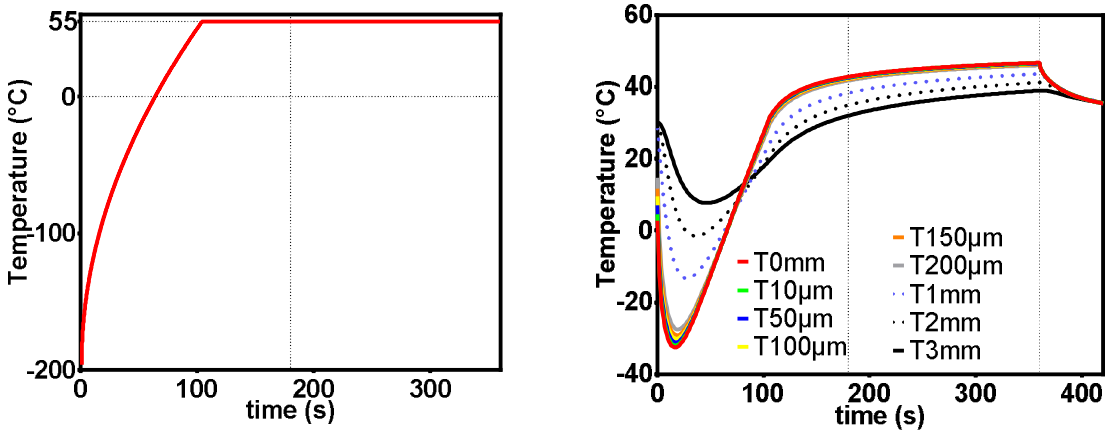

Fig 181 Left: gas temperature. Right: skin temperature for several depths. With the assumption $T_{He} = 24.7\sqrt{t} - 196\ °C$ until $T_{He} = 55\ °C$.

Since it is difficult to imagine that the heat flux due to the plasma-surface interaction is lower in the plasma source than on the surface of the skin, it is perhaps a sign that the modeling of thermal effects by a constant heat transfer $q_{plasma} = Cst$ is inconsistent.

To obtain a skin warm-up curve compatible with the experimental observations, it must be assumed that $T_{He} = 3.5\sqrt{t} - 31\ °C$, which corresponds to $\phi = 1000\ W.m^{-2}$. In this case, the temperatures given in Fig 182 are obtained. On the right side, the red curve represents the temperature at the surface of the skin. It is 17 ° C after 3 min and 31 °C after 6 min. few seconds after the start, skin temperature stabilizes between 7 and 9 ° C, This is consistent with the experiments. The simulation does not predict damage (Fig 183)

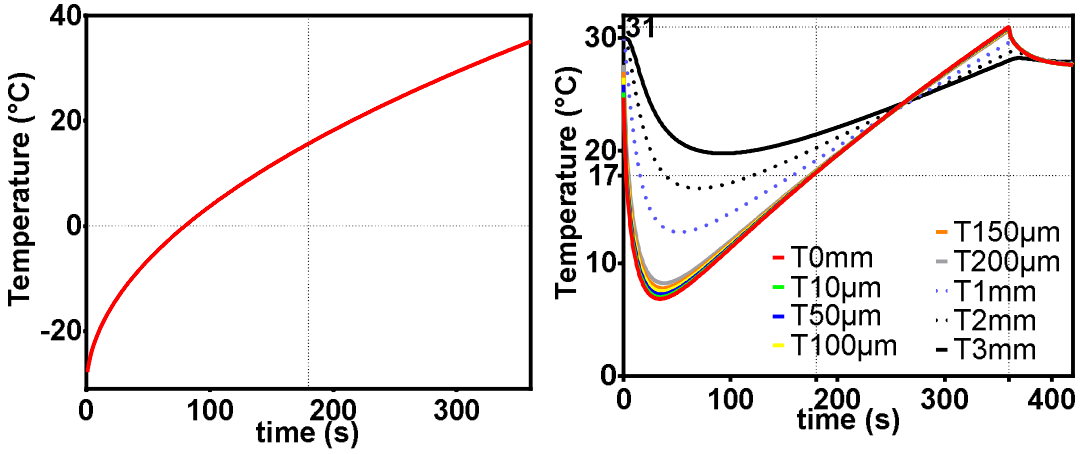

Fig 182 Left: gas temperature. Right: skin temperature for several depths. With the assumption $T_{He}(t) = 3.5\sqrt{t} - 31\ °C$.

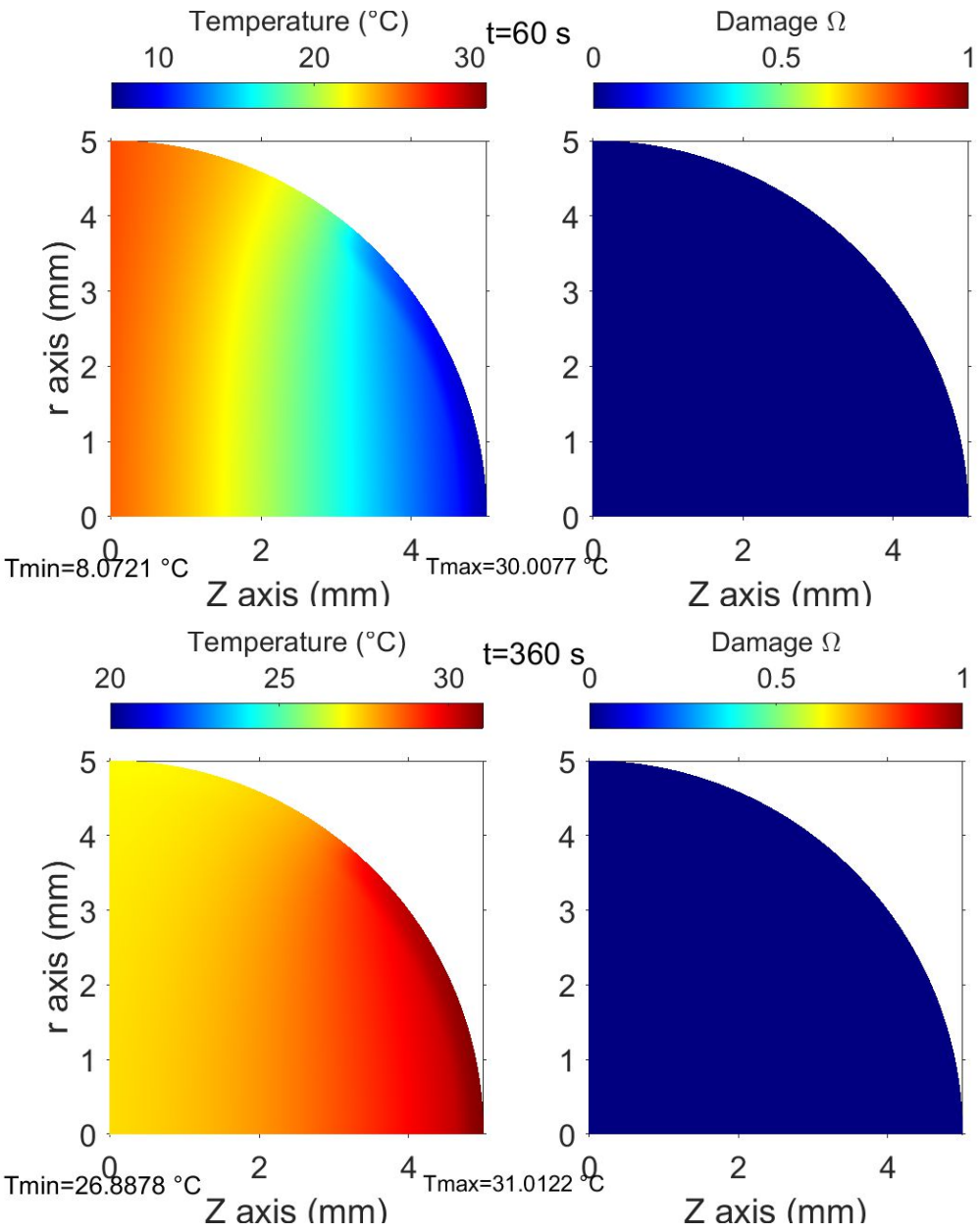

Fig 183 Field of temperature and damages. Top: time t= 60s. Bottom: time t=360s.

VI.2.4 Surface cooling after plasma-treatment

The purpose of this section is to compare the experimental results which regard the cooling of the tumor with the simulations. Several infrared images of the tumor were acquired at different times during the cooling of one tumor. For each image, the maximum temperature of the tumor is recorded. Table 24 shows three pictures of a mouse during the cooling, which follows a 6-min exposure to the refrigerated plasma-jet. This temperature will be compared with the maximum surface temperature given by the simulation (the temperature of the point defined by r = 0 and z = 5 mm).

Table 24 Infrared picture of a tumor treated during 6 min with the refrigerated multi-channel plasma jet. The picture of the second line is acquired 8 s after that of the first line. Picture of the third, 12 seconds later. The three images have the same orientation. The maximum temperature is visible in the third column.

Time	Infrared image	Maximum temperature
The first image defines the time t =0 s	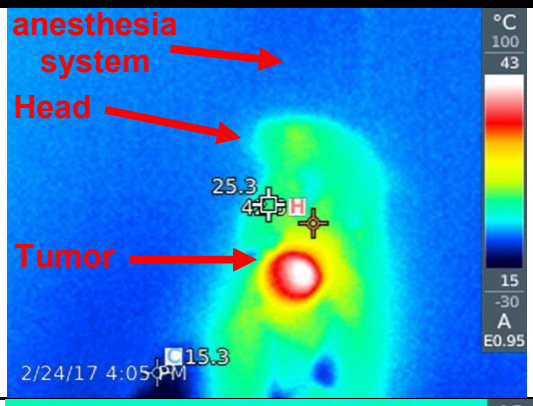	**43** °C
t = 8 s	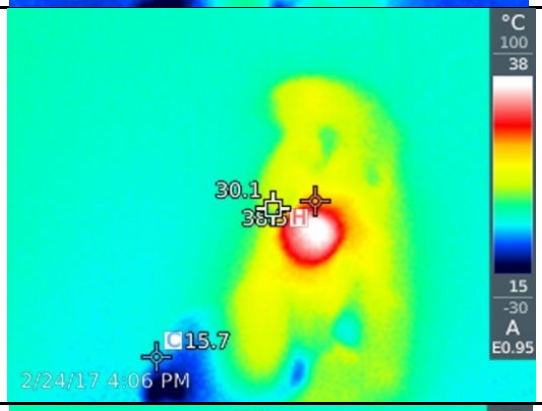	**38.5** °C
t = 12 s	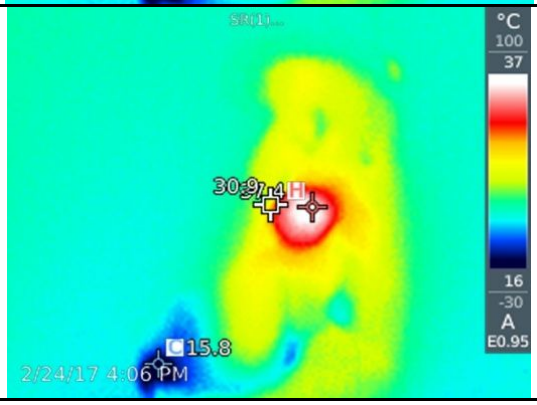	**37.4** °C

Unfortunately, this type of use of infrared images was not foreseen when the experiment took place. The infrared images were used to attest that the tissues were not subjected to hyperthermia. Consequently, there is not many usable data, because it is necessary to have at least two successive pictures of the same tumor. Moreover, there is uncertainty regarding the time between the end of plasma-exposure and the acquisition of the first picture. This time is of the order of five seconds or less, but, without the exact value, it is not possible to use the first image. Only the interval of time between two images (provided by the image metadata) can be exploited. Ideally, it would have been necessary to film the cooling of the skin.

Fig 184 shows the maximum temperature as a function of time for several mice. The first image defines the time $t = 0\ s$. It can be seen that among the measurements which start from the same temperature at $t = 0$ gives dispersed measurements after cooling. Several factors could explain this dispersion:

- Differences in the distributions of temperature $T(\overrightarrow{\boldsymbol{M}})$ from one mouse to another due to the inhomegeity of the treatment, area of plasma-skin interaction.
- Differences in biological parameters of the tumor from one mouse to another $\omega_{tumor}, T_{blood}$.
- Differences in thermal environment, enhancement of the natural convection...

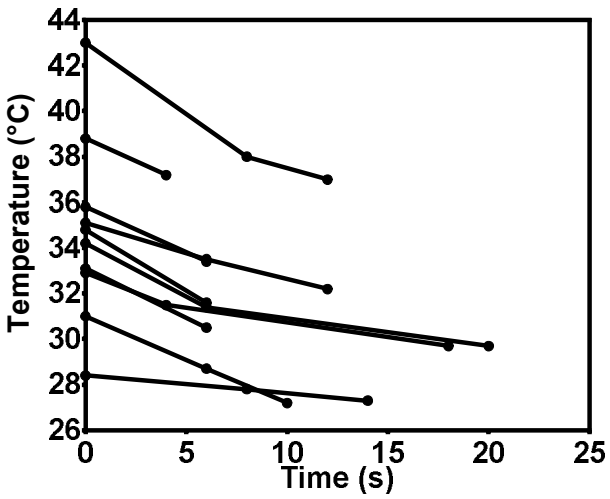

Fig 184 Maximum temperature of the surface of the skin as a function of time. The pictures were acquired during the in-vivo experiments described in section V.3.2. These experiments concern the cooling of the skin after an exposure of 6 min to the refrigerated multichannel plasma-jet.

Fig 184 shows that the speed of cooling is of the order of several[103] °C for 5 s when T>30 °C. Now, we compare this observation with the simulations. The first point (at time t=0 s in Fig 184) of each set of measurements is positioned on the curve which represents the temperature as a function of time.

For the sake of clarity:

- The experimental data are represented by different sets of dots (from A to J). Each set corresponds to the data acquired on one mouse.
- The results of the simulation are represented by a continuous line.

[103] that why it is assumed that final skin temperature was between 45-48°C during non refrigerated multichannel-jet experiments..

- The first point of each set (from A to J) is positioned on the curve. Then, the other points are positioned with respect to the first point according to the measured intervals Fig 184.

The kinetic of the cooling depends on the temperature reached at the end of plasma treatment. However, the treatments were slightly different from one mouse to another since after treatment ($< \sim 5\ s$), the temperature is **31 ± 6°C** (see Fig 154 in V.3.2). Therefore, the initial conditions of the cooling are different from one mouse to another.

The total time of simulation is shown in the panel A of Fig 185. The treatment time of duration tc (indicated in the legend) is followed by cooling. The panel B shows the cooling from the moment the plasma is off. Fig 185 (panel A and B) proves that the rate of cooling at a certain temperature T, for instance, $31\ °C$, depends on the history of cooling/heating since it depends on tc (see the slope of the curve at 31 °C). The lower the maximum temperature reached by the skin, the higher the cooling rate at 31 ° C. This observation enables to obtain simulations results consistent with experimental results with reasonable assumptions about blood temperature/perfusion rate. The panel C shows the cooling curves for two treatment times and three blood temperatures.

It is therefore somewhat futile to try to obtain a curve on which all the points of measurement would be distributed since they correspond to several initial conditions. On the other hand, the approximation should be correct for similar initial conditions. In this case, it means that the initial conditions are within a temperature range with a width of less than 5 ° C. It appears in sub-figure D that:

- The black curve ($tc = 390\ s, Tb = 30\ °C$) is a good fit for the sets of data I and J. These treatments are characterized by the lowest initial temperature.
- The blue curve ($tc = 460\ s, Tb = 30\ °C$) fit the sets A, B, D, E, F, G, and H. These sets have an initial temperature between 33 and 38 °C.
- The set C is fitted by the red curve ($tc = 600\ s, Tb = 30\ °C$). (this result does not have a profound meaning: there is only two points in the set ...)
- The assumption $T_{blood} = 30\ °C$ enables to obtain simulations that explain the rate of cooling. This is a more realistic assumptions than $T_{blood} = 25\ °C$.

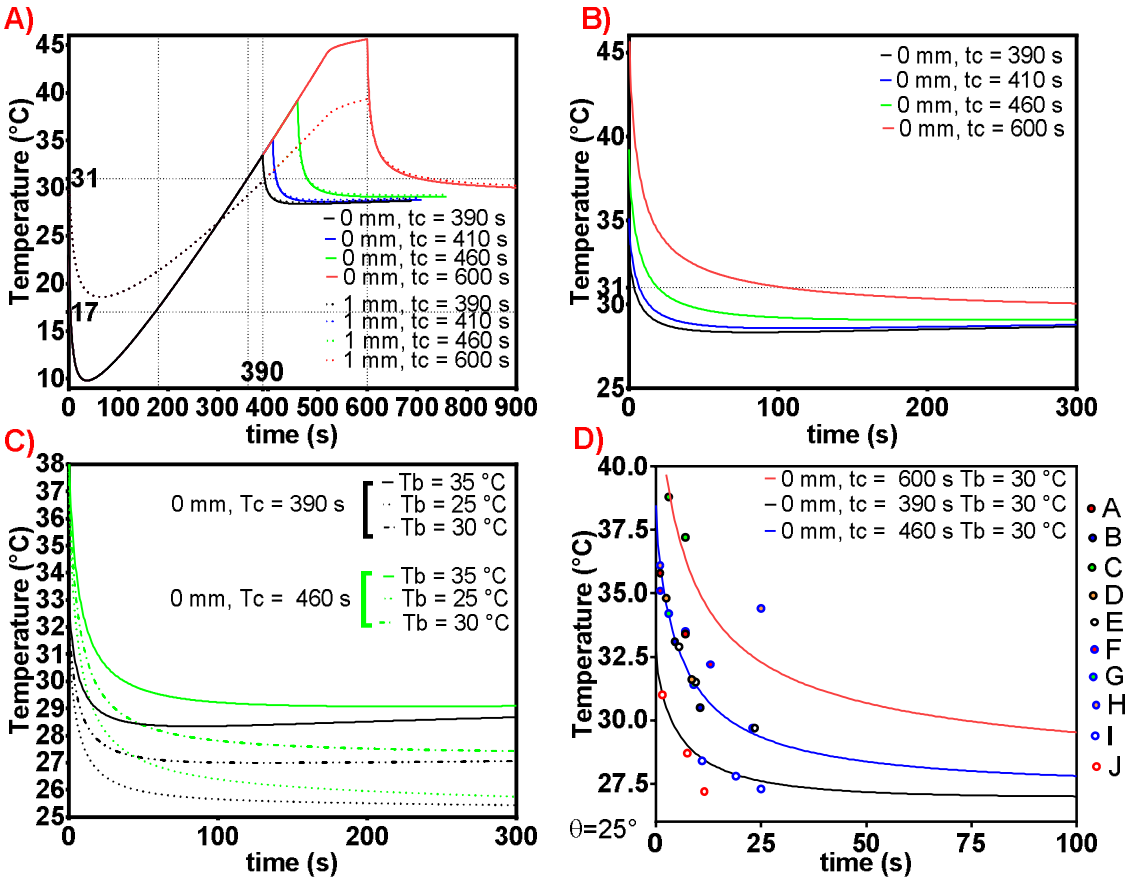

Fig 185 Temperature as a function of time, $\Theta = 25°$. A) for severals time of heating (tc = 390, 410, 460 and 600 s) and two depth (1 mm and 0 mm = surface). Only the phase of cooling is represented in the following figures. Blood temperature = $Tb = 35\,°C$ B) zoom on the cooling phase. The rate of cooling at 31 °C is different for the different durations of heating. C) skin temperature for two durations of treatment and three different temperatures of blood. D) The dots represent the experimental data. The three simulations are made with Tb = 30 ° C and three processing times (tc = 390, 460, 600 s).

In conclusion, the studies of the cooling show that:

1. The mains parameters imply in the cooling are the conduction and the thermal effect of blood perfusion (For the sake of brevity, these points are shown in Appendix G). A mistake in the evaluation of natural convection cannot explain the cooling rates.
2. The area on which the heat transfer takes place is likely smaller than what was previously imagined (see Appendix G). The simulations could be easily generalized to distributions of incident flux of any form.
3. Another interpretation is that the rate of perfusion, ω, is higher than previously modeled.
4. The cooling is a non-steady problem which strongly depends on the initial temperature. This enables to propose more realistic simulations of the cooling according to the range of initial surface temperature.
5. Very simple experiments would make possible to improve the comparisons between simulations and experiments. In particular, the recording of the cooling of the tumor with the thermal camera over time.

To conclude, it appears that dynamics of the cooling is particularly sensitive to the parameters of the model. In contrast, the reliability of the model regarding the prediction of the damage still remains (see Appendix E, where the parameter are modified for a constant surface temperature).

VI.2.5 Single channel jet

The purpose of this section is to simulate the thermal aspects of the single-channel jet. It is assumed that the proportion of consummed energy which heats the tumor is the same for single jet and multijet (without refrigeration). We must also consider that the surface treated is much smaller and that gas flow rate (thus convective heat loss) is smaller. We will begin by studying the convection.

This section uses the same line of arguments and notations as paragraph VI.1.5.6.2. The flow rate is 400 sscm, and the pipe is a cylinder of diameter 3 mm. We assume that the treated area is a portion of sphere defines by half angle to the top $\theta = 19.5\,°$. The boundary has an area of $2\pi r^2(1-\cos(\theta) \cong 9\,mm^2$.

$$\mathrm{U_{He}} = 400\frac{10^{-6}}{60}\frac{1}{\pi(1.5\times10^{-3})^2} = 0.94\ \mathrm{m/s}$$

$$\mathrm{Re} = \frac{\mathrm{U_{He}L}}{\nu_{\mathrm{He}}} = \frac{0.94\ \times 3\times10^{-3}}{12.2\times10^{-5}} = 23.2$$

With z/d=1 which corresponds to this experimental situation; [283] gives $a1 = 1.2$ and $b1 = 4.6$ in the expression of Nusselt number at stagnation point.

$$Nu(r=0) = Re^{\frac{1}{2}}Pr^{\frac{1}{3}}a_1\left(\frac{z}{d}\right)^{-0.11} = 23.2^{\frac{1}{2}}0.680^{\frac{1}{3}}\times 1.2\times(1)^{-0.11} = 4.4$$

$$h_{conv} = \frac{\lambda_{He}Nu}{L} = \frac{15.2\times10^{-2}\times Nu}{3\times10^{-3}} = 50.7\times Nu$$

$$h_{simu} = h_{conv}\times\frac{"Sum\ of\ the\ aera\ of\ stagnations\ regions"}{"boundary\ aera"} = h_{conv}\times\frac{\pi(1.5)^2}{9}$$
$$= 39.4\ \times Nu\ \ \mathrm{W.m^2.K^{-1}}$$

If we assume Nu = 5, thus $h_{simu} = 197\ \mathrm{W.m^2.K^{-1}}$. From the point of view of convective transfers the, situation is very similar with those of the multijet (197 instead of 203 W.m².K^{-1}).

Mean electric power consumed by the multijet was measured at 4 W. In this case, the simulation enables to find the incident heat flux. $q_{plasma} = 7250\,W.m^{-2}$ on 56 mm² reproduce the surface temperature and the observed damage.

Since the power consumption of the single jet is around 400 mW. Plasma-surface interaction should be modeled by $q_{plasma} = \frac{0.4}{4}\frac{7250*56}{9} = 4510\,W.m^{-2}$ by using the assumption that same proportion of electrical power gives thermal transfer.

The temperature increases slightly at the border (Tmax=36°C), but not enough to cause damage (Fig 186). This is consistent with the experiments.

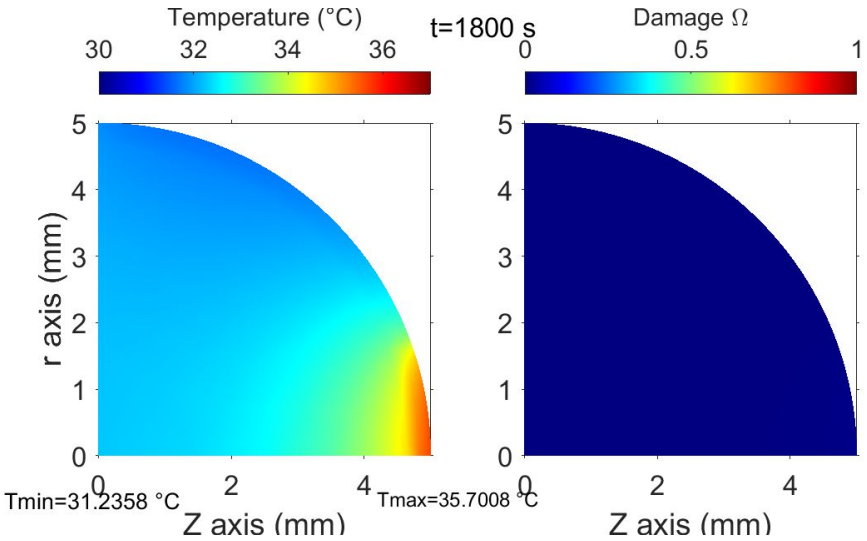

Fig 186 Field of temperature and damages after 30 min.

VI.2.6 Traps of temperature measurements

The purpose of this section is to show that many pitfalls can skew temperature measurements in the context of plasma medicine. The traps are listed one after the other; their existence is proved and quantified by calculation or by the result of simulations.

VI.2.6.1 Spatial resolution

The spatial resolution of a diagnostic describes the distance between two points below which the temperature of the two points cannot be separated. Temperature differences occurring at a smaller spatial scale are spatially averaged. This is an issue in the context of plasma medicine since the sources of heat can be very localized. For example, regarding the single-channel plasma jet, if the target and the source are immobile, it can be estimated that the surface of the skin in contact with the plasma is of the order of 1 mm².

In these circumstances, the spatial resolution of the diagnostics should be small enough; otherwise, the temperature measurement may be biased. Let's examine what happens with three measurement methods, i) infrared thermometer ii) a probe implanted in a biological tissue iii) an infrared camera.

An infrared thermometer provides averaged measurement on a surface called “Field of View”. The size of this surface depends on how far the thermometer is from the surface (see Fig 187). Often a laser is added, to visualize the area on which the measurement is acquired. Generally, the area viewed with the laser corresponds to a surface containing 90% of the signal acquired by the sensor (Fig 187). The minimum resolution is between a few mm and several cm for most infrared thermometers.

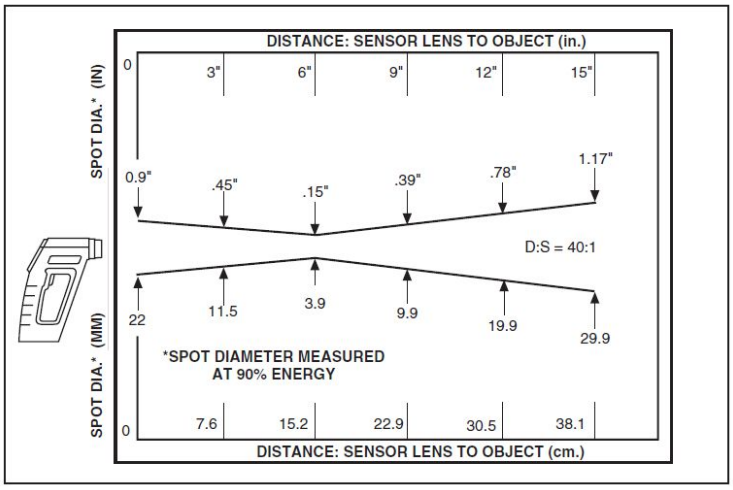

Figure 2-7 Field of View OS53x-CF

Fig 187 Link between the field of view and the distance between the object and the thermometer. The size of the spot represents 90% of the signal received by the sensor in front of a surface having a uniform temperature (manufacturer's data).

To evaluate the extent of the experimental error, we used the results of the simulation program. The parameters of the simulation are really close to those described in section VI.2.5 (simulation of the single jet). It is considered that the treated surface has a radius of 1 mm on the surface of the tumor. The tumor has a diameter of 1 cm. The half-angle to the top is therefore:

$$\theta = \frac{1}{5} \times \frac{180}{\pi} \cong 11.46\,°$$

The heat transfer is therefore done on a total surface of:

$$2\pi(1 - \cos(\theta))r^2 = 3.13\ \mathrm{mm}^2$$

The surface power is equal to $15\,000\ \mathrm{W/m^2}$. Consequently, the total thermal power is around 47 mW. The surface temperature is plotted after 10 minutes of treatment (Fig 188, **red curve**). The steady state has been reached. This surface power is chosen because it enables to exceed the temperature beyond which the damages are irreversible (42 °C). It can be seen that at 1 mm, the temperature is 42 ° C. This is also the maximum radius of the heated area. Two mm from the center, the temperature is equal to 35.1 ° C.

The **black curve** represents the temperature measured by a gun-thermometer, whose the spot of measurement has a radius of 2 mm. Since the temperature is averaged over the surface of the spot, it is considerably underestimated in the hottest area of the tumor.

The **blue curve** represents the averaged temperature on the surface whose radius is indicated in abscissa. This is the value that would provide a thermometer whose spot would have this area. If the thermometer spot has a diameter of 4 mm, the measured temperature is only 39.4 ° C. Under these assumptions, the temperature measurement is biased and hyperthermia is invisible.

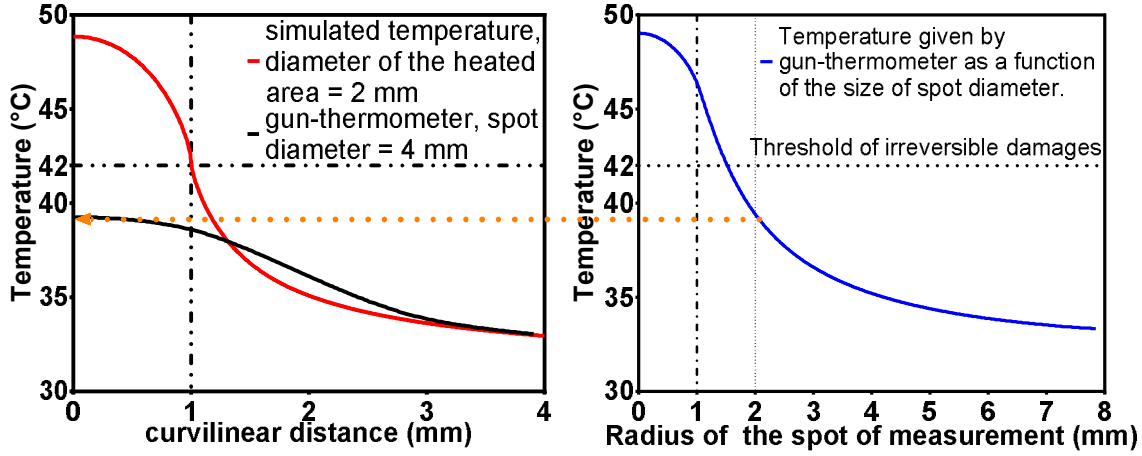

Fig 188 Left: surface temperature after 10 min of treatment (red curve). The incident thermal power is equal to $q_{plasma} = 15\,000\ W.m^{-2}$. The heated area is defined by $\theta = 11.46°$ (the heated area has a radius of 2 mm). The gun-thermometer averages the temperature by a spot of radius 2 mm. The black curve is the temperature given by gun-thermometer as a function of the position of the spot on the surface of the tumor. The average, leads to greatly underestimate the temperature in the hottest area of the tumor. Right: the blue curve represents the temperature measured in the center of the heated surface as a function of measurement spot radius.

The spatial resolution is also an issue for a probe implanted in a biological tissue. The size of the probe is related to the spatial resolution of the measurement. Just below, the biases that can induce the introduction of a probe into a tissue is discussed.

Regarding an infrared camera, the spatial resolution is much higher. It depends on the number of pixels present on the sensor, the optics, the angle under which the object is observed, its distance, the dispersion of the optics... We can estimate the spatial resolution of the image by noting that, on most acquired images, the observed surface has a size of about 5 cm. Since the cameras give an image of 480 by 640 pixels, a single pixel corresponds to approximately 78 µm. This order of magnitude illustrates the fact that thermal imaging has a much better spatial resolution than gun-thermometers.

VI.2.6.2 The time of measurement

The moment at which the measurement is made is a critical point; the previous discussion on the cooling time (section VI.2.4) has shown that the cooling occurs quickly after the end of the plasma treatment.

For example, the experimental results of Table 24 show that the temperature goes from 43 to 38.5 in 8 s. If a measurement is made at the end of the treatment, it is therefore crucial to know exactly when this measurement takes place. Otherwise, there is a risk of underestimating the maximum temperature reached by the tissues.

VI.2.6.3 Thermal conduction smearing

One of the essential qualities of a good sensor is that it does not disturb the measured object. As such, the sensors inserted in the body can induce several biases ([306], p 42 and [307]). One of them is related to the thermal conductivity of the inserted probe. If the inserted probe is too large and provided that the thermal gradients are significant, the thermal conductivity of the probe can lead to a significant underestimation of the tissue temperature. The role of thermal conductivity of the thermocouple leads and the errors

they can induce is shown in [308] and [309]. In particular, these two papers provide comparisons of the measurements made with thermocouples and fluorometric probes fixed at the end of optical fibers. This last measurement technique is much more reliable and has been used by the team of T. Freeman [79]. The operation of these probes is detailed in the review [310].

The thermal behavior of a mouse skin under which a temperature probe has been inserted is simulated. It is considered that the probe used in the work of Vandamme et al. [84] is inserted under the skin of a C57BL/6 mouse. The specifications of the probe are available on the website of the manufacturer and resellers (Fig 189).

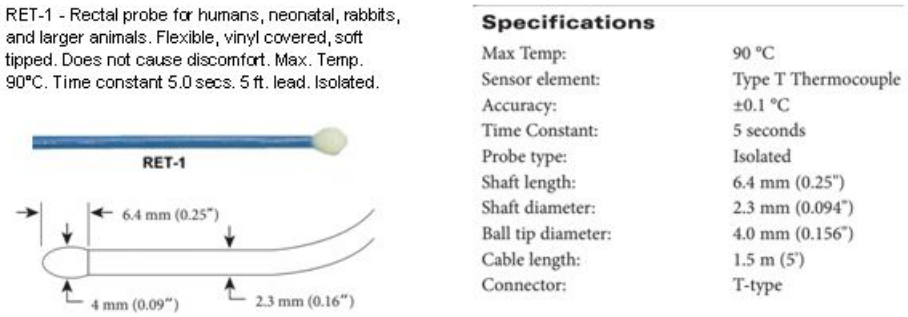

Fig 189 Specifications of the probe Ret-1, (Physitemp Instruments) used in [84]. Manufacturer's data.

The operation of the thermocouples is based on the Seebeck effect [311]. In this sensor, two wires of copper and constantan (copper-nickel alloy) are brought into electrical contact at the end of the sensor (the ball). This pair of metals is used since the sensor is a thermocouple of type T. The two leads of the sensor are electrically and thermally insulated from the outside environment. The thermal properties of cooper and Constantan are described in [311] and [312].

Unfortunately, the exact structure of the probe is not known; neither the metal constituting the ball nor the thickness of the plastic layer (vinyl) covering the sensor. However, this lack of information is not really crucial to realize the simulation since the response time of the sensor is specified (5 s). The response time is the time required for the measured temperature to reach 63% of the maximum value when a temperature step is applied to the sensor. It is sufficient to verify that the simulated sensor has this response time, to simulate how this sensor could disturb the measurements (at least in first approximation).

It is assumed that the sensor is a sphere of diameter $5/32\," \cong 3.97\,mm$. The plastic lasyer has a thickness of 400 µm, the metal part is a sphere of radius $3.17\,mm$. At time $t = 0$, the sensor which has an initial temperature of 20 ° C is immersed in water at 30 ° C. The thermal properties attributed to the metal and to the plastic layer correspond to those of copper and vinyl. The thermal properties and the initial temperature field are below:

$$\begin{aligned}(\rho, C, \lambda, T_{ini}) &= (8900, 385, 390, 20) \quad \text{for} \quad \mathrm{r} \le \mathrm{r_s} - \mathrm{dplas} \\ &= (1200, 900, 0.14, 20) \quad \text{for} \quad \mathrm{r_s} - \mathrm{dplas} \le \mathrm{r} \le \mathrm{r_s} \\ &= (1000, 4180, 0.59, 30) \quad \text{for} \quad \mathrm{r_s} \le \mathrm{r} \le \mathrm{r_{water}}\end{aligned}$$

With, the density ρ in $kg.m^{-3}$, the specific heat C in $J.kg^{-1}.K^{-1}$, the conductivity λ in $W.m^{-1}.K^{-1}$, the thickness of plastic layer $dplas = 400\,\mu m$, the radius of the sensor $r_s = 1.985\,mm$, the radius of the sphere which contains the water $r_{water} = 3 \times r_s$. r_{water}

delineates the boundaries of the model (dirichlet boundary $T = 30\,°C$). The other boundary condition is provided by the symmetry of the problem (perfectly isolating boundary). Fig 190 shows the initial value of the temperature field.

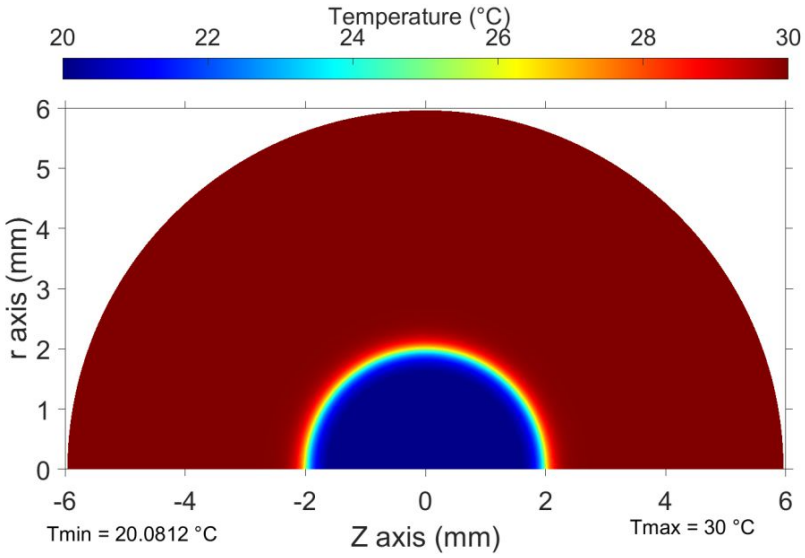

Fig 190 Field of temperature at the beginning of the simulation. Z axis is an axysymetrical axis. The blue zone corresponds to the volume occupied by the thermocouple (metal part + vinyl layer). The whole has an initial temperature of 20 ° C. The red zone represents the water in which the thermocouple is immersed (temperature of 30 ° C).

Fig 191 shows the field of temperature at time $\mathrm{t} = 5\,\mathrm{s}$. The metal part of the thermocouple has a temperature of the order of 26.4 ° C. This value would be displayed by the sensor if we assume that there are not additional thermal losses (due to the thermal conductivity of the leads).

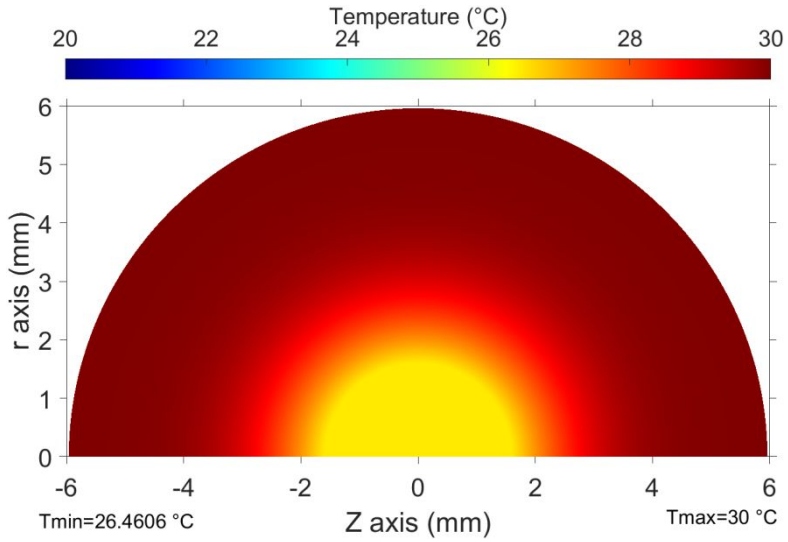

Fig 191 Field of temperature at the time t = 5 s. The metal part of the thermocouple has a temperature of the order of 26.4 ° C. Since the thermocouple has been subjected to a step of 10 ° C, this means that the response time of the sensor is 5 s.

The value of the temperature measured by the thermocouple is represented as a function of time in Fig 192. Subject to a temperature step of 10 ° C in water. It is proved that the response time at 63% is 5 s when the thermocouple is subjected to a temperature step of 10 ° C. This value is in accordance with the manufacturer's

specifications. Finally, the knowledge of the response time of the sensor is sufficient to model its interaction with its thermal environment (at least in first approximation).

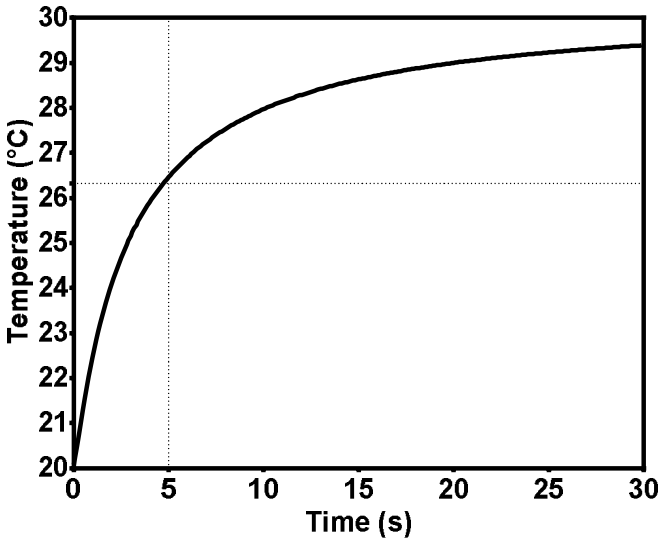

Fig 192 Temperature measurement provided by the simulated thermocouple. It is assumed that the thermocouple which has an initial temperature of 20 ° C is immersed in water at 30 ° C at the time $t = 0\ s$. The temperature is an average of the temperature of the metal part. Since the conductivity of the metal is much greater than that of those of the biological tissue or the layer of vinyl, the temperature of the metal part is almost uniform.

We will now look at the result that this implanted sensor would give under a mouse skin. Does the measurement given by this sensor correctly represent the thermal conditions that the tissue undergoes in the absence of an implanted probe?

Here, the simulation is based on the one presented in section VI.2.2 (non-refrigerated multijet). The structure of the mesh used is shown in Fig 193. The spatial resolution is increased in the skin and the plastic layer surrounding the thermocouple. The metal part does not require a precise description; the thermal gradient will be very low in the metal compared to that of the surrounding tissue, because of its high thermal conductivity.

The thermocouple is implanted just below the skin, the plastic layer of the sensor touches the lower fat layer of the skin at the z-axis. The thermocouple has the dimensions presented above: total diameter of 3.97 mm, including a layer of vinyl of thickness 400 µm. All the other properties of the materials and heat exchanges with the outside: source plasma and convection in the ambient air are already described in VI.2.2 (non-refrigerated multijet) and VI.1.6.

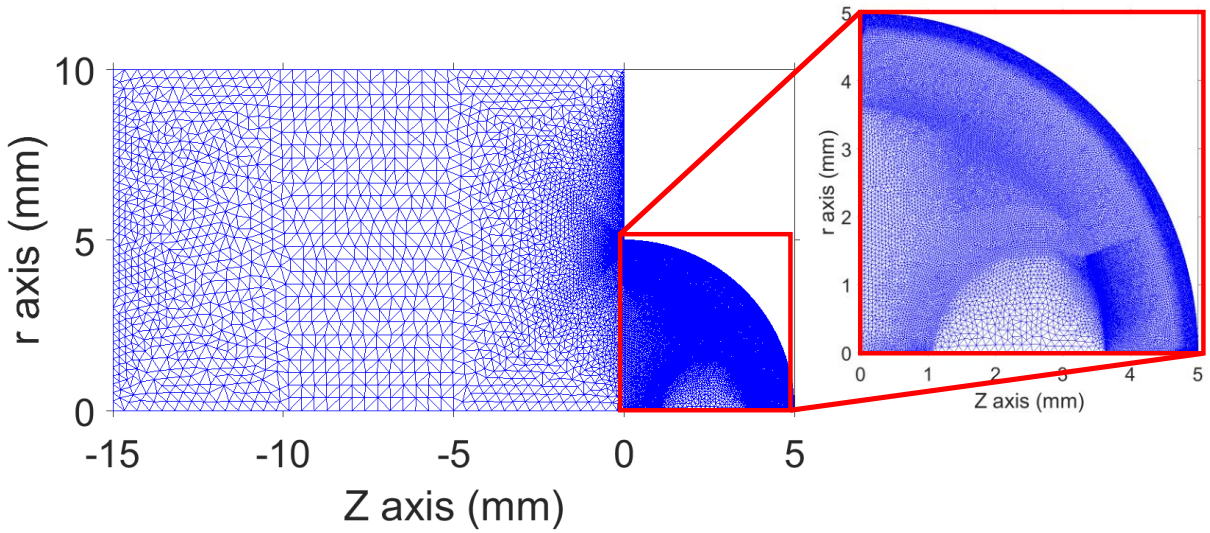

Fig 193 Mesh used in the finite element modeling of a subcutaneously implanted thermocouple.

It turns out that the presence of the thermocouple significantly changes the temperature distribution. Fig 194 shows the field of temperature with (left) or without (right) the thermocouple after 5 minutes of simulation. The heat transport with the surface is changed, which has a significant influence on the value of the surface temperature. Indeed, the maximum temperature is only 45.4 ° C with the thermocouple, against 46.9 ° C. In addition, the temperature measured by the probe (40.8 ° C) is much lower than that of the skin above.

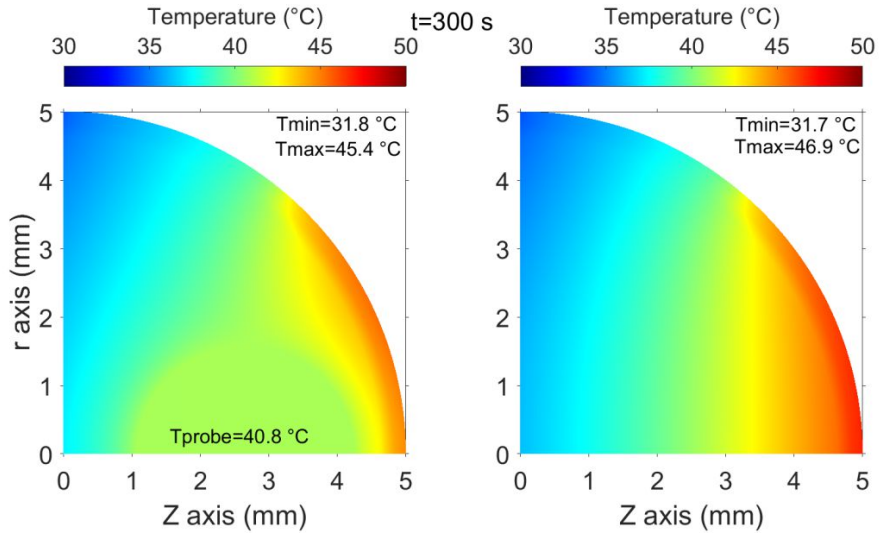

Fig 194 Field of temperature with (left) or without (right) the thermocouple after 5 minutes of simulation. The position of the metal part of the thermocouple is clearly visible on the left side of the figure. The temperature is constant in this semi-circular zone. The maximum temperature reached by the tissue is 1.5 ° C lower in the presence of the probe. After 5 min the thermocouple gives a temperature which is 6.1 °C than surface temperature.

The temperature is plotted at different depths under the skin on the z-axis (Fig 195). The dotted lines represent the simulation made in the presence of thermocouple. It is noted that the probe decreases the temperature of several degrees. This is very significant since the time required for thermal damage to occur is divided by two or three for each degree of hyperthermia added. The dashed black curve represents the temperature that

the thermocouple would measure; it is the average temperature of the metal part of the sensor. The temperature measured by this probe never exceeds 42 ° C. This means that, with this thermocouple, we would never be able to conclude that hyperthermia can play a role.

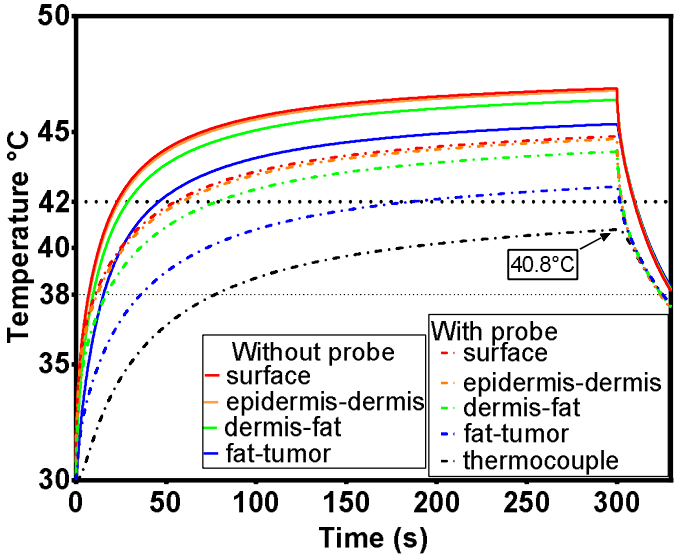

Fig 195 Simulation of the temperature field measured in several depths. Non-refrigerated-multijet

The damages (continuous curves in Fig 196) are therefore much greater than what would be expected according to thermocouple measurements. Moreover, the thermocouple itself causes a decrease in temperature which causes a reduction of the damage.

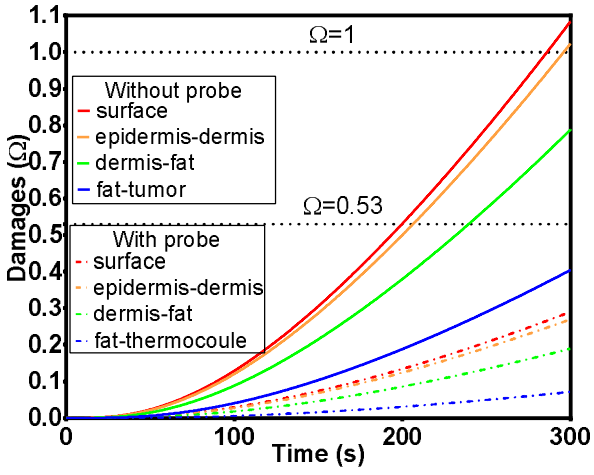

Fig 196 Damages at several depths along z-axis $(r = 0)$. The presence of the thermocouple decreases the temperature, therefore the damage to the tissues.

The study precedence concerns our multi-channel plasma. A significant area of the tumor was covered by plasma. But what happens if the plasma source is slightly smaller? What will be the influence on the temperature measured after the thermocouple?

In the following simulation, we consider that the area of skin in contact with the plasma is defined by the half-angle to the top $\theta = 30°$ (in the previous simulation 50°). The diameter of the disk delimiting the plasma-treated surface is 5.2 mm. Its area is:

$$S = 2\pi r^2(1 - \cos(\theta)) = 0.21\ cm^2$$

It is assumed that the incident thermal power is constant during 12 min: $q_{plasma} = 4000\ W.m^{-2}$. The surface exchanges heat by natural convection with the outside. Fig 197 shows the field of temperature after 10 min. As before, we find that:

- The presence of the thermocouple has a significant influence. With the subcutaneous thermocouple, the maximum temperature reached by the tissues is only 45.5 ° C (49.5 °C without)
- The temperature measured by the thermocouple does not give a true picture of the temperature actually reached by the tissues. Without a thermocouple, a significant part of the skin and subcutaneous tissue has undergone hyperthermia ($T \geq 42\ °C$), while the thermocouple measures a temperature of 38.6 ° C

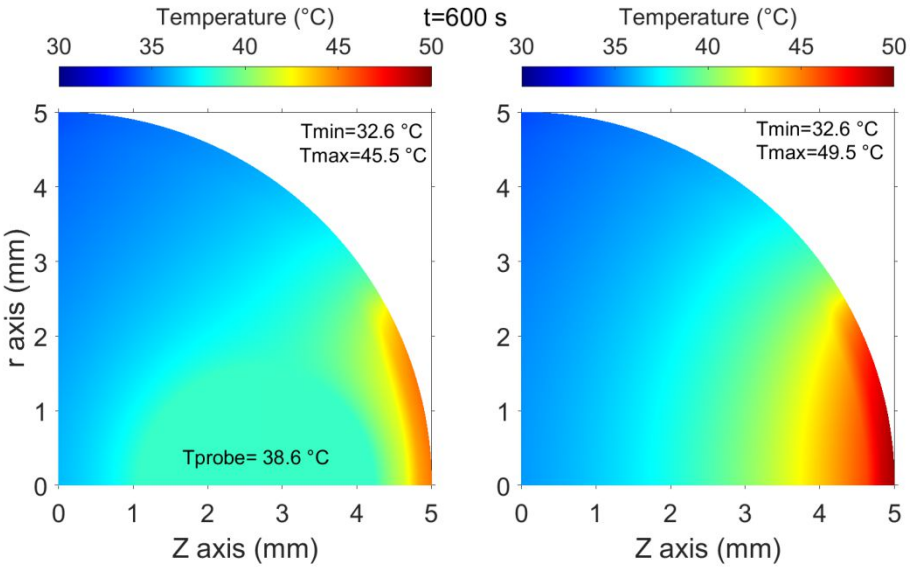

Fig 197 Field of temperature with (left) or without (right) the thermocouple after 10 minutes of simulation. The position of the metal part of the thermocouple is visible: the temperature is constant in this semi-circular zone. The maximum temperature reached by the tissue is 4° C lower when the thermocouple is present. The thermocouple measures a temperature of 38.6 ° C. It is much lower than the temperature that reaches a good part of the tissues in the absence of a thermocouple.

Fig 198 shows the temperature at several depths along the z-axis ($r = 0$). Continuous lines represent temperatures in the absence of a thermocouple. The dotted lines represent the temperatures in the presence of a subcutaneous thermocouple. The dashed black curve is the temperature measured by the thermocouple. This temperature does not exceed 40 ° C while the subcutaneous temperature (at the border fat/tumor = **continuous blue line**) exceeds 42 ° C after 81 s.

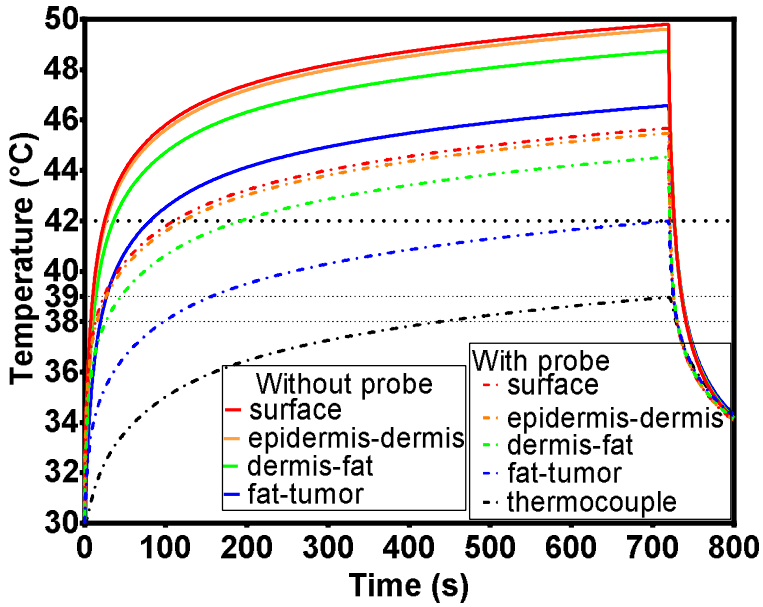

Fig 198 Temperature at several depths along z-axis ($r = 0$). $q_{plasma} = 4000\ W.m^{-2}$, $\theta = 30\ °$. The experimental situation corresponds more or less to that of a DBD treating a surface of 0.21 cm². The diameter of the disk delimiting the plasma-treated surface is 5.2 mm.

With this plasma source, the difference between the temperature measured by the thermocouple and the surface temperature is greater than those measured in the simulation of the non-refrigerated multi-jet. About 10 ° C difference here, 4.6 ° C with the multijet.

The damages (continuous curves in Fig 199) are therefore much greater than what would be expected according to thermocouple measurements. Moreover, the thermocouple itself causes a decrease in temperature which causes a reduction of the damage.

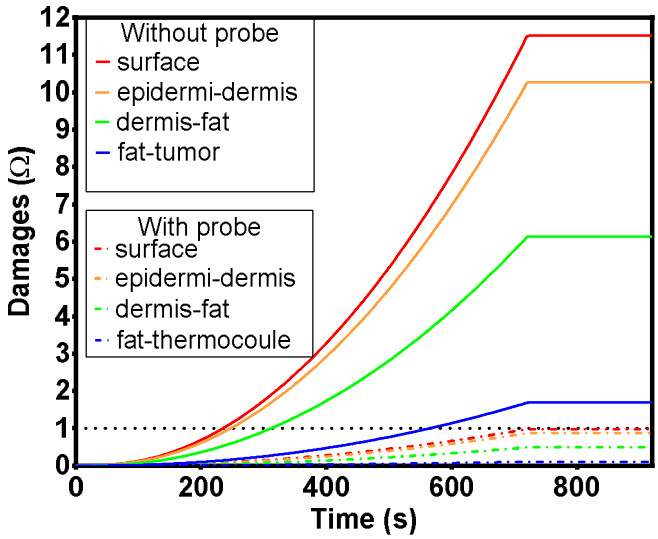

Fig 199 Damages at several depths along z-axis ($r = 0$). The presence of the thermocouple decreases the temperature, therefore the damage to the tissues.

In conclusion, the subcutaneous implantation of thermocouple does not necessarily give a true picture of the temperature that the tissues can undergo in the absence of this

thermocouple. The error will be greater if the thermocouple has a large volume, or if the thermal source is localized. The smallest possible thermocouples should be used; a better solution is to use fluorometric probes placed at the end of optical fibers implanted in the tissues.

VI.2.6.4 Summary of methodological issues

The previous sections discuss methodological issues that are directly specific to plasma-skin interaction.

To conclude, we have to check:

- The range of detection and the accuracy of measurements
- The probe should be placed at a known and measured depth. The Fig 194 and Fig 197 show that the thermal gradients are sharp $\sim 5\ °C/mm$.
- It must be checked that the electric field and / or the deposited charges do not distort the measurements of the sensor. This is another argument in favor of the optical sensors used by the team of T. Freeman [79] . On the other hand, changes in temperature could distort the values provided by an implanted electrochemical probe (pH, O_2, H_2O_2, …)
- An invasive sensor should alter as little as possible the field of temperature. In addition, it must be verified that the temperature measured by a subcutaneous sensor represents a true picture of tissues below which it is implanted. Large thermocouples should be avoided.
- The surface temperature must be measured by a diagnostic that has a suitable spatial resolution. Thermometer-gun should be avoided. At least, in any case, it is necessary to indicate the spatial resolution of the method. It is the same for measurement acquired inside the tissue. The error induced by the thermocouple can also be seen as a problem due to a lack of spatial resolution.
- If a measurement is made after the plasma has been stopped, it is essential to know precisely when.

To conclude, if an invasive measurement method is employed, it is probably better to use the fluorometric method (fluorophore placed at the end of optical fibers) than thermocouples. The ideal would be obvious to use non-invasive methods. Regarding the surface temperature, it is better to use a thermal camera, which provides higher spatial resolution than gun-thermometers.

VI.2.7 Simulation and Modelling of the experiments of Chernets et al. [79]

In this section, the results regarding the simulation of the experiments of Chernets et al. [79] are presented. This team carried out temperature measurements with the method evocated in section VI.2.6.

VI.2.7.1 Temperature in the center of postmortem mouse tumors

Let's start from what has been measured. In the first experiment, the fiber optic sensor was implanted in the center of the 6 mm tumor. The three mice bearing this tumor were freshly sacrificed before the experiment and treated with the ns-pulsed DBD described in the paper. The temperature was measured each minute. The paper specifies that the area of the surface electrode of the DBD is equal to 0.83 cm². This corresponds to the

surface of a 5.14 mm diameter disc. The surface of the skin affected by the plasma is not specified in the paper, but it is reasonable to think that the area of plasma-skin interaction is less than or equal to the surface of the electrode. It is therefore chosen to simulate the skin on a radius 3 times larger so that the boundary condition "$r = 15\,mm$" does not disturb the result. The results of the paper also show that the plasma treatment causes a considerable heating of the tissues including the center of the tumor located at 3 mm of depth.

The experimental results (Table 3, [79]) show that the temperature measured at the center of the tumor reaches a plateau value of 27 ° C higher than the ambient temperature of the tissue. As in the foregoing, a sufficient depth of tissue is simulated so that the thermal disturbance produced by the plasma treatment never reaches the boundary (z = -15 mm) of the simulated domain. Otherwise, it would be necessary to impose a temperature value at the border. Fig 200 and Fig 201 presents the mesh choosen for each layer of the skin. The inner tissues are on the left; the skin is on the right. Apart from the right-hand boundary that takes into account heat losses by convection and radiation, all boundaries are perfectly thermally isolated.

Of course, the thermal properties of the subcutaneous tissues (tumor or normal) are probably different from those modeled. To go further, it would be necessary to take into account the thermal properties of the organs located in the simulated zone. However, Appendix E shows that the thermal properties of the tumor do not fundamentally change the extent of damage in the superficial layers.

In this simulation, the tissue temperature reaches values above 60 °C, which changes the thermal properties of the tissue (thermal conductivity and specific heat). For example, the phospholipids of the membranes undergo phase changes (an increase of specific heat). Generally, this effect is not taken into account, due to the lack of information available in the literature.

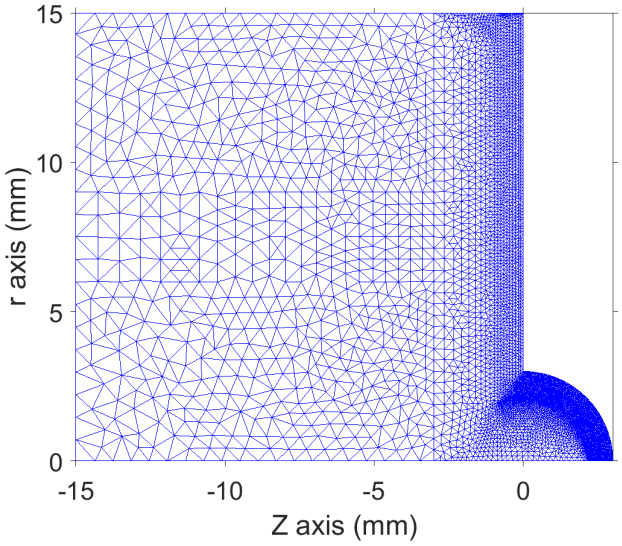

Fig 200 structure of the mesh for the simulation of mouse tumor. The Z axis is an axysymetrical axis. The mesh resolution is increased inside the skin. The tumor has a diameter of 6 mm. The tissues are simulated up to 1.5 cm radius from the center of the tumor.

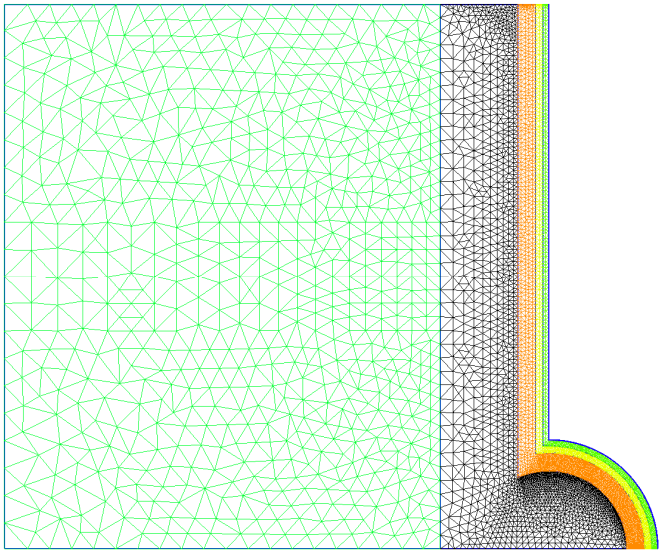

Fig 201 Structure of the mesh. From the outside to the inside: blue = epidermis, green = dermis, yellow = fat layer, orange+black+green = subcutaneous tissues. The thermal properties of subcutaneous tissue are assumed uniform.

The simulation has a total duration of 520 s; the plasma is on for 7 min = 420 s. The initial temperature is 20 °C (thermal equilibrium with the ambient temperature). The plasma-skin interaction is modeled (regarding the thermal aspect) by a constant and uniform heat flux q_{plasma}. The contribution of radiation and natural convection is taken into account in the cooling of the surface. Several values of the plasma-skin interaction surface and q_{plasma} are tested. It is assumed that the postmortem tissue have the same thermal properties than alives tissues. The heat exchanges due to blood perfusion are disabled.

Of course, the way in which heat exchange is modeled is most likely false, especially the assumption of uniformity. Additional dedicated experiments would help to provide answers. The model is simple: it depends on the size of the treated area and the incident heat flux. The question is whether it is possible to obtain simulation results compatible with the experiments by combining the two parameters.

Fig 202 illustrates that the area of the plasma-skin interface has been modified. On the left and in the center, this area is larger than the surface of the tumor. On the right, the surface is defined by the half-angle to the top θ.

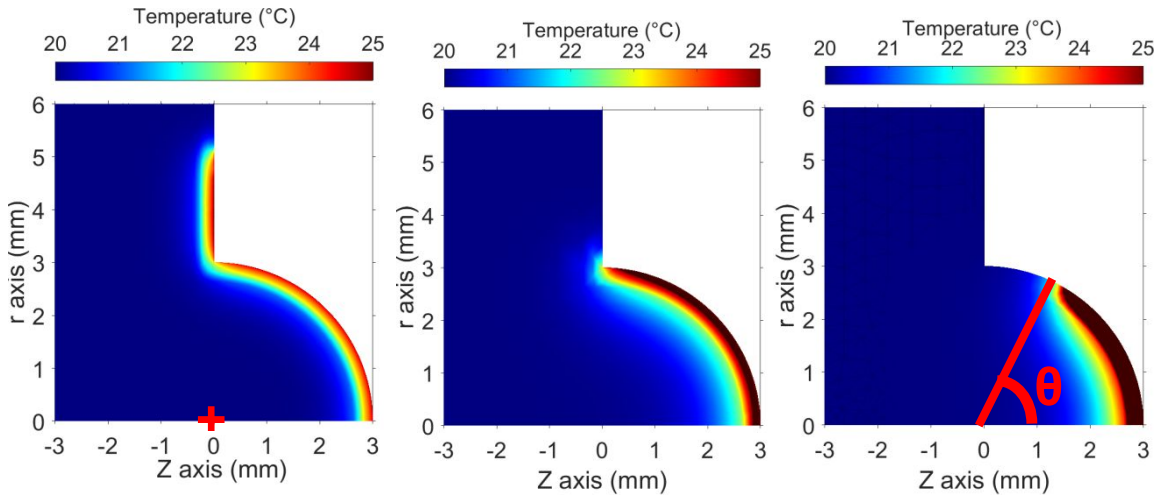

Fig 202 Visualization of the part of the skin that is in contact with the plasma. Left, the treated area has a radius of 5.14 mm. Center, the radius is 3.14 mm. Right, the treated area is defined by $\theta = 60°$. The red cross corresponds to the center of the tumor. The temperature at this point is compared with the reported experimental results.

Fig 203 shows the results of simulations made with large areas of contact (radius = 5.14 or 3.14 mm). The results of the simulations are not very compatible with the experimental measurements. Indeed, the **orange** and **red**, **green** simulations are compatible with the measurement made at $t = 60\,s$. The same simulations do not respect the experimental measurements at $t \geq 120\,s$. By reducing the incident flux, the temperature at time $t \geq 120\,s$ is acceptable (4500 W / cm², **blue** curve), but the temperature at 1 min, is seveal degrees colders than the experiments. This proves that no thermal flux is compatible with the experimental measurements once the area is defined by the radius of 5.14 mm. The result is similar when the radius is 3.14 mm, even if a significant improvement is visible.

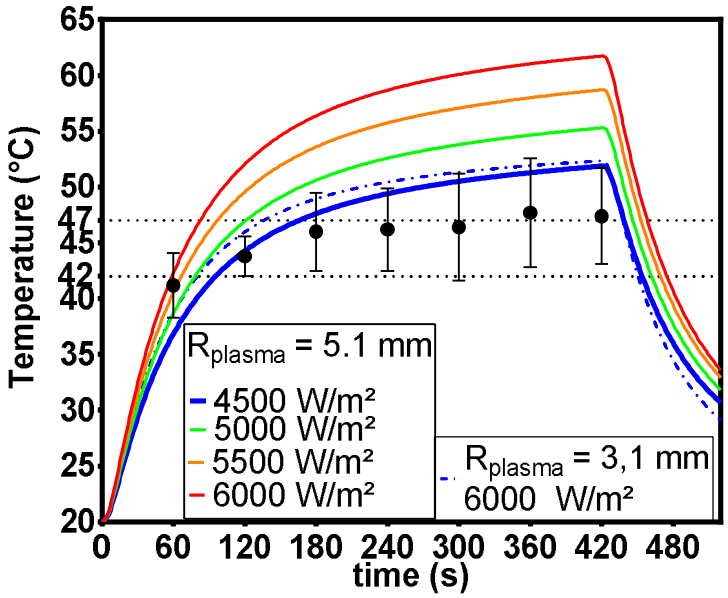

Fig 203 Temperature in the center of the tumor as a function of time. The black dots are the experimental results; the errors bars represent the standard deviation. The solid lines represent the temperature at the center of the tumor, for several values of qplasma. and when the surface of the skin interacting with the plasma has a radius of 5.14 mm. Dotted line = the surface is defined by a disk of radius 3.14 mm.

Fig 204 shows the results obtained for smaller areas on which the heat flux is applied. No perfect agreement is obtained with the experimental results. But the surface fluxes equal to 7000, 11000, or 23000 makes it possible to obtain the best compromises respectively for theta = 80, 60 and 40 °.

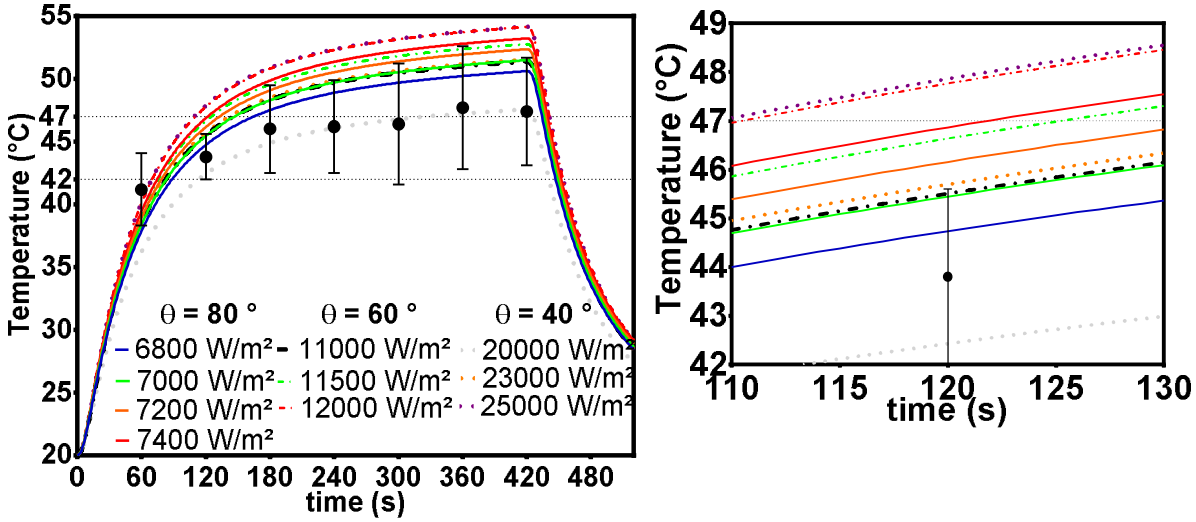

Fig 204 Temperature in the center of the tumor as a function of time. The angle θ defines the surface exposed to the plasma. Simulations performed with the angle θ and incident fluxes are specified in the legends. On the right, zoom between 110 and 130 s.

It is possible that this discrepancy is due to an underestimation of thermal conductivity. Since the mouse has been freshly sacrificed, it is likely that the tissues were soaked with blood that has not coagulated. Even in the absence of cardiac activity, this blood will be able to increase the thermal transport by its convection in the irrigated tissues. Some papers used this notion of effective thermal conductivity (see section VI.1.5.1 and Appendix F).

The results obtained by a slight increase in the conductivity of the inner tissues (an addition of $0.1\,W.m^{-1}.K^{-1}$ to standard value of $0.56\,W.m^{-1}.K^{-1}$) are more compatible with the experimental results (not shown here). But without measure, it is difficult to justify this choice of modeling that would be tinkering. Consequently, the properties of the tissues used are retained. The following simulation is made with the parameter pair $q_{plasma} = 7000\,W.m^{-2}$ and $\theta = 80\,°$ (see Fig 205).

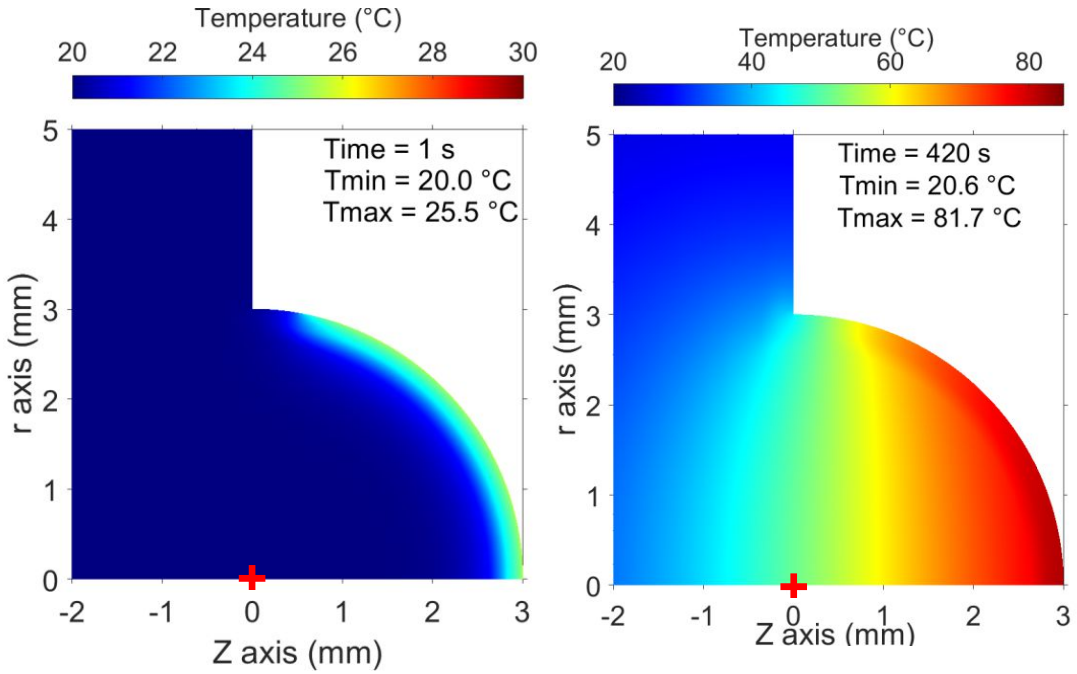

Fig 205 Temperature field. $q_{plasma} = 7000\, W.m^{-2}$, $\theta = 80$ ° Left after 1 s of simulation. It enables to vizualize the surface in contact with the plasma. Right: temperature field after 7 min. The red cross is at the center of the tumor, the temperature is 50.1 ° C after 7 min.

Fig 206 shows the temperature as a function of time at several depths along the Z-axis. The increase of temperature of the superficial layer of the tumor is considerably high, to obtain an increase of 27 ° C in the center of the tumor. This model predicts that the temperature at the fat/tumor interface is around 77°C, while the surface temperature would be of the order of 80 ° C. Heat damage is expected to be devastating in a short time.

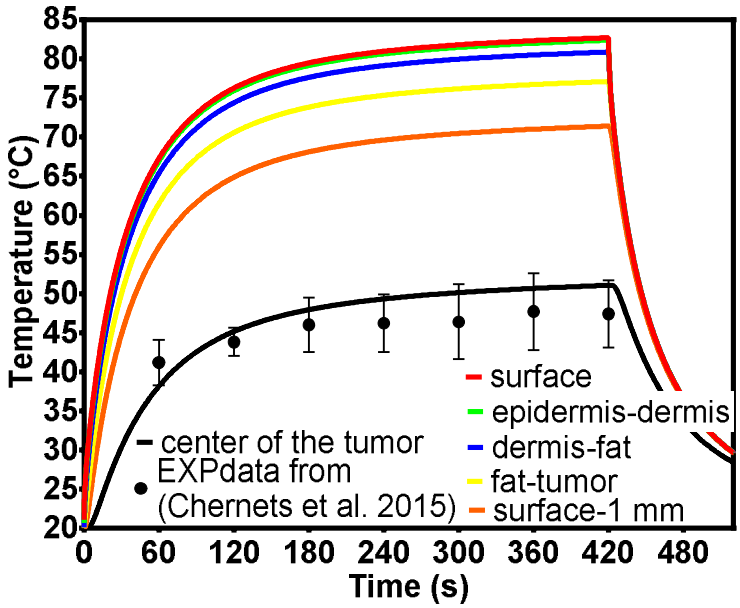

Fig 206 $q_{plasma} = 7000\, W.m^{-2}$, $\theta = 80$ °. The temperature as a function of time at several depths along Z axis. Black dots = experimental data from [79]. the blue curve represents the temperature at the dermis-hypodermis interface.

VI.2.7.2 Living mice

Previous simulations were done in dead mice. What if the animal is alive?

First, it is considered that the initial temperature of the tissue 30 ° C instead of 20 °C. Then we consider that the blood circulation works. With such an initial temperature, an increase of 12 ° C is sufficient to enter in the range of irreversible damages. Fig 207 shows that the damage function Ω reaches the value of $\Omega = 1$ at the center of the tumor after only 87 seconds. It also means that all the tissues above are also severely damaged.$\Omega = 1$ is reached at the fat-tumor interface only after 22 s. Fig 208 enables to view the spatial extension of the damages as a function of time. After 7 min of treatment, a large part of the tumor tissues will die from the consequences of hyperthermia. Only a thin crescent of tumor tissue seems to have been spared.

However, the team of T. Freeman observes total remissions. This observation is compatible with the simulation since the unafected part of the tumor will be touched by heat-induced vascular damages. These damages will induce hypoxia and nutrient depletion of the entire neighborhood, which could die from vascular damages, without even mentioning all the other biological reactions related to hyperthermia (described and discussed in the last section of this chapter).

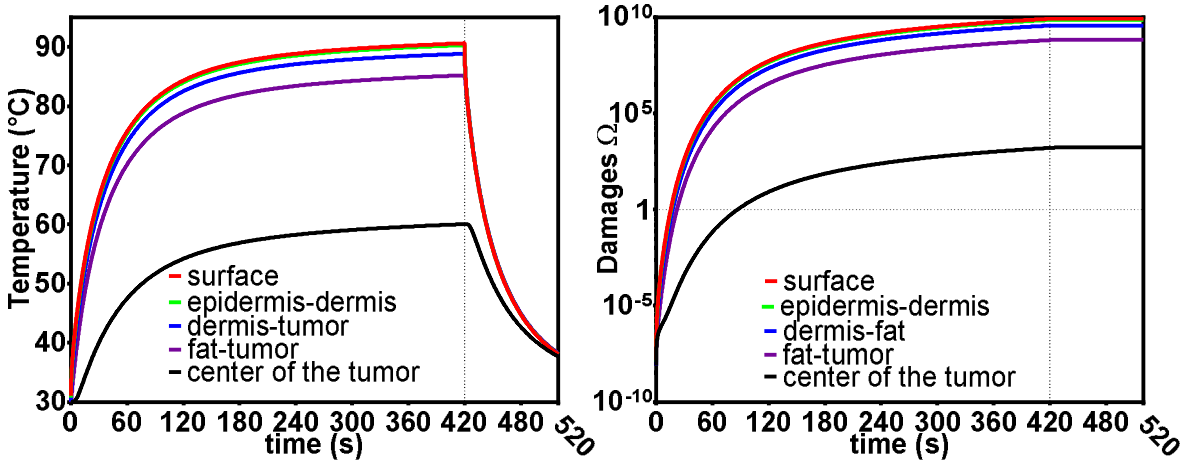

Fig 207 $q_{plasma} = 7000\ W.m^{-2}$, $\theta = 80$ °. Damages and temperature as a function of time at several depths along Z axis. the damage axis is logarithmic.

Other simulations of the experiments of Chernets et al. could be treated by finite element model. The thermal behavior of pork skin can be simulated[104].

[104] It coud be show that the structure of pork skin cannot explain why the temperature of pig skin increases so little compared to mouse skin in the work of Chernets et al. The simulations could also show that a layer of gel with a thickness $\geq 300\ \mu m$ have a very significant effect on the signals of the sensors located 2 mm below the pig skin surface. The simulations are compatible with the experimental results if the gel layer is less than 300 µm thick. Otherwise, the two signals (with / without gel) have a delay incompatible with that reported. Finally, the role of water-evaporation coud be quantified with a modelling of the mass transfer. The damage that a mouse with or without a gel undergoes are compared.

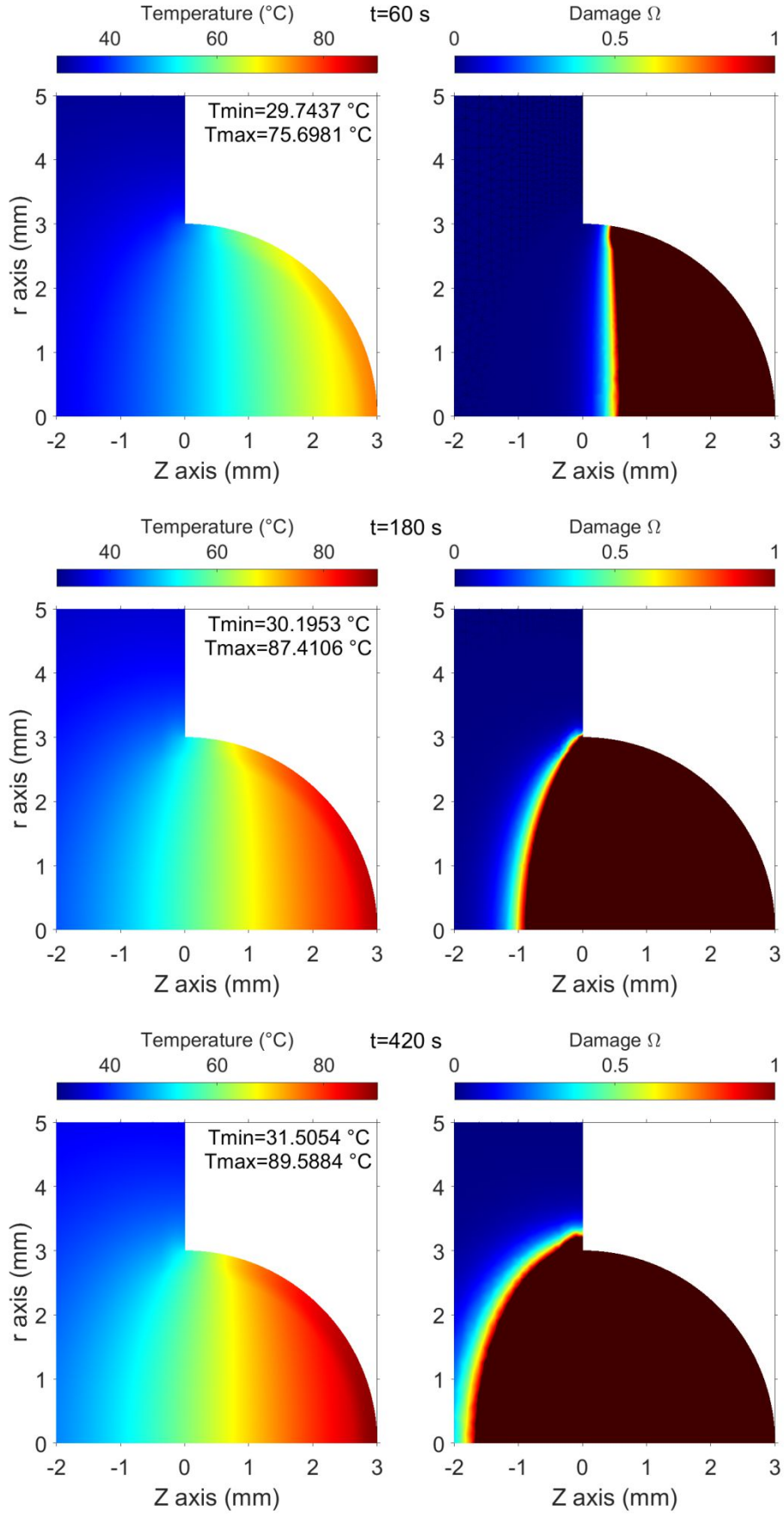

Fig 208 Temperature and damage field after 1, 3 and 7 minutes. $q_{plasma} = 7000\ W.m^{-2}$, $\theta = 80\ °$. In just one minute a considerable part of the tumor has been destroyed.

VI.2.8 In what extent fractioned treatments can be dangerous?

In plasma medicine, it is generally sought to prevent the tissues from heating. The scientific community is aware that hyperthermia can play a biological role. Since the goal is generally to question the working hypothesis according to which it is the chemical species or ,at least, a non-thermal action of cold plasmas which is at the origin of the therapeutic effects; the experimenters seek to get rid of hyperthermia.

Several strategies are possible to avoid hyperthermia. experimenters working with the Kin-Pen09 [313] chose to move the plasma device over the skin to avoid the overheating of the tissues. The addition of a cooling system is another solution. This “cooling strategy” was adopted to carry out the last two experimental campaigns (see sections V.3.1 and V.3.2).

An obvious strategy to prevent hyperthermia is to reduce the duration of plasma exposure. However, it is necessary to maximize the total time of contact of the plasma with the skin to increase the amount of chemical species deposited on the surface. The strategy of fractional treatments is to repeat plasma treatments of a few seconds separated by a cooling time.

The scientific question is to know in what condition this strategy works. We work with the same parameters as those of the previous simulation (Simulation of a tumor treated with the DBD of Chernets et al. with $q_{plasma} = 7000\ W.m^{-2}$ and $\Theta = 80$ °).

First we consider the case of a fractional treatment characterised by the sequence **{plasma on = 5 + cooling by natural convection = 10 s}**.

The damages after 15 min are shown in Fig 209. Consequently, the total time of plasma-skin interaction is equal to 5 min. The damage extends significantly up to 2 mm depth and therefore would have led to severe damage. Note, however, that the damage is much less severe than that produced in 180 s by the device operating continuously (see previous figure, e.g., Fig 208).

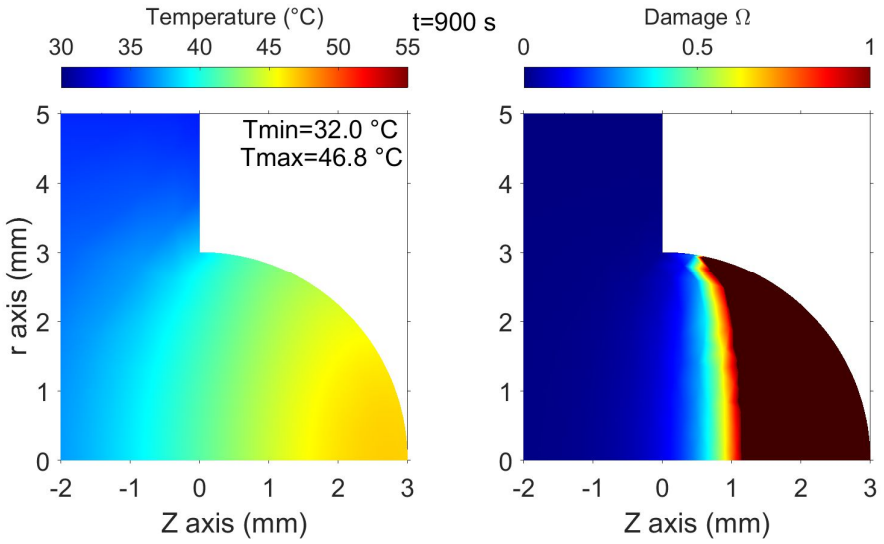

Fig 209 Field of temperature (left) and damage (right) for $q_{plasma} = 7000\ W.m^{-2}$. At time t = 900s, with fractional treatment (plasma on =5 s and cooling = 10 s).

Fig 210 represents the temperature as a function of time at several depths along the Z-axis. The temperature does not increase as much in-depth as on the surface. This

damping is visible as a function of depth. The period of 15 s is clearly visible on the right part of the figure. The left side shows that on average, tissues heat up with the accumulation of the sequences of heating and cooling. The equilibrium between the average incident power and the thermal exchange (conduction, radiation, convection, blood perfusion ...) is obtained after a transient regime (~ 200 s). The accumulation of heat between several treatment sequences is the cause of the damage.

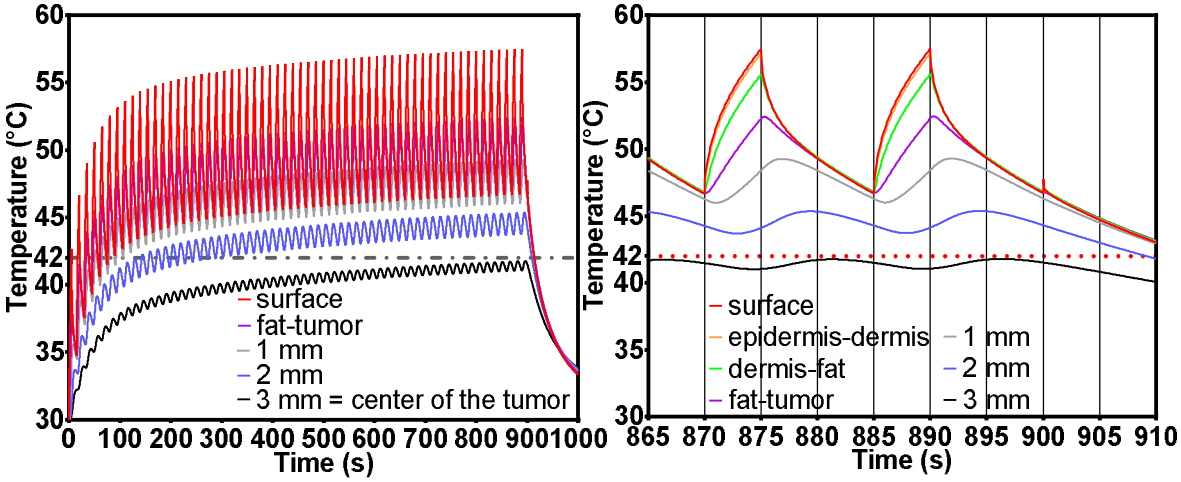

Fig 210 Temperature as a function of time at several depths. The legend designates the depth relative to the surface. The red curve is the surface temperature. $q_{plasma} = 7000\ W/m^2$. It can be seen that there is a temporal response at a timescale longer than the period. The period of 15 seconds is clearly visible. The damping of temperature step is also observed as a function of depth.

In a second step, we consider the case of a DBD fractional treatment characterized by the sequence **{plasma on = 5 + cooling by natural convection = 15 s}**. We consider, as previously, that the total duration of plasma treatment is 5 min (+15 min of cooling by natural convection). Fig 211 is relatively similar from a qualitative point of view. The longer cooling time decreases the maximum temperature of 2 °C at all depths.

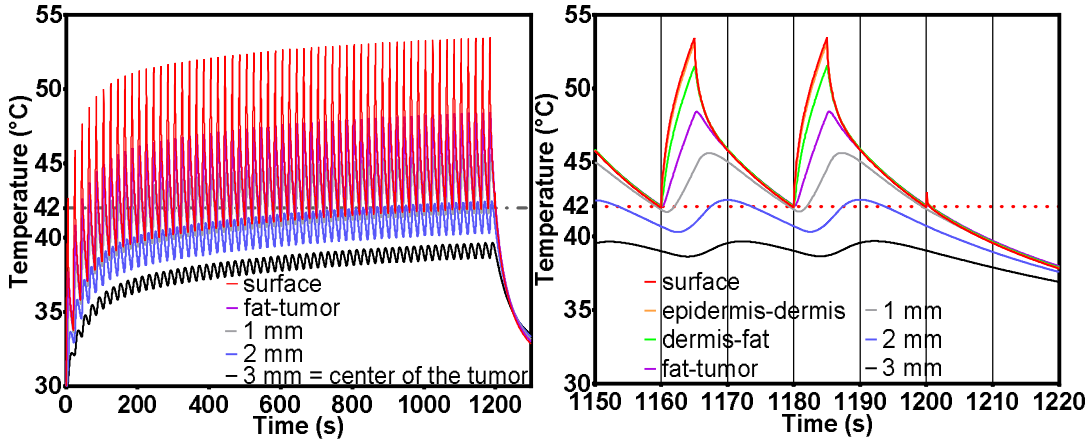

Fig 211 Temperature as a function of time at several depths. The legend designates the depth relative to the surface. The red curve is the surface temperature. $q_{plasma} = 7000\ W/m^2$. It can be seen that there is a temporal response at a timescale longer than the period. The period of 20 seconds is clearly visible. The damping of temperature step is also observed as a function of depth.

The damage map is plotted in Fig 212. The damages are reduced compared to the previous simulation (1 mm of depth along Z axis, 2 mm in the previous simulation).

However, the damage remains severe since the skin is completely destroyed and the tumor is directly damaged[105].

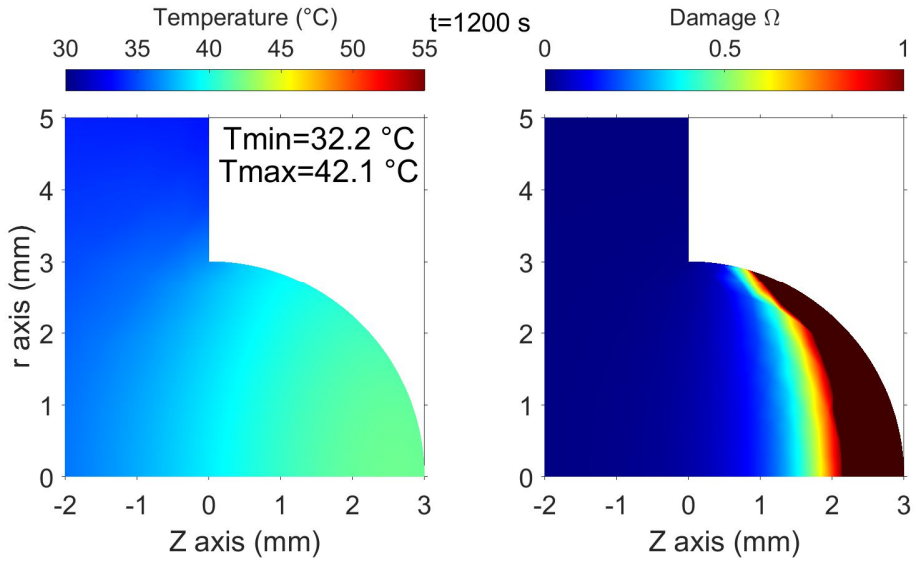

Fig 212 Field of temperature (left) and damage (right) for $q_{plasma} = 7000\ W.m^{-2}$. At time t = 1200s, with fractional treatment (plasma on =5 s and cooling = 15 s).

If the cooling time is 10 or 15 s, the strategy which consists of splitting the treatments into fractions of 5 seconds, doesn't enable to avoid severe thermal damage. What happens if the cooling time is increased?

Simulations were carried out with cooling times between 10 s and 35 s to answer that question. The next two pages contain figures describing the temperature at the beginning of the treatment (Fig 213) and the accumulation of damage during 1000 s [106](Fig 214). The figures representing the temperature during all the treatment are visible in the Appendix H (p 367). It is noted that the surface temperature reached after the first 5-second treatment exceeds the threshold of 42 °C for less than 100 ms. On the other hand, the temperature does not return to its initial value. After the transient regime, the temperature of the biological tissues oscillates around a mean temperature depending on the depth and the cooling time. The higher the average temperature, the more the 5s of plasma will inflict deep damage.

Beyond 25 s of cooling, the damage function **Ω** is less than 1 after 1000 s. In particular **Ω** is less than 0.1 for the upper layer of the tumor. However, damage function is still higher than 0.1 in the dermis with 25 and 30 s of cooling. The dermis is therefore likely to undergo mild hyperthermia. This can cause significant biases since the inflammation of the skin can have side-effects on the anti-tumor response.

The figures in Appendix H show that even with a cooling of 35 s, the 5 minutes of plasma ON, spread over 40 min (2400 s) of operation would cause severe damage to the dermis. The damage function remains below 0.1 at the fat-tumor interface. The solution would then be to have less than 5 s of plasma on. Note that the results obtained here are not intuitive. If an experimenter measures the skin temperature after only 5 seconds and sees that the surface temperature is only 40-42 °C. He might be tempted to use this to justify that his treatment does not heat significantly. This would be an error since this temperature is measured at the beginning of a transient regime. This approach is not

[105] Since skin thickness ~360 µm
[106] This is a realistic treatment time for an animal under anesthesia...

fundamentally exotic in the field of hyperthermia; indeed Kolios et al. [269] conducted a similar study on the damage induced by repetitive heating induced by ultrasound.

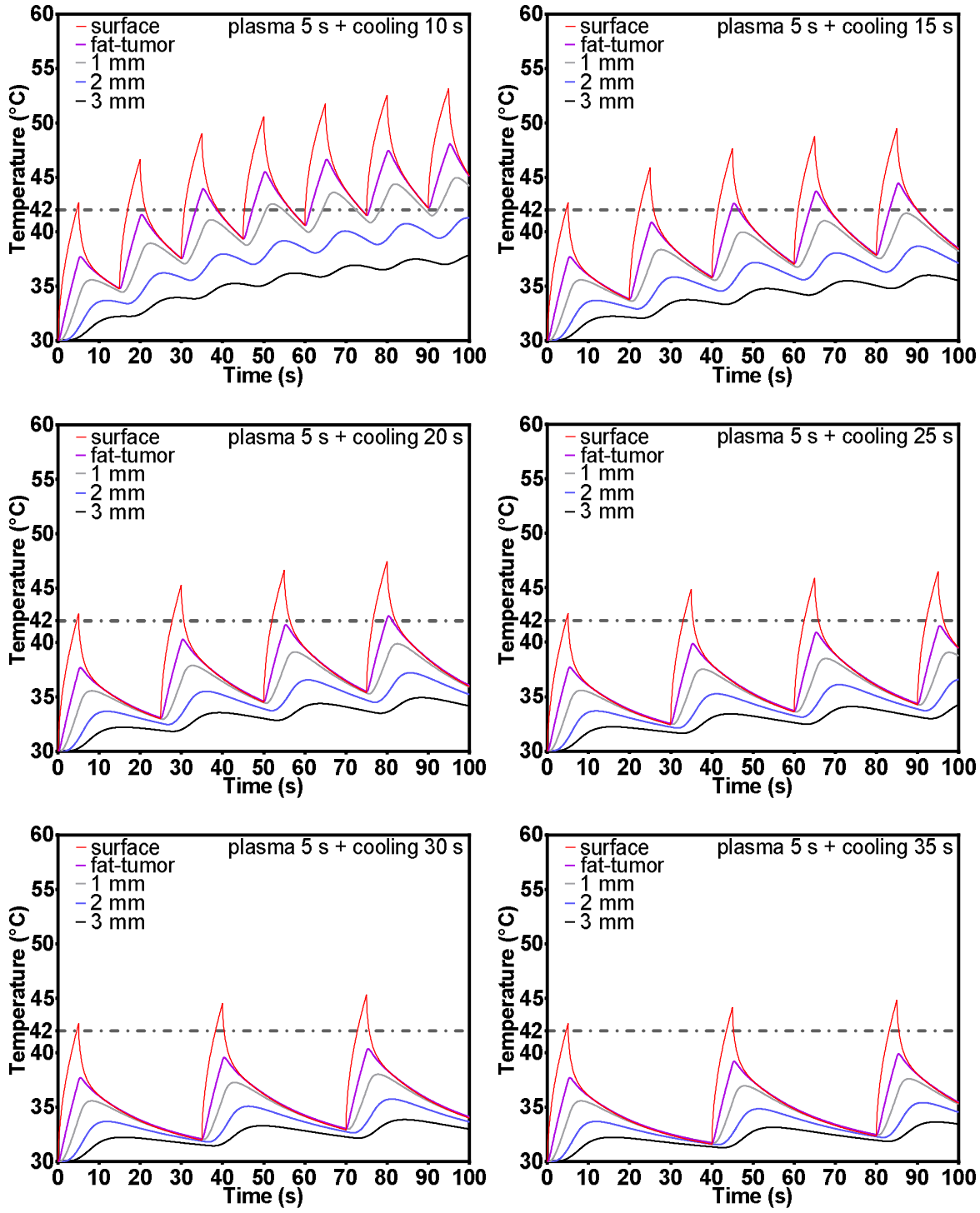

Fig 213 Temperature at the beginning of fractioned treatment. The temperature is measured at several depths along Z axis: surface (red), interface between fatty and dermis layer (pink), 1 mm below the surface (grey), 2 mm below (blue), 3 mm = in the center of the tumor (black). From one sequence to another, the average temperature increases with time. With a longer cooling time, the average temperature reached by the tissues is lower. Even with 35 s of cooling, the temperature reached by the skin is in the regime of moderate hyperthermia for a few seconds.

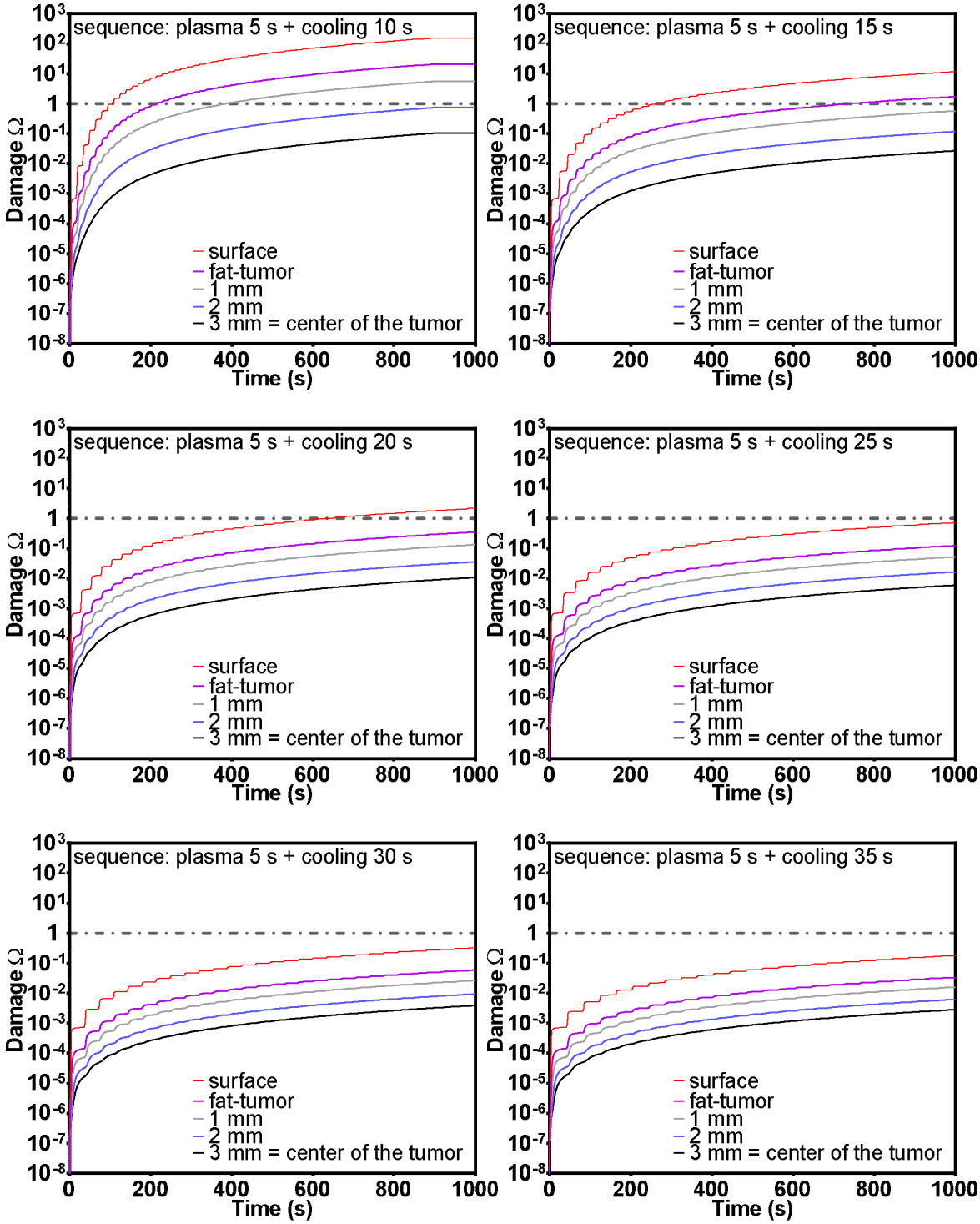

Fig 214 Damage during fractioned treatment. The damage is measured at several depths along Z axis: surface (red), interface between fatty and dermis layer (pink), 1 mm below the surface (grey), 2 mm below (blue), 3 mm = in the center of the tumor (black). Beyond 25 s of cooling, surface damage is less than 1 after 1000 s of treatment. With 10 s of cooling, very significant damage ($\Omega = 1$) reaches a depth of between 2 and 3 mm. With 15 s of cooling, very significant damage ($\Omega = 1$) still reaches the depth of the tumor. Significant damage still reaches the dermis with 20 and 25 s of cooling. This can cause significant biases since the inflammation of the skin can have side-effects on the the anti-tumor response.

VI.2.9 What is the maximum heat flux that a mouse can sustain without damage?

We will now determine the limiting conditions of the incident heat flux (and gas temperature) that can sustain the skin without damage. Even for the long treatments. The experimental configuration of the non-refrigerated multijet is used. It is assumed that there are no damages if $T_{max} \leq 42°C$ after 20 min of treatment; with T_{max}, the maximum temperature.

Fig 215 represents the field of temperature and damages after 20 min of continuous treatment. Plasma surface-interaction is modeled by a constant incident flux q_{plasma} = 5500 W/m². It is considered that the flow of Helium is at room temperature and therefore cools the surface of the skin ($T_{helium} = T_{amb} = 20\,°C$). The maximum temperature is 41.95 °C. It is unlikely that the skin suffer thermal damage, when the thermal flow is less or equal to q_{plasma} = 5500 W/m².

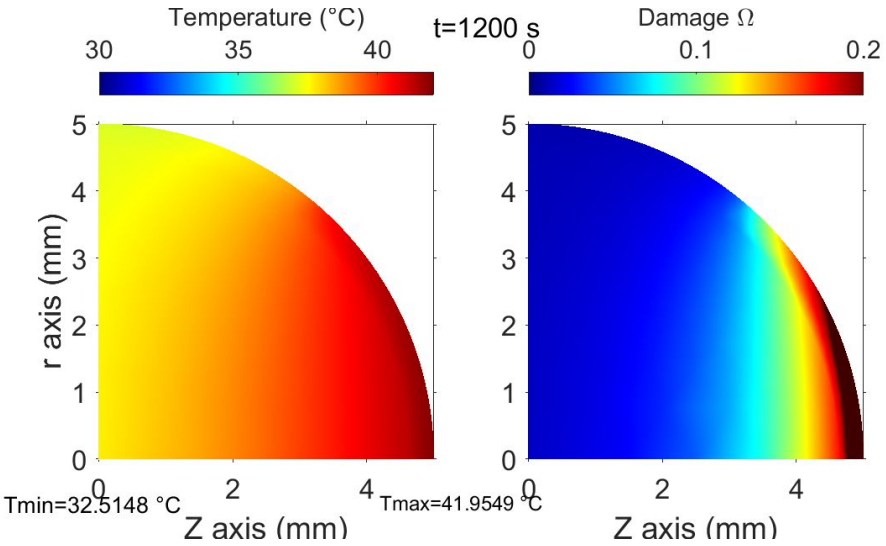

Fig 215 Field of temperature and damage after 20 min with q_{plasma} = 5500 W/m². The convection of helium cools the skin at plasma-skin interface $T_{helium} = T_{amb} = 20\,°C$.

Fig 216 represents a very similar experimental situation. Except that it is assumed that there is no flow of helium to cool the surface. Cooling is ensured by natural convection only with ambient air at $T_{amb} = 20\,°C$. This experimental situation is closer to that of a DBD.

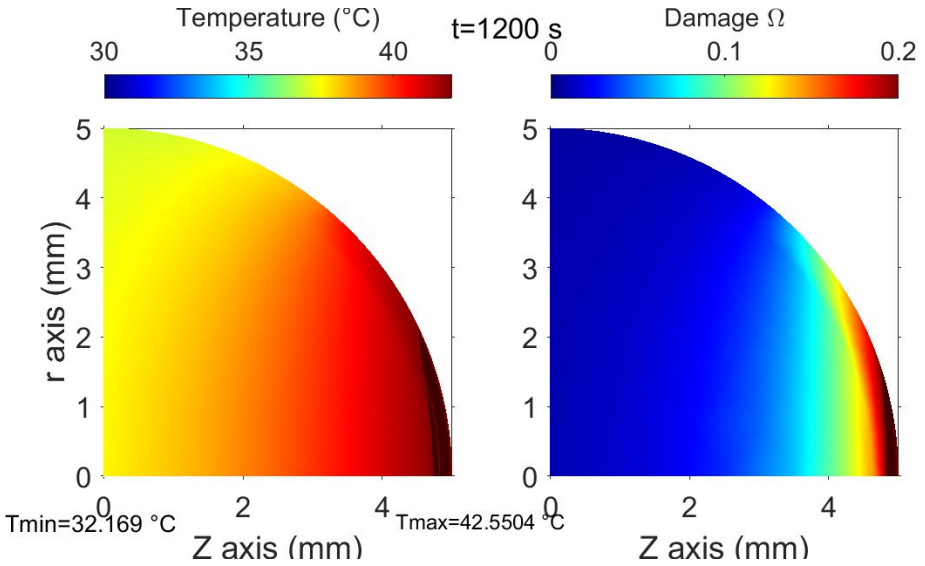

Fig 216 Field of temperature and damage after 20 min with q_{plasma} = 1250 W/m². Natural convection cools the skin at the plasma-skin interface. It is recalled that $T_{amb} = 20\,°C$.

In a similar way, the maximum temperature of helium which does not cause damages can be found. Fig 217 represents the field of temperature and damages after 20 min of treatment. Plasma surface-interaction is modeled by convective transfer due to Helium at temperature $T_{He} = 46\,°C$.

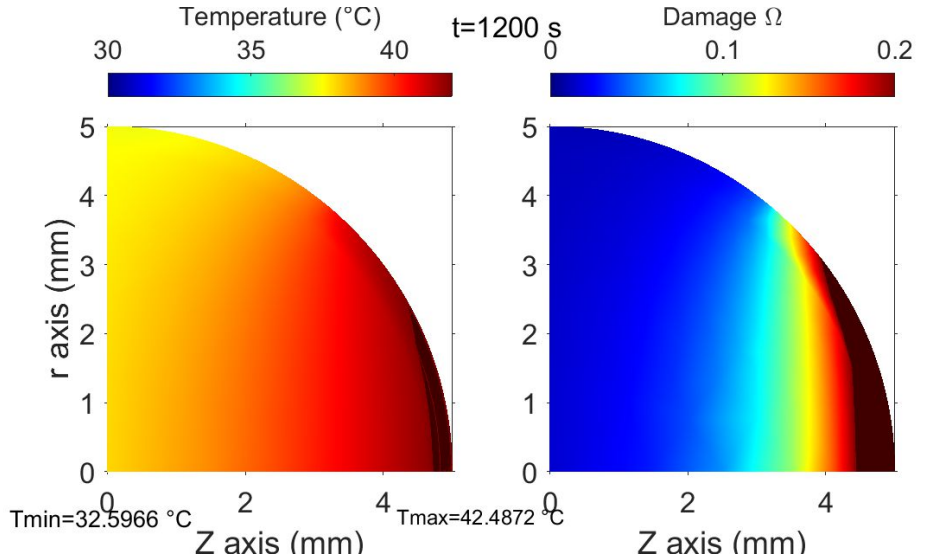

Fig 217 Field of temperature and damage after 20 min. The convection of Helium heats the skin at the plasma-skin interface. Helium temperature of impinging jet is $T_{He} = 46\,°C$

To summarize, we found the treatment conditions to avoid damage to mouse skin. Since the structure of the human skin is different (in particular the epidermis is much thicker, and the blood perfusion is superior), it is likely that the human skin can withstand higher thermal flows. Sweating also enables to evacuate a consequent quantity of heat (absent in mouse).

The influence of the gas flow rate cannot be easily guessed. In one hand, by increasing it, we can expect that gas temperature decreases since our experiments show that the power consumption reaches a plateau when flow rate increases. In other hand, the turbulence at the point of stagnation could considerably increase the value of heat transfer coefficient h (which already increases in $Re^{0.5}$ in laminar regime). Experiments

combining heat transfer and turbulence studies in the presence of plasma discharges are therefore necessary. Spatially resolved diagnostics of plasma should be coupled to optical diagnostics. Fig 218 shows an example of an interferometric figure obtained at the beginning of this work with a Mach-Zehnder interferometer and a pulsed laser at 532 nm. Optical diagnostic should enable the quantification of the turbulence.

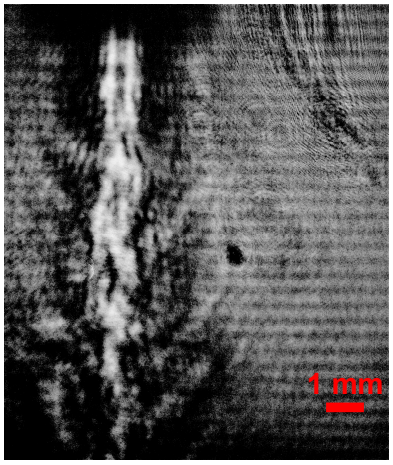

Fig 218 Interferometric image of the flow obtained with a Mach-Zender interferometer. $\lambda = 532\ nm$

VI.2.10 What is the reliability of damages predictions

This paragraph summarizes the results presented in Appendix E. The reliability of simulations has been studied by modifying the four main parameters involved in the prediction of thermal damage.

- Blood perfusion inside the tumor ω_{tumor}
- the thermal conductivity of the tumor λ_{tumor}
- The value of the kinetics parameters A and Ea, which defines the damage function $\Omega = \int_0^t Aexp\left(-\frac{E_a}{RT}\right) dt$
- The area of the plasma-skin interface. The portion of sphere defined by half-angle to the top Θ has an area of $S = 2\pi r^2(1 - \cos(\Theta))$.

Studies were carried out with the previous experimental situation of a DBD operating during 5 s, whereupon the skin cools for 15 s by natural convection and radiation. These treatment sequences are repeated during 20 min so that the total processing time is 5 min. This experimental situation is chosen because the transient responses play a key role in this context. The position and extent of damage are more sensitive to parameter changes than continuous processing by the multijet. Consequently, it would be a stronger result to prove that the damages prediction is quite independent of the model.

As previously, the heat flux $\mathrm{q_{plasma}}$ at the plasma-skin interface is chosen in order to reproduce the temperature field at steady state. Secondly, the map damage is simulated in the case of an intermittent regime with the value of q_{plasma} found in first step. The depth reached by the damage is then compared.

Whatever the parameter among the four considered, the simulation of a “fractioned DBD” always predicts damage that completely destroys the skin. This could be a bias for anti-tumor. Since inflammation and immune reactions are triggered by the thermal damage (see the references and the discussion on thermal effects in the context of antitumor studies, concluding Chapter VI). In all realistic cases, significant damage also occurs in

the upper layers of the tumor (below 4636 µm on r axis). Thus, this reliability study proves undoubtedly that such treatment would induces a thermal bias during in-vivo experiments. The simulations are remarkably insensitive to the values of perfusion rates and thermal conductivity.

In all cases, it was assumed that the heat flux is uniform on the treated surface. This hypothesis is probably false. It would be interesting to find experimentaly the heat flux as a function of the angle θ: $q_{plasma}(\theta)$. Measurements of the temperature field on half-spheres of materials having different radii and a known thermal conductivity should enables to obtain $q_{plasma}(\theta)$. The problem with this kind of experiment will be to know to what extent it enables to deduce the heat flux above a biological tissue which has a different electric conductivity (which could modify the plasma discharge and $q_{plasma}(\theta)$). The passage from the simple isotropic inert model to the anisotropic inhomogeneous material requires precautions. The further step of modeling would be to consider the effects of discharges inhomogeneitie to evaluate if the function $q_{plasma}(\theta)$ has a strong effect to the depth reached by thermal damage at constant incoming power.

VI.2.11 What if the skin is slightly moist?

The case of wet skin could be treated by finite element method. The addition of a gel layer would probably reduce the temperature of the skin and therefore the damages in three different ways.

First, the gel layer adds a thickness of material which adds thermal inertia to the skin. A thermal gradient is established through the gel layer which constitutes a thermal resistance. Second, the diffusion which is orthogonally to the surface significantly reduces the temperature at gel-skin interface, since the thermal conductivity of the gel is greater than that of the epidermis. Finally, the evaporation of the gel considerably reduces the temperature at the surface of the gel (and below) since the specific latent heat of water is of the order of 2500 J per gram of water.

VI.3 Plasma-medicine and hyperthermia, a critical approach of *in-vivo* experiments.

In this section, we will focus on few in-*vivo* plasma experiments. In particular, those that involve treatment of melanoma B16. For each paper, there are two simple questions:

- Do the published studies really exclude the possibility that tissues have been subjected to hyperthermia depending on the measurement method used?
- In the event of a negative answer. In what extent the results obtained could be attributed to hyperthermia? The question of the reliability of measurement methods is addressed by the section VI.2.6. The questioning of the published results is based on the discussions presented therein.

VI.3.1 *In-vivo* experiments involving B16-F10 melanoma

Four recent studies present *in-vivo* results involving plasma treatment of B16 melanoma models. This line of melanoma is well known in the scientific community of hyperthermia. Consequently, the first part of this discussion describes what is known from the effect of hyperthermia alone on this specific line. Then, the four papers are discussed according to the principles discussed above.

VI.3.1.1 What are the effects of the temperature on B16 melanoma growth?

First of all, the temperature is far from being a negligible parameter even below the limit of irreversible damage, especially regarding the anti-tumor response. For example, Kokolus et al .2013 [314] show the effect of the thermal environment of an anti-tumor response. Most animal houses keep mice at a temperature between 20 and 26 °C, which elicits cold stress of the animals. The temperature, called “thermoneutral”, which do not induce thermal stress would be rather of the order of 30-31 °C. The experiments compare the tumor growth of mice housed at thermoneutral temperature **(TT)** or classic sub-thermoneutral **(ST)** temperature. Fig 219 show that the tumors grow significantly faster when mice are exposed to cold stress [314]. Tumor growth is delayed at thermoneutral temperature by 10 days for almost all the lines studied (especially the B16-F10 line). Using immunodeficient lines, the authors were able to show that this behavior is related to a better immune response in the case of thermoneutrality **(TT)**.

It is obvious that this situation has no analogy with hyperthermia experiments (implying moderate or strong hyperthermia during few minutes) in terms of exposure time and temperature. This is an illustration of the strong link between temperature and immune response. For someone with a physicist background, this links seems counter-intuitive at first glance whereas immune response greatly alters tumor growth.

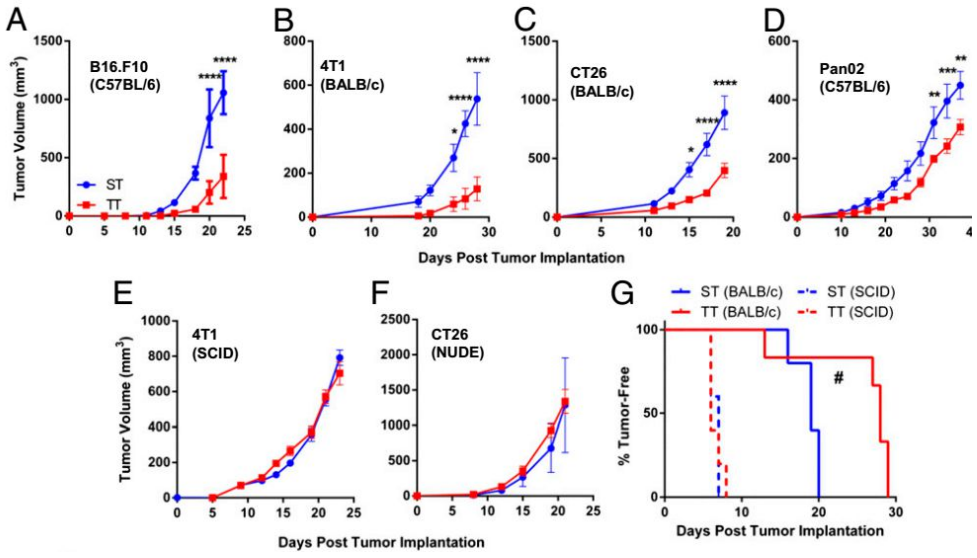

Fig 219 Legend and figures of Kokolus et al. [314]. Maintaining mice at thermoneutral temperature (TT) slows tumor growth in immunocompetent mice but not in immunodeficient mice compared to the mice exposed to sub-thermoneutral temperature (ST). Tumor growth was monitored following injection of (A) 1 × 105 B16. F10 cells into C57BL/6 mice, (B) 1 × 104 4T1 cells into BALB/c mice, (C) 1 × 105 CT26 cells into BALB/c mice or (D) 1 × 105 Pan02 cells into C57BL/6 mice, (E) 1 × 104 4T1 cells into SCID mice, and (F) 1 × 104 CT26 cells into NUDE mice. Data presented as mean ± SEM (n = 5–10; *P < 0.05, **P < 0.01, ***P < 0.001, ****P < 0.0001; Two-way ANOVA with Bonferroni posttests). (G) Tumor incidence was monitored in mice after injection of 1 × 104 CT26 into BALB/c mice or 1 × 103 CT26 cells into SCID mice. Data presented as percent of mice tumor-free (n = 5; #P <0.05; Mantel-Cox test).

Now the discussion will focus on three articles proving and quantifying the sensitivity of B16-F10 melanoma to hyperthermia. These results all relate to *in-vivo* experiments. The modes of exposure to hyperthermia are different in the three cases discussed.

In Li et al. [315], the melanomas are heated at a temperature between 46°C and 55 °C. The tumors are heated with a hot steam flow. The temperature is measured in the center of the tumor with a 0.1 mm thermocouple. This thermocouple size is small enough not to

disturb the measurement (contrary to the case discussed in the section VI.2.6.3 “Thermal conduction smearing”). The tumors are heated for 15 minutes at 46 ° C, 48 °C and 50 ° C (and 10 minutes at 55 ° C). The two figures of [315], Fig 220 and Fig 221, show the tumor volume and survival rates of the groups exposed to hyperthermia compared to control group. The treatments were performed on 5-6 mm tumors.

It appears that tumor growth is considerably slowed down. The survival time of all groups is increased. The groups treated at 50 and 55 ° C contain cases of remission/tumor removal. The group treated at 46 ° C is particularly remarkable since the survival is increased by 15 days.

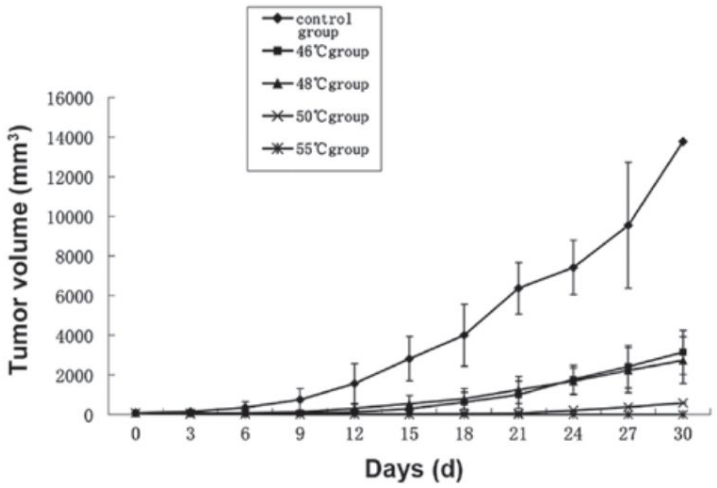

Fig 220 Legend and figures from Li et al. [315] Tumor growth following hyperthermia treatment. All data are expressed as mean ± standard deviation (SD) (n=6)

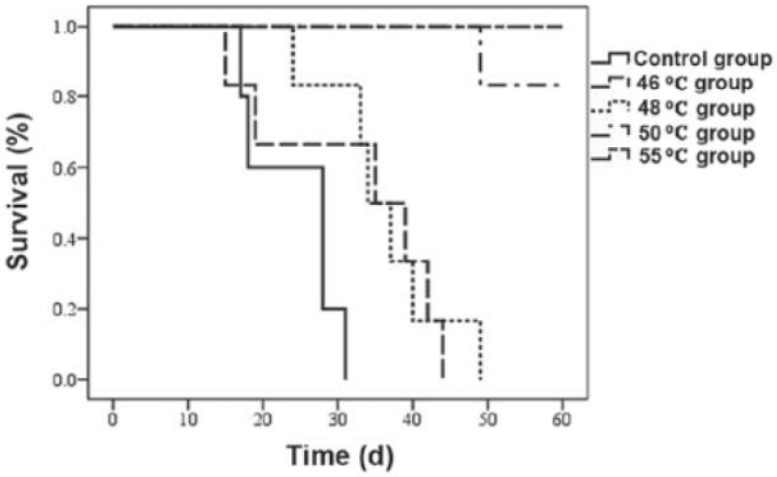

Fig 221 Legend and figures from Li et al. [315] Survival curve over a period of 60 days following hyperthermia treatment. n=6 mice/group, T=0 corresponds to the time of hyperthermia.

Kostenich et al. [316] describe hyperthermia treatment of B16 melanoma by intense light pulses (xenon flash, incoherent broadband 400-800 nm). The pulses have a duration of 2 ms; each pulse deposits 0.6 J / cm² on a disc of diameter 2 cm. The light dose is between 60 and 120 J/cm². Tumors were treated when their diameter was 5 mm. The temperature was measured at different depths with thermocouples:

"Temperature in the tissue during photoirradiation was measured by a quick-response (0.025 s) TEFLON PFA-insulated thermocouple probe coupled to a DigiSense digital thermometer (Cole–Parmer, Niles, Illinois). The thermocouple was inserted into a 21G needle and fixed to three positions in the tissue: under the skin above the tumor surface, and in the tumor at depths of 2 and 4 mm."

The thermocouples are small enough, therefore, the temperature measurement was not biased (see VI.2.6.3 "Thermal conduction smearing"). Four groups were treated with light doses of 60, 72, 90 and 120 J/cm². The figure below shows the results of temperature measurements, as well as the volume of melanomas.

It appears that tumors in the 72 J / cm² group have a significantly slower tumor growth rate than the control group. In this group, the maximum temperature reached respectively at the surface, 2 mm and 4 mm depths are 44-45 ° C, 41 ° C and 39 ° C. Compared to previous paper, melanomas were subjected to much lower hyperthermia. In addition, the dose of 72 J / cm² was delivered in 2 min, since the pulses have a frequency of 1 Hz. The heating time of the tissues is shorter than in previous paper. It may also be noted that the surface tissues reach the temperature of 42 ° C only for a dose of 30 J, so all tissues spend slightly more than one minute at a temperature higher than 42 °C. Even with such small times and temperature, a significant effect is obtained on tumor growth.

It should also be noted that, in two cases, only the upper tissues were exposed to high hyperthermia ($T \geq 42\,°C$). This concern a small volume since the temperature at 2 mm depths is below 42 °C. However these doses of 60 and 72 J / cm² are sufficient to induce a significant effect on the total tumor volume. The paper shows also that a light dose of 120 J/cm² (which corresponds to a temperature of 43 ° C at 4 mm depths after 200) prevent the regrowth of the tumor. The sensitivity to hyperthermia of melanomas is stronger than the first paper could suggest. It is likely that the immune responses associated with mild hyperthermia play a predominant role in these experimental situations.

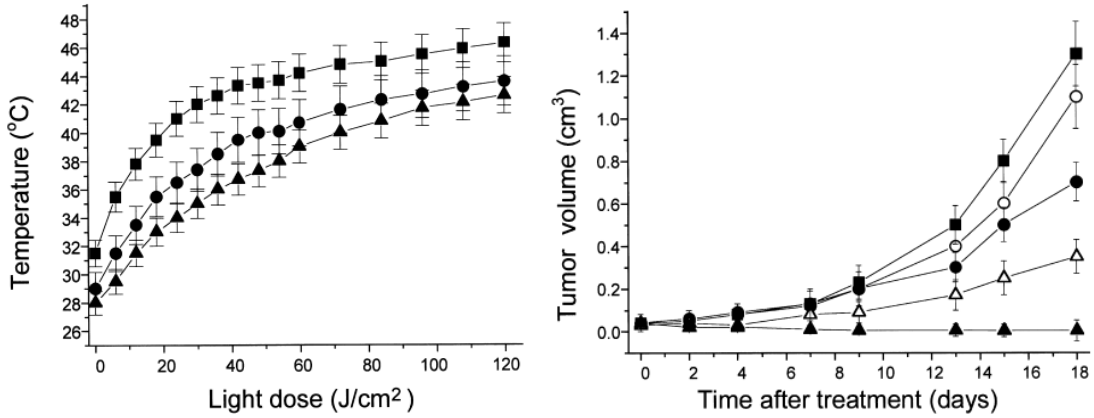

Fig 222 Legend and figures of Kostenich et al. [316] Left: Temperature-time profiles in melanoma B16 tissue above the tumor (square), at depths of 2 mm (circle) and 4 mm (triangle) during pulsed photoirradiation with pulse energy density 0.6 J/cm² and frequency 1 Hz. Five mice in each group were examined. Error bars, SE. Right: B16 melanoma growth curves after pulsed Photothermal therapy. 1 Hz-photoirradiation (0.6 J/cm² per pulse) was performed with light doses of 60 J/cm² (open circle), 72 J/cm² (closed circle), 90 J/cm² (open triangle) and 120 J/cm² (closed triangle). (closed square), untreated control. Ten mice in each group were examined. Error bars, SE.

In the experiments of Werthmöller et al. [317], the hyperthermia is induced by microwave heating. This study presents a comparison of the effect of hyperthermia, irradiation and the combination of both on B16-F10 tumors.

"Treatment of B16-F10 melanomas with ionising radiation and hyperthermia On days 8, 9 and 10 the irradiation was performed. The tumours were locally irradiated with a clinically relevant single dose of 2 Gy using a PRIMART linear accelerator (6MV, Siemens, Munich, Germany). Local hyperthermia was delivered on days 8 and 10, in each case 4 h after RT. To do so the mice were anaesthetised and the tumours were heated locally with microwaves to 41.5 C for 30 min using a BSD50 Hyperthermia System (BSD Medical, Salt Lake City, UT)"

It appears that hyperthermia greatly increases the effect of irradiation. Radiotherapy alone does not enable to induce a difference in tumor growth. The immune response induced is particularly interesting, since B16 melanomas are known to be poor immunogens.

"This suggests that RT in combination with HT induces a tumour microenvironment which is immunogenic and characterised by apoptotic and necrotic tumour cells, presence of the danger signals HMGB1 and HSP70, enhanced infiltration of CD8+ T cells, DCs, and NK cells, and concomitantly decreased infiltration of Treg and MDSC. HT combined with RT can therefore be regarded as a potential in situ tumour vaccinator"

The immune response of B16 melanoma induced by hyperthermia is specifically studied by Kubes et al. [251] and T. Takada et al. [318]. In the first paper, the tissue is heated with microwaves, in the second by magnetite nanoparticles.

More general information on the immune response induced by hyperthermia can be found in section VI.1.3 (Biological effects of hyperthermia) and in the papers [248], [249] and [251] which give a good idea of the number of signaling pathways involved in the response to hyperthermia.

VI.3.1.2 Chernets at al. [79], 2015, melanoma B16/F10

The results presented in [79] are clearly in a range of temperature which elicit anti-tumor response due to hyperthermia. To be convinced, let us recall that the treatment causes a temperature rise of 27 ° C at the center of the tumor of the dead mice. In addition, the simulations show that the temperature rise will be substantially the same in the tumor of living mice, which leads to a temperature of the order of 57 °C. The treatment has a total duration of 7 min. The discussions of the paragraph VI.3.1.1. (especially the papers of Li et al. [315] and Kostenich et al. [316]) show anti-tumor response very similar to those obtained with plasma-treatments. Moreover, these experiments are in a range of temperature containing the temperatures reached by the tumors of Chernets et al. It has even been found that tumor slowing can even be obtained at lower temperatures and for shorter treatments than those induced by plasma-skin interaction. These studies are carried out under biological conditions which are very similar to those of Chernets et al. and are therefore fully valid to make a comparison (mouse species, melanoma line, tumor size, and even position of temperature probe).

The next figure (Fig 223) enables to compare the results of Li et al. [315] with those of Chernets et al. At first glance one could say that the experiments of Li et al. expose the tumors to hyperthermia for a longer time (10 min at 55 °C). But, it is recalled that the time required to inflict a given amount of damage (related to the denaturation of structural proteins) is divided by 2-3 for each additional degree (see VI.1.2 "Orders of magnitude related to hyperthermia"). So, the damage inflicted during plasma-experiment are therefore probably larger. Both results, however, are quite comparable.

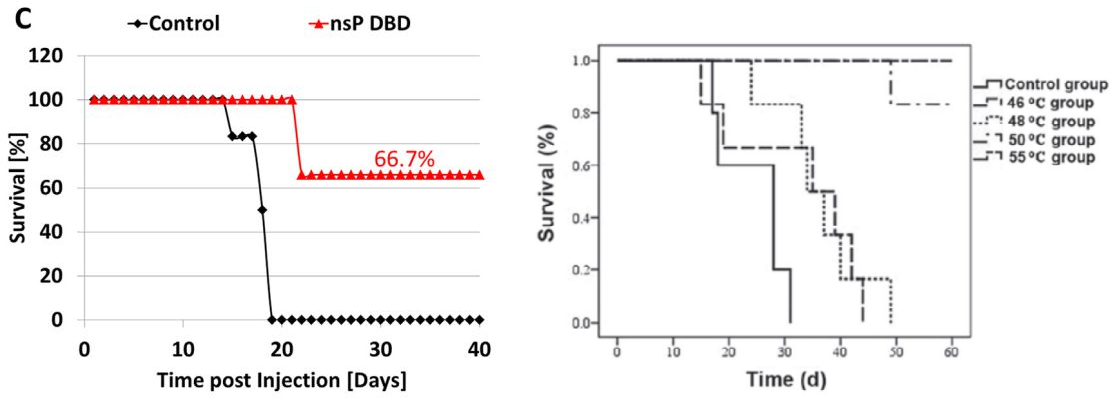

Fig 223 Left, legend and figure 1C from Chernets et al. [79]. Survival for nsP DBD treated tumors (red triangle) and control untreated tumors (black diamond) as a function of time post-injection (n = 6 each) Right: Legend and figures from Li et al. [315] Survival curve over a period of 60 days following hyperthermia treatment. n=6 mice/group, T=0 corresponds to the time of hyperthermia.

The comparison of the results of Chernets et al. and Kostenich et al. [316] is shown in Fig 224. Indeed, in the work of Kostenich et al., tumor ablation is obtained with a light dose equal to 120 J/cm². This corresponds to 200 s of treatment, leading to a temperature at the center of the tumor of 43 °C at the end of the treatment. This thermal stress is lower than that caused by plasma treatment according to the measurements done by Chernets et al.

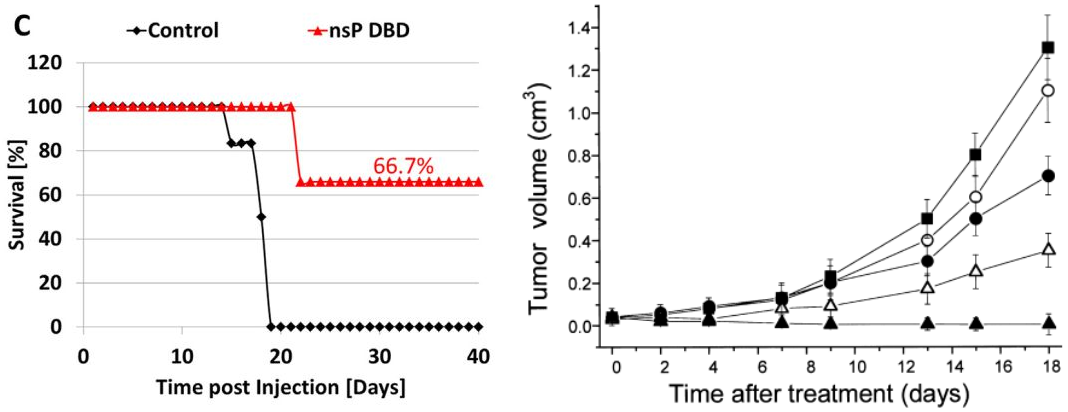

Fig 224 Left, legend and figure 1C from Chernets et al. [79]. Survival for nsP DBD treated tumors (red triangle) and control untreated tumors (black diamond) as a function of time post-injection (n = 6 each). Right: legend and figures of Kostenich et al. [316] B16 melanoma growth curves after pulsed Photothermal therapy. 1 Hz-photoirradiation (0.6 J/cm² per pulse) was performed with light doses of 60 J/cm² (open circle), 72 J/cm² (closed circle), 90 J/cm² (open triangle) and 120 J/cm² (closed triangle). (closed square), untreated control. Ten mice in each group were examined. Error bars, SE.

As a result, the non-thermal effects are entirely masked by the response due to hyperthermia. It turns out that arguments proposed by the authors to justify that hyperthermia plays no role are questionable. However, it leads to very interesting physical questions involving pig-skin and the gel layers covering the differents skins.

To begin, what is the argument proposed by Chernet et al. which leads them to affirm that they observe an effect due to plasma chemistry?

- First, they observed that the anti-tumor response is less efficient when a layer of gel is applied at the surface of the tumor

- Then, they observed that the addition of H_2O_2, to the gel, enables to restore the anti-tumor effect at a level which is similar to those of direct treatment.
- To justify that hyperthermia does not play a role, they do experiments on pig skin. At 2 mm depth, it turns out that the presence of gel does not significantly change the dynamics of heating.

What conclusions do they draw from these observations?

Since the gel does not change the temperature in the center of the pig's skin, they assume that this is also the case for the mouse. So they deduce that the gel only slows the diffusion of the chemical species from the plasma. Then in the experiment with the H_2O_2 gel, it also assumes that the addition of H_2O_2 does not modify the thermal properties, and makes it possible to restore some efficiency to the plasma treatment.

It could be shown by finite element model that:

First of all, the temperature increase is very different in the case of pigskin (+6 °C) and in the case of the freshly sacrificed mouse (+27 °C). The simulations could probably show if the incident thermal flux caused by plasma-surface interaction is very different for the simulation of pig or mouse skin. In a second step, the effect of the gel layer on the skin can be modeled. For low concentrations of glycerol, the thermal properties differ little from those of water [319]. The simulations could probably show that the temperature reached by the skin depends a lot on the thickness of gel.

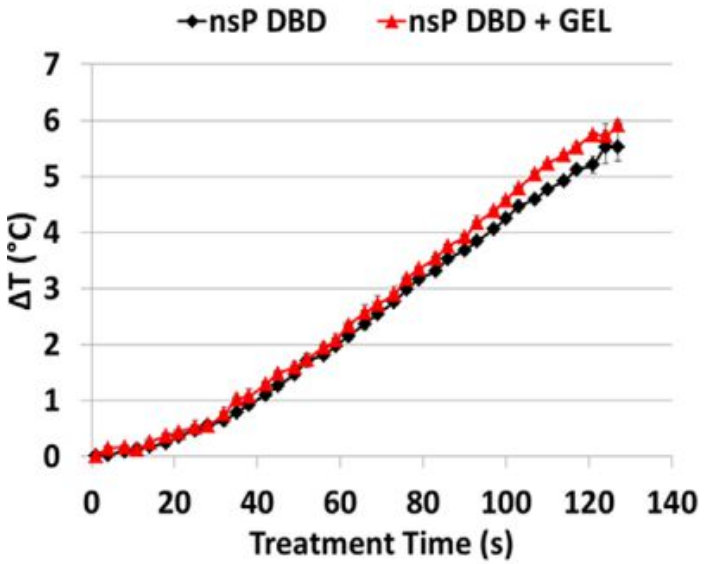

Fig 225 Legend and figure 1C from Chernets et al. [79]. Measurement of temperature 2 mm below the pig skin surface during nsP DBD treatment for 2 min, with or without gel, showed no significant differences (with gel – red triangles; without gel – black diamonds).

Thus the depth of damage depends considerably on gel-layer thickness. Nothing indicates that the thickness has been controlled in the work of Chernets et al. [79]. The difference between survival rates of the “gel” or “gel+H_2O_2” groups with “control group” could be attributed to a lack of control of gel thickness in the experiment. It also turns out that an addition of H_2O_2 increase the thermal conductivity of the gel, which could increases the heating of the skin.

VI.3.1.3 Keidar et al. [12], 2011, melanoma B16/F10

In [12], Keidar et al. report positive results regarding B16-melanoma (C57/BL6) and SCaBER tumor (nude mice). They report that tumor growth rates of B16-melanoma is significantly decreased after cold plasma treatment. They claim that their source does not cause heating of the tissue with the following argument:

"The skin temperature during plasma treatment was measured using an infra-red thermometer (Traceable, Model no. 4470, Control Company, Friendswood, TX, USA) to assess whether the cold plasma effect on cancer tissue is associated with thermal damage. Cold plasma treatment produced an increase in skin temperature of approximately 2°C above room temperature, which is below the temperature needed for thermal damage."

With this instrument, obtaining a spatial resolution of less than 1 mm would require a distance to use the thermometer at less than of 1.1 cm. Moreover, the spatial resolution of this measuring instrument cannot be made arbitrarily small. Before reaching the diffraction limit, the aberrations of the optics, in particular, their dispersions, generally limit the spatial resolution to a few millimeters, this could lead to an underestimation of surface temperature as explained in section VI.2.6.1 (page 226).

Moreover, the mouse skin shows the presence of damage, just after treatment (see Fig 226). This kind of damage is usually associated with a burn as stated in the paper of Dobrynin et al. [78].

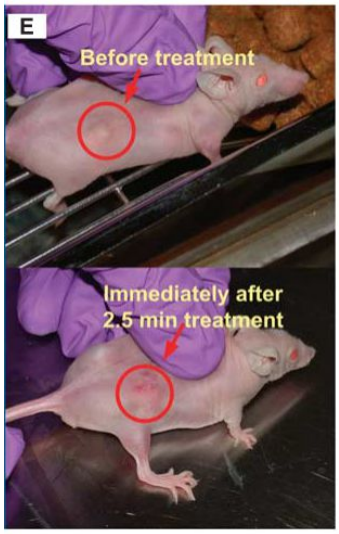

Fig 226 From [12]

If mild-hyperthermia occurs during this treatment, the positive effects of plasma treatment, namely a slowing of tumor growth (Fig 227), could be attributed to thermal effects.

As previously discussed in VI.3.1.1, the thermal sensitivity of B16 melanoma to mild-hyperthermia is so high that a moderate increase in temperature for a relatively short time is enough to slow tumor growth of 10-15 days. The same plasma device was used in another study (Walk et al. [81]).

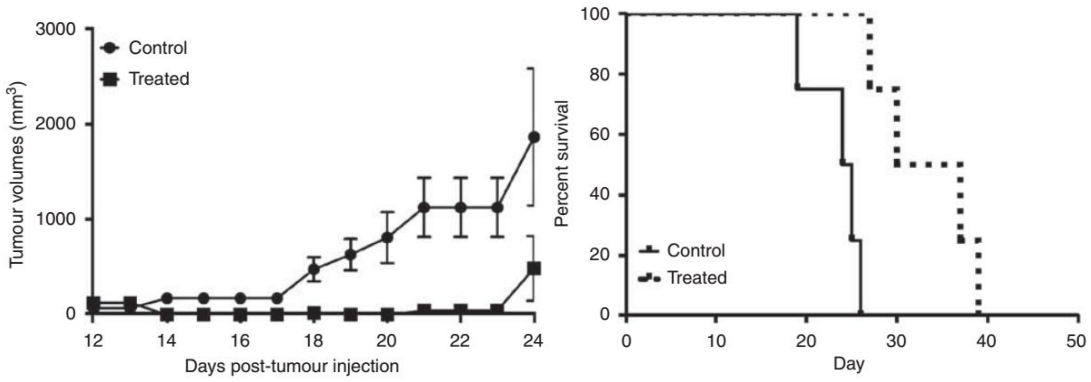

Fig 227 Legend and figure from [12]. Left: cold plasma treatment effect on the growth of established tumour in a murine melanoma model. Right: Cold plasma treatment effect on the mice survival in a murine melanoma model.

The paper of Walk et al. [81] describes the treatment of an *in-vivo* murine model of neuroblastoma (Neuro2a).This paper begins by defining the operating conditions of plasma-device and refers to the paper of Shashurin et al. [320]:

"The CAP device utilized for these experiments was previously described [320] and additionally modified for handheld application of the CAP. All treatments, both in vivo and in vitro were administered at 4 kV using industrial-grade helium at a flow rate of 4l/min

So let's look in the paper of Shashurin et al. [320]. Unfortunately, this paper does not contain temperature measurement. However, Shashurin et al. writes that

"Short-time up to 10 s exposition of the finger to the jet results in a mild sensation of heat in the treated area."

Several remarks can be made about this statement:

It is recalled that human skin is very different from mouse skin (see section VI.1.1, page 173). The thickness of the epidermis is considerably higher for humans (mean value 75 µm-150 µm) than mice (~13 µm). In addition the thickness of the epidermis is greater in body parts exposed to mechanical stress (like the fingers). According to [321], the epidermis of the fingertip has a thickness of $369 \pm 111\ \mu m$. However, the cells signaling the pain or the impression of heat are located in the dermis [210]. Consequently, these cells are protected from heat flow by a particularly thick and insulating layer in humans compared to the mouse. It should also be noted that the sweat phenomenon can consume a large part of the incident heat flux in humans. It turns out also that mice do not have sweat glands (as discussed in section VI.1.5.7, page 196). Because of this, the temperature is necessary greater in mouse skin than in humans for the same treatment.

Consequently, the following argument: **"I put plasma on my finger, I do not feel heat, thus the skin of the mouse will not experience hyperthermia" is <u>false</u>**.

The fact that Shashurin has reported a sensation of heat after only 10 seconds may raise concerns that plasma treatment will heat the skin of the mouse beyond 42 ° C.

Now let's go back to the commentary of Walk et al. [81]. This paper does not contain temperature measurement. The absence of heating is justified by a reference to the paper of Keidar et al. [12].

"CAP therapy provides a unique method of treatment. Unlike argon plasma, cryoablation, or electrocautery, this treatment is atraumatic to the tumor and surrounding tissue. A prior paper utilizing our device investigated surface temperatures during treatment and found a 2°C rise from room temperature

[12]. There is no evidence of thermal damage to skin following treatment. Application of the beam to one's skin is tolerable and pain-free"

We have shown that the temperature measurement used in [12] could be significantly biased. It also turns out that the treatment conditions used on neuroblastoma are different from those used in [12]. Indeed, the helium flow is lower in this studies than that used in [12] (4 l/min *versus* 11 l/min). However, it is likely that a decrease in flow will lead to an increase in gas temperature, as seen by the users of kINPen09 [107].

Fig 228 Legend and figure from [81] . (A) Female A/J mouse with a tumor on the right hind leg (arrowhead). Mice were selected for treatment once tumors reached 5mm in any dimension. (B) The tumor was treated through the skin with CAP for five minutes. (C) View of tumor immediately following treatment. (D) View of right hind leg 25days after CAP therapy demonstrating ablation of the tumor.

VI.3.1.4 Daeschlein et al. [76], 2013, melanoma B16/F10

Daeschlein et al. [76] compare the effects of two plasma sources described below:

1) *"**Atmospheric pressure plasma jet (APPJ), kINPen 09 (Institute for Plasma Science and Technology Greifswald, Greifswald, Germany)**. For a detailed characterization of the APPJ, see Weltmann et al. [323]. Argon as the feed gas flows through the capillary (gas flow rate of about 8 l/min). A radio frequency (RF) voltage (1–5 kV, 1.5 MHz) is coupled to the centre electrode. The temperature at the tip of the beam with a length of up to 12 mm did not surpass 37 °C as a result of the cooling effect by the argon stream together with the electronic regulation when the device works with 60 V [324]."*

2) *"**Dielectric barrier discharge (DBD, CINOGY GmbH, Duderstadt, Germany)**. The second plasma source was a dielectric barrier discharge device. The DBD generates high-voltage pulses (14 kV) across small gaps with the high-voltage electrode being covered with a dielectric barrier made of Macor [325]. The application electrode measures 20 mm. The pulse repetition rate is adjustable between 100 and 400 Hz, which leads to electric powers dissipated in the gas discharge in the range of 167–237 mW [325]."*

The tumors are significantly larger (~8 mm) than those of the experiments of Freeman [79] and Keidar [12] (~5 mm) and are exposed to plasma every day. The conditions of plasma-exposure are specified by:

1) *"Tumors were treated with cold plasma once they were 8 mm in diameter. All treated mice received 2 × 3 min of cold plasma treatment with DBD (30 s interruption after 3 min of treatment) and 5 min with APPJ"*

[107] See [322], however the plasma jet used in this paper (kINPen04) is different in terms of frequency, voltage, and gas flow.

2) *"Treatment with plasma Treatment with DBD (D) was manually performed at a distance of 1–2 mm between electrode and skin. The APPJ (J) treatment was carried out with the tip of the jet just touching the surface and being continuously moved over the whole tumor surface."*

Curiously, the results are not given directly in terms of tumor volumes. The conclusions are drawn from derived quantities: tumor growth acceleration (TGA) and daily volume progression (DVP) in mm^3/day. TGA is the quadratic coefficient of the curve that fit tumor volume as a function of time $V(day) = b0 + b1 * day + b2 * day^2$.

The results show a weaker effect than those observed by the Freeman's and Keidar's teams.

- *"DBD (D) alone caused no and APPJ (J) alone a non-significant (3.6 days) effect on survival" [76]*
- *"Regarding TGA, both plasmas J and D as single treatment caused significant delay of TGA (P = 0.035, respectively 0.063; one-sided t-test) (J with slightly more efficacy than D)" [76]*
- *"In conclusion, CP (J or D) alone can significantly delay melanoma skin tumor growth"[76]*

Now, what data are available regarding the thermal aspect of the two plasma-device.

VI.3.1.4.1 What about hyperthermia and the DBD device used in the paper of Daeschlein et al. [76]?

The paper does not report any measurements made on the tissue itself and is based on the results presented by Kuchenbecker et al. [325]. This paper is a very precise characterization of the thermal and electrical aspects of this plasma source. The measurement method is described by the following statements.

- *"The temperature of the treated surface is measured using a probe consisting of thin round Al-plate."*
- *"The heating of the treated object is studied using probe measurement. The mass of the probe is 0.46 g. The probe is hung on the thin wires with a diameter of 0.27 mm and length of 100 mm. The ends of the wires are connected to the ground. The probe is heated in the discharge for 10 min (see Fig 229). The temperature of the probe is measured with an accuracy of ±0.5 K."*
- *"By means of steady-state temperature difference (T) and the value of the h · A parameter, the heat input is determined. The heat input is calculated by assuming that cooling efficiency of the probe during discharge is equal to that in afterglow. But the gas temperature in the gas gap is clearly higher than outside. Therefore, during active phase of discharge, cooling occurs mainly from one side of the probe plate. The real value of the heat input is in between the values obtained by assuming both sides and one side cooling. We take into account this effect and calculate the heat input for both electrodes assuming that the heating of those are equal. The heat input increases with interelectrode distance (see figure) because averaged current is approximately constant for the discharge in the gas gap broader than 1.0 mm and at the same time the ignition voltage increases"*

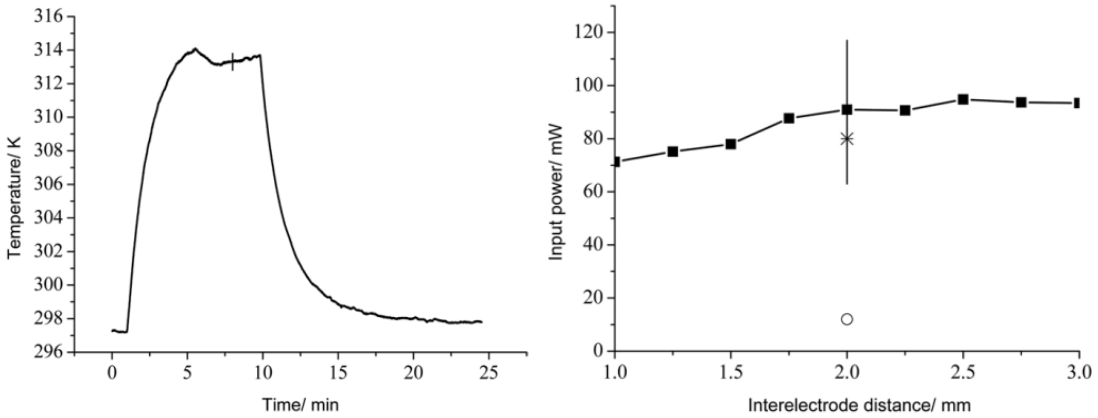

Fig 229 Legend and figures 18 and 19 from Kuchenbecker et al. [325]. Left: Temporal dependence of the probe temperature by heating during 10 min in DBD discharge. Right: Electric power consumed for heating of the electrodes via interelectrode distance (black square). Total electric power dissipated in discharge (star) and in excitation of chemically active species (hollow circle).

Note that the maximum temperature reached by the probe is about 314 K (41 °C). A tissue at this temperature would undergo the modifications associated with moderate hyperthermia (modification of the blood flow, oxygenation ...). In addition, the initial temperature of the probe is 25 ° C, which is 5 ° C lower than the temperature of the skin at the beginning of treatment (30 °C, temperature of the skin after few minutes of anesthesia). If the increment of temperature is the same on the skin, the skin would reach a temperature of 46 ° C.

With the information cited so far, it is not possible to know if the skin will be in a state of hyperthermia or not. Fortunately, the thermal characterization was continued. The paper describes a measurement of the incident heat flux. We will use it to guess the temperature of the skin during the treatment described in Daeschlein et al. [76] Unfortunately, in the absence of measurement of tissue temperature, the result will be more uncertain. We assume that the incident heat is the same as that given in Fig 229 (~80 mW).

The plasma is on for 3 minutes, off for 30 seconds and on for 3 minutes again as in Daeschlein et al. [76]. It is assumed that the tumor has a diameter of 8 mm. The simulation code used is the same as in section VI.2.7.2 (“Living mice”, p 242). The thermal properties of the tissue are those summarized in the tables of the section VI.1.6 (p 200). It is considered that the skin is heated by a constant incident heat flux $q_{plasma} = Cst\ W.m^{-2}$, and cooled by natural convection.

Unfortunately, the area of the plasma-skin interface is not known. Numerical simulationd are done with the two following assumptions:

- Either the surface covered by the plasma has the same dimensions as the inner electrode of the DBD (radius of 9 mm).
- Either the treated area covers only the tumor (radius of 4 mm).

The power per unit area is such that the total power of the incident heat is 80 mW in both cases. Fig 230 shows that the temperature reached by the upper layers of the skin is below the limit of mild-hyperthermia (39 °C). Of course, if the 80 mW were distributed on a smaller area, the temperature increase could be higher.

Note that the surface temperature of the skin is lower than that measured by the probe (32 and 38 ° C against 41 ° C for the metal probe). This is consistent with the fact that

the skin evacuates the heat towards the interior of the body by thermal conduction and thermal exchanges with the blood (In addition to the cooling due to convection and radiation which are also present above the probe). Regarding the paper Kuchenbecker et al. [325], the temperature sensor is not really mentioned (a thermocouple ? a fluoroptic sensor ? only the target is described). Moreover, the proposed modeling does not take into account radiative thermal losses. Without more information about the metal target, it is difficult to know if radiation loss is negligible or not. Indeed, the emissivity of aluminium varies between 0.02 and 0.9 depending on the surface state, the thickness of the oxide layer and alloy. It is recalled that the losses depend on the fourth power of the temperature. The equations representing the cooling of the metal probe must therefore take the form:

$$\frac{\partial(C_h \Delta T)}{\partial t} = \frac{\partial Q}{\partial t} - h.A.\Delta T - \epsilon_{Al}\sigma\left(T^4 - T_{amb}^4\right).A$$

The linearization of the radiative term is valid only when:

$\left(T^2 + T_{amb}^2\right)(T + T_{amb})$ varies little on the range of temperature. The minimum temperature is 25 °C; the maximum temperature is 41 ° C.

Numerical application

With $T_{amb} = 25\ °C$,

$$if\ T = 25\ °C \qquad \left(T^2 + T_{amb}^2\right)(T + T_{amb}) = 1.059 \times 10^8\ \mathrm{K}^3$$

$$if\ T = 41\ °C \qquad \left(T^2 + T_{amb}^2\right)(T + T_{amb}) = 1.147 \times 10^8\ K^3$$

which represents a relative error of only 7%. Consequently, the integration of a term of radiative losses in the term of convection (linear terms) does not cause a significant error. Consequently, these measurements are likely valid, and the simulations confirm that the skin of mice has not been subjected to hyperthermia provided the area exposed to the plasma is sufficiently large, and heat transfer is the same above the skin and above the metal probe.

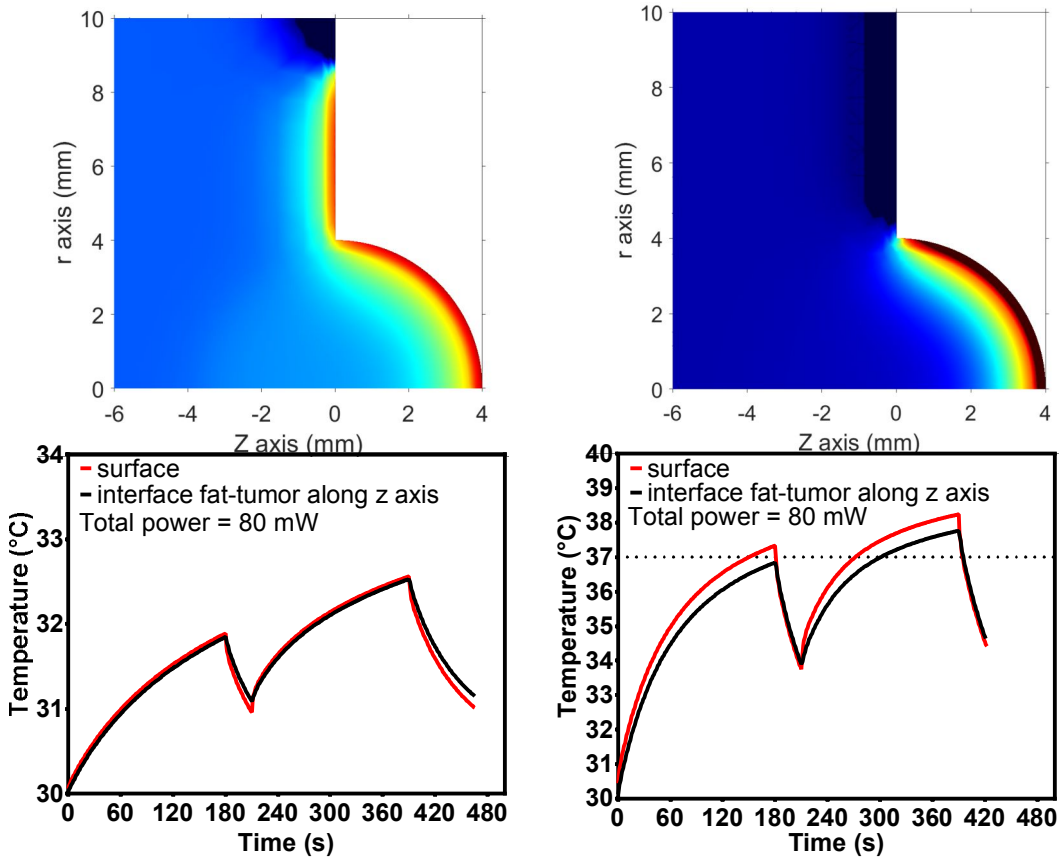

Fig 230 the color map indicates the size of the heated surface during the simulation. On the left, the surface below an 18-mm disc, on the right, only the tumor. The temperature along the z-axis is plotted for two depths: surface = red curve, fat-tumor interface (depth = 364 µm) = black curve. In both cases, the power per unit area is such that the total power of the incident heat is 80 mW. In both cases, the temperature increase experienced by the tissues is lower than the threshold of mild-hyperthermia (39 °C). It depends on the area over which the 80 mW of heat is distributed. The sequence consists of 3 min of plasma on, followed by 30 s plasma-off, the skin cools, followed by another 30 s of plasma

VI.3.1.4.2 What about the kINPen09 used in the paper of Daeschlein et al. [76], (2013)?

The paper [76] of Daeschlein et al. does not report any measurements made on the tissue itself with the kINPen09 and is based on the results of a previous paper.

The statement *"The temperature at the tip of the beam with a length of up to 12 mm did not surpass 37 °C"* has been proven in another paper of the same author [326].

It appears that the operating conditions of the kINPen09 are the same as those of the anti-tumor study. Gas flow, operating Voltage and distance are the same. The green curve (60 V) of Fig 231, describes the temperature in the plasma plume. It is also noted that it is necessary to control the distance of the tip to better than 2 mm since at 10 mm the temperature reaches the threshold temperature of 42 °C.

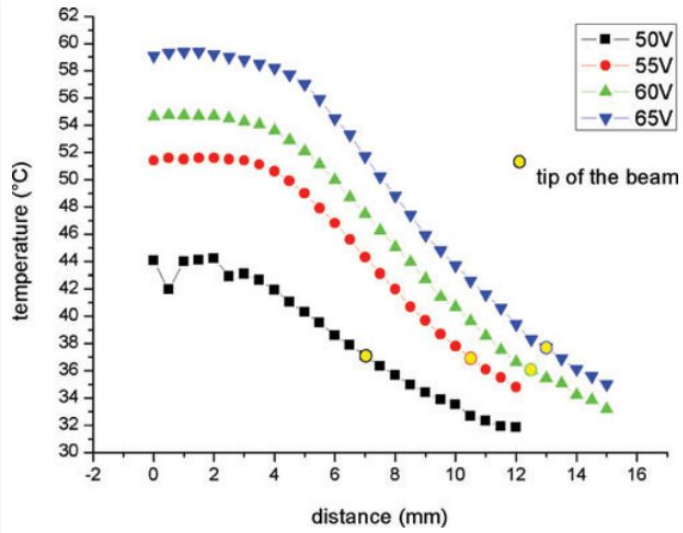

Fig 231 Legend and figure from the paper of Daeschlein et al. (2012) [326]. Temperature profile of the plasma beam.

The paper [323] explains in what operating conditions the kINPen09 can generate excessive heat (In continuous mode, with a flow of 5 slm). The temperature measurement was performed by placing a temperature probe at the center of the gas flow. This probe is fluoroptic: as said before, this probe works by measuring the decreasing fluorescence of molecules placed at the end of the probe[108]. The response time of such probes is generally short[109]. Moreover, they are insensitive to electromagnetic disturbances since the signal is optical.

The only remark that can be made is the size of the probe: its diameter is of the order of 0.8 mm, it means that the measured temperature is averaged over this distance, and therefore the central temperature may be slightly higher than what is claimed (Fig 232).

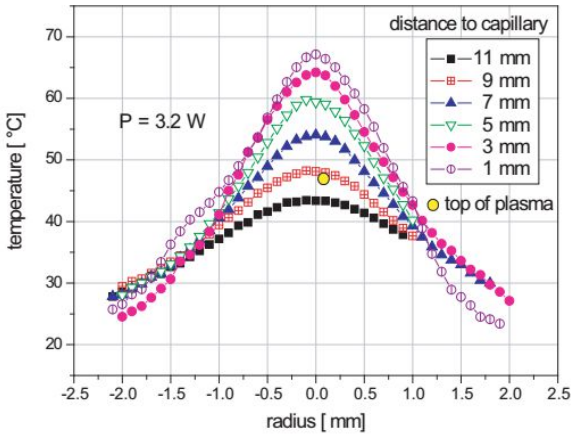

Fig 232 Legend and figure from the paper of Weltmann et al. [323]. Radial temperature profile of the APPJ (Kin-Pen09 parameters: P=3.2 W, U=65 V).

Note also that the size of the plasma corresponds to that of the heating zone simulated in VI.2.6.3. Another criticism concerning this type of measurement is that the nature of the discharge is not necessarily the same above the temperature probe or a mouse.

---

[108] . The results of this probe can be distorted if the fluorophores are exposed to laser IR irradiation [327]. Here, this is probably not relevant.

[109] Since the time needed to thermalize the thin layer of fluorophore can be short.

Under these conditions, the authors claim that it is possible to limit the damage by moving the plasma source quickly above the skin. This is certainly true, for a single passage, but it would be necessary to know how often the plasma source goes back to the same point. Indeed, in a similar way than fractioned treatment, slow heating of the tissues could lead to thermal damage (as explain in VI.2.8, page 244). The APPJ could also be used in burst working mode to reduce the temperature. This seems a very effective way of reducing the temperature, but this is probably done to the detriment of the production of reactive chemical species.

Unfortunately, the following information is missing:

- The temperature measurements of a substrate exposed to the treatment conditions precisely used above the tumor (and not only in the plasma plume).
- As the source is moved manually, it would be interesting to know the pattern described on the surface of the tumor and its frequency of repetition. And the height above the tumor in each point.

Among the plasma sources used, the kin-pen is probably the best thermally characterized. But in the absence of published subtract temperature measurement of temperature under the conditions specifically used by Daeschlein et al., it is not possible to conclude that there is no hyperthermia, strictly speaking.

In a very clever way, the heat flux leaving the plasma has been studied in [323] by measuring the temperature of a copper target (floating electrode). The heat flux is estimated at about 75 mW. Since the plasma is modeled by a cylinder with a radius of 1 mm, we can estimate the value of the incident thermal flux:

$$q_{plasma} = \frac{75 \times 10^{-3}}{\pi(10^{-3})^2} \cong 23\,900\ W.m^{-2}$$

which is an order of magnitude greater than the thermal flux we have determined in VI.2.9 (maximum heat flow without damage for long treatment). This order of magnitude is ultimately very similar to that of laser treatments presented in (VI.1.2 page 175). This is not surprising since, in the absence of displacement, kINPen09 actually causes damage in these operating conditions (continuous mode, 8 L/min). And that's why it was chosen to move the device above the skin.

VI.3.1.5 Mashayekh et al. [77], 2015, melanoma B16/F10

Mashayekh et al. describe treatment of mice bearing melanoma B16/F10 [77]. To ensure that the melanoma has not heated up, an image acquired with a thermal camera is presented. This image is visible on the left side of Fig 233. The target used during this measurement is not specified in the paper. After discussion with one of the authors, A.Mashayekh, it appears that the target is a piece of wood (private communication of A.Mashayekh). As the temperature measurement is done with a thermal camera, it is likely that the spatial resolution is adapted.

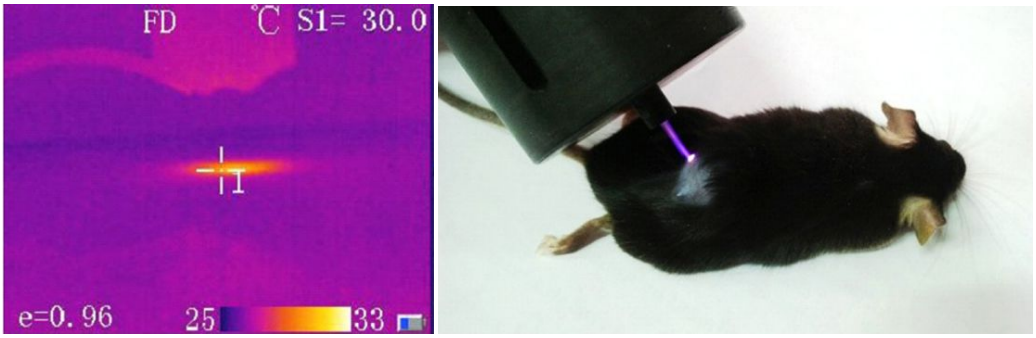

Fig 233 Pictures from Mashayekh et al. [77]

The heating of the wood found on the surface is very low in all the treatment conditions envisaged. A simulation was carried out by modeling the wood with the following thermal properties:

$$\rho = 650\ kg.m^{-3}$$
$$\lambda = 0.16\ W.K^{-1}.m^{-1}$$
$$C = 1600\ J.kg^{-1}.K^{-1}$$

When the plasma-surface interaction surface is modeled by a filament with a diameter of 1 mm (private communication), the temperature at steady state (33°C) is reproduced by the simulation with an incident heat flux 2800 W/m². In these conditions, the total power is equal to 2.2 mW.

On the other hand, it is likely that the nature of the discharge is different above the mouse compares to those above the wood. Indeed the mouse is relatively conductive while dry wood is a good electrical insulator. It is well known that the electrical properties of the target play a key role, for example, on the helium density of the metastable and the entire discharge [39]. It is reasonable to imagine that the same goes for thermal behavior.

The paper shows that plasma treatment is effective against B16 melanoma. However, tumor volumes are given only in standardized form (as shown in Fig 234).

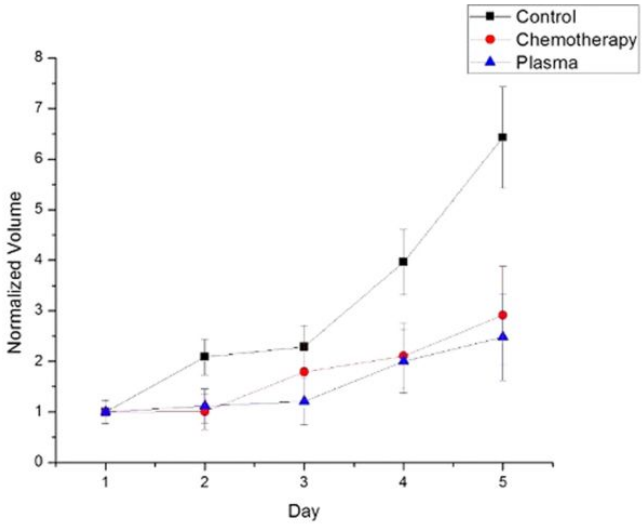

Fig 234 Legend and figures of Mashayekh et al. [77]. In-vivo comparison of different groups

Regarding the condition of the tumor, the author told me that no damage was visible (necrotic or burning damage) at the surface of the tumor (private communication of

A.Mashayekh). In addition, interestingly, the treatments were done on conscious mice that showed no signs of pain (private communication of A.Mashayekh).

Since no temperature measurement was made on the mouse itself, it is not possible to exclude the possibility that the temperature is higher than those measured above wood (since the electrical properties of the two targets are different). The absence of pain and the absence of visible burn should exclude strong hyperthermia. However, mild-hyperthermia (as explain in VI.3.1.1) could explain the slowing of tumor growth.

VI.3.2 Summary of the critical approach

Finally, few papers rigorously control the hyperthermia induced by plasma treatments. Often it is not possible to know if the temperature played a role or not in obtaining the therapeutic effects obtained.

However, the literature concerning the treatment of B16 melanoma shows that mild-hyperthermia can have a significant effect on tumor growth without necessarily producing visible damage. Sometimes some papers are based only on the following statement to exclude the role of hyperthermia: "I put my finger under the plasma-jet, and I did not feel any warm up ". We have shown how false this statement is because of physiological differences between our skin and those of mice.

We need to measure systematically[110] the temperature of the skin during and after the treatment. The simplest solution is to use an infrared camera with sufficient spatial resolution. It is only under these conditions that it will be possible to prove that cold plasmas have a non-thermal antitumoral effect.

On the other hand, if cold plasmas have a thermal effect, it might be interesting to recognize it and exploit this fact to kill cancer.

In the paper of Chernets et al. the temperature is measured with admirable precision at the center of the tumor showing that the hyperthermia cannot be excluded (contrary to what is stated by authors) [79].

In the next two paragraphs and to conclude this critical approach, we will consider which non-thermal biases could also play.

Therapeutic versus preventive treatment

Tumors in humans are not detected until they reach a certain size. However, the effectiveness of therapy will depend significantly on the initial tumor size at which it starts. Consequently, **a**n *in-vivo* model is considered as representative of the effect that would be obtained during therapy, if the tumors have reached few mm before the first treatment. Otherwise, the experience represents the effect of a preventive approach.

Wound healing and Low-Level Laser Therapy (LLLT)

According to the review of Avci et al. [328], LLLT/phototherapy/photobiomodulation refers to the use of photons to alter biological activity, but with light intensity that excludes the possibility of thermal effect. The exact mechanism remains essentially not understood but could be related to the absorption of light by some chromophores located in the mitochondria [328]. LLLT could accelerate wound healing and promote skin rejuvenation. It would be interesting to see if the light produced by plasma discharges

[110] on each mouse and during each treatment.

could produce such effects and contribute to the improvement of wound healing. More information can be found in the following papers: [328]–[332].

VI.4 Conclusion

The development of this chapter started from the observation that, sometimes, cold-plasma experiments involved significant heating of the biological tissue. “Significant” means high enough to induce biological changes in the behavior of the cells constituting the tissue. This chapter contains three main parts:

i. Description of the biological effects of hyperthermia
ii. Modeling of power transfer from plasma to living tissues and subsequent damages.
iii. Compaison of model with in-vivo experiments presented in Chapter V as well as with few article published by other group dealing with the treatment of B16 melanoma

This term deliberately imprecise of “biological changes,” covers a wide variety of modifications regarding the enzymatic activity, the denaturation of proteins, the production of thermo-induced oxidative stress...

Let us briefly summarize the consequences of hyperthermia detailed in section VI.3.

- At the scale of one cell, these changes can lead to its death by a great variety of mechanisms. If the cell survives, it can develop a thermotolerance, making it resistant for several hours to another thermal stress. It is noteworthy that these changes induce radiosensitization of the cells for several hours. This is particularly useful against chemoresistant cancer.
- At the scale of the tissue, the changes vary from a slight increase in tissue oxygenation associated with vasodilatation of blood vessels and slight changes in tissue pH, to the complete destruction of living tissues by necrosis or apoptosis and the total annihilation of the blood network as a result of blood coagulation.
- At the scale of the organism, thermal stress can trigger systemic responses of the immune system.

On purpose, we have not yet spoken of temperature. It is obvious that these phenomena do not occur at any temperature, or with the same amplitude. However, the threshold temperatures delimiting the temperature intervals that defined the magnitude of phenomena depend on several parameters. Among these, I would like to draw attention to the fact that the effects of hyperthermia strongly depend on the species, and organs, and even of the cell type considered.

- mouse skin is more sensitive to hyperthermia than human skin [224], which is important since the majority of in-vivo experiments use mice...
- Some organs are subject to greater damage for the same exposure to hyperthermia
- All the different cells of the same organ do not have the same thermosensitivity.

This greatly complicates the definition of limit temperature. T>~ 45°C is the threshold to obtain a significant ablation in relatively short time (~min).

It appears that there are great similarities between the effects induced by hyperthermia and the effects that the plasma-medicine community has shown in the last ten years.

Since plasma-skin interaction can be at the origin of a warm-up of the skin, a model for studying the propagation of heat through the skin of a mouse has been developed and validated with experimental results. Conversely; this model specifies the characteristic

that a thermal diagnostics must have to obtain reliable measurements of temperatures. The methods of temperature measurement and their scientific description are crucial points. In particular, the spatial resolution of certain infrared thermometers could lead to minimize the measurements of surface temperature

In the present work, the tissues damages are modeled with the denaturation reaction of collagen, the major component of skin. The rate of reaction strongly depends on the temperature. An increase of only 1 ° C divides the time to obtain the same amount of damages by 2 or 3. The degree of burns is linked with the temperature history of the skin with the damage function [210], $\Omega(t) = \int_0^t Aexp(-\frac{E_a}{k_b T(t)})\, dt$, which enables the simulation of thermal damages. Where t is the time, $T(t)$ the temperature as a function of time, A (in s^{-1}) is a constant which depends on the specie and tissue, E_a is the energy of activation of the denaturation. This simulation gives the volume of a subcutaneous tumor subjected to mild hyperthermia. It also describes tissues subjected to higher temperature, which can lead to tissue ablation. Heat burns may affect epidermis, dermis or subcutaneous fat (1st to 3rd-degree heat burn). The severity depends on the time and temperature of exposure.

- The model provides a quantitative approach of the thermal damages which corresponds to the current state of the art. The model takes into accounts
    - The thermal diffusion of heat
    - Radiative exchange
    - Natural and forced convection of heat with ambient air and Helium
    - The effect of blood perfusion
    - The effect of metabolic heat generation
    - The effect of temperature on blood circulation
- The model can reproduce the kinetics of heating and cooling of the surface of the tumor. The sensitivity of the cooling rate to various parameters is studied. The thermal conductivity (not the convection) is the main factor of cooling (see Appendix G).
- The simulation takes into account the specificity of mouse skin compared to human skin, in terms of thickness.
- The heat source due to plasma-skin interaction has been modeled either by the assumption that only hot helium ($T_{He} = 55\,°C$ assumption), or the bombardment of energetic particules ($q_{plasma} = Cst\ (t)$ assumption) is at the origin of the heating.
- We have benchmarked the code by comparison between computational results with time temperature measurements presented in Chapter V. The simulations are consistent with the totality of the experimental observations regarding the temperature and the severity of the damages.
    - Regarding the non-refrigerated multichannel-jet: Skin temperature after treatment of 3 or 5 min was around 45-48°C. Treatment of one min gave no damages. One treatment of three min gave no damages, but the repetition of this treatment at two days intervals gave damages after two or three treatments. Treatment of 5 min systematically gave damages.
    - The simulation of refrigerated multichannel-jet reproduces the evolution of the surface temperature correctly.
    - The treatment with the single jet does not cause any damage.
- The prediction of damages is a reliable result (see Appendix E). In the framework of fractionated treatment, the change in the settings[111] of the model does not

[111] i.e. the thermal conductivity of the tumor, the area of plasma-skin interaction, the value of blood perfusion, the two parameters defining the damage function (A and B)

modify the result in a qualitative way; in the sense of the tumor is always damaged **as long as the simulation correctly reproduces the temperature in the center of the tumor in continuous regime**.

- The simulation can give the conditions for which a plasma treatment can cause mild-hyperthermia without significant thermal damages. This could potentially elicit an additional therapeutic response.
- Particular attention has to be paid to the accumulation of damage during fractioned treatments at high temperature. It appears that the device used by Chernets et al. [79] should be used with a cooling time greater than 25 seconds[112], to avoid the formation of thermal damage in less than 1000 seconds.
- Finite element simulations could show at which point the evaporation over a slightly moistened skin can decrease the damages. For instance, a layer of 100 µm thick decreases the surface temperature reached by the skin by more than 15 ° C (for DBD treatment). The temperature at the center of the tumor loses only 7°C.

As a conclusion, temperature of tissues exposed to non-thermal plasmas should be controlled by appropriate thermal probes associated with models in order to i) discriminate the “plasma effect” such as RONS and electric field, from the effects of hyperthermia, ii) possibly take advantage of a controlled hyperthermia (mild or high) to increase the “plasma effect” , iii) avoid biased experiments when effects of hyperthermia have been neglected.

[112] The repeted sequence is : {cooling=25 seconds + plasma-on = 5 seconds}

General conclusion

The main motivation of this Ph.D. was to evaluate the potentialities of Cold Plasmas sources for cancer treatment. This is a long-term objective; to the date, only few published papers have evidenced antitumor effect of Cold Plasma Treatment. In our work, the priority given to *in-vivo* experiments underlies the whole architecture of this dissertation.

Chapter III is dedicated to the chemistry of plasma-liquid interaction. The plasma-device have been characterized with respect to the amount of H_2O_2, NO_2^-, NO_3^-, and HO° that the device produces per second (production rate in pmol/s) or per J (yield in nmol/J). Regarding, the quantification of HO°, it was found that the yield of the reaction between terephthalic acid (TPA) and hydroxyl radical depends on TPA concentration. In fact, the reaction producing the fluorescent compound is most likely in competition with the recombination reaction of the radicals HO° into H_2O_2. This experimental problem was transformed into a mean to acquire data on the incident flow of HO° by performing measurements with several values of [TPA].

The aim of the parametric studies was not only to understand the plasma-liquid interactions but also to choose the set of parameters which optimize the production of chemical species. The underlying idea is to maximize the biological effect by increasing the amount of species produced. These experiments show that it is possible to optimize the amount of nitrite and nitrate produced in liquid phase by the single-channel jet by choosing $\Phi(He) = 300\ sccm$, when peak to peak voltage is 27.4 kV and height is 5.5 mm. In such condition, the production rate of nitrite is $\sim 750\ pmol.s^{-1}$ and the yield is $\sim 1.2\ nmol.J^{-1}$. By comparing the production rate of nitrites and nitrates for all the devices, it appears that the ratio of the two seems relatively constant: about 4 molecules of nitrate are measured for one molecule of nitrite.

Regarding the single-channel plasma jet[113], the production rate of H_2O_2, NO_2^-, NO_3^- and HO° were measured in the range: 300-1500, 50-1500, 20-4000 and 100-400 pmol.s^{-1} respectively; the yields were in the range 0.7-4, 0.03-1.5, 0.2-9, 0.2-1.1 nmol.J^{-1} respectively.

The question of the chemical dose was also discussed from the point of view of the antioxidant defenses of the tissue. The results obtained suggest that the antioxidant defenses of the skin can considerably limit the ability of H_2O_2 to diffuse deeply into the living tissues. Incidentally, we also explain how the studies [176] and [169] which present an opposite result could have been biased.

Chapter IV described *in-vitro* experiments made with two cell lines TC1 and NRS1. An energy-dependent effect of plasma treatments has been shown on cell viability. It appears that the DBD and the single-channel plasma jet decrease the viability of the cells. The effect on cell-viability is significant after 72h of incubation. Moreover, TC-1 cells have been exposed to increasing concentrations of H_2O_2 (~10-200 µM) and nitrites (10-1000 µM), and a combination of the two. It appears that nitrites play no role in the toxicity of the chemical mixtures. The concentration of H_2O_2 alone explains the decrease in cell viability observed after 72h of incubation. Finally whatever the origin of H_2O_2; DBD, plasma-jet or PAM; the decay of cell viability seems to be identical.

Chapter V describes the results of five *in-vivo* campaigns. Plasma-device and the protocol have evolved towards powerful device. The experiments were performed on two

[113] at 500 Hz

lines of tumors: TC-1 and CT-26 tumors. The experiments were carried out with two Dielectric Barrier Discharge (DBD), the single-channel plasma jet and several multi-channel jets (refrigerated or not). The efficacy of PAM has also been tested *in-vivo.* It has also been attempted to expose the skin to catalase inhibitor, in the hope that it could increase a ROS-mediated effect of cold plasma. These experiments highlight negative results of our tissue-tolerable plasmas sources. Although the last experiment was done with the multi-channel plasma jet show no anti-tumor effect, it was observed that plasma treatment promotes the extension of pre-existing surface necrosis. The only positives results; up to tumoral ablation; were obtained with the plasma device which increases the temperature of the skin (final temperature between 45 and 48 °C).

Chapter VI was dedicated to the thermal aspect of plasma-skin interaction. It addresses the issues related to hyperthermia and its biological effects. Since plasma-skin interaction can be at the origin of a warm-up of the skin, a model for studying the propagation of heat through mouse skin has been developed and validated with experimental results. Conversely; this model specifies the characteristic that a thermal diagnostics must have to obtain reliable measurements of temperatures. The methods chosen to measure the temperature is a crucial point. The spatial resolution of some infrared thermometers could lead to minimize the measurements of surface temperature by several degrees**.**

To sum up, The temperature of tissues exposed to non-thermal plasmas must be controlled by appropriate thermal probes associated with thermal-simulations to :

i) Check the absence of bias regarding the temperature measurements.
ii) Discriminate the “plasma-chemical-action” which would be caused by RONS and/or the pulsed electrical field, from the effects of hyperthermia,
iii) take advantage of controlled hyperthermia (mild or high) to increase the effect of cold plasma.

Regarding hyperthermia and plasma-cancer, one of these two statements is true:

Either hyperthermia contributed significantly to the “plasma-effect” reported in the published *in-vivo* experiments showing positive anti-tumor effects of cold plasma. In this case, it is interesting to study and understand the precise role of hyperthermia in plasma treatment.

Either hyperthermia played no role. Consequently, it would be interesting to study the combination of cold-plasma and hyperthermia. Since such path could considerably increase the effect of cold-plasma treatment.

In both cases, the modeling and the study of hyperthermia in relation to plasma treatments is a positive contribution.

Perspectives

It appears that plasma-medicine is not only an interdisciplinary field full of major scientific challenges such as i) the quantifications of highly reactive radicals, ii) the biochemistry of living organisms, iii) the interpretation of *in-vivo* experiments. Plasma-medicine is also an epistemological trap.

Since cold-plasma treatments can induce biological responses via several modalities: heat, UV, pulsed electrical pulse, charge deposition, reactive oxygen and nitrogen species. It is necessary to increase the level of control of our experiments (particularly regarding thermal aspects among others). The scientific objective is to separate the role of each contribution. However, even the effect of heat, UV or RONS alone is not always detailed in the literature. The data available in the literature often do not correspond

exactly to the experimental situation encountered with plasma medicine. For example, studies concerning hyperthermia and cancer rarely[114] involve small thermal sources located at the surface of the skin.

Consequently, it would be interesting not only to do experiment implying the comparisons of several well-characterized (electrically, chemically...) plasmas-device but also to do *in-vivo* experiments with chemical species, heat, UV, pulsed field alone.

[114] since it is an inefficient way to heat the entire tumor.

Contribution details

Abbreviation of contributors' name:

LPP

B.H = Bruno Honnorat

A.R = Antoine Rousseau

C.D = Constance Duchesnes

B.L = Bo Liu

T.D = Thierry Dufour

S.T = Sébastien Thomassier

LIB

A.D = Alexandre Dizeux

J.G = Jérôme Griffon

L.B = Lori Bridal

D.G = Delphine Le Guillou

CIMI

M.D = Maude Delost

A.G = Aurélien Gaubert,

A.L = Aline Le-Moignic

G.L = Géraldine Lescaille

F.L = François Lemoine.

R.B = Réda Bouras

Engineering

S.T designed and manufactured all the power supply. The Glass-maker of Polytechnique, Jean-Michel Wierniezky, prepare glass-DBD. B.H designed and manufactured all of the other plasma-device: DBD, single-channel plasma jet, multi-channel plasma jet. The high voltage tests, as well as the electrical characterization of the devices, were carried out by B.H. All the mechanical supports made by 3D printing were designed (Openscad) and printed by B.H with a Creat-HS double extrusion (Leapfrog). The program for automatic discharges and energy consumption calculation detection has been coded by B.H.

Chemistry experiments

The procedures for the chemical diagnostics of H_2O_2 (amplex-red + TioSO4) and nitrite (Griess) were developed, calibrated and tested for chemical interference in the

framework of plasma-liquid interaction by B.H. The modified diagnostic of nitrate was developed, tested and used by B.H, C.D and B.L. The development of HO° diagnostic by TPA was developed by B.H. Preliminary experiments showing an effect of [TPA] on final [TPA-OH] were made by B.H. The systematic measurements of [TPA-OH] as a function of variable [TPA] were made by C.D and B.L (results shown in fig 87). The interpretation in term of competition between probing and recombination reaction was proposed and developed by B.H.

The systematic experiments presented in section III.1, III.2 and III.5.3 were done by B.H. The experiments of sections III.3 and III.4 were done by B.H, C.D and B.L.

B.H, A.R, C.D and B.L participated in the interpretation of the results

In-vitro experiments

The preliminary experiments were made by B.H and M. D. M.D prepared, observed and count the cells. B.H treated the wells. M.D, B.H, A.R and L.B participated in the design of the experiments and in the interpretation of the results.

Regarding the systematic experiments presented in section IV.1 and IV.2, M.D prepared, observed and count the cells. B.H treated the wells and measured the energy consumption of the device. M.D, B.H, A.R and L.B participated in the design of the experiments and in the interpretation of the results.

R.B prepared the cells of the three differents cell lines treated during the last *in-vitro* experiment (only two were presented in this manuscript). B.H, G.L and R.B participated in the interpretation of the results.

In-vivo experiment

LIB

D.G, A.D and J.G prepare the CT26 cells, and the implantation of tumor fragment. A.D and J.G performed Ultrasound diagnostics. A.D and J.G performed the injections of PAM. B.H prepared the PAM and performed the other treatments. A.D and J.G performed the analysis of ultrasound data. A.D, J.G, B.H, A.R, L.B participated in the interpretation of the results.

CIMI

M.D, A.L prepared the cells and performed subcutaneous injections into the cheek or flank of the mice. A.L and A.G monitored the size of the tumors (caliper measurements). B.H proceeded to the treatments and performed tissue temperature measurements. A.L, B.H, G.L, A.G, A.R and L.B participated in the interpretation of the results.

Finite element methods applied to hyperthermia

All the simulations by finite elements methods and the instructions enabling to represent them in Matlab were written, tested, benchmarked and implemented by B.H. B.H and A.R participated in the interpretation of the results.

Bibliography

[1] P. Wardman, “Fluorescent and luminescent probes for measurement of oxidative and nitrosative species in cells and tissues: Progress, pitfalls, and prospects,” *Free Radic. Biol. Med.*, vol. 43, no. 7, pp. 995–1022, Oct. 2007.

[2] M. M. Tarpey and I. Fridovich, “Methods of Detection of Vascular Reactive Species,” *Circ. Res.*, vol. 89, no. 3, pp. 224–236, Aug. 2001.

[3] A. S. Wu *et al.*, “Porcine intact and wounded skin responses to atmospheric nonthermal plasma.,” *J. Surg. Res.*, vol. 179, no. 1, pp. e1–e12, Jan. 2013.

[4] Q. S. Yu *et al.*, “Plasma for Bio-Decontamination, Medicine and Food Security,” in *Plasma for Bio-Decontamination, Medicine and Food Security*, Z. Machala, K. Hensel, and Y. Akishev, Eds. Dordrecht: Springer Netherlands, 2012, pp. 215–228.

[5] S. Emmert *et al.*, “Atmospheric pressure plasma in dermatology: Ulcus treatment and much more,” *Clin. Plasma Med.*, Jan. 2013.

[6] M. Vandamme *et al.*, “Antitumor Effect of Plasma Treatment on U87 Glioma Xenografts: Preliminary Results,” *Plasma Process. Polym.*, vol. 7, no. 3–4, pp. 264–273, Mar. 2010.

[7] J. Heinlin *et al.*, “Plasma medicine: possible applications in dermatology.,” *J. Dtsch. Dermatol. Ges. J. Ger. Soc. Dermatol. JDDG*, vol. 8, no. 12, pp. 968–76, Dec. 2010.

[8] J. Ehlbeck *et al.*, “Low temperature atmospheric pressure plasma sources for microbial decontamination,” *J. Phys. Appl. Phys.*, vol. 44, no. 1, p. 013002, Jan. 2011.

[9] J. Heinlin *et al.*, “Plasma applications in medicine with a special focus on dermatology.,” *J. Eur. Acad. Dermatol. Venereol. JEADV*, vol. 25, no. 1, pp. 1–11, Jan. 2011.

[10] G. Isbary, G. Morfill, and J. Zimmermann, “Cold atmospheric plasma: a successful treatment of lesions in Hailey-Hailey disease,” *Arch. Dermatol. Res.*, vol. 147, no. 4, pp. 388–90, 2011.

[11] J. Schlegel, J. Köritzer, and V. Boxhammer, “Plasma in cancer treatment,” *Clin. Plasma Med.*, vol. 1, no. 2, pp. 2–7, Dec. 2013.

[12] M. Keidar *et al.*, “Cold plasma selectivity and the possibility of a paradigm shift in cancer therapy,” *Br. J. Cancer*, vol. 105, no. 9, pp. 1295–1301, Oct. 2011.

[13] M. Vandamme *et al.*, “ROS implication in a new antitumor strategy based on non-thermal plasma,” *Int. J. Cancer*, vol. 130, no. 9, pp. 2185–2194, May 2012.

[14] M. Vandamme, “Les plasmas froids, nouvelle stratégie thérapeutique en cancérologie,” phdthesis, Université d’Orléans, 2012.

[15] S. U. Kalghatgi, G. Fridman, A. Fridman, G. Friedman, and A. M. Clyne, “Non-thermal dielectric barrier discharge plasma treatment of endothelial cells,” in *2008 30th Annual International Conference of the IEEE Engineering in Medicine and Biology Society*, 2008, pp. 3578–3581.

[16] N. Kumar, P. Attri, D. K. Yadav, J. Choi, E. H. Choi, and H. S. Uhm, “Induced apoptosis in melanocytes cancer cell and oxidation in biomolecules through deuterium oxide generated from atmospheric pressure non-thermal plasma jet,” *Sci. Rep.*, vol. 4, p. 7589, Dec. 2014.

[17] S. Arndt *et al.*, “Cold atmospheric plasma, a new strategy to induce senescence in melanoma cells,” *Exp. Dermatol.*, vol. 22, no. 4, pp. 284–289, Apr. 2013.

[18] G. Fridman *et al.*, “Floating Electrode Dielectric Barrier Discharge Plasma in Air Promoting Apoptotic Behavior in Melanoma Skin Cancer Cell Lines,” *Plasma Chem. Plasma Process.*, vol. 27, no. 2, pp. 163–176, Mar. 2007.

[19] J. Y. Kim *et al.*, “Apoptosis of lung carcinoma cells induced by a flexible optical fiber-based cold microplasma,” *Biosens. Bioelectron.*, vol. 28, no. 1, pp. 333–338, Oct. 2011.
[20] J. W. Chang *et al.*, “Non-thermal atmospheric pressure plasma induces apoptosis in oral cavity squamous cell carcinoma: Involvement of DNA-damage-triggering sub-G1 arrest via the ATM/p53 pathway,” *Arch. Biochem. Biophys.*, vol. 545, pp. 133–140, Mar. 2014.
[21] F. Utsumi *et al.*, “Effect of Indirect Nonequilibrium Atmospheric Pressure Plasma on Anti-Proliferative Activity against Chronic Chemo-Resistant Ovarian Cancer Cells In Vitro and In Vivo,” *PLOS ONE*, vol. 8, no. 12, p. e81576, Dec. 2013.
[22] K. Torii *et al.*, “Effectiveness of plasma treatment on gastric cancer cells,” *Gastric Cancer*, vol. 18, no. 3, pp. 635–643, Jul. 2015.
[23] J. Ferlay, D. M. Parkin, and E. Steliarova-Foucher, “Estimates of cancer incidence and mortality in Europe in 2008,” *Eur. J. Cancer*, vol. 46, no. 4, pp. 765–781, 2010.
[24] A. S. Ho, D. H. Kraus, I. Ganly, N. Y. Lee, J. P. Shah, and L. G. Morris, “Decision making in the management of recurrent head and neck cancer,” *Head Neck*, vol. 36, no. 1, pp. 144–151, 2014.
[25] H. Mirghani, F. Amen, F. Moreau, and J. L. St Guily, “Do high-risk human papillomaviruses cause oral cavity squamous cell carcinoma?,” *Oral Oncol.*, vol. 51, no. 3, pp. 229–236, 2015.
[26] M. L. Gillison *et al.*, “Eurogin Roadmap: comparative epidemiology of HPV infection and associated cancers of the head and neck and cervix,” *Int. J. Cancer*, vol. 134, no. 3, pp. 497–507, 2014.
[27] N. Gildener-Leapman, R. L. Ferris, and J. E. Bauman, “Promising systemic immunotherapies in head and neck squamous cell carcinoma,” *Oral Oncol.*, vol. 49, no. 12, pp. 1089–1096, Dec. 2013.
[28] H.-R. Metelmann *et al.*, “Clinical Experience with Cold Plasma in the Treatment of Locally Advanced Head and Neck Cancer,” *Clin. Plasma Med.*, Sep. 2017.
[29] B. Eliasson and U. Kogelschatz, “Modeling and applications of silent discharge plasmas,” *IEEE Trans. Plasma Sci.*, vol. 19, no. 2, pp. 309–323, Apr. 1991.
[30] Y. Sakiyama, D. B. Graves, H. Chang, T. Shimizu, and G. E. Morfill, “Plasma chemistry model of surface microdischarge in humid air and dynamics of reactive neutral species,” *J. Phys. Appl. Phys.*, vol. 45, no. 425201, 2012.
[31] K. D. Weltmann, E. Kindel, T. von Woedtke, M. Hähnel, M. Stieber, and R. Brandenburg, “Atmospheric-pressure plasma sources: Prospective tools for plasma medicine,” *Pure Appl. Chem.*, vol. 82, no. 6, pp. 1223–1237, Apr. 2010.
[32] M. Hoentsch, T. von Woedtke, K.-D. Weltmann, and J. Barbara Nebe, “Time-dependent effects of low-temperature atmospheric-pressure argon plasma on epithelial cell attachment, viability and tight junction formation in vitro,” *J. Phys. Appl. Phys.*, vol. 45, no. 2, p. 025206, Jan. 2012.
[33] C. Hibert, I. Gaurand, O. Motret, and J. M. Pouvesle, “[OH(X)] measurements by resonant absorption spectroscopy in a pulsed dielectric barrier discharge,” *J. Appl. Phys.*, vol. 85, no. 10, pp. 7070–7075, May 1999.
[34] F. Massines, P. Ségur, N. Gherardi, C. Khamphan, and A. Ricard, “Physics and chemistry in a glow dielectric barrier discharge at atmospheric pressure: diagnostics and modelling,” *Surf. Coat. Technol.*, vol. 174–175, no. Supplement C, pp. 8–14, Sep. 2003.
[35] K. V. Kozlov, H.-E. Wagner, R. Brandenburg, and P. Michel, “Spatio-temporally resolved spectroscopic diagnostics of the barrier discharge in air at atmospheric pressure,” *J. Phys. Appl. Phys.*, vol. 34, no. 21, p. 3164, 2001.
[36] E. Robert *et al.*, “Experimental Study of a Compact Nanosecond Plasma Gun,” *Plasma Process. Polym.*, p. NA-NA, Nov. 2009.
[37] E. Stoffels, I. Kieft, and R. Sladek, “Superficial treatment of mammalian cells using plasma needle,” *J. Phys. Appl. …*, vol. 36, no. 2908, 2003.

[38] S. Reuter *et al.*, “From RONS to ROS: Tailoring Plasma Jet Treatment of Skin Cells,” *IEEE Trans. Plasma Sci.*, vol. 40, no. 11, pp. 2986–2993, Nov. 2012.
[39] T. Darny, J.-M. Pouvesle, V. Puech, C. Douat, S. Dozias, and E. Robert, “Analysis of conductive target influence in plasma jet experiments through helium metastable and electric field measurements,” *Plasma Sources Sci. Technol.*, vol. 26, no. 4, p. 045008, 2017.
[40] B. R. Locke, M. Sato, P. Sunka, M. R. Hoffmann, and J.-S. Chang, “Electrohydraulic Discharge and Nonthermal Plasma for Water Treatment,” *Ind. Eng. Chem. Res.*, vol. 45, no. 3, pp. 882–905, Feb. 2006.
[41] K.-D. Weltmann *et al.*, “Antimicrobial treatment of heat sensitive products by miniaturized atmospheric pressure plasma jets (APPJs),” *J. Phys. Appl. Phys.*, vol. 41, no. 19, p. 194008, 2008.
[42] N. N. Misra, K. M. Keener, P. Bourke, J.-P. Mosnier, and P. J. Cullen, “In-package atmospheric pressure cold plasma treatment of cherry tomatoes,” *J. Biosci. Bioeng.*, vol. 118, no. 2, pp. 177–182, Aug. 2014.
[43] V. I. Parvulescu, M. Magureanu, and P. Lukes, *Plasma Chemistry and Catalysis in Gases and Liquids*. John Wiley & Sons, 2013.
[44] T. Adachi, H. Tanaka, S. Nonomura, H. Hara, S. Kondo, and M. Hori, “Plasma-activated medium induces A549 cell injury via a spiral apoptotic cascade involving the mitochondrial–nuclear network,” *Free Radic. Biol. Med.*, vol. 79, pp. 28–44, Feb. 2015.
[45] F. Judée, C. Fongia, B. Ducommun, M. Yousfi, V. Lobjois, and N. Merbahi, “Short and long time effects of low temperature Plasma Activated Media on 3D multicellular tumor spheroids,” *Sci. Rep.*, vol. 6, Feb. 2016.
[46] R. Radi, G. Peluffo, M. N. Alvarez, M. Naviliat, and A. Cayota, “Unraveling peroxynitrite formation in biological systems,” *Free Radic. Biol. Med.*, vol. 30, no. 5, pp. 463–488, Mar. 2001.
[47] N. Romero, A. Denicola, J. M. Souza, and R. Radi, “Diffusion of Peroxynitrite in the Presence of Carbon Dioxide,” *Arch. Biochem. Biophys.*, vol. 368, no. 1, pp. 23–30, Aug. 1999.
[48] J. S. Beckman and W. H. Koppenol, “Nitric oxide, superoxide, and peroxynitrite: the good, the bad, and ugly,” *Am. J. Physiol.-Cell Physiol.*, vol. 271, no. 5, pp. C1424–C1437, 1996.
[49] W. A. Pryor, “Oxy-Radicals and Related Species: Their Formation, Lifetimes, and Reactions,” *Annu. Rev. Physiol.*, vol. 48, no. 1, pp. 657–667, Oct. 1986.
[50] I. Adamovich *et al.*, “The 2017 Plasma Roadmap: Low temperature plasma science and technology,” *J. Phys. Appl. Phys.*, vol. 50, no. 32, p. 323001, Aug. 2017.
[51] P. J. Bruggeman *et al.*, “Plasma–liquid interactions: a review and roadmap,” *Plasma Sources Sci. Technol.*, vol. 25, no. 5, p. 053002, 2016.
[52] S. Samukawa *et al.*, “The 2012 Plasma Roadmap,” *J. Phys. Appl. Phys.*, vol. 45, no. 25, p. 253001, 2012.
[53] A. Duval *et al.*, “Cell Death Induced on Cell Cultures and Nude Mouse Skin by Non-Thermal, Nanosecond-Pulsed Generated Plasma,” *PLOS ONE*, vol. 8, no. 12, p. e83001, Dec. 2013.
[54] P. Ranieri *et al.*, “Nanosecond pulsed Dielectric Barrier Discharge induced Anti-Tumor Effects Propagate Through the depth of Tissue via Intracellular Signaling,” *Plasma Med.*
[55] M. Vandamme *et al.*, “ROS implication in a new antitumor strategy based on non-thermal plasma,” *Int. J. Cancer*, vol. 130, no. 9, pp. 2185–2194, May 2012.
[56] S. j. Munn *et al.*, “European Union Risk Assessment Report. Hydrogen Peroxide. CAS No. 7722-84-1. EINECS No. 231-765-0,” EUR - Scientific and Technical Research Reports, 2003.
[57] “Peroxyde d’hydrogène et solutions aqueuses (FT 123) - Fiche toxicologique - INRS.” [Online]. Available:

http://www.inrs.fr/publications/bdd/fichetox/fiche.html?refINRS=FICHETOX_123. [Accessed: 01-Feb-2017].
[58] B. E. Watt, A. T. Proudfoot, and J. A. Vale, “Hydrogen Peroxide Poisoning,” *Toxicol. Rev.*, vol. 23, no. 1, pp. 51–57, Mar. 2004.
[59] R. M. Howes, “Hydrogen Peroxide: A review of a scientifically verifiable omnipresent ubiquitous essentiality of obligate, aerobic, carbon-based life forms,” *Internet J. Plast. Surg.*, vol. 7, no. 1, Dec. 2009.
[60] J. R. Stone and S. Yang, “Hydrogen Peroxide: A Signaling Messenger,” *Antioxid. Redox Signal.*, vol. 8, no. 3–4, pp. 243–270, Mar. 2006.
[61] E. Tur, L. Bolton, and B. E. Constantine, “Topical hydrogen peroxide treatment of ischemic ulcers in the guinea pig: Blood recruitment in multiple skin sites,” *J. Am. Acad. Dermatol.*, vol. 33, no. 2, Part 1, pp. 217–221, Aug. 1995.
[62] E. Weitzberg, M. Hezel, and J. O. Lundberg, “Nitrate-nitrite-nitric oxide pathway: implications for anesthesiology and intensive care,” *Anesthesiology*, vol. 113, no. 6, pp. 1460–1475, Dec. 2010.
[63] K.-O. Honikel, “The use and control of nitrate and nitrite for the processing of meat products,” *Meat Sci.*, vol. 78, no. 1–2, pp. 68–76, Jan. 2008.
[64] D. Yan, J. H. Sherman, and M. Keidar, “Cold atmospheric plasma, a novel promising anti-cancer treatment modality., Cold atmospheric plasma, a novel promising anti-cancer treatment modality,” *Oncotarget Oncotarget*, vol. 8, 8, no. 9, 9, pp. 15977, 15977–15995, Feb. 2017.
[65] D. Yan, A. Talbot, N. Nourmohammadi, J. H. Sherman, X. Cheng, and M. Keidar, “Toward understanding the selective anticancer capacity of cold atmospheric plasma—A model based on aquaporins (Review),” *Biointerphases*, vol. 10, no. 4, p. 040801, Dec. 2015.
[66] R. Guerrero-Preston *et al.*, “Cold atmospheric plasma treatment selectively targets head and neck squamous cell carcinoma cells,” *Int. J. Mol. Med.*, vol. 34, no. 4, pp. 941–946, Oct. 2014.
[67] X. Han, M. Klas, Y. Liu, M. Sharon Stack, and S. Ptasinska, “DNA damage in oral cancer cells induced by nitrogen atmospheric pressure plasma jets,” *Appl. Phys. Lett.*, vol. 102, no. 23, p. 233703, Jun. 2013.
[68] C.-H. Kim *et al.*, “Effects of atmospheric nonthermal plasma on invasion of colorectal cancer cells,” *Appl. Phys. Lett.*, vol. 96, no. 24, p. 243701, 2010.
[69] P.-M. Girard *et al.*, “Synergistic Effect of H2O2 and NO2 in Cell Death Induced by Cold Atmospheric He Plasma,” *Sci. Rep.*, vol. 6, Jul. 2016.
[70] S. Bekeschus, A. Lin, A. Fridman, K. Wende, K.-D. Weltmann, and V. Miller, “A Comparison of Floating-Electrode DBD and kINPen Jet: Plasma Parameters to Achieve Similar Growth Reduction in Colon Cancer Cells Under Standardized Conditions,” *Plasma Chem. Plasma Process.*, pp. 1–12, Sep. 2017.
[71] M. Schuster *et al.*, “Visible tumor surface response to physical plasma and apoptotic cell kill in head and neck cancer,” *J. Cranio-Maxillofac. Surg.*, vol. 44, no. 9, pp. 1445–1452, Sep. 2016.
[72] T. F. Gajewski, H. Schreiber, and Y.-X. Fu, “Innate and adaptive immune cells in the tumor microenvironment,” *Nat. Immunol.*, vol. 14, no. 10, p. 1014, Oct. 2013.
[73] G. Kroemer *et al.*, “Classification of cell death: recommendations of the Nomenclature Committee on Cell Death 2009,” *Cell Death Differ.*, vol. 16, no. 1, p. 3, Jan. 2009.
[74] L. Zitvogel, L. Apetoh, F. Ghiringhelli, F. André, A. Tesniere, and G. Kroemer, “The anticancer immune response: indispensable for therapeutic success?,” *J. Clin. Invest.*, vol. 118, no. 6, pp. 1991–2001, Jun. 2008.
[75] H. Salmon *et al.*, “Matrix architecture defines the preferential localization and migration of T cells into the stroma of human lung tumors,” *J. Clin. Invest.*, vol. 122, no. 3, pp. 899–910, Mar. 2012.

[76] G. Daeschlein *et al.*, “Comparison between cold plasma, electrochemotherapy and combined therapy in a melanoma mouse model,” *Exp. Dermatol.*, vol. 22, no. 9, pp. 582–586, Sep. 2013.
[77] S. Mashayekh, H. Rajaee, M. Akhlaghi, B. Shokri, and Z. M. Hassan, “Atmospheric-pressure plasma jet characterization and applications on melanoma cancer treatment (B/16-F10),” *Phys. Plasmas*, vol. 22, no. 9, p. 093508, Sep. 2015.
[78] D. Dobrynin *et al.*, “Live Pig Skin Tissue and Wound Toxicity of Cold Plasma Treatment,” *Plasma Med.*, vol. 1, no. 1, 2011.
[79] N. Chernets, D. S. Kurpad, V. Alexeev, D. B. Rodrigues, and T. A. Freeman, “Reaction Chemistry Generated by Nanosecond Pulsed Dielectric Barrier Discharge Treatment is Responsible for the Tumor Eradication in the B16 Melanoma Mouse Model,” *Plasma Process. Polym.*, vol. 12, no. 12, pp. 1400–1409, Dec. 2015.
[80] L. I. Partecke *et al.*, “Tissue Tolerable Plasma (TTP) induces apoptosis in pancreatic cancer cells in vitro and in vivo,” *BMC Cancer*, vol. 12, p. 473, Oct. 2012.
[81] R. M. Walk *et al.*, “Cold atmospheric plasma for the ablative treatment of neuroblastoma,” *J. Pediatr. Surg.*, vol. 48, no. 1, pp. 67–73, Jan. 2013.
[82] S. Mirpour *et al.*, “Utilizing the micron sized non-thermal atmospheric pressure plasma inside the animal body for the tumor treatment application,” *Sci. Rep.*, vol. 6, Jul. 2016.
[83] S. U. Kang *et al.*, “Nonthermal plasma induces head and neck cancer cell death: the potential involvement of mitogen-activated protein kinase-dependent mitochondrial reactive oxygen species,” *Cell Death Dis.*, vol. 5, no. 2, p. e1056, Feb. 2014.
[84] M. Vandamme *et al.*, “Antitumor Effect of Plasma Treatment on U87 Glioma Xenografts: Preliminary Results,” *Plasma Process. Polym.*, vol. 7, no. 3–4, pp. 264–273, Mar. 2010.
[85] M. Vandamme *et al.*, “Response of Human Glioma U87 Xenografted on Mice to Non Thermal Plasma Treatment,” *Plasma Med.*, vol. 1, no. 1, 2011.
[86] E. Robert *et al.*, “Perspectives of endoscopic plasma applications,” *Clin. Plasma Med.*, vol. 1, no. 2, pp. 8–16, Dec. 2013.
[87] L. Brullé *et al.*, “Effects of a Non Thermal Plasma Treatment Alone or in Combination with Gemcitabine in a MIA PaCa2-luc Orthotopic Pancreatic Carcinoma Model,” *PLoS ONE*, vol. 7, no. 12, Dec. 2012.
[88] “ASTM D150 - 11 Standard Test Methods for AC Loss Characteristics and Permittivity (Dielectric Constant) of Solid Electrical Insulation.” [Online]. Available: https://www.astm.org/Standards/D150.htm. [Accessed: 05-Feb-2017].
[89] D. Ashpis, M. Laun, and E. Griebeler, “Progress toward Accurate Measurements of Power Consumption of DBD Plasma Actuators,” in *50th AIAA Aerospace Sciences Meeting including the New Horizons Forum and Aerospace Exposition*, American Institute of Aeronautics and Astronautics.
[90] K. C. Sole, “Recovery of titanium from the leach liquors of titaniferous magnetites by solvent extraction: Part 1. Review of the literature and aqueous thermodynamics,” *Hydrometallurgy*, vol. 51, no. 2, pp. 239–253, Feb. 1999.
[91] F. Baillon, E. Provost, and W. Fürst, “Study of titanium(IV) speciation in sulphuric acid solutions by FT-Raman spectrometry,” *J. Mol. Liq.*, vol. 143, no. 1, pp. 8–12, Sep. 2008.
[92] G. Schwarzenbach, J. Muehlebach, and K. Mueller, “Peroxo complexes of titanium,” *Inorg. Chem.*, vol. 9, no. 11, pp. 2381–2390, Nov. 1970.
[93] K. P. Reis, V. K. Joshi, and M. E. Thompson, “Molecular Engineering of Heterogeneous Catalysts: An Efficient Catalyst for the Production of Hydrogen Peroxide,” *J. Catal.*, vol. 161, no. 1, pp. 62–67, Jun. 1996.

[94] C. N. Satterfield and A. H. Bonnell, “Interferences in Titanium Sulfate Method for Hydrogen Peroxide,” *Anal. Chem.*, vol. 27, no. 7, pp. 1174–1175, Jul. 1955.
[95] J. Serrano, M. Jové, J. Boada, M. J. Bellmunt, R. Pamplona, and M. Portero-Otín, “Dietary antioxidants interfere with Amplex Red-coupled-fluorescence assays,” *Biochem. Biophys. Res. Commun.*, vol. 388, no. 2, pp. 443–449, Oct. 2009.
[96] B. Zhao, F. A. Summers, and R. P. Mason, “Photooxidation of Amplex red to resorufin: Implications of exposing the Amplex red assay to light,” *Free Radic. Biol. Med.*, vol. 53, no. 5, pp. 1080–1087, Sep. 2012.
[97] T. V. Votyakova and I. J. Reynolds, “Detection of hydrogen peroxide with Amplex Red: interference by NADH and reduced glutathione auto-oxidation,” *Arch. Biochem. Biophys.*, vol. 431, no. 1, pp. 138–144, Nov. 2004.
[98] K. M. Robinson and J. S. Beckman, “Synthesis of Peroxynitrite from Nitrite and Hydrogen Peroxide,” vol. 396, B.-M. in Enzymology, Ed. Academic Press, 2005, pp. 207–214.
[99] P. Lukes, E. Dolezalova, I. Sisrova, and M. Clupek, “Aqueous-phase chemistry and bactericidal effects from an air discharge plasma in contact with water: evidence for the formation of peroxynitrite through a pseudo-second-order post-discharge reaction of H 2 O 2 and HNO 2,” *Plasma Sources Sci. Technol.*, vol. 23, no. 1, p. 015019, 2014.
[100] B. Halliwell and J. M. C. Gutteridge, *Free Radicals in Biology and Medicine*. OUP Oxford, 2015.
[101] P. Wardman and L. P. Candeias, “Fenton Chemistry: An Introduction,” *Radiat. Res.*, vol. 145, no. 5, pp. 523–531, May 1996.
[102] M. Saran, C. Michel, K. Stettmaier, and W. Bors, “Arguments against the significance of the Fenton reaction contributing to signal pathways under *in vivo* conditions,” *Free Radic. Res.*, vol. 33, no. 5, pp. 567–579, Jan. 2000.
[103] M. L. Kremer, “The Fenton Reaction. Dependence of the Rate on pH,” *J. Phys. Chem. A*, vol. 107, no. 11, pp. 1734–1741, Mar. 2003.
[104] R. G. Zepp, B. C. Faust, and J. Hoigne, “Hydroxyl radical formation in aqueous reactions (pH 3-8) of iron (II) with hydrogen peroxide: the photo-Fenton reaction,” *Environ. Sci. Technol.*, vol. 26, no. 2, pp. 313–319, 1992.
[105] X. Fang, G. Mark, and C. von Sonntag, “OH radical formation by ultrasound in aqueous solutions Part I: the chemistry underlying the terephthalate dosimeter,” *Ultrason. Sonochem.*, vol. 3, no. 1, pp. 57–63, Feb. 1996.
[106] S. Li *et al.*, “Fluorescence detection of hydroxyl radicals in water produced by atmospheric pulsed discharges,” *IEEE Trans. Dielectr. Electr. Insul.*, vol. 22, no. 4, pp. 1856–1865, 2015.
[107] R. Macedo *et al.*, “Intra-cheek immunization as a novel vaccination route for therapeutic vaccines of head and neck squamous cell carcinomas using plasmo virus-like particles,” *OncoImmunology*, vol. 5, no. 7, p. e1164363, Jul. 2016.
[108] R. Macedo Gonzales, *Development of therapeutic vaccine strategies and pre-clinical animal tumor models for head and neck cancers*. Paris 6, 2015.
[109] F. Tsushima *et al.*, “Predominant expression of B7-H1 and its immunoregulatory roles in oral squamous cell carcinoma,” *Oral Oncol.*, vol. 42, no. 3, pp. 268–274, Mar. 2006.
[110] S. Mogi *et al.*, “Tumour rejection by gene transfer of 4-1BB ligand into a CD80+ murine squamous cell carcinoma and the requirements of co-stimulatory molecules on tumour and host cells,” *Immunology*, vol. 101, no. 4, pp. 541–547, Dec. 2000.
[111] F. A. Villamena, *Molecular Basis of Oxidative Stress: Chemistry, Mechanisms, and Disease Pathogenesis*. John Wiley & Sons, 2013.
[112] A. Dizeux, “Ultrasound characterization of tumor angiogenesis, stiffness and microstructure under conventional and innovative therapies,” phdthesis, Université Pierre et Marie Curie - Paris VI, 2015.

[113] M. Sahni and B. R. Locke, “Quantification of Hydroxyl Radicals Produced in Aqueous Phase Pulsed Electrical Discharge Reactors,” *Ind. Eng. Chem. Res.*, vol. 45, no. 17, pp. 5819–5825, Aug. 2006.
[114] T. J. Mason, J. P. Lorimer, D. M. Bates, and Y. Zhao, “Dosimetry in sonochemistry: the use of aqueous terephthalate ion as a fluorescence monitor,” *Ultrason. Sonochem.*, vol. 1, no. 2, pp. S91–S95, Jan. 1994.
[115] G. Mark *et al.*, “OH-radical formation by ultrasound in aqueous solution – Part II: Terephthalate and Fricke dosimetry and the influence of various conditions on the sonolytic yield,” *Ultrason. Sonochem.*, vol. 5, no. 2, pp. 41–52, Jun. 1998.
[116] S. E. Page, W. A. Arnold, and K. McNeill, “Terephthalate as a probe for photochemically generated hydroxyl radical,” *J. Environ. Monit.*, vol. 12, no. 9, pp. 1658–1665, Sep. 2010.
[117] R. Xiao, Z. He, D. Diaz-Rivera, G. Y. Pee, and L. K. Weavers, “Sonochemical degradation of ciprofloxacin and ibuprofen in the presence of matrix organic compounds,” *Ultrason. Sonochem.*, vol. 21, no. 1, pp. 428–435, Jan. 2014.
[118] G. J. Price and E. J. Lenz, “The use of dosimeters to measure radical production in aqueous sonochemical systems,” *Ultrasonics*, vol. 31, no. 6, pp. 451–456, Nov. 1993.
[119] R. Xiao, D. Diaz-Rivera, Z. He, and L. K. Weavers, “Using pulsed wave ultrasound to evaluate the suitability of hydroxyl radical scavengers in sonochemical systems,” *Ultrason. Sonochem.*, vol. 20, no. 3, pp. 990–996, May 2013.
[120] R. W. Matthews, “The Radiation Chemistry of the Terephthalate Dosimeter,” *Radiat. Res.*, vol. 83, no. 1, pp. 27–41, Jul. 1980.
[121] “Critical Review of rate constants for reactions of hydrated electrons, hydrogen atoms and hydroxyl radicals (·OH/·O− in Aqueous Solution,” *J. Phys. Chem. Ref. Data*, vol. 17, no. 2, pp. 513–886, Apr. 1988.
[122] Pubchem, “TEREPHTHALIC ACID.” [Online]. Available: https://pubchem.ncbi.nlm.nih.gov/compound/7489. [Accessed: 05-Jan-2018].
[123] A. Tauber, H.-P. Schuchmann, and C. von Sonntag, “Sonolysis of aqueous 4-nitrophenol at low and high pH,” *Ultrason. Sonochem.*, vol. 7, no. 1, pp. 45–52, Jan. 2000.
[124] J. Hine and P. K. Mookerjee, “Structural effects on rates and equilibriums. XIX. Intrinsic hydrophilic character of organic compounds. Correlations in terms of structural contributions,” *J. Org. Chem.*, vol. 40, no. 3, pp. 292–298, 1975.
[125] G. P. Bienert, J. K. Schjoerring, and T. P. Jahn, “Membrane transport of hydrogen peroxide,” *Biochim. Biophys. Acta BBA - Biomembr.*, vol. 1758, no. 8, pp. 994–1003, Aug. 2006.
[126] A. S. Verkman, “More than just water channels: unexpected cellular roles of aquaporins,” *J Cell Sci*, vol. 118, no. 15, pp. 3225–3232, Aug. 2005.
[127] T. Henzler and E. Steudle, “Transport and metabolic degradation of hydrogen peroxide in Chara corallina: model calculations and measurements with the pressure probe suggest transport of H2O2 across water channels,” *J. Exp. Bot.*, vol. 51, no. 353, pp. 2053–2066, Dec. 2000.
[128] F. Antunes and E. Cadenas, “Estimation of H2O2 gradients across biomembranes,” *FEBS Lett.*, vol. 475, no. 2, pp. 121–126, Jun. 2000.
[129] R. A. Condell and A. L. Tappel, “Evidence for suitability of glutathione peroxidase as a protective enzyme: Studies of oxidative damage, renaturation, and proteolysis,” *Arch. Biochem. Biophys.*, vol. 223, no. 2, pp. 407–416, Jun. 1983.
[130] V. Rani and U. C. S. Yadav, *Free Radicals in Human Health and Disease*. Springer, 2014.
[131] N. S. Agar, S. M. Sadrzadeh, P. E. Hallaway, and J. W. Eaton, “Erythrocyte catalase. A somatic oxidant defense?,” *J. Clin. Invest.*, vol. 77, no. 1, pp. 319–321, Jan. 1986.

[132] G. F. Gaetani, A. M. Ferraris, M. Rolfo, R. Mangerini, S. Arena, and H. N. Kirkman, “Predominant role of catalase in the disposal of hydrogen peroxide within human erythrocytes,” *Blood*, vol. 87, no. 4, pp. 1595–1599, Feb. 1996.
[133] H. J. Forman, A. Bernardo, and K. J. A. Davies, “What is the concentration of hydrogen peroxide in blood and plasma?,” *Arch. Biochem. Biophys.*, vol. 603, pp. 48–53, Aug. 2016.
[134] A. Sousa-Lopes, F. Antunes, L. Cyrne, and H. s. Marinho, “Decreased cellular permeability to H2O2 protects Saccharomyces cerevisiae cells in stationary phase against oxidative stress,” *FEBS Lett.*, vol. 578, no. 1–2, pp. 152–156, Dec. 2004.
[135] J. J. Thiele, F. Dreher, and L. Packer, “Antioxidant defense systems in skin,” *J. Toxicol. Cutan. Ocul. Toxicol.*, vol. 21, no. 1–2, pp. 119–160, Jan. 2002.
[136] J. J. Thiele, C. Schroeter, S. N. Hsieh, M. Podda, and L. Packer, “The Antioxidant Network of the Stratum corneum,” vol. 29, pp. 26–42, 2001.
[137] B. Halliwell and J. M. C. Gutteridge, “The antioxidants of human extracellular fluids,” *Arch. Biochem. Biophys.*, vol. 280, no. 1, pp. 1–8, Jul. 1990.
[138] S. R. Pinnell, “Cutaneous photodamage, oxidative stress, and topical antioxidant protection,” *J. Am. Acad. Dermatol.*, vol. 48, no. 1, pp. 1–22, Jan. 2003.
[139] M. Rinnerthaler, J. Bischof, M. K. Streubel, A. Trost, and K. Richter, “Oxidative Stress in Aging Human Skin,” *Biomolecules*, vol. 5, no. 2, pp. 545–589, Apr. 2015.
[140] Y. Shindo, E. Witt, and L. Packer, “Antioxidant Defense Mechanisms in Murine Epidermis and Dermis and Their Responses to Ultraviolet Light,” *J. Invest. Dermatol.*, vol. 100, no. 3, pp. 260–265, Mar. 1993.
[141] H. S. Marinho, L. Cyrne, E. Cadenas, and F. Antunes, “Chapter One - The Cellular Steady-State of H2O2: Latency Concepts and Gradients,” in *Methods in Enzymology*, vol. 527, Supplement C vols., E. Cadenas and L. Packer, Eds. Academic Press, 2013, pp. 3–19.
[142] Y. Shindo, E. Witt, D. Han, W. Epstein, and L. Packer, “Enzymic and Non-Enzymic Antioxidants in Epidermis and Dermis of Human Skin,” *J. Invest. Dermatol.*, vol. 102, no. 1, pp. 122–124, Jan. 1994.
[143] Y. Shindo, E. Witt, D. Han, and L. Packer, “Dose-Response Effects of Acute Ultraviolet Irradiation on Antioxidants and Molecular Markers of Oxidation in Murine Epidermis and Dermis,” *J. Invest. Dermatol.*, vol. 102, no. 4, pp. 470–475, Apr. 1994.
[144] B. Kalyanaraman, M. Hardy, R. Podsiadly, G. Cheng, and J. Zielonka, “Recent developments in detection of superoxide radical anion and hydrogen peroxide: Opportunities, challenges, and implications in redox signaling,” *Arch. Biochem. Biophys.*, vol. 617, no. Supplement C, pp. 38–47, Mar. 2017.
[145] G. Valacchi, S. U. Weber, C. Luu, C. E. Cross, and L. Packer, “Ozone potentiates vitamin E depletion by ultraviolet radiation in the murine stratum corneum,” *FEBS Lett.*, vol. 466, no. 1, pp. 165–168, Jan. 2000.
[146] G. Valacchi *et al.*, “Ozone exposure activates oxidative stress responses in murine skin,” *Toxicology*, vol. 179, no. 1, pp. 163–170, Sep. 2002.
[147] G. Valacchi, C. Sticozzi, A. Pecorelli, F. Cervellati, C. Cervellati, and E. Maioli, “Cutaneous responses to environmental stressors,” *Ann. N. Y. Acad. Sci.*, vol. 1271, no. 1, pp. 75–81, Oct. 2012.
[148] R. O. Potts and R. H. Guy, “Predicting Skin Permeability,” *Pharm. Res.*, vol. 9, no. 5, pp. 663–669, May 1992.
[149] M. J. Bartek, J. A. Labudde, and H. I. Maibach, “Skin Permeability In Vivo: Comparison in Rat, Rabbit, Pig and Man,” *J. Invest. Dermatol.*, vol. 58, no. 3, pp. 114–123, Mar. 1972.
[150] S. Mitragotri, “Modeling skin permeability to hydrophilic and hydrophobic solutes based on four permeation pathways,” *J. Controlled Release*, vol. 86, no. 1, pp. 69–92, Jan. 2003.
[151] A. Couto, R. Fernandes, M. N. S. Cordeiro, S. S. Reis, R. T. Ribeiro, and A. M. Pessoa, “Dermic diffusion and stratum corneum: A state of the art review of

mathematical models," *J. Controlled Release*, vol. 177, no. Supplement C, pp. 74–83, Mar. 2014.
[152] T. N. Brown, J. M. Armitage, P. Egeghy, I. Kircanski, and J. A. Arnot, "Dermal permeation data and models for the prioritization and screening-level exposure assessment of organic chemicals," *Environ. Int.*, vol. 94, no. Supplement C, pp. 424–435, Sep. 2016.
[153] S. Mitragotri, "Devices for overcoming biological barriers: The use of physical forces to disrupt the barriers," *Adv. Drug Deliv. Rev.*, vol. 65, no. 1, pp. 100–103, Jan. 2013.
[154] G. Zonios, A. Dimou, and D. Galaris, "Probing skin interaction with hydrogen peroxide using diffuse reflectance spectroscopy," *Phys. Med. Biol.*, vol. 53, no. 1, p. 269, 2008.
[155] O. A. Hatoum, D. G. Binion, H. Miura, G. Telford, M. F. Otterson, and D. D. Gutterman, "Role of hydrogen peroxide in ACh-induced dilation of human submucosal intestinal microvessels," *Am. J. Physiol.-Heart Circ. Physiol.*, vol. 288, no. 1, pp. H48–H54, Jan. 2005.
[156] K. Izu, O. Yamamoto, and M. Asahi, "Occupational Skin Injury by Hydrogen Peroxide," *Dermatology*, vol. 201, no. 1, pp. 61–64, 2000.
[157] S. Nocchi, S. Björklund, B. Svensson, J. Engblom, and T. Ruzgas, "Electrochemical monitoring of native catalase activity in skin using skin covered oxygen electrode," *Biosens. Bioelectron.*, vol. 93, no. Supplement C, pp. 9–13, Jul. 2017.
[158] N. Makino, Y. Mochizuki, S. Bannai, and Y. Sugita, "Kinetic studies on the removal of extracellular hydrogen peroxide by cultured fibroblasts.," *J. Biol. Chem.*, vol. 269, no. 2, pp. 1020–1025, Jan. 1994.
[159] B. A. Wagner, J. R. Witmer, T. J. van't Erve, and G. R. Buettner, "An assay for the rate of removal of extracellular hydrogen peroxide by cells," *Redox Biol.*, vol. 1, no. 1, pp. 210–217, Jan. 2013.
[160] R. Sender, S. Fuchs, and R. Milo, "Revised Estimates for the Number of Human and Bacteria Cells in the Body," *PLOS Biol.*, vol. 14, no. 8, p. e1002533, Aug. 2016.
[161] T. T. Marquez-Lago, D. M. Allen, and J. Thewalt, "A novel approach to modelling water transport and drug diffusion through the stratum corneum," *Theor. Biol. Med. Model.*, vol. 7, p. 33, Aug. 2010.
[162] K. Calabro, A. Curtis, J.-R. Galarneau, T. Krucker, and I. J. Bigio, "Gender variations in the optical properties of skin in murine animal models," *J. Biomed. Opt.*, vol. 16, no. 1, pp. 011008-011008-8, 2011.
[163] Y. Ogura, "Catalase activity at high concentration of hydrogen peroxide," *Arch. Biochem. Biophys.*, vol. 57, no. 2, pp. 288–300, Aug. 1955.
[164] P. Jones and A. Suggett, "The catalase–hydrogen peroxide system. Kinetics of catalatic action at high substrate concentrations," *Biochem. J.*, vol. 110, no. 4, pp. 617–620, Dec. 1968.
[165] A. G. Wiese, R. E. Pacifici, and K. J. A. Davies, "Transient Adaptation to Oxidative Stress in Mammalian Cells," *Arch. Biochem. Biophys.*, vol. 318, no. 1, pp. 231–240, May 1995.
[166] T. Finkel and N. J. Holbrook, "Oxidants, oxidative stress and the biology of ageing," *Nature*, vol. 408, no. 6809, pp. 239–247, Nov. 2000.
[167] M. Keidar, "Plasma for cancer treatment," *Plasma Sources Sci. Technol.*, vol. 24, no. 3, p. 033001, 2015.
[168] W. Murphy, C. Carroll, and M. Keidar, "Simulation of the effect of plasma species on tumor growth and apoptosis," *J. Phys. Appl. Phys.*, vol. 47, no. 47, p. 472001, 2014.
[169] D. Dobrynin, G. Fridman, G. Friedman, and A. A. Fridman, "Deep Penetration into Tissues of Reactive Oxygen Species Generated in Floating-Electrode Dielectric

Barrier Discharge (FE-DBD): An *In Vitro* Agarose Gel Model Mimicking an Open Wound," *Plasma Med.*, vol. 2, no. 1–3, 2012.
[170] M. Beneš, J. Hudeček, P. Anzenbacher, and M. Hof, "Coumarin 6, Hypericin, Resorufins, and Flavins: Suitable Chromophores for Fluorescence Correlation Spectroscopy of Biological Molecules," *Collect. Czechoslov. Chem. Commun.*, vol. 66, no. 6, pp. 855–869, 2001.
[171] S. A. M. van Stroe-Biezen, F. M. Everaerts, L. J. J. Janssen, and R. A. Tacken, "Diffusion coefficients of oxygen, hydrogen peroxide and glucose in a hydrogel," *Anal. Chim. Acta*, vol. 273, no. 1, pp. 553–560, Feb. 1993.
[172] M. M. Tarpey, D. A. Wink, and M. B. Grisham, "Methods for detection of reactive metabolites of oxygen and nitrogen: in vitro and in vivo considerations," *Am. J. Physiol. - Regul. Integr. Comp. Physiol.*, vol. 286, no. 3, pp. R431–R444, Mar. 2004.
[173] I. Snyrychová, F. Ayaydin, and E. Hideg, "Detecting hydrogen peroxide in leaves in vivo - a comparison of methods," *Physiol. Plant.*, vol. 135, no. 1, pp. 1–18, Jan. 2009.
[174] T. E. Tipple and L. K. Rogers, "Methods for the Determination of Plasma or Tissue Glutathione Levels," *Methods Mol. Biol. Clifton NJ*, vol. 889, pp. 315–324, 2012.
[175] F. A. Summers, B. Zhao, D. Ganini, and R. P. Mason, "Chapter One - Photooxidation of Amplex Red to Resorufin: Implications of Exposing the Amplex Red Assay to Light," in *Methods in Enzymology*, vol. 526, Supplement C vols., E. Cadenas and L. Packer, Eds. Academic Press, 2013, pp. 1–17.
[176] N. Gaur *et al.*, "Combined effect of protein and oxygen on reactive oxygen and nitrogen species in the plasma treatment of tissue," *Appl. Phys. Lett.*, vol. 107, no. 10, p. 103703, Sep. 2015.
[177] E. J. Szili, S.-H. Hong, J.-S. Oh, N. Gaur, and R. D. Short, "Tracking the Penetration of Plasma Reactive Species in Tissue Models," *Trends Biotechnol.*, Aug. 2017.
[178] E. J. Szili, J. W. Bradley, and R. D. Short, "A 'tissue model' to study the plasma delivery of reactive oxygen species," *J. Phys. Appl. Phys.*, vol. 47, no. 15, p. 152002, 2014.
[179] Y. S. Choi, S. R. Hong, Y. M. Lee, K. W. Song, M. H. Park, and Y. S. Nam, "Study on gelatin-containing artificial skin: I. Preparation and characteristics of novel gelatin-alginate sponge," *Biomaterials*, vol. 20, no. 5, pp. 409–417, Mar. 1999.
[180] T. He *et al.*, "A 'tissue model' to study the barrier effects of living tissues on the reactive species generated by surface air discharge," *J. Phys. Appl. Phys.*, vol. 49, no. 20, p. 205204, 2016.
[181] T. Kawasaki *et al.*, "Two-dimensional concentration distribution of reactive oxygen species transported through a tissue phantom by atmospheric-pressure plasma-jet irradiation," *Appl. Phys. Express*, vol. 9, no. 7, p. 076202, Jun. 2016.
[182] E. J. Szili *et al.*, "Modelling the helium plasma jet delivery of reactive species into a 3D cancer tumour," *Plasma Sources Sci. Technol.*, vol. 27, no. 1, p. 014001, 2018.
[183] C. O. Gill and J. Bryant, "The contamination of pork with spoilage bacteria during commercial dressing, chilling and cutting of pig carcasses," *Int. J. Food Microbiol.*, vol. 16, no. 1, pp. 51–62, May 1992.
[184] J. Duan, X. Lu, and G. He, "On the penetration depth of reactive oxygen and nitrogen species generated by a plasma jet through real biological tissue," *Phys. Plasmas*, vol. 24, no. 7, p. 073506, Jul. 2017.
[185] G. C. Van de Bittner, E. A. Dubikovskaya, C. R. Bertozzi, and C. J. Chang, "In vivo imaging of hydrogen peroxide production in a murine tumor model with a chemoselective bioluminescent reporter," *Proc. Natl. Acad. Sci. U. S. A.*, vol. 107, no. 50, pp. 21316–21321, Dec. 2010.
[186] M. Schäferling, D. B. M. Grögel, and S. Schreml, "Luminescent probes for detection and imaging of hydrogen peroxide," *Microchim. Acta*, vol. 174, no. 1–2, p. 1, Jul. 2011.

[187] H. Guo, H. Aleyasin, B. C. Dickinson, R. E. Haskew-Layton, and R. R. Ratan, “Recent advances in hydrogen peroxide imaging for biological applications,” *Cell Biosci.*, vol. 4, Oct. 2014.
[188] J. Zielonka, R. Podsiadły, M. Zielonka, M. Hardy, and B. Kalyanaraman, “On the use of peroxy-caged luciferin (PCL-1) probe for bioluminescent detection of inflammatory oxidants in vitro and in vivo – Identification of reaction intermediates and oxidant-specific minor products,” *Free Radic. Biol. Med.*, vol. 99, pp. 32–42, Oct. 2016.
[189] W. Wu *et al.*, “Bioluminescent Probe for Hydrogen Peroxide Imaging in Vitro and in Vivo,” *Anal. Chem.*, vol. 86, no. 19, pp. 9800–9806, Oct. 2014.
[190] K. Kundu, S. F. Knight, N. Willett, S. Lee, W. R. Taylor, and N. Murthy, “Hydrocyanines: A Class of Fluorescent Sensors That Can Image Reactive Oxygen Species in Cell Culture, Tissue, and In Vivo,” *Angew. Chem. Int. Ed.*, vol. 48, no. 2, pp. 299–303, Jan. 2009.
[191] L. Xie, A. S. P. Lin, K. Kundu, M. E. Levenston, N. Murthy, and R. E. Guldberg, “Quantitative imaging of cartilage and bone morphology, reactive oxygen species, and vascularization in a rodent model of osteoarthritis,” *Arthritis Rheum.*, vol. 64, no. 6, pp. 1899–1908, Jun. 2012.
[192] G. S. Wilson and R. Gifford, “Biosensors for real-time in vivo measurements,” *Biosens. Bioelectron.*, vol. 20, no. 12, pp. 2388–2403, Jun. 2005.
[193] G. R. Buettner, B. A. Wagner, and V. G. J. Rodgers, “Quantitative Redox Biology: An approach to understanding the role of reactive species in defining the cellular redox environment,” *Cell Biochem. Biophys.*, vol. 67, no. 2, Nov. 2013.
[194] L. H. Long and B. Halliwell, “Artefacts in cell culture: Pyruvate as a scavenger of hydrogen peroxide generated by ascorbate or epigallocatechin gallate in cell culture media,” *Biochem. Biophys. Res. Commun.*, vol. 388, no. 4, pp. 700–704, Oct. 2009.
[195] J. Sun, X. Zhang, M. Broderick, and H. Fein, “Measurement of nitric oxide production in biological systems by using Griess reaction assay,” *Sensors*, vol. 3, no. 8, pp. 276–284, 2003.
[196] H. Moshage, B. Kok, J. R. Huizenga, and P. L. Jansen, “Nitrite and nitrate determinations in plasma: a critical evaluation.,” *Clin. Chem.*, vol. 41, no. 6, pp. 892–896, Jun. 1995.
[197] G. C. Kim *et al.*, “Air plasma coupled with antibody-conjugated nanoparticles: a new weapon against cancer,” *J. Phys. Appl. Phys.*, vol. 42, no. 3, p. 032005, 2009.
[198] T. Karlsmark *et al.*, “Tracing the use of electrical torture.,” *Am. J. Forensic Med. Pathol.*, vol. 5, no. 4, p. 333, Dec. 1984.
[199] G. Aguilar, B. Majaron, K. Pope, L. O. Svaasand, E. J. Lavernia, and J. S. Nelson, “Influence of nozzle-to-skin distance in cryogen spray cooling for dermatologic laser surgery,” *Lasers Surg. Med.*, vol. 28, no. 2, pp. 113–120, Jan. 2001.
[200] D. Theodorescu, “Cancer Cryotherapy: Evolution and Biology,” *Rev. Urol.*, vol. 6, no. Suppl 4, pp. S9–S19, 2004.
[201] A. A. Gage, J. M. Baust, and J. G. Baust, “Experimental Cryosurgery Investigations In Vivo,” *Cryobiology*, vol. 59, no. 3, p. 229, Dec. 2009.
[202] M. Stanczyk and J. J. Telega, “Thermal problems in biomechanics-a review. Part III. Cryosurgery, cryopreservation and cryotherapy,” *Acta Bioeng. Biomech.*, vol. 5, no. 2, pp. 3–22, 2003.
[203] A. A. Gage, J. A. Caruana, and M. Montes, “Critical temperature for skin necrosis in experimental cryosurgery,” *Cryobiology*, vol. 19, no. 3, pp. 273–282, Jun. 1982.
[204] A. A. Gage, S. Augustynowicz, M. Montes, J. A. Caruana, and D. A. Whalen, “Tissue impedance and temperature measurements in relation to necrosis in experimental cryosurgery,” *Cryobiology*, vol. 22, no. 3, pp. 282–288, Jun. 1985.
[205] Hecht F., “New development in freefem++,” *J. Numer. Math.*, vol. 20, no. 3–4, p. 251, 2013.

[206] F. C. Henriques Jr and A. R. Moritz, “Studies of thermal injury: I. The conduction of heat to and through skin and the temperatures attained therein. A theoretical and an experimental investigation,” *Am. J. Pathol.*, vol. 23, no. 4, p. 530, 1947.
[207] D. Manstein, G. S. Herron, R. K. Sink, H. Tanner, and R. R. Anderson, “Fractional Photothermolysis: A New Concept for Cutaneous Remodeling Using Microscopic Patterns of Thermal Injury,” *Lasers Surg. Med.*, vol. 34, no. 5, pp. 426–438, Jun. 2004.
[208] M. Pasparakis, I. Haase, and F. O. Nestle, “Mechanisms regulating skin immunity and inflammation,” *Nat. Rev. Immunol.*, vol. 14, no. 5, pp. 289–301, May 2014.
[209] A. Abdullahi, S. Amini-Nik, and M. . Jeschke, “Animal Models in Burn Research,” *Cell. Mol. Life Sci. CMLS*, vol. 71, no. 17, pp. 3241–3255, Sep. 2014.
[210] F. Xu and T. Lu, *Introduction to Skin Biothermomechanics and Thermal Pain*. Berlin, Heidelberg: Springer Berlin Heidelberg, 2011.
[211] C. P. Sabino *et al.*, “The optical properties of mouse skin in the visible and near infrared spectral regions,” *J. Photochem. Photobiol. B*, vol. 160, pp. 72–78, Jul. 2016.
[212] K. Parson, *Human Thermal Environments: The Effects of Hot, Moderate, and Cold Environments on Human Health, Comfort and Performance, Second Edition*. CRC Press, 2002.
[213] F. A. Duck, *Physical Properties of Tissues: A Comprehensive Reference Book*. Academic Press, 2013.
[214] M. Wild, D. Folini, C. Schär, N. Loeb, E. Dutton, and G. König-Langlo, “The Earth’s radiation balance and its representation in CMIP5 models,” presented at the EGU General Assembly Conference Abstracts, 2013, vol. 15, pp. EGU2013-1286.
[215] D. A. Torvi and J. D. Dale, “A Finite Element Model of Skin Subjected to a Flash Fire,” *J. Biomech. Eng.*, vol. 116, no. 3, pp. 250–255, Aug. 1994.
[216] A. M. Stoll and L. C. Greene, “Relationship between pain and tissue damage due to thermal radiation,” *J. Appl. Physiol.*, vol. 14, no. 3, pp. 373–382, May 1959.
[217] H. C. HARDEE, D. O. LEE, and W. B. BENEDICK, “Thermal Hazard from LNG Fireballs,” *Combust. Sci. Technol.*, vol. 17, no. 5–6, pp. 189–197, Feb. 1978.
[218] R. B. Roemer, “Thermal Dosimetry,” *SpringerLink*, pp. 119–214, 1990.
[219] M. Jaunich, S. Raje, K. Kim, K. Mitra, and Z. Guo, “Bio-heat transfer analysis during short pulse laser irradiation of tissues,” *Int. J. Heat Mass Transf.*, vol. 51, no. 23–24, pp. 5511–5521, Nov. 2008.
[220] M. W. Dewhirst, J. Abraham, and B. Viglianti, “Chapter Six - Evolution of Thermal Dosimetry for Application of Hyperthermia to Treat Cancer,” in *Advances in Heat Transfer*, vol. 47, J. P. A. and J. M. G. Ephraim M. Sparrow, Ed. Elsevier, 2015, pp. 397–421.
[221] B. L. Viglianti, M. W. Dewhirst, J. P. Abraham, J. M. Gorman, and E. M. Sparrow, “Rationalization of thermal injury quantification methods: Application to skin burns,” *Burns*, vol. 40, no. 5, pp. 896–902, Aug. 2014.
[222] J. Pearce, “Mathematical models of laser-induced tissue thermal damage,” *Int. J. Hyperthermia*, vol. 27, no. 8, pp. 741–750, Dec. 2011.
[223] J. P. Abraham, M. P. Hennessey, and W. J. Minkowycz, “A simple algebraic model to predict burn depth and injury,” *Int. Commun. Heat Mass Transf.*, vol. 38, no. 9, pp. 1169–1171, Nov. 2011.
[224] M. W. Dewhirst, B. L. Viglianti, M. Lora-Michiels, M. Hanson, and P. J. Hoopes, “Basic principles of thermal dosimetry and thermal thresholds for tissue damage from hyperthermia,” *Int. J. Hyperthermia*, vol. 19, no. 3, pp. 267–294, Jan. 2003.
[225] F. K. Storm and D. L. Morton, “Localized hyperthermia in the treatment of cancer,” *CA. Cancer J. Clin.*, vol. 33, no. 1, pp. 44–56, Jan. 1983.
[226] M. P. Law, “Induced thermal resistance in the mouse ear: the relationship between heating time and temperature,” *Int. J. Radiat. Biol. Relat. Stud. Phys. Chem. Med.*, vol. 35, no. 4, pp. 481–485, 1979.

[227] A. R. Moritz and F. C. Henriques Jr, “Studies of thermal injury: II. The relative importance of time and surface temperature in the causation of cutaneous burns,” *Am. J. Pathol.*, vol. 23, no. 5, p. 695, 1947.
[228] J. W. Lee, P. Gadiraju, J.-H. Park, M. G. Allen, and M. R. Prausnitz, “Microsecond thermal ablation of skin for transdermal drug delivery,” *J. Controlled Release*, vol. 154, no. 1, pp. 58–68, Aug. 2011.
[229] J. R. Lepock, “Cellular effects of hyperthermia: relevance to the minimum dose for thermal damage,” *Int. J. Hyperthermia*, vol. 19, no. 3, pp. 252–266, Jan. 2003.
[230] P. de Andrade Mello *et al.*, “Hyperthermia and associated changes in membrane fluidity potentiate P2X7 activation to promote tumor cell death,” *Oncotarget*, vol. 8, no. 40, pp. 67254–67268, Jun. 2017.
[231] W. Leyko and G. Bartosz, “Membrane Effects of Ionizing Radiation and Hyperthermia,” *Int. J. Radiat. Biol. Relat. Stud. Phys. Chem. Med.*, vol. 49, no. 5, pp. 743–770, Jan. 1985.
[232] G. Borasi *et al.*, “Fast and high temperature hyperthermia coupled with radiotherapy as a possible new treatment for glioblastoma,” *J. Ther. Ultrasound*, vol. 4, p. 32, 2016.
[233] M. Ahmed, M. Moussa, and S. N. Goldberg, “Synergy in cancer treatment between liposomal chemotherapeutics and thermal ablation,” *Chem. Phys. Lipids*, vol. 165, no. 4, pp. 424–437, May 2012.
[234] L. Appelbaum *et al.*, “Algorithm Optimization for Multitined Radiofrequency Ablation: Comparative Study in ex Vivo and in Vivo Bovine Liver,” *Radiology*, vol. 254, no. 2, pp. 430–440, Jan. 2010.
[235] C. Rossmann and D. Haemmerich, “Review of temperature dependence of thermal properties, dielectric properties, and perfusion of biological tissues at hyperthermic and ablation temperatures,” *Crit. Rev. Biomed. Eng.*, vol. 42, no. 6, pp. 467–492, 2014.
[236] J. Sun, A. Zhang, and L. X. Xu, “Evaluation of alternate cooling and heating for tumor treatment,” *Int. J. Heat Mass Transf.*, vol. 51, no. 23–24, pp. 5478–5485, Nov. 2008.
[237] A. G. Alzaga, M. Cerdan, and J. Varon, “Therapeutic hypothermia,” *Resuscitation*, vol. 70, no. 3, pp. 369–380, Sep. 2006.
[238] A. K. Li, H. P. Ehrlich, R. L. Trelstad, M. J. Koroly, M. E. Schattenkerk, and R. A. Malt, “Differences in healing of skin wounds caused by burn and freeze injuries.,” *Ann. Surg.*, vol. 191, no. 2, pp. 244–248, Feb. 1980.
[239] S. Singh and S. Kumar, “A Study on the Effect of Metabolic Heat Generation on Biological Tissue Freezing,” *Sci. World J.*, vol. 2013, Nov. 2013.
[240] J. R. Thomas and E. H. N. Oakley, “Nonfreezing cold injury.”
[241] F. Stewart and A. Begg, “Blood flow changes in transplanted mouse tumours and skin after mild hyperthermia,” *Br. J. Radiol.*, vol. 56, no. 667, pp. 477–482, Jul. 1983.
[242] G. Grile, “The effects of heat and radiation on cancers implanted on the feet of mice,” *Cancer Res.*, vol. 23, no. 3, pp. 372–380, 1963.
[243] C. W. Song, A. Lokshina, J. G. Rhee, M. Patten, and S. H. Levitt, “Implication of Blood Flow in Hyperthermic Treatment of Tumors,” *IEEE Trans. Biomed. Eng.*, vol. BME-31, no. 1, pp. 9–16, Jan. 1984.
[244] C. W. Song, “Effect of Local Hyperthermia on Blood Flow and Microenvironment: A Review,” *Cancer Res.*, vol. 44, no. 10 Supplement, p. 4721s–4730s, Oct. 1984.
[245] Z. Vujaskovic *et al.*, “Temperature-dependent changes in physiologic parameters of spontaneous canine soft tissue sarcomas after combined radiotherapy and hyperthermia treatment,” *Int. J. Radiat. Oncol.*, vol. 46, no. 1, pp. 179–185, Jan. 2000.
[246] C. W. Song, H. Park, and R. J. Griffin, “Improvement of Tumor Oxygenation by Mild Hyperthermia,” *Radiat. Res.*, vol. 155, no. 4, pp. 515–528, Apr. 2001.

[247] N. van den Tempel, M. R. Horsman, and R. Kanaar, “Improving efficacy of hyperthermia in oncology by exploiting biological mechanisms,” *Int. J. Hyperthermia*, vol. 32, no. 4, pp. 446–454, May 2016.
[248] S. Toraya-Brown and S. Fiering, “Local tumour hyperthermia as immunotherapy for metastatic cancer,” *Int. J. Hyperthermia*, vol. 30, no. 8, pp. 531–539, Dec. 2014.
[249] B. Frey *et al.*, “Antitumor immune responses induced by ionizing irradiation and further immune stimulation,” *Cancer Immunol. Immunother.*, vol. 63, no. 1, pp. 29–36, 2014.
[250] B. Frey *et al.*, “Old and new facts about hyperthermia-induced modulations of the immune system,” *Int. J. Hyperthermia*, vol. 28, no. 6, pp. 528–542, Sep. 2012.
[251] J. Kubes, J. Svoboda, J. Rosina, M. Starec, and A. Fiserova, “Immunological response in the mouse melanoma model after local hyperthermia,” *Physiol. Res.*, vol. 57, no. 3, p. 459, 2008.
[252] B. Hildebrandt *et al.*, “The cellular and molecular basis of hyperthermia,” *Crit. Rev. Oncol. Hematol.*, vol. 43, no. 1, pp. 33–56, Jul. 2002.
[253] S. Lord-Fontaine and D. A. Averill, “Enhancement of Cytotoxicity of Hydrogen Peroxide by Hyperthermia in Chinese Hamster Ovary Cells: Role of Antioxidant Defenses,” *Arch. Biochem. Biophys.*, vol. 363, no. 2, pp. 283–295, Mar. 1999.
[254] S. Lord-Fontaine and D. A. Averill-Bates, “Heat shock inactivates cellular antioxidant defenses against hydrogen peroxide: protection by glucose,” *Free Radic. Biol. Med.*, vol. 32, no. 8, pp. 752–765, Apr. 2002.
[255] A. Bettaieb, P. K. Wrzal, and D. A. Averill-Bates, “Hyperthermia: Cancer treatment and beyond,” *Cancer Treat. Innov. Approaches*, 2013.
[256] P. S. Yarmolenko *et al.*, “Thresholds for thermal damage to normal tissues: An update,” *Int. J. Hyperth. Off. J. Eur. Soc. Hyperthermic Oncol. North Am. Hyperth. Group*, vol. 27, no. 4, pp. 320–343, 2011.
[257] A. Capon and S. Mordon, “Can Thermal Lasers Promote Skin Wound Healing?,” *Am. J. Clin. Dermatol.*, vol. 4, no. 1, pp. 1–12, Jan. 2003.
[258] J. Heinlin *et al.*, “Plasma applications in medicine with a special focus on dermatology,” *J. Eur. Acad. Dermatol. Venereol.*, vol. 25, no. 1, pp. 1–11, Jan. 2011.
[259] B. C. Wilson and M. S. Patterson, “The physics of photodynamic therapy,” *Phys. Med. Biol.*, vol. 31, no. 4, p. 327, 1986.
[260] M. Leunig *et al.*, “Thermal imaging during photodynamic therapy (PDT),” *Lasers Med. Sci.*, vol. 7, no. 1–4, pp. 477–481, Mar. 1992.
[261] J. H. Kinsey, D. A. Cortese, and H. B. Neel, “Thermal Considerations in Murine Tumor Killing Using Hematoporphyrin Derivative Phototherapy,” *Cancer Res.*, vol. 43, no. 4, pp. 1562–1567, Apr. 1983.
[262] L. O. Svaasand, D. R. Doiron, and T. J. Dougherty, “Temperature rise during photoradiation therapy of malignant tumors,” *Med. Phys.*, vol. 10, no. 1, pp. 10–17, Jan. 1983.
[263] A. R. Moritz, “Studies of thermal injury: III. The pathology and pathogenesis of cutaneous burns. An experimental study,” *Am. J. Pathol.*, vol. 23, no. 6, p. 915, 1947.
[264] K. Pietrucha, “Changes in denaturation and rheological properties of collagen–hyaluronic acid scaffolds as a result of temperature dependencies,” *Int. J. Biol. Macromol.*, vol. 36, no. 5, pp. 299–304, Sep. 2005.
[265] K. R. Diller and J. A. Pearce, “Issues in Modeling Thermal Alterations in Tissues a,” *Ann. N. Y. Acad. Sci.*, vol. 888, no. 1, pp. 153–164, Nov. 1999.
[266] K. R. Diller, “Modeling of Bioheat Transfer Processes at High and Low Temperatures,” *Adv. Heat Transf.*, vol. 22, pp. 157–357, Jan. 1992.
[267] C. Bai and A. S. Lavine, “On Hyperbolic Heat Conduction and the Second Law of Thermodynamics,” *J. Heat Transf.*, vol. 117, no. 2, pp. 256–263, May 1995.

[268] T.-C. Shih, H.-W. Huang, W.-C. Wei, and T.-L. Horng, “Parametric analysis of effective tissue thermal conductivity, thermal wave characteristic, and pulsatile blood flow on temperature distribution during thermal therapy,” *Int. Commun. Heat Mass Transf.*, vol. 52, pp. 113–120, Mar. 2014.
[269] M. C. Kolios, M. D. Sherar, and J. W. Hunt, “Blood flow cooling and ultrasonic lesion formation,” *Med. Phys.*, vol. 23, no. 7, pp. 1287–1298, Jul. 1996.
[270] J. Crezee and J. J. W. Lagendijk, “Experimental verification of bioheat transfer theories: measurement of temperature profiles around large artificial vessels in perfused tissue,” *Phys. Med. Biol.*, vol. 35, no. 7, p. 905, 1990.
[271] J. R. Speakman, “Measuring Energy Metabolism in the Mouse – Theoretical, Practical, and Analytical Considerations,” *Front. Physiol.*, vol. 4, Mar. 2013.
[272] Z.-S. Deng and J. Liu, “Monte Carlo Method to Solve Multidimensional Bioheat Transfer Problem,” *Numer. Heat Transf. Part B Fundam.*, vol. 42, no. 6, pp. 543–567, Dec. 2002.
[273] A. Tsukamoto, K. Serizawa, R. Sato, J. Yamazaki, and T. Inomata, “Vital signs monitoring during injectable and inhalant anesthesia in mice,” *Exp. Anim.*, vol. 64, no. 1, pp. 57–64, 2015.
[274] D. J. Schutt and D. Haemmerich, “Effects of variation in perfusion rates and of perfusion models in computational models of radio frequency tumor ablation,” *Med. Phys.*, vol. 35, no. 8, pp. 3462–3470, Aug. 2008.
[275] S. B. Wilson and V. A. Spence, “A tissue heat transfer model for relating dynamic skin temperature changes to physiological parameters,” *Phys. Med. Biol.*, vol. 33, no. 8, p. 895, 1988.
[276] V. T. Morgan, “The Overall Convective Heat Transfer from Smooth Circular Cylinders,” *Adv. Heat Transf.*, vol. 11, pp. 199–264, Jan. 1975.
[277] J. Taine, E. Iacona, and J.-P. Petit, *Transferts thermiques: Introduction aux transferts d’énergie*. 2008.
[278] C. D. Donaldson, R. S. Snedeker, and D. P. Margolis, “A study of free jet impingement. Part 2. Free jet turbulent structure and impingement heat transfer,” *J. Fluid Mech.*, vol. 45, no. 3, pp. 477–512, Feb. 1971.
[279] C. O. Popiel, T. H. van der Meer, and C. J. Hoogendoorn, “Convective heat transfer on a plate in an impinging round hot gas jet of low Reynolds number,” *Int. J. Heat Mass Transf.*, vol. 23, no. 8, pp. 1055–1068, Aug. 1980.
[280] C. Gau and C. M. Chung, “Surface Curvature Effect on Slot-Air-Jet Impingement Cooling Flow and Heat Transfer Process,” *J. Heat Transf.*, vol. 113, no. 4, pp. 858–864, Nov. 1991.
[281] D. H. Lee, S. Y. Won, Y. T. Kim, and Y. S. Chung, “Turbulent heat transfer from a flat surface to a swirling round impinging jet,” *Int. J. Heat Mass Transf.*, vol. 1, no. 45, pp. 223–227, 2002.
[282] R. Viskanta, “Heat transfer to impinging isothermal gas and flame jets,” *Exp. Therm. Fluid Sci.*, vol. 6, no. 2, pp. 111–134, Feb. 1993.
[283] V. Katti and S. V. Prabhu, “Experimental study and theoretical analysis of local heat transfer distribution between smooth flat surface and impinging air jet from a circular straight pipe nozzle,” *Int. J. Heat Mass Transf.*, vol. 51, no. 17, pp. 4480–4495, Aug. 2008.
[284] H. G. Lee, H. S. Yoon, and M. Y. Ha, “A numerical investigation on the fluid flow and heat transfer in the confined impinging slot jet in the low Reynolds number region for different channel heights,” *Int. J. Heat Mass Transf.*, vol. 51, no. 15, pp. 4055–4068, Jul. 2008.
[285] D. Sahoo and M. A. R. Sharif, “Numerical modeling of slot-jet impingement cooling of a constant heat flux surface confined by a parallel wall,” *Int. J. Therm. Sci.*, vol. 43, no. 9, pp. 877–887, Sep. 2004.
[286] P. M. Brdlik and V. K. Savin, “Heat transfer in the vicinity of the stagnation point in an axisymmetric jet flowing over flat surfaces normal to the flow,” *J. Eng. Phys.*, vol. 10, no. 4, pp. 241–245, Apr. 1966.

[287] R. Gardon and J. C. Akfirat, “The role of turbulence in determining the heat-transfer characteristics of impinging jets,” *Int. J. Heat Mass Transf.*, vol. 8, no. 10, pp. 1261–1272, Oct. 1965.
[288] T. H. van der Meer, “Stagnation point heat transfer from turbulent low reynolds number jets and flame jets,” *Exp. Therm. Fluid Sci.*, vol. 4, no. 1, pp. 115–126, Jan. 1991.
[289] L. C. Burmeister, *Convective Heat Transfer*. John Wiley & Sons, 1993.
[290] J. R. Tallackson, “Thermal transport properties of helium, helium–air mixtures, water, and tubing steel used in the CACHE program to compute HTGR auxiliary heat exchanger performance,” Oak Ridge National Lab., Tenn.(USA), 1976.
[291] W. M. Haynes, *CRC Handbook of Chemistry and Physics, 96th Edition*. CRC Press, 2015.
[292] E. R. Adair and D. R. Black, “Thermoregulatory responses to RF energy absorption,” *Bioelectromagnetics*, vol. 24, no. S6, pp. S17–S38, Jan. 2003.
[293] Z.-S. Deng and J. Liu, “Mathematical modeling of temperature mapping over skin surface and its implementation in thermal disease diagnostics,” *Comput. Biol. Med.*, vol. 34, no. 6, pp. 495–521, Sep. 2004.
[294] G. Havenith *et al.*, “Evaporative cooling: effective latent heat of evaporation in relation to evaporation distance from the skin,” *J. Appl. Physiol. Bethesda Md 1985*, vol. 114, no. 6, pp. 778–785, Mar. 2013.
[295] H. Kersten, H. Deutsch, H. Steffen, G. M. W. Kroesen, and R. Hippler, “The energy balance at substrate surfaces during plasma processing,” *Vacuum*, vol. 63, no. 3, pp. 385–431, Aug. 2001.
[296] E. Tatarova, E. Stoykova, K. Bachev, and I. Zhelyazkov, “Effects of nonlocal electron kinetics and transition from alpha; to gamma; regime in an RF capacitive discharge in nitrogen,” *IEEE Trans. Plasma Sci.*, vol. 26, no. 2, pp. 167–174, Apr. 1998.
[297] P. Faber and L. Garby, “Fat content affects heat capacity: a study in mice,” *Acta Physiol. Scand.*, vol. 153, no. 2, pp. 185–187, Feb. 1995.
[298] Y. S. Touloukian, P. E. Liley, and S. C. Saxena, “Thermophysical Properties of Matter - The TPRC Data Series. Volume 3. Thermal Conductivity - Nonmetallic Liquids and Gases,” Jan. 1970.
[299] R. L. Mcintosh and V. Anderson, “A comprehensive tissue properties database provided for the thermal assessment of a human at rest,” *Biophys. Rev. Lett.*, vol. 05, no. 03, pp. 129–151, Sep. 2010.
[300] K. R. Holmes and M. M. Chen, “Local thermal conductivity of Para-7 fibrosarcoma in hamster,” *Adv. Bioeng.*, vol. 4, pp. 147–149, 1979.
[301] W. T. Stott, M. D. Dryzga, and J. C. Ramsey, “Blood-flow distribution in the mouse,” *J. Appl. Toxicol.*, vol. 3, no. 6, pp. 310–312, Dec. 1983.
[302] F. W. Orr, M. R. Buchanan, and L. Weiss, *Microcirculation in Cancer Metastasis*. CRC Press, 1991.
[303] X. Montet, J.-L. Figueiredo, H. Alencar, V. Ntziachristos, U. Mahmood, and R. Weissleder, “Tomographic Fluorescence Imaging of Tumor Vascular Volume in Mice,” *Radiology*, vol. 242, no. 3, pp. 751–758, Mar. 2007.
[304] H. H. Pennes, “Analysis of tissue and arterial blood temperatures in the resting human forearm,” *J. Appl. Physiol.*, vol. 1, no. 2, pp. 93–122, 1948.
[305] L. Trhlíková, O. Zmeskal, P. Psencik, and P. Florian, “Study of the thermal properties of filaments for 3D printing,” *AIP Conf. Proc.*, vol. 1752, no. 1, p. 040027, Jul. 2016.
[306] E. Moros, *Physics of Thermal Therapy: Fundamentals and Clinical Applications*. Taylor & Francis, 2016.
[307] I. Rivens, A. Shaw, J. Civale, and H. Morris, “Treatment monitoring and thermometry for therapeutic focused ultrasound,” *Int. J. Hyperthermia*, vol. 23, no. 2, pp. 121–139, Jan. 2007.

[308] P. Fessenden, E. R. Lee, and T. V. Samulski, “Direct Temperature Measurement,” *Cancer Res.*, vol. 44, no. 10 Supplement, p. 4799s–4804s, Oct. 1984.
[309] T. V. Samulski, B. E. Lyons, and R. H. Britt, “Temperature measurements in high thermal gradients: II. Analysis of conduction effects,” *Int. J. Radiat. Oncol.*, vol. 11, no. 5, pp. 963–971, May 1985.
[310] E. Schena, D. Tosi, P. Saccomandi, E. Lewis, and T. Kim, “Fiber Optic Sensors for Temperature Monitoring during Thermal Treatments: An Overview,” *Sensors*, vol. 16, no. 7, Jul. 2016.
[311] C. M. Jha, *Thermal Sensors: Principles and Applications for Semiconductor Industries*. Springer, 2015.
[312] R. J. Dickinson, “Thermal conduction errors of manganin-constantan thermocouple arrays,” *Phys. Med. Biol.*, vol. 30, no. 5, p. 445, 1985.
[313] M. S. Mann *et al.*, “Introduction to DIN-specification 91315 based on the characterization of the plasma jet kINPen® MED,” *Clin. Plasma Med.*, vol. 4, no. 2, pp. 35–45, Dec. 2016.
[314] K. M. Kokolus *et al.*, “Baseline tumor growth and immune control in laboratory mice are significantly influenced by subthermoneutral housing temperature,” *Proc. Natl. Acad. Sci.*, vol. 110, no. 50, pp. 20176–20181, Oct. 2013.
[315] D. Y. LI, Y. P. TANG, L. Y. ZHAO, C. Y. GENG, and J. T. TANG, “Antitumor effect and immune response induced by local hyperthermia in B16 murine melanoma: Effect of thermal dose,” *Oncol. Lett.*, vol. 4, no. 4, pp. 711–718, Oct. 2012.
[316] G. Kostenich, T. Babushkina, Z. Malik, and A. Orenstein, “Photothermic treatment of pigmented B16 melanoma using a broadband pulsed light delivery system,” *Cancer Lett.*, vol. 157, no. 2, pp. 161–168, Sep. 2000.
[317] N. Werthmöller, B. Frey, M. Rückert, M. Lotter, R. Fietkau, and U. S. Gaipl, “Combination of ionising radiation with hyperthermia increases the immunogenic potential of B16-F10 melanoma cells in vitro and in vivo,” *Int. J. Hyperthermia*, vol. 32, no. 1, pp. 23–30, Jan. 2016.
[318] T. Takada *et al.*, “Growth Inhibition of Re-Challenge B16 Melanoma Transplant by Conjugates of Melanogenesis Substrate and Magnetite Nanoparticles as the Basis for Developing Melanoma-Targeted Chemo-Thermo-Immunotherapy,” *J. Biomed. Biotechnol.*, vol. 2009, 2009.
[319] Lienhard, *A Heat Transfer Textbook, 4/e*, 4th ed. Cambridge, MA: Phlogiston Press, 2017.
[320] A. Shashurin, M. Keidar, S. Bronnikov, R. A. Jurjus, and M. A. Stepp, “Living tissue under treatment of cold plasma atmospheric jet,” *Appl. Phys. Lett.*, vol. 93, no. 18, p. 181501, Nov. 2008.
[321] J. T. Whitton and J. d. Everall, “The thickness of the epidermis,” *Br. J. Dermatol.*, vol. 89, no. 5, pp. 467–476, Nov. 1973.
[322] R. Foest, E. Kindel, H. Lange, A. Ohl, M. Stieber, and K.-D. Weltmann, “RF Capillary Jet - a Tool for Localized Surface Treatment,” *Contrib. Plasma Phys.*, vol. 47, no. 1–2, pp. 119–128, Feb. 2007.
[323] K.-D. Weltmann *et al.*, “Atmospheric Pressure Plasma Jet for Medical Therapy: Plasma Parameters and Risk Estimation,” *Contrib. Plasma Phys.*, vol. 49, no. 9, pp. 631–640, Nov. 2009.
[324] R. Brandenburg *et al.*, “Antimicrobial Treatment of Heat Sensitive Materials by Means of Atmospheric Pressure Rf-Driven Plasma Jet,” *Contrib. Plasma Phys.*, vol. 47, no. 1–2, pp. 72–79, Feb. 2007.
[325] M. Kuchenbecker, N. Bibinov, A. Kaemlimg, D. Wandke, P. Awakowicz, and W. Viöl, “Characterization of DBD plasma source for biomedical applications,” *J. Phys. Appl. Phys.*, vol. 42, no. 4, p. 045212, 2009.
[326] G. Daeschlein *et al.*, “Cold plasma is well-tolerated and does not disturb skin barrier or reduce skin moisture,” *JDDG J. Dtsch. Dermatol. Ges.*, vol. 10, no. 7, pp. 509–515, Jul. 2012.

[327] A. D. Reid, M. R. Gertner, and M. D. Sherar, “Temperature measurement artefacts of thermocouples and fluoroptic probes during laser irradiation at 810 nm,” *Phys. Med. Biol.*, vol. 46, no. 6, p. N149, 2001.
[328] P. Avci *et al.*, “Low-level laser (light) therapy (LLLT) in skin: stimulating, healing, restoring,” *Semin. Cutan. Med. Surg.*, vol. 32, no. 1, pp. 41–52, Mar. 2013.
[329] J. R. Basford, “Low intensity laser therapy: Still not an established clinical tool,” *Lasers Surg. Med.*, vol. 16, no. 4, pp. 331–342, Jan. 1995.
[330] M. D. Skopin and S. C. Molitor, “Effects of near-infrared laser exposure in a cellular model of wound healing,” *Photodermatol. Photoimmunol. Photomed.*, vol. 25, no. 2, pp. 75–80, Apr. 2009.
[331] P. V. Peplow, T.-Y. Chung, and G. D. Baxter, “Laser Photobiomodulation of Wound Healing: A Review of Experimental Studies in Mouse and Rat Animal Models,” *Photomed. Laser Surg.*, vol. 28, no. 3, pp. 291–325, Dec. 2009.
[332] D. Hawkins, N. Houreld, and H. Abrahamse, “Low Level Laser Therapy (LLLT) as an Effective Therapeutic Modality for Delayed Wound Healing,” *Ann. N. Y. Acad. Sci.*, vol. 1056, no. 1, pp. 486–493, Nov. 2005.
[333] U. Kogelschatz, “Advanced Ozone Generation,” in *Process Technologies for Water Treatment*, Springer US, 1988, pp. 87–118.
[334] “Mesure des caractéristiques des matériaux isolants solides.” [Online]. Available: http://www.techniques-ingenieur.fr/base-documentaire/materiaux-th11/materiaux-a-proprietes-electriques-et-optiques-42375210/mesure-des-caracteristiques-des-materiaux-isolants-solides-d2310/. [Accessed: 05-Feb-2017].
[335] H.-E. Wagner, R. Brandenburg, K. V. Kozlov, A. Sonnenfeld, P. Michel, and J. F. Behnke, “The barrier discharge: basic properties and applications to surface treatment,” *Vacuum*, vol. 71, no. 3, pp. 417–436, May 2003.
[336] M. Valentinuzzi, *Bioelectrical impedance techniques in medicine. Part I: Bioimpedance measurement. First section: General concepts*, vol. 24. 1996.
[337] J. Claudel, *Spectroscopie d’impédance électrique par biocapteur à micro-électrodes : application à la cytométrie de flux de cellules sanguines*. Université de Lorraine, 2013.
[338] M. Sato, T. Ohgiyama, and J. S. Clements, “Formation of chemical species and their effects on microorganisms using a pulsed high-voltage discharge in water,” *IEEE Trans. Ind. Appl.*, vol. 32, no. 1, pp. 106–112, Jan. 1996.
[339] K. C. Hsieh, R. J. Wandell, S. Bresch, and B. R. Locke, “Analysis of hydroxyl radical formation in a gas-liquid electrical discharge plasma reactor utilizing liquid and gaseous radical scavengers,” *Plasma Process. Polym.*, p. n/a-n/a, Mar. 2017.
[340] S. Robl, M. Wörner, D. Maier, and A. M. Braun, “Formation of hydrogen peroxide by VUV-photolysis of water and aqueous solutions with methanol,” *Photochem. Photobiol. Sci.*, vol. 11, no. 6, pp. 1041–1050, 2012.
[341] C. K. WESTBROOK and F. L. DRYER, “A Comprehensive Mechanism for Methanol Oxidation,” *Combust. Sci. Technol.*, vol. 20, pp. 125–140, 1979.
[342] R. Overend and G. Paraskevopoulos, “Rates of hydroxyl radical reactions. 4. Reactions with methanol, ethanol, 1-propanol, and 2-propanol at 296 K,” *J. Phys. Chem.*, vol. 82, no. 12, pp. 1329–1333, Jun. 1978.
[343] G. Heit, A. Neuner, P.-Y. Saugy, and A. M. Braun, “Vacuum-UV (172 nm) Actinometry. The Quantum Yield of the Photolysis of Water,” *J. Phys. Chem. A*, vol. 102, no. 28, pp. 5551–5561, Jul. 1998.
[344] M. G. Gonzalez, E. Oliveros, M. Wörner, and A. M. Braun, “Vacuum-ultraviolet photolysis of aqueous reaction systems,” *J. Photochem. Photobiol. C Photochem. Rev.*, vol. 5, no. 3, pp. 225–246, Dec. 2004.
[345] X.-Y. Yu, “Critical Evaluation of Rate Constants and Equilibrium Constants of Hydrogen Peroxide Photolysis in Acidic Aqueous Solutions Containing Chloride Ions,” *J. Phys. Chem. Ref. Data*, vol. 33, no. 3, pp. 747–763, Aug. 2004.
[346] K. Azrague *et al.*, “Hydrogen peroxide evolution during V-UV photolysis of water,” *Photochem. Photobiol. Sci.*, vol. 4, no. 5, pp. 406–408, 2005.

[347] B. R. Locke and K.-Y. Shih, “Review of the methods to form hydrogen peroxide in electrical discharge plasma with liquid water,” *Plasma Sources Sci. Technol.*, vol. 20, no. 3, p. 034006, 2011.
[348] M. Sahni and B. R. Locke, “Quantification of Reductive Species Produced by High Voltage Electrical Discharges in Water,” *Plasma Process. Polym.*, vol. 3, no. 4–5, pp. 342–354, Jul. 2006.
[349] R. O. Olojo, R. H. Xia, and J. J. Abramson, “Spectrophotometric and fluorometric assay of superoxide ion using 4-chloro-7-nitrobenzo-2-oxa-1,3-diazole,” *Anal. Biochem.*, vol. 339, no. 2, pp. 338–344, Apr. 2005.
[350] G. Bartosz, “Use of spectroscopic probes for detection of reactive oxygen species,” *Clin. Chim. Acta*, vol. 368, no. 1–2, pp. 53–76, Jun. 2006.
[351] T. Toyo’oka, Y. Watanabe, and K. Imai, “Reaction of amines of biological importance with 4-fluoro-7-nitrobenzo-2-oxa-1,3-diazole,” *Anal. Chim. Acta - ANAL CHIM ACTA*, vol. 149, pp. 305–312, Dec. 1983.
[352] B. S. Baines, G. Allen, and K. Brocklehurst, “The highly electrophilic character of 4-chloro-7-nitrobenzofurazan and possible consequences for its applications as a protein-labelling reagent,” *Biochem. J.*, vol. 163, no. 1, pp. 189–192, Apr. 1977.
[353] A. Ikhlaq, D. R. Brown, and B. Kasprzyk-Hordern, “Mechanisms of catalytic ozonation: An investigation into superoxide ion radical and hydrogen peroxide formation during catalytic ozonation on alumina and zeolites in water,” *Appl. Catal. B Environ.*, vol. 129, pp. 437–449, Jan. 2013.

Appendix A Electrical and power measurements

This section describes the results obtained related to the electrical characterization of the device. The first section regards the single-channel jet. The number of discharges, the amount of charges transferred were deduced from the signal acquired with the oscilloscope. The characteristic of the discharge are studied as a function of two parameters: the height above liquid and the helium flow, the other parameter being constant. Significant difference appears according to these two parameters. Such differences are correlated with the change in the chemical properties of the liquid. However, with such result, no causal link can be demonstrated. Perhaps electrical measurement could enable to obtain insight on target chemistry? Significant differences appear between positive and negative discharges.

The second section regards the modeling of the dielectric losses. These loss are often negligible and neglected in plasma-device and depends on the voltage, the frequency and the angle of loss of the dielectric. However, there is some case of practical interest where they can count for almost 10% of the total power consumption (DBD at “High Voltage” and “low” power[115]). Neglecting these losses could lead to an underestimation of the power of some plasma-medicine device. In contrast, the measurement of the angle of loss enables to characterize the aging of the dielectric barrier. This could useful to prevent the electrocution of a patient treated by a reusable device.

In the last section, the consequences of the presence of a living organism are discussed. Experimental results of the equivalent series capacitance and resistance of the mouse are presented.

A-1) Statistical count of discharges, correlation with RONS production.

A-1-1) Method, characteristic times

In the main document, the power consumption of the devices was calculated with the integral of $U \times I$ over an entire period of the power supply. As explained in section V.1.5 (page 129), even if the time of the response of measurement systems is slow, power measurement are correct at the time scale of a period[116] since the response time of the measuring system is small compared to one period.

The measurement system is equivalent to a capacitance C = 11.5 pF placed in parallel with a resistance of 10 MΩ (see Chapter II). The response time is therefore of the order of $\tau = 10\ M\Omega \times 11.5\ pF \cong 0.12\ ms \ll 2\ ms$

Actually, what is called one "discharge" in the rest of this section may be the occurrence of several microdischarges occurring at a time scale smaller than the temporal resolution of our device. When it is found that 90 nC are transferred in a “one” discharge, a current probe with a better temporal resolution[117] could enable to specify if it is several discharges or a “big” single discharge.

---

[115] ~30 kV peak to peak and 100 mW at 500 Hz

[116] Indeed, what is important is to know the amount of charge transferred and measure the voltage across the plasma device at the time of the discharge.

[117] Rogowski coil, inductive groove…

In our condition, with theses plasma-devices[118] and at low frequency (~500 Hz), it turns out that the plasma is not present over a significant part of power supply period (see Fig 235, for instance). The discharges are separated by an interval of time[119] during which the plasma is not present.

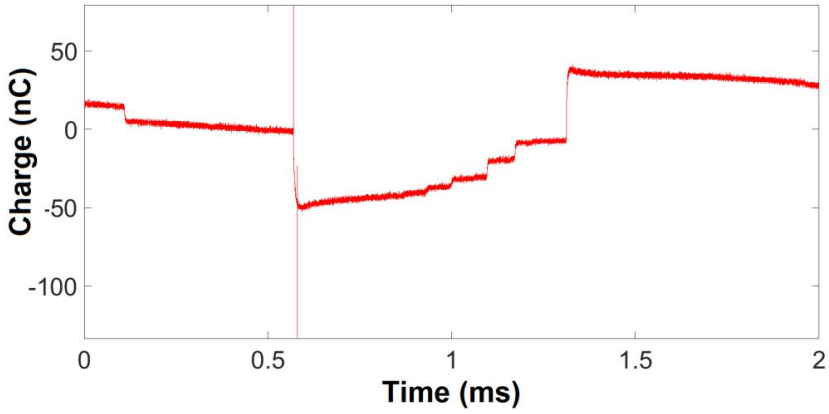

Fig 235 Charge measured at the terminal of the measuring capacitor ($Cm = 104\ nF$). 500 µL of desionised water exposed to the single-channel plasma jet (di=4, H=60 mm, e=1.5) with the set of parameter (helium flow = 350 sscm, Height = 9 mm, Peak to peak voltage = 26.6 kV). Sinusoid power supply of frequency $f = 500\ Hz$

The discharges stop because the surface of the dielectric has been neutralized by the currents circulating in the plasma or the highly conductive medium post streamer. It is interesting to evaluate the characteristic time to replenish the charge of the dielectric. For this, we consider the circuit presented in Fig 236:

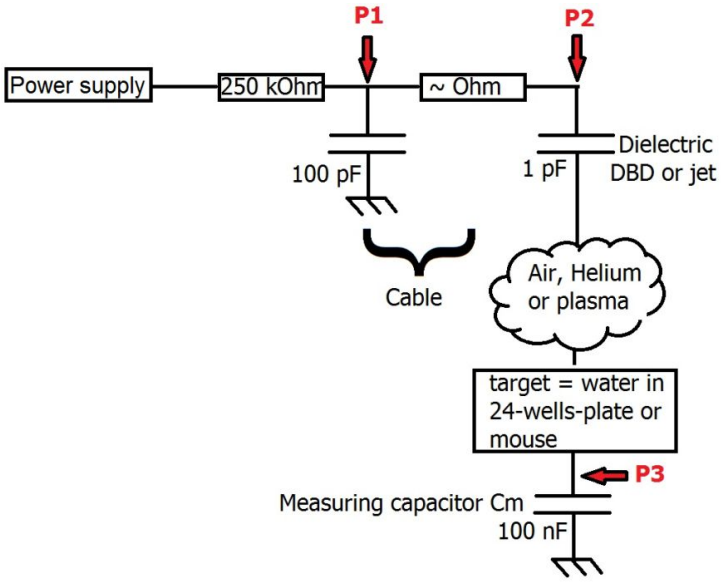

Fig 236 Schematic of the electrical circuit. There is a high voltage resistor between High Voltage power supply and the cable which is connected to the plasma device (the dielectric layer of the device is shown, the rest was not modeled here) We have shown in Chapter II that the capacitance of dielectric layer is ~1 pF (DBD or single-channel plasma-jet). The cable has a length of about 1 m and therefore a capacity of the order of 100 pF (measured and consistent with the manufacturer's data).

[118] i.e the different plasma-jet and the DBD (not shown)
[119] During this, the voltage of the measuring capacity evolves only because of displacement current

Two characteristic time of charge replenishment appears. First, the time needed to charge the capacity of the dielectric layer of plasma-device from the cable which acts as a tank of charges:

$$\tau_1 \sim 1\Omega \times 1\,pF = 1\,ps\ (this\ value\ has\ no\ physical\ meaning\ here)$$

The time obtained is so small, that the AEQS and the modeling in term of electric dipole cease to be valid (it would be necessary to use the equations of the electromagnetism here to obtain realistic times). The time τ_1 is more likely of the order of few ns. Roughly it means that the voltage at the position **P1** of the dielectric is quickly equal to the voltage of the cable.

At 10 kV the amount of charges stored in the cable is of the order ~ 1 µC. The next sections show that this value is very large in front of the quantity of charge conveyed by "one" discharge (~100 nC maximum). The cable, therefore, remains almost at a constant[120] voltage.

Moreover, the characteristic time of cable replenishment is

$$\sim\tau_2 = 250\,k\Omega m \times 100\,pF = 25\,\mu s$$

These characteristic times explain why voltage measurements are the same whatever the position of measurement (**P1** or **P2**) (observed but not shown in this document). This also explains why the drop in voltage is not visible when this cable is connected to the DBD ($\tau_1 \ll response\ time\ of\ PPE20\,kV\ probe$), but visible when the DBD is connected with a simple electric wire (in this case cable capacitance is small, and the time of charge replenishment ~τ_2 and bigger than the response time of PPE20 kV probe[121]).

The two following sections describe statistical count of the discharges produced by the single-channel jet described with the parameter (di=4 mm, e=1.5 mm, H=60 mm, see Chapter II). The waveform is sinusoidal. The electrical circuit corresponds to that described in Fig 236. The target is identical to that used for chemistry studies (in Chapter III): 500 µL of deionized water in 24-wells plate.

The voltage of the power supply was acquired with an oscilloscope (WaveRunner 6 Zi, band-pass =2.5 GHz, Lecroy) connected in **P1** with a probe PPE20kV ($\div 1000$ Lecroy). Passive probes PP08 ($\div 10$) was connected in **P3** to measure the voltage of the measuring capacitance **Cm** (C = 104 nF). The time to obtain 200 acquisitions[122] is ~ 6 min. The power calculated from the integral of $UIdt$, is represented in Fig 237 for the two experiments defined with the parameters:

- Helium Flow= 100-600 sscm. Height= 9 mm, peak to peak Voltage is 26.6 kV
- Helium Flow= 400 sscm. Height= 2-11 mm, peak to peak Voltage is 26.6 kV

[120] at a time scale larger than τ_1 and smaller than the period of power supply…
[121] Bandwith (-3 dB) ~ 100 MHz according to manufacturer's data
[122] This number of acquisitions was chosen because it enables to perform statistics, and because the variation of height due to evaporation is not excessive during the required time.

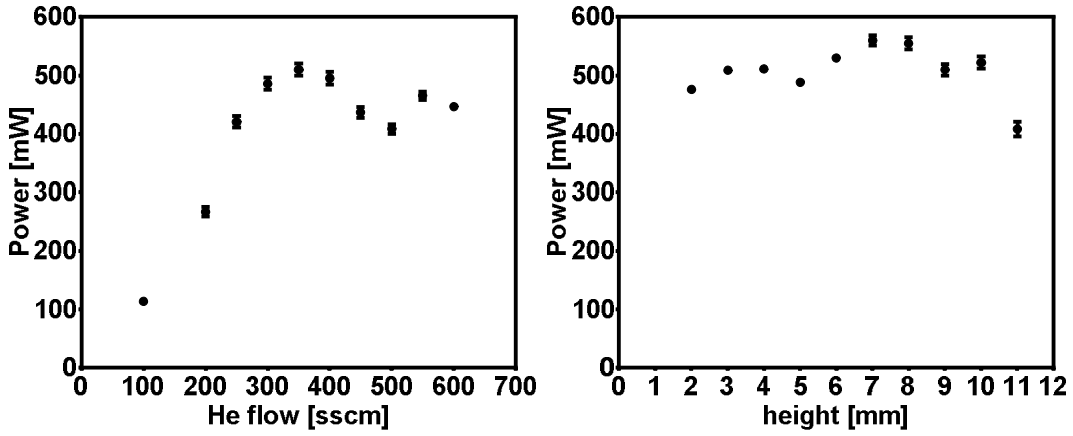

Fig 237 Power (in mW) as a function of Helium flow (left, in sscm) and height (right in mm). Each point represents a single treatment; error bar is the standard error of the mean over 200 acquisitions. Left: height = 9 mm, peak to Peak Voltage= 26.6 kV, helium flow = 100-600 sscm .Right: height = 2-11 mm, peak to Peak Voltage= 26.6 kV, helium flow = 400 sscm.

The power was also calculated by summing the energy consumed by each discharge. The energy of a "single" discharge is calculated by multiplying the amount of charge transferred by the voltage of the power supply when the discharge takes places. It is correct to do this because, in this case, the voltage across the gas is almost identical to that measured at the position **P2** before the discharge. Indeed, it is due to the fact that plasma exists only intermittently and that between discharges, the capacitance of the gas is very small compared to that of the dielectric layer.

Indeed, the impedance of the dielectric is $Z_{die} \sim \frac{1}{jC\omega} = -j\frac{1}{\omega \times 1\ pF}, |Z_{die}| \cong 3.2 \times 10^8\ \Omega$

While the impedance of a cylinder (diameter = 4 mm, length e = 60 mm) of gas is approximately:

$$Z_{gas} = \frac{1}{jC\omega} = -j\frac{e}{\epsilon_0 S\omega}, \qquad thus\ |Z_{gas}| \cong 1.7 \times 10^{11}\ \Omega$$

The voltage across the gas, V_{gas},is given by a voltage divider circuit[123] (almost a capacitive divider):

$$V_{gas} = \frac{Z_{gas}}{(Z_{die} + Z_{gas})} \times V(\boldsymbol{P1}) \cong V(\boldsymbol{P1})$$

The experimental results presented in the next two sections confirm the validity of this alternative means of calculating power (Fig 239 and Fig 243). The data were processed with a Matlab® program to detect the discharges (see section A-5-1), page 308). This code uses the functions of the "Signal Processing Toolbox".

[123] Moreover,the voltage of the target is small (~100 mV) compare to the voltage accross the gas ~ several kV

A-2-1) Adjustable parameter: helium flow

This section regards the results acquired with variables helium flow, the other parameters being constant. The acquisition parameters have been previously described. The single-channel plasma jet operates according to the parameters:

- helium flow = 100-600 sscm
- height = 9 mm
- peak to peak Voltage = 26.6 kV.

The power consumption is shown in the left panel of Fig 237. Automatic waveform processing enables to obtain the distribution of the discharges in terms of transferred charge (abscissa) and initiation voltage of the discharge (ordinate). Each point represents one discharge, the discharges of 200 periods of the power supply were added for each helium flow (Fig 238).

- at 100 sscm, there are mainly less than 10 nC per discharge. Positive or negative discharges have the same behavior.
- The asymmetry between positive and negative charges appears for the flow higher than 200 sscm. Negative discharges carry more charges per event.
- At 550 or 600 sscm, there is a large number of “small” negative discharges which carry less than -10 nC and start between 6 and 13 kV. This population is not found in positive discharges (small number of positive discharges which carry a large number of charges).

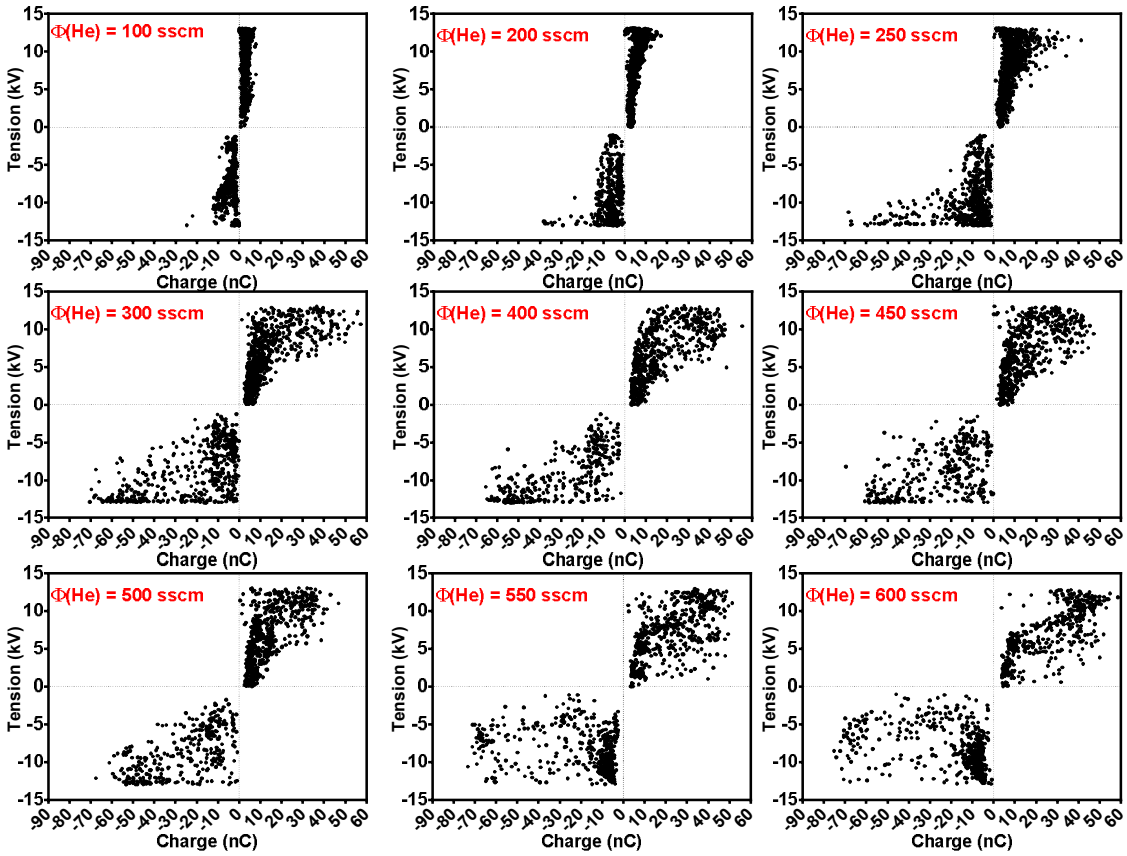

Fig 238 Each point represents “one” discharge. The abscissa is the amount of charges transported during “this” discharge. The ordinate represents the voltage of the power supply at the time of the discharge. Single-channel plasma jet, height = 9 mm, peak to peak Voltage= 26.6 kV, Helium flow =

100-600 sscm. Waveform = sinusoidal, frequency = 500 Hz. Target = 500 µL of deionized water in 24-wells plate. Each figure contains the concatenation of the data of 200 acquisitions. Each acquisition has a duration of 2 ms = one period of the power supply.

It would be interesting to compare this behavior with the simulations of the positive and negative streamer. The accumulation of more results would enable to know the probability of triggering one discharge in each coordinate (amount of charge, Voltage). Note that the difference between positive and negative discharge is not due to an artifact of the program of detection since the peaks are detected from the absolute value of the current.

Fig 239 shows a comparison of the two methods to calculate the power[124] as described in the previous section. Both methods give very similar results; since the mean value differs by less than 3 % for all the flow (except one). It means that almost all the discharges were detected and that the number of false detection remains low. It is also experimental evidence of the validity of the approximation related to the relative impedance of gas (without plasma) and the dielectric layer.

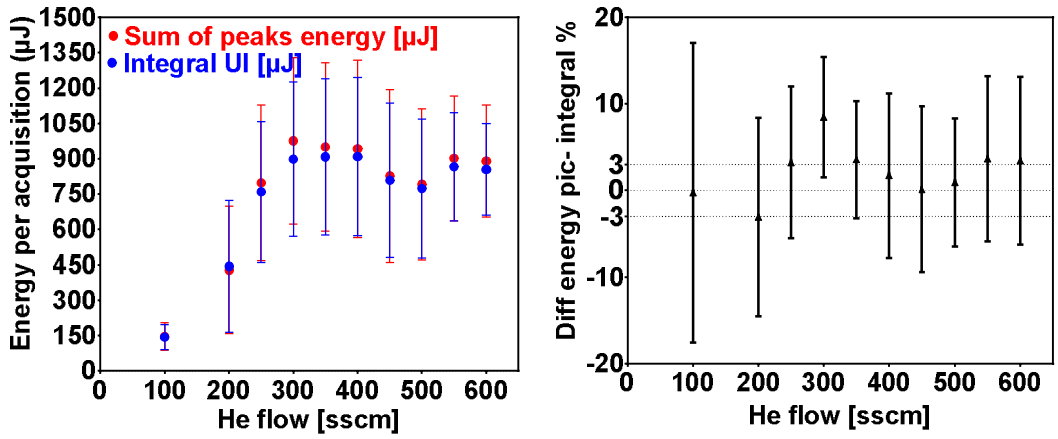

Fig 239 Left: energy consumed per acquisition (average on 200 acquisitions) as a function of Helium flow. **Red** sum of the energy of each peak detected, **Blue**: energy consumption is calculated over the entire period = $\int_0^T UIdt$. The error bars represents the standard deviation of the measurements. Right: percentage of difference between the sum of the energy counted during one period of the power supply for the two methods = $100 \times (\textbf{Sum of peaks} - \textbf{Integral}) / \textbf{Integral}$. It appears that the results of the two methods are similar and consistent.

The amount of positive charge transferred per period of 2 ms is presented in red in Fig 240 (respectively negative in blue). On average, the amount of positive and negative charge is the same (net charge ~ 0).

[124] since power is proportional to the energy summed over an entire period

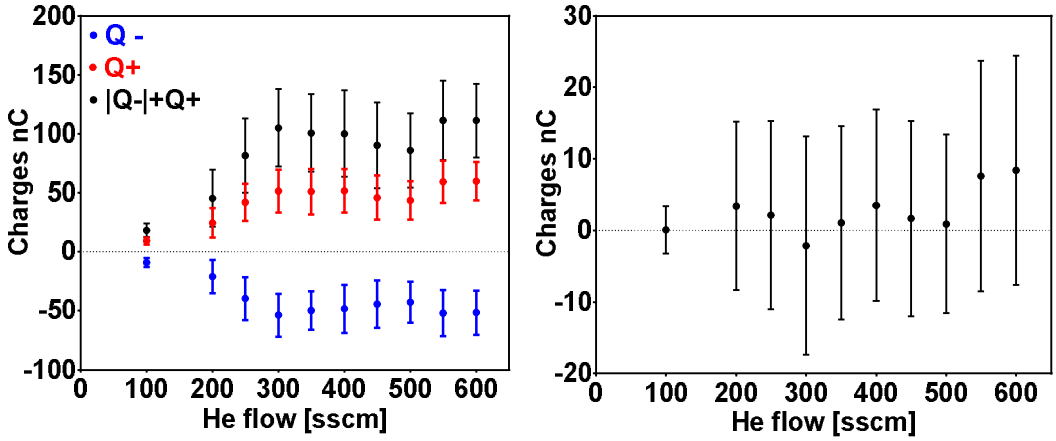

Fig 240 Left: the amount of charge transferred during one acquisition (mean over 200 acquisitions) as a function of helium flow. **Blue** = total amount of negative charge transferred during one acquisition.**Red** = total amount of negative charge transferred during one acquisition. Black = sum of the absolute value of the charge transferred. Right: net number of charge transferred during one period of the power supply. The error bars represent the standard deviation.

The left panel of Fig 241 shows the number of positive and negative discharge which take place on average during one period of 2 ms. There is less negative discharge but each negative discharge transport more charge (except for flow =550 or 600 sscm). So the increase in power should be attributed to an increase in the amount of charge transported per discharge, rather than an increase in the number of discharges.

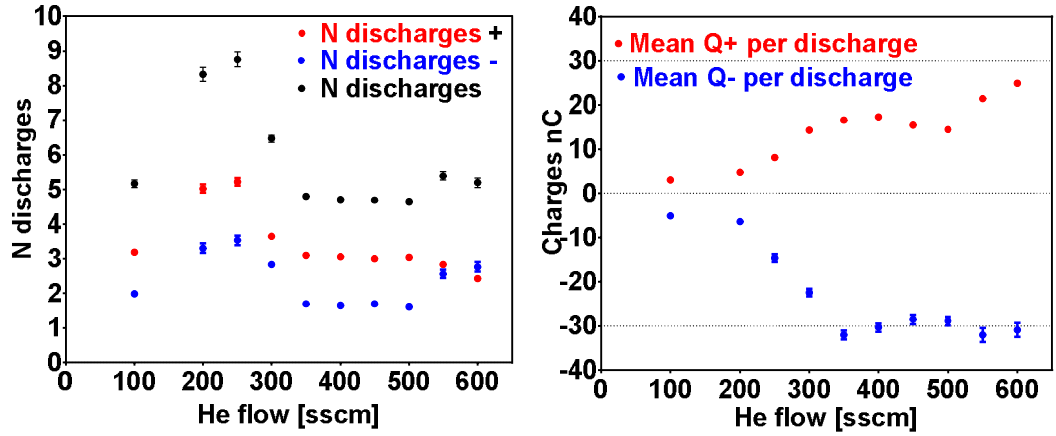

Fig 241 Left: number of discharges per period of the power supply (2 ms) as a function of He flow: **Red** = this discharge transport a positive amount of charges, **Blue** = a negative amount, **Black**: all the discharges. Right, **red** = mean value of the charge per positive discharge, **Blue** = mean value of transferred charge per negative discharge. Average on 200 acquisitions. Error bars represent the standard deviation of the mean.

A-3-1) Adjustable parameter: height above liquid

This section regards the results acquired with variables height above liquid, the other parameters being constant. The acquisition parameters have been previously described. The single-channel plasma jet operates according to the parameters:

- helium flow = 400 sscm

- height = 2-11 mm
- peak to peak Voltage = 26.6 kV.

The power consumption is shown in the right panel of Fig 237. Automatic waveform processing enables to obtain the distribution of the discharges in terms of transferred charge (abscissa) and initiation voltage of the discharge (ordinate). Each point represents one discharge, the discharges of 200 periods of the power supply were added for each height (Fig 242).

- The asymmetry between positive and negative charges appears for all the height. Negative discharges carry more charges per event.
- At small height (2 and 3 mm), the majority of the negative discharge carry ~ -65 nC and start at any negative voltage. Between 4 and 6 mm the distribution of the negative discharges seems to form two families: one at -65 nC and the others in the interval [–20 nC, 0 nC].
- at a great height (10 or 11 mm), the distribution looks like that observed at low helium flow. Perhaps that the composition of the gas phase play a significant role in the pattern of the discharge. On the other hand, perhaps is it possible to adjust the parameter of the device above the patient, in order to reproduce a pattern of reference and then obtain similar chemistry?

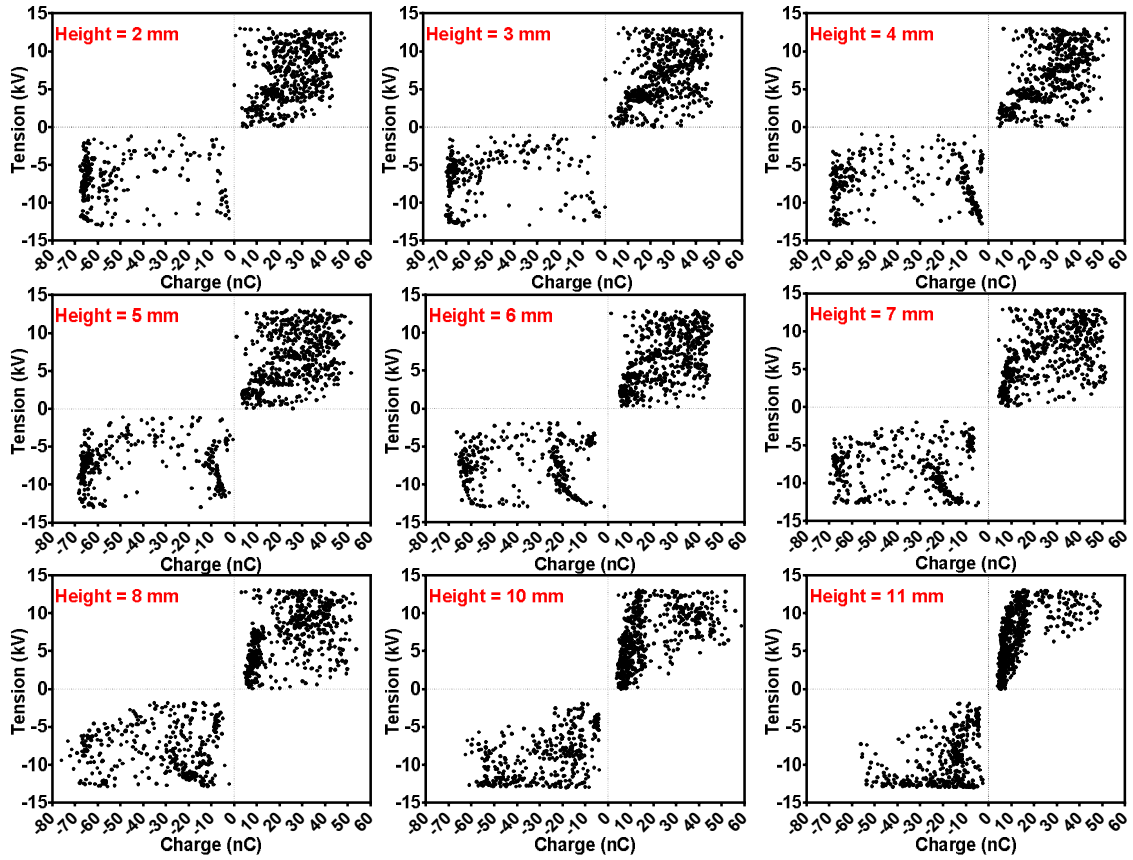

Fig 242 Each point represents "one" discharge. The abscissa is the amount of charges transported during "this" discharge. The ordinate represents the voltage of the power supply at the time of the discharge. Single-channel plasma jet, height = 2-11 mm, peak to peak Voltage= 26.6 kV, helium flow = 400 sscm. Waveform = sinusoidal, frequency = 500 Hz. Target = 500 µL of deionized water in 24-wells plate. Each figure contains the concatenation of the data of 200 acquisitions. Each acquisition has a duration of 2 ms = one period of the power supply.

Once again, it would be interesting to compare these results with the simulations of the positive and negative streamer. Fig 243 shows a comparison of the two methods to calculate the power. Both methods give very similar results; since the mean value differs by less than 3 % for all height.

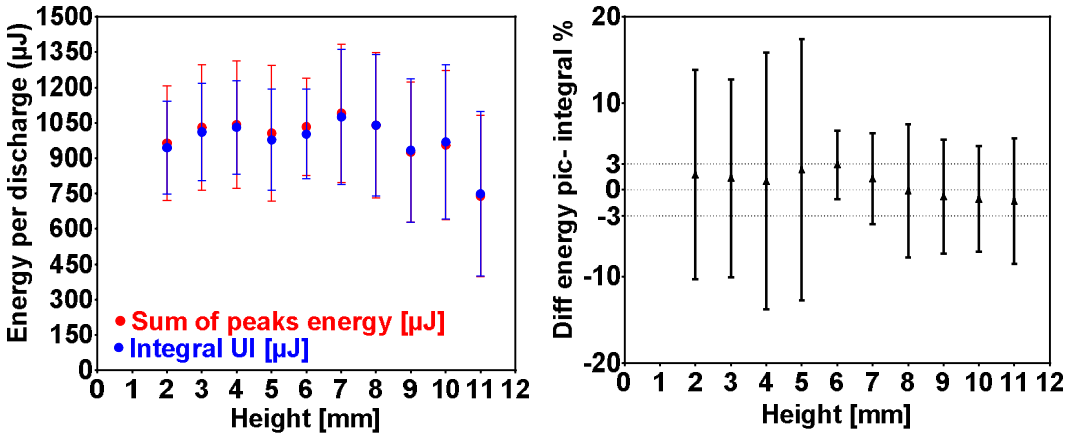

Fig 243 Left: energy consumed per acquisition (average on 200 acquisitions) as a function of height. **Red** sum of the energy of each peak detected, **Blue**: energy consumption is calculated over the entire period = $\int_0^T UIdt$. The error bars represents the standard deviation of the measurements. Right: percentage of difference between the sum of the energy counted during one period of the power supply for the two methods = $100 \times (\mathbf{Sum\ of\ peaks} - \mathbf{Integral})/\mathbf{Integral}$. It appears that the results of the two methods are similar and consistent.

The amount of positive charge transferred per period of 2 ms is presented in red in Fig 244 (respectively negative in blue). On average, the amount of positive and negative charge is the same (net charge ~ 0).

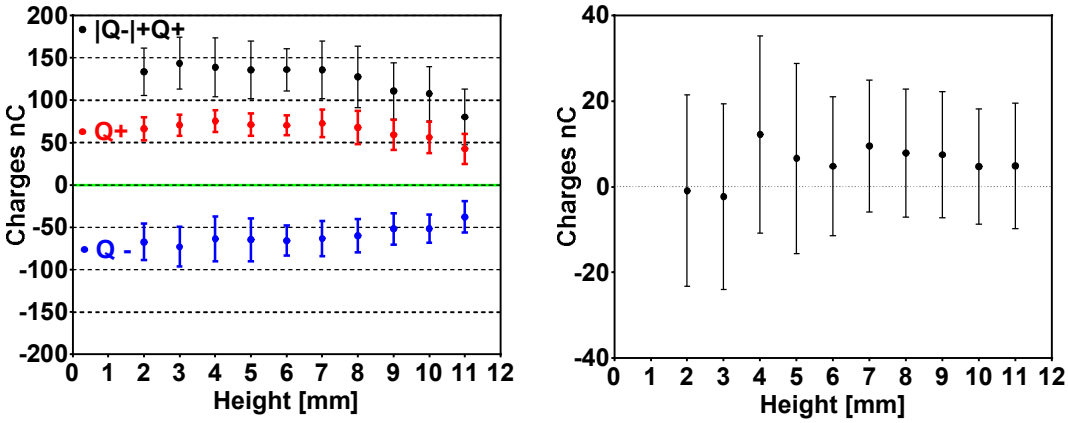

Fig 244 Left: amount of charge transferred during one acquisition (mean over 200 acquisitions) as a function of the height. **Blue** = total amount of negative charge transferred during one acquisition.**Red** = total amount of negative charge transferred during one acquisition. Black = sum of the absolute value of the charge transferred. Right: net number of charge transferred during one period of the power supply. The error bars represent the standard deviation.

The left panel of Fig 245 shows the number of positive and negative discharge which take place on average during one period of 2 ms. There is less negative discharge but each negative discharge transport more charge. The small decrease in power for large height should be attributed to a decrease in the number of charges transported per

discharge, rather than a decrease in the number of discharges (which increase slightly with height).

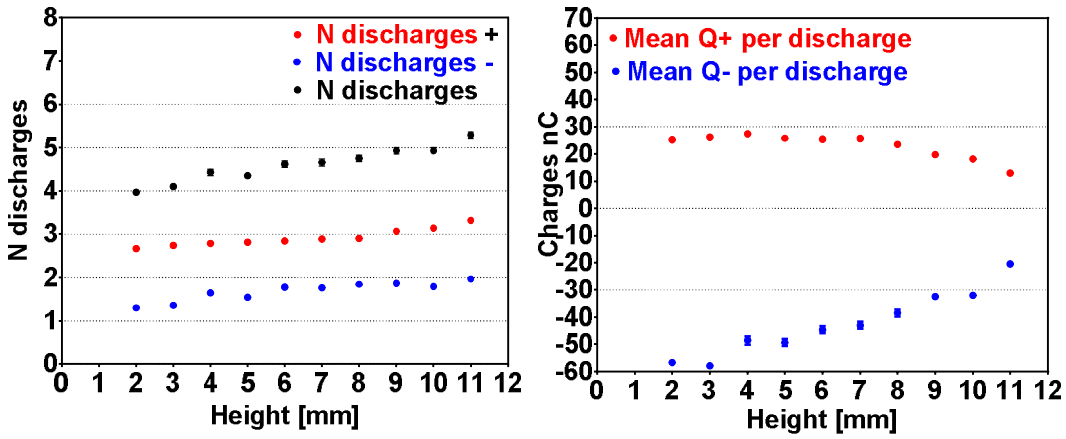

Fig 245 Left: number of discharges per period of the power supply (2 ms) as a function of height: **Red** = this discharge transport a positive amount of charges, **Blue** = a negative amount, **Black**: all the discharges. Right, **Red** = mean value of the charge per positive discharge, **Blue** = mean value of transferred charge per negative discharge. Average on 200 acquisitions. Error bars represent the standard deviation of the mean.

A-4-1) Correlation with RONS production

The production rate of HO° was studied with the reaction which occurs between terephthalic acid (TPA) and hydroxyl radical for several [TPA] during plasma-liquid interaction (Chapter III, section III.5).

The order-of-magnitude presented in section III.5.2 (page 85) propose the value of 16 pmol per second for the production rate of hydroxyl radical when there is only one discharge per half period. According to the previous section, the number of discharge per half period is ~2.5 discharge which would lead to predicting a production rate of 40 pmol/s.

This value is five times below those observed with the single jet studied in Chapter III (~200 pmol/s at 27 kV). However, the comparison is not valid since the power supply are not the same (“square with resonance” for HO° study versus sinusoidal for the statistical study of the discharges). It would be necessary to do additional experiments to go further.

However, since the number of discharge slightly increase with height at (almost) constant power and since the mean amount of charge in one discharge decrease with height like the HO° production rate. Since this correlation is also observed regarding He flown it could be assumed that HO° production depends more on the amount of charges transferred by each discharge. It would be interesting to test this hypothesis.

A-5-1) Matlab program for automatic discharge detection

```
clear all
tic

%ce code permet de faire des statistiques sur le nombre de décharge se
%produisant dans une periode, et sur la quantité de charge véhiculée par
%ses dernières. La configuration experimentale choisie est du type "mesure
```

```
%de lissajous" avec une capacité de mesure CM placé en série avec la cible
%du plasma

kdeb=0; %indice premier et dernier fichier
kfin=200; %201
Cm=104*1e-9; %valeur de la capacité de mesure
corrsonde=1; %1 pour corriger l'effet de la sonde de tension /10 avec les deux paramètres suivants
capacorr=11.5*1e-12; %capacité ajouté par la sonde en // de la capacité de mesure Cm
Rsonde=10*1e6; % résistance existant en parallèle de la capacité de mesure Cm

affichage=1;  % 1 pour afficher et enregistrer les courbes
%%%les paramètres sont à definir avant cette ligne
tcell{1,1}='numero de fichier';
tcell{1,2}= 'le nombre de pics de courants';
tcell{1,3}= 'Energie totale transferée';
tcell{1,4}= 'somme des energie des pics';
tcell{1,5}= 'Numéro du pic de courant';
tcell{1,6}= 'Charge transférée nC';
tcell{1,7}= 'Energie du pic uJ';
tcell{1,8}= 'Tension de départ de la décharge V';
tcell{1,9}= 'Rapport Q/U*1E12';
tcell{1,10}= 'Temps ms';

tcell{1,12}= 'Charge nC';
tcell{1,13}= 'Energie uJ';
tcell{1,14}= 'Tension V';
tcell{1,15}= 'Temps ms';
position=2;

dim1=1;
ratiok=0;

            for k=kdeb:1:kfin

    %SEL1
    sel1(k-kdeb+1,1)=k;
    sel1(k-kdeb+1,3)=0; %initialisation de la valeur

    if k<1000
    basenum=strcat('00',num2str(k));
    end
    if k<100
    basenum=strcat('000',num2str(k));
    end
    if k<10
    basenum=strcat('0000',num2str(k));
    end


     %Chargement des données de la voie "ALIMHT" en memoire
 C1 = load(strcat('C1Title',basenum,'.dat'));
 %origine des temps mise à 0
C1(:,1)=C1(:,1)-C1(1,1);
 temps=C1(:,1);
 C1=C1(:,2);
 FS=1.0/(temps(10001)-temps(1))*1e4; %fréquence d'échantillonge du signal


      %Chargement des données de la voie "CAPACITE CM" en memoire
 C2 = load(strcat('C2Title',basenum,'.dat'));
 C2=C2(:,2);
 %I est le courant tel qu'il est mesuré aux bornes de Cm <> courantde
 %décharge car bande passante plus faible du fait de la capa
 if corrsonde==0
     I=diff(C2)*Cm*FS;
 else
     I=diff(C2).*(Cm+capacorr).*FS+C2(1:end-1)./Rsonde;
 end


  %Effectue une moyenne glissante sur (2*lissage_temporel - 1) points

  if affichage==1
  figure(33)
```

```
 subplot(2,1,1)
 title('charges vehiculées')
 plot(temps,C2*Cm*1e9,'r-');
 xlabel ('Temps (s)', 'FontSize', 16)
ylabel ('Charge (nC)', 'FontSize', 16)
xlim([temps(1),temps(end)])
ylim([min(C2*Cm*1e9) max(C2*Cm*1e9)])

subplot(2,1,2)
 title('courant')
  end

 Nzero=1001;        %taille fit
C2lisse=abs(sgolayfilt(I,5,  Nzero));
lissage_temporel=300.0;    %Lissage temporelle detection
C2l1 = filter(ones(1,lissage_temporel)/lissage_temporel,1, C2lisse);
C2l2 = filter(ones(1,lissage_temporel)/lissage_temporel,1, C2lisse(end:-1:1,:));
C2l2=C2l2(end:-1:1,:);
C2lisse=(lissage_temporel*(C2l1+C2l2)- C2lisse)/(2*lissage_temporel-1);

C2lisse=detrend(C2lisse);
C2lisse(1:Nzero)=0;
C2lisse(end-Nzero:end)=0;

%[pks,locs,w,p]=findpeaks(C2lisse,FS,'MinPeakDistance',3e-
5,'Annotate','extents','SortStr','descend','WidthReference','halfheight','MinPeakWidth',10*1e-6);
[pks,locs,w,p]=findpeaks(C2lisse,FS,'MinPeakHeight', 2e-5,'MinPeakDistance',7e-
5,'Annotate','extents','SortStr','descend','WidthReference','halfheight','MinPeakWidth', 6e-7);

if affichage==1
findpeaks(C2lisse,FS,'MinPeakHeight', 2e-5,'MinPeakDistance',7e-
5,'Annotate','extents','SortStr','descend','WidthReference','halfheight','MinPeakWidth', 6e-7);
end

%ENREG
  dim1=dim1+1;
tcell{dim1,1}=k;
tcell{dim1,2}=size(locs,1);


%Calcul de l'integrale u*I lissage de l'integrale du courant
lissage_temporel2=10.0;
C2l1 = filter(ones(1,lissage_temporel2)/lissage_temporel2,1,I);
C2l2 = filter(ones(1,lissage_temporel2)/lissage_temporel2,1,I(end:-1:1,:));
C2l2=C2l2(end:-1:1,:);
C2lisser=(lissage_temporel2*(C2l1+C2l2)-I)/(2*lissage_temporel2-1);

integrenergy=trapz(C2lisser.*C1(1:end-1))*1e6/FS;
tcell{dim1,3}=integrenergy; %dissipé dans le dispositif plasma + pertes dielectriques en µJ
deb=dim1;


tableaustringC2=cell(size(locs,1),1);
sumenergy=0;
fauxpic=0;


clear charge tension indicechargeavant indicechargeapres signepicC tableaustringC2 vraipic positif
negatif
for tmpk=1:1:size(locs,1)
    %determination du signe du courant repéré
    indicepourlesignedeC2=find(temps<=locs(tmpk)+1e-8 & locs(tmpk)-1e-8<=temps);
    % moyenne autour de la localisation entre -10 et + 10 ns
    signepicC2(tmpk)=sign(mean(C1(indicepourlesignedeC2)));
    pks(tmpk)=signepicC2(tmpk)*pks(tmpk);
    %tension de départ de la décharge
    indicedepart=find(temps<=locs(tmpk) & locs(tmpk)-2e-6<=temps);
    tension(tmpk)=mean(C1(indicedepart));

    %determination de la charge transferée
     indicechargeavant=find(temps<=locs(tmpk)-2e-5 & locs(tmpk)-3e-5<=temps);
     indicechargeapres=find(temps<=locs(tmpk)+3e-5 & locs(tmpk)+2e-5<=temps);
```

```
     if size(indicechargeapres,1)==0
         indicechargeapres=size(C2,1);
     end

     if size(indicechargeavant,1)==0
         indicechargeavant=1;
     end


charge(tmpk)=(mean(Cm*C2(indicechargeapres))-mean(Cm*C2(indicechargeavant)))*1e9; %en nC
tableaustringC2(tmpk)=cellstr([num2str(tmpk) ' charge' num2str(charge(tmpk)) ]);

  %ENREGISTREMENT POUR CHAQUE DECHARGE DE CHAQUE ACQUISITION
  dim1=dim1+1;

tcell{dim1,5}= tmpk;
tcell{dim1,6}= charge(tmpk); %charge arrivant dans Cm
tcell{dim1,7}= charge(tmpk)*tension(tmpk)*1e-9*1e6; %en µJ
tcell{dim1,8}= tension(tmpk)/1000;
tcell{dim1,9}= charge(tmpk)/tension(tmpk)*1e12*1e-9; % en pF
tcell{dim1,10}= mean(temps(indicechargeapres))*1e3; % en ms
if charge(tmpk)*tension(tmpk)*1e-9*1e6<0
fauxpic=fauxpic+1;
vraipic(tmpk)=0;
   positif(tmpk)=0;
    negatif(tmpk)=0;
else
sumenergy=sumenergy+charge(tmpk)*tension(tmpk)*1e-9*1e6;
tcell{position,12}= charge(tmpk);
tcell{position,13}= charge(tmpk)*tension(tmpk)*1e-9*1e6;
tcell{position,14}= tension(tmpk)/1000;
tcell{position,15}=  mean(temps(indicechargeapres))*1e3;
position=position+1;
vraipic(tmpk)=1;
if charge(tmpk)>0
   positif(tmpk)=1;
    negatif(tmpk)=0;
else
    negatif(tmpk)=1;
    positif(tmpk)=0;
end


end

end

if size(locs,1)>0
tcell{deb,4}=sumenergy; %'somme des energie des pics';   sum(charge.*tension*1e-9*1e6)
tcell{deb,2}=size(locs,1)-fauxpic;
if integrenergy~=0
   ratio=(sumenergy-integrenergy)/integrenergy;
else
    ratio=0;
end
tcell{deb+1,4}=ratio;
ratiok=ratiok+1;
ratiotablr(ratiok)=ratio;
Ndischarge(ratiok)=size(locs,1)-fauxpic;
tablecharge(ratiok,1)=sum(abs(charge.*vraipic));  %charges absolue transferées dans l'acquisition
tablecharge(ratiok,2)=sum(charge.*vraipic);%Charge moyenne transférée dans l'acquision
tablecharge(ratiok,3)=mean(abs(charge.*vraipic));  %charges absolue transferées en moyenne par
décharges
tablecharge(ratiok,4)=sum(charge.*positif);%somme charges positives
tablecharge(ratiok,5)=sum(charge.*negatif);%somme charges negatives
tablecharge(ratiok,6)=sum(positif);%nombres decharges positives
tablecharge(ratiok,7)=sum(negatif);%nombres decharges negatives
if tablecharge(ratiok,6)>0
tablecharge(ratiok,8)=tablecharge(ratiok,4)/tablecharge(ratiok,6);%moyenne charge decharges
positives
end

if tablecharge(ratiok,7)>0
```

```
tablecharge(ratiok,9)=tablecharge(ratiok,5)/tablecharge(ratiok,7);%moyenne charfe decharges
negatives
end

end

tableaustringC2=cellstr(tableaustringC2);

if affichage==1
text(locs,abs(pks),tableaustringC2);
end


  tcell{1,20}= 'n° fichier';
  tcell{1+k-kdeb+1,20}=k;
  tcell{1,21}= 'Integral energy µJ';
  tcell{1+k-kdeb+1,21}=integrenergy;
  tcell{1,22}= 'Sum pic µJ';
  tcell{1+k-kdeb+1,22}=sumenergy;
  tcell{1,23}= '% diff';
  tcell{1+k-kdeb+1,23}=ratio*100;
tablecharge(ratiok,10)=integrenergy; % integrale energy de U I
tablecharge(ratiok,11)=sumenergy;    %Somme des pics d'énergie


  tcell{1,24}= 'N discharges';
  tcell{1+k-kdeb+1,24}=size(locs,1)-fauxpic;
  tcell{1,25}= 'Decharges +';
  tcell{1+k-kdeb+1,25}=tablecharge(ratiok,6);
  tcell{1,26}= 'Decharges -';
  tcell{1+k-kdeb+1,26}=tablecharge(ratiok,7);


  tcell{1,27}= 'Somme totale des charges';
  tcell{1+k-kdeb+1,27}=tablecharge(ratiok,2);
  tcell{1,28}= 'Somme valeur absolue des charges';
  tcell{1+k-kdeb+1,28}=tablecharge(ratiok,1);
  tcell{1,29}= 'Somme charges +';
  tcell{1+k-kdeb+1,29}=tablecharge(ratiok,4);
  tcell{1,30}= 'Somme charges -';
  tcell{1+k-kdeb+1,30}=tablecharge(ratiok,5);


    tcell{1,31}= 'Moyenne decharges +';
  tcell{1+k-kdeb+1,31}=tablecharge(ratiok,8);
  tcell{1,32}= 'Moyenne decharges -';
  tcell{1+k-kdeb+1,32}=tablecharge(ratiok,9);

  if affichage==1
saveas(gcf, ['fichier_', num2str(k),'_Reperagepics'],'png')
  end
    k
    ratio*100
  end


  tcell{1,17}= '%diff sumpic and integral';
  tcell{2,17}=mean(ratiotablr)*100;
  tcell{1,18}= '%std';
  tcell{2,18}=std(ratiotablr)*100;
  tcell{1,19}= '%sem';
  tcell{2,19}=std(ratiotablr)*100/sqrt(size(tablecharge,1));



  tcell{3,17}= 'mean Ndischarge';
  tcell{4,17}=mean(Ndischarge);
  tcell{3,18}= '%std';
  tcell{4,18}=std(Ndischarge);
  tcell{3,19}= '%sem';
  tcell{4,19}=std(Ndischarge)/sqrt(size(tablecharge,1));


   tcell{6,17}= 'mean';
```

```
tcell{6,18}= 'Std';

tcell{7,16}= 'Integral energy';
tcell{8,16}= 'Sum pic';
tcell{9,16}= 'Decharges +';
tcell{10,16}= 'Decharges -';
tcell{11,16}= 'Somme totale des charges';
tcell{12,16}= 'Somme valeur absolue des charges';
tcell{13,16}= 'Somme charges +';
tcell{14,16}= 'Somme charges -';
tcell{15,16}= 'Moyenne charges +';
tcell{16,16}= 'Moyenne charges-';


tcell{7,17}=mean(tablecharge(:,10));
tcell{8,17}= mean(tablecharge(:,11));
tcell{9,17}= mean(tablecharge(:,6));
tcell{10,17}= mean(tablecharge(:,7));
tcell{11,17}= mean(tablecharge(:,2));
tcell{12,17}= mean(tablecharge(:,1));
tcell{13,17}= mean(tablecharge(:,4));
tcell{14,17}= mean(tablecharge(:,5));
tcell{15,17}= mean(tablecharge(:,8));
tcell{16,17}= mean(tablecharge(:,9));


tcell{7,18}= std(tablecharge(:,10));
tcell{8,18}= std(tablecharge(:,11));
tcell{9,18}= std(tablecharge(:,6));
tcell{10,18}= std(tablecharge(:,7));
tcell{11,18}= std(tablecharge(:,2));
tcell{12,18}= std(tablecharge(:,1));
tcell{13,18}= std(tablecharge(:,4));
tcell{14,18}= std(tablecharge(:,5));
tcell{15,18}= std(tablecharge(:,8));
tcell{16,18}= std(tablecharge(:,9));


%SEM
tcell{7,19}= std(tablecharge(:,10))/sqrt(size(tablecharge,1));
tcell{8,19}= std(tablecharge(:,11))/sqrt(size(tablecharge,1));
tcell{9,19}= std(tablecharge(:,6))/sqrt(size(tablecharge,1));
tcell{10,19}= std(tablecharge(:,7))/sqrt(size(tablecharge,1));
tcell{11,19}= std(tablecharge(:,2))/sqrt(size(tablecharge,1));
tcell{12,19}= std(tablecharge(:,1))/sqrt(size(tablecharge,1));
tcell{13,19}= std(tablecharge(:,4))/sqrt(size(tablecharge,1));
tcell{14,19}= std(tablecharge(:,5))/sqrt(size(tablecharge,1));
tcell{15,19}= std(tablecharge(:,8))/sqrt(size(tablecharge,1));
tcell{16,19}= std(tablecharge(:,9))/sqrt(size(tablecharge,1));


xlswrite('Resultat.xls',tcell);
         toc
```

A-2) Dielectric losses

First, we give orders of magnitude that are relevant for the material which is used. Second, we give a model for dielectric losses in the framework of Dielectric Barrier Discharge. We explain, why we need to take into account dielectric losses, on the contrary of Kogelschatz et al. [333]. We are led to distinguish two sources of loss: one due to low-frequency currents (polarization of the dielectric due to the power supply) and one at high frequency due to short pulse discharges. Calculation of loss at low frequencies is made with Fourier series decomposition of the high voltage signal.

The short pulse current is modeled by a triangular pulse in a first approach. A parametric study enables to find the value of the losses according to the parameter of the models (pulse duration, capacitance, the angle of loss).

A-1-2) Order of magnitude

In the presence of an electric field, the dipoles constituting the dielectric orient themselves in the direction of the field. The material polarizes and surface charges (bonds) appear. Thus a plate of a material (Linear, homogeneous, isotropic) of relative permeability ε_r of surface S and of thickness e behaves like a capacitor of capacitance $C = \varepsilon_0 \varepsilon_r S/e$ when edge effects are negligible (see [88] for the calculation of edge effects).

The dielectric strength of a material is the maximum difference of potential that can be applied of a given thickness without electrical breakdown. It is expressed in kV/mm. [334] give typical value: 20 kV/mm for soda-calcium glass, 24 kV/mm for polyamide-imide and more than 100 kV/mm for mica. Dielectric strength decrease with the temperature, heating can lead to thermal breakdown.

The transverse resistivity of insulators is typically between 10^{11} Ω.cm and 10^{18} Ω.cm. For example: 10^{12} Ω.cm for soda-lime glass, 10^{17} Ω.cm for polyamides-imides. For comparison: copper resistivity is 17 10^{-9} Ω.cm, gold 22 10^{-9} Ω.cm. The current is only defined by the value of the transverse resistance for a constant potential difference.

In a dielectric exposed to a variable electric field, the material undergoes additional heating. This electric heating is at the basis of the operation of microwave ovens. Heating losses can be modeled by adding an Equivalent Serie Resistance ($\mathbf{R_S}$) in series with the equivalent capacitance of the dielectric. The general expression giving the power absorbed by the dielectric is expressed:

$$P = 2\pi f \varepsilon_0 \varepsilon'_r \tan(\delta) E^2 V = R_S {I_{RMS}}^2$$

with

- E: uniform electric field of frequency f applied to the material.
- I_{RMS}: RMS intensity.
- V: volume of dielectric material.
- ε'_R: real part of the relative permeability of the material
- $\tan(\delta)$: tangent of the angle of loss (angle measuring the deviation from the phase shift of π/2 between the current and the voltage across a capacitor). We have: $tan\delta = \varepsilon'_R/\varepsilon''_r$ with ε''_r : the imaginary part of the relative permeability

$\tan\delta$ is connected to the capacitance of the electrical plate by $\tan(\delta) = R_s C\omega$. Therefore $R_s(\nu) = \frac{\tan(\delta)}{2\pi\nu C}$

Orders of magnitude of $\tan(\delta)$ from [334] are shown in Table 25. The loss angle may increase with the frequency (look at polyacetal row in the table).

Material	tan(δ)
soda-lime glass	$1.5\ 10^{-2} \rightarrow 6\ 10^{-2}$ at 50 Hz
Borosilicate glass (for example pyrex)	$3.5\ 10^{-3}$ at 50 Hz
Ceramic alumina	10^{-3} at 50 Hz
Polyethylene	$2\ 10^{-4}$ at 50 Hz
polyamide-imide	$3\ 10^{-2}$ at 50 Hz
Polyacetal	10^{-3} at 50 Hz and $6\ 10^{-3}$ at 1 MHz

Table 25 Orders of magnitude of $\tan(\delta)$ for different material from [334].

A-2-2) Model of dielectric losses in the framework of DBD

Polarization(s) of a material

A material polarizes when displacements of charge carriers relative to each other under the effect of an external electric field make it possible to form dipoles or redirect pre-existing dipole. There are therefore several types of polarization, depending on the type of charge carrier involved.

Electronic polarization is due to a relative displacement of the nucleus of the atom with respect to the set of electrons that surround it. All atoms exhibit, this type of polarization which is established in a very short time, and remains sensitive to frequencies exceeding those of visible light. This is why electronic polarization is often referred to as optical polarization.

Ionic polarization is found in ionic crystals (for example NaCl). It results from the displacement in opposite directions of positives and negatives ions. This polarization is established more slowly than the previous one; it manifests itself to frequencies between the microwaves and the infrared.

Orientation polarization. Most often, a molecule formed of different atoms possesses a spontaneous dipole moment that is independent of the existence of an external field. In the absence of such a field, these moments are oriented in a random manner, so that there are no observable macroscopic polarization. Under the effect of a field, on the other hand, moments tend to line up. This result in a polarization called orientation polarization, occurring up to frequencies between 1 kHz and 1 MHz. In addition to this orientation phenomenon, the field can vary the moment of the molecule, by deformation of its orbitals.

Interfacial polarization.

Charges carriers, which are never totally absent in a dielectric, migrate under the effect of the field and tend to concentrate around defects such as impurities, gaps, grain boundary, etc. The polarization resulting from the local accumulations of loads due to all the migration phenomena is grouped under the name of interfacial polarization. This polarization is characterized by the longest settling time of all: it can reach several minutes and even more.

Polarisability and Debye equation

Let us consider a dipole of moment $\vec{p}$ in an externe electric field $\vec{E}$. Potentiel energy of this dipole is:

$$E_{pot} = -\vec{p}.\vec{E}$$

The potential energy is minimal if the dipole is aligned with $\vec{E}$. A set of identical electrical dipoles of polarization p are distributed in energy according to a Boltzmann distribution:

$n(E_{pot}) = n_0 exp\ (-\frac{E_{pot}}{k_B T})$,

with $n(E_{pot})dE_{pot}$ the volumic density of dipole with an energy in the interval $[E_{pot}, E_{pot} + dE_{pot}]$. n_0 is a normalization factor, which is determined by the integral of the Boltzmann function over the energies space. This integral must be equal to the density of dipoles.

$$n_{dipole} = \int_{-pE}^{pE} n_0 exp\ (-\frac{E_{pot}}{k_B T})\, dE_{pot} = "density\ of\ dipole"$$

We defined z-axis along the electric field. Therefore a dipole which makes an angle θ with z axis has energy:

$$E_{pot}(\theta) = -pEcos(\theta)$$

The average polarization P is calculated by integrating the projections of the dipoles on the z-axis.

$$P = \int_{-pE}^{pE} p\ cos\left(\theta(E_{pot})\right) n(E_{pot})\, dE_{pot}$$

Moreover $dE_{pot} = pEsin(\theta)d\theta$ and by changing the variable

$$P = \int_0^{\pi} pcos(\theta) n_0 \exp\ (\frac{pEcos(\theta)}{k_B T}) sin(\theta) d\theta$$

By performing the same operation with the normalization factor:

$$P = n_{dipole} p\ \frac{\int_0^{\pi} cos(\theta) exp\ (\frac{pEcos(\theta)}{k_B T}) sin(\theta) d\theta}{\int_0^{\pi} exp\ (\frac{pEcos(\theta)}{k_B T}) sin(\theta) d\theta} = n_{dipole} p \frac{\int_{-1}^{1} x exp\ (\frac{pEx}{k_B T}) dx}{\int_{-1}^{1} exp\ (\frac{pEx}{k_B T}) dx}$$

$$= n_{dipole} p\ L(\frac{pE}{k_B T})$$

With L the function of Langevin such as $L(x) = \coth(x) - \frac{1}{x} = \frac{x}{3} + O_0(x^3)$ for small value of x.

order of magnitude of $\frac{pE}{k_B T}$:

- Permanent moment p of water is around $6.3\ 10^{-30}\ C.m.$
- E is around $20\ kV.mm^{-1} = 2\ 10^7\ V.m^{-1}$

$k_B T = 0.025\ eV$ for T =20 °C and $k_B T = 6.7\ meV$ for T=77.4 K (temperature of liquid nitrogen). Therefore at 20°C : $\frac{pE}{k_B T} = 0.031$, at T=77.4 K $\frac{pE}{k_B T} = 0.12$.

Consequently, the linear approximation of Langevin function is true, even in our “worst” experimental conditions: dielectric in liquid nitrogen and strong field. Finally, we have:

$$P = n_{dipole}\frac{p^2E}{3k_BT} = n_{dipole}\epsilon_0\alpha_{or}E$$

α_{or} is called orientation polarizability. The previous calculation is valid in static mode. Now we will see how to get the results in sinusoidal regime.

Two factors influence the orientation of permanent dipoles:

- The thermal agitation, which can be assimilated to the action of shocks inflicted on the dipoles.
- The local field $\vec{E}$

These shocks enable to reorient a part of the dipoles at any time t_1. These dipoles are distributed according to the statistical distribution of Boltzmann which depends on the orientation of the electric field $\vec{E}(t_1)$. The effect of shocks is predominant[125] with respect to that of the local field which tends to align the dipoles parallel to each other (except in ferroelectric materials). We can assume, as a first approximation, that the orientation of a dipole does not vary in the absence of shocks. On the other hand, since the dipoles are not coupled to each other, it is reasonable to assume that, immediately after a shock, the energy of a dipole is distributed according to the corresponding Boltzmann distribution defined by the value of the local field at the time of the shock.

We need to evaluate the number of dipoles $dn(\theta)$ that have undergone **a last shock** at time $\theta = t - t_1$ (see Fig 246).The average frequency of the shocks $1/\tau$ does not depend on $\vec{E}$ and therefore on time. There is no correlation between energy before impact and after shock. The shock can be considered instantaneous. $dn(\theta)$ depends only on the time interval θ. The number of dipoles $dn(\theta)$ undergoing their last shock between θ and θ + dθ is proportional to the frequency of the shocks and proportional to the number of dipole $n(\theta)$ that have not yet undergone a shock. Their number decreases with θ.

$$dn(\theta) = -n(\theta)\,1/\tau\,d\theta$$

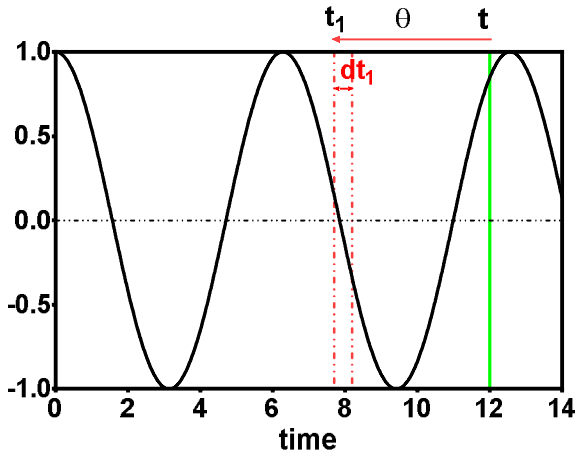

Fig 246 Polarization at time t is the sum of the polarization of each dipole. Among these dipoles, some experienced their last shock between t1 and t1 + dt1. This shock caused them to adopt a distribution of energy and therefore of orientation corresponding to the value of the electric field at time t1.

[125] Since $\frac{pE}{k_BT} \ll 1$

By integration, with the condition $n(\theta = 0) = n_{dipole}$, we obtain $n(\theta) = n_{dipole}\exp\left(-\frac{\theta}{\tau}\right)$

In sinusoidal regime, the electric field has this expression $E = E_a Re(e^{j\omega t})$.
thus, $dP = \frac{p^2 E_a}{3k_B T}\exp(j\omega t_1)dn(t_1) = \frac{-p^2 E_a}{3k_B T}\exp(j\omega(t-\theta))dn(\theta)$
whence the complex expression of P:

$$P = \int_0^{+\infty} \frac{-p^2 E_a}{3k_B T}\exp\big(j\omega(t-\theta)\big)\frac{-n_{dipole}}{\tau}\exp\left(-\frac{\theta}{\tau}\right)d\theta = \frac{p^2 E_a n_{dipole}}{3k_B T\tau}\int_0^{+\infty}\exp\left(j\omega(t-\theta)-\frac{\theta}{\tau}\right)d\theta$$

and $P = \frac{p^2 E_a n_{dipole}}{3k_B T\tau}\frac{-1}{j\omega+\frac{1}{\tau}}\exp(j\omega t)[0-1] = \frac{p^2 E_a n_{dipole}}{3k_B T}\frac{1}{j\omega\tau+1}\exp(j\omega t)$

Thus real expression of P is expressed by Debye equation:

$$P = n_{dipole}\frac{p^2}{3k_B T}Re\left(\frac{E}{1+j\omega t}\exp(j\omega t)\right)$$

Complex permittivity and dielectric losses, definitions

According to Clausius-Mossotti relation: $\frac{\epsilon_r - 1}{\epsilon_r + 2} = \frac{n_{dipole}\,\alpha}{3}$, which enables to infer the value of real and imaginary part of the relative permeability.

A-3-2) Losses in the framework of Dielectric Barrier Discharge

Kogelschatz describes in the paper [333] why it does not take into account dielectric losses : *"The area inside the closed curve is proportional to the energy dissipated in the discharge during one cycle. The dielectric behaves like an ideal capacitance and does not noticeably dissipate power. This can easily be checked: as long as U < Umin the curve collapses to a line on the oscilloscope."*.

In the devices used by Kogelshatz, the generator supplies charges immediately after one microdischarge of few nC. The new charges elicit immediately another micro-discharge of few nC which enable to maintain a constant difference of potential across the gas gap. In our case the situation is very different: instead of "small" micro-discharges of few nC or less which occurs continuously after the supply voltage has reached ignition voltage; we have discharges of several tens of nC which occurs quite randomly. Instead of having a smooth parallelogram, the Lissajous curves of our devices (DBD and plasma-jet) looks like those shown in Fig 247. Consequently, the voltage across the dielectric layers of our device could be higher than the voltage that would be reached if the discharge was ignited continuously as soon as voltage exceeded ignition voltage.

Moreover, by choosing a Voltage slightly below the ignition voltage, we have been able to check that the line turns into an ellipse (weakly open). A metal electrode connected to ground (via the measuring capacitor) was taped at the outside of the DBD and enables the direct observation of dielectric losses.

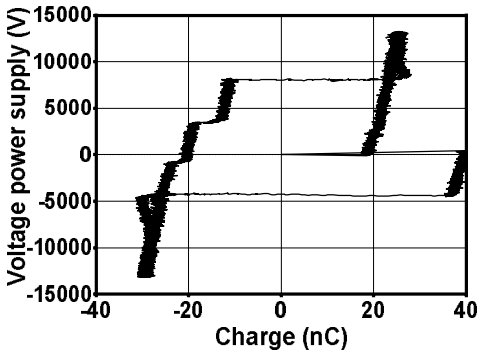

Fig 247 Lissajous curve for He-single jet. Helium Flow= 600 sscm. Height= 9 mm, peak to peak Voltage is 26 kV. waveform is sinusoidal. Power is 447±7 mW. Single jet parameter : di=4 mm, e=1.5 mm. Target is 500 µL of demineralized water in 24 wells costar plate

Regarding the ozoner, the dielectric losses are negligible compared to the mean power of the device. We distinguish two field of dielectric loss: one due to low[126] frequency currents and one at high frequency (~50 MHz-GHz) due to short pulse discharge (~1 ns - 20 ns).

A-4-2) Dielectric losses at low frequency

In the first section, the dielectric losses due to the polarization of dielectric barrier will be quantified. The losses are evaluated in the case of the sinusoid power supply and then if the power supply is not sinusoidal.

We have seen that a small number of discharges are observed per period. Under these conditions, there is no "active plasma phase" during which a multitude of micro-discharges enables to build a constant potential across the gas gap. Calculations of losses from experimental signals are discussed in paragraph A-2-4-b) . They were made by decomposing the current into Fourier series (see Matlab program described in section A-2-4-c).

A-2-4-a) Sinusoidal power supply, order-of-magnitude calculations

We consider a dielectric barrier of capacitance 3 pF, which corresponds to the value of the measured and calculated capacitance value of the DBD actually used above the mice. We assume that $\tan(\delta) = 5\ 10^{-3}$, which correspond to the loss angle of glass. It is assumed that the voltage has following waveform: $V(t) = V_0 \cos(\omega t)$ with frequency $\nu = \frac{\omega}{2\pi} = 500\ \mathrm{Hz}$ and amplitude $V_0 = 15\ \mathrm{kV}$.

Under these conditions, the current has the amplitude:

$$I = C\omega V_0 = 3\ 10^{-12} \times 2\pi \times 500 \times 1.5\ 10^{4} \cong 141\ \mu A$$

Whence, RMS value of current is $I_{RMS} = 100\ \mu A$.

According to the section A-1-2), equivalent series resistance representing dielectric losses is:

$$R_S = \frac{\tan(\delta)}{2\pi\nu C} = \frac{5\ 10^{-3}}{3000\pi \times 10^{-12}} \cong 531\ \mathrm{k\Omega}$$

[126] $\leq 500\ kHz$ essentially due to the polarisations curent elicited by power supply

Therefore, the power of dielectric losses is:

$$P = R_S {I_{RMS}}^2 = 5.31\ 10^5 \times (1.41 \times 10^{-4})^2 \cong 10.5\ mW$$

and energy of losses during one period of the power supply is $\mathrm{E} \cong 21.1\ \mu\mathrm{J}$. Since the mean power consumption of dielectric barrier discharge which was used is around 100 mW, dielectric losses are not always negligible.

A-2-4-b) What if the voltage is not sinusoidal?

The voltage at the terminals of the dielectric can be decomposed into the sum of sines and cosines function. This signal is real and periodic at the frequency $\frac{1}{\mathrm{T}} = 500\ \mathrm{Hz}$: therefore Fourier series has real coefficients. Experimentally we will start from the current flowing through the device. The voltage of power supply is plotted in red in Fig 248. The voltage at the terminal of condensers $\mathrm{Cm} = 104\ \mathrm{nF}$ is shown in blue. The current is deduced from the value of the voltage at the terminals of the capacitor. The bandwidth of this method is limited. This is not an issue since we consider only low-frequency losses (several-fold the frequency of power supply). Fourier series takes the following form:

$$I(t) = A_0 + \sum_{n=1}^{+\infty} A_n \cos(\omega n t) + B_n \sin(\omega n t)$$

with:

$$A_n = \frac{2}{T}\int_0^T I(t)\, cos(\omega n t)\, dt, \qquad B_n = \frac{2}{T}\int_0^T I(t)\, sin(\omega n t)\, dt \text{ for } n \geq 1$$

and $$A_0 = \frac{1}{T}\int_0^T I(t)\, cos(0)\, dt.$$

In this section, we will compute the value of the dielectric losses which occurs in a layer of dielectric material of capacitance 3 pF characterized by the angle of losses $\tan(\delta) = 5 \times 10^{-3}$. The signal used is plotted in Fig 248. It will be assumed that this signal is periodic, the decomposition in Fourier series will lead us to estimate the value of the dielectric losses that can be expected.

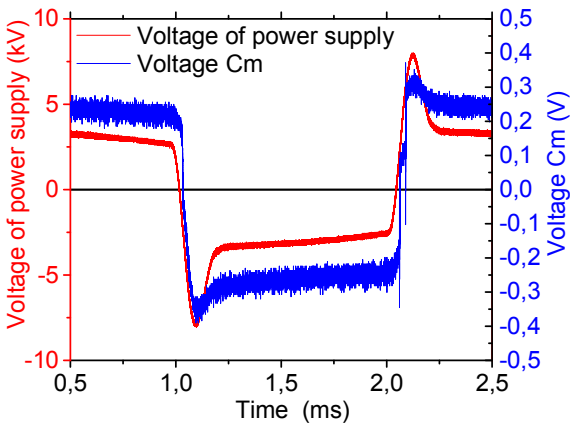

Fig 248 Red, voltage of the power supply during one period of the power supply (2 ms), Blue, voltage at the terminal of measuring capacitor. There are three discharges during this acquisition (sampling frequency = 25 MHz)

Let's look at the signal in more detail. Fig 249 shows that, for each discharge, the amount of charges and the energy consumption can be deduced. It appears that the energy consumption is ~323 µJ over one period of 2 ms. It means that if this signal was periodic, the average power of the device would be ~160 mW.

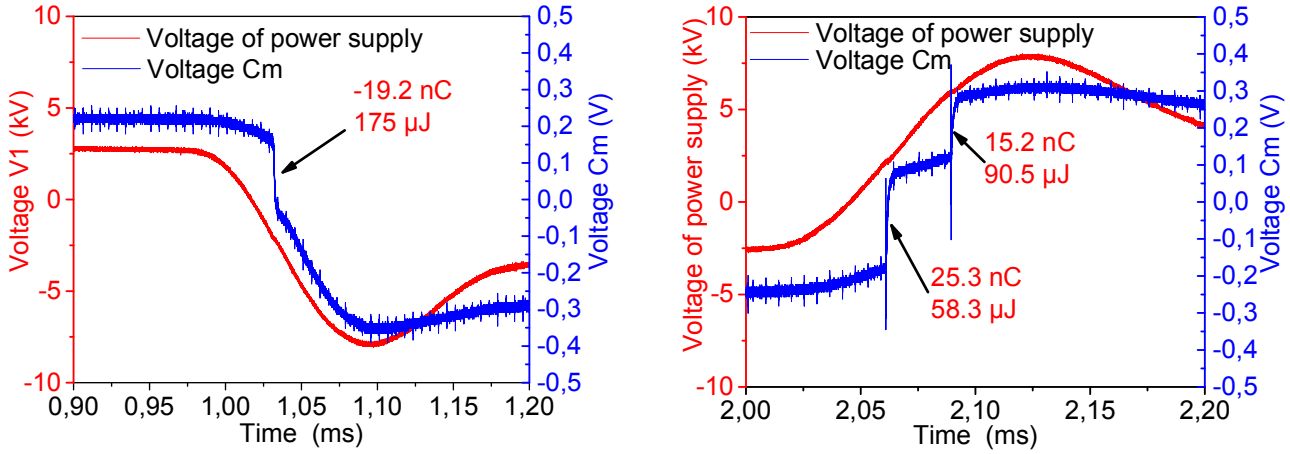

Fig 249 Details of Fig 248. Red: voltage of power supply. Blue: voltage at the terminal of condenser Cm. Left, one discharge during negative phase of the power supply. Right : Two discharges during the positive phase of power supply. The amounts of switched charges, as well as the energy consumed, are shown in red. Total energy consumption is ~ 324 µJ.

The left panel of Fig 250 describes the energy consumption of the whole device over the entire period. This energy[127] ~ 333 µJ is obtained by numerical integration and contain energy consumption due to plasma-discharge and dielectric losses. This value is consistent with those found by the summation of the energy associated with each discharge (~323 µJ) and would correspond to a power of 160 mW. The right panel shows the value computed for the losses over this period as a function of the number of harmonics included in the calculation. The dielectric losses are limited to a value of 27.2 µJ (~ 8 %) which correspond to ~14 mW. Computations were made with the program given in next paragraph.

It would be interesting to be particularly careful when plasma power is “low” (~100 mW in such conditions). Since a significant proportion of the power consumption measured by integral method[128] could be made of dielectric losses.

[127] As explained in section V.1.5 (page 129), the “overshoot” of the integral $E(t) = \int_0^t U(t') \times I(t')dt'$ has no physical meaning. On the contrary, the values obtained after the damping of this transient regime have one meaning. hence the value of 333 µJ

[128] which is strictly equivalent to Lissajous method i.e. the calculation of an inner area...

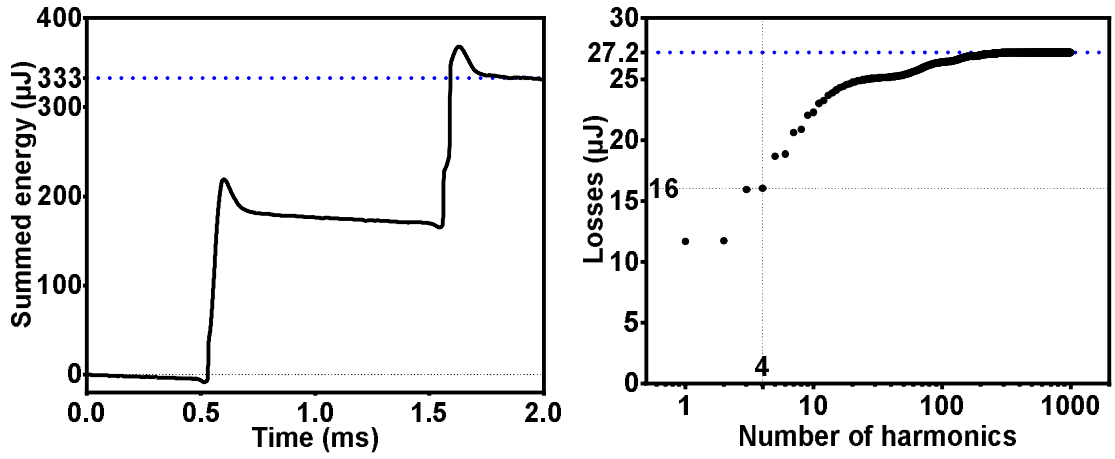

Fig 250 **Left**: energy consumption over one period. This curve is $E(t) = \int_0^t U(t') \times I(t')dt'$ where U is the voltage of the power supply, and I is the current flowing through measuring capacitor (see Chapter II, section II.2 page 34). With this method total energy consumption is ~ 333 µJ, this value is consistent with those found by the summation of the energy associated with each discharge. **Right**: dielectric losses computed with Fourier series as a function of the number of harmonic include in the sum. The fact that this curve reaches the value 16 µJ when N=4, means that the sum of the dielectric losses associated with the frequency f_1=500 Hz, f_2=1000 Hz, f_3= 1500 Hz, f_4 = 2000 Hz is equal to $16\ \mu J$. The dielectric losses are computed for a dielectric layer of capacitance $C = 3\ pF$ and the angle of losses δ such that $tan(\delta) = 5 \times 10^{-3}$. The energy of the dielectric losses would be ~27.2 µJ per period (which would represent a power of 13.6 mW)

A-2-4-c) Matlab program for the summation of dielectric losses

```
clear x y T A Af Bf aff afff affff listefreq pertefreq Rpertes signalcondensateur
format longeng


Nharm=1000;                                %Number of harmonics
 close all

cm=104*1e-9;
Rsonde=10*1e6;

C=3*1e-12;                                 %equivalent series capacitance
tandelta=5e-3;                  %angle of losses


t=CC21;
t=transpose(t(1:end-1)-t(1));     %- 1 due to diff
signalcondensateurCM=CC22;
%smoothing
% raw data have a temporal resolution of 4ns, windows = 4 µs
windowSize=500;
taille=2*windowSize-1;
V=signalcondensateurCM;
            V1 = filter(ones(1,windowSize)/windowSize,1,V);
            V2 = filter(ones(1,windowSize)/windowSize,1,V(end:-1:1,:));
            V2=V2(end:-1:1,:);
            V=(windowSize*(V2+V1)-V)/(2*windowSize-1);
            V=V(taille:end-taille,:);
signalcondensateurCM=V;
t=t(taille:end-taille);

x=cm.*diff(signalcondensateurCM)./(t(2)-t(1))+signalcondensateurCM(1:end-1)/Rsonde;

% V=CC12
%V=x;
%             V1 = filter(ones(1,windowSize)/windowSize,1,V);
%             V2 = filter(ones(1,windowSize)/windowSize,1,V(end:-1:1,:));
```

```
%             V2=V2(end:-1:1,:);
%             V=(windowSize*(V2+V1)-V)/(2*windowSize-1);
%             V=V(taille:end-taille,:);
% x=V;
%

vvv(1,1)=t(1)*1e3;
vvv(1,2)=sss(1)*1e6;
for nn=100:100:498003
    vvv(nn/100.0,1)=t(nn)*1e3;
    vvv(nn/100.0,2)=sss(nn,1)*1e6;
end


T=t(end)-t(1);

N=length(t);
A=zeros(2,N);
A(1,:)=t;
A(2,:)=x;




y=zeros(1,N);
Af=zeros(1,Nharm);
Bf=zeros(1,Nharm);
A0=1/T*trapz(A(1,:),A(2,:).*cos(0.*t));
y=A0;
affichage=0;

    for n=1:Nharm
       % for n=2*1e6-20:2*1e6

        Af(n)=2/T*trapz(A(1,:),A(2,:).*cos(n*(2*pi)/T*t));
        Bf(n)=2/T*trapz(A(1,:),A(2,:).*sin(n*(2*pi)/T*t));
        y=y+Af(n)*cos(n*2*pi/T*t)+Bf(n)*sin(n*2*pi/T*t);
         if (mod(n+1,1)==0)
           q=n/Nharm*100
        listefreq=1/T:1/T:Nharm/T;
        Rpertes=tandelta./(C*2*pi*listefreq);
        pertefreq=Rpertes.*(Af.^2+Bf.^2)*1*T; %energy

        PerteBF=sum(pertefreq(1:10));
        perteTot=sum(pertefreq);
        affichage=affichage+1;
        aff(affichage)=n;
        afff(affichage)=perteTot;
        affff(affichage)=PerteBF;
        figure(4)
        plot(aff,afff,'r',aff,affff,'b');
         pause(0.01);
         end

        end


figure(1)
plot(t,transpose(y(1,1:N))-x,'b+')

figure(2)
plot(t,x,'b+');
hold on;
plot(t,transpose(y(1,1:N)),'r')



listefreq=1/T:1/T:Nharm/T;
Rpertes=tandelta./(C*2*pi*listefreq);
pertefreq=Rpertes.*(Af.^2+Bf.^2)*1*T; %energy

PerteBF=sum(pertefreq(1:10));
perteTot=sum(pertefreq);
```

A-5-2) Experimental observation of the aging of DBD device

The measurement of $\tan(\delta)$ characterizes the dielectric barrier of our DBD device, and so, enables to compute dielectric losses. However, these measurements can also be used to follow the aging of the dielectric layer. Indeed, in the practical case of medical treatment, it would be useful to know when one DBD-device should be change to avoid the occurrence of dielectric breakdown and thus electrical shocks.

The measurements of the capacitance and angle of loss of our DBD-device were performed after several hours of aging with a LCR-meter (Keysight, reference Ref E4980AL-032 20Hz to 300 kHz with DCR) equipped with an adapted alligator clip (Keysight 16089D-FG Alligator Clip Lead).

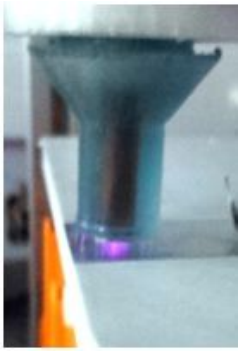

Fig 251: head of the DBD

The head of the DBDs was held by a vise. The coaxial cable and all the mobile parts were also fixed on the table.

One of the crocodile clips is connected to the heart of the coaxial cable connected to the inner part of the DBD. The second is connected to an 18 mm wide aluminum strip bonded to the surface of the DBD (rectangular, length ~3 cm). The measurements were repeated 10 times by changing aluminum strip. The ground[129] was connected to the external conductor of the coaxial cable. Settings of the RLC-meter:

- mode = Cs-D, i.e. measure the equivalent series resistances
- level = 2 V, amplitude of test voltage
- frequency $F = 5\,kHz$.
- measurement time = 240 ms (LONG) averaged over 64 acquisitions.

First, the measurements were done with a newly manufactured device (Fig 252, zero hours of aging). We obtain a capacitance equal to $C_S = 2.25 \pm 0.05\,pF$ and $\tan(\delta) = 0.147 \pm 0.005$. The DBD was powered[130] during 12 hours in front of a conductive tape connected to the ground. The measurements were repeated with the same protocol (aging = 12 h). As the measured aging is not significant, we performed the treatment above a liquid target for 12 additional hours (aging = 24 h). The capacitance does not decrease significantly; it means that the surface is not significantly eroded. However, a significant difference is observed regarding the value of **tan (δ)**.

In this case, there is actually aging of the materials due to the degradation of the upper layers of the dielectric layer. This evolution is visible by eye since the plastic becomes slightly opaque. The faster aging above the liquid may be due to the production of more reactive species in the gas phase above the water. These species could lead to accelerated degradation of the plastic.

[129] provided by another lead of the RLC-meter).
[130] sinusoid power supply, ~30 kV peak to peak.

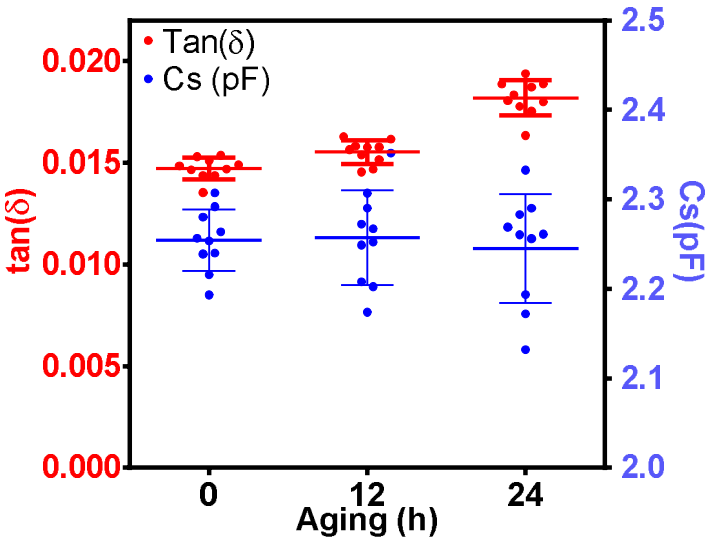

Fig 252 Red, angle of loss of the dielectric layer of blue resin DBD (see II.1.3, page 29) just after manufacturing (0 h), after 12 h of functioning over a solid target (aluminum plate connected to the ground). After this step, the aging was done during 12 h above liquid layer (aging = 24 h). Blue: capacitance of the device as a function of aging. Error bar represents the standard deviation of 10 independent measurements.

A-6-2) Dielectric losses at high-frequency

Model

When one of the discharges takes place an intense current flow for a period of time of the order of few ns ([335] and own results). Each discharge carries a quantity of charge: between 0.1 nC and few tens of nC ([335] and own results). This transitional current is also at the origin of dielectric losses. The question is whether they can be neglected or not. The current pulse is modeled by a triangular pulse. The first step is to obtain the Fourier transform of this pulse. The second step is to sum the energy of the losses for each frequency. We use the **assumption** $\tan(\delta) = Cst$ to known the equivalent resistance R_S for each frequency. This is true as a first approximation according to [334] and the results regarding blue resin.

Fourier transform of a triangular pulse

Let us consider a triangular current pulse defined by the parameters A and T_1 respectively the amplitude and the half of the pulse duration. Pulse is of the the form:

$$I(t) = \begin{cases} 0, \ t \leq -T_1 \ or \ t \geq T_1 \\ A\left(1 + \frac{t}{T_1}\right), \ -T_1 \leq t \leq 0 \\ A\left(1 - \frac{t}{T_1}\right), \ 0 \leq t \leq T_1 \end{cases}$$

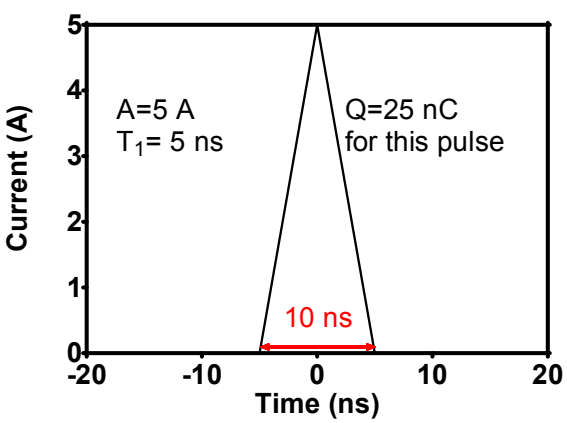

The derivative I' of I is:

$$I'(t) = \frac{A}{T_1} rect\left(t + \frac{T_1}{2}\right) - \frac{A}{T_1} rect\left(t - \frac{T_1}{2}\right)$$

with

$$rect(X) = \begin{cases} 1, & -\frac{T_1}{2} \le t \le \frac{T_1}{2} \\ 0, & otherwise \end{cases}$$

We defined the Fourier transform $F[g]$ of the function $(g: t \to g(t))$ as $\left(F[g]: \nu \to \int_{-\infty}^{+\infty} g(t) e^{-2i\pi\nu t} dt\right)$.

So Fourier transform of rect is: $F[rect](\nu) = \int_{-\infty}^{+\infty} rect(t) e^{-2i\pi\nu t} dt = T_1\, sinc(\pi\nu T_1)$

Let us consider Fourier transform of I':

$$F[I'](\nu) = \frac{A}{T_1}\left[\mathrm{e}^{\frac{2i\pi\nu T_1}{2}} T_1 sinc(\pi\nu T_1) - e^{-\frac{2i\pi\nu T_1}{2}} T_1 sinc(\pi\nu T_1)\right]$$
$$= \frac{A}{T_1}\left[2iT_1 \sin(\pi\nu T_1) sinc(\pi\nu T_1)\right]$$

Since $F[I'](\nu) = 2i\pi\nu F[I](\nu)$,

$$F[I](\nu) = AT_1 sinc^2(\pi\nu T_1)$$

Dielectric loss of one pulse

The amount of energy of dielectric losses for the frequencies in the interval $[\nu, \nu + d\nu]$ is:

$$R_s(\nu)|F[I](\nu)|^2 d\nu.$$

Since $R_s(\nu) = \frac{\tan(\delta)}{2\pi\nu C}$,

$$R_s(\nu)|F[I](\nu)|^2 \underset{\nu \to 0}{\sim} \frac{1}{\nu}\frac{\tan(\delta)}{2\pi C}$$

Therefore, the integral of the spectral density of energy is divergent in 0. This non-physical behavior is due to the limits of the modeling: actually $\tan(\delta)$ is a function of ν. Since the experiment itself has a finite duration, it is legitimate to introduce a cut-off: $1/T_0$. At high frequency the integral is convergent. Calculations were made with "integral" function of MATLAB. Cut-off was chosen at f = 10^{-3} Hz. Since $\tan(\delta)$ increases wit the frequency f, this model gives a lower bound of dielectric losses. In the following figures, the power of the dielectric losses is computed with the assumptions that there are two pulses per period. The parametric study presented in Fig 253, Fig 254, Fig 255 and Fig 256 show that the power of the dielectric losses depends on:

- the amount of charge transported
- the duration of the pulse
- the angle of losses
- the capacitance of the dielectric layer

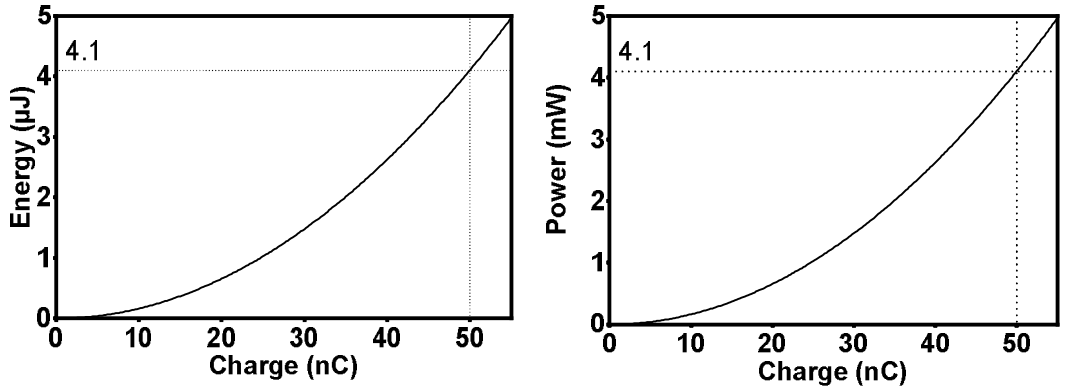

Fig 253 Parameter = transported charge. Dielectric losses for a triangular pulse. The pulse has a duration of 10 ns. The charge (and the amplitude of current pulse) is variable. The dielectric layer has a capacitance C=3 pF and $tan(\delta) = 5\ 10^{3}$ is the langle of loss. Left: energy losses for 1 pulse in µJ as a function of carried charge in nC. Right: power consumption of the losses with the assumption of 1 discharge by half-period at 500 Hz.

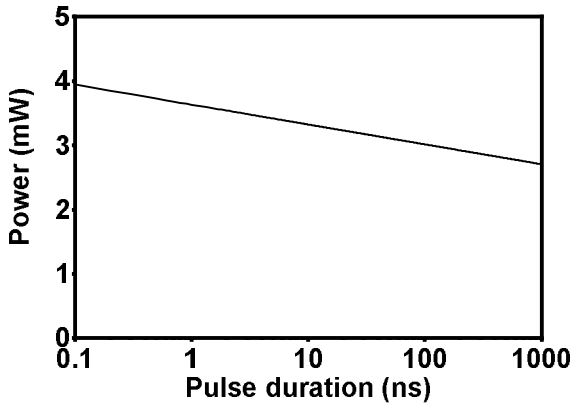

Fig 254 Parameter = pulse duration. Dielectric losses for a triangular pulse. The carried charge is 45 nC. The dielectric layer has a capacitance C = 3 pF and $tan(\delta) = 5\ 10^{-3}$ is the tangent of the angle of loss. Power consumption of the losses as a function of pulse duration in ns. Assumption "one discharge by half-period at 500 Hz".

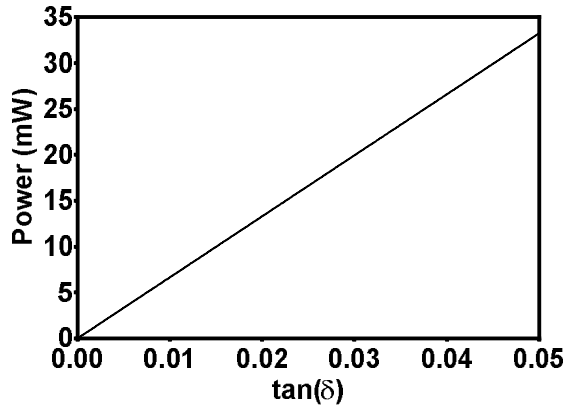

Fig 255 Parameter = loss angle. Dielectric losses for a triangular pulse. The carried charge is 45 nC. The dielectric layer has a capacitance C=3 pF, and $tan(\delta)$ is variable. Power of the losses as a function of $tan(\delta)$ with the assumption "1 discharge by half-period at 500 Hz".

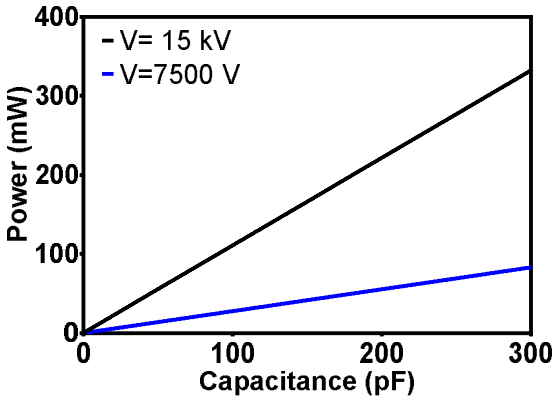

Fig 256 Parameter = capacitance. Dielectric losses for a triangular pulse. **Black:** Voltage of discharge ignition = 15 kV. **Blue** : ignition = 7500 V. The dielectric layer has a capacitance between 1 and 300 pF, $tan(\delta) = 5\ 10^{-3}$.Power of the losses as a function of capacitance for a constant Voltage. Assumption: "one discharge by half-period at 500 Hz".

A-3) What if there is a mouse in the electrical circuit?

During *in-vivo* experiments, the cold plasma is directly in contact with the skin of the mouse. It is essential to know the electrical characteristics of the treated target to ensure that power measurement was not biased by the Joule effect occurring in the skin of the mouse. Equivalent series resistance and capacitance were measured with a RLC-meter[131] to understand the electrical behavior of the mouse skin. The upper part of the tumor was connected to the RLC-meter with a cut piece of an ECG electrode (whitesensor, distrimed). The conductive gel was placed around the tumor (without covering it) in the same way that in the *in-vivo* experiments (section V.2 and following). This gel was used to prevent the current from flowing through the internal organs. The second lead was connected to the ECG electrode fixed at ~ 3 cm from the tumor (similar to in-vivo experiments). A conductive path was established between this ECG electrode and the gel located near the tumor (similar to *in-vivo* experiments). The mouse was under anesthesia.

Equivalent series **resistance** and **capacitance** were measured for several frequencies between 100 Hz and 300 KHz (Fig 257 Log-Log scale). The capacitance decrease with frequency from 488 nF to 1.45 nF. Equivalent series resistance decreases also from $14\ k\Omega$ to $1\ k\Omega$.

The existence of a slope break in Cs(f) curve near to the frequency $f = 1\ kHz$ probably reflects the fact that it is not the same biological structure that contributes mainly to the total capacitance of this piece of skin before and after this frequency. It would be interesting to repeat such experiments (this measurement was made on a single mouse) and to interpret the slope break with the references [336], [337].

[131] The same device was used in section A-5-2). Keysight RLC-meter, Ref E4980AL-032 20Hz to 300 kHz and 16089D-FG Alligator Clip Lead (4 Clips)

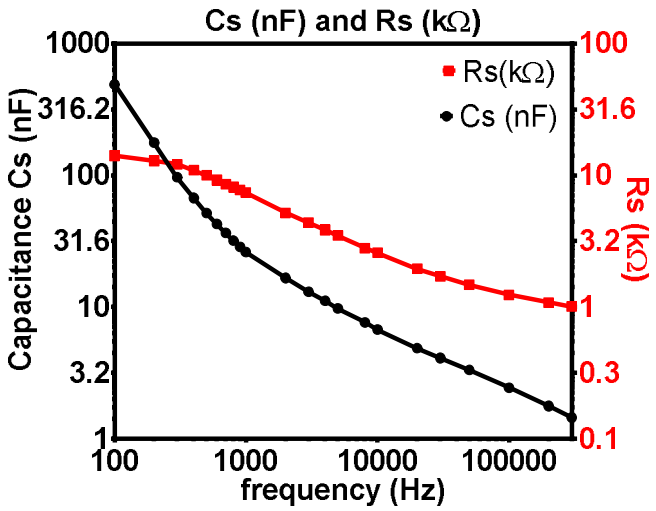

Fig 257 Capacitance (in nF) and equivalent series resistance acquired at the surface of the skin with the LCR meter (E4980AL from Keysight®).

Regarding power measurement, Fig 258 shows that charges movement take place in ~ 1 µs (acquired in-vivo, sampling frequency = 10 MHz). Consequently, at this time scale, the resistance is probably ~ 1 $k\Omega$ or below according to previous figure. This is consistent with the response time $\tau = RC$ deduced from the electrical circuit equivalent to {mouse skin + measuring capacitor Cm = 100 nF + measuring system} that should be equivalent to a capacitor $C \cong 1.5\,nF$ in series with a resistor $R = 1\,k\Omega$.

$$\tau = RC = 1.45\ \mu s$$

Moreover, the additional resistance does not contribute significantly to the power consumption. Indeed, if it is assumed that the current last ~1 µs in the skin and transport ~ 100 nC (the upper limit of the charges transported during "one" discharge); the current is ~0.1 A. Energy consumption will be $\sim 1\ \mu s \times RI^2 \cong 10^{-6} \times 10^{3} \times 10^{-2} \sim 10\ \mu J$. Whereas the total energy consumption associated with such discharge is around $1000\ \mu J$ (see the order of magnitude presented in Fig 239, page 304 which is remain suitable for this calculation). So even in an extreme case (that of a powerful discharge which transport 100 nC) the energy dissipated by the joule effect in mouse skin should not contribute significantly to the overall energy balance.

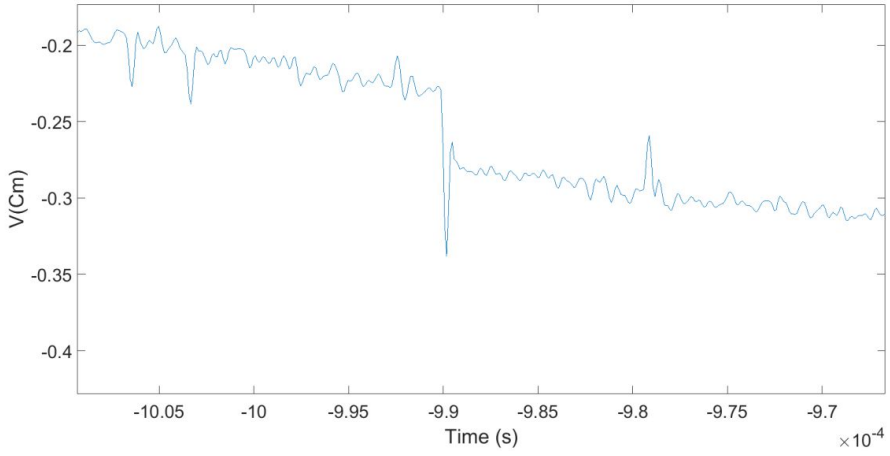

Fig 258 example of signal measured with the capacitor connected to the mouse. Response time is approximately ~ 1 µs

Appendix B Scavenging of HO° by methanol

B-1) Methanol: an efficient scavenger of HO°

The purpose of these experiments was, initially, to precise the origin of H_2O_2 in liquid solution. Sato et al. [338] and Hsieh et al. [339] make the assumption that H_2O_2 in the liquid phase is mostly produced by the recombination of hydroxyl radicals.

$$OH° + OH° \rightarrow H_2O_2 \ (k_{recombination} = 5.5 \times 10^9 \ M^{-1}s^{-1}) \quad [338]$$

These hydroxyls radicals would originate directly from the plasma phase or would be a by-product linked to the production of solubilized electrons, or destruction of water molecules.

Scavengers such as methanol or ethanol react very quickly with hydroxyls radicals ($k_{ethanol} = 10^9 \ M^{-1}s^{-1}$, $k_{methanol} = 5 \times 10^8 \ M^{-1}s^{-1}$ at $pH = 7$ according to [338]. The reaction constant of the hydroxyl radical with its scavengers is slightly weaker than the reaction of the radical with itself ($k_{recombination} = 5.5 \times 10^9 \ M^{-1}.s^{-1}$, [121]). However, it should be considered that the concentration of the scavenger is in large excess:

$$[R - OH] \sim 1M \gg [OH°].$$

Therefore, the speed of reaction with scavenger is several orders of magnitude higher. If the hydroxyl radicals are at the origin of H_2O_2 in liquid phase, the addition of scavenger capturing OH° should decrease the production of H_2O_2.

This is what Hsieh et al. describe in the paper [339]. The scavenging agent is ethanol in liquid phase; the plasma source is a gliding arc. H_2O_2 concentration is measured with $TiOSO_4$ diagnostic.

Sato et al. also observe a decrease in the production of H_2O_2 in the presence of methanol or ethanol [338]. In this case, plasma source is an underwater discharge generated with High Voltage pulses. The concentration of H_2O_2 is measured indirectly with Glucose CII-Test Wako Method that measures the total quantity of oxidizing species: addition of catalase which destroys H_2O_2 allows to assert that H_2O_2 is predominantly formed among the oxidizing species.

The results presented in the following sections show different results from those of Sato et al. [338] and Hsieh et al. [339]. H_2O_2 is not only formed in the presence of methanol, but also there is a slight increase in the production of H_2O_2 in the presence of methanol compared to pure water.

First, it was checked that methanol is an efficient scavenger of HO°. Fig 259 gives the fluorescence of several solutions at the emission and excitation wavelength[132] of TPA-OH. Seven experiments were made in duplicate. From left to right:

- A well which contains 500 µL of [TPA]=4.11 mM, [KOH]=20 mM, was treated by the single-channel plasma jet. Unfortunately, treatment conditions were not correctly recorded[133] but were the same for all wells. After the experiment 50 µL

[132] Fluorometer parameter are λex=317nm, λem=435nm, with Δλ= 5 nm for excitation and emission, see section II.3.4.2 page 54).
[133] treatment conditions were probably: 27 kV peak to peak, 500 sscm, 3 min, height= 5 mm since we choose the standard condition used during parametric experiment

of pure methanol and 950 µL of untreated TPA+KOH solution were mixed with this solution in a spectroscopic cuvet (PMMA)

- A well which contains 500 µL of [TPA]=4.11 mM, [KOH]=20 mM, was treated by the single-channel plasma jet, and then mixed with 1000 µL of untreated TPA+KOH solution in a spectroscopic cuvet.
- A well which contains 500 µL of [TPA]=4.11 mM, [KOH]=20 mM and 1 ppmv of methanol, was treated by the single-channel plasma jet, and then mixed with 1000 µL of untreated TPA+KOH solution in a spectroscopic cuvet.
- A well which contains 500 µL of [TPA]=4.11 mM, [KOH]=20 mM and 10 ppmv of methanol, was treated by the single-channel plasma jet, and then mixed with 1000 µL of untreated TPA+KOH solution in a spectroscopic cuvet.
- 1500 µL of untreated TPA+KOH solution (i.e. [TPA]=4.11 mM, [KOH]=20 mM)
- 500 vµL of untreated TPA+KOH solution+1 ppmv of methanol mixed with 1000 µL of untreated TPA+KOH solution
- 500 vµL of untreated TPA+KOH solution+10 ppmv of methanol mixed with 1000 µL of untreated TPA+KOH solution

The comparison of the first and second column shows that methanol does not significantly modify the fluorescence of TPA-OH.

The comparison of column five, six and seven prove that methanol does not increase the fluorescence of TPA (excited in the range of wavelength for TPA-OH detection).

Consequently, the comparison of column one, three, four and five, show that methanol is a competitive scavenger with respect to TPA. An order-of-magnitude calculation enables to check this:

We use the order of magnitude of [HO°] found in section III.5.2 (page 85): $[HO°] = 6.9 \times 10^{-4}\ M$.

1-Recombination reaction:

$$\frac{d[HO°]}{dt} = -2k_2[HO°]^2 = -5.24\ \times 10^3\ mol.L^{-1}.s^{-1}$$

2- Scavenging reaction (with [TPA]=4.11 mM)

$$\frac{d[HO°]}{dt} = -k_1[TPA][HO°] = -9.36\ \times 10^3\ mol.L^{-1}.s^{-1}$$

3—scavenging due to 1 ppmv methanol, $[CH_3OH] \cong 0.025\ M$

$$\frac{d[HO°]}{dt} = -5 \times 10^8 \times [CH_3OH][HO°] = -8.6\ \times 10^3\ mol.L^{-1}.s^{-1}$$

3'—scavenging due to 10 ppmv methanol, $[CH_3OH] \cong 2.5\ M$

$$\frac{d[HO°]}{dt} = -5 \times 10^8 \times [CH_3OH][HO°] = -860\ \times 10^3\ mol.L^{-1}.s^{-1}$$

Note that the speed of reaction 3 is comparable with those of reaction 1 and 2, this is consistent with the fact that the third column (from the left of Fig 259) show a significant decrease in TPA-OH production, without a total cancel of TPA-OH production. This experiment confirms the value of the order of magnitude of [HO°] found in Chapter III.

The speed of reaction 3' is 100-fold higher than others reactions, that's why methanol entirely scavenge the production of TPA-OH (column four from the left of Fig 259).

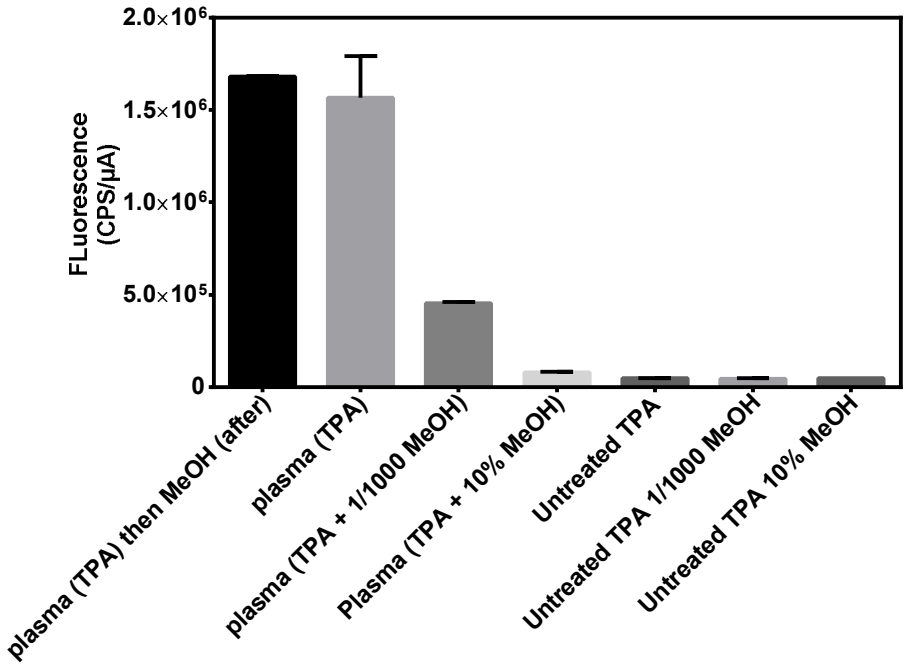

Fig 259 Methanol is an efficient scavenger of HO°. Duplicate experiment. The treatment conditions were the same for the four first column but have not been adequately recorded. see footnote 133

B-2) H_2O_2 production in plasma-treated methanol solution

protocol and experimental setup. Solutions of 1 mL were prepared by mixing water and methanol in varying proportions. We use the approximation that the total volume is the sum of the volume of each solution. These solutions are in the wells of a 24-well plate (Costar®). Solutions are treated for 6 min with the single-plasma-jet (di=3, e=1.5, H=60). We use the "square+resonnance" power supply (as in the experiments described in Chapter III), with a peak to peak voltage of 30 kV. He flows is 600 sscm. and the output of the jet is 3 mm above the liquid. After each treatment, 100 µL of the $TiOSO_4$ solution at 2% is added to the well. Thus, dismutation of H_2O_2 is avoided as much as possible. $TiOSO_4$ is not in solution before plasma treatment. This choice prevents eventual interference[134].

Since methanol has a density and molar mass different from that of water: molar ration of CH_3OH is not proportional to the proportion by volume (Fig 260, left): by mixing 900 µL of methanol with 100 µL of water the molar proportion of methanol is only 80%. Since methanol is more volatile than water, the samples prepared with higher concentration of

[134] Moreover one of our experiment show that the addition of TiOSO4 solution do not indue an interference caused by the formation of peroxinitrite from H_2O_2 and nitrite in acidic medium. Since TiOSO4 is added after plasma-liquid interaction, the kinetic of peroxinitrite formation (several min see II.3.3.1, page46) is negligible compared to the speed of formation of coloured complex (quasi instantaneous)

methanol undergone increased evaporation[135]. Consequently, the volume of the wells containing methanol is lower than those containing water (Fig 260, right panel).

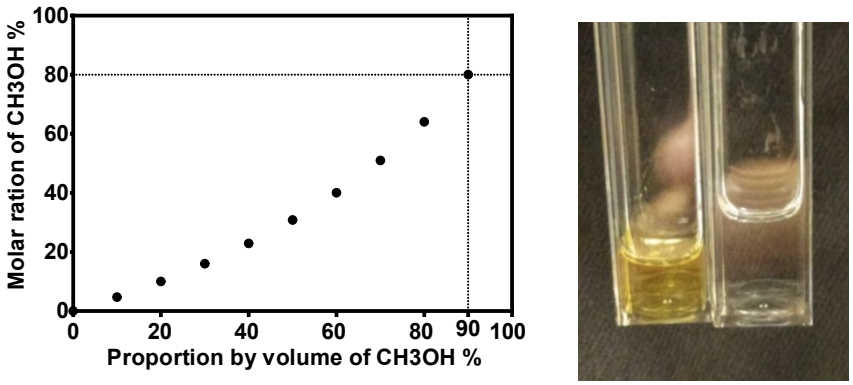

Fig 260 Left: Since methanol has a density and molar mass different from that of water: molar ration of CH_3OH is not proportional to the proportion by volume. **Right**: comparison of a blank of 1100 µL (700 µL methanol+300 µL H_2O+100 µL TiOSO4 2 w%.), with the remaining volume after treatment + 100 µL of TiOSO4. Yellow color proves that H_2O_2 is present. Approximately half of the methanol evaporates in each well.

Methanol is added to the treated solutions to compensate this evaporation. A blank solution which has the same composition than the treated solution (+100 µL of $TiOSO_4$) were prepared. Methanol is added to the treated solution mixed with 100 µl of $TiOSO_4$ so that the mass of the two cuvets are equal. Since methanol is more volatile than water, it is reasonable to replace the entire evaporated volume by methanol[136]. A schematic of the protocol is shown in Fig 261.

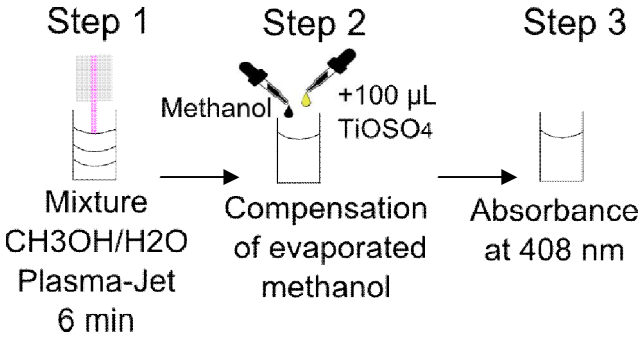

Fig 261 First, 1 mL of a mixture of methanol/water is exposed to single-channel plasma jet for 6 min (height = 3 mm, He flow = 600 sscm, Voltage = 30 kV). Just after the treatment 100 µL of $TiOSO_4$ were added. Then, the volume of evaporated methanol is compensated by adding methanol in the cuvet. Finally, the absorbance of the solution is measured at 408 nm; the value is proportional to the final H_2O_2 concentration in the treated sample.

Results During these experiments, the proportion by volume of methanol is modified between 10% and 90%. The nature of the solvent is modified, and this could have effects (called solvatochromic) on the absorption spectra of the chemical species. In particular

[135] The liquid-vapor diagram for water-methanol mixture has no azeotrope (instead of ethanol-water mixture for instance). Since the boiling point of methanol is 64.2 °C at atmospheric pressure, the impinging jet cause an increased evaporation compared to the pure water solution. The vapor is enriched in methanol, and it could be shown that the majority of the evaporated volume consists of methanol.

[136] In reality, water also evaporates. But even replacing a small part of the water evaporated with methanol is not an issue because it has no influence on the absorbance of the solutions and the measurement of H_2O_2, this point is discussed with Fig 262.

$TiOSO_4$ and the colored species formed with its reaction with H_2O_2. The absorbance at 408 nm of blank solutions containing a variable proportion of methanol +100 µL $TiOSO_4$ at 2 w% is plotted in the left panel of Fig 262 to address this question. The level of the signal is in the amplitude of noise originating from the individual difference between cuvets ($\sim 10^{-2}$). This graph proves that there is no solvatochromic effect related to $TiOSO_4$ in the methanol-water mixture.

The right panel of Fig 262 shows that there is not solvatochromic effect related to the colored product formed by the reaction between H_2O_2 and $TiOSO_4$.

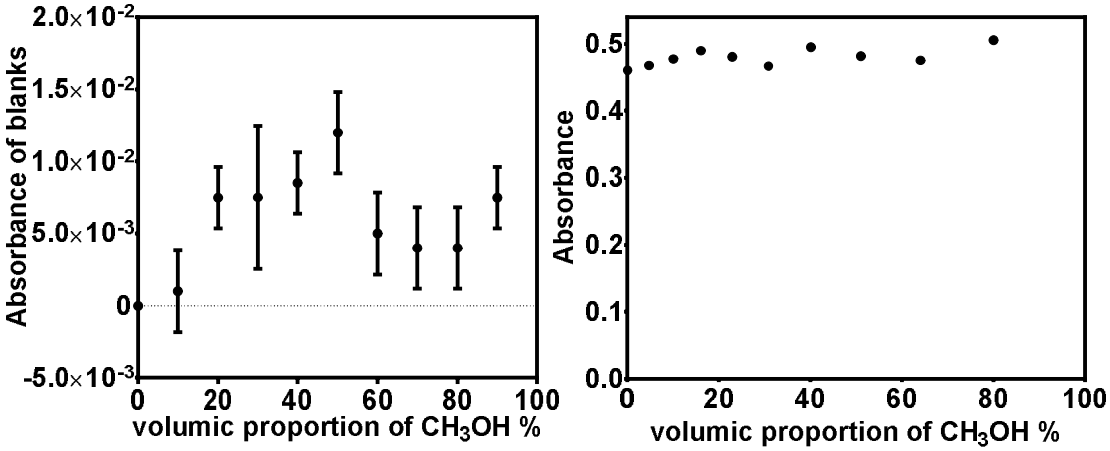

Fig 262 **Left:** Absorbance at $\lambda = 408\,nm$ of blanks solutions containing 100 µL of $TiOSO_4$ 2 w% and 1000 µL of water-methanol solutions with variable proportion of methanol. This graph proves that there is no solvatochromic effect on $TiOSO_4$. **Right** Absorbance at 408 nm of cuvets containing variable proportions of methanol,100 µL of $TiOSO_4$ solution at 2 w% and 8 µL of H_2O_2 at 0.3 w% ; $[H_2O_2]$=637 µM in 1108 µL. Blank is pure water + 100 µL $TiOSO_4$ solution. This graph proves that methanol does not destroy H_2O_2 and that there is no solvatochromic effect on the coloured complex.

However, we could imagine that changing the solvent could change the nature of the plasma discharge (especially its power). This is not the case as shown in Fig 263.

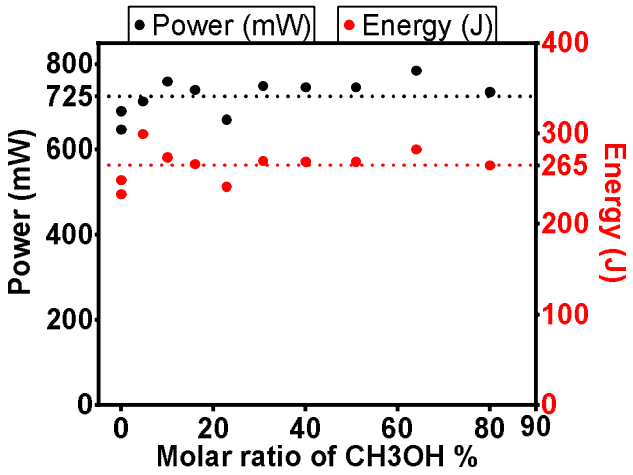

Fig 263 energy and power consumption associated with each treatment. (height = 3 mm, He flow = 600 sscm, Voltage = 30 kV). single experiment.

The absorbance of samples treated by plasma is plotted in Fig 264. It appears that the scavenging of HO° by methanol does not decrease the production of H_2O_2 in liquid

phase even if the concentration of methanol is high enough to prevent[137] the recombination reaction: $OH° + OH° \rightarrow H_2O_2$. On the contrary, it seems that the absorbance at 408 nm and so the production of H_2O_2 is higher with methanol than without. How to explain this?

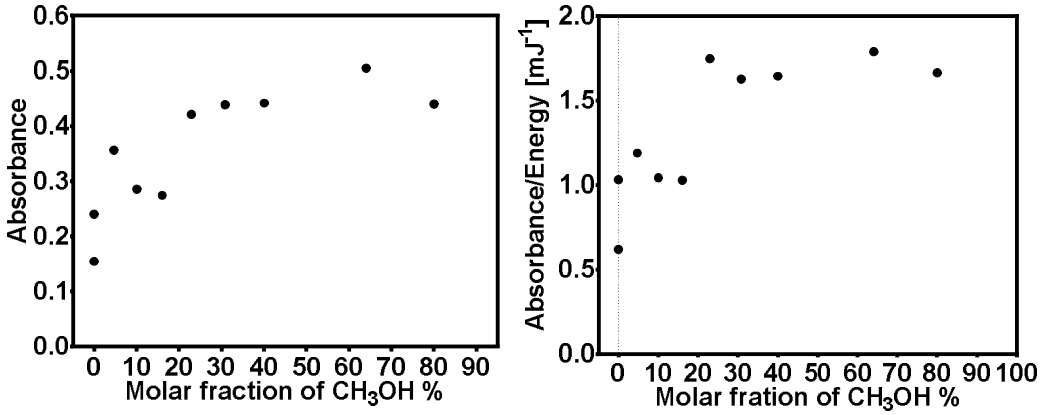

Fig 264 Left panel: absorbance at $\lambda = 408\ nm$ of the samples exposed to the single-channel plasma jet for 6 min (height = 3 mm, He flow = 600 sscm, peak to peak voltage = 30 kV). Single experiment. Each sample has a volume of 1 mL with the molar fraction of methanol shown in abcissa. Before absorbance measurements, 100 µL of $TiOSO_4$ were added and the evaporated-volum was compensated (according to the previous protocol described in Fig 261). Right panel: absorbance divided by energy consumption

Discussion

It turns out that the radical chemistry does not stop with the reaction between HO° and methanol:

$$\boldsymbol{CH_3OH + HO° \rightarrow °CH_2OH + H_2O \qquad k = 10^9\ M^{-1}s^{-1}}$$ [340]

This radical can react with dissolved oxygen leading to the formation of $HO_2°$ and then H_2O_2. The reactions invovled in the production of H_2O_2 are described in detail in the papers of Robl et al. [340] and Westbrook et al. [341]. The presence of methanol or ethanol increase the production of H_2O_2 (Fig 265). More work would be needed to obtain a more precise comparison between photolysis experiments and plasma experiments. In particular, chemistry calculations should enables to compare the increase in H_2O_2 production with the modeling. This type of simulation is potentially easy to carry out since the reactions and, reaction constants are well known from photolysis experiment [342]–[346]. However, it would be interesting to have superoxide measurement to model this kind of experiment.

How to explain the discrepancy between this result (an increase in H_2O_2 production when the [MeOH]↗) compare to those of Hsieh et al. [339] **and Sato et al.** [338]**?**

In the work of Hsieh et al. it is likely that the solution is deoxygenated since the liquid is enclosed in a cavity purged with Ar and Co flux [339]. This could limit the reaction following the formation of $°\boldsymbol{CH_2OH\ or\ CH_3O}°$ with O_2 and thus the formation of H_2O_2.

[137] note that 1 ppmv of methanol is enough to compete with TPA+OH reaction according to the previous section, and here it is far higher

In the paper[138] of Sato et al. [338] the fact that H_2O_2 does not increase with MeOH or EtOH concentration is probably due to more complex reasons, perhaps related to the nature of the discharge (underwater discharge). It should also be checked that the presence of scavenger does not cause interference in the operation of the chemical diagnosis (Glucose CII-Test Wako Method).

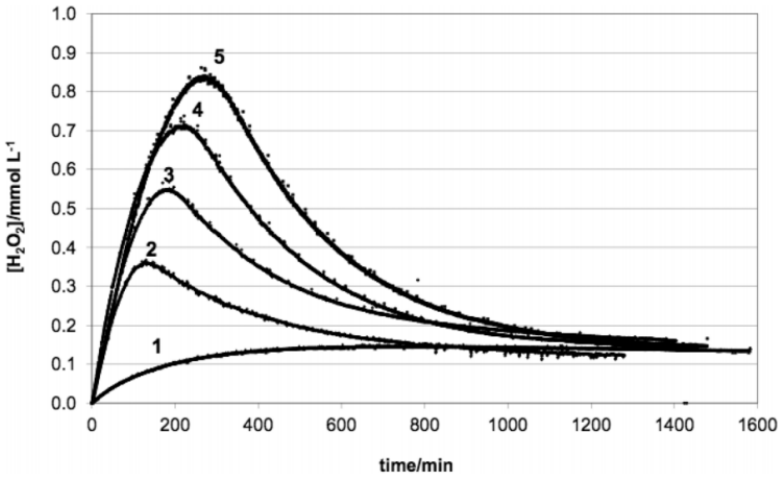

Fig 265 Legend and figure from the work of Robl et al. Evolution of [H_2O_2] produced by VUV-photolysis (172 nm) of O2-saturated aqueous CH3OH of varying initial concentrations. [CH3OH]0: (1) 0 mM; (2) 0.25 mM; (3) 0.50 mM; (4) 0.75 mM; (5) 1.00 mM. [340] © The Royal Society of Chemistry and Owner Societies 2012

More discussion would be needed to precise the complete radical chemistry of the liquid phase and the link between HO° and H_2O_2 like those conducted by Locke et al. [347] and Sahni et al. [113], [348]. It would be interesting to compare such result with spatially resolved simulation. During this thesis, we have also observed the discoloration of methylene blue, which is generally attributed to the action of HO°. It would be interesting

[138] Note also that the following statement of paper [338] is debatable: *"2) total oxidation without H_20_2 (a catalase is used to selectively remove the H_2O_2) ... This method determined that the only oxidizing agent present in significant amounts was H_2O_2"*. Since catalase (and SOD) are also scavenger of HO° (Buxton et al. [121]). One of our experiment show that increasing concentration of catalase decrease the production of TPA-OH. during plasma exposure (see the following figure) (Single channel jet, time = 2 min, voltage = 30 kV, height = 14 mm, Helium flow = 200 sscm, liquid volume = 500 µL power 539 ± 14 mW, triplicate experiment). The addition of an enzyme has a considerable influence on liquid chemistry.

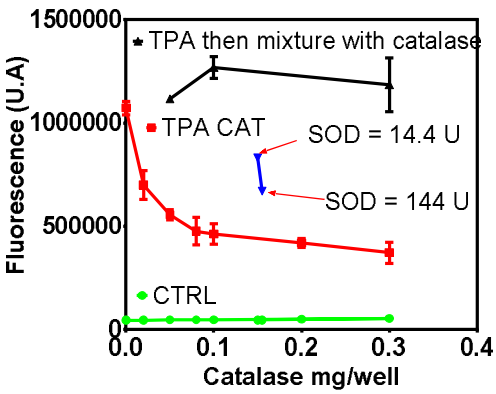

to compare this result with those obtained with TPA even if the methylene blue chemistry is not precisely known.

Appendix C *in-vitro* experiments, additional data

For the experiments which involve an incubation time of 24 and 48 hours, the flow of helium is 400 sscm, the distance between the nozzle and the surface of the liquid is about 3 mm. Peak to peak voltage is around 18.5 kV for the following energies: {2.5, 5, 10, 15, 20, 25, 30, 40, 50 J}. It takes about 5 min to reach the energy of 50 J. For higher target energies, the peak-to-peak voltage is increased to decrease the total treatment time. The following targets of energy {50, 70, 80,100, 200 J}, are reached with a peak-to-peak voltage of 30 kV. It takes about 5 min to obtain 200 J. Most treatments are done in duplicate.

Fig 266 shows the count obtained after 24h of incubation (trypan blue diagnostic). This is a comparison between the effect of direct treatments (plasma-jet, red dots) and PAM treatments (orange dots).

During direct treatments, the wells containing the cells and the medium are treated with the single-channel plasma jet. The plasma plume touches the surface of the liquid. PAMs are prepared from the complete medium (without cells). Just after the preparation of PAM, the medium in which the cells are immersed is replaced by the PAM (less than 1 min after its preparation). Since the treatments exhibit significant variability, it would be necessary to use more replicates. The results were grouped by the range of energy. No significant differences appear between treated and untreated wells since the error bars of the treatments done at the energy $E = 200\,J$ are just below those of the untreated group. Moreover, there is no significant difference between direct and indirect treatments.

Therefore, it can be concluded that no deleterious effect on viability occurs after 24 hours of incubation in this range of energy.

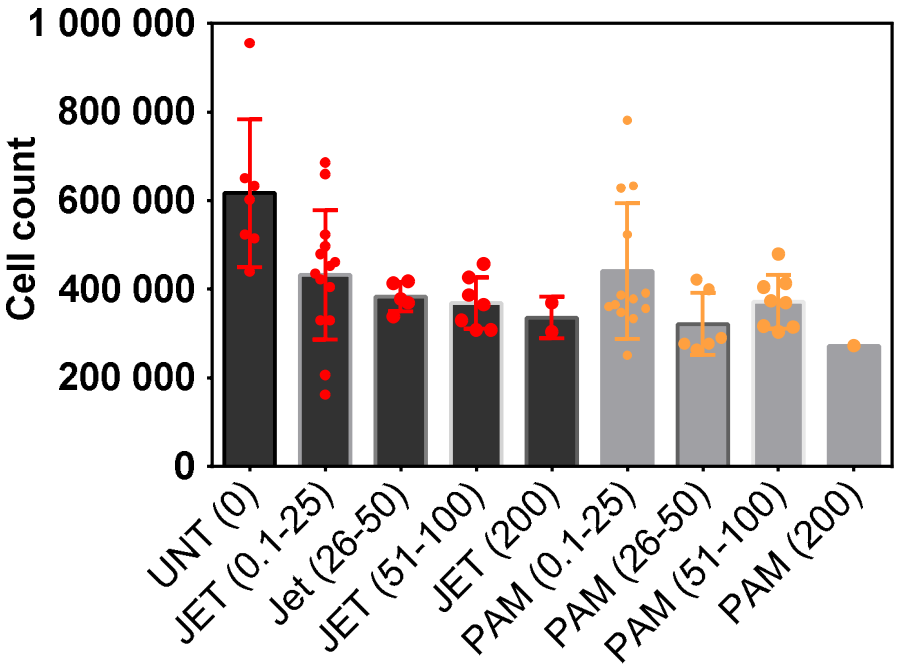

Fig 266 Cell count of living cell after 24 h of incubation. The error bars represent the standard deviation of the data. The red dots represent the results of direct plasma treatments. Orange dots represent the results of indirect treatments (PAM). The number in brackets refers to the range of energy pooled in the bar. For example, "Jet (26-50)" means that the cell counts of treatments with an energy between 26 and 50 J are pooled.

Fig 267 shows the results of trypan blue diagnostic after 48h of incubation. The red dots represent the results of direct plasma jet treatments. The treatments were grouped by energy range. The conclusions are precisely the same as after 24 hours of incubation. It can be concluded that no significant deleterious effect appears after 48 hours of incubation with this range of energy. No significant differences appear between direct and PAM treatments (orange dots).

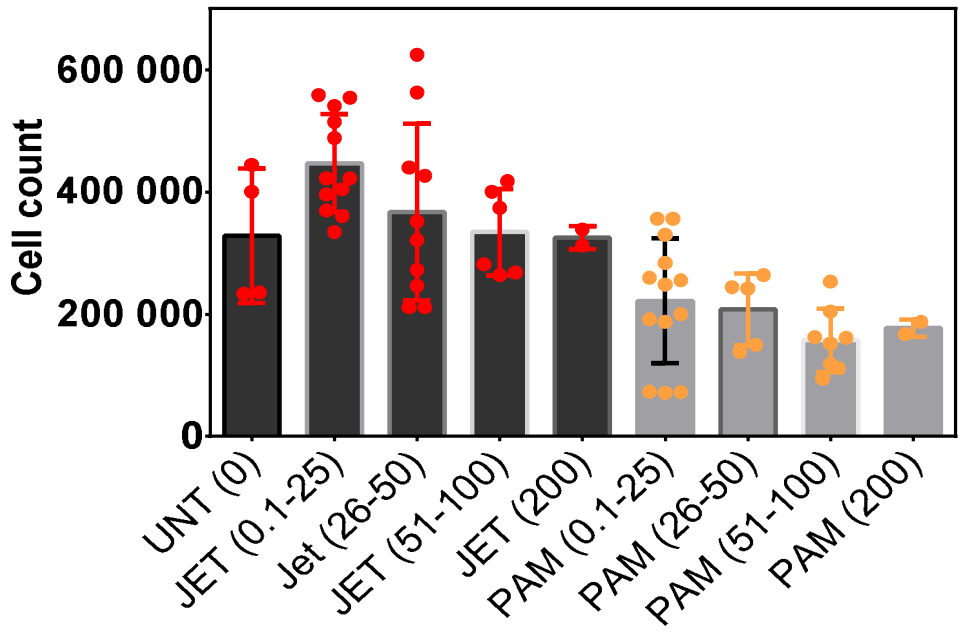

Fig 267 Cell count of living cell after 48 h of incubation. The error bars represent the standard deviation of the data. The red dots represent the results of direct plasma jet treatments. Orange points represent the results of indirect treatments by PAM. The number in brackets refers to the range of energy pooled in the bar. For example, "Jet (26-50)" means that the cell counts of treatments with an energy between 26 and 50 J are pooled.

Fig 268 shows the results of trypan blue diagnostic after 72h of incubation. The blue dots (black bars) represent the results of plasma jet treatments. The green dots represent the cell counts after exposure to H_2O_2 diluted in the medium.

The treatment conditions have been slightly modified. Half of the plates were treated with a flow rate of 400 sscm, with a height of 9.7 mm between the surface of the liquid and the nozzle. The other plates were treated at 200 sscm and a height of 1.7 mm. Similarly, the targeted energies (100 and 200 J) were carried out with a peak-to-peak voltage of 30 kV while the other energies (2, 4, 5, 6, 8, 10, 20, 50 J) were reached with a peak-to-peak voltage of 19-20 kV. At 30 kV, 200 J are approximatively equivalent to one treatment of 4 min. 6 min of treatment are needed at 19-20 kV to obtain 50 J.

The cell division rate is unusually high as evidenced by the control group (over 2 million cells). The results of the untreated group are dispersed. However, the effect on cell viability is significant after 72h of incubation. The error bars represent the standard deviation of the data. The analysis of the results did not show any significant differences

for the same energy in the two conditions of treatments (200 sscm/1.7 mm vs. 400 sscm/9.7 mm). Consequently, the results of the two plates have been pooled.

The treatment at $E = 10\,J$ is placed under the same brakets since the wells are exposed to a concentration of 40 µM of H_2O_2, which corresponds to the concentration of H_2O_2 produced by the plasma for this energy. The second brace corresponds to 50 J/200 µM.

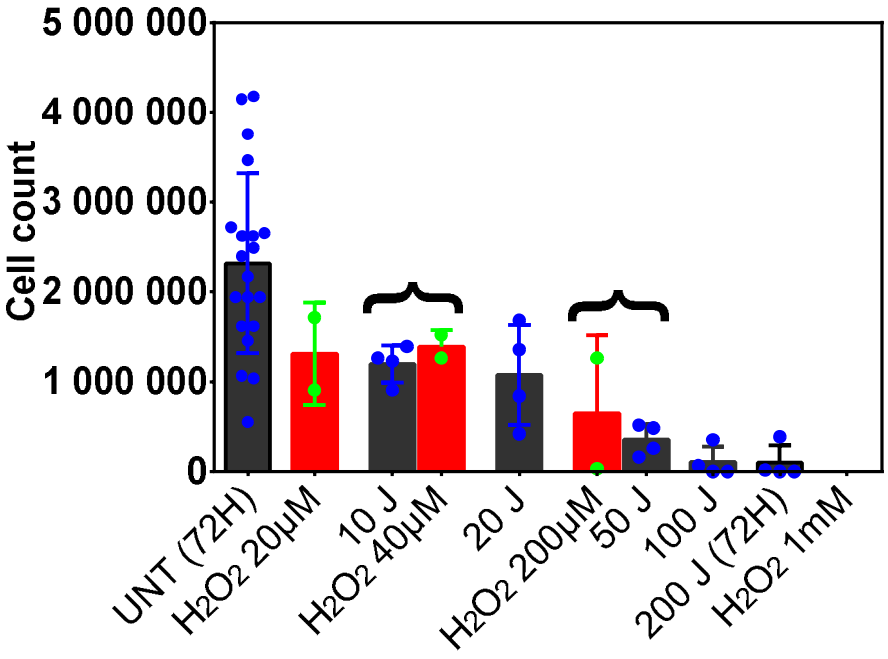

Fig 268 Cell count of living cell after 72 h of incubation. The numbers in the brackets describe the range of energy consumption measured during the experiment.

Appendix D Benchmark of the simulation

The simulations produce realistic behaviors regarding the propagation of heat. This point, although necessary, is not enough; the result must be numerically exact. To check that, we compare the result given by the simulation and an exact analytical solution. The main point to test is that the program correctly models the propagation of heat by conduction.

As a benchmark, we consider a homogeneous material bar subjected to constant heat flux. [277] give an analytical expression of the temperature inside at depth x, for any time t.

$$\boldsymbol{T(x,t) = T_{ini} + \frac{2\,\phi\sqrt{t}}{\sqrt{\lambda\rho C}} \int_{x/(2\sqrt{at})}^{\infty} erfc(u)du \;\; (t \geq 0)}$$

Where $\mathbf{T_{ini}}$ is the initial temperature of the material, $\boldsymbol{\phi}$ the thermal flux in $\mathbf{W.m^{-2}}$, $\boldsymbol{\lambda}$ the thermal conductivity in $\boldsymbol{W.m^{-1}.K^{-1}}$, $\boldsymbol{\rho}$ the density in $\boldsymbol{kg.m^{-3}}$, C the specific heat in $\boldsymbol{J.kg^{-1}.K^{-1}}$. $\boldsymbol{x = 0}$ corresponds to the surface of the material, x is positive inside the bar. $\boldsymbol{erfc}$ is the complementary error function :

$$\boldsymbol{erfc(x) = 1 - \frac{2}{\sqrt{\pi}} \int_{x}^{\infty} e^{-t^2}\, dt}$$

First of all, the usual conditions of temporal and spatial resolution are chosen to do the comparison with the benchmark (these conditions are discussed in VI.1.7.2). Regarding the spatial resolution, the size of the mesh is around 10 µm in the first few hundred micrometers (see the mesh Fig 269). The temporal resolution is 0.05 s.

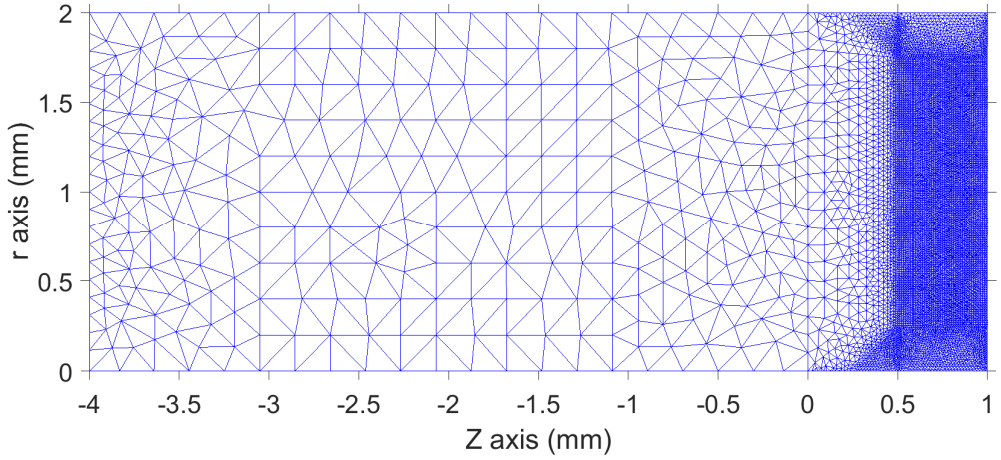

Fig 269 Mesh of the bar in the "usual conditions" of spatial resolution. $z = 1$, corresponds to $x = 0$, in the analytical expression. All boundaries are insulating except the boundary definded by $x = 0$ where the thermal flux is equal to 10,000 W / m².

The parameters of the modeling are given below:

Size of the cylinder: radius = 2 mm, length L = 5 mm

$\lambda = 0.5\, W.K^{-1}.m^{-1}$

$\rho = 1500\, kg.m^{-3}$

$C = 3600\, J.kg^{-1}.K^{-1}$

$$\text{diffusivity } a = \frac{\lambda}{\rho C} \cong 9.3 \times 10^{-8}\ m^2.s^{-1}$$
$$\phi = 10\,000\ W.m^{-2}$$

Note that the diffusivity, the length of the bar, and the total duration of the simulation ($T = 10s$) satisfy the condition of validity of the analytical expression:

$L^2/a \cong 270\ s \gg T = 10\ s$ ([277])

The integral of erfc is computed with the Simpson's rule. Fig 270 shows the comparison between the simulation and the exact solution. The error is between -0.05 and 0.05 °C below 10 µm. Logically, the error regarding the surface temperature is more important in the first moments. In the simulations of Chapter VI, the flow imposed is lower, which will further reduce the error. The precision achieved is therefore relatively good, in any case, sufficient compared to other uncertainties regarding the skin model and the modeling of damages.

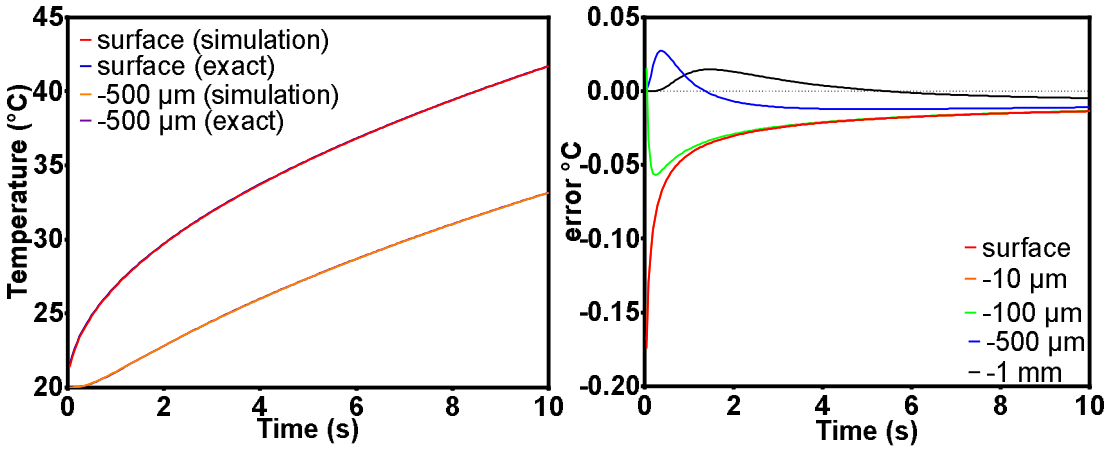

Fig 270 Comparison of the simulation with the exact analytical solution. The temporal resolution is $dt = 0.05\ s$. Left, the curves describing the temperature at the surface and at 500 µm depth are confounded. Right: the error defined by "results of the simulation" minus "analytical solution is plotted as a function of time.

What happens if the temporal resolution is reduced? In Fig 271, the temporal resolution of the simulation is decreased to dt = 0.5 s. The error is approximately multiplied by three. The error is close to one-tenth of a degree, which is excessive, so all the results presented in Chapter VI were made with a temporal resolution of 0.05 or 0.01 seconds.

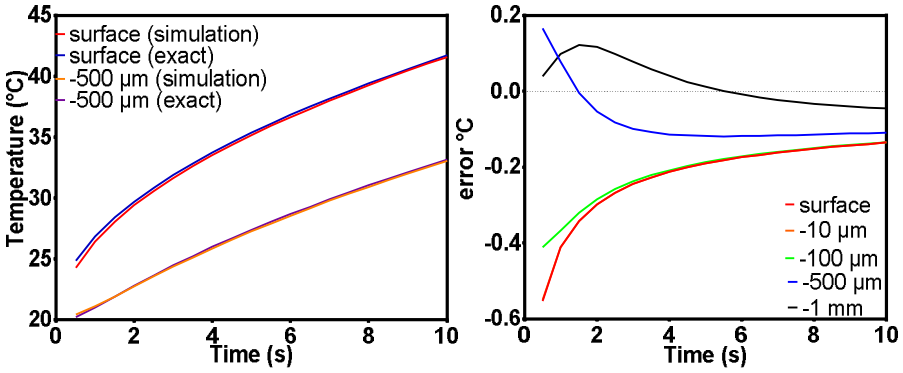

Fig 271 Comparison of the simulation with the exact analytical solution. The temporal resolution is $dt = 0.5\ s$.

What happens if the spatial resolution is reduced? The number of points defining the boundary is approximately divided by 20 in the next simulation (Fig 272). The temporal resolution is still 0.05 s.

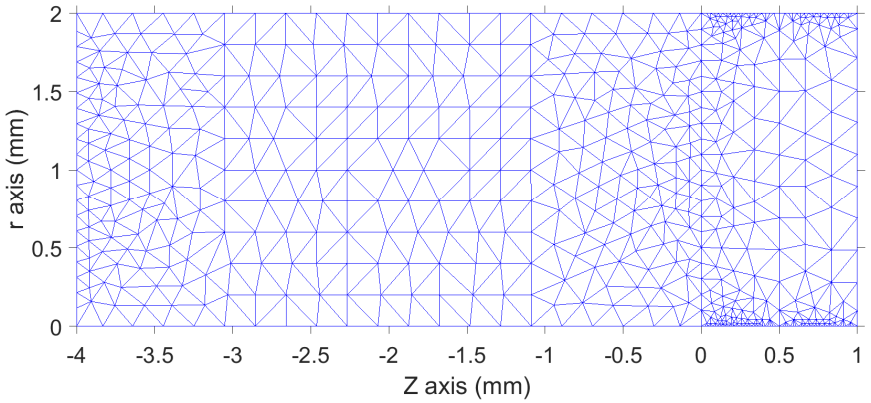

Fig 272 Mesh of the bar when the spatial resolution is reduced. $z = 1$, corresponds to $x = 0$, in the analytical expression. All boundaries are insulating except the boundary definded by $x = 0$ where the thermal flux is equal to 10,000 W / m².

Surprisingly, the error made is quite similar to that obtained with a more refined mesh (see Fig 273). It is recalled that in the finite element simulations any field is interpolated by polynomials of degree 2. Finally, this degree of interpolation enables to represent the temperature field with few exactly calculated points.

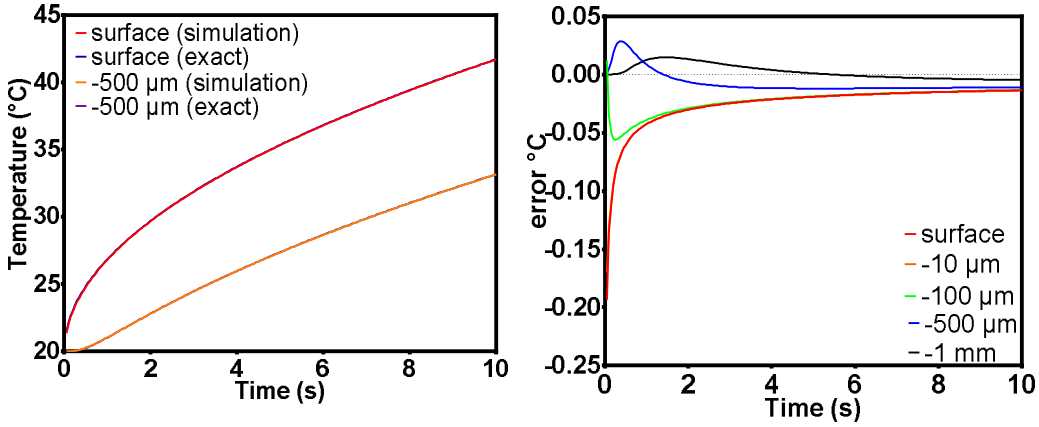

Fig 273 Comparison of the simulation with the exact analytical solution. $dt = 0.05\ s$. The spatial resolution has been decreased compared to that of Fig 270.

Appendix E The reliability of damage prediction

The section VI.1.6 describes thermal properties chosen to model the tumor. However, these values suffer from strong uncertainties. The aim of this section is to study the influence of the thermal properties on the damage field for a known temperature field.

Therefore, we will not only have to modify the thermal parameters of the model but also modify the incident plasma power so that the model can reproduce the observed experimental temperature field.

The four parameters considered are:

- The area of plasma-skin interface (parameter Θ)
- The value of blood perfusion inside the tumor ω_{tumor}
- The thermal conductivity of tumor tissue λ_{tumor}
- The value of A and Ea in the expression of damage function $\Omega = \int_0^t Aexp\left(-\frac{E_a}{RT}\right)dt$

We choose to study the behavior of the skin submitted to the fractioned treatment described in section VI.2.8 “fractioned treatment”. More particularly, we are interested in the heating scheme:

$$\{5\ s\ of\ heating\ due\ to\ plasma + 15\ s\ of\ cooling\}\ repeated\ during\ 20\ min$$

In such experimental situation, the transient thermal responses of the skin play a key role. The position and extent of damage are, therefore, more sensitive to parameter changes than continuous treatment.

As previously, there are two steps: first, we reproduce the temperature distribution in dead mice at thermal equilibrium by modifying q_{plasma}. Then the damage are calculated in the case of a living mouse submitted to fractionned treatment with the value of q_{plasma} found in the first step. All the results are compared to the damage field obtained after 1200 seconds of simulation (see section VI.2.8, page 244). Fig 274 shows damage map after 1200 seconds.

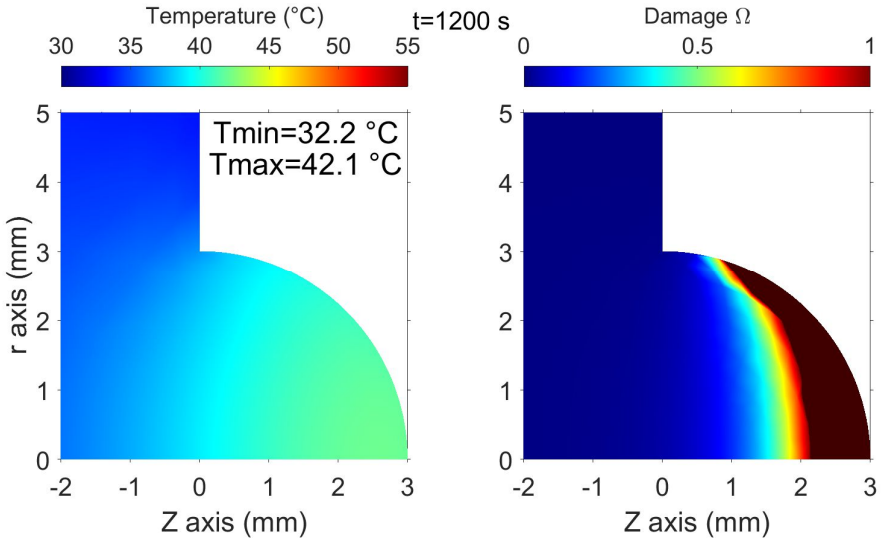

Fig 274 Field of temperature (left) and damage (right) for $q_{plasma} = 7000\ W.m^{-2}$. $\Theta = 80°$ At time t = 1200s, with fractional treatment (plasma on =5 s and cooling = 15 s).

E-1) Area of plasma-skin interface

It is recalled that, in this simulation, the area of the plasma-skin interface is the portion of the sphere defined by half-angle to the top Θ. Thus, the plasma-skin interface has an area:

$$S = 2\pi r^2(1 - \cos(\Theta))$$

What happens if the area of plasma-skin interaction decreases? Here, we consider that $\Theta = 40\,°$ (instead of $\Theta = 80\,°$). The value of the incident power needed has already been calculated to be ~ 23 000 W/m² (instead of 7000 W/m²). Fig 275 shows this result; this is a part of the curves shown in Fig 204 which has already been discussed in the main document. The temperature modeled in the center of the tumor (orange dotted curve) is consistent with the experimental values (error bar and black dots) measured by Chernets et al. [79].

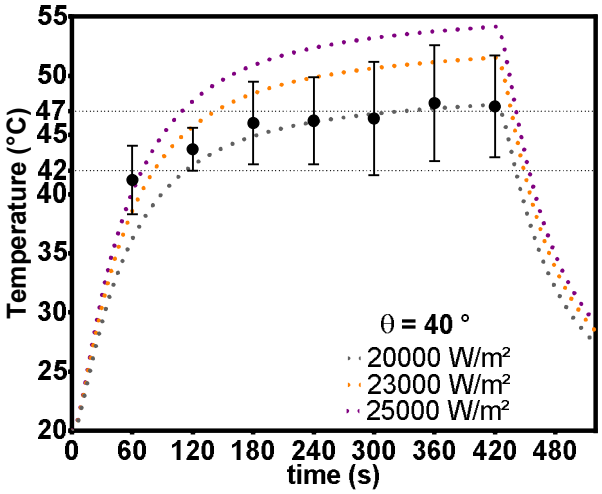

Fig 275 Temperature in the center of the tumor as a function of time. Comparison of the temperature modeled in the center of the tumor for three incident power (dotted line), with the experimental value measured by Chernets et al. [79]. postmortem mouse tumors.

The radial diffusion of heat causes a rapid decrease in temperature as a function of depth. Since the plasma-skin interface is smaller, the radial diffusion is more efficient to decrease the temperature as a function of depth and time.

The total incident thermal power is

$$P = \mathrm{q}_{\mathrm{plasma}} S \cong 304\,mW$$ (instead of 327 mW in the case 7000 W/m², $\Theta = 80°$)

The result of the simulation in "fractioned mode" (Fig 276), shows that the damage extends much more deeply in the case $\Theta = 40\,°$ than in the case $\Theta = 80\,°$. The damaged depth is around 1800 µm against 1000 µm for $\Theta = 80\,°$. Finally, it is found that the area of plasma-skin interaction has a strong influence on the depth of damage for the same distribution of temperature in the center of post-mortem tumor.

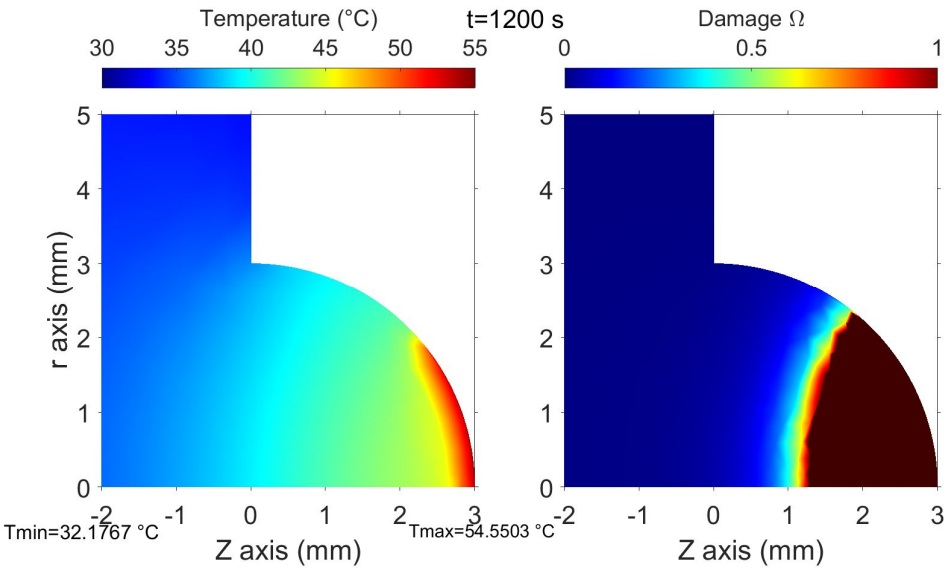

Fig 276 Field of temperature and damage for $q_{plasma} = 23\,000\,W.m^{-2}$ and $\Theta = 40°$. At time t = 1200s, with fractionned DBD protocol (plasma on =5 s + cooling = 15 s) during 20 min.

E-2) Blood perfusion of tumor

As explained in section VI.1.6 and according to [302], the perfusion rate of mouse tumor is between 0.01 and 0.22 ml/min/g. We will consider the two extreme values of perfusion rate: 0.01 and 0.22 ml/min/g which corresponds respectively to

$$\text{min:}\quad \omega_0 = 1.67 \times 10^{-4}\, ml.s^{-1}.ml^{-1}$$

$$\text{max:}\quad \omega_0 = 3.7 \times 10^{-3}\, ml.s^{-1}.ml^{-1}$$

It is recalled that in the simulations presented in Fig 274, blood perfusion is

$$\omega_0 = 1.33 \times 10^{-3}\, ml.s^{-1}.ml^{-1} \approx 0.08\ \text{ml.min}^{-1}.\text{g}^{-1}$$

Fig 277 and Fig 278 show that at the end of the treatment of 1200 s; the extension of damage is higher for the higher value of perfusion rate. At first glance, this is surprising. This is due to the fact that in the overheated volume, blood perfusion reach quickly zero because of vessels damages. The increase in tumor blood perfusion is not efficient to decrease the temperature of this part of the tumor.

In the part of the tumor that is not heated, an increase in blood perfusion also increase the mean temperature of the tissue (if tissues temperature is below the arterial temperature of 35 °C). Indeed, in the case of “max perfusion”, the minimum temperature of the tissue is 33.6 °C after 1200 seconds, whereas it is only 29.5 °C for “min perfusion”. This increased in average temperature is high enough to hide the positive effect of better blood perfusion on mild-heated area.

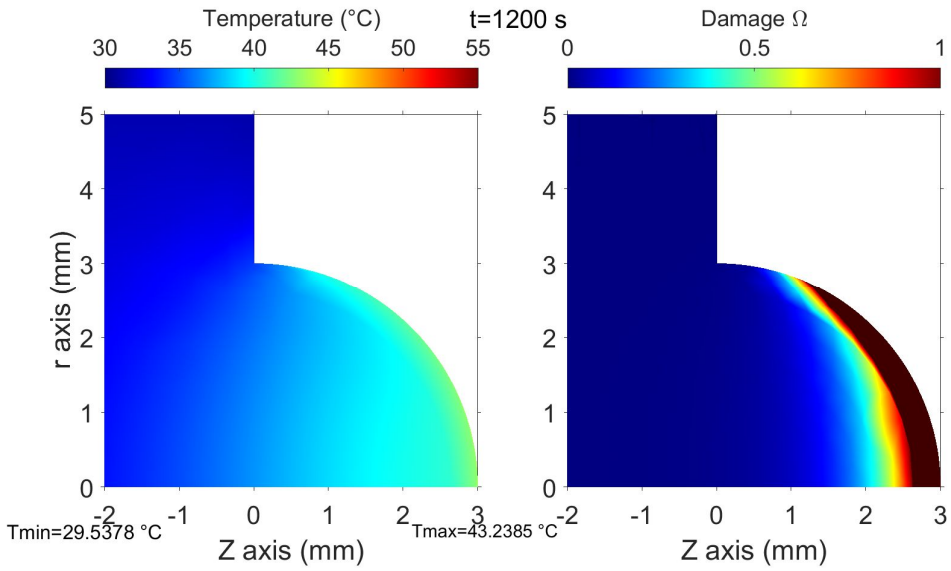

Fig 277 Field of temperature and damage for the blood perfusion $\omega_0 = 1.67 \times 10^{-4}\ ml.s^{-1}.ml^{-1}$ (which corresponds to the minimum)

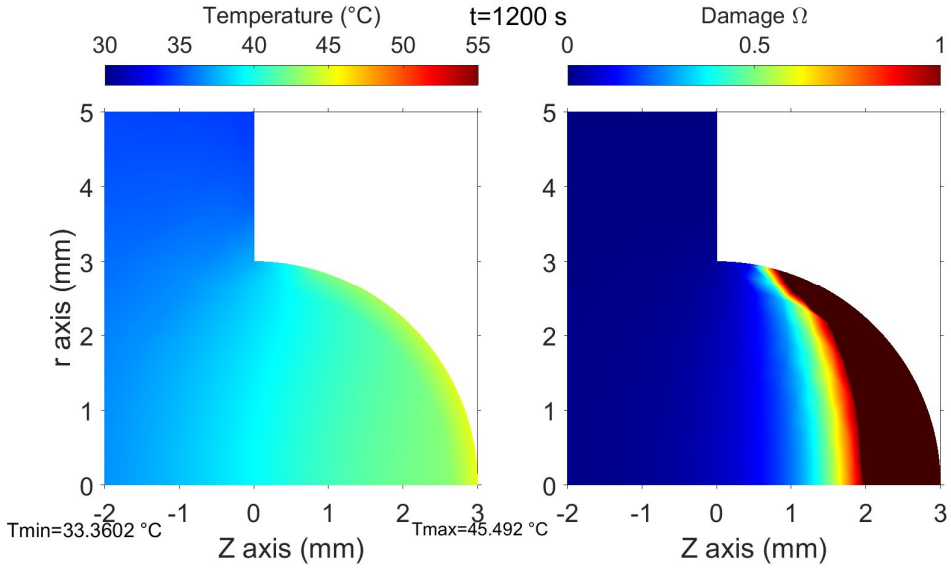

Fig 278 Field of temperature and damage for the blood perfusion $\omega_0 = 3.7 \times 10^{-3}\ ml.s^{-1}.ml^{-1}$ (which corresponds to the maximum)

Finally, the blood perfusion of the tumor has a strong influence on the extent of the damage. If we consider the effect of damage to blood vessels and the increase in average temperature induced by higher blood perfusion can lead to paradoxical effects: an increase in blood perfusion leads to more damages... In all case, the skin and the tumor are always deeply damaged whatever the blood perfusion. With more moderate heating, such a paradoxical effect does not occur, because the entire heated zone does not undergo enough damage to induce a cut in the blood circulation and we observe that an increase in blood flow reduces the damage.

E-3) Thermal conductivity

In this section, the thermal conductivity of the tumor tissue is modified compared to the value $\lambda_{tumor} = 0.561\ W.m^{-1}.K^{-1}$ used for the simulation whose damage are plotted in Fig 274

A change in conductivity considerably changes the value of center temperature obtained in post-mortem model. It is, therefore, necessary to find the q_{plasma} which reproduce the temperature in the center of the tumor.

This work is done for the two conductivities. $\lambda_{tumor} = 0.2\ W.m^{-1}.K^{-1}$, which represents the conductivity of the most insulating soft tissu, the fatty tissu and $\lambda_{tumor} = 0.7\ W.m^{-1}.K^{-1}$ which would be a soft tissu with the conductivity of water (higher than all known value of conductivity).

However for $\lambda_{tumor} = 0.2\ W.m^{-1}.K^{-1}$, it appears that it is impossible to find a good compromise which enables to reproduce the experimental data. Fig 279 show that it is impossible to obtain temperature value at t=60 s and a correct temperature for t= 5, 6 or 7 min whatever q_{plasma}.

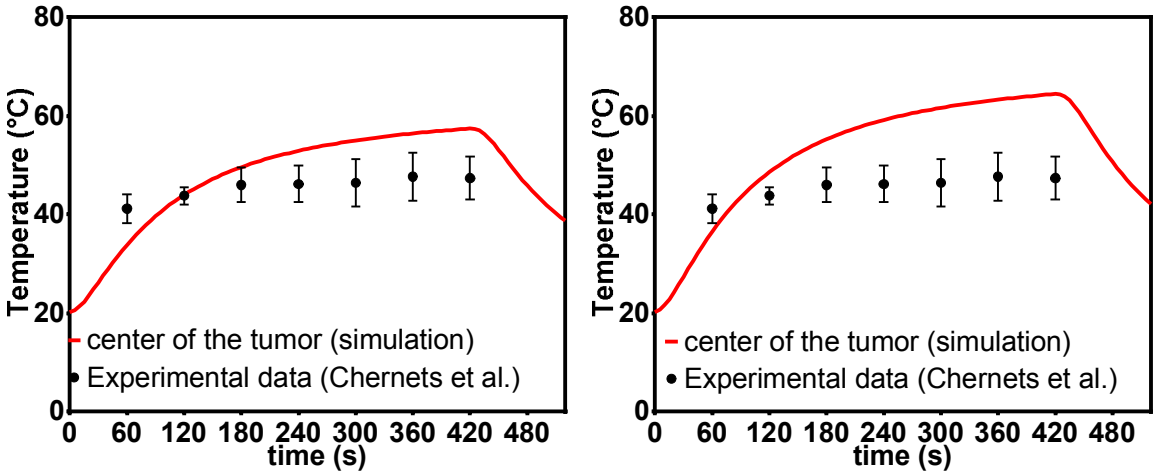

Fig 279 Temperature in the center of the tumor as a function of time for $q_{plasma} = 5000\ W/m^2$ (left) and $q_{plasma} = 6000\ W/m^2$ with $\lambda_{tumor} = 0.2\ W.m^{-1}.K^{-1}$.

An acceptable compromise can be obtained for $\lambda_{\mathrm{tumor}} \geq 0.4\ \mathrm{W.m^{-1}.K^{-1}}$. For $\lambda_{tumor} = 0.4\ \mathrm{W.m^{-1}.K^{-1}}$, $q_{plasma} = 6000\ W.m^{-2}$

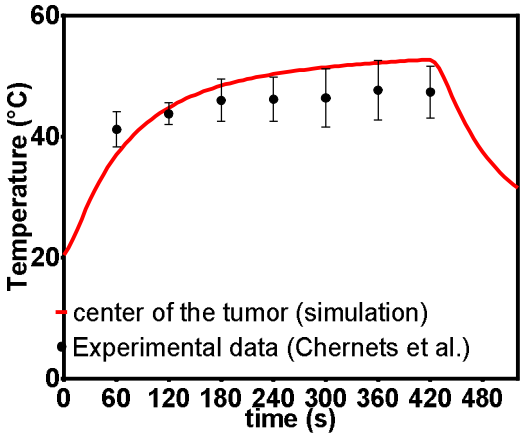

Fig 280 Temperature in the center of the tumor (r=0, z=0). $q_{plasma} = 6\,000\,W/m^2$ and $\lambda_{tumor} = 0.7\,W.m^{-1}.K^{-1}$.

Fig 281 shows the fields of damage after the fractionated treatment. The extent of damage observed is very similar to the case $\lambda_{\mathrm{tumor}} = 0.56\,\mathrm{W.m^{-1}.K^{-1}}$

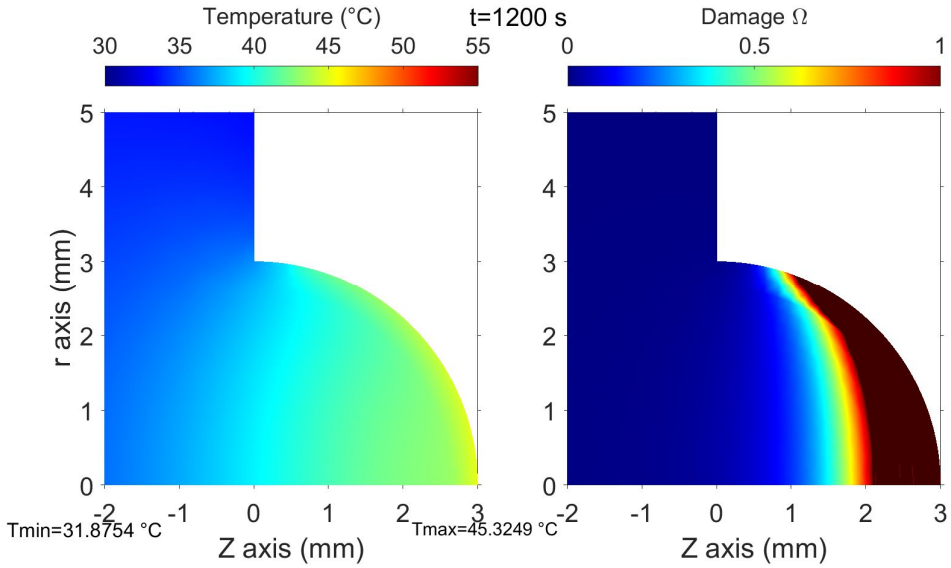

Fig 281 Field of temperature and damage for $\lambda_{tumor} = 0.4\,W.m^{-1}.K^{-1}$ and $q_{plasma} = 6000\,W.m^{-2}$.

For $\lambda_{tumor} = 0.7\,W.m^{-1}.K^{-1}$, the choice $q_{plasma} = 8\,000\,W.m^{-2}$ enables to reproduce the temperature in the center of the tumor (Fig 282).

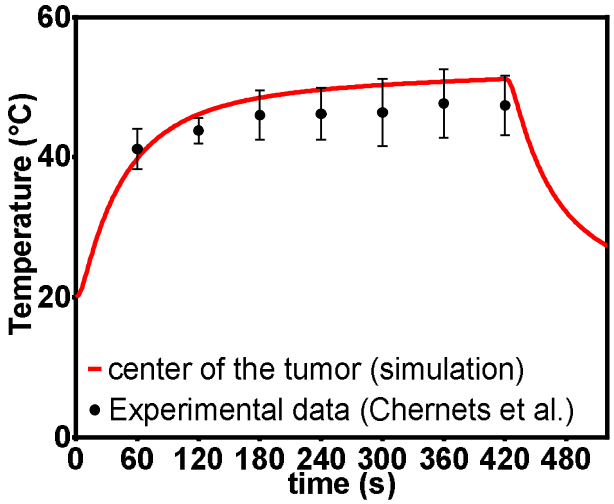

Fig 282 Temperature in the center of the tumor (r=0, z=0). $q_{plasma} = 8\,000\ W/m^2$ and $\lambda_{tumor} = 0.7\ W.m^{-1}.K^{-1}$.

Fig 283 shows that damages are very close to the case $\lambda_{tumor} = 0.56\ W.m^{-1}K^{-1}$ (Fig 274). Finally the value of the thermal conductivity of the tumor does not question the reliability of damage prediction since the qualitative result "at least a part of the tumor has been exposed to strong hyperthermia" remain true.

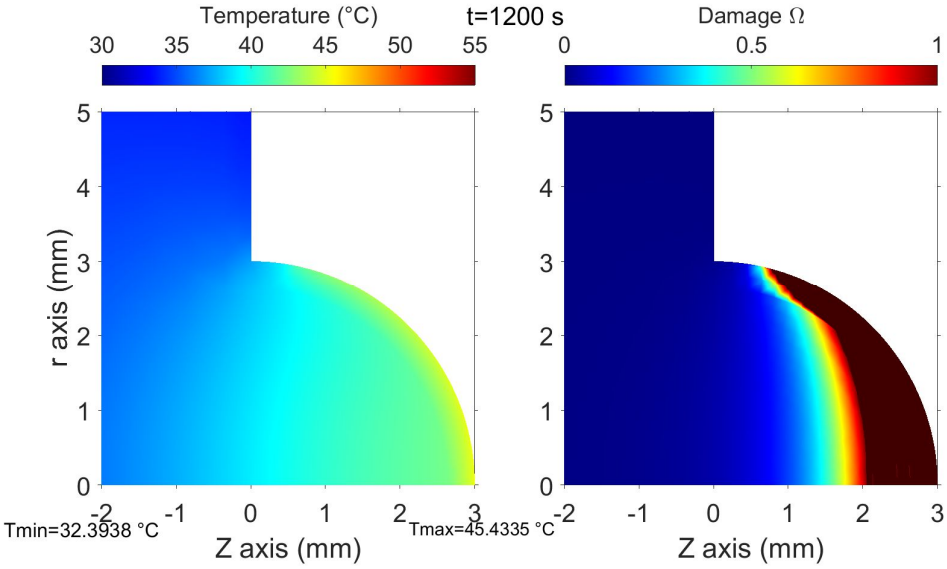

Fig 283 Field of temperature and damage for $\lambda_{tumor} = 0.7\ W.m^{-1}.K^{-1}$ and $q_{plasma} = 8000\ W.m^{-2}$. At time t = 1200s, with fractioned treatment protocole (plasma on =5 s + cooling = 15 s).

E-4) Expression of thermal damages

The expression of damage function takes the form $\Omega = \int_0^t Aexp\left(-\frac{E_a}{RT}\right) dt$, where Ea is an energy of activation, and A a factor in s^{-1}. The literature proposes several values of the coefficients A and Ea. The majority of studies involve human, rat or pig skin. Different coefficients are sometimes defined according to the temperature range used, the skin layer studied (dermis or epidermis). Relatively few studies are available. The values obtained are to be considered with caution. It may happen that the coefficients obtained

vary according to the method of heating the skin and the position of the heated zone. The book ([210], page 48) review 15 differents values of A and Ea. Six of them were selected since they correspond to the temperature range encountered in the center of mouse tumor. Four additional values of (Ea, A) were considered ([215]).The data are grouped in Table 26.

Table 26 Coefficients are defining damages functions. The first pair of coefficient dam1 is used in all other simulations outside this section. The data are valid for human skin and tissues except for dam 3 and dam 7, which concern rat and pig skin respectively. No mouse-specific data were found.

Index	Ea (J/mol)	A (s^{-1})	Reference	Comment
dam1	5.064×1e5	2.984×1e80	[274]	Used in all other simulations of the thesis
dam2	4.6×1e5	2.86×1e69	[210]	Dermis, whole range of T,
dam3	3.06×1e5	1.606×1e45	[210]	Rat skin collagen, birefringence 40-60 °C
dam4	4.6×1e5	1.43×1e72	[210]	Epidermis, whole range of T
dam5	6.27×1e5	3.1×1e98	[210]	Dermis, $T \leq 50$
dam6	6.69×1e5	9.389×1e104	[210]	Dermis $50 \leq T \leq 60$
dam7	3.39×1e5	4.11×1e53	[210]	Porcine epidermis, $48 \leq T \leq 57$
dam8	55 000×8.31	1.43×1e72	[215]	Human epidermis
dam9	55 000×8.31	2.86×1e69	[215]	Human dermis
dam10	93 535×8.31	2.185×1e124	[215]	$44 \leq T \leq 50$ human epidermis
	39 109×8.31	1.823×1e51		$50 \leq T$ human epidermis
dam11	50 000×8.31	4.32×1e64	[215]	$44 \leq T \leq 50$ human dermis
	80 000×8.31	9.39×1e104		$50 \leq T \leq 60$ human dermis

One could be discouraged by such a disparity, which enables to predict everything and its opposite. Fortunately, we have experimental data. The data acquired during the treatments performed with the non-refrigerated multijet are used. It is recalled that the incident power $q_{plasma} = 7250\ W.m^{-2}$ was chosen so that the simulation reproduces the surface temperature actually observed. By repeating these simulations with the pairs of values proposed in the Table 26; we can see if there are major inconsistencies between the severity of damage predicted and observed. Table 27 gives the qualitative result of these simulations. Three pairs of values yield results consistent with experimental observations. All other simulations predict a total absence of damage after 5 min of treatment.

Table 27 Summary of results obtain during the simulation obtain during treatment with the nonrefrigerated multi-jet ($q_{plasma} = 7250\ W.m^{-2}$, $\Theta = 50\ °$)

Index	Simulation of non-refrigerated multi-channels plasma jet
dam1	See section VI.2.2.1, consistent
dam2	No damage at all, after 5 min
dam3	No damage at all, after 5 min
dam4	No damage at all, after 5 min
dam5	No damage at all, after 5 min
dam6	No damage at all, after 5 min
dam7	No damage at all, after 5 min
dam8	consistent with damages observed
dam9	No damage at all, after 5 min
dam10	consistent with damages observed
dam11	No damage at all, after 5 min

This can be explained by the fact that in most cases the damage function is defined in a phenomenological way. More often, what is measured is the time necessary to produce

burns of the first, second, or third degree. Since the dermis and epidermis are thicker (at least 10 times in humans than in mouse); the exposure time for observing significant damage is more delayed in human than in mouse. Not only, the thickness that must be overcome by thermal diffusion is thicker, but blood perfusion removes more heat in a bigger volume and slows down the heating. Consequently, the values (A, Ea) tend to simulate less severe damage than in the case of faster heating.

These coefficients lead to an underestimation of Ω because the thinner skin of mouse has a faster response to thermal disturbances. Moreover, the coefficients that describe damage to human epidermis are more adapted than those dealing with human dermis since, in this situation, the error induced by the delay is smaller. This explains why simulation based on dam8 and dam10 functions give a result consistent with the observation.

Dam7 function describes the behavior of epidermis at a higher temperature ($48 \leq T \leq 57$) than the one observed. Since the program cancels the increase of damage for out-of-range temperature; it is logical to fail in the prediction of damages (even if this function describes the epidermis).

dam4 function describes the thermal response of epidermis in the context of flash fire. Torvi et al. also observe that this precise function gives less damage and is inconsistent[139] with others damages functions [215].

Dam1 function regards the damage induced by RF heating [274], the propagation of thermal disturbances is not slowed down by the skin. Consequently, it seems logical that such coefficients correctly predicted the nature of the damage observed in the experiment.

The results of the simulation of an intermittent DBD treatment (plasma on = 5 s, cooling by natural convection = 15 s) are shown in Fig 284 and Fig 285, respectively for the damages functions dam8 and dam10.

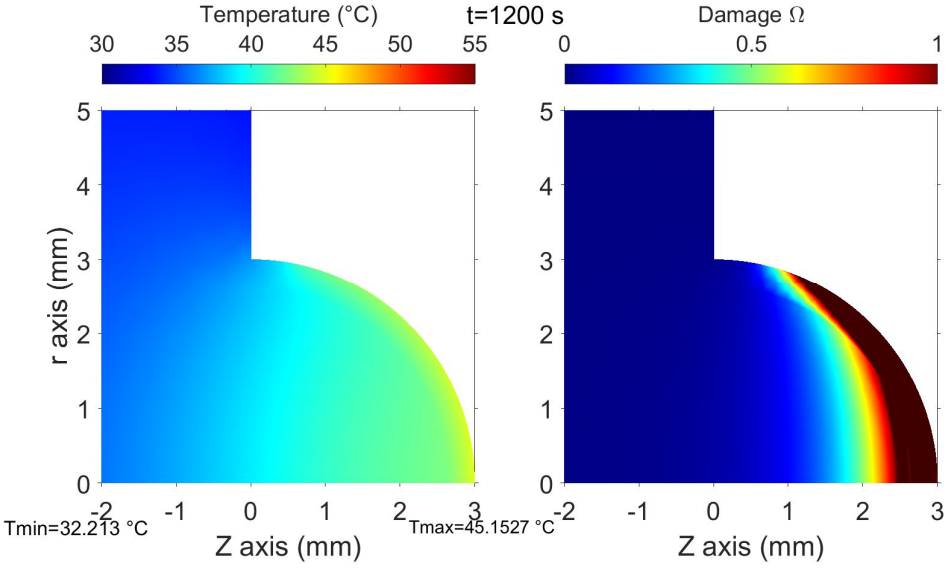

Fig 284 Field of temperature and damage for damage function dam8. At t = 1200s, with "intermittent DBD protocol (plasma on =5 s + cooling = 15 s).

[139] I was unable, however, to find the paper which contains the original data (Mehta A K, Wong F C. Measurement of Flammability and Burn Potential of Fabrics. Full Report from Rules Research Laboratory, 1973).

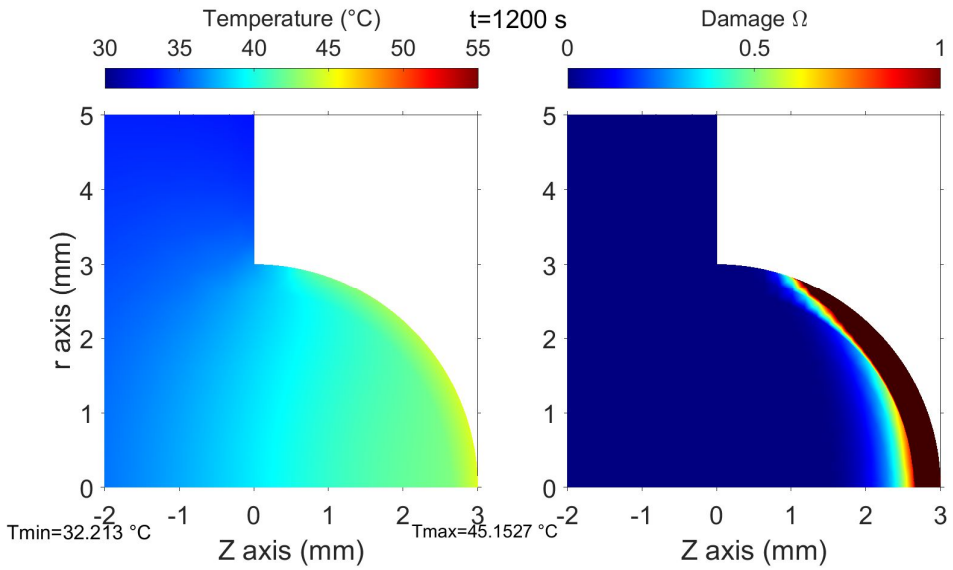

Fig 285 Field of temperature and damage for damage function dam10. At t = 1200s, with "intermittent DBD protocole (plasma on =5 s + cooling = 15 s).

Damage is slightly deeper for dam8 than dam10. The extent of damage predicted by dam1 (Fig 274) is very similar to that of dam8. In the three cases considered, the epidermis and the dermis are entirely destroyed. In all cases, subcutaneous fat and the external part of the tumor.

To summarize, changing the damage functions does not question the reliability of the results of the simulation. A choice of damage function compatible with our results leads to predict that the protocol of fractionated treatment completely destroys the skin of the mouse and a part of the tumor.

Whatever the parameter considered, the simulation of "intermittent DBD" always predicts damage that completely destroys the skin. This could be a bias since inflammation, and immune reactions are triggered by the thermal damage (see the references and the discussion on thermal effects in the context of antitumor studies, concluding Chapter VI). In all realistic cases, significant damage also occurs also in the upper layers of the tumor.

Appendix F Effective tissue thermal conductivity

aThe convective transport of heat could be modeled by considering an effective thermal conductivity value λeff which depends linearly on blood perfusion. This model is the subject of a recent paper, and the relevance of this model is not fully established. Further informations can be found in the paper [268] and [270].

According to the work of Kolios et al. [269]

$\lambda_{eff} = \lambda_{tumor}(1 + \alpha\omega)$ with $\alpha = 0.12$ (ml/100g/min)$^{-1}$, which gives $\alpha = 720$ (ml/g/s)$^{-1}$.

The following simulation was done with the model described in section VI.2.2.1 (page 210) i.e., model of the non-refrigerated multijet. The thermal conductivity is modified according to the expression of Kolios et al. [269]. Energy exchanges due to blood circulation are disabled since the effective conductivity is another tool to take into account the convective transfer of heat due to blood. The damage to blood vessels is taken into account. In this simulation $q_{plasma} = 7250\ W.m^{-2}$. This model of thermal conductivity increases the diffusion of heat in skin and tumor leading to a smaller temperature than observed and successfully modeled with the parameter $q_{plasma} = 7250\ W.m^{-2}$ in section VI.2.2.1.

With such a model it would be necessary to increase the incidental power to obtain a simulation consistent with experiments. It could be done without difficulties. The results given by this model does not really differ fundamentally, except that the parameters characterizing convective transfer due to blood perfusion are less known and questionable...

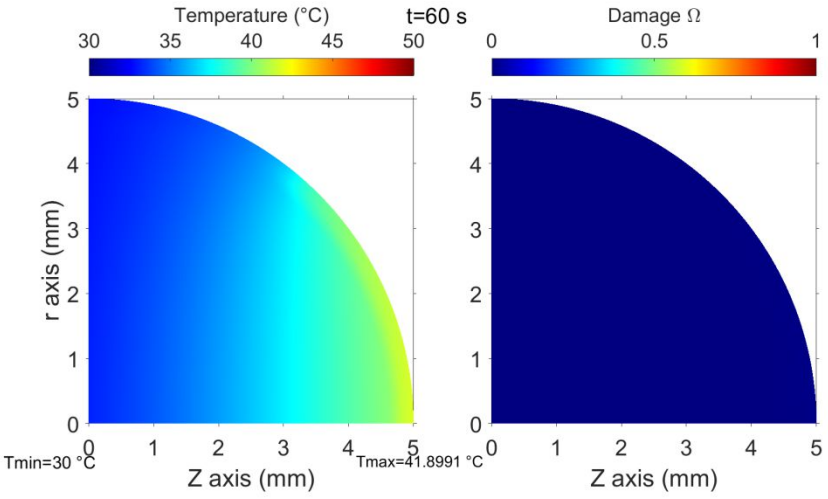

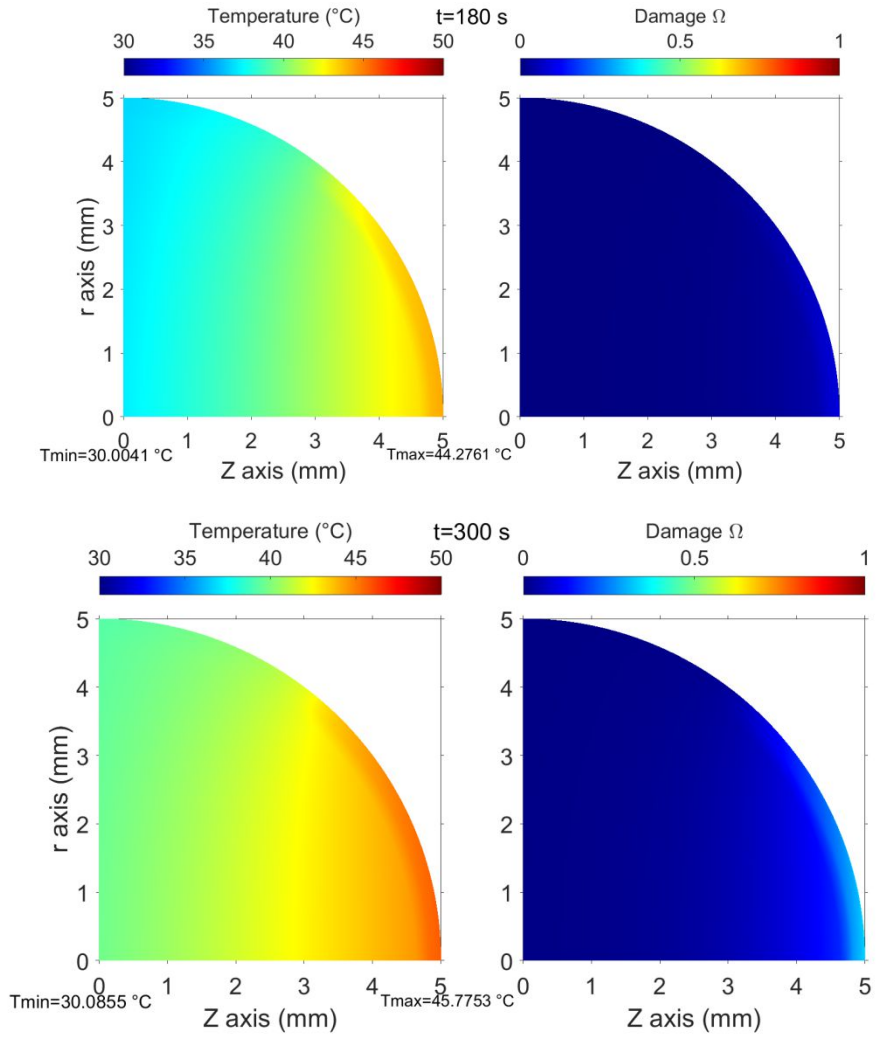

Fig 286 Damage and temperature map after one, three or five minutes of treatments. $q_{plasma} = 7250\ W.m^{-2}$, $\theta = 80°$.

Appendix G Which parameters play in the cooling of the skin after treatment?

The purpose of this part is to compare the results concerning the cooling of the treated surface with the result given by the simulations. The section 0 gives an example of this kind of measurements. Several infrared images of the tumor are acquired at different times during the cooling of one tumor. For each image, the maximum temperature reached at the surface of the tumor is recorded. Table 24 shows three pictures of a mouse during the cooling, which follows a 6-min exposure to the refrigerated plasma-jet. The three images have the same orientation. The maximum temperature is visible in the third column. This temperature will be compared with the maximum surface temperature given by the simulation (the temperature of the point defined by r = 0 and z = 5 mm).

Table 28 Infrared picture of a tumor treated during 6 min with the refrigerated multi-channel plasma jet. The picture of the second line is acquired 8 s after that of the first line. Picture of the third, 12 seconds later.

Time	Infrared image	Maximum temperature
The first image defines the time t =0 s	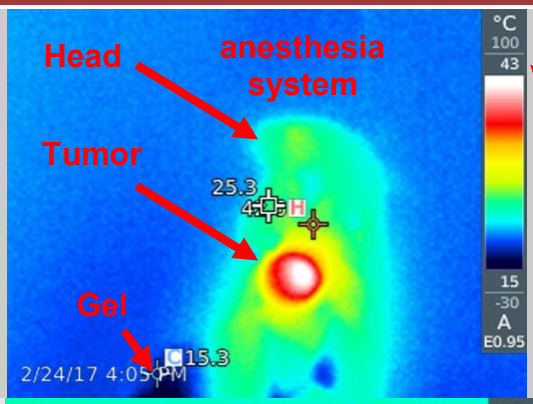	**43** °C
t = 8 s	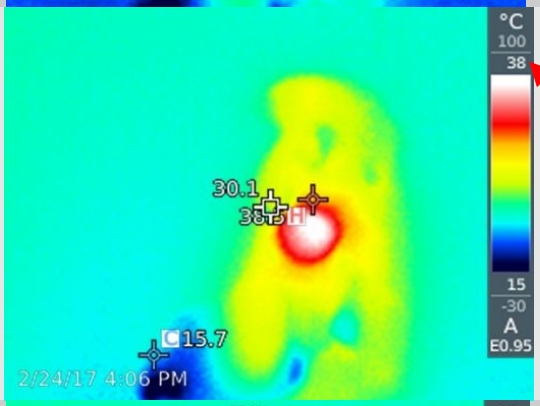	**38.5** °C
t = 12 s	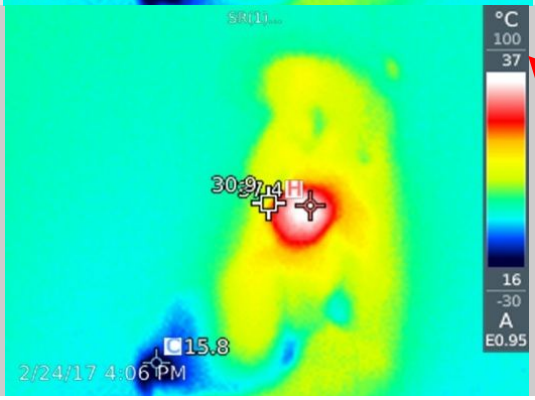	**37.4** °C

Unfortunately, this type of use of infrared images was not foreseen at the time of the experiment. The infrared images were used to attest that the tissues were not subjected to hyperthermia. Consequently, there is not many usable data because it is necessary to have at least two successive pictures of the tumor. Moreover, there is uncertainty regarding the time between the end of plasma-exposure and the acquisition of the first picture. This time is of the order of five seconds or less, but, without the exact value, it is not possible to use the first image. Only the time difference between two images (provided by the image metadata) can be exploited. Ideally, it would have been necessary to film the cooling of the skin, with a scale of length in the field of observation.

Fig 184 shows the maximum temperature as a function of time for several mice. The time of the first image defines the time $t = 0\ s$. It can be seen that among the measurements which start from the same temperature at $t = 0$ gives dispersed measurements after cooling. Several factors could explain this dispersion:

- Differences in the distributions of temperature $T(\overrightarrow{\boldsymbol{M}})$ from one mouse to another due to the inhomegeity of the treatment.
- Differences in biological parameters of the tumor from one mouse to another $\omega_{tumor}, T_{blood}$.
- Differences in thermal environment, enhancement of the natural convection...

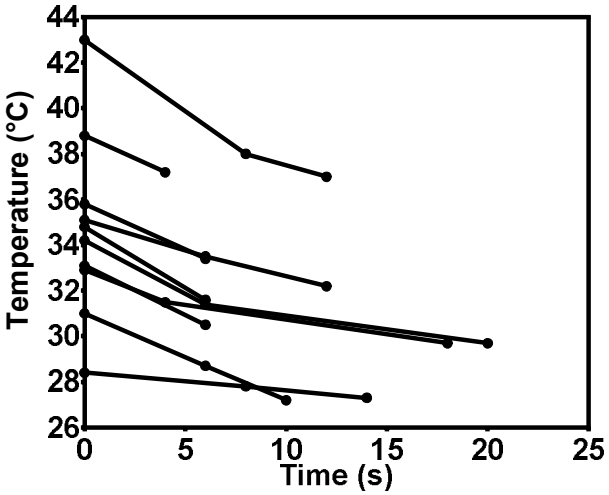

Fig 287 Maximum temperature of the surface of the skin as a function of time. The pictures were acquired during the in-vivo experiments described in section 0. These experiments concern the cooling of the skin after an exposure of 6 min to the refrigerated multichannel plasma-jet.

Fig 184 shows that the speed of cooling is of the order of several °C for 5 s when T>30 °C. Now, we compare this observation with the simulations. The first point (at time t=0 s in Fig 184) of each set of measurements is positioned on the curve which represents the temperature as a function of time. The next step is to see if the points of the same measurement group are distributed on the simulated curve or not. It would be possible to quantify the proximity of the experimental points with the simulated curve. But here we will only proceed with a purely graphic approach, the results being rather eloquent. Moreover, the lack of experimental points and the uncertainty associated with the latter would make this type of quantification unnecessary in our experimental situation.

For the sake of clarity:

- The experimental data are represented by different sets of dots (from A to J). Each set corresponds to the data acquired on one mouse.
- The results of the simulation are represented by a continuous line.
- The first point of each set (from A to J) is positioned on the red curve called “last fit”. Then, the other points are positioned with respect to the first point according to the values shown in Fig 184. The simulation producing this curve will be described later. The experimental points should be replaced on each curve to visualize in what extent the simulation is consistent with experimental results. However, this would make the figures illegible. Consequently, the experimental data are only represented with the temporals offsets associated with the curve “last-fit”. For the needs of the present discussion, it is sufficient.

Fig 288 compare the cooling of the skin predicted by the simulations of the multichannel plasma jet and the experimental results. It is recalled that, in this case, the source is <u>not</u> refrigerated (section VI.2.2). The simulations are exactly the same than in the subsections VI.2.2.1 and VI.2.2.2. The area of the plasma-skin interface is defined by the angle $\Theta = 50\,°$. The arterial temperature of the blood is assumed to be equal to 35°C. The two simulations regard the two alternatives envisaged (i, black) heat transfer is constant and equal to $7250\ W.m^{-2}$, the gas is at $T = Tamb = 20\,°C$ (ii, blue) heat transfer at the interface is due to the convection of Helium at $T = 55\,°C$. It may seem surprising that the rate of cooling is different for these two simulations even though the same surface temperature is reached in both cases. In fact, the field of temperature is imposed by the value of the heat transfer at the interface. Heat transfer imposed in the simulation “hot helium” has this magnitude:

$$q_{due\ to\ hot\ He} \approx 203 \times (55 - 45) = 2030\ W.m^{-2}$$

Since this value is lower than $q_{plasma} = 7250\ W.m^{-2}$. The gradient of temperature which ensure the flux imposed at the interfce is less abrupt for “hot helium” simulation. The temperature is higher below the surface, resulting in a slower cooling rate. It appears that the rate of cooling predicted by the simulations is inconsistent with experimental data. In the simulations, the cooling is too slow (several tens of seconds to lose 2 °C). In the next paragraph, we see what happens, when we used the refrigerated device.

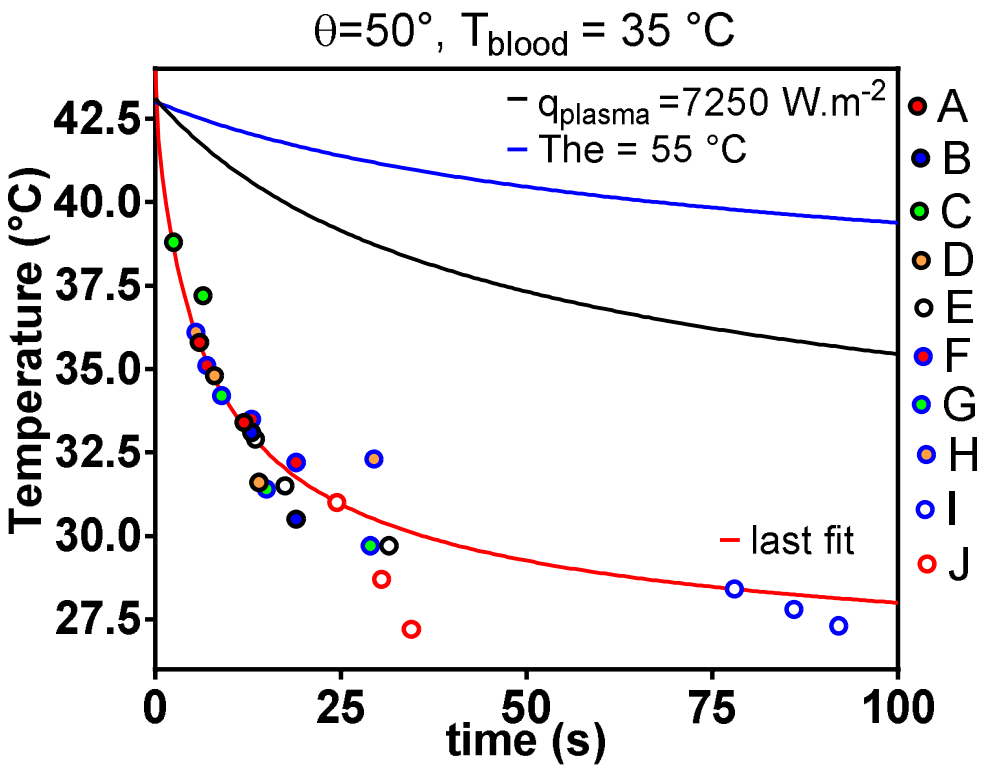

Fig 288 Cooling of the skin as a function of time. Experimental data are represented by the dots from A to J. Lines represents the simulations. Black curve corresponds to the cooling of the surface after treatment by the multichannel jet simulated in the section VI.2.2.1 (heat transfer is a constant $q_{plasma} = 7250\, W.m^{-2}$). Blue curve is the cooling of the surface after a treatment by the multichannel jet simulated in the section VI.2.2.2 (heat transfer is due to the convection of Helium at 55 °C). The blood has an arterial temperature $T_{blood} = 35\,°C$. Plasma-skin interface has an area defined by the half angle to the top $\Theta = 50$ °.. The cooling predicted by the blue and black curve is too slow to be consistent with the experimentales data.

Fig 289 describes the cooling of the surface when several parameters are modified. The following points are analyzed:

- The speed of cooling when the device is refrigerated or not.
- The effect of a 10% increase in the heat transfer coefficient due to the natural convection. Indeed, there might be a difference between the model of natural convection and the reality. It may be that a slight increase in the heat transfer coefficient h_{conv} could increase therate of cooling so that the simulation would be consistent with the experiment.
- The effect of changes in the value of the arterial temperature of the blood. It is recalled that the contribution of blood perfusion in heat exchanges takes the form: $q_{perf} = \omega_{tissu}\rho_{blood}c_{blood}(T - T_a)\ in\ W.m^{-3}$. A change in the value of T_a, the arterial temperature enables to emulate a higher perfusion rate or a lower blood temperature. T_a is modeled in the interval [25°C; 35 °C]. For instance, a volume of tissue at 40 ° C will exchange 3 times more energy when the blood is modeled at 25 ° C than when modeled at 35 ° C. It is unlikely that the temperature of the blood entering the tissue is only 25 ° C, although the blood may be somewhat cooled before reaching the tumor and the fact that the mice sometimes seemed to be close to the hypothermia. On the other hand, it is conceivable that the rate of perfusion is greater than that which has been modeled so far (see the section Physical properties of living tissues VI.1.6 and the Table 23).

It appears that the modification of these parameters does not significantly modify the temperature of the skin during the treatment. It is recalled that in the case of the refrigerated device, the temperature of the skin is simulated by the convection of helium at temperature

$$T_{He}(t) = 3.5\sqrt{t} - 31\ °C \qquad \text{for} \quad 3.5\sqrt{t} - 31\ °C \leq 55\ °C$$

$$T_{He}(t) = 55\ °C \qquad \text{for} \quad 3.5\sqrt{t} - 31\ °C > 55\ °C$$

The fives simulations of the refrigerated devices verify the experimental criteria:

- At the beginning, the temperature of the skin is between 8 and 10 °C.
- The mean temperature is 17 °C after 3 min.
- The mean temperature is 31 °C after 6 min.

It is sufficient to imagine that the plasma source operates a little longer than 6 min to obtain higher temperatures (~45 °C). The curve which corresponds to the cooling of the point of coordinates (r = 0, z = 5) is recorded as soon as the treatment is stopped. The skin cools in ambient air (natural convection). The cooling is plotted for the temperatures below 43 °C.

Fig 289 includes the three same curves that the Fig 288. Black and blue curves represent the cooling after treatment by the non-refrigerated plasma-jet. The red curve is associated with a simulation presented in the last part of this section.This curve gives the time offset of the experimental points.

The five other curves correspond to the simulations of the refrigerated plasma-jet. The black dotted lines show the cooling under the conditions that were studied in the section VI.2.3 (refrigerated multijet, blood temperature at 35 ° C, no change in natural convection). At first glance, it is surprising that the cooling rate is faster than that of the blue curve. This is caused by the fact that the steady state is not reached when the plasma is switched off. Consequently, even if the surface temperature is the same, the underlying tissues are colder when treated by the refrigerated jet. This increases the cooling rate of the surface.

Except for the convection, the pink curve is calculated in the same conditions than the black dotted (refrigerated multijet, blood temperature at 35 °C). The efficiency of natural convection (NC) is increased by 10%; to that end, heat transfer coefficient is multiplied by 1.1.

$$\mathrm{q_{conv}} = 1.1 \times \mathrm{h(Ts - Tair)} = 1.1 \times 5.21 \times (\mathrm{Ts - Tair})^{1.188}\ \mathrm{W.m^{-2}}$$

It appears that the black dotted line curve is above the pink one. This is consistent. However, the influence on the cooling rate is quite low. It can be noted that the cooling rate predicted by these two curves is still inconsistent with the experimental data. The natural convection rate would have to be several orders of magnitude higher than the value calculated so far to obtain a result consistent with the experiment. This hypothesis is not realistic despite the assumptions made for the calculation of the natural convection rate. The reality is that the surface is not cooled by the exterior for the essentials, but from the inside with heat transfer caused by blood perfusion and conduction.

The three last curves (orange line, dotted green, blue dotted) show what happens when the arterial temperature is changed. These three curves are below the previous ones, which is quite coherent. By decreasing the blood temperature / increasing the perfusion rate, the amount of energy removed from the surface is increased. Unfortunately, the rate of cooling is still incompatible with the experimental results (in particular for the points 31 and 35 ° C). And yet, assuming that the blood is 10 ° C colder is a rather

extreme hypothesis. To summarize, none of the three parameters mentioned above can be used to simulate the rate of cooling of tumors satisfactorily. Even when combined (cold blood + increased convection + refrigerated device).

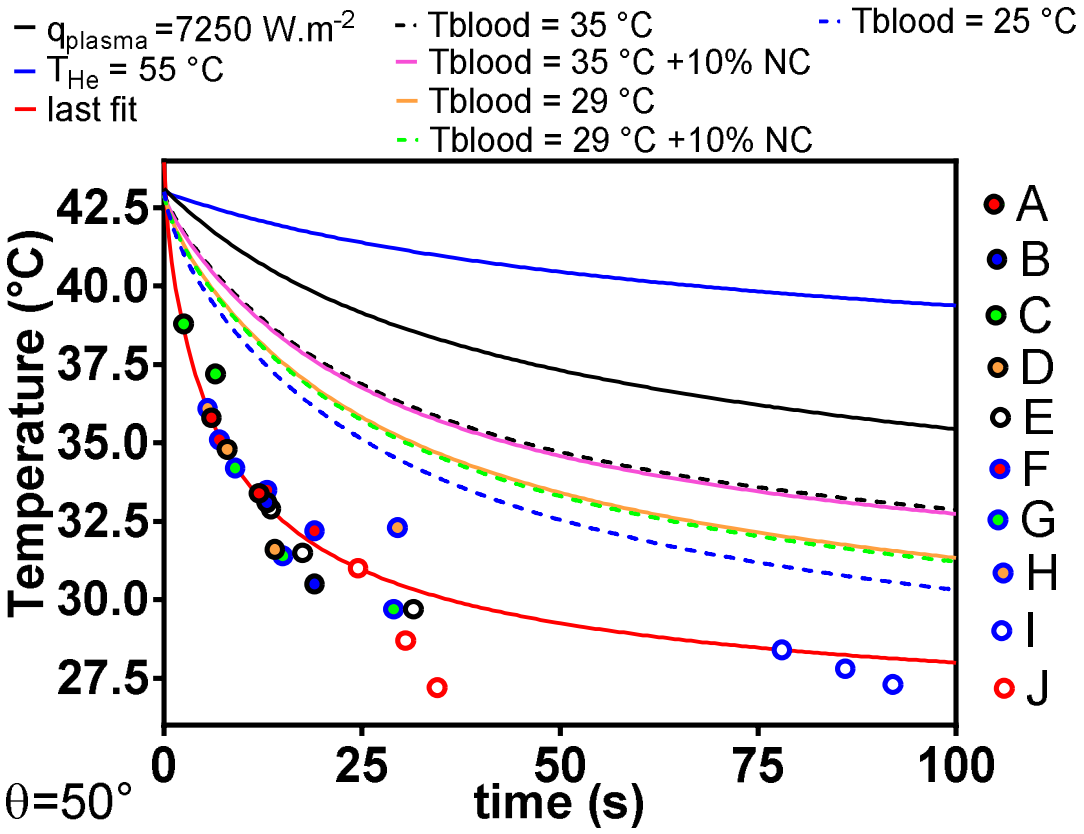

Fig 289 Cooling of the skin as a function of time. Non-refrigerated device: continuous black and blue line. These two curves, as well as the red curve, are the same in the previous figure (see Fig 288 for a detailed description). Refrigerated device: dotted black line, dotted blue line, dotted green line, orange and pink line. The arterial temperature of the blood is indicated in the legends of the curves. The value of the heat transfer coefficient was increased by 10% in the case of pink and green dotted curves. $\Theta = 50\,°$. Experimental data are represented by the dots from A to J. Lines represent the simulations

Until then we have assumed that the surface undergoing the thermal flux is defined by the half angle at the apex $\Theta = 50\,°$, which defined a circle of diameter $d \cong 8.7\,mm$, and area $S = 2\pi r^2(1-\cos(\Theta)) \cong 56\,mm^2$ on the surface of the sphere.

This value of Θ is of the order of magnitude of the size covered by the plasma (according to the pictures). On the other hand, nothing ensures that the heat transfer is efficient over the totality of this portion of the sphere. The distribution of filaments striking the surface is also not known, but it can be assumed that the density of filaments is greater directly below the gas stream than at the side. The area of heat transfer is likely smaller. Θ is divided by two in the following paragraphs.

The procedure is exactly the same as described in the sections VI.2.2.2 and VI.2.3. First, the temperature of helium gas is found. The temperature and the simulated damage must verify the following conditions:

- Skin temperature after treatment of 3 or 5 min was around 45-48 °C.
- Treatment of one min gave no damages.
- One treatment of three min gave no damages, but the repetition of this treatment at two days intervals gave damages after two or three treatments.

- Treatment of 5 min systematically gave damages.

The value $T_{He} = 64\,°C$ enables to verify all of theses conditions. Fig 290 proves the previous assertions. $T_{He} = 65\,°C$ is also suitable. On the other hand, a temperature of 66°C produces too much damage.

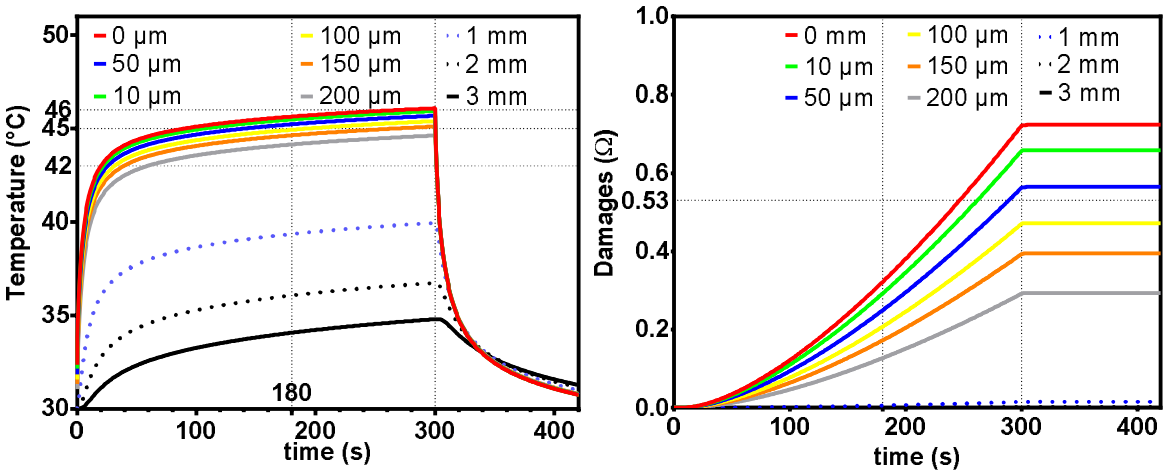

Fig 290 Temperature and damage as a function of time, for several depths under the plasma-skin interface. This device is not refrigerated. $\Theta = 25\,°$, $T_{He} = 64\,°C$. The red curve represents the surface temperature of the tumor. The temperatures reached at 3 min and 5 min are compatible with the experimental observations. The level of damage caused at 50 µm of depth (blue curve) makes it possible to conclude that one third of the thickness of the dermis is severely damaged.

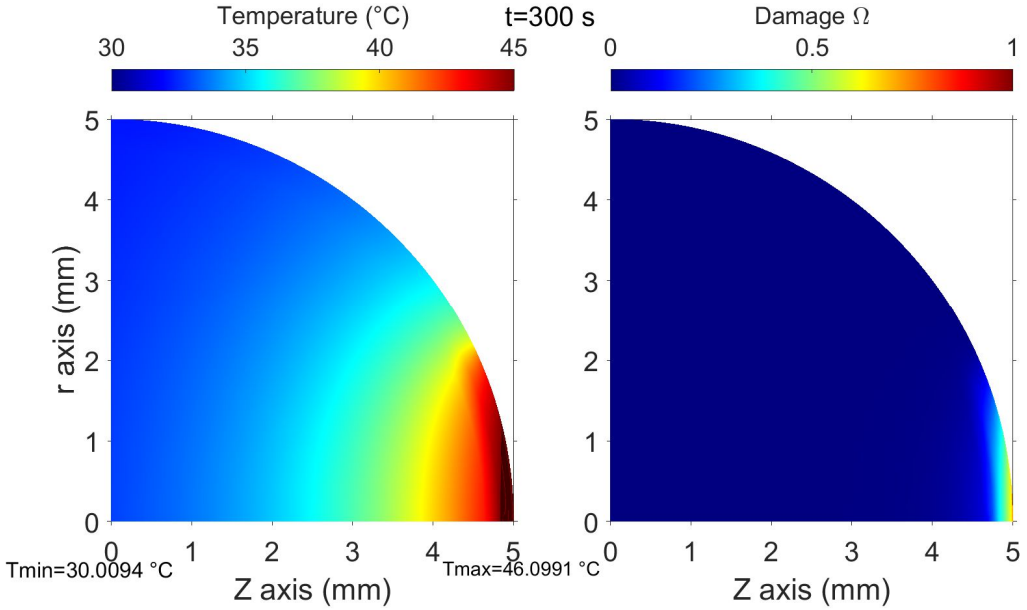

Fig 291 Field of temperature and damage at the time t= 5 min. This device is not refrigerated. $\Theta = 25\,°$, $T_{He} = 64\,°C$. The level of damage obtained is consistent with the experimental observations.

As described in the section VI.2.3, the choice of a function, $T_{He}(t)$, that describes the temperature of the gas over time; enables to reproduce the temperature of the skin. The following three criteria must be verified.

- At the beginning, the temperature of the skin is between 8 and 10 °C.
- The mean temperature is 17 °C after 3 min.

- The mean temperature is 31 °C after 6 min.

The red curve of Fig 292 proves that these criteria are checked by the function:

$$T_{He}(t) = -24 + \frac{t}{550}\left(64 - (-24)\right) \text{°C} \qquad \text{for} \quad t \leq 550$$

$$T_{He}(t) = 64 \text{°C} \qquad \text{for} \quad t \geq 550$$

where t is expressed in seconde and T_{He} in °C. Note that a linear function has been chosen. The choice of a function in $A\sqrt{t} + B$ do not provide a simulation that respects the previous criteria (deviation of several °C regarding the surface temperature). Even if the dependence in $\sqrt{t}$ has more physical meaning (despite the severe limitations of this model), it is desirable to choose the best fit of the experimental data.

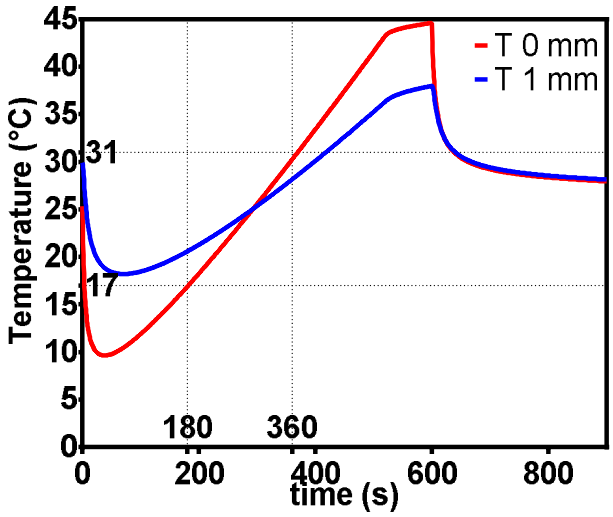

Fig 292 Red: temperature of the point (r=0, z=5 mm), at the surface of the skin. Blue: 1 mm below the surface. The red curve passes through the coordinates (180 s, 17 ° C), (360 s, 31 ° C). $T_{blood} = 35\ °C$. $T_{He} = 64\ °C$. $\Theta = 25\ °$.

The curves representing the cooling of the skin were extracted for several values of T_{blood} (Fig 293). Green, black and blue lines represents the cooling of the skin at (r=0 mm, z=5 mm) for the non-refrigerated multichannel-jet. The other curves correspond to the refrigerated device.

First, the comparison of green and blue curves show that the decrease of Θ increases the speed of cooling. The diffusion of heat in the radial direction (along r axis r) is more efficient in the cooling of surface when Θ is small. On the contrary, when Θ is large, the diffusion in the vicinity of the point (r = 0, z = 5 mm) is almost a 1-D-diffusion along to z. Consequently, less efficient in the cooling of heated area.

Again, the curves derived from the simulations of refrigerated devices are below those of non-refrigerated device. A decrease in blood temperature results in an increase in the rate of cooling. It turns out that orange and red curves (called “last fit” in the previous figure), are more compatible with the experimental data. The cooling rate of the experimental points between 31 ° C and 40 ° C is correctly predicted.

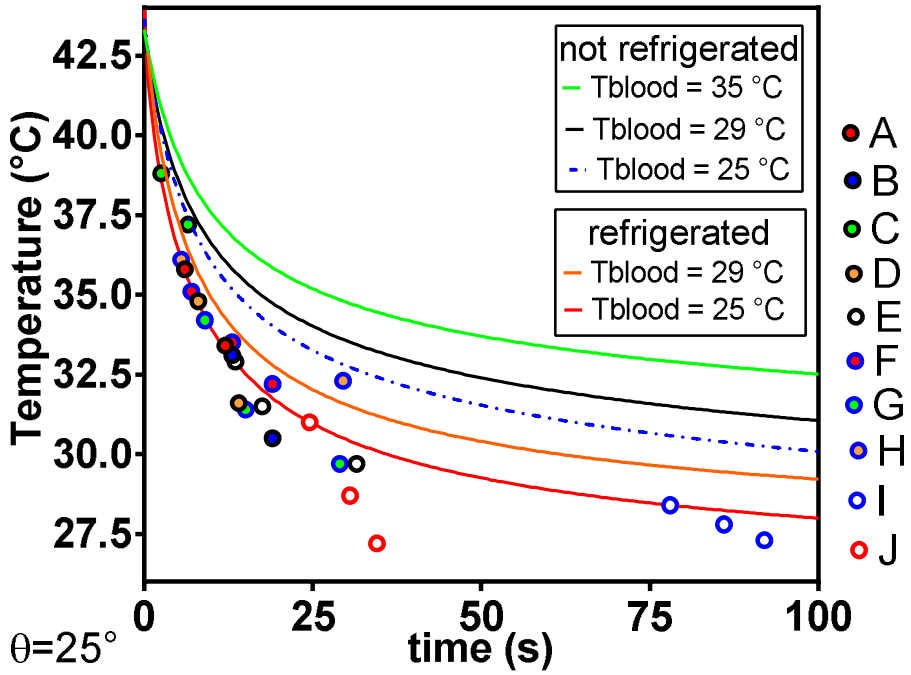

Fig 293 Cooling of the skin as a function of time. Non-refrigerated device: black green and blue. Refrigerated device: orange and red. The arterial temperature of the blood is indicated in the legends of the curves. $\Theta = 25\,°$. Experimental data are represented by the dots from A to J. Lines represent the simulations.

On the other hand, the predicted cooling rate for the set of points I and J are clearly false. It would be possible to decrease the angle Θ to obtain a rate of cooling consistent with all of the experimental results. However, it would be interesting to raise another problem of the intellectual approach adopted until then.

The cooling depends on the initial conditions. However, the experimental measurements are dispersed. The treatments were slightly different from one mouse to another, resulting in an average final temperature of 31 ° C **with** a standard deviation of 6°C (see Fig 154) before cooling. Therefore, the initial conditions are different from one mouse to another.

The totality of the simulation is represented in sub-figure A of Fig 185. The processing time of duration tc (indicated in the legend) is followed by cooling in the ambient air (natural convection). The sub-figure B shows the curves which represent the cooling with the same temporal origin. The Fig 185 (sub-figure A and B) prove that the rate of cooling at a certain temperature T, for instance, $31\,°C$, depends on the duration of treatment tc (see the slope of the curve at 31 °C). The lower the maximum temperature reached by the skin, the higher the cooling rate at 31 ° C. It also becomes possible to have simulations consistent with experimental results with less extreme assumptions about blood temperature / perfusion rate. The sub-figure C shows the cooling curves for two treatment times and three blood temperatures.

It is therefore somewhat futile to try to obtain a curve on which all the points of measurement would be distributed since they correspond to several initial conditions. On the other hand, the approximation should be correct for similar initial conditions. In this case, it means that the initial conditions are within a temperature range with a width of less than 5 ° C. It appears in sub-figure D that:

- The black curve ($tc = 390\ s, Tb = 30\ °C$) is a good fit for the sets of data I and J (at least, a better fit than that shown in Fig 293). These treatments are characterized by the lowest initial temperature.
- The blue curve ($tc = 460\ s, Tb = 30\ °C$) fit the sets A, B, D, E, F, G, and H. These sets have an initial temperature between 33 and 38 °C.
- The set C is fitted by the red curve ($tc = 600\ s, Tb = 30\ °C$). (this result does not have a profound meaning: there is only two points in the set ...)
- The assumption $T_{blood} = 30\ °C$ enables to obtain simulations that explain the rate of cooling. This is a more realistic assumptions than $T_{blood} = 25\ °C$.

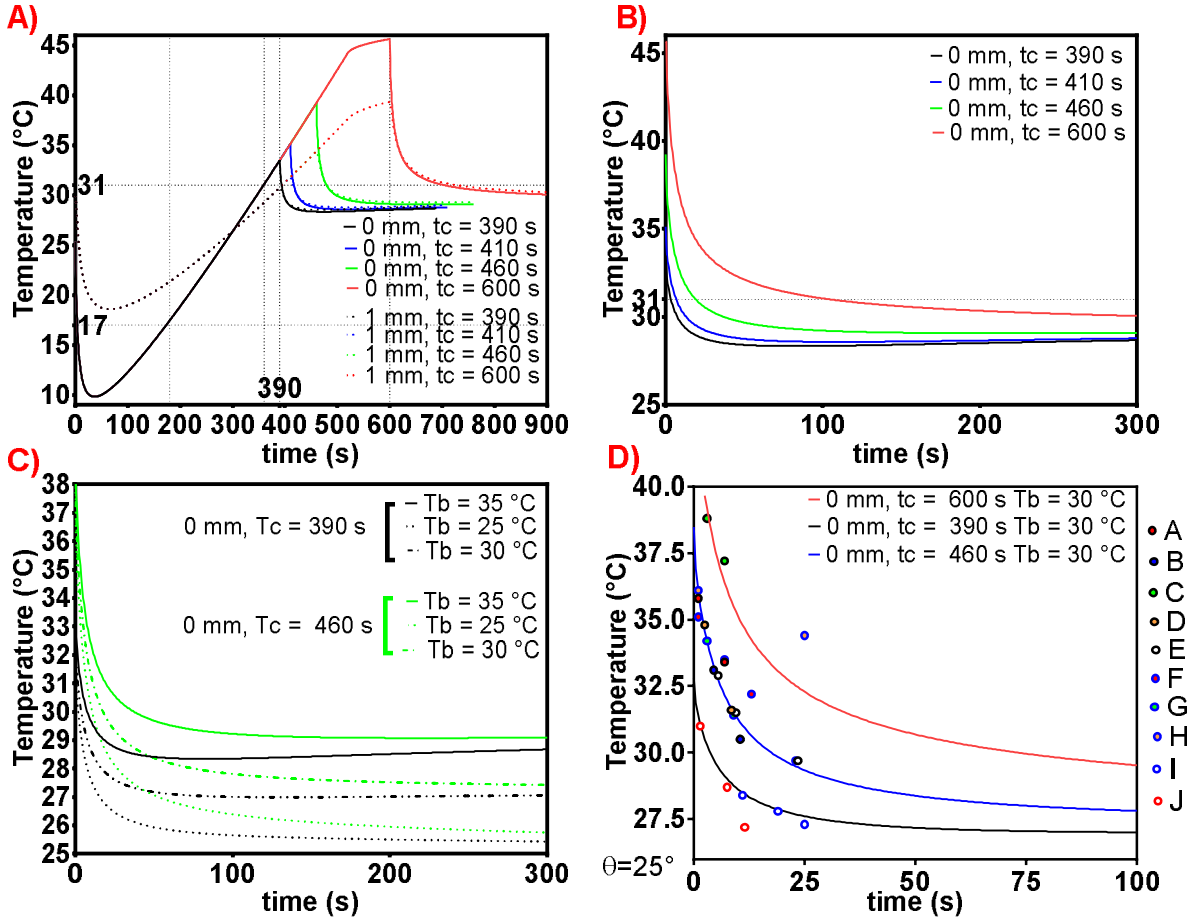

Fig 294 Temperature as a function of time, $\Theta = 25°$. A) for severals time of heating (tc = 390, 410, 460 and 600 s) and two depth (1 mm and 0 mm = surface). Only the phase of cooling is represented in the following figures. Blood temperature = $Tb = 35\ °C$ B) zoom on the cooling phase. The rate of cooling at 31 °C is different for the different durations of heating. C) skin temperature for two durations of treatment and three different temperatures of blood. D) The dots represent the experimental data. The three simulations are made with Tb = 30 ° C and three processing times (tc = 390, 460, 600 s).

In conclusion, the studies of the cooling show that:

1. The mains parameters imply in the cooling are the conduction and the thermal effect of blood perfusion. The possible errors in the terms which represent the natural convection cannot explain the values of the cooling rates.
2. The area on which the heat transfer takes place is likely smaller than what was previously imagined. It would be interesting to couple electrical measurements with thermal measurements (to find out if the numbers of filaments striking the surface and their distribution alone are sufficient to predict the heating of the

surface, or whether the quantity of charges transferred by each filament plays a role). The simulations could be easily generalized to distributions of incident flux of any form. For instance, $q_{plasma}(\alpha) = q_0 \exp\left(-\frac{\alpha^2}{2\beta^2}\right)$. Where α is an angle, and β the characteristic angular size of the heated area.

3. The cooling of the tumor may be slightly more effective than previously thought. In combination with the effect of the area, $T_{blood} = 30\ °C$ enables to reproduces the value of the cooling rate. Another interpretation, is that the rate of perfusion, ω, is higher than previously modelled. Beware; the two interpretations are not mathematically equivalents: the two factors play in a non-trivial way on the asymptotic temperature reached.
4. The cooling is a non-steady problem which strongly depends on the initial temperature. This enables to propose more realistic simulations of the cooling according to the range of initial surface temperature.
5. Very simple experiments would make possible to deepen the comparisons between simulations and experiments. In particular, the recording of the cooling of the tumor with the thermal camera in the form of a film. The film should start at a known time after the end of the treatment. It would be wise to have a length scale in the field of view, by bonding a metal strip (different emissivity) of known length to the skin surface of the mouse. The curvature of the tumor could be problematic.

This section concerns the cooling phase whose dynamics are particularly sensitive to the parameters of the model. In contrast, the reliability of the model regarding the prediction of the damage still remains with larger modifications of the model (see Appendix E). However, this section is not useless. It is not only a test of the model and its limitations; it is also the first step of a work enabling a better understanding of the heating during plasma-skin interaction.

Plasma-skin interaction has been modeled either by the assumption that only hot helium ($T_{He} = 55\ °C$ assumption), or the ionic bombardment of the surface ($q_{plasma} = Cst\ (t)$ assumption) is at the origin of skin heating. This can guide, in the choice of an experimental setup which could really prove or question these assumptions.

Appendix H Fractioned treatment: temperature and damage as a function of time

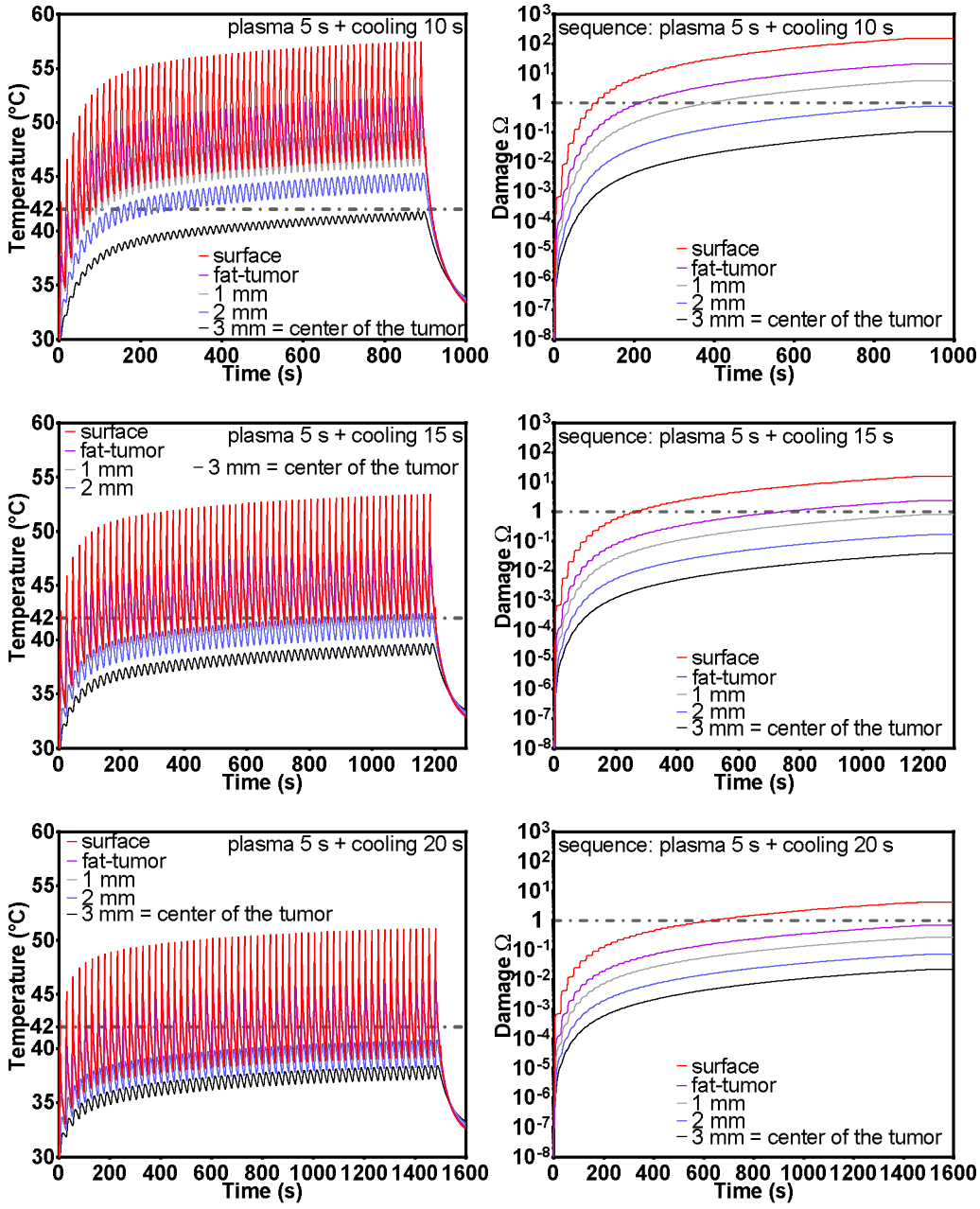

Fig 295 Temperature and damage as a function of time. Fractioned treatments. $q_{plasma} = 7000\ W.m^{-2}$, $\theta = 80\ °$.

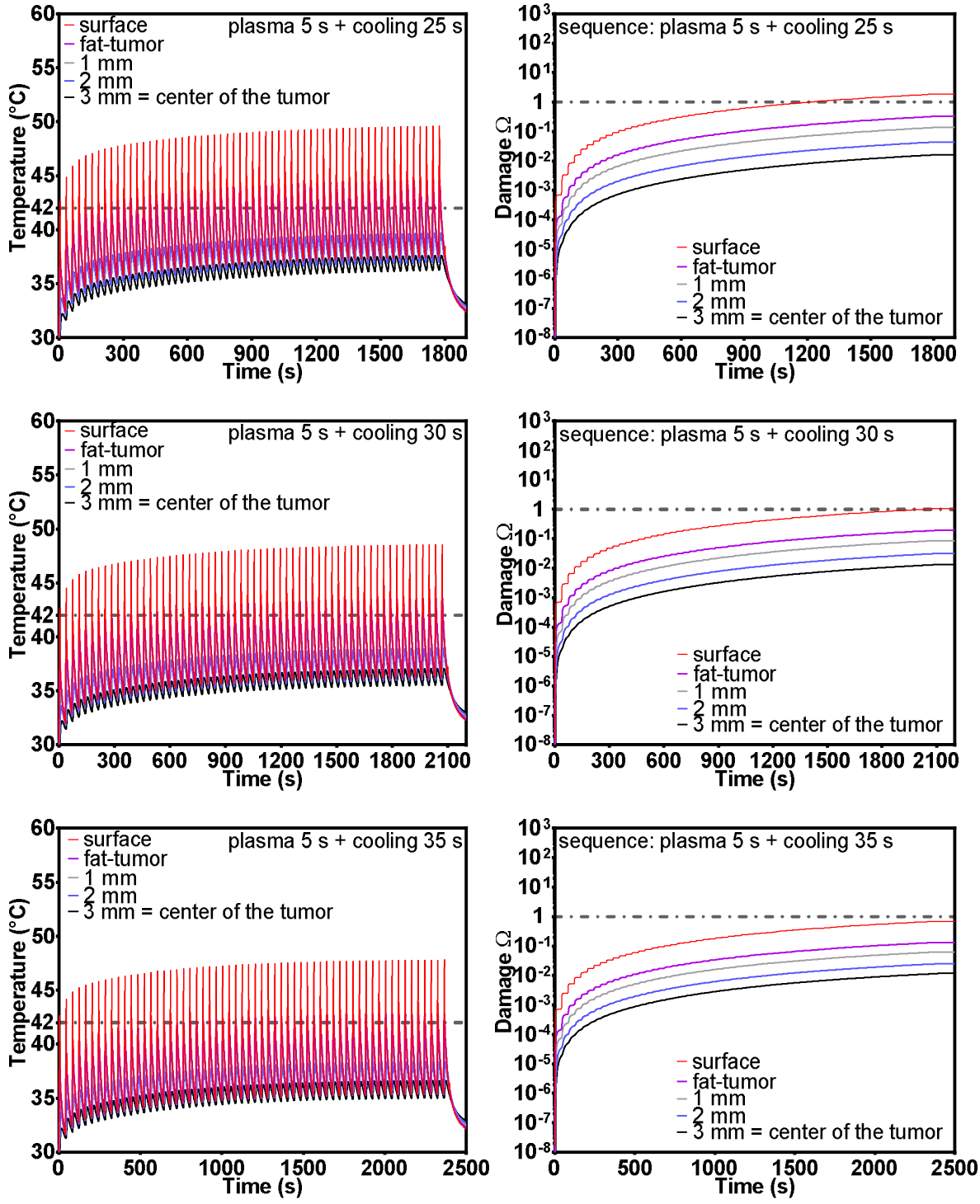

Fig 296 Temperature and damage as a function of time. Fractioned treatments. $q_{plasma} = 7000\, W.m^{-2}$, $\theta = 80$ °.

Appendix I FreeFEM++ instructions for the simulation of heat propagation

```
real actev=0,actrad=1,actcv=1;
// CHOOSE 0 or 1 to take into account or not FOR evaporation, radiation, convection
real actplasma=1;                    // constant flux or not (for test)
real actvesseldamage=1;              //1 for the effect of damage on blood vessel
real actmeta=1,actblood=1;           // activity of metabolism, activity of blood perfusion
string expname="continuous-7000-80-alive"; //NAME OF EXEPERIMENT

real qqq=7000; //INCIDENT POWER: W/m²
real degc=80; //angle to the top defining the aera hitten by Helium flow and plasma //50.7238 utilisé ici

//FOR THE SIMULATION OF A DBD WITH ALTERNATING PHASES OF HEATING AND COOLING
real DBDinter=2; // 1= YES, 2= NO

//Mouse anesthesia
real anesthesia=0; //0 =anesthesia, 1= awake

//MESH RESOLUTION
int vite=1; //FOR FAST SIMULATIONS, this factor decrease the number of vertex at each boundary. Decrease the
spatial resolution


//TIME
real T=420+100, dt=0.05;      //T= Total time of simulation, dt = temporal resolution

//FIELD of temperature at t=0 s
func v0=(anesthesia==0)*(273.15+30.001)+(anesthesia==1)*(273.15+33);
//ROOM TEMPERATURE
real Tamb=20+273.15;

real depimesh=13*1e-6,ddermmesh=162*1e-6,dadiposemesh=189*1e-6; //definition of layer thickness for C57BL6
//real depimesh=12.08*1e-6,ddermmesh=156.65*1e-6,dadiposemesh=168*1e-6; //definition for BALBC
real dexttum=500*1e-6; //TUMOR EXTERN PART = 500 µm under the tumor_subcutaneous fat interface
//THE SPATIAL RESOLUTION OF the calculation was increased in this region of interest

//BOUNDARIES DEFINITION
//!!! b != a was not implemented in the definition of physical field (lambda, density,..)
//b was implemented in the definition of boundaries, use only a=b
real a=0.3*1e-2, b=0.3*1e-2; //little and big half size of ellipsoide in m V=pi/6*a*b*b

real b2=4*a;       //couche de peau qui n'est pas sous la tumeur, voir schéma
real a2=4*a;       //tissus en dessous de la tumeur
real a3=a;         //ditance de la frontière du calcul HR,au centre de la tumeur de rayon 3 mm il faut que a3>=a-
z4


//Definition des 4 profondeurs associés à chaque couche et des quatres rayons
real z1=depimesh;
real z2=depimesh+ddermmesh;
real z3=depimesh+ddermmesh+dadiposemesh;
real z4=depimesh+ddermmesh+dadiposemesh+dexttum;

real r1=a-z1;
real r2=a-z2;
real r3=a-z3;
real r4=a-z4;

//Definition des 4 angles associés à chacune des couches du prog, degc déjà defini
real th1=asin(z1/r1);
real th2=asin(z2/r2);
real th3=asin(z3/r3);
real th4=asin(z4/r4);

//DECLARATION of BOUNDARY HANDLE
int C1=99, C2=98,C3=97,
C4=96,C5=95,C6=94,C7=93,C8=92,C9=91,C10=90,C11=89,C12=88,C13=87,C14=86,C15=85,C16=84,C17=83,C18=82,C19=81,C20=80
,C21=79,C17p=78,C18p=77,C19p=76,C20p=75;

border b1(t=0,a3+r4){x=-a3+t; y=0; label=C1;}
border bo2(t=0,dexttum){x=r4+t; y=0; label=C2;}
border b3(t=0,dadiposemesh){x=r3+t; y=0; label=C3;}
border b4(t=0,ddermmesh){x=r2+t; y=0; label=C4;}
border b5(t=0,depimesh){x=r1+t; y=0; label=C5;}


border b6(t=0,degc/180*pi){ x=a*cos(t);y=a*sin(t);label=C6;}
border b7(t=degc/180*pi,pi/2.0){x=a*cos(t); y=a*sin(t); label=C7;}
border b8(t=0,b2){x=0;y=a+t;label=C8;}
```

```
border b9(t=0,z1){x=-t;y=b2+a;label=C9;}
border b10(t=0,z2-z1){x=-z1-t;y=b2+a;label=C10;}
border b11(t=0,z3-z2){x=-z2-t;y=b2+a;label=C11;}
border b12(t=0,z4-z3){x=-z3-t;y=b2+a;label=C12;}
border b13(t=0,a3-z4){x=-z4-t;y=b2+a;label=C13;}
border b14(t=0,a2+a-a3){x=-a3-t;y=b2+a;label=C14;}
border b15(t=0,b2+a){x=-a2-a;y=b2+a-t;label=C15;}
border b16(t=0,a2+a-a3){x=-a2-a+t;y=0;label=C16;}
border b17(t=0,pi/2+th1){x=r1*cos(t);y=r1*sin(t);label=C17;}
border b17p(t=0,r1*(1-cos(th1))+z1+b2){x=-z1;y=r1*sin(pi/2+th1)+t;label=C17p;}
border b18(t=0,pi/2+th2){   x=r2*cos(t);y=r2*sin(t);label=C18;}
border b18p(t=0,r2*(1-cos(th2))+z2+b2){x=-z2;y=r2*sin(pi/2+th2)+t;label=C18p;}
border b19(t=0,pi/2+th3){x=r3*cos(t);y=r3*sin(t);label=C19;}
border b19p(t=0,r3*(1-cos(th3))+z3+b2){x=-z3;y=r3*sin(pi/2+th3)+t;label=C19p;}
border b20(t=0,pi/2+th4){x=r4*cos(t);y=r4*sin(t);label=C20;}
border b20p(t=0,r4*(1-cos(th4))+z4+b2){x=-z4;y=r4*sin(pi/2+th4)+t;label=C20p;}
border b21(t=0,b2+a){x=-a3;y=b2+a-t;label=C21;}

//MESH GENERATION
//THIS IS THE NUMBER OF VERTICES ON BOUNDARIES


mesh Th=buildmesh(b1(30)+
                          bo2(20)+
                          b3(20)+
                          b4(20)+
                          b5(20)+
                          b6(100)+
                          b7(80)+
                          b8(80)+
                          b9(20)+
                          b10(20)+
                          b11(20)+
                          b12(20)+
                          b13(20)+
                          b14(20)+
                          b15(20)+
                          b16(20)+
                          b17(120/vite)+b17p(120/vite)+
                          b18(120/vite)+b18p(120/vite)+
                          b19(120/vite)+b19p(120/vite)+
                          b20(120/vite)+b20p(120/vite)+
                          b21(40));

plot(Th,wait=1);
savemesh(Th,expname+" "+"Th.am_fmt");

fespace Vh(Th,P2); //space of function


//Position points de mesures
real actpunc=1; //1 TO PRODUCE A .txt file, which contain temperature and damage information for the point of
coordiantes (puncx(i),puncy(i))
real [int] puncx=[a,a-depimesh,a-depimesh-ddermmesh,a-depimesh-ddermmesh-dadiposemesh,a-500*1e-6,a-1e-3,a-2e-
3,a-3e-3];
real [int] puncy=[0,0,0,0,0,0,0,0];//coordx //coordy


//CONDUCTION
real rhoepi=1500;           //density 1200 kg/m3 of stratum corneum
real Cepi= 3600;            //massic specific heat 3600 J/kg/K of stratum corneum
real coepi=0.235;           //conductivity of stratum corneum layer
//the four next functions define density, specific heat and conductivity of the tumor drom following parameters

real depi=depimesh,dderm=ddermmesh,dadipose=dadiposemesh; //thickness of three different layers of mouse skin m
real rhoderm=1116,rhoadipose=971,rhotumor=1050;          //density of different layer
real Cderm=3300,Cadipose=3700,Ctumor=3669;              //specific heat of different layer
real coderm=0.445,coadipose=0.21,cotumor=0.561;         //thermal conductivity
//fat 2700 J/kg/K, lean 3669 (FABER 95), coadipose=0.185

func norme=sqrt(x^2+y^2);
func anglatmp=y/x*(x!=0);

func rhotiss=rhotumor+(rhoepi-rhotumor)*(norme(x,y)>=r1)*(norme(x,y)<=a)*(x>=-z1)
                                    +(rhoepi-rhotumor)*(norme(x,y)>a)*(x>=-z1)*(x<=0)
                                    +(rhoderm-rhotumor)*(norme(x,y)>=r2)*(norme(x,y)<r1)*(x>=-z2)
                                    +(rhoderm-rhotumor)*(norme(x,y)>r1)*(x>=-z2)*(x<=-z1)
                                    +(rhoadipose-rhotumor)*(norme(x,y)>=r3)*(norme(x,y)<r2)*(x>=-z3)
                                    +(rhoadipose-rhotumor)*(norme(x,y)>r2)*(x>=-z3)*(x<=-z2);

func Ctiss=Ctumor+(Cepi-Ctumor)*(norme>=r1)*(norme<=a)*(x>=-z1)
                                    +(Cepi-Ctumor)*(norme>a)*(x>=-z1)*(x<=0)
                                    +(Cderm-Ctumor)*(norme>=r2)*(norme<r1)*(x>=-z2)
                                    +(Cderm-Ctumor)*(norme>r1)*(x>=-z2)*(x<=-z1)
                                    +(Cadipose-Ctumor)*(norme>=r3)*(norme<r2)*(x>=-z3)
```

```
                                    +(Cadipose-Ctumor)*(norme>r2)*(x>=-z3)*(x<=-z2);

Vh lambda=cotumor+(coepi-cotumor)*(norme>=r1)*(norme<=a)*(x>=-z1)
                                    +(coepi-cotumor)*(norme>a)*(x>=-z1)*(x<=0)
                                    +(coderm-cotumor)*(norme>=r2)*(norme<r1)*(x>=-z2)
                                    +(coderm-cotumor)*(norme>r1)*(x>=-z2)*(x<=-z1)
                                    +(coadipose-cotumor)*(norme>=r3)*(norme<r2)*(x>=-z3)
                                    +(coadipose-cotumor)*(norme>r2)*(x>=-z3)*(x<=-z2);

func k=lambda/(rhotiss*Ctiss); //thermal diffusivity lambda/(rho*C) m²/s as a function of space

//CONVECTION (these coefficient are redefined in time dependent loop)
Vh hwithHe=0, hwithouthel=0;        //heat convective coefficient W/m²/K
Vh The=0;                           // temperature of Helium K
Vh alpha, alphahe;                  //heat convective coefficient divided by rho*Ctiss at the extern boundary

//RADIATION (urad2 coefficient are redefined in time dependent loop)
Vh urad2=0; //temperature of the room for radiative heat exchange K
Vh rad=5.67e-8/(rhoepi*Cepi); //Stefan-Boltzmann constant divided by rho*Ctiss at the extern boundary of the
skin (stratum corneum)

//METABOLISM power release of the cells during their life (higher in tumor).
//qmet is in W/m3
real qderm=200, qadipose=5, qtumor=7700; //W/m²
//qtumor=4200*(1-anesthesia)+anesthesia*7700;
Vh qmet=qderm*(sqrt(x^2+y^2)<a-depi)*(sqrt(x^2+y^2)>=a-depi-dderm)+qadipose*(sqrt(x^2+y^2)<a-depi-
dderm)*(sqrt(x^2+y^2)>=a-depi-dderm-dadipose) +qtumor*(sqrt(x^2+y^2)<a-depi-dderm-dadipose);
func qred=qmet/(rhotiss*Ctiss)*actmeta;

//BLOOD PERFUSION (defined here, no time dependance (assumption))
real rhoblood=1060;                         //blood density 1000 kg/m3 //bioheat transfer liu p231
real Cblood=3770;                           // massic specific heat of blood 4200 J/kg/K
real Tblood=35+273.15+anesthesia*2; //Blood temperature : 35 with anesthesia, 37 without
real bloderm=0.00133, bloadipose=0.0005,blotumor=0.0013*(1-anesthesia)+0.01*anesthesia; //ml/s/ml
//REDEFINI DANS LA BOUCLE DEPENDANT DU TEMPS POUR PRENDRE EN COMPTE L'effet des domages et de la température sur
la circulation sanguine
Vh omegaval=blotumor*(sqrt(x^2+y^2)<a-depi-dderm-dadipose)+bloadipose*(sqrt(x^2+y^2)>=a-depi-dderm-
dadipose)*(sqrt(x^2+y^2)<=a-depi-dderm)+bloderm*(sqrt(x^2+y^2)<a-depi)*(sqrt(x^2+y^2)>=a-depi-dderm); // omegab
en ml/s/ml represents blood perfusion, values are chosen from papers, in the tumor or not, during anesthesia or
not
Vh omegab=omegaval*rhoblood*Cblood/(rhotiss*Ctiss)*actblood; // unis s^-1
Vh DS=1;
Vh relativeperf=0;

//PARAMETER FOR SKIN EVAPORATION (defined here)
real RH=0; //relative humidity of air

//ENERGY DEPOSITION DUE TO PLASMA (redefined in temporal loop)
real qplasm = 0.0; //Thermal flux due to plasma surface interaction W/m²
real qpla=qplasm/(rhoepi*Cepi);

//DAMAGES FUNCTION
Vh damageadd=0, damage=0, dameageperfusion=0; //integral of Omega=Aexp(-Ea/RT)
real A, B, Aperfusion,Bperfusion;
A=2.984*1e80;// A en s^-1 //Les deux autres variables sont attribuées dans la boucle dépendant du temps.
B=5.064*1e5/8.31;//   B = Ea/R en /K

Vh vold,w,v,cc2,cc3,cr2,cr3,qev2,qev3,vaff; //variables for the resolution,v is the field of temperature, w a
function of the same regularity than v for the resolution.
int optp=1; //optp=0 No mesh optimization, optp=1, mesh optimization (solver)
v=v0; //INITIALISATION

//PROBLEM DEFINITION, WEAK FORMULATION
problem thermaxi(v,w)=int2d(Th,optimize=optp)((v*w/dt + k*(dx(v)*dx(w) + dy(v)*dy(w)))*y)-
int2d(Th,optimize=optp)(vold*w*y/dt)+
int1d(Th,C6,optimize=optp)(cr2*y*v*w)-
int1d(Th,C6,optimize=optp)(cr2*y*The*w)+
int1d(Th,C7,optimize=optp)(cr2*y*v*w)-
int1d(Th,C7,optimize=optp)(cr2*y*The*w)+
int1d(Th,C8,optimize=optp)(cr3*y*v*w)-
int1d(Th,C8,optimize=optp)(cr3*y*Tamb*w)+
int1d(Th,C6,optimize=optp)(cc2*y*v*w)-
int1d(Th,C6,optimize=optp)(cc2*y*The*w)+
int1d(Th,C7,optimize=optp)(cc2*y*v*w)-
int1d(Th,C7,optimize=optp)(cc2*y*The*w)+
int1d(Th,C8,optimize=optp)(cc3*y*v*w)-
int1d(Th,C8,optimize=optp)(cc3*y*Tamb*w)-
int2d(Th,optimize=optp)(qred*w*y)+
int2d(Th,optimize=optp)(omegab*v*w*y)-
int2d(Th,optimize=optp)(omegab*Tblood*w*y)+
int1d(Th,C6,optimize=optp)(y*qev2*v*w)-
int1d(Th,C6,optimize=optp)(y*qev2*The*w)+
int1d(Th,C7,optimize=optp)(y*qev2*v*w)-
int1d(Th,C7,optimize=optp)(y*qev2*The*w)+
int1d(Th,C8,optimize=optp)(y*qev3*v*w)-
```

```
int1d(Th,C8,optimize=optp)(y*qev3*Tamb*w)-
int1d(Th,C6,optimize=optp)(y*qpla*w);//

//dirichlet = value of the function at the boundarie +on(C4,v=37+273.15)+on(C5,v=37+273.15);
//Neumann = imposer la valeur de la dérivée fonction à la frontière commande fait avect int1d sur la frontière;
//ROBIN as previous + v dependance

//OPENING OF PUNC.TXT file for writing
string namepunc=expname+ " punc.txt";
{ofstream fff(namepunc);

//TIME LOOP
for(real t=0;t<=T;t+=dt){
    vold=v;
    //Loop FOR NON-LINEAR RESOLUTION
                for(int m=0;m<2;m++){

                        //PLASMA-SURFACE INTERACTION
                        qplasm=qqq*(t<=420);
                        if (DBDinter==1) qplasm=qqq*(t%15<=5)*(t<=900);
                        qpla=qplasm/(rhoepi*Cepi)*actplasma;

//TEMPERATURE OF HELIUM, and temperature of radiative environnment seen by the surface which interact with
plasma
                        The=Tamb;
                        urad2=The;

                        //CONVECTION
                        hwithHe=(5.21 * (abs(v-The))^0.188);
                        hwithouthel=(5.21 * (abs(v-Tamb))^0.188); //NATURAL CONVECTION

                        alphahe=hwithHe/(rhoepi*Cepi);
                        alpha=hwithouthel/(rhoepi*Cepi);
                        cc2= alphahe*actcv;
                        cc3= alpha*actcv;

                        //RADIATION
                        //division by (rhoepi*Cepi) was include in the definition of rad
      cr2= (actrad==1)*rad * (v+urad2)*(v^2+urad2^2);
                        cr3= (actrad==1)*rad * (v+Tamb)*(v^2+Tamb^2);

                //BLOOD PERFUSION
                rhoblood=1060;                      //blood density 1000 kg/m3 //bioheat transfer liu p231
                Cblood=3770;                                //  massic specific heat of blood 4200 J/kg/K
                Tblood=35+273.15+anesthesia*2; //Blood temperature : 30 with anesthesia, 37 without

                bloderm=0.00133;                                    //ml/s/ml
                bloadipose=0.0005;                                 //ml/s/ml
                blotumor=0.00133*(1-anesthesia)+0.01*anesthesia;    //ml/s/ml

                if (actvesseldamage==0)
                {
//THE EFFECT OF TEMPERATURE AND DAMAGES ON BLOOD PERFUSION ARE DIASBLED
omegaval=blotumor+(-blotumor)*(norme>=r1)*(norme<=a)*(x>=-z1)
                        +(-blotumor)*(norme>a)*(x>=-z1)*(x<=0)
                        +(bloderm-blotumor)*(norme>=r2)*(norme<r1)*(x>=-z2)
                        +(bloderm-blotumor)*(norme>r1)*(x>=-z2)*(x<=-z1)
                        +(bloadipose-blotumor)*(norme>=r3)*(norme<r2)*(x>=-z3)
                        +(bloadipose-blotumor)*(norme>r2)*(x>=-z3)*(x<=-z2);
omegab=omegaval*rhoblood*Cblood/(rhotiss*Ctiss)*actblood; // unis s^-1
}
else{
//THE EFFECT OF TEMPERATURE AND DAMAGES ON BLOOD PERFUSION ARE ACTIVATED
// (The damage function is not the same for blood vessels, value from the paper of D. J. Schutt and D.
Haemmerich: RF ablation perfusion model 2008)
Aperfusion=1.98*1e106;
Bperfusion=6.67*1e5/8.314;
damageperfusion=damageperfusion+Aperfusion*exp(-Bperfusion/v)*dt;
DS=1-exp(-damageperfusion);
relativeperf=(30*DS+1)*(DS<=0.02)+(-13*DS+1.86)*(DS>0.02)*(DS<=0.08)+(-0.79*DS+0.884)*(DS>0.08)*(DS<=0.97)+(-
3.87*DS+3.87)*(DS>0.97)*(DS<=1)+0; //VOir papier pour explication

//CALCULATION OF BLOOD PERFUSION

omegaval=blotumor+(-blotumor)*(norme>=r1)*(norme<=a)*(x>=-z1)
                        +(-blotumor)*(norme>a)*(x>=-z1)*(x<=0)
                        +(bloderm-blotumor)*(norme>=r2)*(norme<r1)*(x>=-z2)
                        +(bloderm-blotumor)*(norme>r1)*(x>=-z2)*(x<=-z1)
                        +(bloadipose-blotumor)*(norme>=r3)*(norme<r2)*(x>=-z3)
                        +(bloadipose-blotumor)*(norme>r2)*(x>=-z3)*(x<=-z2);

omegab=omegaval*rhoblood*Cblood/(rhotiss*Ctiss)*actblood*relativeperf; // unis s^-1

}
//RODENTS DO NOT SWEAT !!!!!!!!!
```

```
//EVAPORATION actev=0 or 1, to take evaporation into account or not
//HUMAN FORMULATION
                            qev2= (actev==1)*(v>Tamb)*(v>273.15)*abs(v-Tamb)/(v-Tamb)*9.66*1e-8*(abs(v-
Tamb))^(0.25-1)*(10^(0.0265*v)-RH*10^(0.0265*Tamb))/(rhoepi*Cepi);
                            qev3= (actev==1)*(v>The)*(v>273.15)*abs(v-The)/(v-The)*9.66*1e-8*(abs(v-The))^(0.25-
1)*(10^(0.0265*v)-RH*10^(0.0265*The))/(rhoepi*Cepi);
      thermaxi; //RESOLUTION WITH UMFPACK SOLVER
    }    //END OF NON LINEAR LOOP

                  vaff=v-273.15; //Conversion in °C for vizualization
                  string afff="t="+real(t)+" s T  Tc = "+vaff(0,0);

                  Vh damageaff;
                  damageadd=A*exp(-B/v)*dt;
                  damage=damage+damageadd;
                  //plot(DS,value=true,fill=true,cmm=afff);
                  plot(vaff,value=true,fill=true,cmm=afff);
                  //plot(relativeperf,value=true,fill=true,cmm=afff);
                  //plot(damageadd,value=true,fill=true,cmm=afff+" DAMAGE ADD");
                  //plot(damage,value=true,fill=true,cmm=afff+" SUM");

//SAVING OF TEMPERATURE AND DAMAGE FIELDS (on each vertex)
string name=expname+ " t="+real(t/dt)+"data.txt";
{ofstream ff(name); //Th(i) verteri, Th(k) Triangle k
for (int i=0;i<Th.nv;i++)
ff<<vaff(Th(i).x,Th(i).y)<<" "<<damage(Th(i).x,Th(i).y)<<endl;
}

//SAVING OF TEMPERATURE AND DAMAGE OF SEVERAL POINTS OF INTEREST (Defined by coordinate in vector puncx and
puncy.
if (actpunc==1){
fff<<t<<" ";
for (int co1=0; co1<8;co1++){
fff<<vaff(puncx(co1),puncy(co1))<<" "<<damage(puncx(co1),puncy(co1))<<" ";
}
fff<<endl;
}

}
}
plot(vaff,value=true,wait=1,fill=true);
```

Appendix J Matlab instructions for displaying damage and heat map

```
clear all;                              % matlab file is in the same folder than .edp file
exp='DBDinter9700dt1dam10';     % name of experiment
T=900;                          %Total time
dt=0.01;                                %Temporal resolution

%MIN ET MAX OF TEMPERATURE AND DAMAGE COLORBARS
mint=30;
maxt=65;

mindam=0;
maxdam=1;
%SIZE (in mm) OF Z AND R AXIS
xmin=4;
xmax=5;
ymin=0;
ymax=1;
%NUMBER OF TIME-STEP BETWEEn EACH PICTURE
past=2*dt;
nbframe=20; %framerate of movie

%READING MESH FILE (see FREEFEM++ doc, for the structure of mesh file)
fiche=fopen(strcat(exp,' Th.am_fmt'),'r');
formatSpec = '%f %f %f %f';
sizeA = [2 1];
a = fscanf(fiche,formatSpec,sizeA);
a=a.';
nbv=a(1,1);
nbt=a(1,2);
sizeB = [3 nbt];
nu=fscanf(fiche,formatSpec,sizeB);
nu=nu.';
sizeC= [2 nbv];
c=fscanf(fiche,formatSpec,sizeC);
c=c.';
reft=fscanf(fiche,formatSpec,nbt);
reft=reft.';

refs=fscanf(fiche,formatSpec,nbv);
refs=refs.';
fclose(fiche);

%CONVERSION IN MM OF THE COORDINATE OF EACH VERTEX
for i=1:nbv
x(i)=c(i,1)*1e3;
y(i)=c(i,2)*1e3;
end

verts = c*1000; %verts =contain the coordinate of each vertex in mm
faces = nu;             %face =contain the index (in table c) of the three vertex defining one
triangle

%LOADING OF FIRST FILE
dataf=fopen(strcat(exp,' t=',num2str(0/dt),'data.txt'),'r') ;
data=fscanf(dataf,'%f %f',[2,nbv]);
data=data.'; %transposition
fclose(dataf);
cdat=data(:,1);
cdat2=data(:,2);

%OPENING OF TEMPORARY MOVIE FILE
F= struct('cdata',[],'colormap',[]);
v = VideoWriter(strcat(exp,' ','Temperature-Damage','.avi'));
v.FrameRate = nbframe;
open(v)

%MAXIMIZATION OF FIG WINDOW
fig=figure('Name','Temperature Damage','NumberTitle','off');
set(fig,'Units','normalized')
```

```
set(fig,'Position',[0,0.0444,1.0000,0.8759])

%TIME LOOP
for t = 0:past:T
%SUBPLOT TEMPERATURE
pos = [0.05 0.15 0.5 0.77];             %position of subplot
left=subplot(1,2,1,'Position',pos);

%PATCHING AND AXIS CHARACTERISTIC OF LEFT SUBPLOT
p=patch('Faces',faces,'Vertices',verts);
set(p,'FaceColor','interp','FaceVertexCData',cdat,'EdgeColor','interp','LineWidth',0.001,'CDataMap
ping','scaled')
axis equal
ax = gca();
ax.FontSize = 25;
ax.TickDir = 'out';
ax.Box = 'on';
xlabel('Z axis (mm)')
ylabel('r axis (mm)')
xlim([xmin xmax])
ylim([ymin ymax])

set(gca,'CLim',[mint maxt])
cc = colorbar;
cc.Label.String = 'Temperature (°C)';
cc.Location='northoutside';
colormap(jet(5000));                    %Number of colors defining colorbar


%SUBPLOT DAMAGES
pos2 = [0.45 0.15 0.5 0.77];            %position of subplot
right=subplot(1,2,2,'Position',pos2);   %handle of subplot
xlabel('Z axis (mm)')
%ylabel('r axis (mm)')
xlim([xmin xmax])
ylim([ymin ymax])

p2=patch('Faces',faces,'Vertices',verts);
set(gca,'CLim',[mindam maxdam])
ccc = colorbar;
ccc.Label.String = 'Damage \Omega';
colormap(jet(5000));                    %Number of colors defining colorbar
ccc.Location='northoutside';
%PATCHING AND AXIS CHARACTERISTIC OF RIGHT SUBPLOT
set(p2,'FaceColor','interp','FaceVertexCData',cdat,'EdgeColor','interp','LineWidth',0.001,'CDataMa
pping','scaled')
axis equal

ax2 = gca();
ax2.FontSize = 25;
ax2.TickDir = 'out';
ax2.Box = 'on';


t/T*100 %DISPLAY PERCENTAGE BEFORE END

%OPENING AND READING OF DATA FILE
dataf=fopen(strcat(exp,' t=',num2str(t/dt),'data.txt'),'r') ;
data=fscanf(dataf,'%f %f',[2,nbv]);     %FIRST LINE=TEMPERATURE, SECOND LINE=DAMAGE
data=data.';
fclose(dataf);
cdat=data(:,1);
cdat2=data(:,2);

%REPATCHING OF OBJECT p (map of temperature)
set(p,'FaceColor','interp','FaceVertexCData',cdat,'EdgeColor','interp','LineWidth',0.001,'CDataMap
ping','scaled');
xlim([xmin xmax])
ylim([ymin ymax])
dim = [.30 .4 .3 .4];
stri = strcat('t=',num2str(t), ' s');
% tex1 = annotation('textbox',dim,'String',stri,'FitBoxToText','on','LineStyle','none');
% tex1.FontSize = 25;
```

```
%REPATCHING OF OBJECT p2 (map of damage)
set(p2,'FaceColor','interp','FaceVertexCData',cdat2,'EdgeColor','interp','LineWidth',0.001,'CDataM
apping','scaled');
xlim([xmin xmax])
ylim([ymin ymax])

%DISPLAY TEMPERATURE MIN and MAX and Time on fig
dim2 = [.45 .705 .3 .3];
tex2 = annotation('textbox',dim2,'String',stri,'FitBoxToText','on','LineStyle','none');
tex2.FontSize =25;
%pause(0.5)

dim3 = [.05 0 .3 .1];
tex3 = annotation('textbox',dim3,'String',strcat('Tmin=',num2str(min(cdat)),'
°C'),'FitBoxToText','on','LineStyle','none');
tex3.FontSize =20;
dim4 = [.4 0 .3 .1];
tex4 = annotation('textbox',dim4,'String',strcat('Tmax=',num2str(max(cdat)),'
°C'),'FitBoxToText','on','LineStyle','none');
tex4.FontSize =18;
    drawnow();
    writeVideo(v,getframe(fig));
%     tex1.delete
if (t<T)
    tex2.delete
    tex3.delete
    tex4.delete
end
end
close(v);       %SAVING MOVIE
                %IN ORDER TO SAVE ONLY ONE FIGURE, USE .bmp to keep axis definition at time T
```

Appendix K VBS code for the calculation of power in real time with an oscilloscope

This code works on Lecroy oscilloscopes equipped with the Xdev option which enable to customize the operations performed on waveforms. In order to minimize the numerical error, the signals must be represented on the whole screen (in order to maximize the step in voltage).

```
Function Update() 'VBS code
        coeffaffichage=1e7 'This coefficient enables the display and the calculation of the
integral of power

        capa=100*1e-9'value of the capacitance Cm = 100 nF
        Rsonde=10e6     'probe resistance = equivalent resistance of measurement system
        fs=10*1e6       'frequency of sampling
        ts=1.0/fs       'time between two samples

        startData = 0
        endData = InResult1.Samples
        scaledData1 = InResult1.DataArray(True)
        scaledData2= InResult2.DataArray(True)

        Redim Tension(endData)  'High voltage,
        Redim ucm(endData)              'Voltage cross the capacitance
        Redim Courant(endData)  'current

        For i = 0 To endData-1-1
        Tension(i)=scaledData1(i)
        ucm(i)=scaledData2(i)
        ucm(i+1)=scaledData2(i+1)
        Courant(i)=capa*(ucm(i+1)-ucm(i))/ts+ucm(i)/Rsonde 'current crossing the DBD
        Next

        'This code provides the sliding average on 2 *taillefen-1 samples
        'LastPoint = endData - 1 '
        'ReDim lisse1(endData)
        'ReDim lisse2(endData)
        'For i = 0+taillefen To LastPoint-taillefen
        '       somme1=0
        '       somme2=0
        '       For j=i-taillefen TO i+taillefen
        '       somme1 = somme1+scaledData1(j)
        '       somme2 = somme2+scaledData2(j)
        '       Next
        '       lisse1(i)=somme1/(2*taillefen+1)
        '       lisse2(i)=somme2/(2*taillefen+1)*capa
        'Next
        'OutResult.DataArray(True) = lisse1 'ou 2 affichage du signal lissé

        OutResult.Samples=endData  ' Trace length + 1

ReDim somme(endData)    'contains the primitiv function of power as a function of t

somme(0)=0
for i=1 TO endData-1 'integral calculation
somme(i)=somme(i-1)+coeffaffichage*((Tension(i-1)*Courant(i-1)-ucm(i-1)*ucm(i-1)/Rsonde)*Ts)
Next
OutResult.DataArray(True) = somme

End Function
```

Appendix L NBD-CL, a probe for superoxide radical?

During this thesis, we have also tried to measure the production of superoxide radical of the single-channel plasma jet in the liquid phase. A fluorescent probe has been particularly tested: 4-Chloro-7-nitrobenzo-2-oxa-1,3 diazole (abbreviated NBD-Cl) purchased from Sigma-aldrich (reference : 25455-25G). The chemical structure of NBD-CL is visible in Fig 297.

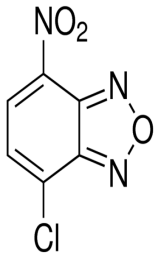

Fig 297 NBD-Cl = 4-chloro-7-nitrobenzo-2-oxa-1,3-diazole, CAS Number 10199-89-0

The reaction product of this probe with O_2^- absorbs at $\lambda = 470\,nm$ (maximum of absorbance). The solution is clear yellow. The maximum fluorescence is around 560 nm (see Fig 298 & Fig 299). These values are consistent with those reported in the literature [349], [350].

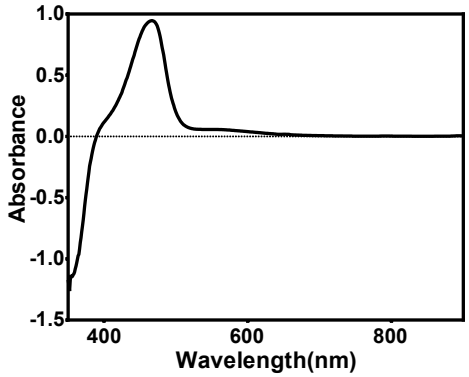

Fig 298 absorbance of a solution of NBD-CL put in contact with KO2(s). Blank = before the addition of few mg of KO2(s).

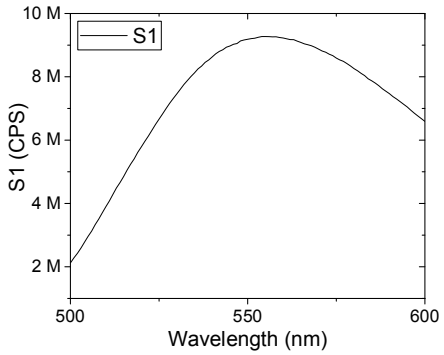

Fig 299 Fluorescence signal of a solution of NBD-CL exposed to KO2 (s), emission spectrum (λex=460 nm, λem= adjustable, Δλex=10, Δλem=5nm). Blank = before the addition of few mg of KO2(s).

This probe is mentioned in the review of Bartosz, which describe the functioning of several RONS-probes [350]. According to the work of Olojo et al. (and own experiments), the fluorescence of the product is enhanced by the addition of an organic solvent prior to measurement [349]. We use acetonitrile in a proportion of 2/3.

NBD-CL has also been used for years to detect amino, imino acids and amines [351]. Baines et al. precise that NBD-CL is an electrophilic reagent [352].

The crucial point with this probe is that Ikhlaq et al. report that H_2O_2 and HO° doesn't interfere with NBD-Cl [353]. This characteristic makes it very attractive for the study of the plasma-liquid interaction (see Fig 300). Ikhlaq et al. prepare a mixture of H_2O_2 and NBD-CL at a concentration of 294 µM and 50 µM respectively to prove that. No change in fluorescence was observed after 1 hour of reaction. The absence of interference due to HO° was investigated using tertiary butyl Alcohol as HO° scavenger. The absence of interferences caused by H_2O_2 was also evoked by Olojo et al.:

"Additional experiments (data not shown) confirmed that the presence of biological species, such as H_2O_2, NADH, NADPH, and NAD^+, does not interfere with NBD-Cl reactions and especially its ability to quantify superoxide ion in solution." [349].

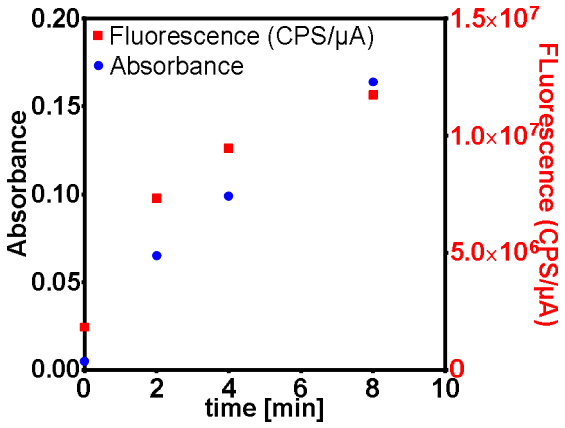

Fig 300 Absorbance and fluorescence of a solution made with 500 µL of PBS1X + 5 µL of NBD-Cl at 450 µM. After treatment: addition of 1000 µL of PBS1X and then absorbance measurement ($\lambda = 470\ nm$). Subsequently, 100 µL of acetonitrile are added, enough to enhanced the fluorescence ($\lambda_{ex} = 470\ nm,\ \lambda_{em} = 560\ nm, \Delta\lambda(ex\ \&\ em) = 10\ nm$). single-channel jet: helium flow=1000 sscm, peak to peak voltage = 28.7 kV, height ~ 5.5 mm. Power ~ 490 mW. Mean value of duplicate experiment.

However, my own tests showed the existence of a reaction between H_2O_2 and NBD-Cl leading to the production of a fluorescent product. This test was done in the range of concentration encountered during plasma-liquid interaction ($[H_2O_2] = 2\,mM$, [NBD-Cl]=450 µM). It is perhaps this difference in terms of concentration that explains this discrepancy between our observation and those of Olojo et al. and Ikhlaq et al.

The use of catalase enzyme do not enable to prevent this interference by the scavenging of H_2O_2.: more precisely we did not find the range of catalase concentration which scavenges efficiently H_2O_2 without causing a strong modification of the absorbance or fluorescence spectra.

Appendix M Design of refrigerated multi-channel jet

The following lines describe the design of the multi-channel plasma jet in the software OpenScad.

```
$fn=80;
ddie=1.4;
difference(){
    union(){
 //corps
        translate([-13,-10,0]) cube(size=[22,100,4.4+3+2]);
        translate([-23,7,0]) cube(size=[11,43,4.4+3+2+1]);
        translate([-29,16,0]) cube(size=[14,28,4.4+3+2+1]);
//fixation support
   hull(){
    #translate([-13+10,59.5-10,0]) cylinder(d=25,h=4);
    #translate([-47,59.5+40,0]) cylinder(d=6.5+9,h=4);
    #translate([-47+25,59.5+40,0]) cylinder(d=6.5+9,h=4);
    #translate([-47+2*25,59.5+40,0]) cylinder(d=6.5+9,h=4);
   }
//acces HT
        translate([-70,65,0]) cube(size=[60+0.1,16.5,10.5+6]);
// acces gaz
         translate([-54.5,22.5,0]) cube(size=[28,14,13]);
  //embout
   //accès refoidissement azote
   translate([-13+22,8,0]) cube(size=[22,44,5+2.8]);
   translate([25,8,0]) cube(size=[6,44,6.5+4]);
   difference(){
       translate([-13+22,8,0]) cube(size=[22,44,5+2.8+45]);
       translate([-13+3+22,8+3,5+2.8]) cube(size=[22-6,44-6,45.1]);
   }
   difference(){
       hull(){
       translate([-13+22,8,5+2.8+45]) cube(size=[22,44,0.1]);
        translate([-13+3+22-15-3,8+3-15-3,5+2.8+45+20]) cube(size=[22+15,44-6+30+6,0.05]);
       }
  #hull(){
  translate([-13+3+22,8+3,5+2.8+45]) cube(size=[22-6,44-6,0.1]);
  translate([-13+3+22-15,8+3-15,5+2.8+45+20]) cube(size=[22-6+15,44-6+30,0.1]);
     }
   }
   //embout
   difference(){
   hull(){
   translate([30,12,0]) cube([2,34,10]);
   translate([30+20,12+9.75-2,0]) cube([2,15+4,10]);
   }
       //embout
    #translate([70-7,29,-1]) cylinder(d=30,h=20);
   }
    }
    //acces gaz
  #translate([-60+5,59.5/2,7.2/2+3]) rotate([0,90,0]) cylinder(d=7.2,h=25);
    //liaison acces gaz, production de plasma
  #translate([-8+1-10,3+8+(1.5+1.5)*(3-1)+1,3.5]) rotate([0,0,180-40])
cube(size=[19,1.5*1.5,1.5*4/1.5]);
  #translate([-8+1-10,4+8+(1.5+1.5)*(7-1)+1,3.5]) rotate([0,0,180]) cube(size=[17,1.5*1.5,4]);
  #translate([-8+1-10-2,5+8+(1.5+1.5)*(10.5-1)+1,3.5]) rotate([0,0,180+40])
cube(size=[17,1.5*1.5,4]);
  #translate([-8+3-13-1,3+8+(1.5+1.5)*(1-1)+1,3.5])  cube(size=[2,34.5,4]);

//    #translate([62,59.5/2+12,4.5]) rotate([90,0,0]) cylinder(d=6,h=24);
    //acces embout
    //liaison extreme-gauche
    #translate([9+20,12,3.5]) cube(size=[1.5,1.5*5,3]);
        //liaison gauche
    #translate([9+20,21,3.5]) cube(size=[1.5,1.5*3,3]);
        //liaison centre
```

```
    #translate([9+20,27,3.5]) cube(size=[1.5,1.5*3,3]);
        //liaison droit
    #translate([9+20,33,3.5]) cube(size=[1.5,1.5*3,3]);
    //extr droite
    #translate([9+20,39,3.5]) cube(size=[1.5,1.5*5,3]);
    //centre
    #translate([9+20,2+4+7+5+5.5*2,3.5]) rotate([0,6,0]) cube(size=[30,1.5,1.5]);
    #translate([9+20,2+4+7+5+5.5*2,3.5]) rotate([0,-6,0]) cube(size=[30,1.5,1.5]);
    //extreme gauche
    #translate([0,-5.5*2,0]){
    translate([9+20,15+5.5*2,3.5]) rotate([0,6,18]) cube(size=[30,1.5,1.5]);
    translate([9+20,15+5.5*2,3.5]) rotate([0,-6,18]) cube(size=[30,1.5,1.5]);
    }
        //extreme droite
    #translate([0,5.5*2,0]){
    translate([9+20,20+5.5*2,3.5]) rotate([0,6,-18]) cube(size=[30,1.5,1.5]);
    translate([9+20,20+5.5*2,3.5]) rotate([0,-6,-18]) cube(size=[30,1.5,1.5]);
    }
            //droite
    #translate([0,5.5*1,0]){
    translate([9+20,2+4+7+5+5.5*2,3.5]) rotate([0,6,-9]) cube(size=[30,1.5,1.5]);
    translate([9+20,2+4+7+5+5.5*2,3.5]) rotate([0,-6,-9]) cube(size=[30,1.5,1.5]);
    }
         //gauche
    #translate([0,-5.5*1,0]){
    translate([9+20,17+5.5*2,3.5]) rotate([0,6,9]) cube(size=[30,1.5,1.5]);
    translate([9+20,17+5.5*2,3.5]) rotate([0,-6,9]) cube(size=[30,1.5,1.5]);
    }
    //fixation support
    #translate([-47,59.5+40-1]) cylinder(d=6.5,h=6);
    #translate([-47+25,59.5+40,-1]) cylinder(d=6.5,h=6);
    #translate([-47+2*25,59.5+40,-1]) cylinder(d=6.5,h=6);
    //pente douce
    hull(){
        translate([-10+2.5,4,3.5+1.5-0.1]) cube(size=[10,1.5*5+4*4+2*10+8,0.001]);
        translate([-10-2,4,3.5+1.5-0.1+ddie+3.1]) cube(size=[10+3+6,1.5*5+4*4+2*10+8,0.001]);
    }
    //hypothèse conducteur de largeur 4mm, 3 mm de part et d'autre +2.5 de part et d'autre pour la
pente douce
    //rainures gaz
    for(k=[1:1:12]){ //ces rainures ont une longeur de 36mm !!! +2 mm pour la HT+2 mm pour la
masse : écart de 32 mm ? est ce trop peu ?
        #translate([-8-10,4+8+(1.5+1.5)*(k-1),3.5]) cube(size=[38+10,1.5,1.5]);
    }
    //acces HT
    #translate([-16,65+16.5/2,16.5/2]) rotate([0,-90,0]) cylinder(d=10.5,h=56);
    translate([-22,65+16.5/2+-5,16.5/2+2]) cube(size=[20,10,10]);
    #translate([-22+13,16.5/2-15,5+1.4]) cube(size=[13,90,10]);
    #translate([-22,65+16.5/2-5,5]) cube(size=[10,10,10]);
}
```